

SPATIAL-SPECTRAL APPROACHES TO EDGE DETECTION IN
HYPERSPECTRAL REMOTE SENSING

by

Cary M. Cox
A Dissertation
Submitted to the
Graduate Faculty
of
George Mason University
in Partial Fulfillment of
The Requirements for the Degree
of
Doctor of Philosophy
Earth Systems and Geoinformation Sciences

Committee:

_____	Dr. Anthony Stefanidis, Dissertation Director
_____	Dr. Arie Croitoru, Committee Member
_____	Dr. Ronald Resmini, Committee Member
_____	Dr. Viviana Maggioni, Committee Member
_____	Dr. Anthony Stefanidis, Department Chairperson
_____	Dr. Donna M. Fox, Associate Dean, Office of Student Affairs & Special Programs, College of Science
_____	Dr. Peggy Agouris, Dean, College of Science
Date: _____	Spring Semester 2017 George Mason University Fairfax, VA

Spatial-Spectral Approaches to Edge Detection in Hyperspectral Remote Sensing

A Dissertation submitted in partial fulfillment of the requirements for the degree of
Doctor of Philosophy at George Mason University

by

Cary M. Cox
Master of Science
American Military University, 2004
Master of Science
University of North Texas, 2003
Bachelor of Arts
University of Texas at Austin, 2001

Director: Anthony Stefanidis, Professor
Department of Earth Systems and Geoinformation Sciences

Spring Semester 2017
George Mason University
Fairfax, VA

Copyright 2017 Cary M. Cox
All Rights Reserved

DEDICATION

For constant Dad. For faithful Mom. And for beloved Shan, Jackson, Wyatt John Cox, Anson and Caroline.

ACKNOWLEDGEMENTS

I would like to thank the many friends and colleagues who have made this dissertation possible. It is through the esteemed instruction and mentorship of Dr. Ron Resmini that I was inspired and equipped to walk this path. His countless hours of instruction, motivation and patient guidance across a decade of triumphs, setbacks and setbacks overcome made this study a reality. A deepest thank you, Ron. Dr. Anthony Stefanidis taught me scientific focus and is the gentleman to thank for my dissertation coming in under 1000 pages – thank you, Tony, and blessings to Peggy and Chloe. Thank you to Dr. Arie Croitoru for teaching me the value of empiricism, to Dr. Viviana Maggioni for inspiring me to build a literature review worthy of my research aspirations, to Dr. Richard Gomez for my earliest instruction on what it means to advance science, to Dr. Jeff Nettles for his instruction on IDL programming, and to Mr. Chris Simi for instructing me in the artful balance between basic research and applied research. I also am indebted to Mr. Jeff Glickman and Mr. Richard Gillespie of the International Group for Historic Aircraft Recovery for providing me with hyperspectral test data collected during their tireless pursuit of Amelia Earhart’s final story. Warmest regards to Mr. Frank Strickland for providing me with the professional time and space I needed to simultaneously bring this work to a close and uphold the responsibilities of a husband and father. For pointing my compass towards a lifelong study of geography, Dr. Robert K. Holz and Dr. Christopher Shane Davies of the University of Texas at Austin have earned my sincerest appreciation. Finally, I extend my deepest gratitude to the Admiral of the Ocean Sea for teaching me to keep sailing, through mutiny, storm and human doubt.

TABLE OF CONTENTS

	Page
List of Tables	x
List of Figures	xv
List of Equations	xxviii
Abstract	xxx
Purpose.....	1
Advance the Science of Spatial-Spectral Edge Detection Methods.....	1
Advance GeoInformation Science into Underserved Research Areas.....	2
Demonstrate Utility against Challenging, Non-Traditional HSI Datasets	8
Background.....	12
Hyperspectral Remote Sensing	16
Hyperspectral Remote Sensing Applications	23
Hyperspectral Remote Sensing Platforms and Data Types	39
The Hyperspectral Processing Chain.....	51
Traditional Panchromatic Edge Detection Methods	62
The Roberts Operator	64
The Sobel Operator.....	67
The Canny Operator	71
A Note on the Substantive Differences between Edge Detection and Segmentation ...	77
Multispectral Edge Detection Methods.....	80
MSI Band-by-Band Edge Detection Methods.....	80
The Tensor Gradient for MSI Edge Detection	88
SAM and ED Applications to MSI Edge Detection	97
Level Set Edge Detection for MSI Edge Detection.....	97
Hyperspectral Edge Detection Methods.....	103
The Tensor Gradient for HSI Edge Detection	110
The Hyperspectral/Spatial Detection of Edges (HySPADE)	119

Level Set Edge Detection for HSI Edge Detection	126
Hypotheses	131
Experiment #1: Gradient-Based Edge Detection Method	132
Experiment #2: HySPADE Edge Detection Method.....	133
Experiment #3: Level Set-Based Edge Detection Method.....	134
Key Science Questions.....	135
What is an Edge in Hyperspectral Space?.....	136
Which Matters More, Spatial or Spectral Resolution?	137
Data.....	139
Overhead – Reno, Nevada USA.....	141
Overhead – Cuprite, Nevada USA	144
Overhead – Indian Pines, Indiana USA	147
Overhead – Deepwater Horizon Oil Spill, Gulf of Mexico	151
Ground-Based – Larkhaven	154
Ground-Based – Granite VNIR.....	157
Ground-Based – Granite NIR/SWIR.....	160
Ground-Based – South African Core Samples.....	163
Ground-Based – Aluminum Panel	166
Microscene – Rare Target on Sand	171
Microscene – Chemical Array on Sand.....	174
Microscene – Cloth Threads on Sand	178
Methodology.....	181
Preprocessing	189
Edge Detection: Di Zeno-Based Gradient Approach for HSI.....	196
Edge Detection: A New HySPADE Approach Combining ED and SAM	207
Edge Detection: A Level Set Edge Detection Approach for HSI	221
Algorithm Evaluation.....	228
Likert Scale Scoring	230
Ground Truthing	232
Information Content at Interest Points.....	237
Global Measures of Coherence.....	246
Image Subtraction.....	252

Intuitive Interpretation.....	252
Final Evaluation Matrices.....	253
Experiments	259
Di Zenzo-Based Gradient Findings.....	259
Overhead – Reno, Nevada USA	263
Overhead – Cuprite, Nevada USA	271
Overhead – Indian Pines, Indiana USA.....	288
Overhead – Deepwater Horizon Oil Spill, Gulf of Mexico.....	297
Ground-Based – Larkhaven.....	306
Ground-Based – Granite VNIR	314
Ground-Based – Granite NIR/SWIR.....	321
Ground-Based – South African Core Samples	329
Ground-Based – Aluminum Panel.....	335
Microscene – Rare Target on Sand.....	342
Microscene – Chemical Array.....	348
Microscene – Cloth Threads.....	355
HySPADE Findings	361
Overhead – Reno, Nevada USA	364
Overhead – Cuprite, Nevada USA	365
Overhead – Indian Pines, Indiana USA.....	370
Overhead – Deepwater Horizon Oil Spill, Gulf of Mexico.....	372
Ground-Based – Larkhaven.....	375
Ground-Based – Granite VNIR	376
Ground-Based – Granite NIR/SWIR.....	378
Ground-Based – South African Core Samples	380
Ground-Based – Aluminum Panel.....	382
Microscene – Rare Target on Sand.....	384
Microscene – Chemical Array.....	386
Microscene – Cloth Threads.....	388
Level Set Edge Detection Findings.....	390
Overhead – Reno, Nevada USA	391
Overhead – Cuprite, Nevada USA	392

Overhead – Indian Pines, Indiana USA.....	397
Overhead – Deepwater Horizon Oil Spill, Gulf of Mexico.....	399
Ground-Based – Larkhaven.....	402
Ground-Based – Granite VNIR	403
Ground-Based – Granite NIR/SWIR.....	405
Ground-Based – South African Core Samples	407
Ground-Based – Aluminum Panel.....	409
Microscene – Rare Target on Sand.....	411
Microscene – Chemical Array.....	413
Microscene – Cloth Threads.....	415
Analysis and Evaluation	418
Di Zenzo-Based Gradient Analysis and Evaluation.....	418
Overhead – Reno, Nevada USA	419
Overhead – Cuprite, Nevada USA	424
Overhead – Indian Pines, Indiana USA.....	440
Overhead – Deepwater Horizon Oil Spill.....	446
Ground-Based – Larkhaven.....	451
Ground-Based – Granite VNIR	455
Ground-Based – Granite NIR/SWIR.....	460
Ground-Based – South African Core Samples	466
Ground-Based – Aluminum Panel.....	469
Microscene – Rare Target on Sand.....	476
Microscene – Chemical Array.....	482
Microscene – Cloth Threads.....	487
HySPADE Analysis and Evaluation	491
Overhead – Reno, Nevada USA	492
Overhead – Cuprite, Nevada USA	494
Overhead – Indian Pines, Indiana USA.....	503
Overhead – Deepwater Horizon Oil Spill.....	505
Ground-Based – Larkhaven.....	507
Ground-Based – Granite VNIR	509
Ground-Based – Granite NIR/SWIR.....	512

Ground-Based – South African Core Samples	514
Ground-Based – Aluminum Panel.....	516
Microscene – Rare Target on Sand.....	518
Microscene – Chemical Array.....	520
Microscene – Cloth Threads.....	523
Level Set Edge Detection Analysis and Evaluation.....	525
Overhead – Reno, Nevada USA.....	526
Overhead – Cuprite, Nevada USA.....	529
Overhead – Indian Pines, Indiana USA.....	537
Overhead – Deepwater Horizon Oil Spill.....	539
Ground-Based – Larkhaven.....	542
Ground-Based – Granite VNIR.....	544
Ground-Based – Granite NIR/SWIR.....	546
Ground-Based – South African Core Samples.....	548
Ground-Based – Aluminum Panel.....	550
Microscene – Rare Target on Sand.....	552
Microscene – Chemical Array.....	554
Microscene – Cloth Threads.....	556
Conclusions and Further Research.....	558
Algorithm Conclusions.....	558
Further Research.....	591
Appendix A: Full Experimental Results.....	594
Gradient-Based Edge Detection Results.....	594
HySPADE Edge Detection Results.....	632
Level Set-Based Edge Detection Results.....	670
Appendix B: Likert Scoring.....	708
Bibliography.....	714

LIST OF TABLES

Table	Page
Table 1: Comparison of Traditional Edge Detection Methods.....	76
Table 2: Hyperspectral Dataset Overview	139
Table 3: Overhead HSI Dataset #1 - VNIR/SWIR Reno, Nevada USA [96].....	142
Table 4: Overhead VNIR/SWIR Hypercube - Cuprite, NV USA [96].....	145
Table 5: Overhead VNIR/SWIR Hypercube - Indian Pines Agriculture [259].....	148
Table 6: Overhead VNIR/SWIR Hypercube - Deepwater Horizon Oil Spill [96]	152
Table 7: Ground-Based VNIR Hypercube - Larkhaven	155
Table 8: Ground-Based VNIR Hypercube - Granite Slab	158
Table 9: Ground-Based NIR/SWIR Hypercube - Granite Slab.....	161
Table 10: Ground-Based NIR/SWIR Hypercube - South African Core Samples	164
Table 11: Ground-Based NIR Hypercube - Aluminum Aircraft Panel	169
Table 12: Ground-Based VNIR Hypercube - Rare Targets on Sand Microscene	172
Table 13: Ground-Based NIR/SWIR Hypercube - Chemical Array Microscene.....	175
Table 14: Key to Chemicals in Chemical Array Microscene	177
Table 15: Ground-Based VNIR Hypercube - Threads on Sand Microscene.....	179
Table 16: Notional Ordinal Rank Metric – Single Algorithm, Single Dataset.....	230
Table 17: Notional Ordinal Rank Metric – All Algorithms, Single Dataset	255
Table 18: Notional Final Ordinal Rank Metric – Criteria Aggregation, Single Dataset	256
Table 19: Notional Final Ordinal Rank Metric – Data Input Aggregation, Single Dataset	257
Table 20: Notional Final Ordinal Rank Metric –All Algorithms, All Datasets.....	257
Table 21: Notional Final Ordinal Rank Metric –All Data Inputs, All Datasets	258
Table 22: Notional Ordinal Rank Metric – All Algorithms, All HSI Applications.....	258
Table 23: Gradient Evaluation Measurements for Reno, NV Overhead VNIR/SWIR Data	420
Table 24: Interest Points for Reno VNIR/SWIR Data.....	421
Table 25: Benchmark Vertical Edge Points for Reno VNIR/SWIR Data	422
Table 26: Benchmark Horizontal Edge Points for Reno VNIR/SWIR Data	423
Table 27: Benchmark Single-Point Intersections for Reno VNIR/SWIR Data.....	423
Table 28: Gradient Evaluation Measurements for Cuprite FL #1 Overhead VNIR/SWIR	425
Data.....	425
Table 29: Interest Points for Cuprite VNIR/SWIR Flight Line #1 Data	426
Table 30: Benchmark Vertical Edge Points for Cuprite VNIR/SWIR Flight Line #1 Data	426

Table 31: Benchmark Horizontal Edge Points for Cuprite VNIR/SWIR Flight Line #1 Data.....	427
Table 32: Benchmark Single Point Intersections for Cuprite VNIR/SWIR Flight Line #1 Data.....	427
Table 33: Gradient Evaluation Measurements for Cuprite FL#2 Overhead VNIR/SWIR Data.....	429
Table 34: Interest Points for Cuprite VNIR/SWIR Flight Line #2 Data	430
Table 35: Benchmark Vertical Edge Points for Cuprite VNIR/SWIR Flight Line #2 Data	430
Table 36: Benchmark Horizontal Edge Points for Cuprite VNIR/SWIR Flight Line #2 Data.....	431
Table 37: Benchmark Single-Point Intersections for Cuprite VNIR/SWIR Flight Line #2 Data.....	431
Table 38: Gradient Evaluation Measurements for Cuprite FL #3 Overhead VNIR/SWIR Data.....	433
Table 39: Interest Points for Cuprite VNIR/SWIR Flight Line #3 Data	434
Table 40: Benchmark Vertical Edge Points for Cuprite VNIR/SWIR Flight Line #3 Data	434
Table 41: Benchmark Horizontal Edge Points for Cuprite VNIR/SWIR Flight Line #3 Data.....	435
Table 42: Benchmark Single-Point Intersections for Cuprite VNIR/SWIR Flight Line #3 Data.....	435
Table 43: Gradient Evaluation Measurements for Cuprite FL #4 Overhead VNIR/SWIR Data.....	437
Table 44: Interest Points for Cuprite VNIR/SWIR Flight Line #4 Data	438
Table 45: Benchmark Vertical Edge Points for Cuprite VNIR/SWIR Flight Line #4 Data	438
Table 46: Benchmark Horizontal Edge Points for Cuprite VNIR/SWIR Flight Line #4 Data.....	439
Table 47: Benchmark Single-Point Intersections for Cuprite VNIR/SWIR Flight Line #4 Data.....	439
Table 48: Gradient Evaluation Measurements for Indian Pines, IN Overhead VNIR/SWIR Data	441
Table 49: Interest Points for Indian Pines VNIR/SWIR Data	443
Table 50: Benchmark Vertical Edge Points for Indian Pines VNIR/SWIR Data.....	444
Table 51: Benchmark Horizontal Edge Points for Indian Pines VNIR/SWIR Data.....	445
Table 52: Benchmark Single-Point Intersections for Indian Pines VNIR/SWIR Data ..	445
Table 53: Gradient Evaluation Measurements for Deepwater Horizon Overhead VNIR/SWIR Data	447
Table 54: Interest Points for Deepwater Horizon VNIR/SWIR Data.....	449
Table 55: Benchmark Vertical Edge Points for Deepwater Horizon VNIR/SWIR Data	450
Table 56: Benchmark Horizontal Edge Points for Deepwater Horizon VNIR/SWIR Data	450

Table 57: Benchmark Single-Point Intersections for Deepwater Horizon VNIR/SWIR Data	451
Table 58: Gradient Evaluation Measurements for Larkhaven Ground-Based VNIR Data	452
Table 59: Interest Points for Larkhaven VNIR Data	454
Table 60: Benchmark Vertical Edge Points for Larkhaven VNIR Data.....	454
Table 61: Benchmark Horizontal Edge Points for Larkhaven VNIR Data	455
Table 62: Benchmark Single-Point Intersections for Larkhaven VNIR Data	455
Table 63: Gradient Evaluation Measurements for Granite Ground-Based VNIR Data .	456
Table 64: Interest Points for Granite VNIR Data	458
Table 65: Benchmark Vertical Edge Points for Granite VNIR Data.....	459
Table 66: Benchmark Horizontal Edge Points for Granite VNIR Data.....	459
Table 67: Benchmark Single-Point Intersections for Granite VNIR Data	460
Table 68: Gradient Evaluation Measurements for Granite Ground-Based NIR/SWIR Data	461
Table 69: Interest Points for Granite NIR/SWIR Data	463
Table 70: Benchmark Vertical Edge Points for Granite NIR/SWIR Data.....	464
Table 71: Benchmark Horizontal Edge Points for Granite NIR/SWIR Data	465
Table 72: Benchmark Single-Point Intersections for Granite NIR/SWIR Data	465
Table 73: Gradient Evaluation Measurements for Core Sample Ground-Based NIR/SWIR Data.....	467
Table 74: Interest Points for South African Core Sample NIR/SWIR Data.....	468
Table 75: Benchmark Vertical Edge Points for South African Core Sample NIR/SWIR Data.....	469
Table 76: Benchmark Horizontal Edge Points for South African Core Sample NIR/SWIR Data.....	469
Table 77: Benchmark Single-Point Intersections for South African Core Sample NIR/SWIR Data	469
Table 78: Gradient Evaluation Measurements for Aluminum Panel Ground-Based VNIR Data.....	471
Table 79: Interest Points for Aluminum Panel VNIR Data	474
Table 80: Benchmark Vertical Edge Points for Aluminum Panel VNIR Data.....	474
Table 81: Benchmark Horizontal Edge Points for Aluminum Panel VNIR Data	475
Table 82: Benchmark Single-Point Intersections for Aluminum Panel VNIR Data	475
Table 83: Gradient Evaluation Measurements for Rare Target on Sand Microscene VNIR Data.....	477
Table 84: Interest Points for Rare Target on Sand VNIR Data	479
Table 85: Benchmark Vertical Edge Points for Rare Target on Sand VNIR Data.....	480
Table 86: Benchmark Horizontal Edge Points for Rare Target on Sand VNIR Data.....	481
Table 87: Benchmark Single Point Intersections for Rare Target on Sand VNIR Data.	481
Table 88: Gradient Evaluation Measurements for Chemical Array Microscene NIR/SWIR Data.....	483
Table 89: Interest Points for Chemical Array NIR/SWIR Data	485
Table 90: Vertical Edge Points for Chemical Array NIR/SWIR Data	486

Table 91: Horizontal Edge Points for Chemical Array NIR/SWIR Data	486
Table 92: Single-Point Intersections for Chemical Array NIR/SWIR Data	487
Table 93: Gradient Evaluation Measurements for Cloth Thread Microscene VNIR Data	488
Table 94: Interest Points for Cloth Threads VNIR Data.....	489
Table 95: Benchmark Vertical Edge Points for Cloth Threads VNIR Data	490
Table 96: Benchmark Horizontal Edge Points for Cloth Threads VNIR Data.....	491
Table 97: Benchmark Single-Point Intersections for Cloth Threads VNIR Data.....	491
Table 98: HySPADE Evaluation Measurements for Reno VNIR/SWIR Data.....	493
Table 99: HySPADE Evaluation Measurements for Cuprite FL #1 Overhead VNIR/SWIR Data	495
Table 100: HySPADE Evaluation Measurements for Cuprite FL #2 Overhead VNIR/SWIR Data	498
Table 101: HySPADE Evaluation Measurements for Cuprite FL #3 Overhead VNIR/SWIR Data	500
Table 102: HySPADE Evaluation Measurements for Cuprite FL #4 Overhead VNIR/SWIR Data	502
Table 103: HySPADE Evaluation Measurements for Indian Pines Overhead VNIR/SWIR Data.....	504
Table 104: HySPADE Evaluation Measurements for Deepwater Horizon Overhead VNIR/SWIR Data	506
Table 105: HySPADE Evaluation Measurements for Larkhaven Ground-Based VNIR Data.....	508
Table 106: HySPADE Evaluation Measurements for Granite Ground-Based VNIR Data	510
Table 107: HySPADE Evaluation Measurements for Granite Ground-Based NIR/SWIR Data.....	513
Table 108: HySPADE Evaluation Measurements for Core Sample Ground-Based NIR/SWIR Data	515
Table 109: HySPADE Evaluation Measurements for Aluminum Panel Ground-Based VNIR Data	517
Table 110: HySPADE Evaluation Measurements for Rare Target on Sand Microscene VNIR Data	519
Table 111: HySPADE Evaluation Measurements for Chemical Array Microscene NIR/SWIR Data	522
Table 112: HySPADE Evaluation Measurements for Cloth Threads Microscene VNIR Data.....	524
Table 113: Level Set Evaluation Measurements for Reno, NV Overhead VNIR/SWIR Data.....	527
Table 114: Level Set Evaluation Measurements for Cuprite FL #1 Overhead VNIR/SWIR Data.....	530
Table 115: Level Set Evaluation Measurements for Cuprite FL #2 Overhead VNIR/SWIR Data.....	532

Table 116: Level Set Evaluation Measurements for Cuprite FL #3 Overhead VNIR/SWIR Data.....	534
Table 117: Level Set Evaluation Measurements for Cuprite FL #4 Overhead VNIR/SWIR Data.....	536
Table 118: Level Set Evaluation Measurements for Indian Pines Overhead VNIR/SWIR Data.....	539
Table 119: Level Set Evaluation Measurements for Deepwater Horizon Overhead VNIR/SWIR Data.....	540
Table 120: Level Set Evaluation Measurements for Larkhaven Ground-Based VNIR Data.....	543
Table 121: Level Set Evaluation Measurements for Granite Ground-Based VNIR Data.....	545
Table 122: Level Set Evaluation Measurements for Granite Ground-Based NIR/SWIR Data.....	547
Table 123: Level Set Evaluation Measurements for Core Sample Ground-Based NIR/SWIR Data.....	549
Table 124: Level Set Evaluation Measurements for Aluminum Panel Ground-Based VNIR Data.....	551
Table 125: Level Set Evaluation Measurements for Rare Target on Sand Microscene VNIR Data.....	553
Table 126: Level Set Evaluation Measurements for Chemical Array Microscene NIR/SWIR Data.....	555
Table 127: Level Set Evaluation Measurements for Cloth Threads Microscene VNIR Data.....	557
Table 128: Disaggregated Evaluation Matrix for All Algorithms and HSI Data Input Types.....	559
Table 129: Aggregated Evaluation Matrix for All Algorithms and HSI Data Input Types.....	564
Table 130: Aggregated Evaluation Matrix for All Algorithms and HSI Datasets.....	565
Table 131: Disaggregated Evaluation Matrix for All Algorithms and HSI Datasets.....	568
Table 132: Strongest 30 Individual Tests According to Canny Evaluation Results.....	569
Table 133: Evaluation Matrix for Spatial Resolution.....	572
Table 134: Evaluation Matrix for Spectral Resolution.....	574
Table 135: Evaluation Matrix for Spectral Bandpass.....	577
Table 136: Aggregated Evaluation Matrix for HSI Applications.....	578
Table 137: Disaggregated Evaluation Matrix for HSI Applications.....	580
Table 138: Key Conclusions for All Algorithms, Input Data Types and Applications..	584
Table 139: Experiment #1 Hypotheses Evaluation.....	585
Table 140: Experiment #2 Hypotheses Evaluation.....	586
Table 141: Experiment #3 Hypotheses Evaluation.....	588

LIST OF FIGURES

Figure	Page
Figure 1: Comparative Scarcity of Edge Detection Research	4
Figure 2: Hyperspectral Studies as an Underserved Research Area.....	5
Figure 3: AmericaView Community Recommendations for Future Landsat Capabilities [2].....	7
Figure 4: Hyperspectral Edge Detection Methods as an Emerging Field.....	8
Figure 5: Distribution of Literature Review Source Material.....	12
Figure 6: Publication Timeline for Cited Sources	14
Figure 7: Reflective and Emissive Portions of the Electromagnetic Spectrum [5]	17
Figure 8: HSI Sensors Collect Hundreds of Narrow, Contiguous Channels	18
Figure 9: Irradiance and Radiance Spectra	19
Figure 10: MSI Spectra Compared to HSI Spectra [11], [12], [13].....	21
Figure 11: Hydrocarbon Absorption Features	23
Figure 12: Traditional HSI Classification Plane for Vegetation Studies.....	25
Figure 13: Supervised Classification of HSI Data for Mineral Mapping in Cuprite, NV USA.....	26
Figure 14: Urban Feature Mapping Derived from VNIR/SWIR HSI Data	28
Figure 15: Trace Chemical Detection Using NIR HSI Data of a Human Handprint	30
Figure 16: Supervised HSI Detection of Sub-Visual Fruit Defects.....	31
Figure 17: Spectral Similarity among Normal and Bruised Regions on Kiwi Fruit.....	32
Figure 18: Key Petroleum Absorption Features in HSI Reflectance Data [78].....	34
Figure 19: HSI Reflectance Spectra of Deepwater Horizon Oil Emulsions [78]	35
Figure 20: Deepwater Horizon Oil Spill Mapping Derived from AVIRIS HSI Data [78]	36
Figure 21: Linear Anomalies in a Homogenous Manmade Material [81].....	38
Figure 22: Cracks in Solar Cells as Identified by an HSI Image Classification Approach	39
Figure 23: AVIRIS Scan of a Missile Field Test Site, New Mexico, U.S.A.	41
Figure 24: Pushbroom Scanning and Whiskbroom Scanning	42
Figure 25: ProSpecTIR Sample HSI Datasets	44
Figure 26: Hyperion HSI Data of Washington, D.C. USA.....	45
Figure 27: Ground-Based HSI Sensor Configurations [62], [29], [108]	47
Figure 28: Very High Spatial-Resolution Laboratory HSI Measurement of Granite Sample.....	49
Figure 29: HSI Microscene Data Collection [110].....	50
Figure 30: True Color HSI Microscene Data and Material Key [110]	50

Figure 31: From Radiance to Reflectance, The Four Stages of the Hyperspectral Processing Chain.....	51
Figure 32: Radiative Transfer Contributions to QUAC [9]	54
Figure 33: Roberts Cross-Gradient Kernels [127]	65
Figure 34: Roberts Edge Plane for High-Contrast Panchromatic Imagery [129].....	66
Figure 35: Roberts Edge Plane for Challenging, Non-Traditional Imagery [132]	67
Figure 36: Sobel Operator 3 x 3 Kernels [137].....	68
Figure 37: Sobel Edge Plane for Challenging, Non-Traditional Imagery [132].....	69
Figure 38: Sobel Edge Plane for High-Contrast Panchromatic Imagery [129]	71
Figure 39: The Canny Operator's Five Steps [143]	74
Figure 40: Canny Operator's Application to Manufacturing Processes [152]	75
Figure 41: Limitations of Euclidean Distance in MSI Space [189].....	82
Figure 42: Broken, Noisy Edges in Canny Planes Derived from 4-Band MRI [187]	83
Figure 43: Edge-Informed Image Classification Results [190]	85
Figure 44: Edge-Informed Region Growing Results [191]	86
Figure 45: Canny-Derived Edge Information from an Ordered Scalar Multispectral Image [192].....	86
Figure 46: Canny-Derived Edge Information from an Ordered Scalar Hyperspectral Image [192].....	87
Figure 47: Morphology Operators Improve Edge Detection Plane [193]	88
Figure 48: Graphical Representation of the Di Zenzo Gradient Operator	91
Figure 49: MSI Gradient Feature Space Edge Results [197].....	93
Figure 50: Edge Results Derived from MSI Gradient Image [198].....	94
Figure 51: The Clifford Gradient's Poor Performance Against Low-Contrast Edges [199]	95
Figure 52: MSI Edge Results Based on Newton's Law of Gravitational Motion [200] ...	96
Figure 53: Evolving a Level Set Function to Detect Edges.....	100
Figure 54: Translating the Level Set Functional Against a Three-Band Image [206]....	102
Figure 55: Rotation-Variant Template Matching [221].....	104
Figure 56: Paskaleva's Edge Signature Approach to Image Classification [220].....	106
Figure 57: Bakker and Schmidt's Modified Laplace Operator Results [153].....	108
Figure 58: NDVI-Informed Fuzzy Edge Map Using HYDICE VNIR/SWIR Data [215]	109
Figure 59: Research Gap for Gradient-Based Hyperspectral Edge Detection.....	111
Figure 60: Comparison of Chromatic Gradient and Prewitt Results [216]	114
Figure 61: Non-Maxima Suppression Results [217]	117
Figure 62: Edge Plane Derived from Band Weighting [218]	118
Figure 63: HySPADE's First Three Processing Steps [219].....	120
Figure 64: HySPADE's Final Three Steps [219]	121
Figure 65: HySPADE Edge Map for Urban Features [249]	122
Figure 66: HySPADE Edge Map for Discrete Alunite Deposits [250]	123
Figure 67: HySPADE Edge Map Derived from LWIR HSI Data [251]	124
Figure 68: HySPADE Edge Maps of the Human Tongue [252]	125
Figure 69: Research Gap for Level-Set-Based Hyperspectral Edge Detection	127

Figure 70: Incorporating Spectral Edge Information into a Level-Set-Based Algorithm [253].....	128
Figure 71: Level-Set Edge Detection Improved by Incorporating HSI Data [203].....	130
Figure 72: Overhead VNIR/SWIR Hypercube, Reno, NV USA - Color Infrared Bands 34, 55, 99 [96].....	143
Figure 73: Sample VNIR/SWIR Reflectance Spectra from Reno, NV Hypercube.....	144
Figure 74: Overhead VNIR/SWIR Hypercube, Cuprite, NV USA - Color Infrared Bands 17, 28, 50 [96].....	146
Figure 75: Sample VNIR/SWIR Radiance Spectra from Cuprite, NV Hypercube.....	147
Figure 76: Sample VNIR/SWIR Radiance Spectra from Indian Pines, IN Hypercube..	149
Figure 77: Overhead VNIR/SWIR Hypercube, Indian Pines, IN USA - Color Infrared Bands 16, 26, 50 [259].....	150
Figure 78: Overhead VNIR/SWIR Hypercube, Deepwater Horizon - Color Infrared Bands 36, 57, 101 [96].....	153
Figure 79: Sample VNIR/SWIR Radiance Spectra from Deepwater Horizon Hypercube.....	153
Figure 80: Ground-Based VNIR Hypercube, Larkhaven - Color Infrared Bands 35, 60, 109.....	156
Figure 81: Sample VNIR Radiance Spectra from Larkhaven Hypercube.....	156
Figure 82: Ground-Based VNIR Hypercube, Granite Slab - True Color Bands 10, 25, 40.....	159
Figure 83: Sample VNIR Reflectance Spectra from Granite Hypercube.....	159
Figure 84: Ground-Based NIR/SWIR Hypercube. Granite Slab - False Color Bands 15, 31, 73.....	162
Figure 85: Sample NIR/SWIR Reflectance Spectra from Granite Hypercube.....	163
Figure 86: Ground-Based NIR/SWIR Hypercube. South African Core Samples - False Color Bands 47, 50, 98.....	165
Figure 87: Sample NIR/SWIR Reflectance Spectra from South African Core Sample Hypercube.....	165
Figure 88: Amelia Earhart's Planned and Hypothesized South Pacific Flight Paths [262].....	166
Figure 89: Amelia Earhart's Lockheed Elektra Affixed with the "Miami Patch" in 1937 [264].....	168
Figure 90: Aluminum Aircraft Panel Recovered on the Island of Nikumaroro in 1991 [264].....	168
Figure 91: Aluminum Aircraft Panel VNIR Data - True Color Bands 18, 35, 53.....	170
Figure 92: Sample VNIR Radiance Spectra from Aluminum Aircraft Panel Hypercube.....	171
Figure 93: Ground-Based VNIR Hypercube, Rare Targets on Sand Microscene - Color Infrared Bands 25, 41, 76.....	173
Figure 94: Sample VNIR Reflectance Spectra from Rare Target on Sand Microscene..	174
Figure 95: Ground-Based NIR/SWIR Hypercube, Chemical Array Microscene – False Color Bands 15, 31, 73.....	176
Figure 96: Sample NIR/SWIR Reflectance Spectra from Chemical Array Microscene	178

Figure 97: Ground-Based VNIR Hypercube, Threads on Sand Microscene – True Color Bands 10, 25, 40.....	180
Figure 98: Sample VNIR Reflectance Spectra from Cloth Threads on Sand Microscene	180
Figure 99: General Methodology Components.....	184
Figure 100: Preprocessing Component.....	190
Figure 101: Post-QUAC Bad Bands Requiring Removal.....	193
Figure 102: SMACC Abundance Planes from Cloth Threads on Sand Microscene Data	195
Figure 103: RX Anomaly Plane for the Aluminum Aircraft Panel VNIR Hypercube ...	196
Figure 104: Compression Component for the Di Zenzo HSI Edge Detection Algorithm	198
Figure 105: PCA Transform Results Obtained from the Reno VNIR/SWIR Cube	199
Figure 106: The Di Zenzo Multidimensional Gradient Edge Detection Process for HSI	201
Figure 107: The Di Zenzo-Based Algorithm as Applied against an Example	203
Figure 108: Geometric Outputs of the Di Zenzo-Based Edge Detection Algorithm Workflow	204
Figure 109: Sample Spectra from Synthetic Dataset	206
Figure 110: Gradient Demonstration against Synthetic HSI Dataset	206
Figure 111: Gradient Test against Synthetic HSI Data, VIS Bands Only	207
Figure 112: HySPADE Intermediate Edge Plane Testing against Cuprite Flight Line #4 VNIR/SWIR Data	210
Figure 113: HySPADE Intermediate Edge Plane Testing against Cuprite Flight Line #4 VNIR/SWIR Data	211
Figure 114: Compression Component for the Improved HySPADE HSI Edge Detection Algorithm.....	214
Figure 115: The Improved HySPADE Edge Detection Process for HSI.....	216
Figure 116: HySPADE Demonstration against Synthetic HSI Dataset.....	221
Figure 117: Level Set Initial Curve Testing against Cuprite Flight Line #4 VNIR/SWIR Data.....	223
Figure 118: Level Set Time Step Testing against Cuprite Flight Line #4 VNIR/SWIR Data.....	225
Figure 119: Level Set Iteration Testing against Cuprite Flight Line #4 VNIR/SWIR Data	226
Figure 120: Level Set-Based Algorithm Demonstration against Synthetic HSI Dataset	228
Figure 121: Likert Scale for Canny's False Positive Criterion	231
Figure 122: Cuprite, NV USA Ground Truth Map [278]	234
Figure 123: Indian Pines, IN USA Ground Truth Map [259].....	235
Figure 124: Rare Target on Sand Ground Truth Information [258]	236
Figure 125: Chemical Array Ground Truth Information	236
Figure 126: Cloth Threads on Sand Ground Truth Information	237
Figure 127: Interest Points Detected on Van Gogh's Sower Painting [279].....	238
Figure 128: Evaluation Workflow for Fundamental Edge Point Information Content ..	242

Figure 129: Fundamental Edge Point Identification	243
Figure 130: Isolating the Top 1% of Edge Pixels in the Edge Plane	244
Figure 131: Edge Pixel Collinearity Evaluation Methodology.....	248
Figure 132: Edge Pixel Single-Point Intersection Evaluation Methodology.....	250
Figure 133: Suboptimal Gradient-Based Edge Planes from Otsu Thresholding	260
Figure 134: Otsu-Injected False Positives, False Negatives and Broken Edges.....	261
Figure 135: Gradient Experiment for Reno, NV Overhead VNIR/SWIR Data, Unstretched	264
Figure 136: Data Exploration for the Reno, NV USA Hypercube	265
Figure 137: SMACC Endmembers for the Reno, NV USA Hypercube.....	266
Figure 138: Saturation within the Reno, NV Hypercube - Color Infrared Bands 34, 55 and 99.....	267
Figure 139: RX Anomaly Plane for Reno, NV USA Hypercube	268
Figure 140: RX Anomaly Spectra for Reno, NV USA Hypercube	269
Figure 141: Optimal Threshold for PCA Cube, Reno, NV VNIR/SWIR.....	270
Figure 142: Optimal Threshold for MNF Cube, Reno, NV VNIR/SWIR.....	271
Figure 143: Gradient Experiment for Cuprite Overhead VNIR/SWIR Data, Flight Line #1, Unstretched	272
Figure 144: Gradient Experiment for Cuprite Overhead VNIR/SWIR Data, Flight Line #2, Unstretched	273
Figure 145: Gradient Experiment for Cuprite Overhead VNIR/SWIR Data, Flight Line #3, Unstretched	274
Figure 146: Gradient Experiment for Cuprite Overhead VNIR/SWIR Data, Flight Line #4, Unstretched	275
Figure 147: Data Exploration for the Cuprite Hypercube, Flight Line #1	276
Figure 148: Data Exploration for the Cuprite Hypercube, Flight Line #2.....	277
Figure 149: Data Exploration for the Cuprite Hypercube, Flight Line #3.....	278
Figure 150: Data Exploration for the Cuprite Hypercube, Flight Line #4.....	278
Figure 151: SMACC Endmembers for the Cuprite Hypercube, Flight Line #1	279
Figure 152: SMACC Endmembers for the Cuprite Hypercube, Flight Line #2.....	280
Figure 153: SMACC Endmembers for the Cuprite Hypercube, Flight Line #3	280
Figure 154: SMACC Endmembers for the Cuprite Hypercube, Flight Line #4	281
Figure 155: RX Anomaly Plane for Cuprite Hypercube, Flight Line #1	282
Figure 156: RX Anomaly Plane for Cuprite Hypercube, Flight Line #2.....	282
Figure 157: RX Anomaly Plane for Cuprite Hypercube, Flight Line #3.....	282
Figure 158: RX Anomaly Plane for Cuprite Hypercube, Flight Line #4.....	283
Figure 159: Optimal Threshold for PCA Cube, Cuprite Flight Line #1	284
Figure 160: Optimal Threshold for MNF Cube, Cuprite Flight Line #1	284
Figure 161: Optimal Threshold for PCA Cube, Cuprite Flight Line #2	285
Figure 162: Optimal Threshold for MNF Cube, Cuprite Flight Line #2	285
Figure 163: Optimal Threshold for PCA Cube, Cuprite Flight Line #3	286
Figure 164: Optimal Threshold for MNF Cube, Cuprite Flight Line #3	286
Figure 165: Optimal Threshold for PCA Cube, Cuprite Flight Line #4	287
Figure 166: Optimal Threshold for MNF Cube, Cuprite Flight Line #4	287

Figure 167: Gradient Experiment for Indian Pines Overhead VNIR/SWIR Data, Unstretched	290
Figure 168: Radiance Data Exploration for the Indian Pines Hypercube	290
Figure 169: Indian Pines QUAC Results	291
Figure 170: Indian Pines Bad Band Removal	292
Figure 171: Reflectance Data Exploration for the Indian Pines Hypercube	293
Figure 172: SMACC Endmembers for the Indian Pines Hypercube	294
Figure 173: RX Anomaly Plane and Saturation Source for Indian Pines Hypercube - Color Infrared Bands 16, 26, 50	295
Figure 174: Optimal Threshold for PCA Cube, Indian Pines VNIR/SWIR	296
Figure 175: Optimal Threshold for MNF Cube, Indian Pines VNIR/SWIR	297
Figure 176: Gradient Experiment for Deepwater Horizon Overhead VNIR/SWIR Data, Unstretched	298
Figure 177: Data Exploration for the Deepwater Horizon Hypercube	300
Figure 178: Deepwater Horizon QUAC Results	302
Figure 179: SMACC Endmembers for the Deepwater Horizon Hypercube	303
Figure 180: RX Anomaly Plane for Deepwater Horizon Hypercube	303
Figure 181: RX Anomaly Plane and Saturation Source for Deepwater Horizon Hypercube - Color Infrared Bands 36, 57, 101	304
Figure 182: Optimal Threshold for PCA Cube, Deepwater Horizon VNIR/SWIR	305
Figure 183: Optimal Threshold for MNF Cube, Deepwater Horizon VNIR/SWIR	306
Figure 184: Gradient Experiment for Larkhaven Ground-Based VNIR Data, Unstretched	307
Figure 185: Radiance Data Exploration for the Larkhaven Hypercube	308
Figure 186: Larkhaven VNIR Radiance Data Optimized for QUAC and Visualization - Color Infrared Bands 35, 60, 109	309
Figure 187: Reflectance Data Exploration for the Larkhaven Hypercube	310
Figure 188: SMACC Endmembers for the Larkhaven Hypercube	311
Figure 189: RX Anomaly Plane for Larkhaven Hypercube	312
Figure 190: Optimal Threshold for PCA Cube, Larkhaven VNIR	313
Figure 191: Optimal Threshold for MNF Cube, Larkhaven VNIR	314
Figure 192: Gradient Experiment for Granite Ground-Based VNIR Data, Unstretched	315
Figure 193: Data Exploration for the Granite VNIR Hypercube	317
Figure 194: SMACC Endmembers for the Granite VNIR Hypercube	318
Figure 195: RX Anomaly Plane for Granite VNIR Hypercube	319
Figure 196: Optimal Threshold for PCA Cube, Granite VNIR	320
Figure 197: Optimal Threshold for MNF Cube, Granite VNIR	320
Figure 198: Gradient Experiment for Granite Ground-Based NIR/SWIR Data, Unstretched	322
Figure 199: Data Exploration for the Granite NIR/SWIR Hypercube	323
Figure 200: SMACC Endmembers for the Granite NIR/SWIR Hypercube	325
Figure 201: RX Anomaly Plane for Granite NIR/SWIR Hypercube	326
Figure 202: Single-Band Sensor Anomalies in Granite NIR/SWIR Hypercube	327
Figure 203: Optimal Threshold for PCA Cube, Granite NIR/SWIR	328

Figure 204: Optimal Threshold for MNF Cube, Granite NIR/SWIR	328
Figure 205: Gradient Experiment for South African Core Sample Ground-Based NIR/SWIR Data, Unstretched.....	330
Figure 206: Data Exploration for the South African Core Sample Hypercube	331
Figure 207: SMACC Endmembers for the South African Core Sample NIR/SWIR Hypercube	332
Figure 208: RX Anomaly Plane for South African Core Sample NIR/SWIR Hypercube	333
Figure 209: Optimal Threshold for PCA Cube, South African Core Sample NIR/SWIR	334
Figure 210: Optimal Threshold for MNF Cube, South African Core Sample NIR/SWIR	334
Figure 211: Gradient Experiment for Aluminum Aircraft Panel Ground-Based VNIR Data, Unstretched.....	336
Figure 212: Data Exploration for the Aluminum Aircraft Panel Hypercube.....	337
Figure 213: Aluminum Aircraft Panel Bad Band Removal	338
Figure 214: SMACC Endmembers for the Aluminum Aircraft Panel VNIR Hypercube	339
Figure 215: RX Anomaly Results for Aluminum Aircraft Panel VNIR Hypercube - True Color Bands 18, 35, 53	340
Figure 216: Optimal Threshold for PCA Cube, Aluminum Aircraft Panel VNIR	341
Figure 217: Optimal Threshold for MNF Cube, Aluminum Aircraft Panel VNIR	341
Figure 218: Gradient Experiment for Rare Target on Sand VNIR Data, Unstretched ...	343
Figure 219: Data Exploration for the Rare Target on Sand Hypercube	344
Figure 220: SMACC Endmembers for the Rare Target on Sand Hypercube.....	345
Figure 221: RX Anomaly Plane for Rare Target on Sand Hypercube	346
Figure 222: Optimal Threshold for PCA Cube, Rare Target on Sand VNIR	347
Figure 223: Optimal Threshold for MNF Cube, Rare Target on Sand VNIR	347
Figure 224: Gradient Experiment for Chemical Array NIR/SWIR Data, Unstretched ..	349
Figure 225: Data Exploration for the Chemical Array Hypercube.....	351
Figure 226: SMACC Endmembers for the Chemical Array Hypercube	352
Figure 227: RX Anomaly Plane and Spectra for Chemical Array Hypercube	353
Figure 228: Optimal Threshold for PCA Cube, Chemical Array NIR/SWIR	354
Figure 229: Optimal Threshold for MNF Cube, Chemical Array NIR/SWIR	354
Figure 230: Gradient Experiment for Cloth Threads VNIR Data, Unstretched	356
Figure 231: Data Exploration for the Cloth Thread Hypercube	357
Figure 232: SMACC Endmembers for the Cloth Threads Hypercube	358
Figure 233: RX Anomaly Plane for Cloth Thread Hypercube	359
Figure 234: Optimal Threshold for PCA Cube, Cloth Threads VNIR	360
Figure 235: Optimal Threshold for MNF Cube, Cloth Threads VNIR	360
Figure 236: Suboptimal Results from Otsu Histogram Thresholding of the Reno Reflectance Edge Plane.....	362
Figure 237: A Strong Bimodal Distribution Explains Suboptimal Otsu Thresholding Performance	362

Figure 238: Optimal Histogram Stretch for HySPADE Edge Planes	363
Figure 239: Improved Results from Optimized Histogram Thresholding of the Reno Reflectance Edge Plane.....	364
Figure 240: HySPADE Experiment for Reno, NV Overhead VNIR/SWIR Data, Linear Stretch of Strong Edge Pixels, Threshold at 40 Intermediate Planes from 0.10 σ to 4.0 σ	365
Figure 241: HySPADE Experiment for Cuprite Overhead VNIR/SWIR Data, Flight Line #1, Linear Stretch of Strong Edge Pixels, Threshold at 40 Intermediate Planes from 0.10 σ to 4.0 σ	367
Figure 242: HySPADE Experiment for Cuprite Overhead VNIR/SWIR Data, Flight Line #2, Linear Stretch of Strong Edge Pixels, Threshold at 40 Intermediate Planes from 0.10 σ to 4.0 σ	368
Figure 243: HySPADE Experiment for Cuprite Overhead VNIR/SWIR Data, Flight Line #3, Linear Stretch of Strong Edge Pixels, Threshold at 40 Intermediate Planes from 0.10 σ to 4.0 σ	369
Figure 244: HySPADE Experiment for Cuprite Overhead VNIR/SWIR Data, Flight Line #4, Linear Stretch of Strong Edge Pixels, Threshold at 40 Intermediate Planes from 0.10 σ to 4.0 σ	370
Figure 245: HySPADE Experiment for Indian Pines Overhead VNIR/SWIR Data, Linear Stretch of Strong Edge Pixels, Threshold at 40 Intermediate Planes from 0.10 σ to 4.0 σ	372
Figure 246: HySPADE Experiment for Deepwater Horizon Overhead VNIR/SWIR Data, Linear Stretch of Strong Edge Pixels, Threshold at 40 Intermediate Planes from 0.10 σ to 4.0 σ	374
Figure 247: HySPADE Experiment for Larkhaven VNIR Data, Linear Stretch of Strong Edge Pixels, Threshold at 40 Intermediate Planes from 0.10 σ to 4.0 σ	376
Figure 248: HySPADE Experiment for Granite Ground-Based VNIR Data, Linear Stretch of Strong Edge Pixels, Threshold at 40 Intermediate Planes from 0.10 σ to 4.0 σ	378
Figure 249: HySPADE Experiment for Granite Ground-Based NIR/SWIR Data, Linear Stretch of Strong Edge Pixels, Threshold at 40 Intermediate Planes from 0.10 σ to 4.0 σ	380
Figure 250: HySPADE Experiment for South African Core Sample Ground-Based NIR/SWIR Data, Linear Stretch of Strong Edge Pixels, Threshold at 40 Intermediate Planes from 0.10 σ to 4.0 σ	382
Figure 251: HySPADE Experiment for Aluminum Aircraft Panel Ground-Based VNIR Data, Linear Stretch of Strong Edge Pixels, Threshold at 40 Intermediate Planes from 0.10 σ to 4.0 σ	384
Figure 252: HySPADE Experiment for Rare Target on Sand VNIR Data, Linear Stretch of Strong Edge Pixels, Threshold at 40 Intermediate Planes from 0.10 σ to 4.0 σ	386
Figure 253: HySPADE Experiment for Chemical Array NIR/SWIR Data, Linear Stretch of Strong Edge Pixels, Threshold at 40 Intermediate Planes from 0.10 σ to 4.0 σ	388
Figure 254: HySPADE Experiment for Cloth Threads VNIR Data, Linear Stretch of Strong Edge Pixels, Threshold at 40 Intermediate Planes from 0.10 σ to 4.0 σ	390

Figure 255: Level Set Experiment for Reno, NV Overhead VNIR/SWIR Data, Initial Curve at Image Center, Initial Radius 1/8 Longest Dimension, Single-Pixel Stepping, 0.1 Second Time Step, Maximum 20 Iterations	392
Figure 256: Level Set Experiment for Cuprite Overhead VNIR/SWIR Data, Flight Line #1, Initial Curve at Image Center, Initial Radius 1/8 Longest Dimension, Single-Pixel Stepping, 0.1 Second Time Step, Maximum 20 Iterations	394
Figure 257: Level Set Experiment for Cuprite Overhead VNIR/SWIR Data, Flight Line #2, Initial Curve at Image Center, Initial Radius 1/8 Longest Dimension, Single-Pixel Stepping, 0.1 Second Time Step, Maximum 20 Iterations	395
Figure 258: Level Set Experiment for Cuprite Overhead VNIR/SWIR Data, Flight Line #3, Initial Curve at Image Center, Initial Radius 1/8 Longest Dimension, Single-Pixel Stepping, 0.1 Second Time Step, Maximum 20 Iterations	396
Figure 259: Level Set Experiment for Cuprite Overhead VNIR/SWIR Data, Flight Line #4, Initial Curve at Image Center, Initial Radius 1/8 Longest Dimension, Single-Pixel Stepping, 0.1 Second Time Step, Maximum 20 Iterations	397
Figure 260: Level Set Experiment for Indian Pines Overhead VNIR/SWIR Data, Initial Curve at Image Center, Initial Radius 1/8 Longest Dimension, Single-Pixel Stepping, 0.1 Second Time Step, Maximum 20 Iterations	399
Figure 261: Level Set Experiment for Deepwater Horizon Overhead VNIR/SWIR Data, Initial Curve at Image Center, Initial Radius 1/8 Longest Dimension, Single-Pixel Stepping, 0.1 Second Time Step, Maximum 20 Iterations	402
Figure 262: Level Set Experiment for Larkhaven VNIR Data, Initial Curve at Image Center, Initial Radius 1/8 Longest Dimension, Single-Pixel Stepping, 0.1 Second Time Step, Maximum 20 Iterations.....	403
Figure 263: Level Set Experiment for Granite Ground-Based VNIR Data, Initial Curve at Image Center, Initial Radius 1/8 Longest Dimension, Single-Pixel Stepping, 0.1 Second Time Step, Maximum 20 Iterations	405
Figure 264: Level Set Experiment for Granite Ground-Based NIR/SWIR Data, Initial Curve at Image Center, Initial Radius 1/8 Longest Dimension, Single-Pixel Stepping, 0.1 Second Time Step, Maximum 20 Iterations	407
Figure 265: Level Set Experiment for South African Core Sample Ground-Based NIR/SWIR Data, Initial Curve at Image Center, Initial Radius 1/8 Longest Dimension, Single-Pixel Stepping, 0.1 Second Time Step, Maximum 20 Iterations	409
Figure 266: Level Set Experiment for Aluminum Aircraft Panel Ground-Based VNIR Data, Initial Curve at Image Center, Initial Radius 1/8 Longest Dimension, Single-Pixel Stepping, 0.1 Second Time Step, Maximum 20 Iterations	411
Figure 267: Level Set Experiment for Rare Target on Sand VNIR Data, Initial Curve at Image Center, Initial Radius 1/8 Longest Dimension, Single-Pixel Stepping, 0.1 Second Time Step, Maximum 20 Iterations	413
Figure 268: Level Set Experiment for Chemical Array NIR/SWIR Data, Initial Curve at Image Center, Initial Radius 1/8 Longest Dimension, Single-Pixel Stepping, 0.1 Second Time Step, Maximum 20 Iterations	415

Figure 269: Level Set Experiment for Cloth Threads VNIR Data, Initial Curve at Image Center, Initial Radius 1/8 Longest Dimension, Single-Pixel Stepping, 0.1 Second Time Step, Maximum 20 Iterations.....	417
Figure 270: Strongest Gradient Evaluation Results for Reno, NV Overhead VNIR/SWIR Data, Unstretched.....	419
Figure 271: Strongest Gradient Evaluation Results for Cuprite FL #1 Overhead VNIR/SWIR Data, Unstretched.....	425
Figure 272: Strongest Gradient Evaluation Results for Cuprite FL #2 Overhead VNIR/SWIR Data, Unstretched.....	428
Figure 273: Strongest Gradient Evaluation Results for Cuprite FL #3 Overhead VNIR/SWIR Data, Unstretched.....	432
Figure 274: Strongest Gradient Evaluation Results for Cuprite FL #4 Overhead VNIR/SWIR Data, Unstretched.....	436
Figure 275: Strongest Gradient Evaluation Results for Indian Pines, IN Overhead VNIR/SWIR Data, Unstretched.....	440
Figure 276: Similarity among Adjacent Vegetation Classes in the Indian Pines VNIR/SWIR Hypercube	442
Figure 277: Strongest Gradient Evaluation Results for Deepwater Horizon Overhead VNIR/SWIR Data, Unstretched.....	446
Figure 278: Strongest Gradient Evaluation Results for Larkhaven Ground-Based VNIR Data, Unstretched.....	452
Figure 279: Strongest Gradient Evaluation Results for Granite Ground-Based VNIR Data, Unstretched.....	456
Figure 280: Strongest Gradient Evaluation Results for Granite Ground-Based NIR/SWIR Data, Unstretched.....	461
Figure 281: Strongest Gradient Evaluation Results for Core Sample Ground-Based NIR/SWIR Data, Unstretched.....	466
Figure 282: Strongest Gradient Evaluation Results for Aluminum Panel Ground-Based VNIR Data, Unstretched.....	470
Figure 283: False Positive Spectra from Aluminum Panel VNIR Data	473
Figure 284: Strongest Gradient Evaluation Results for Rare Target on Sand Microscene VNIR Data, Unstretched.....	476
Figure 285: Delineation of Single-Pixel Neodymium Oxide Target	478
Figure 286: Strongest Gradient Evaluation Results for Chemical Array Microscene NIR/SWIR Data, Unstretched.....	482
Figure 287: False Alarm Spectra from the Sand Background on the Chemical Array Data	484
Figure 288: Strongest Gradient Evaluation Results for Cloth Threads Microscene VNIR Data, Unstretched.....	487
Figure 289: Strongest HySPADE Evaluation Results for Reno VNIR/SWIR Data, Linear Stretch of Strong Edge Pixels, Threshold at 40 Intermediate Planes from 0.10σ to 4.0σ	493

Figure 290: Strongest HySPADE Evaluation Results for Cuprite FL #1 Overhead VNIR/SWIR Data, Linear Stretch of Strong Edge Pixels, Threshold at 40 Intermediate Planes from 0.10σ to 4.0σ	495
Figure 291: Strongest HySPADE Evaluation Results for Cuprite FL #2 Overhead VNIR/SWIR Data, Linear Stretch of Strong Edge Pixels, Threshold at 40 Intermediate Planes from 0.10σ to 4.0σ	497
Figure 292: Strongest HySPADE Evaluation Results for Cuprite FL #3 Overhead VNIR/SWIR Data, Linear Stretch of Strong Edge Pixels, Threshold at 40 Intermediate Planes from 0.10σ to 4.0σ	499
Figure 293: Strongest HySPADE Evaluation Results for Cuprite FL #4 Overhead VNIR/SWIR Data, Linear Stretch of Strong Edge Pixels, Threshold at 40 Intermediate Planes from 0.10σ to 4.0σ	501
Figure 294: Strongest HySPADE Evaluation Results for Indian Pines Overhead VNIR/SWIR Data, Linear Stretch of Strong Edge Pixels, Threshold at 40 Intermediate Planes from 0.10σ to 4.0σ	504
Figure 295: Strongest HySPADE Evaluation Results for Deepwater Horizon Overhead VNIR/SWIR Data, Linear Stretch of Strong Edge Pixels, Threshold at 40 Intermediate Planes from 0.10σ to 4.0σ	506
Figure 296: Strongest HySPADE Evaluation Results for Larkhaven Ground-Based VNIR Data, Linear Stretch of Strong Edge Pixels, Threshold at 40 Intermediate Planes from 0.10σ to 4.0σ	508
Figure 297: Strongest HySPADE Evaluation Results for Granite Ground-Based VNIR Data, Linear Stretch of Strong Edge Pixels, Threshold at 40 Intermediate Planes from 0.10σ to 4.0σ	510
Figure 298: Strongest HySPADE Evaluation Results for Granite Ground-Based NIR/SWIR Data, Linear Stretch of Strong Edge Pixels, Threshold at 40 Intermediate Planes from 0.10σ to 4.0σ	512
Figure 299: Strongest HySPADE Evaluation Results for Core Sample Ground-Based NIR/SWIR Data, Linear Stretch of Strong Edge Pixels, Threshold at 40 Intermediate Planes from 0.10σ to 4.0σ	515
Figure 300: Strongest HySPADE Evaluation Results for Aluminum Panel Ground-Based VNIR Data, Linear Stretch of Strong Edge Pixels, Threshold at 40 Intermediate Planes from 0.10σ to 4.0σ	517
Figure 301: Strongest HySPADE Evaluation Results for Rare Target on Sand Microscene VNIR Data, Linear Stretch of Strong Edge Pixels, Threshold at 40 Intermediate Planes from 0.10σ to 4.0σ	519
Figure 302: Strongest HySPADE Evaluation Results for Chemical Array Microscene NIR/SWIR Data, Linear Stretch of Strong Edge Pixels, Threshold at 40 Intermediate Planes from 0.10σ to 4.0σ	521
Figure 303: Strongest HySPADE Evaluation Results for Cloth Threads Microscene VNIR Data, Linear Stretch of Strong Edge Pixels, Threshold at 40 Intermediate Planes from 0.10σ to 4.0σ	524

Figure 304: Strongest Level Set Evaluation Results for Reno, NV Overhead VNIR/SWIR Data, Initial Curve at Image Center, Initial Radius 1/8 Longest Dimension, Single-Pixel Stepping, 0.1 Second Time Step, Maximum 20 Iterations	527
Figure 305: Strongest Level Set Evaluation Results for Cuprite FL #1 Overhead VNIR/SWIR Data, Initial Curve at Image Center, Initial Radius 1/8 Longest Dimension, Single-Pixel Stepping, 0.1 Second Time Step, Maximum 20 Iterations	529
Figure 306: Strongest Level Set Evaluation Results for Cuprite FL #2 Overhead VNIR/SWIR Data	532
Figure 307: Strongest Level Set Evaluation Results for Cuprite FL #3 Overhead VNIR/SWIR Data	534
Figure 308: Strongest Level Set Evaluation Results for Cuprite FL #4 Overhead VNIR/SWIR Data	536
Figure 309: Strongest Level Set Evaluation Results for Indian Pines Overhead VNIR/SWIR Data, Initial Curve at Image Center, Initial Radius 1/8 Longest Dimension, Single-Pixel Stepping, 0.1 Second Time Step, Maximum 20 Iterations	538
Figure 310: Strongest Level Set Evaluation Results for Deepwater Horizon Overhead VNIR/SWIR Data, Initial Curve at Image Center, Initial Radius 1/8 Longest Dimension, Single-Pixel Stepping, 0.1 Second Time Step, Maximum 20 Iterations	540
Figure 311: Strongest Level Set Evaluation Results for Larkhaven Ground-Based VNIR Data, Initial Curve at Image Center, Initial Radius 1/8 Longest Dimension, Single-Pixel Stepping, 0.1 Second Time Step, Maximum 20 Iterations	543
Figure 312: Strongest Level Set Evaluation Results for Granite Ground-Based VNIR Data, Initial Curve at Image Center, Initial Radius 1/8 Longest Dimension, Single-Pixel Stepping, 0.1 Second Time Step, Maximum 20 Iterations	545
Figure 313: Strongest Level Set Evaluation Results for Granite Ground-Based NIR/SWIR Data, Initial Curve at Image Center, Initial Radius 1/8 Longest Dimension, Single-Pixel Stepping, 0.1 Second Time Step, Maximum 20 Iterations	547
Figure 314: Strongest Level Set Evaluation Results for Core Sample Ground-Based NIR/SWIR Data, Initial Curve at Image Center, Initial Radius 1/8 Longest Dimension, Single-Pixel Stepping, 0.1 Second Time Step, Maximum 20 Iterations	549
Figure 315: Strongest Level Set Evaluation Results for Aluminum Panel Ground-Based VNIR Data, Initial Curve at Image Center, Initial Radius 1/8 Longest Dimension, Single-Pixel Stepping, 0.1 Second Time Step, Maximum 20 Iterations	551
Figure 316: Strongest Level Set Evaluation Results for Rare Target on Sand Microscene VNIR Data, Initial Curve at Image Center, Initial Radius 1/8 Longest Dimension, Single-Pixel Stepping, 0.1 Second Time Step, Maximum 20 Iterations	552
Figure 317: Strongest Level Set Evaluation Results for Chemical Array Microscene NIR/SWIR Data, Initial Curve at Image Center, Initial Radius 1/8 Longest Dimension, Single-Pixel Stepping, 0.1 Second Time Step, Maximum 20 Iterations	554
Figure 318: Strongest Level Set Evaluation Results for Cloth Threads Microscene VNIR Data, Initial Curve at Image Center, Initial Radius 1/8 Longest Dimension, Single-Pixel Stepping, 0.1 Second Time Step, Maximum 20 Iterations	556
Figure 319: Optimal MNF HSI Data Improving Gradient Edge Detection Performance	560

Figure 320: Optimal MNF HSI Data Improving HySPADE Edge Detection Performance	561
Figure 321: Level Set Edge Detection Algorithm's False Negative Example	563
Figure 322: Sample of Top Performing Individual Tests	571
Figure 323: Likert Scale for Canny's False Negative Criterion	709
Figure 324: Likert Scale for Canny's Localization Criterion.....	710
Figure 325: Likert Scale for Canny's robustness to noise Criterion	711
Figure 326: Likert Scale for Canny's Single-Point Response Criterion	712
Figure 327: Likert Scale for Canny's Unbroken Edges Criterion	713

LIST OF EQUATIONS

Equation	Page
Equation 1: QUAC's Radiative Transfer Model [9]	53
Equation 2: The Reed-Xiaoli Anomaly Detector [4].....	56
Equation 3: Euclidean Distance [117]	57
Equation 4: Spectral Angle Mapper [117]	58
Equation 5: Spectral Matched Filter [4].....	59
Equation 6: The Adaptive Cosine Estimator (ACE) [4]	59
Equation 7: Normalized Difference Vegetation Index [4].....	60
Equation 8: The Linear Mixture Model [4]	61
Equation 9: Roberts Cross-Gradient Operator [127]	65
Equation 10: The Sobel Operator [137].....	68
Equation 11: Two-Dimensional Gaussian Filter [1].....	72
Equation 12: Di Zenzo's Gradient Magnitude	89
Equation 13: Di Zenzo's Gradient Direction	89
Equation 14: Di Zenzo's Tensor Components	90
Equation 15: Di Zenzo's Maximum Edge Strength Along the Direction of Greatest Change	90
Equation 16: A Traditional Parametric Active Contour [213].....	98
Equation 17: Minimizing the Level Set Energy Functional [213], [210]	98
Equation 18: The Spectral Angle Mapper as a Statistical Measure of Dissimilarity [153]	108
Equation 19: Hyperspherical Coordinate Representation [216]	113
Equation 20: The Scalar Gradient Magnitude	115
Equation 21: The Scalar Gradient Direction.....	115
Equation 22: Non-Maxima Suppression Criteria [217]	116
Equation 23: Otsu's Class Weight Calculation [268]	186
Equation 24: Otsu's Mean Calculation [268]	187
Equation 25: Otsu's Class Variance Calculation [268]	187
Equation 26: Otsu's Within-Class Variance Calculation [268].....	188
Equation 27: Euclidean Distance Calculation for Improved HySPADE.....	208
Equation 28: Sweet et al's Correlation Measurement [273]	208
Equation 29: The Spectral Similarity Metric [273]	209
Equation 30: Level Set Initial Curve	222
Equation 31: The Zero Level Set of a Function.....	224
Equation 32: Discretization of the Level Set Function [211]	225
Equation 33: Level Set Evolution [211]	225

ABSTRACT

SPATIAL-SPECTRAL APPROACHES TO EDGE DETECTION IN HYPERSPECTRAL REMOTE SENSING

Cary M. Cox, Ph.D.

George Mason University, 2017

Dissertation Director: Dr. Anthony Stefanidis

This dissertation advances geoinformation science at the intersection of hyperspectral remote sensing and edge detection methods. A relatively new phenomenology among its remote sensing peers, hyperspectral imagery (HSI) comprises only about 7% of all remote sensing research – there are five times as many radar-focused peer reviewed journal articles than hyperspectral-focused peer reviewed journal articles. Similarly, edge detection studies comprise only about 8% of image processing research, most of which is dedicated to image processing techniques most closely associated with end results, such as image classification and feature extraction. Given the centrality of edge detection to mapping, that most important of geographic functions,

improving the collective understanding of hyperspectral imagery edge detection methods constitutes a research objective aligned to the heart of geoinformation sciences.

Consequently, this dissertation endeavors to narrow the HSI edge detection research gap by advancing three HSI edge detection methods designed to leverage HSI's unique chemical identification capabilities in pursuit of generating accurate, high-quality edge planes. The Di Zenzo-based gradient edge detection algorithm, an innovative version of the Resmini HySPADE edge detection algorithm and a level set-based edge detection algorithm are tested against 15 traditional and non-traditional HSI datasets spanning a range of HSI data configurations, spectral resolutions, spatial resolutions, bandpasses and applications.

This study empirically measures algorithm performance against Dr. John Canny's six criteria for a good edge operator: false positives, false negatives, localization, single-point response, robustness to noise and unbroken edges. The end state is a suite of spatial-spectral edge detection algorithms that produce satisfactory edge results against a range of hyperspectral data types applicable to a diverse set of earth remote sensing applications. This work also explores the concept of an edge within hyperspectral space, the relative importance of spatial and spectral resolutions as they pertain to HSI edge detection and how effectively compressed HSI data improves edge detection results.

The HSI edge detection experiments yielded valuable insights into the algorithms' strengths, weaknesses and optimal alignment to remote sensing applications. The gradient-based edge operator produced strong edge planes across a range of evaluation measures and applications, particularly with respect to false negatives, unbroken edges,

urban mapping, vegetation mapping and oil spill mapping applications. False positives and uncompressed HSI data presented occasional challenges to the algorithm. The HySPADE edge operator produced satisfactory results with respect to localization, single-point response, oil spill mapping and trace chemical detection, and was challenged by false positives, declining spectral resolution and vegetation mapping applications.

The level set edge detector produced high-quality edge planes for most tests and demonstrated strong performance with respect to false positives, single-point response, oil spill mapping and mineral mapping. False negatives were a regular challenge for the level set edge detection algorithm. Finally, HSI data optimized for spectral information compression and noise was shown to improve edge detection performance across all three algorithms, while the gradient-based algorithm and HySPADE demonstrated significant robustness to declining spectral and spatial resolutions.

PURPOSE

The guiding principles for this dissertation are to: 1) advance remote sensing science into underserved research areas, 2) measure algorithm performance against challenging and non-traditional datasets, and 3) maximize the generalizability of new algorithms.

Advance the Science of Spatial-Spectral Edge Detection Methods

The chief objective of this dissertation is to advance the science of spatial-spectral edge detection methods as applied to hyperspectral imagery (HSI). For the purposes of this study, an edge is defined as a linear or curvilinear multi-pixel spatial and spectral discontinuity separating chemically distinct materials. This edge model extends the traditional edge model to include material composition. For the purposes of this dissertation, an edge is defined as a closed linear or curvilinear multi-pixel spatial and spectral discontinuity separating chemically distinct materials. The edge model explicitly states that an edge occurs only between chemically (i.e., spectrally) distinct materials and is not due to illumination or single-band grayscale intensity differences, weathering effects or other material behaviors or collection parameters that can confuse a single material as multiple materials.

The approach herein modifies for HSI and applies three unique spatial-spectral algorithms and measures their performance against traditional remote sensing datasets (i.e., overhead imagery) as well as against challenging, non-traditional datasets such as microscene and drill-core spectral imagery. This dissertation also links the algorithms' performances to the edge detection literature by comparing their performance to traditional edge detection methods (e.g., Roberts and Sobel) as applied to spectral imagery on a band-by-band basis. Most importantly, this dissertation empirically measures algorithm performance against Dr. John Canny's six criteria for a good edge operator: false positives, false negatives, localization, single-point response, robustness to noise and unbroken edges [1]. The end state is a suite of spatial-spectral edge detection algorithms that produce improved edge results against a range of hyperspectral data types applicable to a diverse set of earth remote sensing applications.

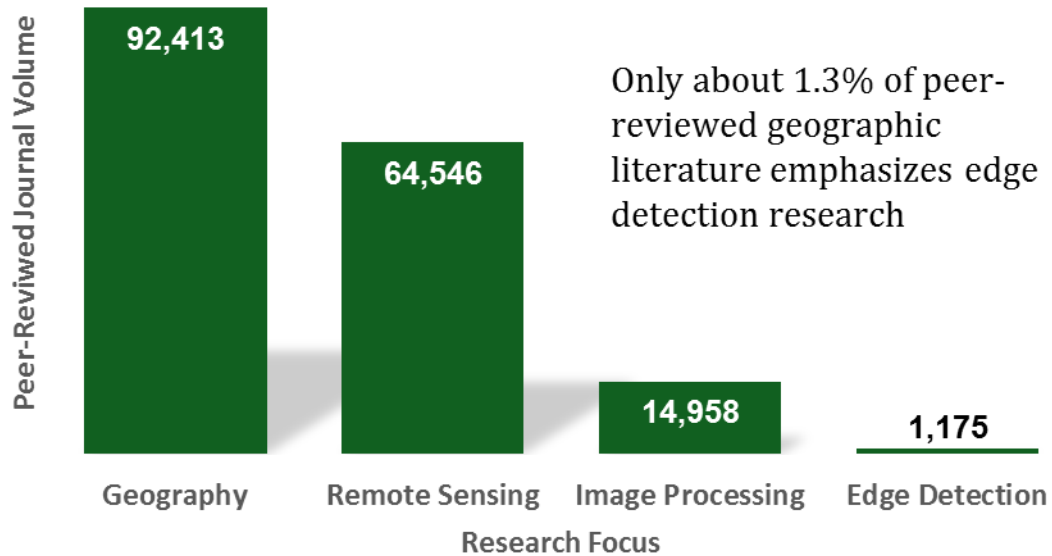
Advance GeoInformation Science into Underserved Research Areas

The second objective of this dissertation is to advance GeoInformation science into relatively underserved research areas, namely edge detection and hyperspectral studies. Consider Figure 1, which demonstrates that within the body of peer-reviewed GeoInformation science, edge detection studies comprise a surprisingly small 1.3% of all GeoInformation research and only about 8% of image processing research. The balance of image processing research emphasizes traditional image processing approaches such as denoising, image segmentation, pattern recognition, feature extraction, etc., while edge detection methods are routinely deemphasized below their more specialized and scene-specific image classification cousins. Put another way, remote sensing researchers tend

to emphasize image processing techniques that are most closely associated with end results (e.g., image classification) at the expense of key enabling techniques such as edge detection. Consequently, this dissertation chooses to advance the science of edge detection methods as opposed to maturing/refining other, more thoroughly understood research areas.

Additionally, this study chooses edge detection methods over other image processing techniques due to its centrality to the essence of geographic study: mapping. Edge detection outputs are much closer to what a geographer wants to see for mapping purposes compared to image classification, denoising or dimensionality reduction outputs. Indeed, properly extracted high-quality edges are a prerequisite to precise, high-quality mapping – the original and still most widely recognized purpose of geographers.

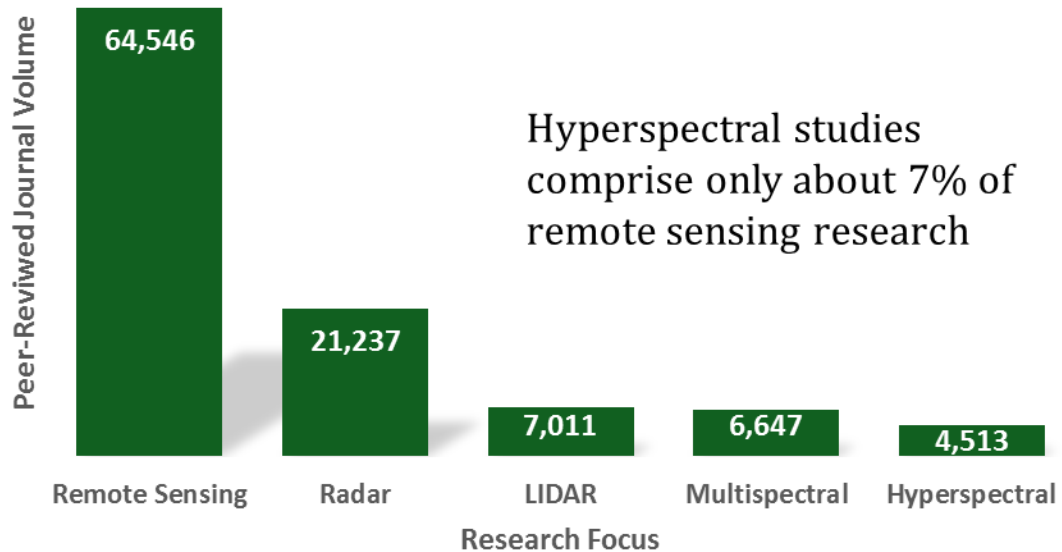
This work also recognizes the disadvantages of edge detection techniques, namely that they are sensitive and that pixel response can vary widely according to collection environment. Look angle, illumination, sensor noise, and limited spatial resolution have a long history of confounding otherwise capable edge detection techniques. This dissertation accepts the challenge of these limitations and endeavors to demonstrate that its edge detection algorithms can leverage the robust spectral character of HSI data to mitigate edge detector performance vagaries.



Source: Peer-Reviewed Journal Titles Held by George Mason University Library; Surveyed 15JUL2016

Figure 1: Comparative Scarcity of Edge Detection Research

Similarly, hyperspectral research comprises only about 7% of all remote sensing research, and less than 5% of all GeoInformation research as seen in Figure 2. There are five times as many radar-focused peer-reviewed journal articles than hyperspectral-focused peer-reviewed journal articles. Clearly, the scientific community’s collective understanding of hyperspectral science is far less than that of traditional remote sensing phenomenologies such as radar and panchromatic imaging. Therefore, in the spirit of advancing remote sensing science into underserved research areas, this work pursues hyperspectral remote sensing methods rather than other, more widely utilized remote sensing phenomenologies.



Source: Peer-Reviewed Journal Titles Held by George Mason University Library; Surveyed 15JUL2016

Figure 2: Hyperspectral Studies as an Underserved Research Area

Hyperspectral data's ability to be optimized according to remote sensing application also makes it an attractive choice for research. For example, HSI's chemical identification capability allows it to be fine-tuned to detect materials central to an application, such as oil spill mapping and mineral mapping. Both oil spill mapping and mineral mapping benefit from hyperspectral data collected between 0.4 μ m and 2.5 μ m, as opposed to gaseous emission applications that benefit from longwave infrared wavelengths (8.0 μ m and 12.0 μ m). Measuring the relative performance of various spectral band combinations promises to illuminate optimal collection parameters from both a purely scientific perspective as well as an applications perspective. Therefore,

HSI data are an attractive choice for a research effort premised on demonstrating wide applicability across remote sensing applications.

Additionally, as seen in Figure 3, the demand for hyperspectral data is quite strong, as evidenced by the leading earth remote sensing scientists' call for hyperspectral capabilities on future Landsat missions [2]. Pairing this strong demand for future HSI capabilities with the comparatively thin HSI literature suggests an interesting conclusion: researchers will receive more hyperspectral data but will require improved understanding in order to maximize its application. Consequently, this dissertation chooses to advance the science of hyperspectral remote sensing as opposed to developing other, more thoroughly understood remote sensing phenomenologies.

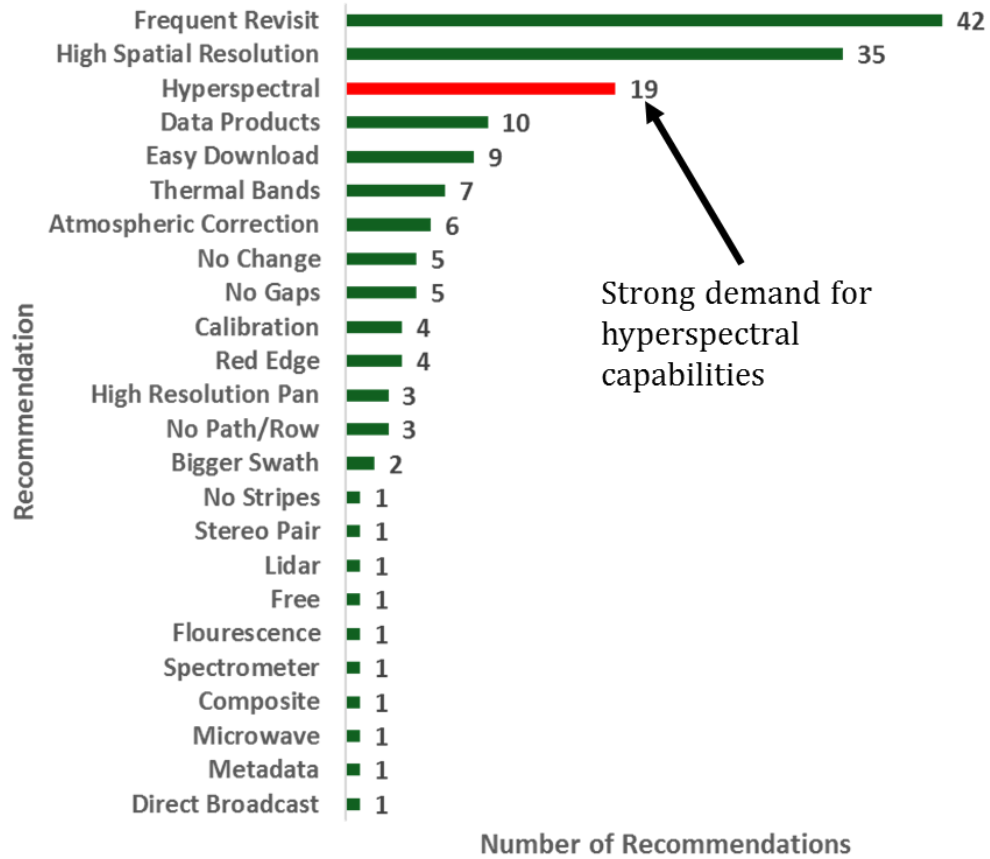
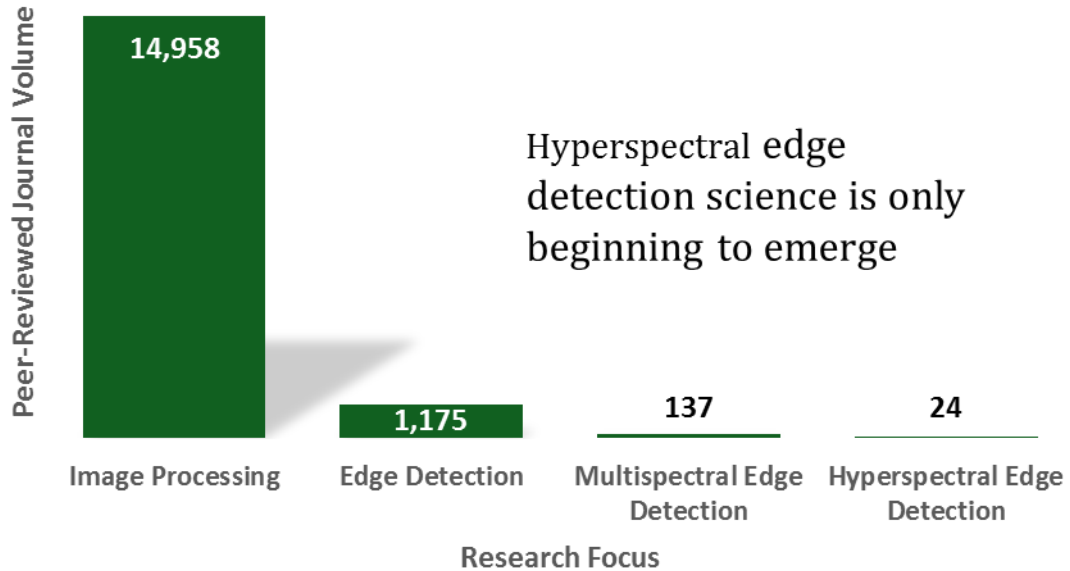


Figure 3: AmericaView Community Recommendations for Future Landsat Capabilities [2]

Most importantly, the intersection between hyperspectral remote sensing and edge detection algorithms represents a clear gap in the scientific literature. Figure 4 demonstrates that among the almost 15,000 peer-reviewed image processing articles, only 24 (i.e., 0.2%) pursue hyperspectral edge detection techniques as their primary research effort. This is a surprisingly low number given the maturity of traditional panchromatic edge detection methods and the strong potential for extracting edge information from

high spectral resolution data. In order to help close this dissertation gap, this dissertation advances the understudied field of hyperspectral edge detection algorithms.



Source: Peer-Reviewed Journal Titles Held by George Mason University Library; Surveyed 15JUL2016

Figure 4: Hyperspectral Edge Detection Methods as an Emerging Field

Demonstrate Utility against Challenging, Non-Traditional HSI Datasets

Regular readers of the remote sensing literature will likely agree that most peer-reviewed research utilizes only a small set of well-understood datasets and that researchers tend to favor conservative methods due to their increased likelihood of success and suitability for publication (i.e., acceptance of negative results into the peer-reviewed literature is quite rare). Spectral scientists, in particular, make such regular use

of the same well-behaved datasets that the data have developed nicknames, such as “the Cuprite data” and “the Indian Pines data.” The regular use of common HSI datasets makes sense: researchers want to measure their new algorithm against existing algorithms in a controlled test made possible only by using the same data for both algorithms. Similarly, researchers prefer calibrated, orthorectified data due to their predictability and stability. The relative scarcity of HSI datasets compared to more long-tenured data types like panchromatic and MSI data also explains the narrow variety of data sets appearing in the HSI literature.

For control purposes, this study similarly measures its new algorithms’ performances against common datasets such as “the Cuprite data.” However, the tests herein also extend HSI edge detection science to challenging, non-traditional datasets such as microscene data, geologic core sampling data, ocean data and material data collected from an aluminum panel possibly traceable to Amelia Earhart’s Lockheed Model 10 Elektra aircraft. Similarly, this study does not rely on orthorectified imagery due to its scarcity among real-world HSI datasets. Nor does this dissertation confine its experiments to perfectly radiometrically calibrated HSI data for the same reason – real-world HSI data ranges from the poorly calibrated to the accurately calibrated.

By testing against both traditional and non-traditional data, this dissertation remains tethered to the well-understood, controlled approaches that constitute the majority of peer-reviewed publications while expanding the scientific horizon to datasets that could yield new insights and avenues of research. The emphasis on relevance to real-world HSI applications (e.g., oil spill mitigation, historic aircraft recovery, etc.)

extends throughout this study in order to maximize the immediate contributions to applied science. Consequently, orthorectified, well-calibrated data make only a rare appearance herein in order to closely model the work environment of field scientists, technicians and engineers.

The challenging, non-traditional HSI datasets were chosen to stress this study's algorithms in several ways, one of which is through the geographic uncertainty of edges. "Where is the edge of the forest" is a common question posed among researchers pursuing edge detection methods. The task of precisely localizing an edge along the edge of a forest, for example, is challenged by the gradual diminution of trees as the forest thins into open plain. Obligated by empirical evaluation methods to precisely define at which pixels a forest ends and plains begin, the researcher must overcome this uncertainty in a rigorous manner that makes sense within the intended remote sensing application. This study is no different in this regard, and expects to be challenged by geographic uncertainties within its non-traditional oil spill mapping and mineral mapping datasets. Specifically, this study addresses geographic uncertainty on a case by case basis according to the intended HSI application. For example, oil spill mapping applications err on the conservative side of determining oil slick extent by including areas only lightly affected by intruding oil. This dissertation follows this convention by increasing the meaningfulness of weak edge pixels in oil spill mapping data – a methodology intended to strike a reasonable balance between scientific consistency and real world behavior.

Given the risk inherent in testing against non-traditional, challenging datasets, a note on negative results is warranted. The scientific community tends to reward positive

results published in peer-reviewed forums, which is understandable – positive results are much more interesting and extendable compared to negative results that appear much more like a scientific dead end. The stigma of failure also clings to negative results, which discourages publication and further study.

Unfortunately, an approach that values only positive results is discordant with the scientific method, which views positive and negative findings equally and assigns value only when a hypothesis is rigorously supported or not supported by those findings. The scientific method values both supported and unsupported hypotheses because both add clarity to the aggregate scientific understanding – the true value is in the tested hypothesis (the actual scientific understanding), not the findings (the measures by which researchers achieve the understanding). Consequently, this dissertation pursues a hypothesis-driven approach in which positive and negative results are valued only to the extent that they rigorously support or do not support a hypothesis. Departing from the traditional conservative approach to remote sensing research, this dissertation deems a negative finding just as welcome as a positive finding so long as it rigorously illuminates the hypothesis. The goal is improved scientific understanding, not flashy, positive findings.

BACKGROUND

This work's literature review emphasizes the peer-reviewed literature in order to maximize the reliability of its hypotheses, methodology and findings, but considers all relevant sources of information to include industry websites (e.g., NASA, USGS, etc.), remote sensing textbooks, conference proceedings and published theses. Figure 5 presents the distribution of sources underpinning this study, fully 81% of which are peer-reviewed journal articles.

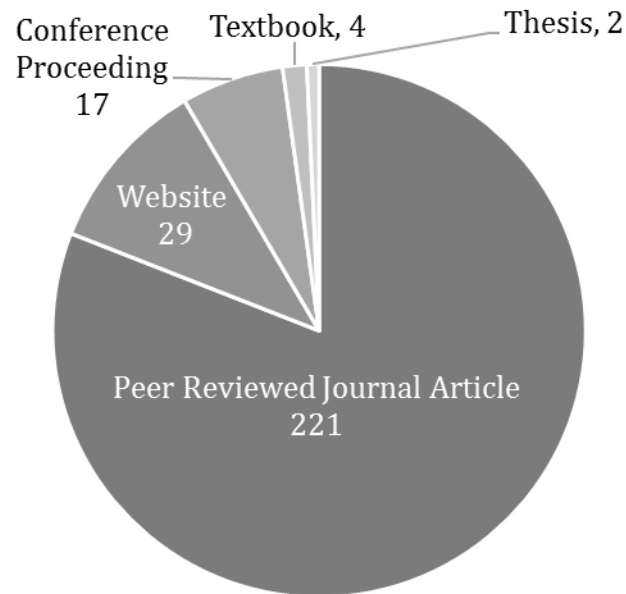


Figure 5: Distribution of Literature Review Source Material

Figure 6 presents evidence of the relative newness of HSI research within the scientific literature, particularly with respect to HSI edge detection methods. Specifically, 50% of this dissertation’s cited sources were published in since 2011, the year in which this dissertation proposal was approved. Nearly 80% of this dissertation’s sources were published in the last ten years – a pattern that closely mirrors the overall trend of HSI peer-reviewed publication. The emerging nature of HSI research serves as both a challenge to this study, which was obliged to stay current with the literature on a monthly basis, and an opportunity to explore largely unstudied avenues of research. Ultimately, closely adhering to the peer-reviewed literature serves as a mitigating factor for the forced reliance on relatively new research.

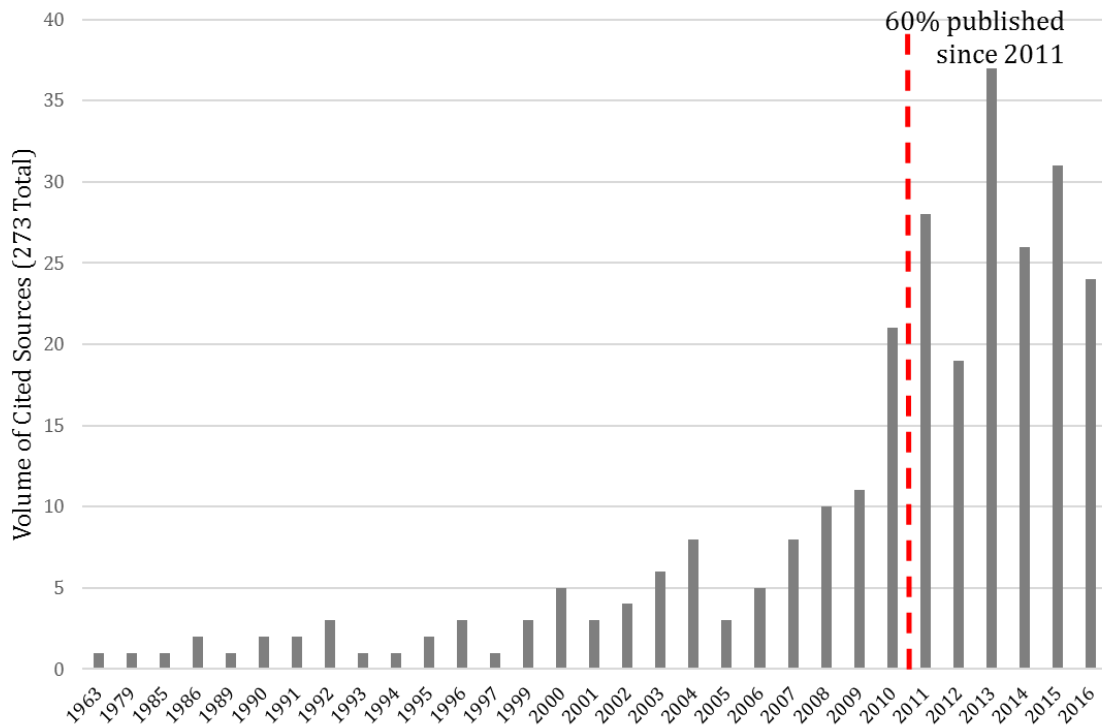


Figure 6: Publication Timeline for Cited Sources

Earth remote sensing is the science of detecting, classifying, identifying, and measuring surface materials collected by a sensor operating away from the surface. The majority of remote sensing research addresses the data analysis component of the remote sensing processing chain – a process whose outcome depends heavily on how effectively algorithms can derive information from imagery. Alongside traditional image processing efforts such as noise reduction and image classification, edge detection methods play a prominent role in the analysis component of the remote sensing processing chain.

Edge detection methods are singularly focused on identifying discontinuities within the image, and generate as output an edge map delineating the image's constituent regions. In most cases, researchers design edge detection algorithms that emphasize the spatial information in the data, whether the algorithms are designed for noise reduction, image classification, edge detection, etc. Relatively few algorithms simultaneously leverage the spatial and spectral dimensions of remote sensing data, in part due to the complexity of collecting data with spectral resolutions sufficient to support robust spectral analysis. The relative newness of high spectral resolution data also has limited the availability of spatial-spectral edge detection algorithms as researchers continue to focus on high resolution panchromatic imagery and five- to ten-band multispectral imagery (MSI). Only in the last few years have focal plane, telescope, and data storage technologies improved to the point that engineers can design and build cost-effective high spatial resolution imagers equipped with high spectral resolutions. Put simply, research

into panchromatic edge detection techniques began in the 1960s and has a twenty-year head start on spectral edge detection techniques which began appearing only in the 1980s.

The traditional approach to remote sensing problem solving also explains the slow advance of spatial-spectral edge detection algorithms. Traditional remote sensing research methods tend to rely on either the spatial dimension or the spectral dimension – a practice borne of the natural tradeoff between spatial and spectral resolutions and the emphasis on specialization within the research community. Naturally, researchers were obliged to develop algorithms aimed exclusively at either the spatial or the spectral information in the data.

Beginning in the late 1980s with the advent of NASA's hyperspectral imagery (HSI) AVIRIS sensor, researchers first began to simultaneously exploit the spatial and spectral dimensions in a scene [3]. Researchers tended to follow one of two research paths depending on which remote sensing school of thought they followed. Unsurprisingly, traditional digital image processing experts emphasized the spatial content of spectral data while spectral scientists naturally designed their algorithms to take advantage of spectral content. Little overlap occurred, and spectral-only algorithms flourished more broadly as research flowed to the newly-opened field. Consequently, most of the early decades of HSI research tended to emphasize the newly available spectral information at the expense of the spatial.

The result is that the majority of edge detection algorithms available for hyperspectral imagery are either well-known panchromatic spatial algorithms modified for spectral imagery, or are algorithms that operate solely in spectral space. Hyperspectral

algorithms working in both spatial and spectral space are comparatively rare and certainly not in the mainstream of spectral analysis and exploitation workflows – correcting this deficiency is the central aim of this work.

Hyperspectral Remote Sensing

All remote sensing systems fall into one of two categories: active or passive.

Active remote sensing systems generate their own illumination source, such as synthetic aperture radar (SAR) and light detection and ranging (LIDAR) systems. The majority of systems, however, are passive remote sensors that rely on reflected solar radiation or on the earth's emitted thermal energy to generate an image composed of individual picture elements, or pixels. In remote sensing, a pixel represents a numerical value associated with the image brightness in a particular band at a particular ground sample point, and is generally understood to be the smallest coherent element in a two-dimensional image [4].

Passive systems can further be divided into panchromatic (PAN), MSI, and HSI systems. PAN systems typically collect photons across a single broad band in the visible (VIS) region of the electromagnetic spectrum or the thermal infrared (TIR) region, such as a forward-looking infrared (FLIR) system. MSI systems typically detect energy in several broad, generally noncontiguous bands spanning the VIS and near-infrared (NIR) channels. MSI systems often include shortwave infrared (SWIR) channels and occasionally incorporate longwave infrared (LWIR) channels, as well. Figure 7 presents a high-level overview of the reflective and emissive bands ranging from the VIS to the LWIR [5].

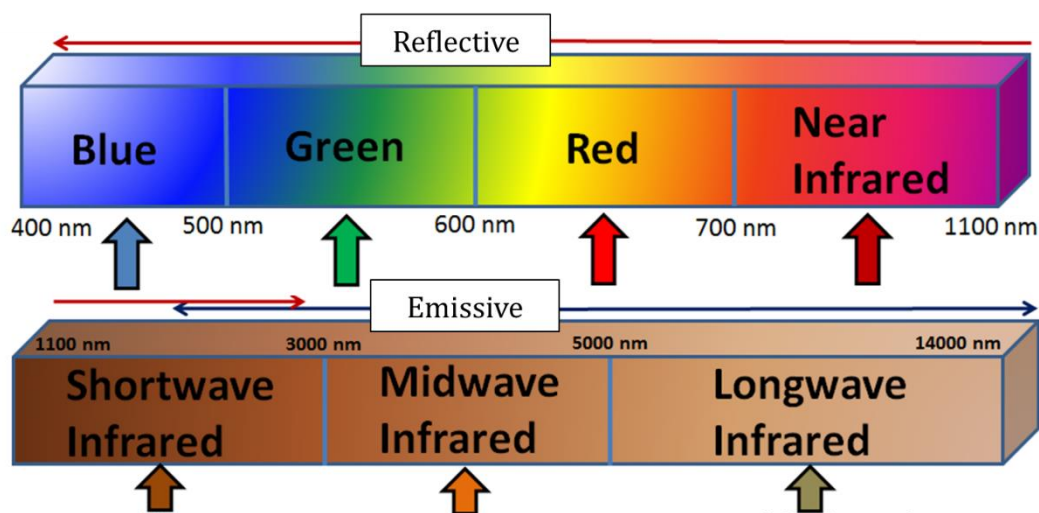


Figure 7: Reflective and Emissive Portions of the Electromagnetic Spectrum [5]

HSI remote sensing systems extend the capabilities of MSI and panchromatic systems by sampling data across hundreds of very narrow, contiguous channels across the VNIR, SWIR, or LWIR bands, as seen in Figure 8. For example, the typical HSI focal plane will generate a spectral resolution on the order of 10 nm in the visible and near-infrared channels, and gradually widens with increasing wavelength. Comparatively, the spectral resolution for the typical MSI sensor will vary from 60 nm to over 200 nm spanning 8 to 20 noncontiguous channels. The finer spectral resolution and the arrangement of contiguous sampling locations allow the hyperspectral sensor to generate a much more accurate estimate of the spectral properties of the materials captured within any given pixel – the chief advantage of HSI systems.

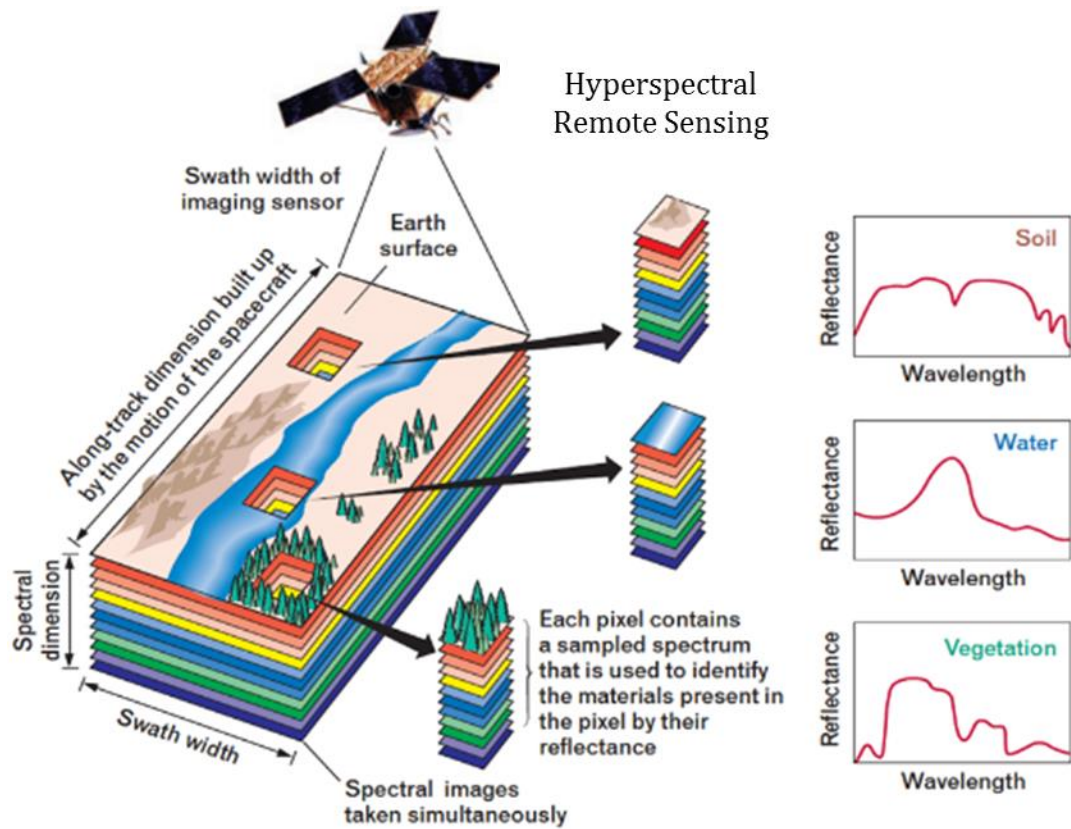


Figure 8: HSI Sensors Collect Hundreds of Narrow, Contiguous Channels

HSI comes in several forms. Radiance data, more formally known as reflected solar irradiance, is the signal or input at the sensor's aperture. Commonly referred to as at-aperture radiance, radiance data contains the spectral information for all features in the field of view, including ground materials, atmospheric constituents, and sensor noise. Figure 9 contains example data plots for exoatmospheric solar irradiance (i.e., the sun's electromagnetic signature before it enters earth's atmosphere) and at-aperture radiance [6].

Note that the radiance data plot is characterized absorption features absent in the irradiance curve. These absorption features occur at specific wavelengths according to

how the matter's chemical composition and (in the case of solids) crystalline structure affect electromagnetic energy's interactions: reflection (scattering), absorption and transmission. During HSI algorithm execution, absorption features serve as diagnostic markers by which the algorithms can discriminate among materials.

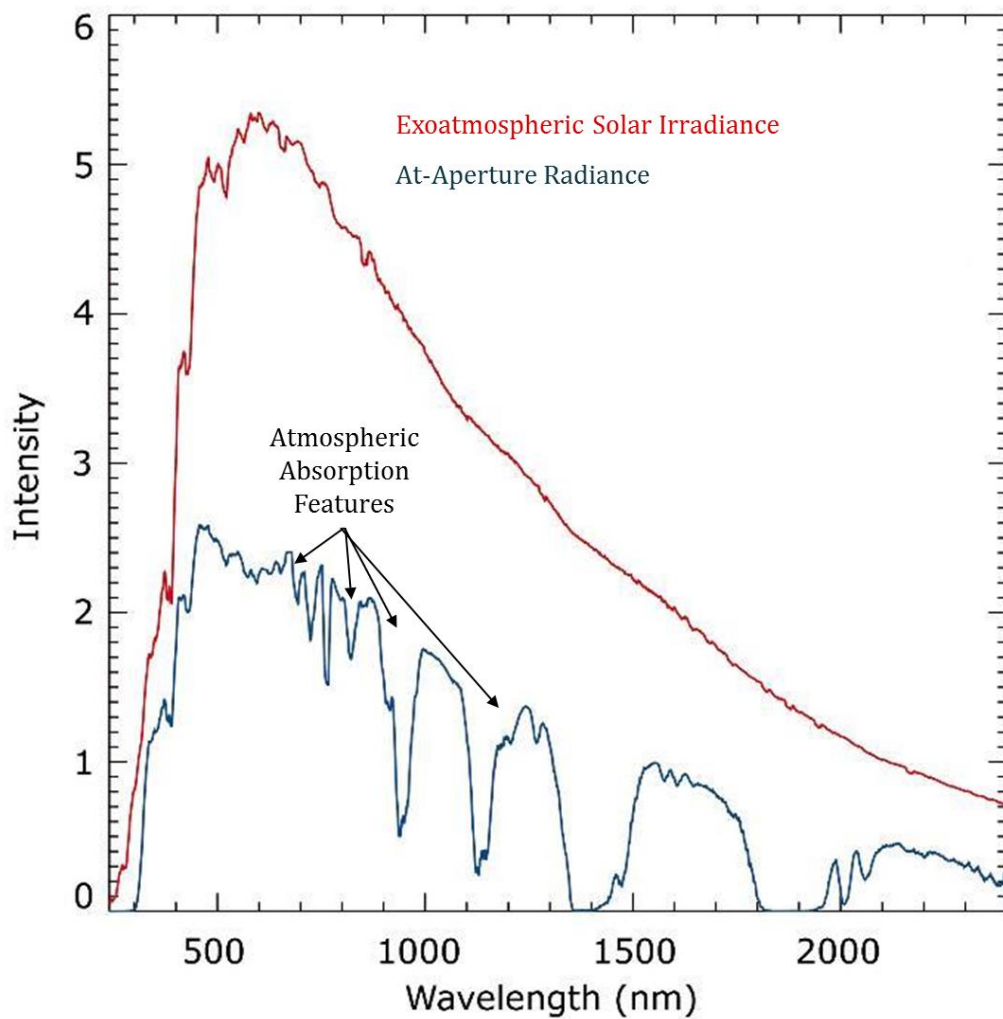


Figure 9: Irradiance and Radiance Spectra

While hyperspectral radiance data have some utility for material identification and mapping [7] and [8], HSI researchers use radiance data primarily for developing atmospheric correction algorithms [9], [10]. HSI atmospheric correction algorithms attempt to remove atmospheric absorption and scattering effects from radiance data in order to generate reflectance data containing spectral information attributable only to ground materials. I.e., atmospheric correction algorithms ingest radiance data and output reflectance data optimized for earth remote sensing applications and algorithm development.

When the reflectance data for a given pixel are viewed as a function of wavelength, the resulting curve is known as the reflectance spectrum, or simply spectrum, of that particular pixel. The spectrum can be thought of as the “fingerprint” or signature of the pixel’s material(s), and is simply the graphical representation of the apparent reflectance plotted as a function of wavelength. Figure 10 provides an example of the difference between MSI and HSI reflectance spectra: hyperspectral data from the United States Geological Survey, space-based MSI data from NASA’s Moderate Resolution Imaging Spectroradiometer (MODIS) sensor, and space-based MSI data from NASA’s Landsat TM7 imager [11], [12], [13].

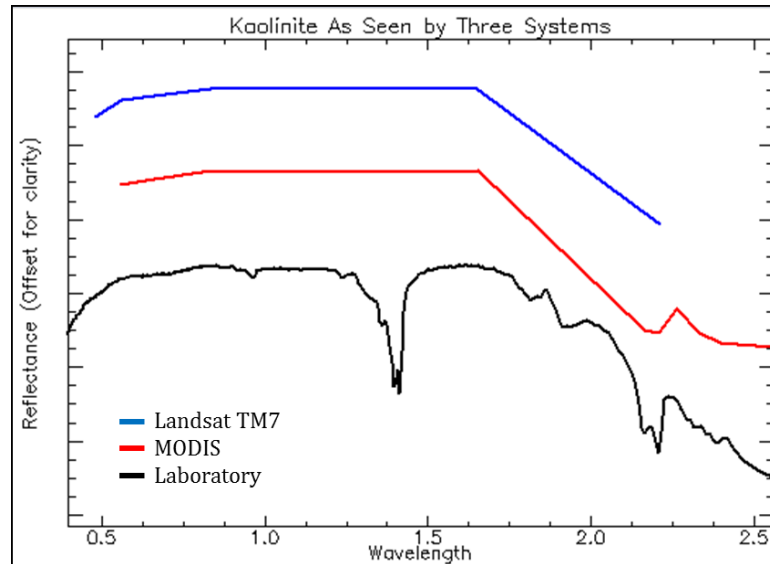


Figure 10: MSI Spectra Compared to HSI Spectra [11], [12], [13]

The lab spectrum is an example of how an HSI sensor would sample a material (e.g., with a spectral sampling interval on the order of 1 nm), while the MODIS and Landsat TM7 spectra represent examples from MSI sensors. The differences among the sensors and spectra are many and have direct implications for how efficiently features can be separated from their backgrounds, classified, measured and dissected by edges. For example, consider the lab spectrum for kaolinite in Figure 10. The diagnostic absorption features near 1.41 μm and the doublet at 2.20 μm are clearly identifiable among the non-diagnostic portions of the spectrum – a dynamic colloquially referred to as “spectral flavor.” As seen in the MODIS channels, the doublet at 2.20 μm is measured only as a single reflectance minimum, which has little diagnostic value compared to the spectra of similar minerals. Similarly, the spectral flavor near 1.41 μm and 2.20 μm in the Landsat TM7 data is completely lost in the low spectral resolution sampling. This

“washing out” of spectral flavor increases to the point of impossibility the difficulty of confidently separating kaolinite from similarly reflecting minerals. Clearly, as spectral resolution improves for a given spatial resolution, the ability to separate target from background improves.

As seen in Figure 10, the ability of HSI sensors to maximize the spectral information within each pixel allows the researcher to identify and quantify specific materials based on their spectral reflectance properties, or signature – a direct extension of the ability of MSI data to classify and discriminate among earth materials. Indeed, material identification and quantification are the chief objectives of HSI data exploitation, a process that relies entirely on separating the target from the background through spectroscopic analysis. Spectroscopic analysis is able to identify materials by measuring the shape and location of diagnostic absorption features visible in the HSI spectra. Absorption features are defined as wavelengths of absorptions visible in spectra as dips in the reflectance values at known wavelengths [4].

For example, consider the diagnostic absorption features for hydrocarbon-bearing materials as seen in Figure 11 [14]. Key hydrocarbon absorption features are located at 1.18 μm , 1.38 μm , 1.72 μm , and the characteristic hydrocarbon plateau extends from 2.3 μm to 2.45 μm . Occasionally, small hydrocarbon absorption features also appear between 2.3 μm and 2.45 μm . The doublet centered on 1.72 μm is particularly strong, and the 1.38 μm feature is typically obscured by atmospheric water vapor. The spectrum of any material that contains hydrocarbons, such as plastics, will often contain these features, particularly the 1.72 μm doublet.

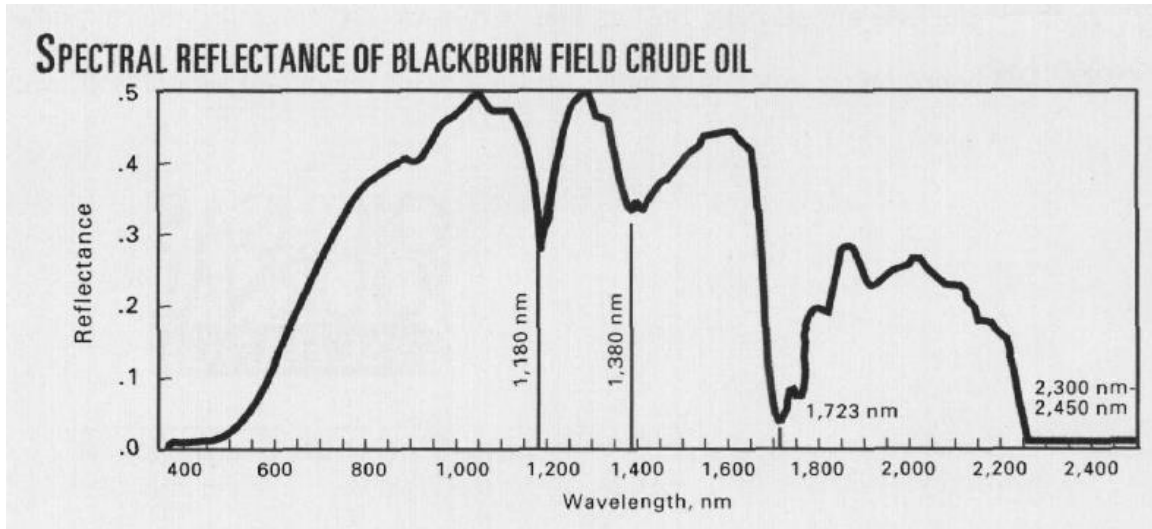


Figure 11: Hydrocarbon Absorption Features

As explained in detail in the Methodology section, this dissertation applies robust image processing techniques to compress the spectral information in HSI data [4], [15]. Specifically, this study applies the well-known principal components analysis (PCA) and minimum noise fraction (MNF) transforms to each dataset in order to take advantage of dimensionality reduction. For the sake of rigor, the methodology tests full PCA cubes and compressed PCA cubes for each algorithm against each dataset. Particularly for the compressed PCA cube tests, which span only the high-information PCA bands, HSI data is highly compressed within a few bands.

Hyperspectral Remote Sensing Applications

Researchers collect hyperspectral data in support of a variety of traditional scientific and commercial interests. Vegetation mapping, mineral mapping and urban feature mapping are examples of some of the most common applications routinely

informed by hyperspectral data. For example, spectral imaging techniques (both MSI and HSI) have long been used to support crop health assessments, mostly through the use of vegetation indices such as the normalized difference vegetation index (NDVI) [16], [17], [18], [19], [20], [21], [22], [23]. Researchers also have applied hyperspectral-based approaches to vegetation mapping, [24], [25], [26], [27], [28], [29] invasive vegetation species identification [30], [31], [32], [33], [34] and vegetation disease detection [35], [36], [37], [38], [39]. Interestingly, all of these methods approach hyperspectral vegetation analysis from an image classification/target detection perspective – vegetation edge detection is simply an artifact for these methods, but will be a primary objective of the research performed herein.

For example, consider the vegetation classification methodology and results achieved in [29], which is representative of HSI research for vegetation problem sets. The well-classified results are seen in Figure 12. The researchers used a partial least squares image classification algorithm to distinguish grass weeds and broadleaf weeds from soils and wheat plants, and their approach emphasized the spectral content of only the red-edge bands. Indeed, the vast majority of HSI vegetation studies utilize only with the red-edge bands and ignore the remaining several hundred HSI channels.

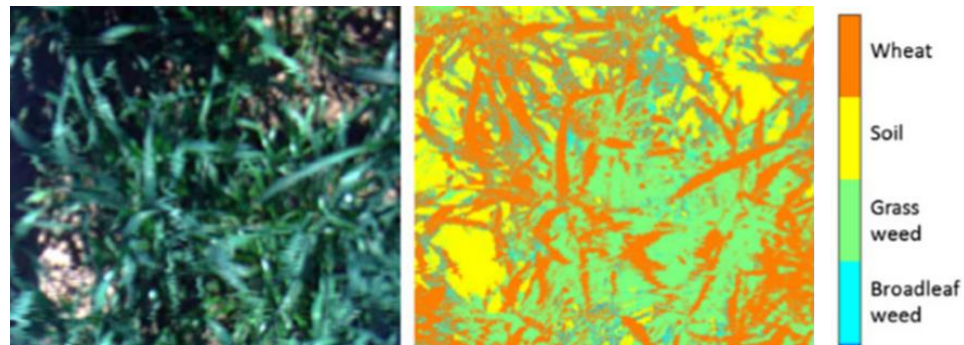


Figure 12: Traditional HSI Classification Plane for Vegetation Studies

Vegetation image classification algorithms certainly should emphasize the red-edge bands, but this narrow focus on a few spectral channels distinguishes the image classification approach from edge detection approaches that nearly always use all available spectral information. Vegetation segmentation methods must emphasize the discriminating red-edge bands to whether “these pixels are broadleaf weeds and those pixels are wheat,” while an edge detection algorithm could use the full spectral range to declare that “these pixels are edge pixels between two different materials regardless of what they happen to be.” Indeed, the research executed herein will advance the science by measuring how effectively full-spectrum edge detection methods can discriminate the boundary between vegetation classes.

Hyperspectral data also have been used with great success to support geological exploration and mapping efforts [40], [41], [42], [43], [44]. Researchers have ably parsed hyperspectral imagery containing large assemblages of common minerals such as kaolinite, alunite and calcite [43], and also have found success mapping less common minerals such as those associated with gold mineralization [45]. Much like vegetation

mapping efforts, however, most mineral mapping efforts follow a workflow in which the algorithms search for spectral similarities among pixels – edge information is incidental to these approaches.

For example, consider the mineral mapping methodology and results achieved in [41], which is highly representative of traditional HSI mineral mapping efforts in that it uses automated identification techniques to classify scene minerals. As seen in Figure 13, [41]’s automated (i.e., unsupervised) HSI classification method produced coherent results for a complex overhead HSI dataset collected over Cuprite, Nevada USA. The Cuprite data is one of the most extensively studied mineral-rich HSI dataset in the HSI literature, and [41]’s automated approach reliably segmented six distinct minerals: kaolinite, alunite, muscovite, silica, buddingtonite and calcite.

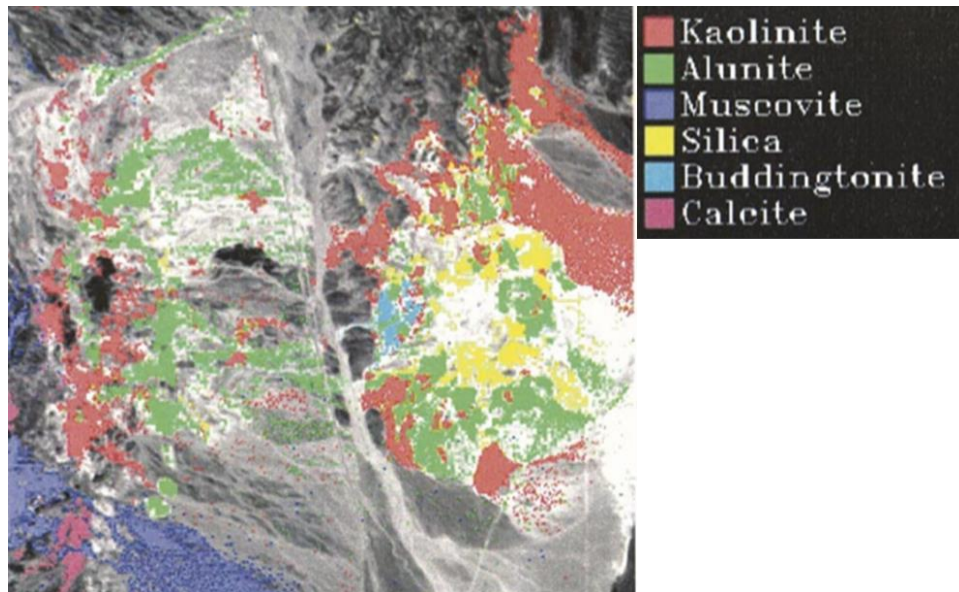


Figure 13: Supervised Classification of HSI Data for Mineral Mapping in Cuprite, NV USA

Automated classification techniques are common to mineral and vegetation mapping efforts because *a priori* knowledge of complex mineralogy and vegetation scenes is difficult to achieve. HSI mineral and vegetation mapping efforts regularly use unsupervised segmentation methods to organize a large set of similar, unknown scene materials. Supervised methods are typically used when ground truth information is available. The common link between mineral mapping and vegetation mapping is the reliance on continuity-based methods, as opposed to the discontinuity-based methods characteristic of the edge detection methods developed in this dissertation.

Additionally, the HSI literature contains hundreds of examples of how HSI data can contribute to urban feature mapping; e.g., [46], [47], [48], [49], [50]. HSI is particularly useful for urban mapping techniques given the high spectral contrast between typical urban land cover classes such as vegetation, soil, asphalt, shadows, metal, plastic and water. Much like vegetation mapping and geologic mapping, HSI urban mapping techniques usually employ continuity-based image classification approaches to segment the image into homogenous, non-overlapping regions. Edge considerations for urban HSI data are much less common [51], [52].

For example, consider the traditional approach to urban feature mapping as evidenced by [53], which begins with prior knowledge of the urban materials' HSI signatures (i.e., a continuity-based approach). In this case, [53] collected VNIR/SWIR field spectra for a range of asphalt surface conditions and then used those signatures to classify asphalt surface conditions imaged by an airborne HSI sensor. As seen in Figure 14, the approach relied on image classification techniques to map urban features

distinguishable by their linear irregularities (e.g., cracks and fissures in the asphalt surface), which is indicative of the HSI literature's prevailing preference for continuity-based approaches to urban feature mapping, even in the presence of distinct linear features.

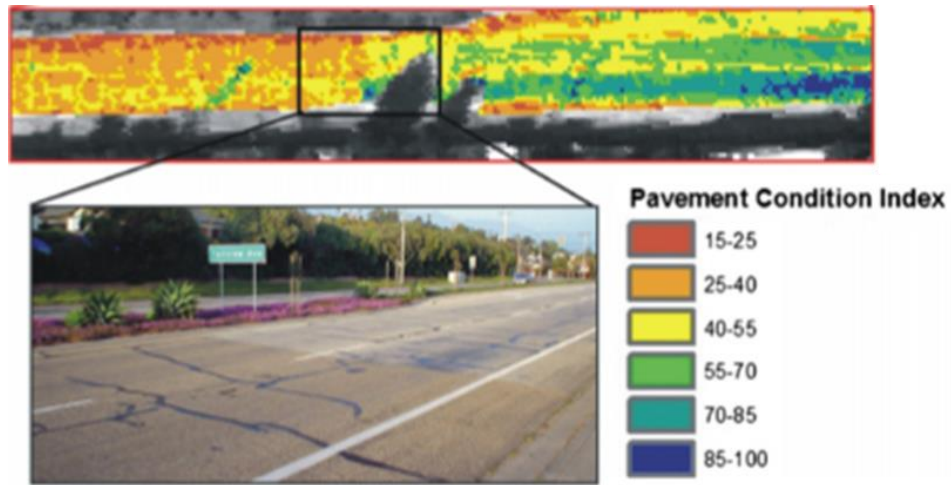


Figure 14: Urban Feature Mapping Derived from VNIR/SWIR HSI Data

In addition to conventional HSI applications, several boutique HSI applications deserve attention, such as trace chemical detection, oil spill mapping and material analysis. HSI's very high spectral resolution frequently enables it to detect very small quantities of a specific target material or chemical, sometimes at the subpixel level (i.e., a positive detection wherein the target material composes less than 100% of the pixel). Researchers have demonstrated HSI's ability to detect trace quantities of explosives such as dynamite, TNT, RDX, PETN and weaponized ammonium nitrate [54], [55], [56], [57], [58], [59], [60], [61]. These efforts are challenging because the target material is present

only in very small amounts, where high spectral resolution sampling is required to confidently detect and identify the chemical.

For example, consider the trace chemical detection results demonstrated by [54], which relied on HSI's high spectral resolution and a supervised classification approach to detect dynamite traces in handprints. The high-confidence results seen in Figure 15 are representative of HSI's ability to detect and identify trace materials present in only a small cluster of pixels or even a single pixel, as can be seen in the lower right of the image plane. However, researchers typically approach trace material detection problems only from an image classification perspective requiring *a priori* knowledge of target chemicals. These methods are difficult to generalize to uncharacterized datasets given the large volume of explosive chemicals that could be present. Therefore, the HSI literature currently relies heavily on assumptions regarding which chemicals are likely to be present, and could benefit from discontinuity-based edge detection research that does not assume prior knowledge of target material.

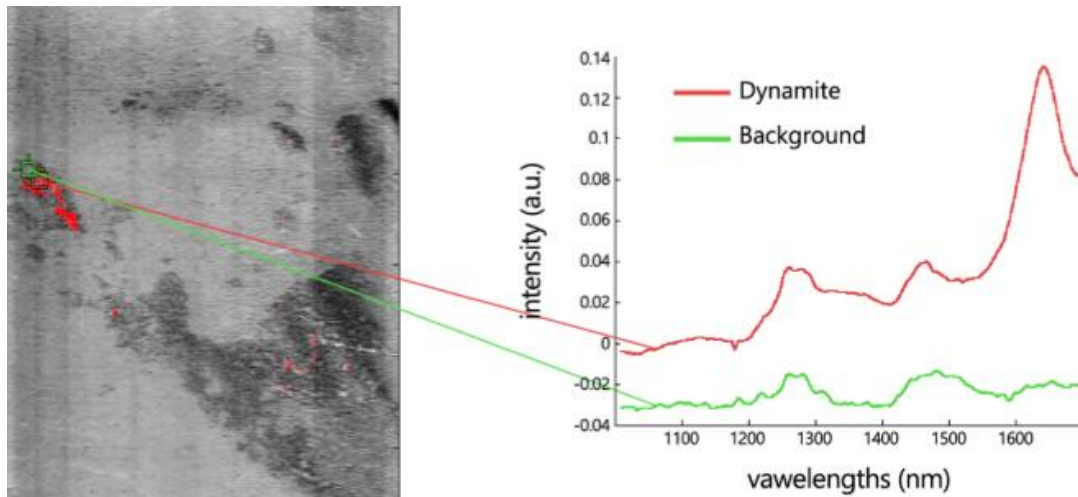


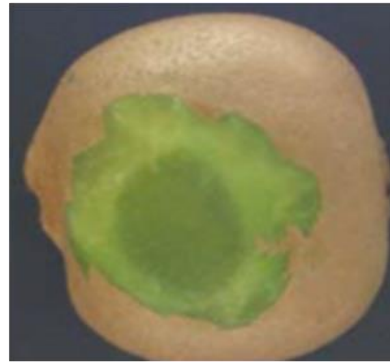
Figure 15: Trace Chemical Detection Using NIR HSI Data of a Human Handprint

Finally, HSI’s sampling advantage over MSI is on full display when searching for other sparse targets in complex backgrounds such as the detection of rare earth mineral traces [62], [63], underwater targets [64], [65] and sub-visual imperfections on food surfaces [66], [67]. For example, consider the results in [66], which used VNIR/SWIR “fruit bruise” signatures to reliably identify sub-visual bruising regions on the surface of kiwi fruit. Figure 16 presents the kiwi fruit samples and bruised detection plane, which clearly distinguishes bruised pixels from non-bruised pixels. Most importantly, note the highly similar spectral signatures of unbruised and bruised regions as depicted in Figure 17, which is an excellent example of HSI’s ability to discriminate between similar materials.

Sub-Visual Bruising on
Kiwi Fruit



Skin Peeling Reveals
Subcutaneous Bruising



HSI-Detected Bruising
on Unpeeled Kiwi Fruit

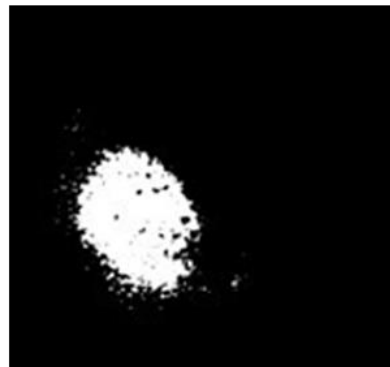


Figure 16: Supervised HSI Detection of Sub-Visual Fruit Defects

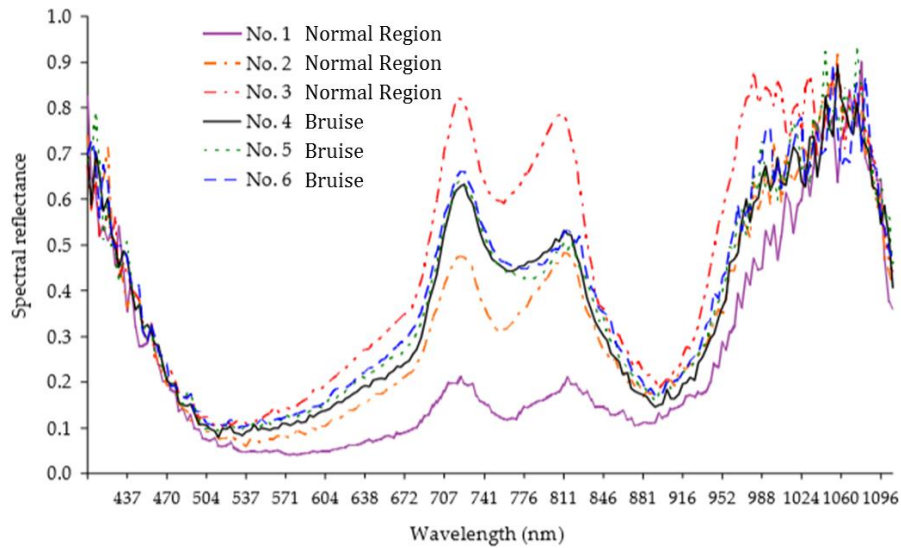


Figure 17: Spectral Similarity among Normal and Bruised Regions on Kiwi Fruit

While [66]’s results are encouraging from an image classification perspective, they rely heavily on accurate sampling of a scene-dependent signature, the kiwi bruise. Apple bruising, orange bruising, etc. are likely to present dissimilar bruise signatures, and orientation and lighting variabilities could also degrade [66]’s approach if applied to other materials. Indeed, the peer-reviewed HSI literature is dominated by scene-specific image processing techniques that take a “map the extent of this specific material” approach as opposed to a “delineate the boundaries of all materials in the scene” approach, which constitutes a well-respected but much smaller component of the literature. The disparity is understandable: supervised image processing techniques are more likely to generate satisfactory, publishing-friendly results than unsupervised results that operate with no knowledge of target and background materials and therefore are less likely to generate clean, crisp results. As will be seen, this dissertation directly addresses

this disparity by advancing HSI practice into the more challenging, unsupervised space of measuring boundaries around sparse, unknown materials.

Using HSI data to map oil spills is another relatively new application of HSI data. Only since the Deepwater Horizon oil spill have researchers accelerated the development of hyperspectral methods for estimating oil spill coverage on a water background [68], [69], [70], [71], [72], [73], [74], [75], [76], [77], [78] although a few pre-Deepwater Horizon studies produced favorable results, as well [79], [80]. These approaches are notable for their similarity – all of them approach oil spill detection from a continuity-based, image classification perspective and are dominated by simple band-ratio techniques. In general, all peer-reviewed HSI oil spill detection methods employ a supervised approach to quantifying and characterizing oil spill coverage by feeding the algorithms prior knowledge of an oil pixel’s spectral signature. None of the existing methods pursue oil spill mapping from a purely unsupervised, discontinuity-based approach that would be less scene-dependent and more robust to the highly variable oil-water reflectance signature.

For example, consider the methodology and results in [78], which is representative of the dominant approach of using continuity-based methods to map the extent of oil spills and characterize their physical characteristics (i.e., oil thickness, oil/water emulsion ratios, etc.). Figure 18 presents petroleum’s key reflectance absorption features that represent the spectral landmarks by which the researchers measure the similarity between pre-measured oil signatures and scene pixels. Specifically, [78] uses a simple least-squares fit to measure the correlation between

Deepwater Horizon oil spill pixels and known VNIR/SWIR signatures for different oil and oil/water emulsion signatures, which vary significantly according to the oil's surface thickness, emulsion ratio, surface winds, organic compounds present in the oil, etc., The least-squares goodness of fit approach is a commonly used image classification technique, but its sensitivity to intensity makes it a curious choice given the variability of oil emulsion reflectance spectra. Figure 19 contains an example of how surface conditions and oil/water mixing ratios can alter the position and intensity of the key absorption features in oil emulsion reflectance spectra.

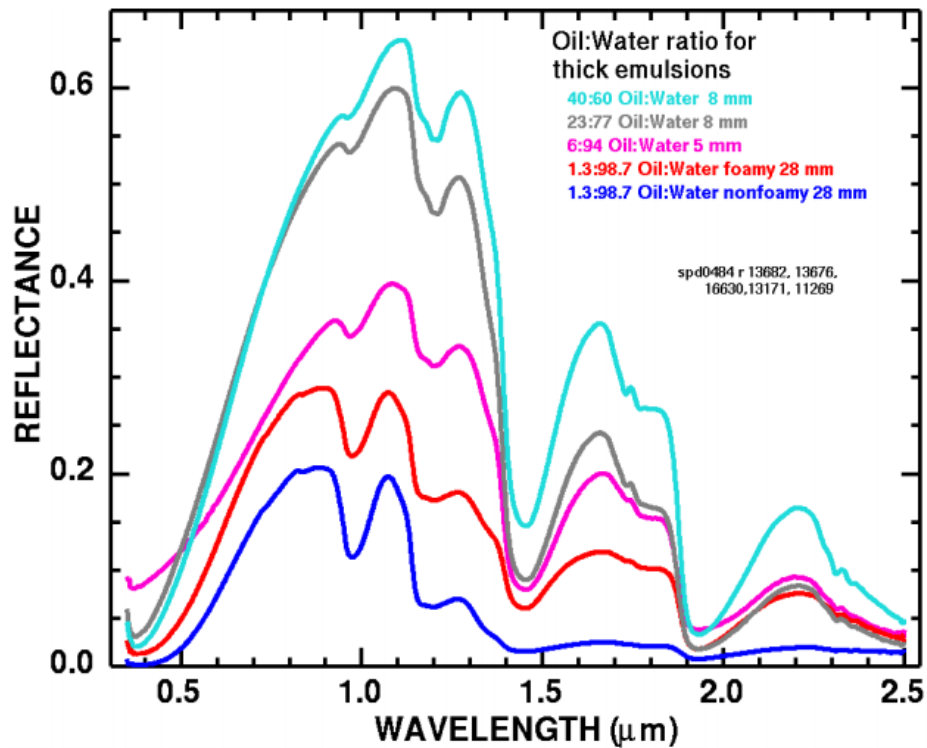


Figure 18: Key Petroleum Absorption Features in HSI Reflectance Data [78]

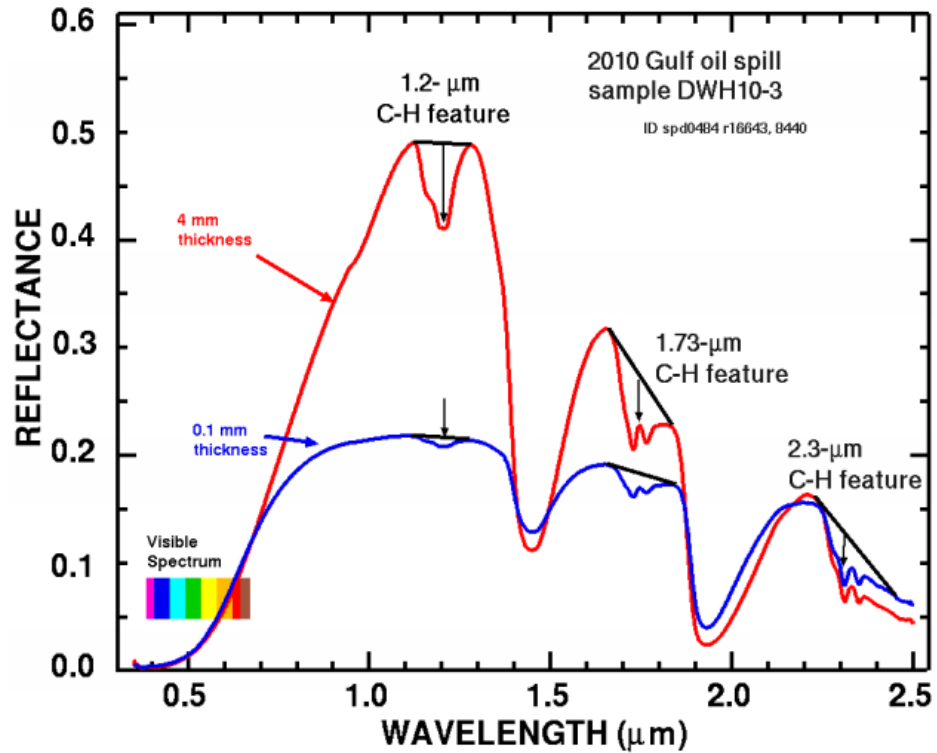


Figure 19: HSI Reflectance Spectra of Deepwater Horizon Oil Emulsions [78]

Figure 20 demonstrates that [78] generated satisfactory detection planes and was able to use HSI data to reliably detect and characterize oil spills on seawater. However, their results are at risk of being scene-dependent since their continuity-based methodology depends on detailed and extensive knowledge of a wide range of possible oil and oil/water mixture signatures in the Gulf of Mexico immediately after the Deepwater Horizon spill. Specifically, the authors fully characterized the unique background and target materials for that particular spill in those particular waters before applying a simple statistical similarity metric to determine goodness of fit between HSI scene pixels and fully characterized target materials.

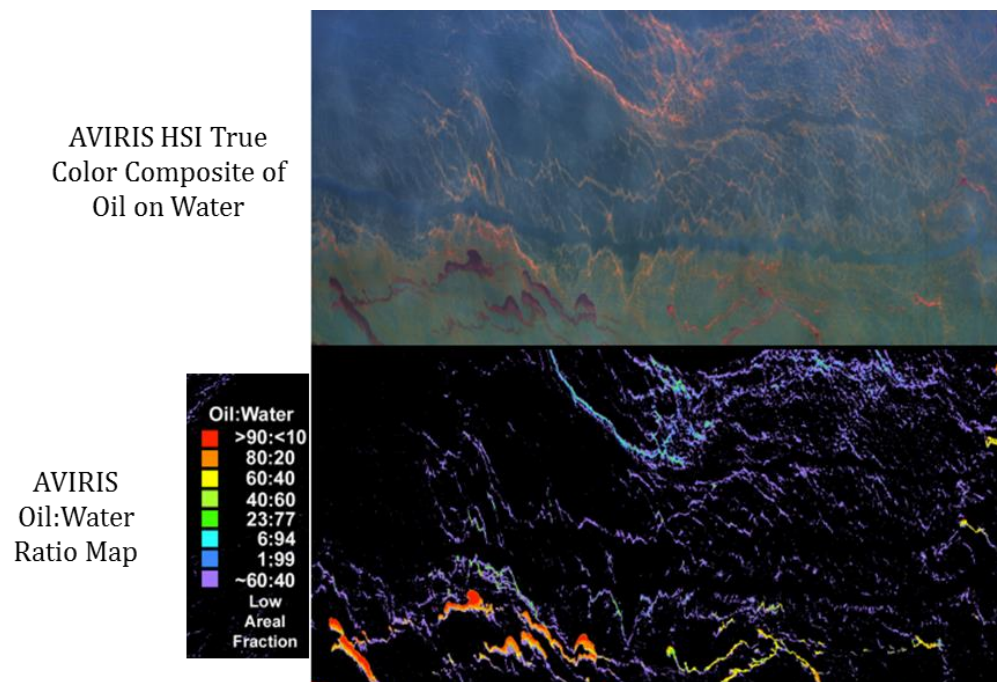


Figure 20: Deepwater Horizon Oil Spill Mapping Derived from AVIRIS HSI Data [78]

The emphasis on oil spill characterization and extent mapping to the exclusion of oil spill boundary identification represents a curious research gap given the utility of simply knowing the boundary between the oil spill and clean seawater as quickly as possible (i.e., first responders simply need to know where to position oil booms and other capture equipment, and they need to know it as soon as possible). As such, this dissertation endeavors to begin closing that gap by demonstrating the analytic speed, accuracy, and generalizability of edge detection methods for oil spills.

Finally, a small population of researchers spanning several scientific fields have used hyperspectral imaging to measure the surface homogeneity of manmade materials. Researchers have used HSI image classification and anomaly detection techniques to detect tampering on plywood cargo containers [81], measure surface patterns in

pharmaceutical tablets [82] [83], assess staining on historical documents [84], detect cracks in solar cells [85], characterize metallic pigments [86], and monitor a textile lamination process [87]. The breadth of HSI applications is impressive, but all of these studies employ either image classification or anomaly detection methods – none of them apply edge detection methods to their problem set, leaving a clear gap in the scientific literature for edge detection methods as applied to homogenous manmade material analysis.

However, the anomaly detection results in [81] strongly suggest that edge detection methods could be useful for measuring the homogeneity of manmade materials. Rivera [81] applied discontinuity-based anomaly detection methods to identify surface anomalies on wooden cargo containers in order to identify cargo tampering and smuggling activity. As seen in Figure 21, the approach produced reliable results in which linear surface anomalies are clearly recognizable. Given that anomaly detectors are discontinuity-based algorithms just like edge detection algorithms, [81]’s results lend optimism to the idea that HSI edge detection algorithms could map linear surface anomalies in manmade materials.

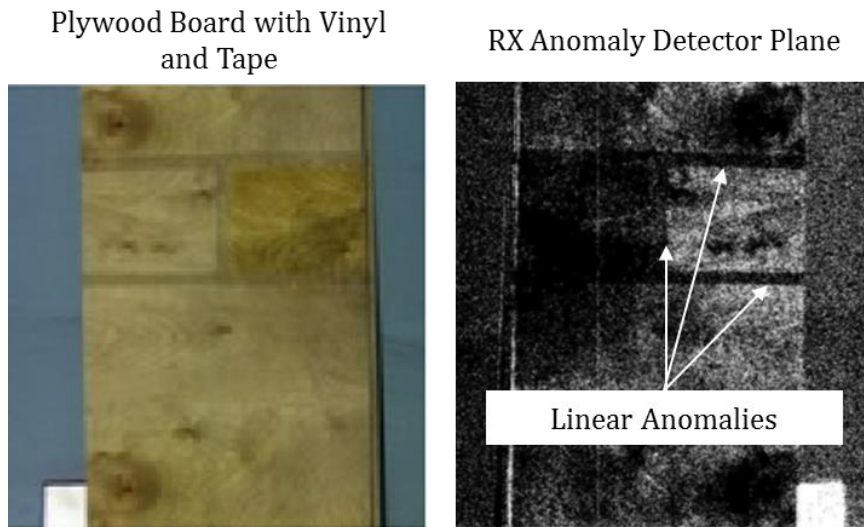


Figure 21: Linear Anomalies in a Homogenous Manmade Material [81]

In fact, an edge detection approach could produce superior results since it would measure edge discontinuities within a smaller neighborhood without considering the overall scene statistics as is done with the RX anomaly detector in [81]. The noisy RX plane in Figure 21 is an example of how anomaly detectors leveraging background statistics dominated by very similar pixels can struggle to generate clean anomaly planes.

Another interesting attempt to identify linear anomalies in manmade materials is seen in [85], which uses an image classification approach to identify cracks in solar panel cells. The approach is notable in the sense that rather than using an edge detector to locate the long, narrow cracks in the panels, it uses a common HSI image classification technique to identify a spectral signature the authors assert is unique to the crack itself. As seen in Figure 22, the approach generated reliable results, but the authors neither explain why they did not use an HSI edge detection method or at least generate a

conventional HSI edge plane for comparison. Clearly, the HSI edge detection literature could benefit from an examination of HSI edge detection methods as applied to manmade materials.

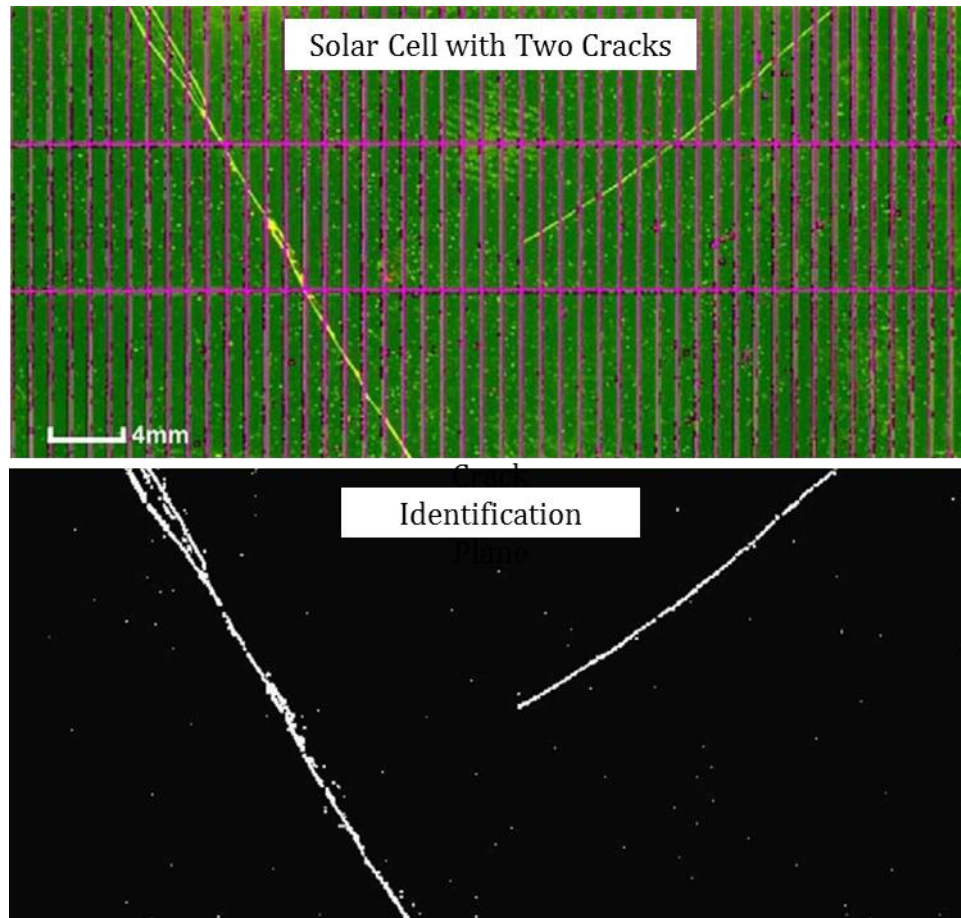


Figure 22: Cracks in Solar Cells as Identified by an HSI Image Classification Approach

Hyperspectral Remote Sensing Platforms and Data Types

To support the broad range of HSI applications, researchers collect HSI data from a variety of remote sensing platforms. The most common form of HSI collection is via

overhead platforms such as aircraft and spacecraft. Overhead assets typically provide optimal visibility of surface targets, particularly in rough terrain, and they can collect large volumes of data per collection mission. HSI at-aperture radiance data collected via overhead platforms must be corrected to reflectance, however, which adds complexity to HSI processing. For most earth remote sensing applications, overhead HSI collection is the preferred method due to its ability to reliably image large areas of variable terrain.

One of the most well-known airborne systems is NASA's Airborne Visible/Infrared Imaging Spectrometer (AVIRIS), which first began collecting HSI data in the late 1980's and has the most extensive data presence in the HSI literature [88]. AVIRIS collects spectral data across 224 channels spanning the VNIR/SWIR from 0.4 μm to 2.5 μm with a bandwidth of 10nm. AVIRIS collects data at a spatial resolution typically between 10m and 20m depending on the altitude of the collection, which varies between 4km and 20km above ground level (AGL) depending on the specific collection platform [88]. Figure 23 presents an example of a typical AVIRIS HSI image of manmade activity in rough terrain. Due to its data availability, history of reliable results and well-respected calibration methods, researchers regularly use AVIRIS data in a variety of earth remote sensing applications such as mineral mapping [89], oil spill environmental impact assessments [90], and forest fire severity measurements [91].



Figure 23: AVIRIS Scan of a Missile Field Test Site, New Mexico, U.S.A.

Like many airborne HSI sensors, AVIRIS is a whiskbroom sensor, meaning that the scan mirror oscillates back and forth across the scene, collecting one pixel at a time in only one direction [4]. The chief advantage of the whiskbroom approach is that every HSI scene pixel is imaged by the same single detector, meaning that the scene is collected with uniform radiometric sensitivity. Uniform sensitivity is highly desirable for many HSI applications, particularly atmospheric correction algorithm development.

Whiskbroom sensors like AVIRIS also generate smile-free data. The majority of HSI sensors are pushbroom and thus are impacted to some degree by spectral smile and keystone. The disadvantage of whiskbroom scanners is that aircraft velocity and

scanning speed must be tightly correlated to avoid pixel smearing, and the modest per-pixel dwell time limits spatial and spectral resolution. Figure 24 presents an overview of whiskbroom scanning and its close cousin, pushbroom scanning [92].

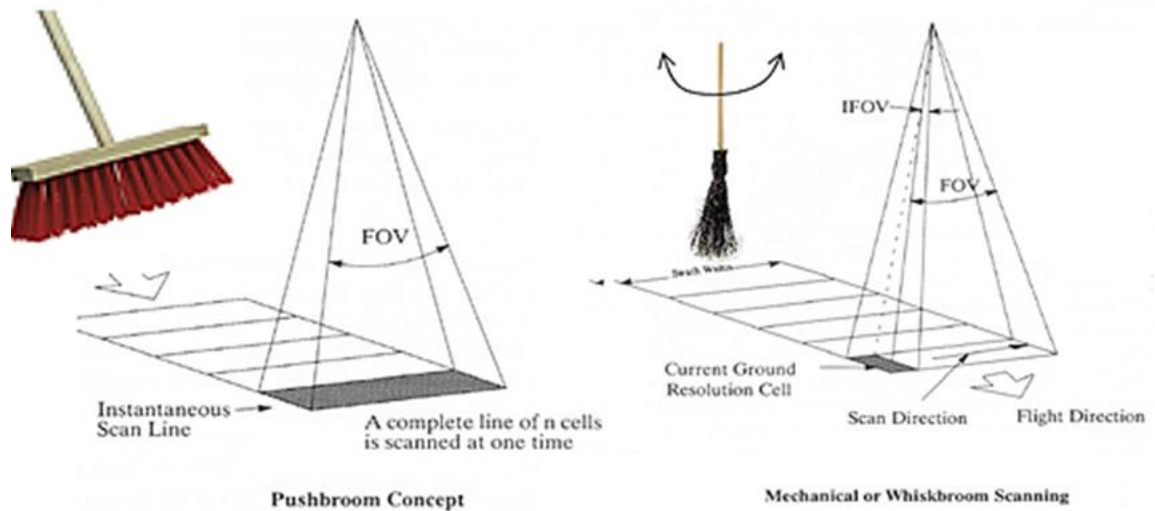


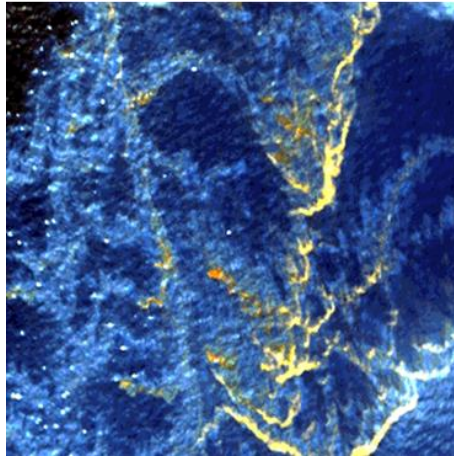
Figure 24: Pushbroom Scanning and Whiskbroom Scanning

Alternatively, airborne data can be collected by a pushbroom sensor that uses the collection platform's forward motion to build the HSI dataset one full line at a time [93]. In this manner, the pushbroom sensor uses a fixed detector array to collect the scene at a pixel width corresponding to the exact number of array detectors. The chief advantage of a pushbroom scanner is that it generates superior spatial and spectral resolution by virtue of its longer dwell time per pixel compared to a whiskbroom scanner. The pushbroom's fixed array can collect more light from a given pixel than can a whiskbroom's oscillating configuration that must move rapidly from pixel to pixel to build the scene.

The primary disadvantage of a pushbroom scanner is that its many detectors collect with unequal radiometric sensitivities. Additionally, whiskbroom scanners generate radiometrically consistent HSI datasets, while pushbroom scanners maximize spatial and spectral resolution. The optimal configuration depends entirely on the intended HSI application. Ultimately, all HSI sensors require calibration, and are generally HSI scanner type-agnostic.

An increasingly popular source for airborne HSI data is the ProSpecTIR hyperspectral sensor. SpecTIR is a private firm integrating airborne hyperspectral instruments specializing in VNIR/SWIR collections. ProSpecTIR's VNIR/SWIR sensors typically collect up to 620 channels between 0.4 μm and 2.45 μm and are designed with earth remote sensing applications in mind [94]. Additionally, the spatial resolution can vary between 0.52 m and 3.34 m depending on the focal length settings and altitude [95]. Figure 25 presents two of the most well-known ProSpecTIR datasets [96].

ProSpecTIR Deepwater
Horizon Oil Spill Data



ProSpecTIR Beltsville,
Maryland Data

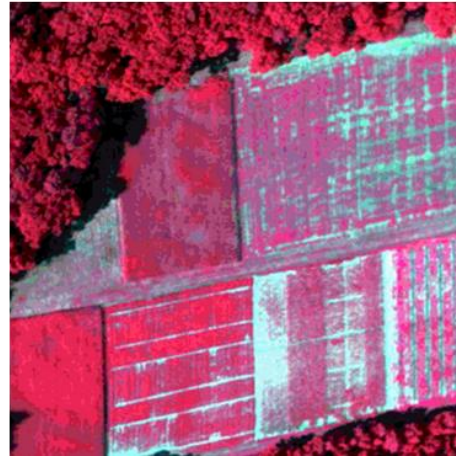


Figure 25: ProSpecTIR Sample HSI Datasets

SpecTIR is an attractive source for airborne data because it makes several ProSpecTIR datasets available for free, including a VNIR/SWIR cube over the Deepwater Horizon spill and a VNIR/SWIR cube over agricultural and other vegetation targets at Beltsville, MD [96] as seen in Figure 25. Like AVIRIS, ProSpecTIR has been used to support a variety of applications such as the oil spill and leaky pipeline detection [77], [79], [97], mineral mapping [98], [99], [100], urban feature mapping [53], vegetation health mapping [101], [102], [103] and invasive species detection [104].

Spacecraft, such as satellites, collect HSI data in the much the same manner as airborne collection platforms. Spaceborne sensors typically collect in a pushbroom configuration, such as NASA's well-known EO-1/Hyperion sensor [105]. Hyperion also is emblematic of the key drawback of spaceborne HSI sensors: spatial resolution. Although Hyperion collects a healthy volume of 220 VNIR/SWIR bands across a 7.5km

swath, it can achieve only 30m ground sampling distance (GSD) [105]. This spatial resolution limitation common to spaceborne HSI sensors typically limits their application to natural resource applications such as mining, geology, forestry, agriculture, and environmental management [106]. Figure 26 contains an example of Hyperion data collected over Washington, D.C [107]. Note the limited spatial resolution, which is likely to limit reliable edge detection results to the boundaries between major land cover classes such as urban, vegetation and water.



Figure 26: Hyperion HSI Data of Washington, D.C. USA

Ground-based sensors are another common method for collecting HSI data. Although they do not share the synoptic advantages of its airborne and spaceborne cousins, ground-based sensors' close proximity to their targets lends them significant advantages is spatial resolution. They also are much more affordable than overhead systems. Ground-based sensors' main advantage, however, is their deployment flexibility. Deployable from a variety of configurations, they can collect a wide range of targets indoors in laboratory settings, in outdoor settings looking outward at the horizon

or downward on a material, or in indoor settings looking at assembly line components, food safety materials, etc.

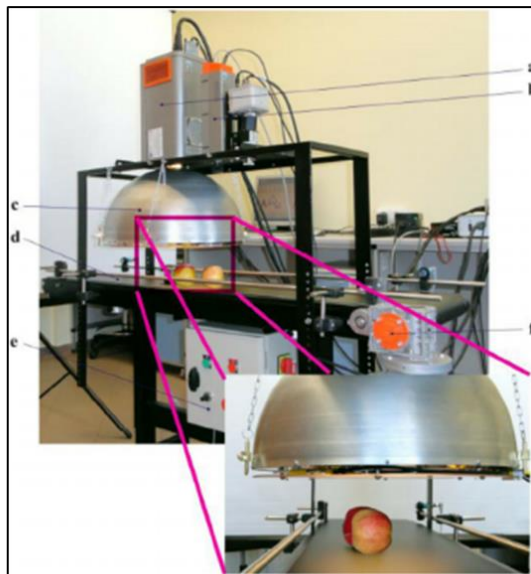
For example, consider the outdoor downward looking configuration in Figure 27. Close-access, downward looking collections are the most commonly employed configurations and are the optimal configuration for measuring *in situ* ground materials [29]. Additionally, consider the outward looking configuration in Figure 27.

Researchers frequently use outward looking configurations to collect HSI data on vertical features such as rock faces [62]. The hyperspectral data collected by both outdoor configurations typically are indistinguishable when collected under similar environmental conditions and range to target, as well.

Outdoor Downward Looking Configuration



Indoor Downward Looking Configuration



Outward Looking Configuration

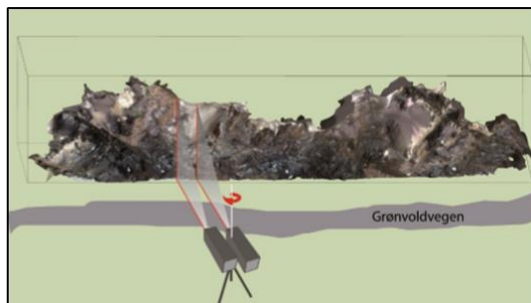


Figure 27: Ground-Based HSI Sensor Configurations [62], [29], [108]

Indoor downward looking configurations such as the one seen in Figure 27 are the optimal configuration for collecting pure spectra under controlled conditions in a

laboratory [108]. Researchers working in a lab can control incident lighting, easily correct the impact of the atmosphere around the sample in order to more closely approximate the samples' true reflectance signature than overhead sensors that must overcome uncontrolled environmental conditions such as adjacency effects.

For edge detection research, lab collections provide two key advantages compared to overhead collections: very-high spatial resolution measurements and measurements of subpixel features. For example, researchers can attach powerful optics to laboratory HSI sensors, enabling very-high spatial resolution measurements of complex materials such as mineral assemblages, as seen in Figure 28 [109]. The resulting datasets contain a unique combination of high spectral resolution and high spatial resolution – optimal conditions for edge detection research attempting to maximize the utility of spatial and spectral information. Figure 28 also demonstrates how laboratory collections enable the collection of sub-visual features such as the complex arrangement of constituent minerals within a rock sample.



Figure 28: Very High Spatial-Resolution Laboratory HSI Measurement of Granite Sample

An emerging class of ground-based HSI data is known as microscene data. Engineered by the researcher, an HSI microscene is a lab-based configuration of specific materials of interest, confusers and background materials in pre-determined quantities and arrangements according to the researcher's needs [110]. HSI microscene data are fully customizable datasets designed to simulate real-world conditions in a controlled environment. The microscene approach enjoys many advantages including cost, ease of use, repeatability and controllability. Most importantly, microscene data can serve as a reliable analogue for real-world data, as demonstrated in [110]. Figure 29 presents an example of how a laboratory HSI sensor collects against a microscene configured within a petri dish, while Figure 30 contains an example of the collected microscene [110].

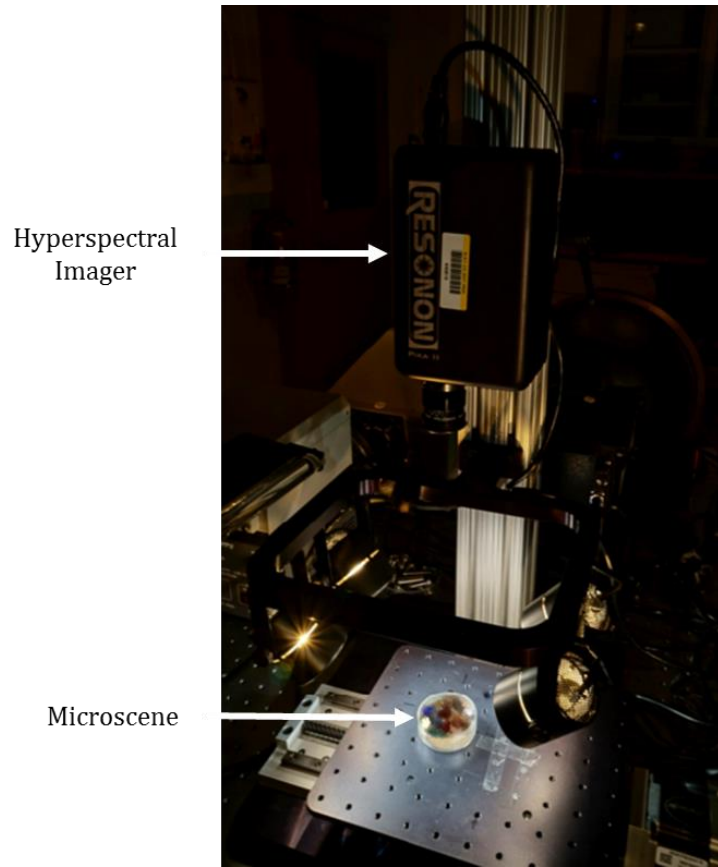


Figure 29: HSI Microscene Data Collection [110]

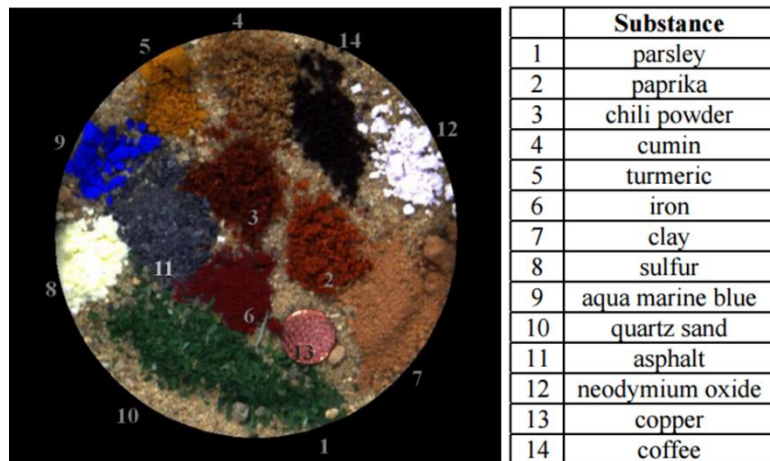


Figure 30: True Color HSI Microscene Data and Material Key [110]

The Hyperspectral Processing Chain

As seen in Figure 31, the full hyperspectral exploitation process spans four distinct stages: Atmospheric Correction, Detection, Identification, and Quantification. Following the receipt of radiance data from the sensor, researchers use atmospheric correction algorithms to generate apparent reflectance data on which the rest of the processing chain depends. The Quick Atmospheric Correction (QUAC) algorithm and the Fast Line-of-Sight Atmospheric Analysis of Spectral Hypercubes (FLAASH) algorithm are the two most commonly used atmospheric correction methods in hyperspectral remote sensing [9], [10], [111], [112]. Due to its speed, reliability and ease of use, QUAC has become the most popular method for removing atmospheric effects (e.g., scattering and absorption) from radiance data, and generally produces results comparable to the more robust FLAASH method.

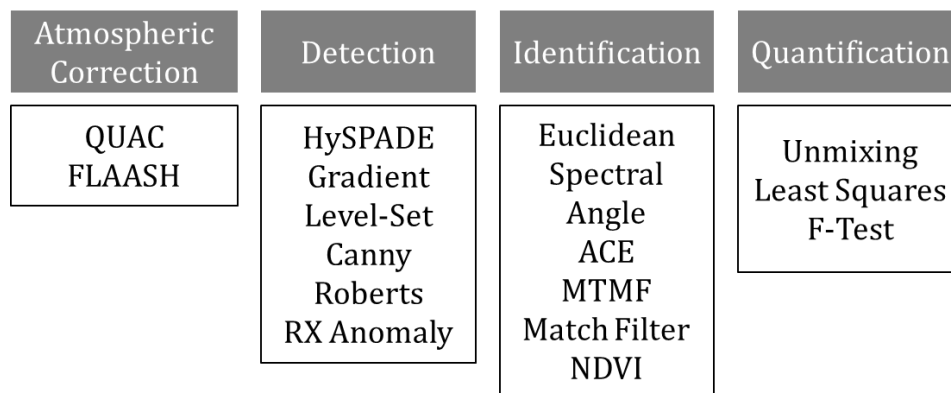


Figure 31: From Radiance to Reflectance, The Four Stages of the Hyperspectral Processing Chain

QUAC's primary advantage is that it uses in-scene techniques for estimating reflectance, as opposed to FLAASH which requires the researcher to provide atmospheric modeling inputs which may or may not be known or discoverable. Indeed, the difficulty of identifying FLAASH's atmospheric model input parameters in the absence of high quality metadata renders FLAASH unusable for most HSI data, particularly challenging, non-traditional HSI datasets that typically lack robust atmospheric metadata. QUAC overcomes the metadata problem by relying on in-scene parameters to correct for atmospheric absorption and scattering effects, and therefore is the optimal atmospheric correction algorithm for this study's challenging and non-traditional HSI datasets and applications.

Additionally, QUAC's in-scene approach is optimized for VNIR/SWIR hyperspectral data, which makes it an excellent choice for the VNIR/SWIR tests in this work [9]. QUAC is used in this work wherever possible due to its consistently demonstrated ability to quickly and reliably generate reflectance data from a wide variety of sensor viewing angles, sun angles, illumination intensities, radiometric calibration errors and wavelength calibration errors, and its ability to estimate reflectance from scenes containing complex natural backgrounds and manmade materials [10]. Considering the diversity of HSI applications and datasets addressed by this dissertation, QUAC's flexibility and accuracy make it the most attractive and expedient choice for the atmospheric correction phase of the HSI processing chain.

Accepting radiance data as input, QUAC begins retrieving approximate reflectance spectra by assuming a linear relationship between spectral reflectance and

measured radiance, a good approximation for most scenes [9]. QUAC then uses in-scene information to derive the key atmospheric compensation parameters such as aerosol optical depth, column water vapor and visibility. Next, QUAC uses these atmospheric compensation parameters to develop the radiation-transfer model seen in Equation 1.

$$\rho_j(\lambda) = A(\lambda) + B(\lambda)\rho_j^o + C(\lambda) \langle \rho(\lambda) \rangle$$

Equation 1: QUAC's Radiative Transfer Model [9]

In Equation 1, $\rho_j(\lambda)$ is the radiance at the j'th pixel for a spectral band centered at wavelength λ , ρ_j^o is the true reflectance at the j'th pixel, and $\langle \rho(\lambda) \rangle$ is the spatially averaged surface reflectance. A, B and C are coefficients that describe the atmospheric transmission and scattering effects as seen in Figure 32, where A accounts for light that never encounters the surface but is scattered and absorbed within the atmosphere, B accounts for the direct sun-surface-sensor path transmittance traceable to a single pixel, and C accounts for diffuse transmittance paths traceable to adjacent pixels scattering their information into the sensor [9]. Ultimately, QUAC's Equation 1 uses solely in-scene information to output an atmospheric model unique to the hyperspectral scene.

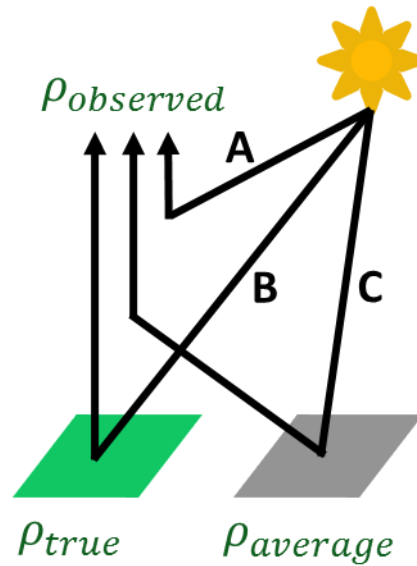


Figure 32: Radiative Transfer Contributions to QUAC [9]

With the radiative transfer model in place, QUAC then uses an endmember extraction tool to identify at least ten diverse pixel spectra (i.e., unique materials) within the scene. By identifying several unique materials, QUAC can estimate the baseline and standard deviation curves for the scene – two of the three inputs needed for atmospheric correction (the radiative transfer model is the third input). Next, QUAC measures the baseline spectrum by identifying the lowest radiance value at each channel for each material, and calculates the standard deviation curve for the collective diverse pixel spectra. With the radiative transfer model, baseline spectrum and standard deviation curve in place, QUAC atmospherically corrects the hyperspectral radiance data to apparent reflectance [9].

Most versions of QUAC, including the one available in ENVI, also attempt to remove the major atmospheric water vapor absorption bands centered at 1.38 μm and

1.88 μm and occasionally some of the low signal to noise (SNR) bands that appear at the extreme upper and lower wavelength ranges of a sensor. However, QUAC often fails to remove a sufficient number of bands near 1.38 μm and 1.88 μm and nearly always fails to remove all of the noisy bands at the extremes. Additionally, QUAC often fails to properly compensate for the 0.760 μm oxygen band, particularly in scenes with little to no vegetation. None of these irregularities present a barrier to research but occasionally require the researcher to manually remove additional bad bands. Given the non-traditional and challenging datasets examined herein, additional bad band removal likely will be required to maximize the quality of QUAC's apparent reflectance estimate.

With reflectance data in hand and the atmospheric correction phase complete, the hyperspectral processing chain advances to the detection process in which the researcher endeavors to extract unique scene elements, such as anomalous materials, edge features, etc. Note that the detection phase is distinct from the identification phase, which attempts to assign a material composition (e.g., alunite, plastic, broadleaf weed, etc.) to a detected scene element. HSI detection algorithms necessarily pursue a discontinuity-based strategy in which the algorithm attempts to declare that a given pixel is unlike its neighbors, be it an anomalous pixel, an edge pixel, an error pixel, etc. Additionally, HSI detection methods tend to be much more generalizable than their image classification peers since they do not require *a priori* knowledge of the materials for which to search.

HSI target detection simply extends the yield from visual examination by making extensive use of the spectral content of the data, most commonly through statistical and geometric measurements in n -dimensional space. However, the objective of target

detection remains the same regardless of data type: identify anomalous pixels for further examination. For example, hyperspectral detection algorithms such as the Reed-Xiaoli (RX) anomaly detector are akin to the literal visual detection methods used for panchromatic imagery in the sense that the detection algorithm searches the scene for a small number of incongruous pixels surrounded by background pixels [113], [114].

As seen in Equation 2, the RX anomaly detector simply calculates the Mahalanobis distance between a sample pixel vector (x) and the scene's mean vector (μ) normalized by the scene's covariance matrix (C). When the vector distance exceeds a user-defined threshold, RX declares the sample pixel to be an anomaly.

$$RX \text{ Anomaly Score} = (x - \mu)^T C^{-1} (x - \mu)$$

Equation 2: The Reed-Xiaoli Anomaly Detector [4]

For the research in this dissertation, the important aspect of RX anomaly detector implementation is the absence of a specific target spectrum. In this manner, RX is representative of HSI detection algorithms in that it will extract discontinuities in the scene without identifying them – a very useful precursor to the next step in the HSI processing chain, identification. Given their centrality to this dissertation, HSI edge detection methods are given full descriptions in later sections – RX is presented here as an introduction to discontinuity-based HSI detection algorithms.

Following the detection process, the HSI processing chain advances to the identification process in which the researcher attempts to either identify all materials in the scene or identify all instances of a specific material in a scene. In both cases, the

researcher knows what materials he or she is looking for, and often uses the results from the detection process to narrow down the scene to the areas of highest interest.

The algorithms used in the identification step of the hyperspectral processing chain mark a clear departure from the methods available to panchromatic and most multispectral efforts. As discussed, the spectral content of HSI data allows scientists to not only distinguish among different materials but to put a specific name to them. For example, most MSI identification methods will identify a pixel as vegetation, bare earth, etc., while HSI identification algorithms can identify the pixel as polypropylene [115], magnesite [116], etc.

HSI identification algorithms can be grouped into three classes: geometric, statistical, and spectroscopic [4]. Geometric algorithms such as spectral angle mapper (SAM) and Euclidean distance (ED) attempt to characterize a pixel vector based on its spatial orientation in n -dimensional space. For example, ED measures the straight line distance between two samples as seen in Equation 3, where x is the reference spectrum, y is the pixel spectrum, and K is the number of spectral channels [117].

$$\|x - y\| = \sqrt{\sum_{k=1}^K (x_k - y_k)^2}$$

Equation 3: Euclidean Distance [117]

ED is sensitive to pixel intensity because it measures the straight-line distance between the vector endpoints, meaning that it frequently underestimates the similarity between

two similar samples collected at different illumination levels. For example, shadowing effects caused by rugged terrain or a low sun angle can inject uncertainty into ED results.

In contrast, SAM measures the angular distance θ between a reference spectrum x and a pixel vector y in n -dimensional space where a small angular distance indicates similar spectra, as seen in Equation 4 [117].

$$\theta = \cos^{-1} \frac{x^T y}{\|x\| \|y\|}$$

Equation 4: Spectral Angle Mapper [117]

Researchers frequently use SAM as an identification tool because it considers only the angle between the target and reference tool, meaning that it is insensitive to intensity. Consequently, SAM tends to be more reliable than ED within a given scene due to variations in intensity common to remote sensing data. However, SAM's chief limitation is that it does not consider the covariance of the background statistics, meaning that it can perform poorly against highly mixed pixels [118].

Statistical measurements overcome the mixed pixel limitations by characterizing the fundamental statistical parameters of HSI data in n -dimensional space, the mean vector and the covariance matrix. For example, one of the most commonly used statistical target detection algorithms is the spectral matched filter (SMF) as given in Equation 5, where x is the target vector, y is the sample vector, m is the background mean spectrum, and S^{-1} is the sample background covariance matrix [4].

$$SMF(y) = (x - m)^T S^{-1}(y - m)$$

Equation 5: Spectral Matched Filter [4]

SMF measures the similarity between two vectors by projecting a demeaned and whitened target vector onto a demeaned and whitened reference vector [4]. The advantage in operating in whitened space is that the algorithm can remove much of the background signal from the pixel spectrum, thereby increasing the likelihood of detection compared to a geometric algorithm that struggles to detect subpixel targets.

A significant portion of the remaining statistical tools are based on or similar to MF, including the adaptive cosine estimator (ACE) and the mixture-tuned matched filter (MTMF). ACE, in particular, has proven to be a reliable statistical algorithm applicable to a wide variety of backgrounds and targets [119]. As seen in Equation 6, ACE is simply the MF normalized by the product of the magnitude of the reference spectrum in the MF space and the magnitude of the pixel spectrum in MF space, where x is the reference vector, y is the pixel vector, S^{-1} is the sample background covariance matrix, and m is the mean background vector [4], [120].

$$ACE = \frac{[(t - m)^T S^{-1}(x - m)]^2}{[(t - m)^T S^{-1}(t - m)][(x - m)^T S^{-1}(x - m)]}$$

Equation 6: The Adaptive Cosine Estimator (ACE) [4]

Occasionally, ACE is treated as a geometric algorithm since it executes the SAM computation in whitened space by inserting the inverse covariance matrix into each of the

three dot products computed by SAM, making the ACE result equal to the cosine square of the angle between the target pixel and sample pixel in whitened space [4], [117], [119]. That this dissertation treats ACE as a statistical algorithm since it is treated as such in most of the literature.

Spectroscopic algorithms comprise the final class of spectral identification algorithms and attempt to take advantage of diagnostic sections of spectra in n -dimensional space, such as key absorption features or the position of the red edge [121], [122]. The most common type of spectroscopic algorithm is a normalized index consisting of two or more bands. Equation 7 presents the most widely used index is the normalized difference vegetation index (NDVI), which attempts to identify vegetation by normalizing the difference between the intensity in the NIR channels and the green channels by the sum of the selected channels [123].

$$NDVI = \frac{(\rho_{NIR} - \rho_{Red})}{(\rho_{NIR} + \rho_{Red})}$$

Equation 7: Normalized Difference Vegetation Index [4]

Researchers have developed dozens of spectroscopic NDVI variants to identify vegetation and to measure vegetation health [38]. For example, researchers have tested a variety of indices to measure the efficiency with which vegetation is able to use incident light for photosynthesis. The photochemical reflectance index (PRI) is one such index, which measures carotenoid pigment coverage by calculating the normalized difference between reflectance at the 531nm band and the 570nm band [124]. The PRI's calculated

index value is a measure of plant health rather than simply vegetation identification, and is characteristic of the many similar spectroscopic indices that explore the relationships between a small set of spectral channels to measure plant health. Ultimately, spectroscopic algorithms are useful for narrow vegetation studies, but their reliance on a few select spectral channels tends to ignore the chief contribution of HSI data: high spectral resolution.

Although not advanced in this work, the HSI processing chain's final phase, quantification, warrants mention. The primary objective of the HSI algorithms in the quantification/measurement phase is to determine the fractional abundance of a given material within an individual pixel [4]. For example, linear spectral unmixing models assume that a pixel spectrum is a linear combination of all of the pure endmember spectra present within the material, meaning that if the endmembers are known, a set of linear equations can be used to determine the fractions for each material [4]. The majority of HSI unmixing algorithms are based on the linear mixture model seen in Equation 8, where R_x is the reflectance of a given pixel in the x th of z spectral bands, n is the number of mixture components (i.e., cover types), f_i is the fractional component of endmember i , a_{xi} is the reflectance of endmember i in spectral band x , and e_x is the error at spectral band x [125].

$$R_x = \sum_{i=1}^n a_{xi} f_i + e_x$$

Equation 8: The Linear Mixture Model [4]

Although quantification algorithms such as spectral unmixing typically are applied much later than edge detection efforts in the HSI processing chain, edge results as pursued in this dissertation can inform spectral unmixing algorithm development and application. For example, HSI edge detection algorithms are going to find linear discontinuities in the scene, which will often present as the most heavily mixed pixels along the boundaries of two different materials. Edge maps, therefore, can serve as cueing mechanisms for unmixing algorithms searching for the most heavily mixed pixels.

At the conclusion of a full HSI processing chain, every material in the HSI data cube has been detected, identified, and measured for abundance. Of course, not all steps need to be performed for every target, and not all targets are always identified. Additionally, many applications do not require the full chain and need only a component to achieve success. For example, urban feature mapping does not require HSI quantification algorithms to be successful, nor does atmospheric correction research require anomaly detection algorithms to create usable atmospheric models. The right balance of HSI processing chain elements is ultimately up to the researcher and the application under study.

Traditional Panchromatic Edge Detection Methods

For most of remote sensing's history, researchers have developed edge detection methods primarily for panchromatic imagery – a reality that makes sense considering that panchromatic sensors have dominated the overwhelming majority of remote sensing history. Traditional edge detection methods apply a kernel-based approach to measure edge strength in one or more directions within a single band, meaning that they tend to

exploit local scene information to identify edges in a single gray-scale image.

Understanding this history and recognizing how traditional, panchromatic edge detection methods can be optimized for HSI data is a key prerequisite for charting the course towards new HSI edge detection methods.

Traditional panchromatic edge detection approaches typically measure the similarity of pixel digital counts (i.e. gray-levels) in a local area defined by an n -sided kernel [126]. In such cases, a kernel is convolved across an $i \times j$ scene to generate an $i \times j$ output plane in which each pixel represents the kernel's calculation over the same pixel in the original image. After the algorithm applies a threshold to the output plane, the remaining pixels represent what are known as edge pixels and are typically rendered as gray-to-white pixels in the edge plane.

Importantly, most edge detection algorithms operate on a per pixel basis rather than on the scene in its entirety. This realization leads to a necessary clarification of the general objective of an edge detection algorithm. One could argue that rather than finding edges among different materials, edge detection algorithms identify individual pixels that are different from the pixels in their neighborhood in a very specific way, namely that the pixel is at a crucial position along a gradient. In this manner, traditional panchromatic edge detection algorithms are similar to many HSI anomaly detection algorithms in the sense that they both attempt to use a kernel convolution to identify pixels with unique characteristics or a change between neighboring pixels. This overlapping functionality explains why anomaly detection algorithms and edge detection algorithms both operate

with the detection phase of the HSI processing chain, and helps justify why this study's HSI edge detection algorithms emphasize discontinuities in HSI data.

Finally, this dissertation measures edge detector performance according to the six criteria established by Canny [1]. First, the edge detector should perform with low false positive and false negative rates such that real edges in the scene should not be missed and that false edge pixels should not be returned. Secondly, the edge detector should correctly localize the edge points such that the operator's edge pixels should be as close as possible to the center of the true edge. Thirdly, the detector should generate only one response to a single edge [1]. Canny's minor criteria such as robustness to noise and unbroken edges also are considered, as well.

The Roberts Operator

Among traditional edge detection methods, the Roberts edge detection algorithm is one of the simplest and most well-understood panchromatic edge detection algorithms in the scientific literature. As seen in Figure 33, the algorithm functions as a regional operator by convolving two 2×2 kernels that use cross differences to calculate a gradient magnitude image [15], [127]. Specifically, by measuring the sum of the squares of the differences in intensity between diagonally adjacent pixels, the Roberts operator generates an approximation to the continuous gradient at the interpolated point, but not at the actual point [128].

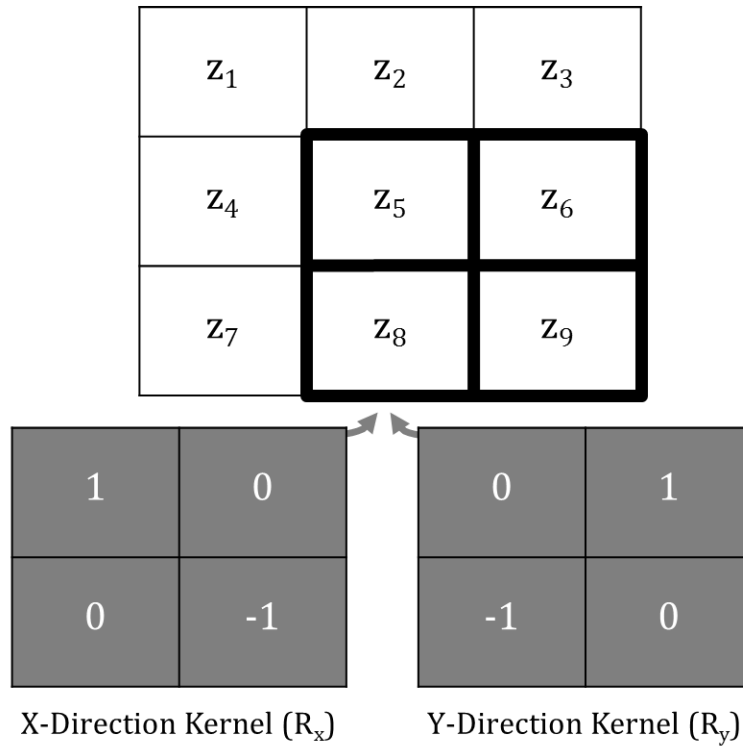


Figure 33: Roberts Cross-Gradient Kernels [127]

Optimized to respond most strongly to 45° edges, the Roberts operator convolves the two kernels in Figure 33 to calculate the cross gradient partial derivatives according to Equation 9 in which $R_{i,j}$ is the computed derivative value (i.e., the pixel's edge strength or the probability of an edge passing through pixel i, j) and Z_n is a scene pixel as depicted in Figure 33 [127].

$$R_{i,j} = \sqrt{(Z_8 - Z_6)^2 - (Z_5 - Z_9)^2}$$

Equation 9: Roberts Cross-Gradient Operator [127]

The Roberts operator is attractive for many panchromatic applications due to its simplicity, computational speed and generally reliable results against edges where there is a rapid change in intensity (i.e., high-contrast edges) [129], [130], [131]. For example, consider the Roberts edge plane in Figure 34 [129]. In the presence of the high-contrast edges between dark chromosomes against a white background, Roberts generates clean, reliable edge planes at high computational speeds. Robert's primary advantage is to quickly identify easy-to-find edges – a useful edge detection method for applications characterized by imagery with highly-controlled backgrounds such as seen in the medical sciences.

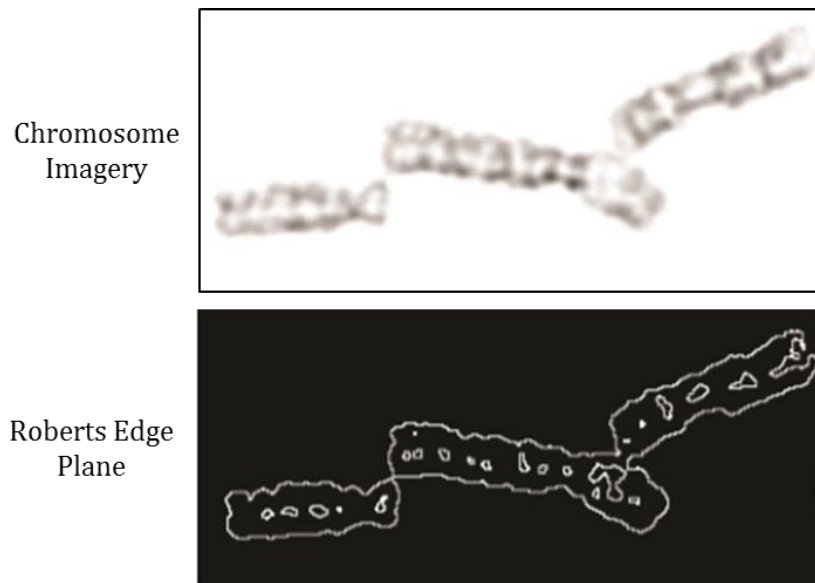


Figure 34: Roberts Edge Plane for High-Contrast Panchromatic Imagery [129]

However, Robert's spatially short gradient measurements can limit its ability to detect minor edges in non-traditional, challenging imagery and its ability to detect edges in the presence of noise [132], [133], [134], [135], [136]. For example, consider the weak Roberts edge plane in Figure 35, which was generated from wood grain imagery with subtle, low-contrast edges. As seen, Roberts generated broken, partial edge information, which is characteristic for Roberts' results against low-contrast edges. Ultimately, this dissertation expects Roberts' demonstrated limitations to restrict its ability to extract reliable edge information from the challenging, non-traditional imagery pursued herein.

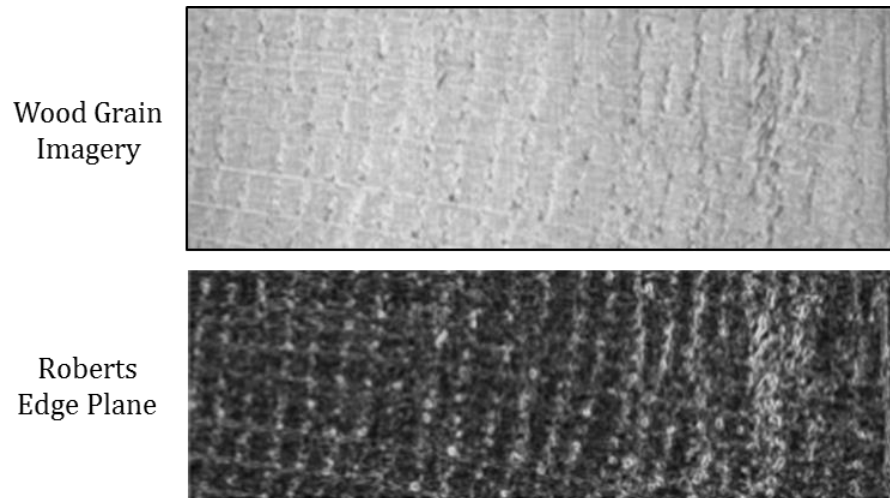


Figure 35: Roberts Edge Plane for Challenging, Non-Traditional Imagery [132]

The Sobel Operator

To improve upon Robert's 2 x 2 cross-gradient sampling, the Sobel operator employs 3 x 3 kernels to measure the cross-gradient strength of edge information in

panchromatic imagery, as seen in Figure 36 [15], [137]. Optimized to detect vertical and horizontal edges, the Sobel operator is more isotropic than the bi-directional Roberts operator because its 3 x 3 kernels aggregate all four possible central gradient estimates obtainable in a 3 x 3 neighborhood [137]. Specifically, the Sobel operator averages the four directions as seen in Equation 10 where S_x and S_y correspond to the Sobel masks in Figure 36, and $S_{i,j}$ is the edge strength at pixel i,j [137].

$$S_{i,j} = \sqrt{S_x^2 + S_y^2}$$

Equation 10: The Sobel Operator [137]

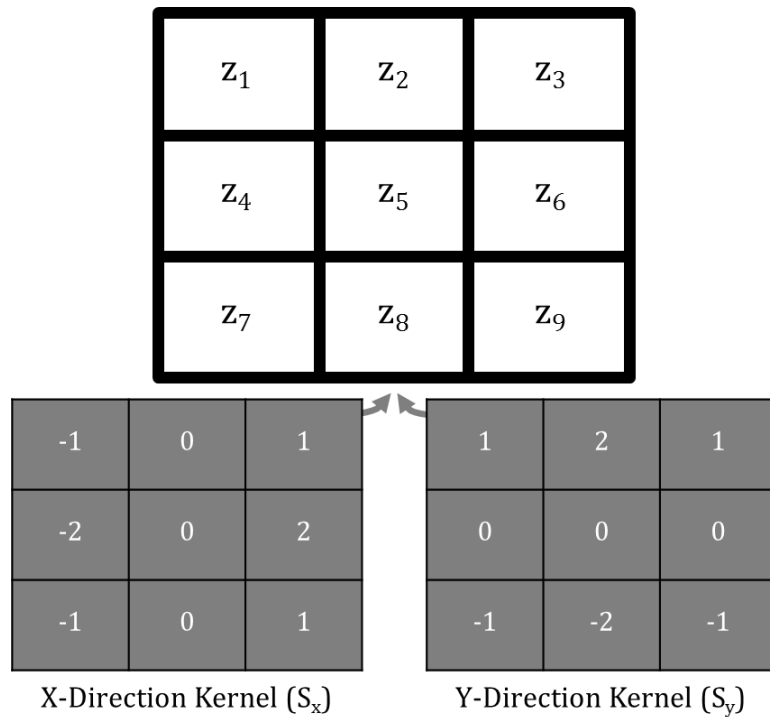


Figure 36: Sobel Operator 3 x 3 Kernels [137]

The Sobel operator is a popular choice among researchers due to its isotropic behavior, computational speed, low false negative rate and improved ability against low-contrast edges in the presence of noise [132], [138], [139], [140], [141]. For example, compare the Robert's edge plane in Figure 35 to the Sobel edge plane in Figure 37 [132]. Note that where the Roberts operator was unable to extract meaningful edge information from the wood grain imagery, Sobel was able to generate a coherent edge map containing vertical and horizontal edges. The Sobel operator's more precise gradient measurements and improved isotropy clearly mark it as an improvement over the Roberts operator, and also explains why edge detection researchers typically use it for baseline comparison purposes more frequently than they use Roberts.

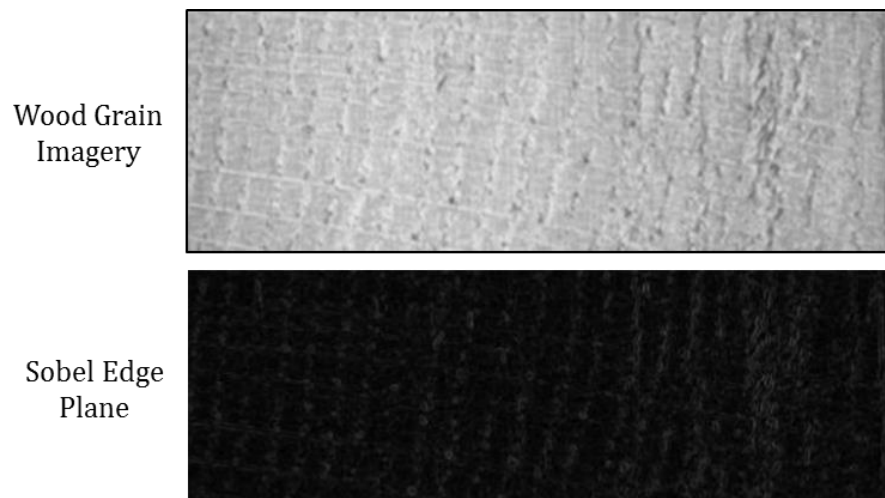


Figure 37: Sobel Edge Plane for Challenging, Non-Traditional Imagery [132]

The Sobel operator's primary disadvantages are that it is not optimized for edge detection accuracy and can obscure closely-spaced edges [15], [129], [142], meaning that

the operator is adequate for detecting edges, but it does not always render them in the correct position in the edge plane. Instead, Sobel's Gaussian-like smoothing behavior adds uncertainty to its results, which present as broad, multi-pixel (i.e., smoothed) edge lines as opposed to crisp, single-pixel edge lines. For many applications, simply knowing that an edge is present is sufficient, but for applications that require precise edge mapping, more robust edge detection techniques are required.

For example, consider the Sobel edge plane in Figure 38, which is the Sobel companion to the precise Roberts edge plane in Figure 34 [129]. While the Roberts edge plane is characterized by crisp, single-pixel edges, the Sobel edge plane is composed of broad, imprecise edges that obscure the internal detail evident in the Robert's plane and fail to communicate a clear edge location. To summarize, Robert's excels at generating clean, crisp edge information but with a high false negative rate, while Sobel has a low false negative rate but struggles to generate highly accurate edge information.

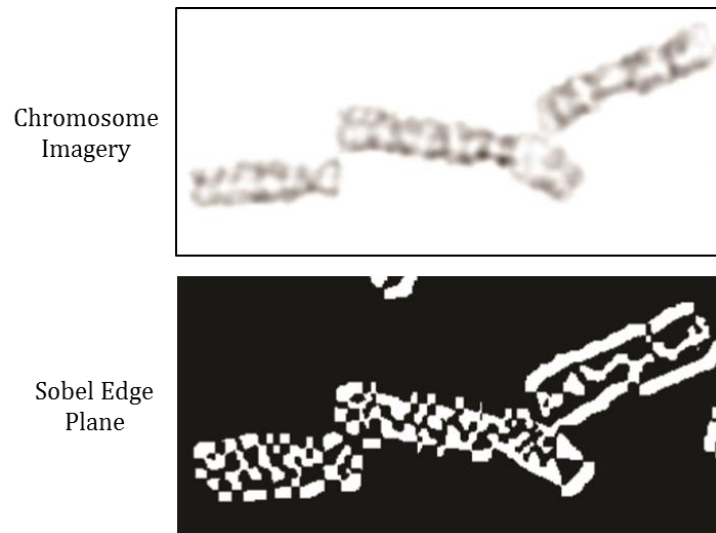


Figure 38: Sobel Edge Plane for High-Contrast Panchromatic Imagery [129]

The Canny Operator

A third example of a traditional panchromatic edge detection algorithm is the well-known Canny edge detector. Generally agreed to be the most effective traditional edge detection algorithm, the Canny edge detector attempts to satisfy the three primary edge detection criteria: 1) perform at a low error rate, 2) closely localize the edge points, and 3) generate a single edge point response for all edges [15], [1].

Canny seeks to satisfy these criteria through a four-step process [15], [1]. First, a small (usually 3 x 3) two-dimensional Gaussian operator is convolved across the image to smooth out the noise according to Equation 11 [1]. The smoothing step is designed to eliminate the most significant noise in the image without eliminating edge information. Smaller Gaussian filters (e.g., 3 x 3) will eliminate less noise than their larger counterparts (e.g., 5 x 5) but will be less likely to remove edge information, hence their predominance in most Canny applications.

$$G(x, y) = \frac{1}{2\pi\sigma^2} e^{\left(-\frac{x^2}{2\sigma^2}\right)}$$

Equation 11: Two-Dimensional Gaussian Filter [1]

Canny's second step calculates the gradient magnitude and direction at each pixel by convolving the smoothed image with the Sobel operator as described in Equation 10 and Figure 36 [137]. Although any gradient operator (e.g., Roberts) would work in Canny's second step, the traditional application of the Canny algorithm incorporates the Sobel.

The third step represents the contribution from Canny. Canny realized that since the magnitude of the edges are computed using a gradient, each of the edges in the output image usually will manifest as a local maximum surrounded by broad ridges on either side (i.e., perpendicular non-maxima edge information). Canny's third step attempts to thin these edges down to only those points that comprise the local maximum, thereby mapping the edge to its precise dimension and location [1].

The algorithm accomplishes this thinning through a process known as nonmaxima suppression, which removes nonmaxima edge points by tracing along each edge and removing those pixels that are weaker than one of their neighbors in a given direction [1]. In this manner, the Canny operator sets to zero pixels that are adjacent to the maximum-strength edge pixels, thereby rendering a single, precise edge in the edge plane. This step effectively satisfies edge criteria #2 and #3 (localization and single-point response) for a Sobel edge plane, which satisfies criterion #1, low error rate.

Canny's final step serves as a simple polishing process to eliminate false edge points. Specifically, the final step uses hysteresis thresholding to link broken edges, thereby rendering unbroken edge lines to the maximum possible extent [1]. Hysteresis thresholding, or double thresholding, establishes a lower threshold to eliminate false alarms and an upper threshold to identify the strongest edge pixels. Once the false alarms have been removed by the lower threshold, connectivity analysis can link the remaining non-zero pixels to the strongest edge pixels. The final output should appear as a network of solid, thin edges with few breaks and few, if any, wide ridges.

Figure 39 presents examples of the full Canny process for both a crisp panchromatic image and a noisy panchromatic image [143]. Notice that the primary difference between the images during the gradient measurement step that the edges in the noisy image tend to be less strong and more broken. I.e., Sobel does not miss many edges in the noisy image, but it renders them with less strength, or confidence. The output of Canny's nonmaxima suppressed step shows superior, more coherent results (as expected) for the less noisy image, particularly around the subject's eyes. However, Canny still generates quite satisfactory results for the noisy image during the nonmaxima suppression step, and both nonmaxima suppressed outputs demonstrate superior localization compared to the simple gradient planes – a chief benefit of Canny's nonmaxima innovation. Finally, Canny's hysteresis thresholding generates excellent edge information for the non-noisy image by linking the small gaps along the edges, which is particularly noticeable along the subtle facial features. While Canny renders Lena more recognizably from the non-noisy image, the Canny-generated edge

information extracted from the noisy image is notably superior to a simple Sobel plane with respect to localization and single-pixel edges.

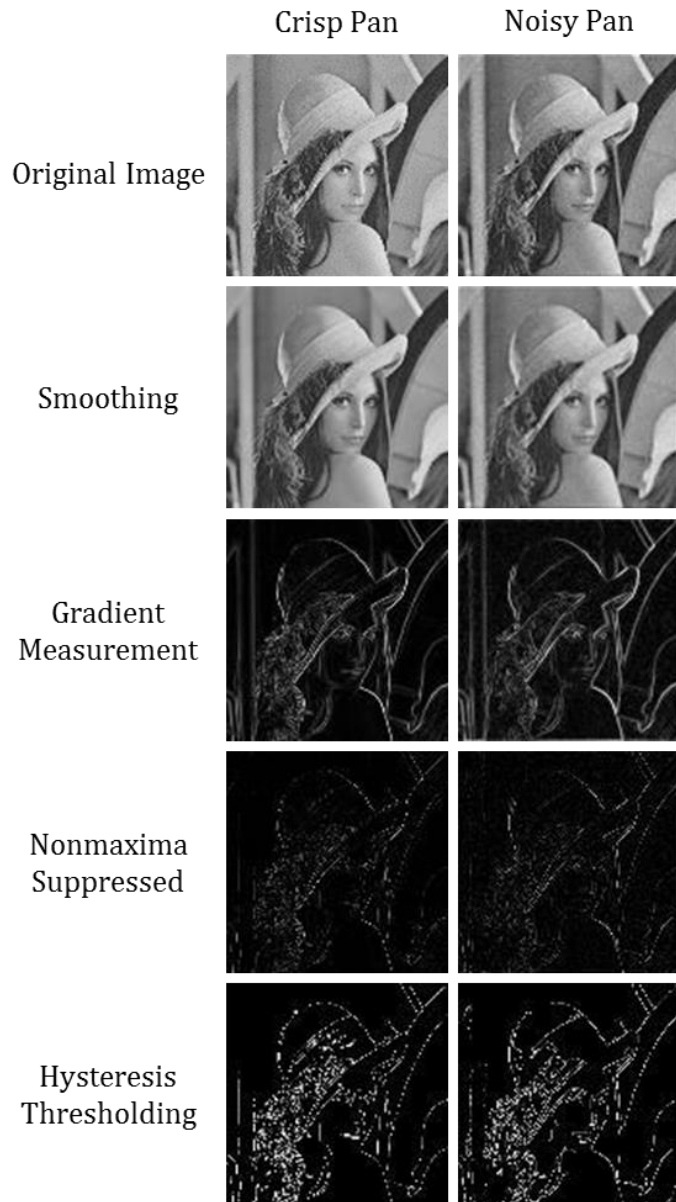


Figure 39: The Canny Operator's Five Steps [143]

Given Canny's deserved reputation as an optimal edge operator, researchers have enlisted its services (and its variants) to inform a diverse array of applications, including medical imaging [144], [145], [146] coastline extraction [147], airborne navigation [148], kiwifruit harvesting [149] and manufacturing quality control [150], [151], [152]. For example, Canny's ability to generate accurately localized single-pixel edges makes it an attractive choice for manufacturing applications that require high precision, such as safety and reliability inspections for welded components [152].

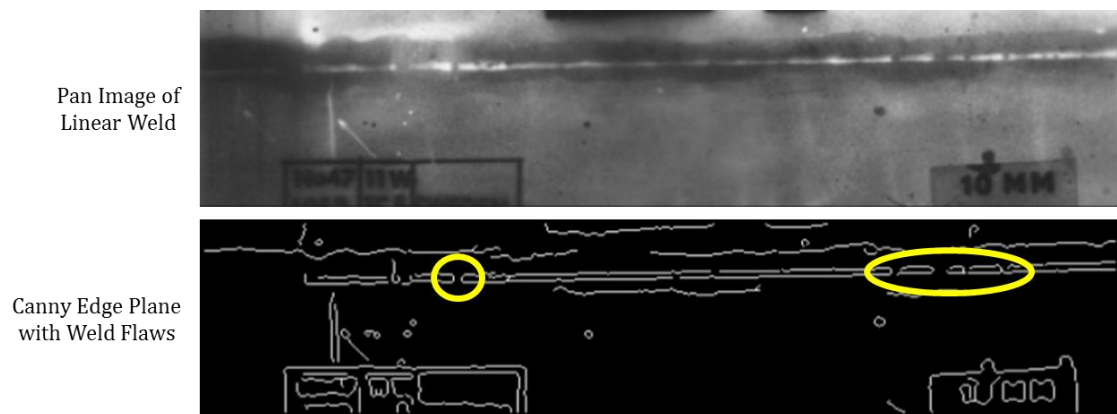


Figure 40: Canny Operator's Application to Manufacturing Processes [152]

Figure 40 presents a Canny edge plane containing the precise locations of weld flaws (circled in yellow) and is an excellent example of how Canny's nonmaxima suppression and hysteresis thresholding processing can detect very small edge breaks. Considering the Sobel operator's ability to detect similarly small edge breaks in Figure

38, Sobel likely would miss the narrow breaks along the weld, which are diagnostic of small weld defects that can have significant implications for safety and reliability.

Table 1 summarizes the strengths and weaknesses of the three traditional edge detection methods examined herein: Roberts, Sobel, and Canny. As with most applications, the primary tradeoff is between performance and speed. Roberts and Sobel are comparatively fast compared to the multi-step Canny process, but Canny produces more accurate, localized and single-point edges than either Sobel or Roberts.

Table 1: Comparison of Traditional Edge Detection Methods

Operator	Strengths	Weaknesses
Roberts	<ul style="list-style-type: none"> • Simple • Fast 	<ul style="list-style-type: none"> • Sensitivity to noise • Biased to 45° edges • Inaccuracy, especially against low-contrast edges
Sobel	<ul style="list-style-type: none"> • Simple • Fast • Accurate 	<ul style="list-style-type: none"> • Sensitive to noise • Poor localization • Difficulty against closely spaced edge features • Multi-point edge response
Canny	<ul style="list-style-type: none"> • Accurate • Good localization • Single edge point response • Robust to noise 	<ul style="list-style-type: none"> • Slower processing speed

Ultimately, researchers must choose the appropriate operator by considering the application’s accuracy requirements, expected scene backgrounds and speed requirements. For baseline comparison purposes, this dissertation tests all three

operators' performance against all datasets in order to compare the new algorithms' performance to the performance of the most well-understood edge operators.

A Note on the Substantive Differences between Edge Detection and Segmentation

Before surveying the multispectral edge detection literature, a note is warranted on the important algorithm differences between edge detection methods and image segmentation methods as they exist within the MSI literature. The two approaches frequently overlap in day-to-day MSI remote sensing discourse, but their methods are mathematically distinct. Specifically, MSI edge detection is premised on locating discontinuities within an image, while image segmentation is premised on organizing continuities within the image.

Edge detection methods look for differences among adjacent pixels while segmentation methods measure spectral and/or spatial similarity to organize an image into homogenous, non-overlapping regions. Bakker and Schmidt similarly state that edge detection is based upon the detection of local variations (i.e. discontinuities or transitions) which mainly correspond to the boundaries of homogeneous objects in the image [153]. The end states of the methods are similar, but distinct in the sense that edge detection methods detect a boundary between these two regions, while segmentation methods detect spectrally similar materials.

Indeed, the MSI segmentation literature reflects a clear emphasis on continuity-based algorithms. For example, most MSI image segmentation methods fall into one of three groups: spatial neighborhood-based methods, spectral clustering-based methods and region-growing methods. Neighborhood-based methods typically implement an image

classification operator for measuring the spectral similarity between a known target pixel and one or more of its immediate neighbors or near-neighbors [154], [155], [156], [157], [158], [159], [160], [161], [162], [163], [164], [165], [166] . These approaches typically assume foreknowledge of what representative spectral parameters to look for and are generally not suitable for identifying spectrally mixed, discontinuous edge pixels. Indeed, neighborhood-based methods sometimes “back into” edge information, but their algorithm approaches are clearly designed to identify similar pixels over a small spatial neighborhood in the scene.

Spectral clustering-based segmentation methods attempt to identify homogenous, non-overlapping regions by grouping spectrally similar pixels in n -dimensional space rather than according to their immediate spatial neighbors [167], [168], [169], [170], [171], [172], [173], [174], [175], [176], [177]. The central idea behind these segmentation methods is to segment the image from a spectral perspective rather than a spatial one – the spatial continuities appear only after the clustered pixels are remapped into their original spatial positions. As expected, clustering-based MSI segmentation methods borrow generously from traditional clustering techniques such as k-means clustering [169], [175], [176] and fuzzy c-means clustering [168], [170], [171], [174]. All of these approaches are similar in the sense that they parse the image for spectral similarity among pixels – any edge information present in the final output is simply an artifact of clustering-based MSI segmentation methods.

Finally, a smaller volume of MSI image segmentation approaches apply region growing techniques to aggregate spectrally similar pixels [178], [179], [180], [181],

[182]. As first hypothesized in [183], region growing methods for MSI segmentation populate an MSI dataset with random or logically placed seeds that then automatically grow to include spatially adjacent pixels until the mass forms a homogenous segment based on spatial and spectral similarity (usually a thresholded distance from the mean). Unlike MSI edge detection methods, MSI region growing segmentation methods emphasize pixel similarity, not continuity. Indeed, MSI region growing segmentation techniques are subject to challenging over-segmentation problems since they are so sensitive to the region growing similarity threshold. Consequently, any superficial edge information derivable from these techniques is typically weak and unreliable – not a surprising result given that the aim of the techniques is to identify continuities.

Ultimately, segmentation algorithms that measure continuity simply are not optimized for rendering quality measurements of an image's discontinuities. Segmentation algorithms present edge information as an implied by-product of identifying homogenous regions, but their algorithm processes are engineered to extract homogenous, non-overlapping image regions. Indeed, authors of MSI segmentation methods clearly appreciate the difference, as evidenced by their independent treatment of edge detection or smoothing techniques within a larger image processing chain emphasizing image segmentation [162], [163], [166], [176], [178], [179], [180], [182]. Given the difference between MSI edge detection and MSI segmentation, this study relies predominantly on the MSI edge detection literature discussed in the next several sections.

Multispectral Edge Detection Methods

The image processing literature contains many MSI edge detection techniques for earth remote sensing data. Most techniques fall into one of two broad categories: 1) band-by-band methods or 2) gradient-based methods. Band-by-band edge detection methods operate independently on each MSI band before deriving a final measure via an aggregation operation like summation or the root mean squared (RMS) calculation. Gradient-based methods attempt to derive meaning from the relationships among bands by operating on multiple bands simultaneously. A handful of techniques fall outside of these two main categories into a third, much smaller category: level-set based MSI edge detection algorithms that take advantage of the powerful non-linear capabilities of level-set mathematics.

While many MSI edge detection techniques produce satisfactory results, they frequently suffer from the same common weaknesses observed in single-band edge detection efforts. Common limitations include sensitivity to noise, poor results between low contrast areas, noisy edge planes, broken edges and a tendency to perform satisfactorily only under optimal conditions. Many MSI edge detection algorithms in the peer-reviewed research also are highly scene-dependent – a generally unwanted characteristic if the algorithm is intended to be used against a broad variety of remote sensing applications and datasets.

MSI Band-by-Band Edge Detection Methods

The simplicity of MSI band-by-band edge detection methods makes them an attractive choice for researchers. Band-by-band approaches can be thought of as a straightforward extension of traditional panchromatic edge detection methods to

multispectral imagery. Edge operators execute against one band at a time with no consideration given to the edge information available in other bands. The single-band results are then combined into a single grayscale image in which each pixel's digital number (DN) represents the aggregate edge information for all bands at that pixel.

While these techniques often generate usable edge information, they tend to produce noisy, broken edges and perform satisfactorily only under optimal conditions. The two most likely explanations for these limitations are the limited spectral resolution of MSI data and the inability of these algorithms to exploit the edge relationships among bands.

A review of the MSI edge detection literature demonstrates that researchers have developed several MSI band-by-band edge approaches not for earth remote sensing data, but for medical imagery [184], [185], [186], [187], [188]. Although the MSI bands in MRI imagery are not reliable analogues for the MSI bands in earth remote sensing data (i.e., the MRI bands are spatial transverses of a given object rather than bands corresponding to different wavelength sampling), many of the MRI edge techniques have objectives similar to MSI edge techniques and therefore are worthy of mention. For example, medical researchers have developed edge detection techniques for reducing noise in magnetic resonance imagery (MRI). One simple approach passed a 3 X 3 filter across a 32-band MRI to measure the n -dimensional Euclidean distances among the center pixel and the surrounding eight pixels [189]. When a Euclidean distance exceeded a user-defined threshold, the filter declared the center pixel to be an edge pixel.

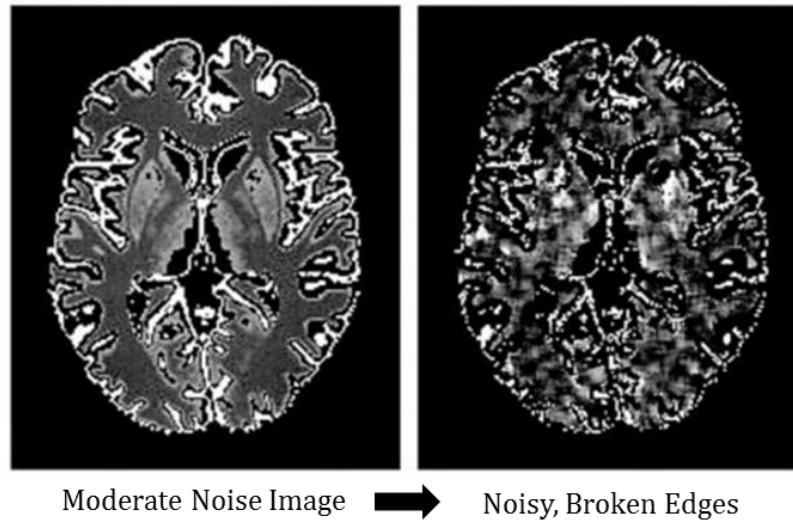


Figure 41: Limitations of Euclidean Distance in MSI Space [189]

While this approach produced satisfactory results for very low noise imagery (as would be expected), it performed poorly against moderate and high noise imagery as seen in Figure 41. The most likely explanation for the poor edge results against moderate and high noise imagery is Euclidean distance's sensitivity to intensity and the relatively low spectral contrast among a limited number of MRI bands. For noisy images, Euclidean distance tends to generate a suboptimal volume of false positives as it alarms on artificially bright or dark pixels. The result is the noisy edge plane characterized by broken edges as seen in Figure 41.

An intensity insensitive method like the spectral angle mapper (SAM) would probably have produced superior noise reduction results. For this very reason, the edge detection methods tested in this dissertation emphasize operators that are insensitive to intensity or employ methods to reduce intensity-related artifacts. Through the principal

components transformation, [189] would have been able to minimize the noise in the MRI data before executing the edge detection techniques, which would likely have produced a superior edge plane.

Another band-by-band edge detection approach for MRI data simply applied the Canny edge operator against the individual MRI bands and summed the results [187]. As seen in Figure 42, the edges are noisy, broken and for some low-contrast edges, completely absent. These modest results are fairly typical for MRI edge efforts that employ a traditional band-by-band edge detection approach such as Canny or Sobel [188]. Similarly to [189], the edge results in [187] undoubtedly suffer from the limited edge information extractable from a four-band image processed on a band-by-band basis.

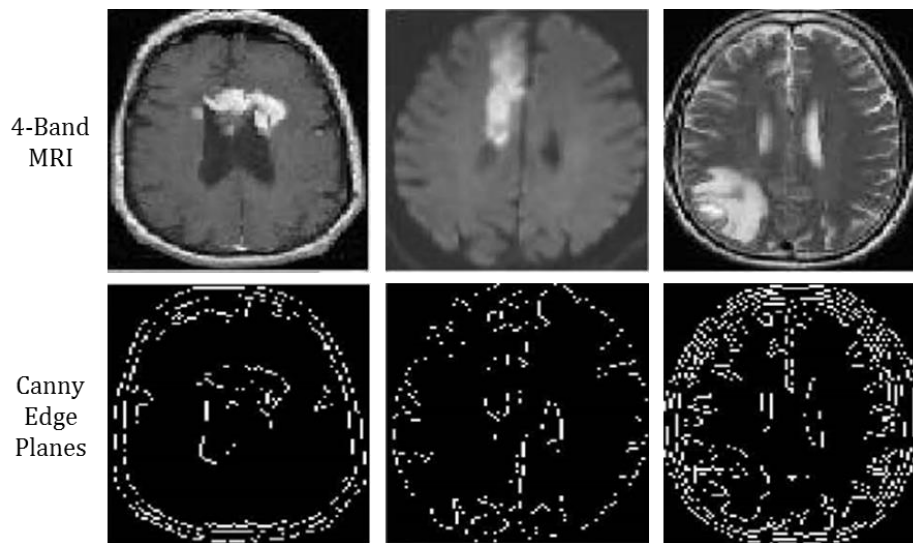


Figure 42: Broken, Noisy Edges in Canny Planes Derived from 4-Band MRI [187]

Additionally, the weak natural correlation among MRI bands limits how well they can cooperate to produce edge information, which clearly caps the edge results obtainable from a band-by-band approach to MRI edge detection methods. This limitation is absent in edge detection processes performed on earth remote sensing data since adjacent electromagnetic spectral bands are naturally organized along a clear electromagnetic spectrum as opposed to MRI data composed of disparate, omnidirectional radiofrequency bands. Given these substantive differences between multiband MRI data and multiband MSI data, and the modest edge results derived from MRI data, this study emphasizes edge techniques for earth remote sensing data.

Band-by-band MSI edge detection approaches frequently employ edge detection methods within a broader image processing chain, and many of them rely on the Canny operator to extract edge information. For example, [190] integrates edge detection techniques within an image classification workflow. Within the image classification workflow, [190] uses the Canny edge detector to generate pixel edge strength measures, which are then fed back into the workflow to help corroborate the independent image classification processing. As seen in Figure 43, the edge-guided image classification results demonstrate the utility of integrating edge detection techniques within broader image processing efforts.



Figure 43: Edge-Informed Image Classification Results [190]

Similarly, [191] also integrated Canny-derived MSI edge detection results into a broader image processing workflow for image classification. After applying the Canny edge detection filter to identify edge pixels within a four-band SPOT-5 MSI datacube, [191] used the strongest MSI edge pixels as seeds for a region growing routine designed to classify ocean regions and aquaculture regions. In this way, MSI edge information serves as a starting point for image classification. As seen in Figure 44, MSI edge detection techniques can help derive clear, single-pixel boundaries between spectrally similar targets such as water and aquaculture.

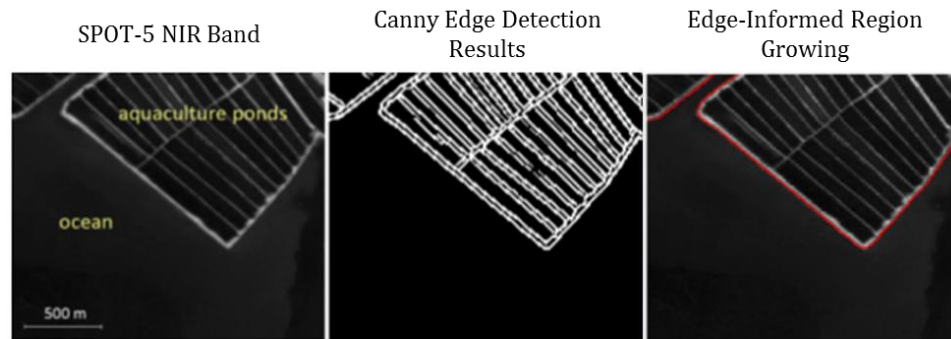


Figure 44: Edge-Informed Region Growing Results [191]

While many MSI edge detection approaches use the Canny edge detection filter on the discrete MSI bands, [192] applies it against a processed image wherein each pixel represents an ordering scalar derived from the respective pixel's spectral vector. This approach is notable in that it executes the Canny operator against a preprocessed grayscale image rather than the original MSI image. As seen in Figure 45, executing Canny against the ordered scalar image produces respectable results, albeit with noisy and frequently broken edges.

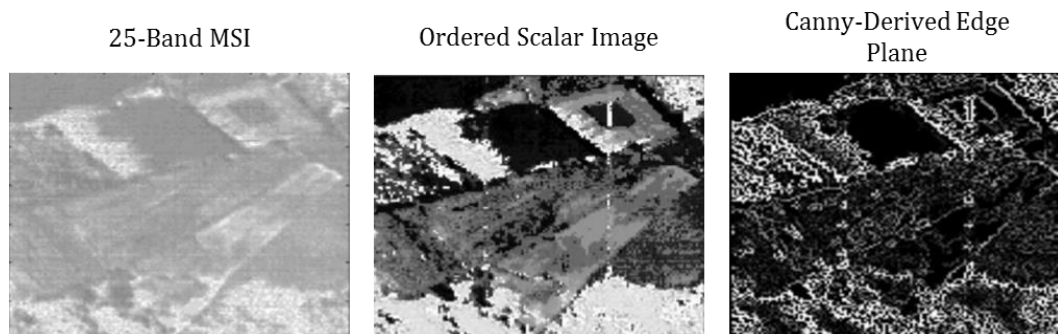


Figure 45: Canny-Derived Edge Information from an Ordered Scalar Multispectral Image [192]

Interestingly, [192] also executed their approach against a 220-band HSI image but generated only modest edge results as seen in Figure 46. The authors do not speculate on the modest HSI results, but the most likely explanations are 1) the HSI data was not corrected to reflectance and/or 2) the HSI data was not compressed via a principal components transform. As will be detailed later, the research performed in this dissertation compresses HSI data prior to edge detection processes in order to maximize results.

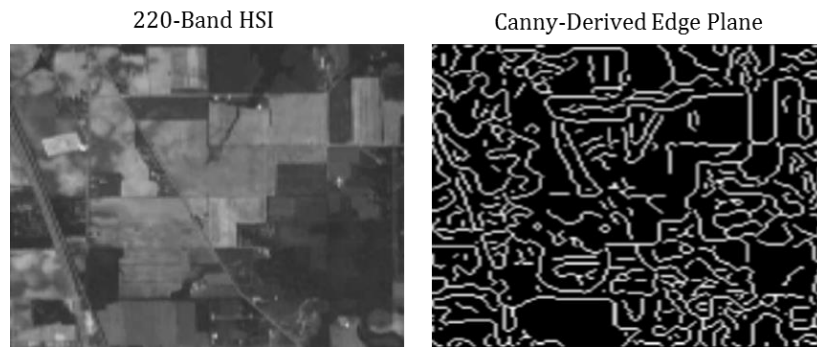


Figure 46: Canny-Derived Edge Information from an Ordered Scalar Hyperspectral Image [192]

Other approaches have applied post-processing techniques to improve outputted edge detection planes. The method detailed in [193] applies simple dilation and erosion morphology filters as a post-processing step to improve MSI edge detection results. By applying erosion and dilation operators to smooth the Canny edge results, [193] demonstrates that simple morphology operators can help mitigate noisy, broken MSI edges often derived from traditional panchromatic edge detection methods.

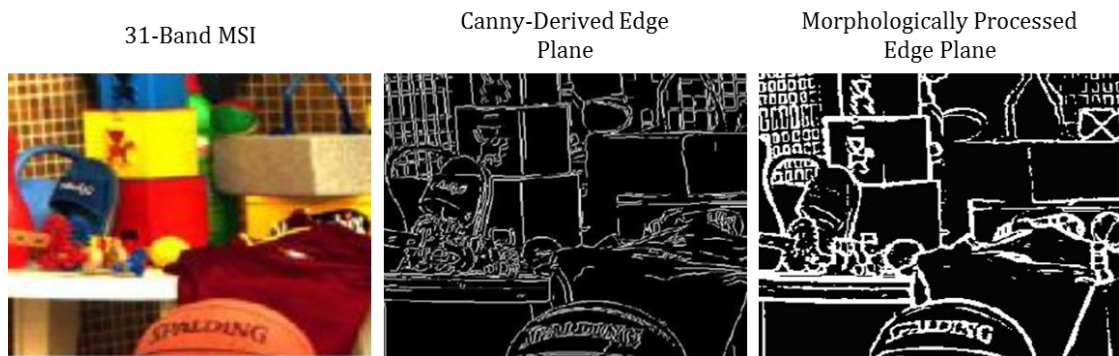


Figure 47: Morphology Operators Improve Edge Detection Plane [193]

The Tensor Gradient for MSI Edge Detection

Publishing within the field of computer vision in 1986, Di Zenzo [194] pioneered the extension of single-band gradient techniques to multispectral imagery. Before Di Zenzo's findings, computer vision and remote sensing practitioners simply applied difference operators to individual spectral bands and combined the results by taking the root mean square, the sum, the maximum of absolute values, etc. Di Zenzo recognized that single-band techniques did not use edge evidence in one component to reinforce edge evidence along the same direction in other components. Di Zenzo suggested treating MSI data as a vector field, and demonstrated that applying the tensor gradient against MSI could measure how effectively the image's spectral bands cooperated to communicate edge information [194]. Specifically, Di Zenzo's approach extended single-band techniques by measuring the direction along which the image's rate of change is maximum as well as the magnitude of the rate of change. He then combined the direction and magnitude to create a gradient that took advantage of the relationships among all of the data's spectral bands.

Di Zeno considered a three-band MSI image as a function mapping a two-dimensional representation of the image plane comprised of real numbers into the red-green-blue (RGB) space where the color components are $R(x, y)$, $G(x, y)$ and $B(x, y)$. In vector space, the full image can be denoted as the function $f(x, y) = (R(x, y), G(x, y)$ and $B(x, y))$ with unitary vectors \mathbf{r} , \mathbf{g} , \mathbf{b} associated with the red, blue and green axes, respectively. Di Zeno then suggests that the vectors $f_h, h = 1, 2$ can be understood as seen in Equation 12, where both \mathbf{u} and \mathbf{v} are functions in the x, y plane for a given pixel.

$$\mathbf{u} = \frac{\partial R}{\partial x} \mathbf{r} + \frac{\partial G}{\partial x} \mathbf{g} + \frac{\partial B}{\partial x} \mathbf{b}$$

$$\mathbf{v} = \frac{\partial R}{\partial y} \mathbf{r} + \frac{\partial G}{\partial y} \mathbf{g} + \frac{\partial B}{\partial y} \mathbf{b}$$

Equation 12: Di Zeno's Gradient Magnitude

Equation 13 presents the angle between the pixel's \mathbf{u} and \mathbf{v} vectors as

$$\theta = \frac{1}{2} \tan^{-1} \left(\frac{2g_{xy}}{(g_{xx} - g_{yy})} \right)$$

Equation 13: Di Zeno's Gradient Direction

where the tensor components are

$$g_{xx} = \mathbf{u} \times \mathbf{u} = \left| \frac{\partial R}{\partial x} \right|^2 + \left| \frac{\partial G}{\partial x} \right|^2 + \left| \frac{\partial B}{\partial x} \right|^2$$

$$g_{yy} = \mathbf{v} \times \mathbf{v} = \left| \frac{\partial R}{\partial y} \right|^2 + \left| \frac{\partial G}{\partial y} \right|^2 + \left| \frac{\partial B}{\partial y} \right|^2$$

$$g_{xy} = \mathbf{u} \times \mathbf{v} = \frac{\partial R}{\partial x} \frac{\partial R}{\partial y} + \frac{\partial G}{\partial x} \frac{\partial G}{\partial y} + \frac{\partial B}{\partial x} \frac{\partial B}{\partial y}$$

Equation 14: Di Zenzo's Tensor Components

Note that at this point in the process, the algorithm has identified the magnitude of the x-direction and y-direction edge strength as well as the direction of the maximum rate of change. Missing is the magnitude of the edge strength along the direction of maximum change. Equation 15 provides Di Zenzo's final calculation to determine magnitude (i.e., edge strength) along the direction of maximum change. Note that Equation 15 functions in the spirit of the gradient by accepting as input a pixel's x-direction magnitude, y-direction magnitude and the direction of maximum change at that pixel.

$$F(\theta) = \sqrt{\{(g_{xx} + g_{yy}) + \cos 2\theta(g_{xx} - g_{yy}) + 2g_{xy} \sin 2\theta\}}$$

Equation 15: Di Zenzo's Maximum Edge Strength Along the Direction of Greatest Change

In plain language, Equation 14 generates the gradient magnitudes in the x-direction and y-direction by combining the MSI cubes' red, green and blue information, while Equation 13 generates the direction of greatest change (i.e., the angle) as a function of the cross products derived in Equation 14. Di Zenzo then proposes finding the magnitude of the vector aligned to the maximum rate of change according to Equation

15. The output from Equation 15 applied to each pixel is assigned as the DN to the corresponding pixel in the output edge plane.

As described above in the Purpose section, a central aim of this study is to advance Di Zenzo's gradient measurement approach into hyperspectral space. Figure 48 presents a graphical representation of how the Di Zenzo gradient operates, where the gradient at pixel g is derived from the gradients within the red, green and blue bands of a three-color image.

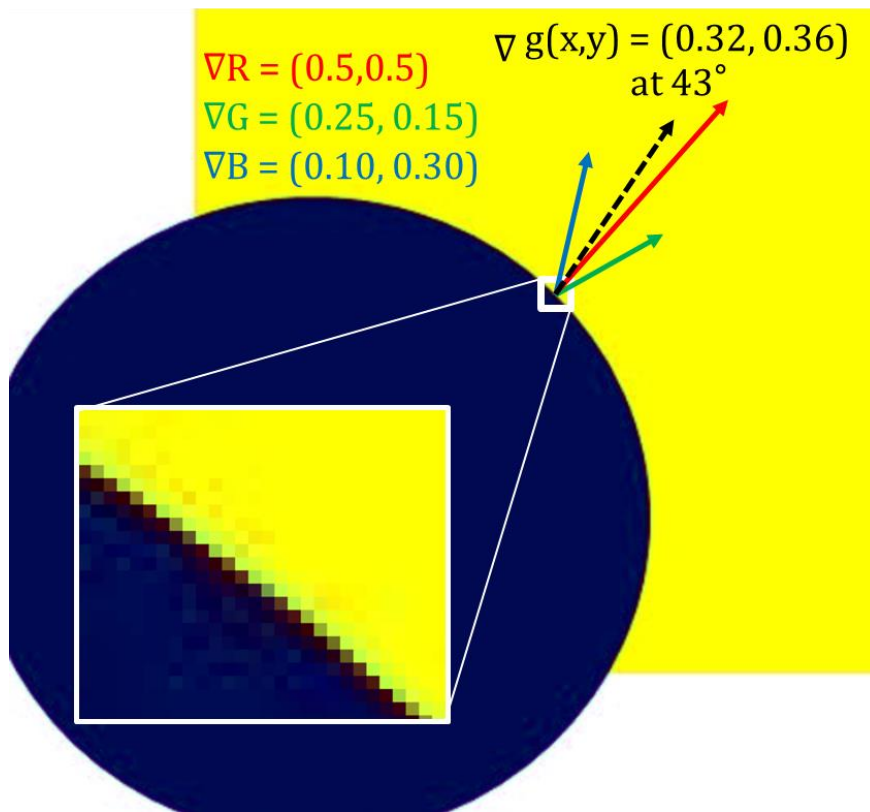


Figure 48: Graphical Representation of the Di Zenzo Gradient Operator

Di Zenzo's multispectral gradient ideas inspired subsequent research efforts. Cumani [195] was the first to extend Di Zenzo's algorithm approach to real imagery, and he determined that there were limitations when extending one-band theories to multiband images. Most importantly, Cumani found that emphasizing maximum gradient variations during edge detection operations frequently led to broken edge lines since maximum gradient variations occurred only sparsely along a given edge. This limitation makes sense for multispectral imagery, where intermittent spectral sampling often leads to stepwise-like results during analysis. As will be discussed, the research conducted herein will measure to what extent the contiguous, narrow band sampling of HSI can overcome the stepwise limitations observed in Cumani's results.

Several authors have built upon the gradient work pioneered by Di Zenzo and Cumani [196]. An interesting extension of gradient-based edge detection methods to MSI imagery is seen in [197], which populates a new feature space by measuring the spatial gradient magnitudes of all pixels over all spectral bands to generate a gradient magnitude feature space. Inside this new gradient magnitude feature space, edge pixels tend to concentrate in small, salient clusters. The key advantage of [197]'s approach is that it uses the global, structural scene information to extract edges as opposed to extracting edges based on local scene information.

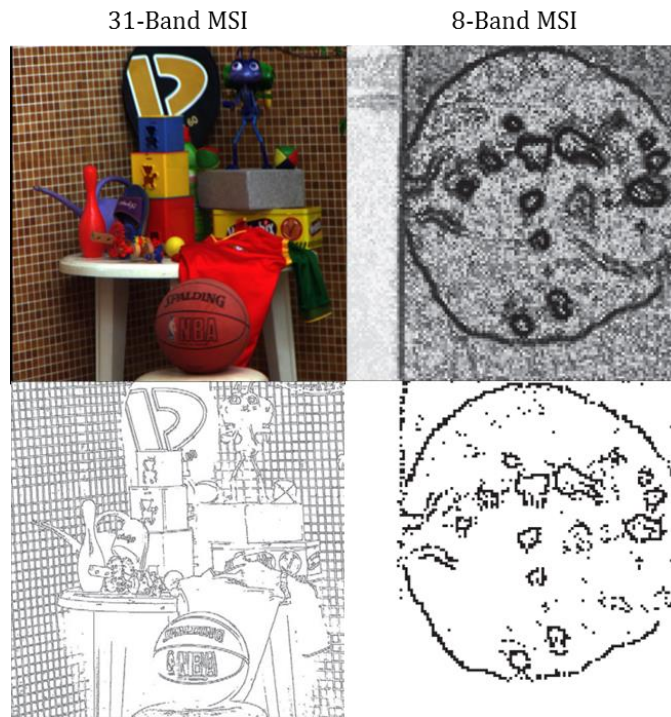


Figure 49: MSI Gradient Feature Space Edge Results [197]

As seen in Figure 49, the results demonstrate the ability of gradient-based edge detection methods to detect edges within complex images and generate low-noise, edge planes. In particular, notice the gradient-based method’s ability to overcome the noise in the right-side image. Although many of the edges are broken, they are still discernable – a respectable result given that the algorithm had only eight noise bands on which to operate. The primary reason that this approach was able to overcome significant background noise was because it deliberately isolated signal from noise by virtue of its novel MSI gradient feature space. Based on the success of [197], this dissertation takes a similarly deliberate approach to noise mitigation by applying a principal components transformation to HSI data prior to executing edge operators.

Another gradient-based edge detection method [198] creates a new “MSI gradient image” wherein each pixel represents the spectral gradient maximum in any direction from that given pixel. Similarly to [189], [198] then passes a 3 X 3 Euclidean distance filter across the new MSI gradient image to identify edge pixels. As seen in Figure 50, the Euclidean distance filter generated satisfactory results when applied against the MSI gradient image derived from 4-band MSI data. The results are particularly notable considering the low spatial resolution of the ASTER data, suggesting that gradient-based edge detection methods perform well even against low spatial resolution imagery.

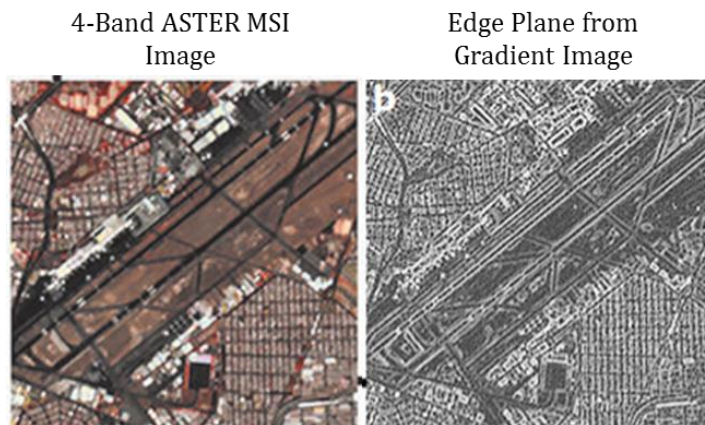


Figure 50: Edge Results Derived from MSI Gradient Image [198]

Another approach [199] extends MSI gradient techniques beyond the conventional n-dimensional vector space by treating each MSI pixel as a Clifford algebraic value in Clifford algebra space (i.e., geometric algebra space). In this manner, [199] reinforced Di Zenzo’s hypothesis that edge detection techniques leveraging the

quantitative relationships among MSI bands are more powerful than edge techniques that simply aggregate the results of single-band operators executing on each MSI band.



Figure 51: The Clifford Gradient's Poor Performance Against Low-Contrast Edges [199]

While the Clifford gradient generated satisfactory edge results against high-contrast areas, the operator failed to reliably detect low-contrast edges between similar areas as seen in Figure 51. Additionally, several moderate-contrast edges were missed, and thin edges were frequently missed. Although [199] does not address these limitations, insufficient spectral resolution or limitations of Clifford algebra are possible explanations for the Clifford gradient's inability to discriminate edges between similar materials.

A novel approach to MSI edge detection is presented in [200], which develops an edge detection method based on Newton's law of universal gravity. Specifically, the method treats every pixel as if it was a celestial body, and calculates pixel gradient edge

strength according to Newton's law. While an interesting approach, its real strength is attributable to its simultaneous treatment of the edge relationships among all MSI bands, as opposed to a band-by-band approach.



Figure 52: MSI Edge Results Based on Newton's Law of Gravitational Motion [200]

As seen in Figure 52, the approach generated satisfactory results against 31-band MSI data – edges are fairly narrow and contiguous, and noise is minimal. Compared to the Clifford algebra approach described in [199], the approach in [200] generated superior results. One possible explanation for the different results is the superiority of vector-based edge detection methods over Clifford algebraic approaches. The volume of MSI edge detection literature based on vector space as opposed to geometric algebra space suggests the same.

SAM and ED Applications to MSI Edge Detection

While the MSI literature contains many single-band and gradient-based edge detection methods, the same cannot be said for MSI edge methods based on spectral angle mapper and Euclidean distance. Researchers have applied the spectral angle mapper and the Euclidean distance algorithms to multispectral image classification efforts [201], [202], but the peer-reviewed scientific literature is devoid of research applying SAM and ED to multispectral edge detection efforts. Such a wide research gap is not terribly surprising given the limitations of discriminating materials in limited n -dimensional space, but the gap's size is certainly indicative of the scientific community's nascent understanding of spectral-based edge detection methods for multispectral data.

Identifying this dissertation gap is important in the sense that it speaks to how much the MSI edge detection literature relies on an image's spatial component to detect edges. The gap also indicates that HSI spatial-spectral edge detection algorithms that incorporate SAM and ED are pioneering new understanding within the scientific literature – a central aim of this dissertation. Indeed, a later section details how this dissertation advances the science by incorporating ED into an existing HSI spatial-spectral edge detection algorithm.

Level Set Edge Detection for MSI Edge Detection

Although not as severe as the research gap in SAM-based and ED-based MSI edge detection approaches, the scientific literature lacks a robust body of level set-based MSI edge detection research [203], [204], [205], [206], [207], [208], [209]. When adapted to multispectral imagery, traditional level-set based edge detection methods attempt to evolve an active contour model (i.e., an active snake, curve, surface or

balloon) to edge pixels as described in the widely cited Chan-Vese work [210] and [211]. The seminal level set work within the field of mathematics was pioneered by Osher and Sethian, upon which all other level set research is based [212].

Specifically, level-set based MSI edge detection methods operate very similarly to classic level set implementations by evolving a parametric contour around an edge until it reaches a minimum energy level according to Equation 16, Equation 17 and Figure 53. In Equation 16 and Equation 17, C is a closed, two-dimensional parametric curve, s is the curve's arc length, x and y are the curve's coordinates, E_{curve} is the energy of the curve to be minimized, E_{image} represents the image energy as represented by an object's edge pixel intensities, E_{int} is the parametric curve's internal energy according to its elasticity/tension and its rigidity (i.e., smoothness), and E_{con} is the constraint energy for inserting optional external constraints to the energy functional [213]. Finally, the functional derivatives of the image, scene and constraint energies constitute the energies minimized by the level set function [214].

$$C(s) = (x(s), y(s))$$

Equation 16: A Traditional Parametric Active Contour [213]

$$E(C(s)) = \int_0^1 E_{curve}(C(s)) ds = \int_0^1 [E_{image}(C(s)) + E_{int}(C(s)) - E_{con}(C(s))] ds$$

where $E(C(s)) \rightarrow \text{minimum}$

Equation 17: Minimizing the Level Set Energy Functional [213], [210]

In simplest terms, a level set-based edge detection algorithm attempts to minimize the sum of the pixel and active contour energies in order to position an edge curve at points of maxima while keeping the curve as smooth as practical; the constraint energy is an optional, but frequently implemented, factor [210]. Figure 53 demonstrates, for example, how the level set method could evolve a conical surface to find the edges of a circular object. In Figure 53, the red conical surface is the level set function that translates up and down until it finds the “best fit” between the function and the target feature. This “best fit” is defined as the zero level set because it is the collection of points for which the level set function returns zero height (i.e., a “level” height to the image plane). Ultimately, the level set function outputs this collection of points as the edge curve since it is the level set at which the sum of the scene and edge curve energies (i.e., derivatives) are minimal.

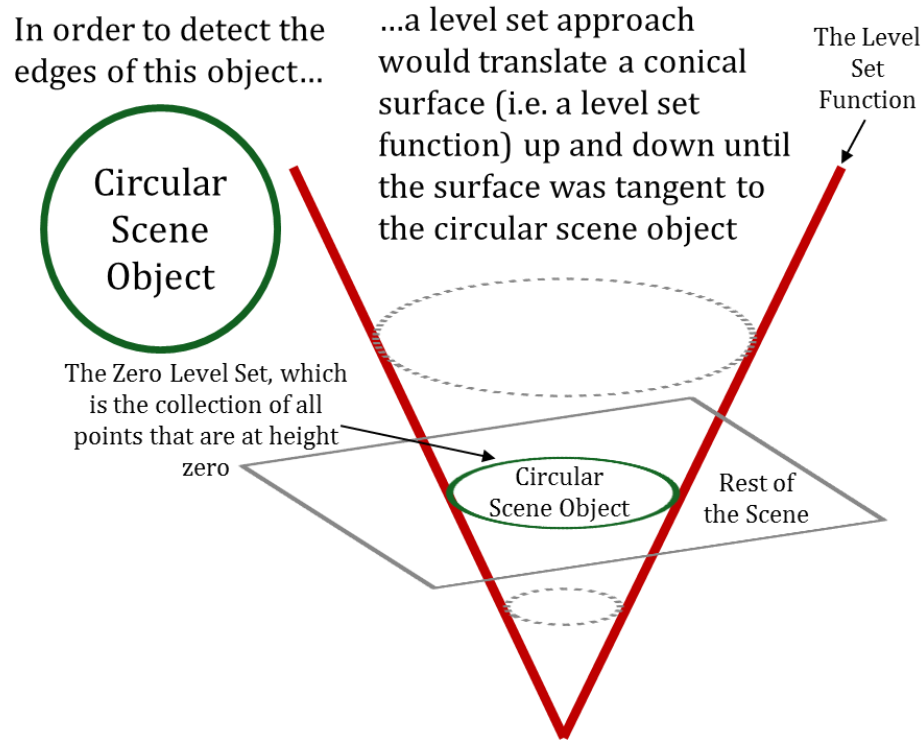
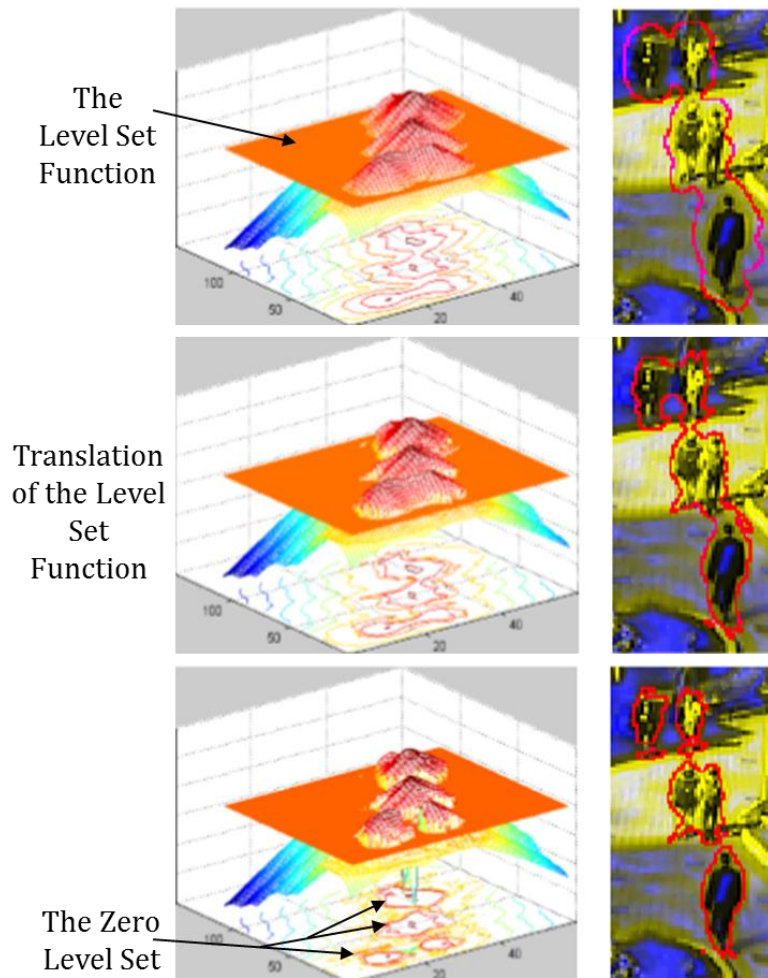


Figure 53: Evolving a Level Set Function to Detect Edges

While Figure 53 presents a simple example using a circle and a vertically translating cone, practical level set implementations must apply much more complex shapes operating in complex motions in order to detect the edges of irregularly shaped scene objects. Level set implementations need not take an “outside in” approach, either. They may execute from as an “inside out,” balloon-like operator that begins within the object and expands to “fill” the object according to the minimum level set. Level set approaches also usually operate against all objects in a scene, which results in highly irregular zero level sets.

Another key element to understand about level set methodologies is that they attempt to overcome the directional biases (i.e., Roberts is biased to 45° edges, Sobel is biased to vertical and horizontal edges, etc.) of classic kernel-based approaches by fitting a highly flexible surface to scene objects in n -dimensional space. For example, a level set approach to panchromatic images would operate in two-dimensional space, while a level set approach to 10-band MSI data would operate in 10-dimensional space.

Level set approaches for MSI data attempt to take leverage MSI's additional spectral information to build a more intelligence level set function, or surface. For example, consider Figure 54 which demonstrates how a level set algorithm would evolve a contour inward towards object boundaries in a two-band multispectral image [206]. In the top frame, the level set function initially returns high-energy contours that are widely distanced around the objects to be circumscribed. As the level set function translates downward in the middle frame, the contours more closely outline the scene objects, and in the final frame the level set function returns tightly spaced, minimal energy contours around each object. Such is the effectiveness of evolving an active contour against multidimensional imagery. As the imagery increases in dimension, the level set surface increases in complexity. In Figure 54, a simple plane can capture both spectral dimensions, but a three-dimensional surface would be required to operate against three-band MSI, a 10-dimensional surface would be required to execute against 10-band MSI, etc. Ultimately, an n -dimensional level set function is required to service an n -dimensional dataset.



*Note that the level set visualization is inverted relative to the scene as depicted on the right

Figure 54: Translating the Level Set Functional Against a Three-Band Image [206]

As one would expect from a shallow literature pool, level set research for MSI data has identified several challenges that higher spectral resolution could help overcome, including how to handle touching or overlapping objects [206], how to detect edges in high-noise environments [208] and how to preserve fine edge details in the final edge map [205]. These challenges indicate that the level set capabilities are outpacing the

spectral capacity of low spectral resolution data, thereby suggesting that level set applications for HSI data will likely yield improved results.

Hyperspectral Edge Detection Methods

Hyperspectral edge detection methods borrow liberally from the traditional and MSI edge detection literature, hence the foregoing literature review of traditional and MSI methods and applications. Recall Figure 4, however, which demonstrated that only a handful of HSI-specific edge detection articles populate the peer-reviewed scientific literature. Among these contributors, two primary algorithm categories appear: unsupervised HSI spatial-spectral edge detection methods [153], [215], [216], [217], [218], [219] and image classification methods masquerading as HSI spatial-spectral edge detection algorithms [220], [221]. Before reviewing the relevant HSI edge detection literature, however, the reader will benefit from a brief clarification regarding several HSI image processing techniques that can be confused with HSI edge detection methods.

First, the latter category of HSI image classification methods appearing as HSI edge detection algorithms is uniquely enabled by the material detection capability of HSI technologies, and merits discussion before proceeding to a review of the HSI edge detection methods relevant to this study. For example, [221] developed a rotation-variant template matching (RTM) algorithm that rotates a 3×1 kernel (or template) in 45° increments at each pixel to measure the spectral closeness and spatial alignment between the template's user-defined endmembers and the neighboring pixels' endmembers. Specifically, RTM populates a kernel with two endmember spectra that are known to exist in the scene, and then uses that kernel to find neighboring pixels that are most

continuous with the kernel's endmembers, which suggests a boundary between the two pure endmembers as seen in Figure 55. RTM then repeats this process for every other unique pair of endmembers specific to that particular scene, applying the kernel as a miniature image to measure the continuity between the hyperspectral image and the miniature image.

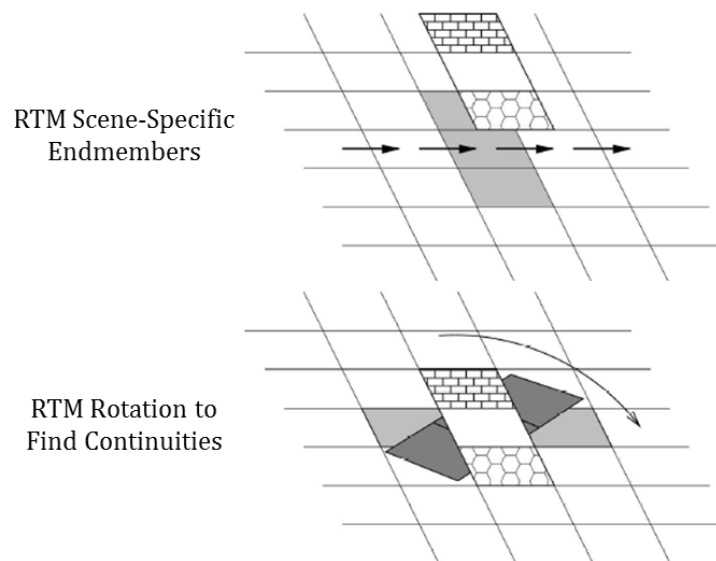


Figure 55: Rotation-Variant Template Matching [221]

The use of the term “suggests” in the previous paragraph is deliberate – RTM does not directly localize edges by finding discontinuities among adjacent pixels, it only implies edge information in the same manner as a continuity-based image classification map suggests edge pixels. Consequently, RTM is best understood as a novel advancement of HSI image classification methods, rather than as an HSI edge detection

method. The scientific literature supports this characterization, as well. Of the eight peer-reviewed journal articles that cite [221] in an applications context, all eight of them use RTM to classify a hyperspectral image containing specific materials of interest [222], [223], [224], [225], [226], [227], [228], [229]. All but one of the citing articles was authored or co-authored by the first author of [221], as well, which further suggests that the RTM algorithm was originally designed as an image classifier, not an edge detector. Ultimately, the critical difference between the RTM approach to edge detection and the edge detection methods pursued in this study is that the RTM methodology uses supervised, continuity-based, scene-dependent mathematics while this dissertation and its supporting literature use unsupervised, discontinuity-based, generalizable mathematics to generate edge maps.

Another interesting example of an HSI image classifier masquerading as an HSI edge detection method is seen in [220], which advances the novel idea of using a material-specific HSI edge signature to identify the boundaries between previously-identified materials. Specifically, [220] proposes two-model based HSI algorithms that first build a set of edge signatures using all unique combinations of the scene-specific materials, and then use those edge signatures to drive an image classification process that generates an image classification plane for each edge signature. [220] then combines the edge signature classification planes into a final classification map that looks strikingly like an edge map as seen in Figure 56.

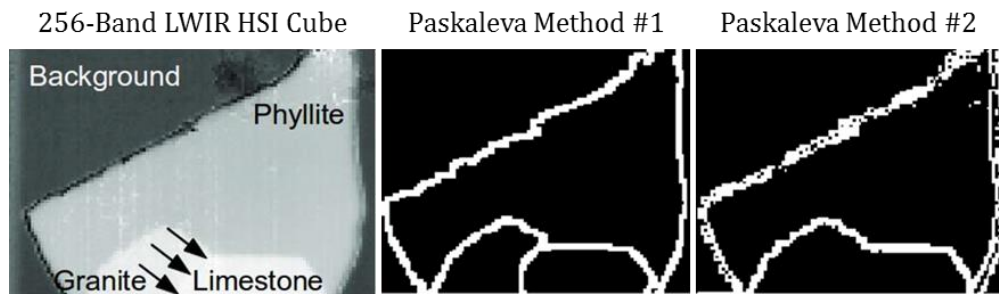


Figure 56: Paskaleva's Edge Signature Approach to Image Classification [220]

Paskaleva et al's concept of an edge signature is unique, but algorithmically the approach is a continuity-based image classification method. Specifically, [220]'s first algorithm uses a band-ratio technique to identify edge signatures unique to the scene, while the second algorithm uses a k -nearest neighbor classifier to generate a large set of candidate edge signatures unique to the scene. Paskaleva et al's approaches produce satisfactory results, but they clearly function as continuity-based image classifiers and therefore do not align to the discontinuity-based edge detection methods advanced by this dissertation.

Additionally, some HSI image filtering and HSI visualization/fusion efforts use edge preservation considerations to measure filter effectiveness [230], [231], [232]. First demonstrated in the landmark Perona and Malik work on anisotropic diffusion [233], image filtering methods incorporating edge preservation considerations use edge persistence as a qualitative criterion for estimating how effectively the filter reduces noise without eliminating edge information. In these cases, edge consideration efforts simply amount to the researcher visually judging the change in edge rendering between pre- and

post-filtering images – a heuristic process that is materially distinct from a rigorous, image processing-based edge detection function that generates edge maps by quantitatively detecting scene discontinuities. Furthermore, some HSI filtering efforts specifically design their filtering process to eliminate minor edges, which are treated as scene noise and therefore targeted for removal by an optimal HSI image filter – such efforts clearly do not behave like edge detectors. Since the image filtering research efforts that use edge preservation criteria do not directly inform edge detection methods, they are largely beyond the scope of this dissertation.

Directly within the scope of this dissertation, however, is the first category of HSI edge detection methods: unsupervised, discontinuity based edge detection methods. For example, [153] develops a spatial-spectral HSI edge detector that generates a dissimilarity map (i.e., an edge plane) by convolving the full HSI datacube with a modified Laplace operator in vector space rather than on a band-by-band basis. Specifically, [153] replaces the Laplace operator’s scalar absolute differences between neighboring pixels with the spectral angle between equivalent neighbors, translates a window operator across and down the scene, and outputs a single edge plane in which pixel values correspond to dissimilarity scores as measured by the spectral angle. As seen in Equation 18, [153] employs SAM as a statistical measure of dissimilarity by taking advantage of the fact that the cosine of the spectral angle is equivalent to the correlation coefficient (CC) of the observations \vec{v} and \vec{w} .

$$\cos(\text{SAM}(\vec{v}, \vec{w})) = \frac{\sum_{k=1}^n v_k w_k}{\sqrt{\sum_{k=1}^n v_k^2} \sqrt{\sum_{k=1}^n w_k^2}} = CC(\vec{v}, \vec{w})$$

Equation 18: The Spectral Angle Mapper as a Statistical Measure of Dissimilarity [153]

Figure 57 presents the results of [153]’s spatial-spectral HSI edge detection algorithm as applied to 128-band VNIR/SWIR HyMap cube. As shown, the spatial-spectral (i.e., Laplace-Spectral Angle) edge detection algorithm produced satisfactory edge information with an acceptable amount of noise.

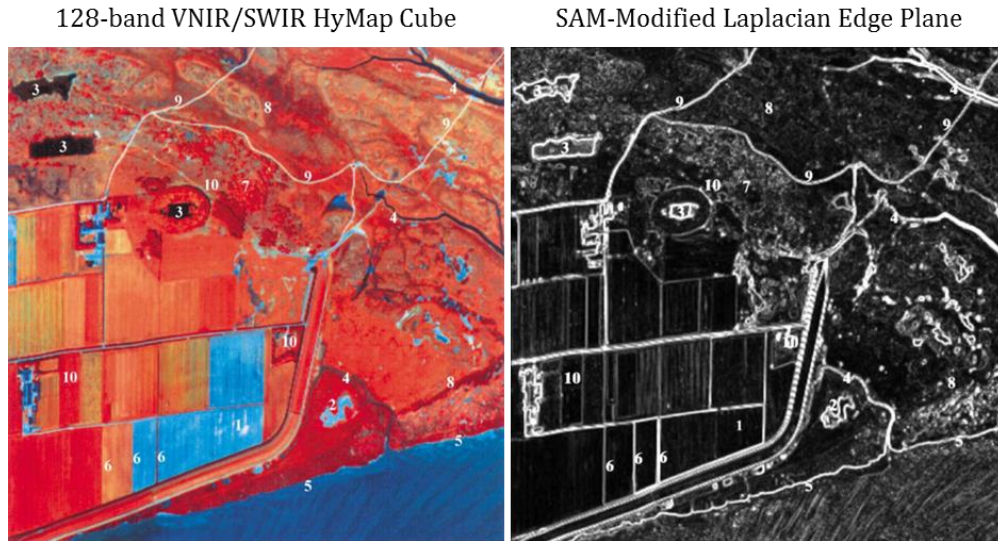


Figure 57: Bakker and Schmidt's Modified Laplace Operator Results [153]

Another spatial-spectral HSI edge detection algorithm is presented in [215], which uses the NDVI to generate a fuzzy edge map in which each pixel’s value reflects the number of bands that were identified as containing edge information. Designed for

heavily vegetated HSI scenes, [215]’s edge detection algorithm fuses a traditional MSI-derived NDVI plane with the data’s independent spectral components as derived from an independent component analysis (ICA). The combined plane is then mined for edges according to a traditional application of the Canny edge detection algorithm and smoothed for noise, resulting in a fuzzy edge map in which pixels are flagged as edge pixels according to how many times (up to the number of spectral bands) Canny alarmed on an edge pixel in the fused plane.

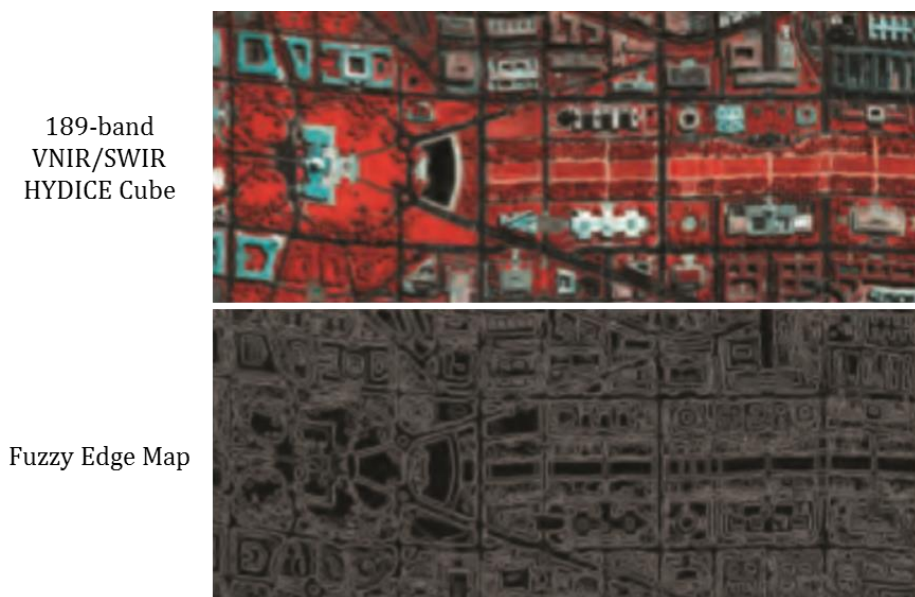


Figure 58: NDVI-Informed Fuzzy Edge Map Using HYDICE VNIR/SWIR Data [215]

Figure 58 presents the results of the algorithm when executed against a 189-band VNIR/SWIR HYDICE cube. The modest edge information is indeed fuzzy (i.e., poorly localized), as noted by the authors, largely due to the overreliance on the sparse spectral

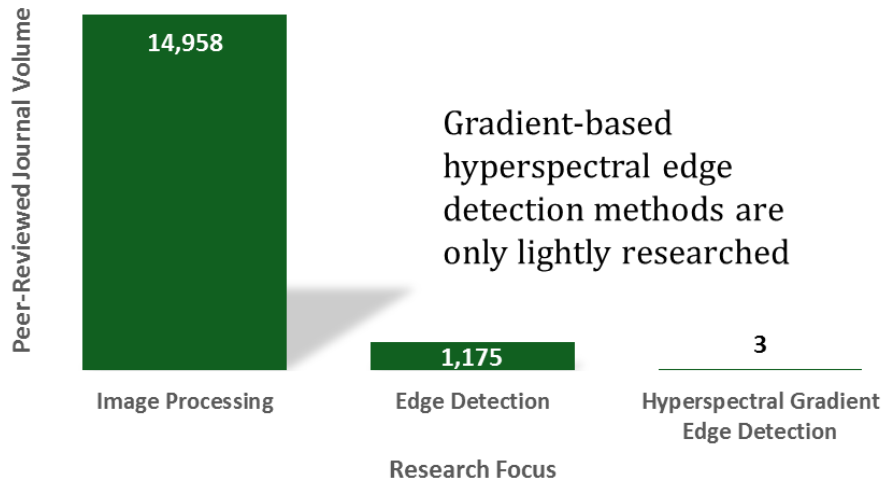
contrast achievable by the two-band NDVI implementation. Sufficient to inform the author's overall image classification objective, [215]'s results fall short of an optimal edge map extractable from hyperspectral data.

The remaining spatial-spectral HSI edge detection algorithms fall into three distinct classes that have direct bearing on the direction of this dissertation: gradient-based edge detection methods, the unique Hyperspectral/Spatial Detection of Edges (HySPADE) method and level-set-based edge detection methods. Accordingly, this study affords each class a focused review.

The Tensor Gradient for HSI Edge Detection

Figure 59 demonstrates why this dissertation endeavors to advance the scientific community's understanding of Di Zenzo's edge detection gradient as tested against hyperspectral imagery – only a handful of peer-reviewed journal articles pursue gradient-based HSI edge detection algorithms as their primary objective. While Di Zenzo's work has been available since 1982, researchers in the relatively new field of hyperspectral remote sensing have de-prioritized gradient-based HSI edge detection developments in favor of integrating simple gradient implementations within more widely studied image processes such as noise reduction in HSI data [234], [235], [236], anomaly detection [237], image fusion [238], [239], dimensionality reduction [240] and HSI image classification [241], [242], [243], [244], [245], [246], [247], [248]. The prioritization makes sense given the general scarcity of edge detection research as seen in Figure 1 (i.e., researchers are more likely to pursue the most well-understood methods when beginning

research into new imaging modalities), but it has created the gap in HSI edge detection research that this study seeks to inform.



Source: Peer-Reviewed Journal Titles Held by George Mason University Library; Surveyed 15JUL2016

Figure 59: Research Gap for Gradient-Based Hyperspectral Edge Detection

The gradient-based HSI research efforts employ the gradient in either spatial and/or spectral space in order to inform the primary image processing technique, but none of them apply the gradient primarily in pursuit of discontinuity-based edge detection research. Most of them use the gradient in either the spatial or spectral dimension to the exclusion of the other, as well. Simply stated, gradient-based HSI research has borrowed from Di Zenzo, but few efforts have attempted to improve upon his ideas as applied to hyperspectral imagery edge detection methods.

For example, [235] and [234] apply Di Zenzo's gradient concept in spectral space in order to improve anisotropic diffusion techniques, but they do not execute the gradient to detect discontinuities in the spatial dimension. Similarly, [237] and [240] apply gradient measures in spectral space (i.e., the rate of change among spectral bands within a single pixel) but stop short of applying the gradient to find discontinuities in the spatial dimension. Finally, gradient-based image classification schemes use Di Zenzo's unaltered gradient in a variety of ways, including only in spectral space [242], within an intermediate noise-reduction step [243] and to identify gradient minima for classification seeds [244], [247]. None of them use the gradient to generate edge maps derived from adjacent pixel discontinuities.

Although many research efforts, as shown, have extended Di Zenzo's gradient work to multispectral edge detection or incorporated it into other HSI image processing efforts, very few have adopted or advanced his gradient-based edge detection methods for hyperspectral data [216], [217], [218]. For example, [216] adapted Di Zenzo's gradient to an HSI edge detection method designed to detect edges in the presence of strong illumination effects. Specifically, [216] developed a chromatic-only version of the Di Zenzo gradient that operates only against the chromatic dimensions of HSI data to the exclusion of the illumination dimension. [216] achieves the decomposition of the HSI chromatic (i.e., angular) and illumination (i.e., vector magnitude) dimensions by converting an HSI dataset's Cartesian coordinates to hyperspherical coordinates in which the illumination and chromatic dimensions are separated according to Equation 19, where p is the hyperspectral pixel color in n -dimensional Euclidean space, l is the vector

magnitude (i.e., illumination dimension), and $\{\theta_1, \theta_2, \theta_3, \dots, \theta_n\}$ are the angular parameters (i.e., chromatic dimensions) [216].

$$p = \{l, \theta_1, \theta_2, \theta_3, \dots, \theta_n\}$$

Equation 19: Hyperspherical Coordinate Representation [216]

This separation of illumination information and chromatic information enables the chromatic gradient to execute independently against the chromatic information, thereby eliminating edge noise attributable to illumination effects. Figure 60 compares [216]’s approach compared to a traditional Prewitt kernel convolution as applied to a 128-band hyperspectral image ranging from 0.3 μm to 1.0 μm . The target is a plastic ball on a homogeneous green background. In the initial results, note how the Prewitt operator fails to distinguish between the plastic ball and its shadow, and how it responds strongly to the specular reflection on the surface of the ball – both of which are indicators of Prewitt’s sensitivity to illumination effects. Comparatively, the chromatic gradient delineated a clear edge between the ball and its shadow in the initial results, and responded much more appropriately to the specular reflection.

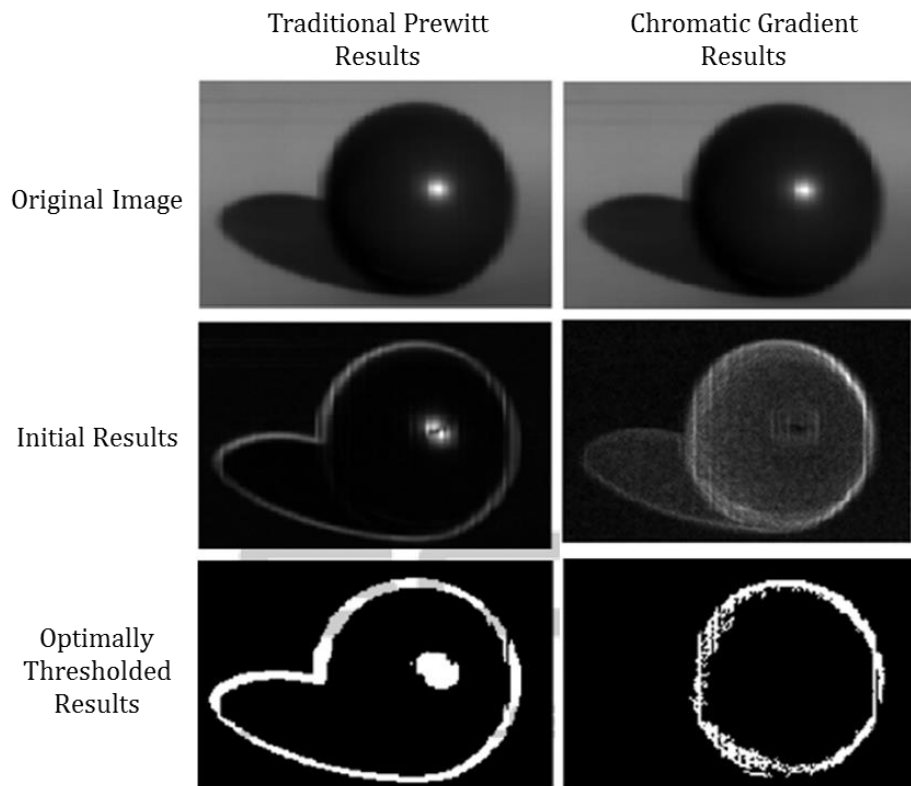


Figure 60: Comparison of Chromatic Gradient and Prewitt Results [216]

Thresholding did not improve the Prewitt filter’s final results, but the optimally thresholded chromatic gradient results indicate a clear, unbroken boundary surrounding the ball. Most importantly, the shadow boundary and specular reflection boundary disappear after thresholding, thereby validating the extension of Di Zenzo’s gradient to a chromatic gradient capable of mitigating illumination effects.

Another effort to extend Di Zenzo’s gradient-based approach to hyperspectral remote sensing is [217], which develops a modified Di Zenzo gradient method designed to improve edge localizations, which frequently appear as wide, unlocalized ridges in

simple applications of the Di Zenzo gradient. Specifically, [217] employs a non-maxima suppression scheme to optimize the partial derivatives of individual HSI bands such that they contain only those contributions directed towards their associated local scalar gradient maxima. Following a two-dimensional Gaussian smoothing to reduce scene noise within each band, [217] next computes the scalar gradient magnitude (M_{bf}) and direction (θ_{bf}) according to Equation 20 and Equation 21, respectively, in which I is an n -band HSI image, b denotes the specific band, x and y represent spatial image coordinates, I_{bf} represents a Gaussian-smoothed version of I_b , I_{bf}^x represents the partial derivative in the x -direction and I_{bf}^y represents the partial derivative in the y -direction.

$$M_{bf}(x, y) = \sqrt{\{I_{bf}^x(x, y)\}^2 + \{I_{bf}^y(x, y)\}^2}$$

Equation 20: The Scalar Gradient Magnitude

$$\theta_{bf}(x, y) = \tan^{-1}\left(\frac{I_{bf}^y(x, y)}{I_{bf}^x(x, y)}\right)$$

Equation 21: The Scalar Gradient Direction

With the scalar gradient magnitude and direction, [217] then executes the non-maxima suppression scheme against each individual HSI band. The non-maxima suppression step attempts to identify the highly localized edge points in the gradient field by suppressing spurious edge responses around the local maxima – the presumably true edge points. Specifically, [217] parses the scalar gradient direction into four discrete orientations, $\theta_1 = 0^\circ$, $\theta_2 = 45^\circ$, $\theta_3 = 90^\circ$ and $\theta_4 = 135^\circ$ before convolving a 3 x 3 kernel (β)

at each pixel in order to locate the discrete orientation ($\theta_k, k \in \{1,2,3,4\}$) closest to $\theta_{bf}(x, y)$. To then isolate the true HSI edge points, [217] then suppresses the corresponding gradient magnitude $M_{bf}(x, y)$ if and only if it's value is smaller (i.e., non-maxima) than one of its two adjacent neighbors ($\{\beta_1, \beta_2\} \in \beta$) along θ_k as represented in Equation 22. In Equation 22, M_{bf}^n is the non-maximally suppressed version of M_{bf} containing only those gradient magnitudes associated with extremely localized, true edge pixels.

$$M_{bf}^n(x, y) \begin{cases} 0 & \text{if } M_{bf}(x, y) < \beta_1 \text{ or } M_{bf}(x, y) < \beta_2, \text{ otherwise} \\ M_{bf}(x, y) & \end{cases}$$

Equation 22: Non-Maxima Suppression Criteria [217]

The end result of [217]'s non-maxima suppression scheme is a set of partial derivatives I_{bf}^x and I_{bf}^y optimized for a Di Zenzo-based gradient calculation in the sense that they represent only the gradient magnitudes of the true edge points. The subsequent gradient operation therefore will execute against only localized edge points and is much more likely to generate discrete edges as oppose to broad ridges attributable to non-maxima edge information. Importantly, [217] advances the science not by modifying Di Zenzo's gradient itself, but by leveraging the spectral advantage of HSI imagery to compress a pre-processed dataset prior to a gradient operation. Finally, Figure 61 presents [217]'s performance as executed against a 191-band urban HYDICE image. Note that [217]'s preprocessing non-maxima step enabled the subsequent gradient

operation to generate more localized edges than the same gradient was able to generate using unsuppressed data.

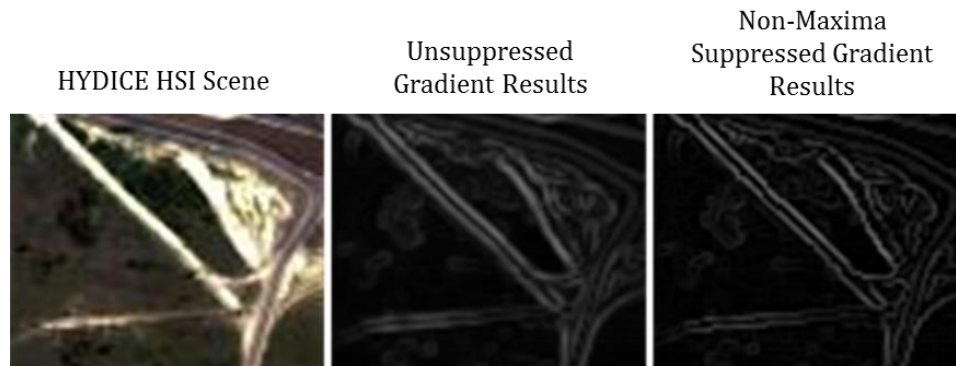


Figure 61: Non-Maxima Suppression Results [217]

Another effort to extend Di Zenzo’s gradient-based approach to hyperspectral remote sensing is [218], which applies a weighted post-processing step to a Di Zenzo gradient-derived structure tensor – a process that attempts to improve upon Di Zenzo’s implicit assumption that all bands contain equal volumes of edge information and therefore merit equal weighting. [218] uses a pixel-based weighted zero mean gradient in which the weights are constructed by comparison with a normalized median. Put more simply, [218] uses a post-gradient processing step to weight more strongly those pixels whose gradient measure indicates that the pixel is an edge pixel.

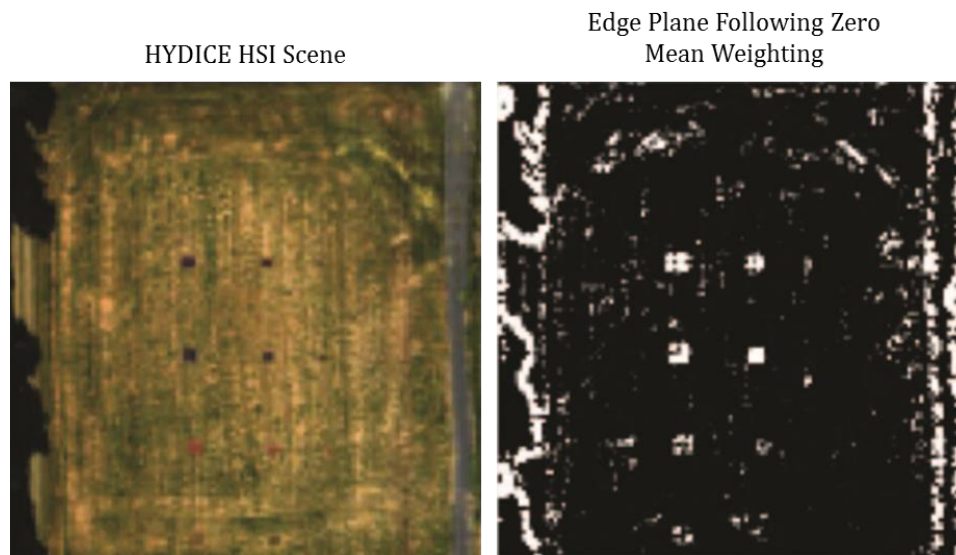


Figure 62: Edge Plane Derived from Band Weighting [218]

The methodology in [218] essentially assigns its weights based on whether a pixel's median gradient measure as represented within the structure tensor exceeds a pre-determined threshold. Pixels exceeding the threshold will necessarily have stronger gradients than pixels falling below the threshold and accordingly will receive more weight. The ultimate contribution of [218] is its exploration of weighting edge pixels according to their likely edge information, which is more robust than the standard histogram stretch used to optimize gradient planes. Figure 62 presents [218]'s results as executed against a 145-band VNIR/SWIR HYDICE dataset, which unfortunately is not an optimal dataset for testing edge detection algorithms due to its weak spatial resolution and small scene features. Nonetheless, the results are satisfactory in the sense that the approach ably delineated the boundaries between field and forest, and between the field and the square array panels.

As shown, the gradient-based edge detection literature for HSI data is minimal, but promising. For example, [216] demonstrated that Di Zenzo's gradient can be used to decompose chromatic and illumination information within an HSI scene, thereby enabling an edge detector to overcome false edges attributable to shadows and specular reflections. Additionally, [217] demonstrated the utility of exploiting the rich spectral content of HSI data prior to executing edge detection operations – a finding that has direct bearing on the gradient-based method tested by this dissertation. Finally, [218] showed that post-weighting a Di Zenzo-gradient derived structure tensor on a per-pixel basis could improve the edge detection process.

The Hyperspectral/Spatial Detection of Edges (HySPADE)

Rare is the hyperspectral edge detection algorithm that takes full advantage of HSI's spatial and spectral information. One such example is the HySPADE algorithm as proposed by Resmini [219], [249] and advanced by Cox [250]. HySPADE's chief contribution to the HSI edge detection science is that it weaves either Euclidean distance or the spectral angle mapper (SAM) algorithm into the hypercube's spatial structure in a manner that uses both spatial and spectral information to detect edges within the scene.

Specifically, the HySPADE algorithm generates an output cube wherein each band is the spectral angle between a given pixel and every other pixel in a scene or $n \times n$ window, and the output cube has as many bands as the original scene has pixels. For example, each pixel in Band 1 in the output cube is the spectral angle between that pixel and pixel (1,1) in the input cube; each pixel in Band 2 is the spectral angle between that pixel and pixel (1,2) in the input cube; each pixel in Band 3 is the spectral angle between

that pixel and pixel (1,3) in the input cube, and so on. In this manner, HySPADE generates an output plane where the strength of a given edge is a function of both its spatial position in the cube and its spectral similarity to every other pixel in the scene. Figure 63 presents the first three steps of the HySPADE algorithm.

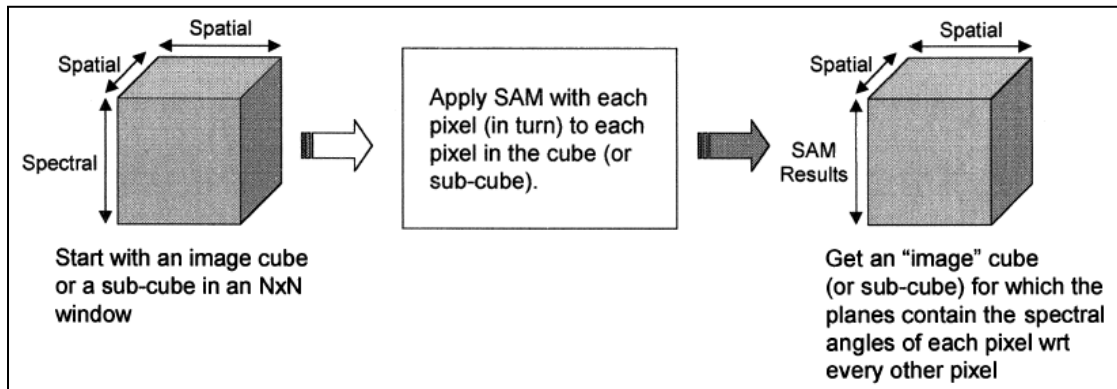


Figure 63: HySPADE's First Three Processing Steps [219]

Next, using a user-defined variance threshold (i.e., a multiple of the standard deviation, such as 0.25σ , 0.75σ , 1.00σ , etc.), HySPADE executes a one-dimensional, first-order finite-difference edge detection operation on each pixel in the output cube. Each pixel is scored according to how many times the detector identifies an edge in the spectrum, and a two-dimensional plane is generated wherein each pixel's value is equal to how many times an edge was detected within the SAM-cube spectrum for that pixel. For example, if the spectrum of a given pixel in the output cube contains five bands whose first-order differences exceed the user-defined threshold, that pixel would have a score of five in the final two-dimensional output plane.

The final output edge plane is a reflection of the highest measured spectral angle at every pixel combined into a single plane, meaning that band selection is not necessary because the best edge pixel (for each pixel in the original cube as detected by ED or SAM) is automatically included in the output plane [250]. The researcher can then simply observe or histogram stretch the edge plane to measure and optimize the derived edge information. Figure 64 presents the final edge detection process as executed by HySPADE.

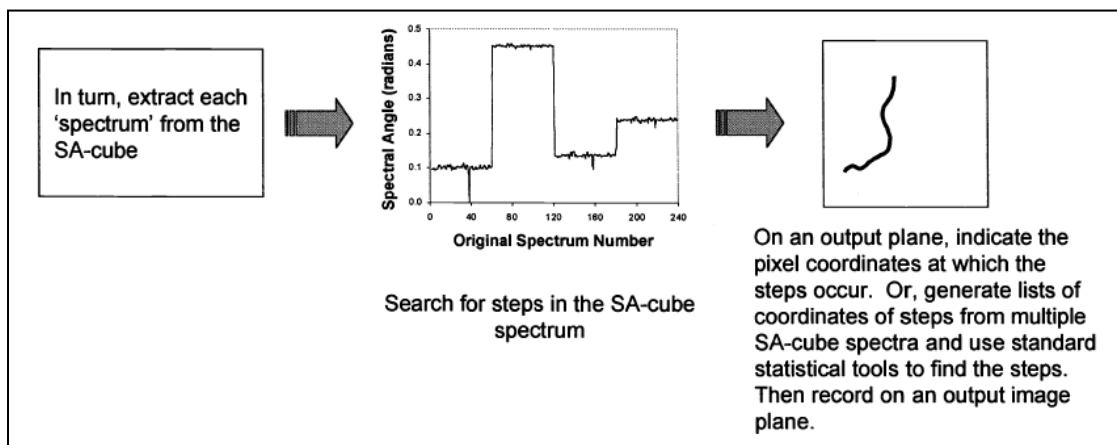


Figure 64: HySPADE's Final Three Steps [219]

HySPADE's unique integration of HSI's spatial and spectral information has demonstrated a reliable ability to detect edges among both manmade and natural targets, including mineral assemblages [219], [250]. For example, Figure 65 presents HySPADE's measurements against urban features in a 350-band VNIR/SWIR reflectance

cube collected by the ProSpecTIR HSI sensor [249]. Note that building outlines, roadways and the boundaries between water and vegetation are easily discernable.



Figure 65: HySPADE Edge Map for Urban Features [249]

Additionally, [250] measured HySPADE's performance against mineral assemblages as seen in Figure 66 [250]. In the discrete test, [250] determined that HySPADE reliably delineated the boundary between alunite and its adjacent minerals, albeit with broken edges. However, HySPADE did not perform well against the non-alunite mineral assemblages to the left of the discrete alunite piles, although limited

spatial resolution and heavily mixed pixels probably served as a limiting factor. These results suggest that additional HySPADE improvements are necessary to satisfy Canny's criteria for a good edge detector – a central objective of this dissertation.

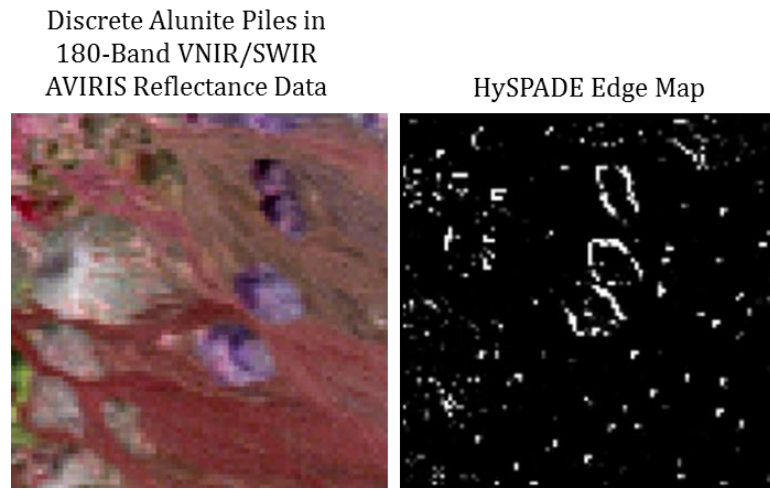


Figure 66: HySPADE Edge Map for Discrete Alunite Deposits [250]

An additional test of HySPADE's ability to support mineral mapping is seen in Figure 67, in which SAM version of HySPADE was tested against a higher spatial resolution 200-band LWIR (7.0 μ m to 11.5 μ m) emissivity dataset containing limestone and granite [251]. Note that in this case, HySPADE generated an unbroken boundary around the bottom mineral feature, but did so by producing a broad, unlocalized edge. The improved spatial resolution likely enabled HySPADE to generate the unbroken edge, but the results are limited from a localization perspective.

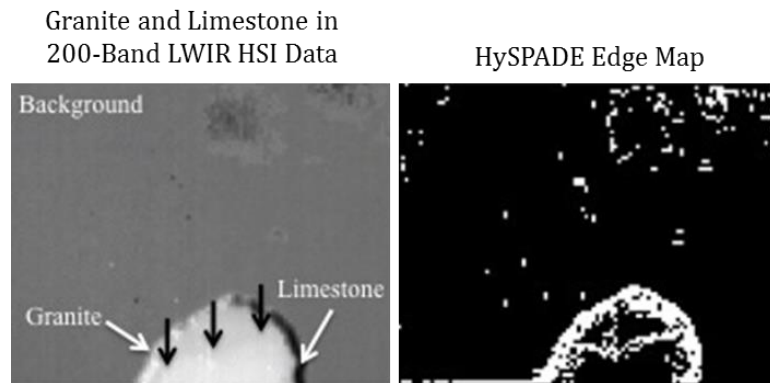


Figure 67: HySPADE Edge Map Derived from LWIR HSI Data [251]

HySPADE has also demonstrated an ability to detect edges in medical HSI data. For example, [252] used HySPADE to map ridges and patterns on the human tongue. As seen in Figure 68, HySPADE generated satisfactory edge maps from 150-band VNIR (0.4 μm to 1.0 μm) HSI data collected against human tongues. For the medical diagnostic purposes examined in [252], the HySPADE edge map contains clean, unbroken edges. Additionally, histogram stretching eliminated nearly all of the background noise, and the edges are more localized than were generated from the mineral assemblage data.

An interesting observation related to [252]’s results is that the edge map is entirely a function of illumination, not a chemical difference between the tongue crevices and the unbroken tongue surface – both are comprised of the same human tissue. The authors do not comment on this illumination dependency, but it suggests that HySPADE can generate satisfactory edge information based on illumination alone. The findings also recall [216]’ gradient-based illumination isolation approach discussed in [216], which indicated that satisfactory edge planes could be derived solely from an HSI scene’s

chromatic information to the exclusion of all illumination information. [252]’s results suggest a similar independency, but from the opposite perspective: reliable edge mapping can rely solely on illumination information to the exclusion of chromatic information. Ultimately, both [216] and [252] speak to the flexibility and broad utility of applying spatial-spectral edge detection algorithms to hyperspectral data.

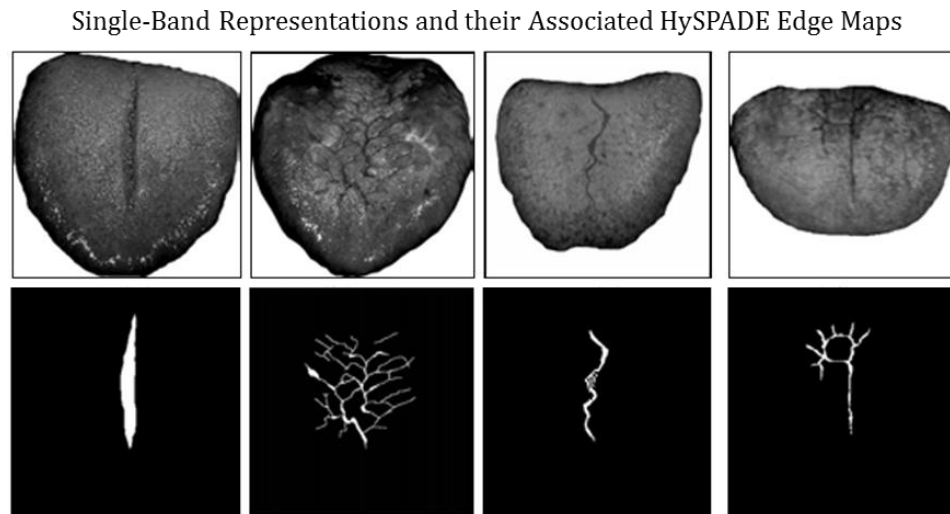


Figure 68: HySPADE Edge Maps of the Human Tongue [252]

Before concluding the HySPADE literature review, the Paskaleva et al HySPADE commentary warrants discussion [220]. Specifically, Paskaleva et al mischaracterize HySPADE by stating that it “utilizes solely spectral information to unveil the boundaries of the material composition” [220]. As demonstrated above, this is clearly not the case – HySPADE uses both spatial and spectral scene information to extract edges. Furthermore, Paskaleva et al incorrectly state that HySPADE has a “high computational

cost [which] makes it hard for the user to fine tune its tolerances, which is a clear disadvantage of the HySPADE algorithm” [220]. In practice, HySPADE’s C++ algorithm executes in less than a minute against a standard 200+ band HSI scene. Most would agree that a sub-minute algorithm does not impose high computational costs.

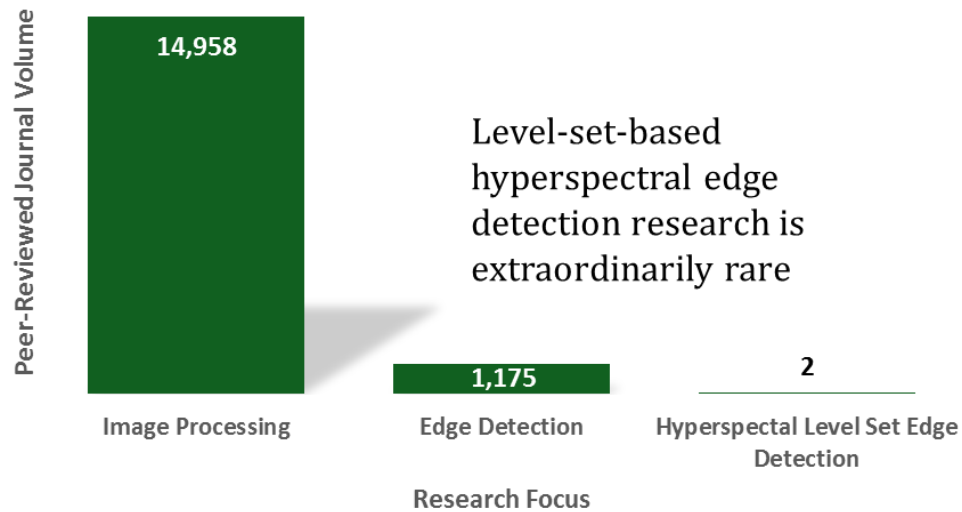
Finally, Paskaleva et al’s use of HySPADE as a comparative edge detector vis-à-vis their own proposed algorithms lacks rigor given that HySPADE is an unsupervised edge detector and Paskaleva et al’s proposed algorithms are all supervised, image classification algorithms (albeit “edge” classification algorithms). In general, supervised image classification algorithms should compare their performance to other supervised image classification algorithms, not unsupervised edge detection algorithms.

The preceding criticism of [220]’s peer-reviewed IEEE publication is not intended to cast doubt on their proposed algorithms – indeed, they produce reliable, scene-specific edge maps. Instead, the criticism is intended to emphasize the scientific community’s fledgling understanding of HSI edge detection algorithms. That a peer-reviewed journal article could contain such an inaccurate mischaracterization of a well-documented HSI edge detection algorithm speaks to the scarcity of experienced HSI edge detection peer reviewers, and by extension, the scarcity of HSI edge detection research.

Level Set Edge Detection for HSI Edge Detection

Among the avenues of research pursued herein, level-set-based edge detection methods for hyperspectral imagery have the smallest footprint in the peer-reviewed scientific literature. As seen in Figure 69, level-set-based edge detection research for HSI data is nearly non-existent – only two such efforts exist [203], [253]. Similar to the trend

in gradient-based HSI edge detection methods, level-set extensions to HSI tend to emphasize image classification applications to the exclusion of nearly all other image processing techniques, most likely due to the increased probability of research success for a supervised image classification method compared to an unsupervised edge detection method [254], [255], [256], [257]. Even with the small body of work, however, level-set-based HSI edge detection techniques appear quite promising.



Source: Peer-Reviewed Journal Titles Held by George Mason University Library; Surveyed 15JUL2016

Figure 69: Research Gap for Level-Set-Based Hyperspectral Edge Detection

For example, [253] incorporated a spatial-spectral edge detection term into a level-set evolution with the objective of using HSI edge information to slow and stop the level-set evolution along an edge. The only limitation of [253]’s approach is that the

edge detection step was scene-specific and subordinated to the larger image segmentation process. The researchers primed their edge detection subroutine (pursuant to the larger image classification objective) to search for the boundary between a known material and a known background, but the results are still suggestive that a level-set-based edge detection approach to HSI data can produce satisfactory results.



Figure 70: Incorporating Spectral Edge Information into a Level-Set-Based Algorithm [253]

Figure 70 presents a comparison between [253]’s algorithm when it incorporates the spectral edge information and when it operates without the spectral information. The left hand plate shows that without the spectral edge detection process, the level-set evolution fails to properly delineate the boundary between the similarly-toned clothing on the two passersby. The right hand plate demonstrates that incorporating high spectral resolution data into a level-set-based edge detection method can significantly improve edge detection accuracy, particularly between two similar materials – an achievement not

possible with lower-resolution MSI or PAN data. Ultimately, [253]’s results suggest that a level-set-based edge detection method can generate accurate edge results.

Another level-set-based HSI edge detection approach for hyperspectral imagery is given in [203], which develops a region-based level-set-based edge detection algorithm optimized to detect sharp corners. Specifically, [203] equips a level-set evolution process with a corner-preserving term that adjusts to how quickly the spectral gradient is changing from pixel to pixel. By considering the rate at which the spectral gradient is changing at any given point, [203] is able to generate more accurate corner edges due to its ability to take advantage of the fact that rapidly changing edges are more easily recognized in higher spectral resolution data. Specifically, [203]’s algorithm shows improved edge performance along sharp corners because it considers the edge information contained in dozens of narrow, contiguous channels, not simply the edge information available in one or a few bands.



Figure 71: Level-Set Edge Detection Improved by Incorporating HSI Data [203]

Figure 71 presents a comparison between [203]’s algorithm when it incorporates 168 bands of spectral edge information and when it executes without the benefit of hyperspectral information. While the corner-optimized results show improved edge accuracy at corners detected in the non-optimized results, more interesting is the spectrally-equipped version’s improved accuracy on corners that the non-optimized version missed. The elongated corner on the image’s lower left is the most prominent example of how incorporating spectral information into a level-set-based HSI edge detection method can improve edge detection accuracy.

HYPOTHESES

The chief objective of this dissertation is to advance the state-of-the-art practice of spatial-spectral edge detection methods for hyperspectral imagery. The primary approach is a simultaneous maximization of the spatial and spectral information inherent in a hyperspectral image cube to an extent that has not been documented in the literature, with an expectation that edge detection performance will produce satisfactory (i.e., usable) results for a variety of remote sensing applications. Specifically, this study advances three distinct spatial-spectral edge detection algorithms for HSI data: a gradient-based HSI edge detection algorithm, an improved HySPADE algorithm and a level-set-based HSI edge detection algorithm.

This study executes its experiments in alignment with the traditional form of the scientific method, which dictates that a given experiment begins with a null hypothesis (H_0), or a statement of no difference or differences. The experiment then tests a series of alternative hypotheses whose corpus of results is used to determine whether the null hypothesis is supported or non-supported. In the instance where the null hypothesis is supported or partially supported, I endeavor to identify explanatory factors including algorithm limits, spatial resolution limits, spectral resolution limits, scene noise, the inherent challenge imposed by a dataset, etc. In the instance where the null hypothesis is not supported by the alternative hypotheses' findings, this dissertation clearly identifies

the conditions under which the null hypothesis was rejected in order to maximize the repeatability of the experiments.

In either circumstance, this dissertation declares an advancement of the science according to the negative findings argument detailed in the Purpose section. Namely, this study deems a negative finding to be just as welcome as a positive finding so long as it rigorously illuminates the hypothesis. This experimental approach's ultimate objective is to improve scientific understanding, be it via positive results that suggest avenues of further research or via negative results that suggest the limits of current technologies.

Finally, the below description of the null and alternative hypotheses is intentionally high-level in order to communicate the overall intent of each experiment, which is to measure each algorithm's performance against each dataset according to Canny's criteria for a good edge detector.

Experiment #1: Gradient-Based Edge Detection Method

H_0 = The gradient-based edge detection algorithm will demonstrate average performance with respect to six edge operator evaluation criteria: false positives, false negatives, localization, single-pixel response, robustness to noise and unbroken edges.

H_1 = The gradient-based edge detection algorithm will demonstrate superior performance with respect to false positives.

H_2 = The gradient-based edge detection algorithm will demonstrate superior performance with respect to false negatives.

H_3 = The gradient-based edge detection algorithm will demonstrate superior performance with respect to localization.

H_4 = The gradient-based edge detection algorithm will demonstrate superior performance with respect to single-pixel response.

H_5 = The gradient-based edge detection algorithm will demonstrate superior performance with respect to robustness to noise.

H_6 = The gradient-based edge detection algorithm will demonstrate superior performance with respect to unbroken edges.

H_7 = The gradient-based edge detection algorithm will demonstrate superior performance against compressed PCA and MNF datasets compared to full reflectance, PCA and MNF hypercubes.

H_8 = The gradient-based edge detection algorithm will be more robust to declining spatial resolution compared to declining spectral resolution.

Experiment #2: HySPADE Edge Detection Method

H_0 = The improved HySPADE edge detection algorithm will demonstrate average performance with respect to six edge operator evaluation criteria: false positives, false negatives, localization, single-pixel response, robustness to noise and unbroken edges.

H_1 = The improved HySPADE edge detection algorithm will demonstrate superior performance with respect to false positives.

H_2 = The improved HySPADE edge detection algorithm will demonstrate superior performance with respect to false negatives.

H_3 = The improved HySPADE edge detection algorithm will demonstrate superior performance with respect to localization.

H_4 = The improved HySPADE edge detection algorithm will demonstrate superior performance with respect to single-pixel response.

H_5 = The improved HySPADE edge detection algorithm will demonstrate superior performance with respect to robustness to noise.

H_6 = The improved HySPADE edge detection algorithm will demonstrate superior performance with respect to unbroken edges.

H_7 = The improved HySPADE edge detection algorithm will demonstrate superior performance against compressed PCA and MNF datasets compared to full reflectance, PCA and MNF hypercubes.

H_8 = The improved HySPADE edge detection algorithm will be more robust to declining spatial resolution compared to declining spectral resolution.

Experiment #3: Level Set-Based Edge Detection Method

H_0 = The level set-based edge detection algorithm will demonstrate average performance with respect to six edge operator evaluation criteria: false positives, false negatives, localization, single-pixel response, robustness to noise and unbroken edges.

H_1 = The level set-based edge detection algorithm will demonstrate superior performance with respect to false positives.

H_2 = The level set-based edge detection algorithm will demonstrate superior performance with respect to false negatives.

H_3 = The level set-based edge detection algorithm will demonstrate superior performance with respect to localization.

H_4 = The level set-based edge detection algorithm will demonstrate superior performance with respect to single-pixel response.

H_5 = The level set-based edge detection algorithm will demonstrate superior performance with respect to robustness to noise.

H_6 = The level set-based edge detection algorithm will demonstrate superior performance with respect to unbroken edges.

H_7 = The level set-based edge detection algorithm will demonstrate superior performance against compressed PCA and MNF datasets compared to full reflectance, PCA and MNF hypercubes.

H_8 = The level set-based edge detection algorithm will be more robust to declining spatial resolution compared to declining spectral resolution.

Key Science Questions

This dissertation informs a range of scientific questions of interest and addresses both the scientific perspective and the applications perspective. Due to the relative newness of HSI data and its significant departure from conventional remote sensing capabilities, HSI research has challenged several traditional image science understandings. For example, Paskaleva et al's [220] concept of a hyperspectral edge signature challenges the accepted understanding of an edge pixel as a discontinuity relative to its neighbors, and Resmini's HySPADE algorithm suggests that spatial and spectral information can be woven together in a manner that is uniquely optimized for edge detection processes. Below are a series of key questions that this study explores in an effort to shed light on how this dissertation's findings align to existing conventions

and how they create new insights and understandings in hyperspectral image science. The key science questions also attempt to blend both pure scientific research with the practical perspective of real-world applications.

What is an Edge in Hyperspectral Space?

This question has a different meaning in spatial space than it does in spectral space. For example, for panchromatic imagery an edge is defined simply as a line dividing pixels with different monochromatic intensities according to a given threshold. In hyperspectral imagery however, there are hundreds of intensity measurements per pixel (as opposed to just one for panchromatic) and therefore hundreds of potential discrete differences between the two pixels – a reality that is further complicated by the fact that when arranged sequentially, the hundreds of intensity measurements (i.e., bands) can be displayed and measured in a variety of ways, including as n -dimensional vectors in n -dimensional space, as data points in a multivariate statistical distribution, or as a two dimensional spectral curve (i.e., a spectrum—a plot of reflectance vs. wavelength).

Put simply, the presence of high-dimensional spectral information complicates the traditional understanding of an edge. This dissertation seeks to inform a new, more precise definition of edges that accommodates the unique contributions of hyperspectral data. For the purposes of this work, an edge is defined as a linear or curvilinear multi-pixel spatial and spectral discontinuity separating spectrally distinct *materials*.

Edges also have different meaning from a scientific perspective compared to an applications perspective. For example, a scientific perspective would define an edge as a yes or no proposition; either the pixel is the boundary between two materials, or it is not.

Researchers regularly pursue this perspective by testing their algorithms against synthetic datasets (or favorably contrived, real examples) characterized by unambiguous and essentially single pixel boundaries between materials. There is great value in this approach in the sense that it establishes an empirical and easily quantified baseline of performance that can be readily compared to other algorithms. Indeed, this study agrees with the value of baselining algorithm performance and pursues this approach by testing its algorithms against a rigorously constructed synthetic HSI dataset designed for edge detection evaluation.

This dissertation also recognizes that applied remote sensing problems treat edges as a matter of degree; namely, some pixels are more strongly edge pixels than another. This reality stems from the geographic (and image formation) uncertainty of where one object begins and where another begins, particularly for natural features whose boundaries nature has blended together. This study tests several types of real-world remote sensing scenes in order to measure algorithm performance from an applications perspective. By testing from both the scientific and applications perspective, this dissertation seeks a balance between basic research and applied research such that both communities merit its findings.

Which Matters More, Spatial or Spectral Resolution?

The dichotomy between spatial and spectral resolution is fundamental to the resolution challenge facing many remote sensing applications. Given the general tradeoff between spatial and spectral resolution, engineers and remote sensing scientists typically “can’t have it both ways” – they usually have to choose either high spatial resolution or

high spectral resolution depending on their specific need. Or as is often the case, they simply must work with whatever data is available, even if it is not the optimal balance of spatial and spectral resolution for the application at hand.

This dissertation seeks to take advantage of its broad sampling of challenging, non-traditional datasets by measuring algorithm performance as a function of spatial and spectral resolutions. For example, for short, high-contrast edges such as those commonly found in urban settings, lower spatial resolutions sufficient to simply resolve the edge will likely dominate the spatial/spectral tradeoff; i.e., spatial resolution is likely to be more valuable for applications in which the materials contrast strongly in the spectral dimension.

Conversely, less distinct boundaries between similar materials such as those found in geologic or other natural settings will likely benefit from superior spectral resolution at the expense of spatial resolution. For applications in which the materials are spectrally similar or strongly mixed, such as mineral mapping of small scale remote sensing scenes, spectral resolution is likely to be more important than spatial resolution. Ultimately, this study seeks to inform the spatial-spectral resolution question by measuring a range of spatial and spectral resolutions against a variety of datasets spanning the range of conventional and straightforward to the unconventional and challenging.

DATA

In order to robustly measure accuracy, localization and single-edge response, this dissertation tests its edge detection algorithms against HSI datasets spanning a broad range of spectral regions, spectral resolutions, spatial resolutions, collection platforms, irradiance sources, scene content, viewing/illumination geometries and complexity.

Table 2 presents an overview of this work’s overhead, ground-based and microscene HSI databases.

Table 2: Hyperspectral Dataset Overview

Hyperspectral Dataset	Wavelengths	Bands	Spatial Resolution
Reno, Nevada	0.4 μ m – 2.5 μ m	356	~8m
Cuprite, Nevada	0.39 μ m – 2.45 μ m	178	4m
Indian Pines, Indiana	0.40 μ m – 2.50 μ m	224	~20m
Deepwater Horizon, Gulf of Mexico	0.39 μ m – 2.45 μ m	360	2.2m
Larkhaven Terrace, Virginia	0.4 μ m – 1.0 μ m	128	~5cm
Fujian Granite Slab #1	0.45 μ m – 0.88 μ m	72	~2mm
Fujian Granite Slab #2	0.92 μ m – 2.50 μ m	164	~2mm
South Africa Core Sample	1.00 μ m – 2.51 μ m	72	~1cm
Aluminum Panel	0.4 μ m – 1.0 μ m	128	~5mm
Rare Target on Sand	0.44 μ m – 0.88 μ m	72	~2mm
Chemical Array on Sand	0.90 μ m – 2.51 μ m	168	~2mm
Cloth Threads on Sand	0.40 μ m – 0.85 μ m	80	~2mm

Overhead datasets constitute most HSI datasets available in the open source. This work considers three very different airborne VNIR/SWIR HSI datasets in order to

measure algorithm performance against both traditional and non-traditional datasets. Algorithm results against traditional overhead datasets are useful because they provide a baseline for comparing the results obtained herein to those in the literature. The non-traditional datasets are useful because they enable measurement of the algorithms' generalizability and unique capabilities. The two traditional overhead datasets are an airborne VNIR/SWIR datacube of a mixed urban/vegetation scene in Reno, Nevada, and an airborne VNIR/SWIR datacube of Cuprite, Nevada. The non-traditional dataset is an airborne VNIR/SWIR datacube of the Gulf of Mexico after the Deepwater Horizon oil spill.

Ground-based datasets appear frequently in the peer-reviewed HSI literature due to their ease of acquisition, suitability as controlled, well-truthed scenes, and the availability of (relatively) inexpensive ground-based HSI sensors. This study considers five ground-based datasets covering a broad range of remote sensing applications and difficulty. Three of the ground-based datasets capture traditional scenes, including two hypercubes containing high-spatial resolution HSI data of granite slabs, one imaged in the VNIR and one imaged in the NIR/SWIR. The third traditional ground-based dataset is the Larkhaven dataset, which contains a building façade and an automobile. The first non-traditional dataset is a NIR/SWIR hypercube of South African core samples. The second challenging, non-traditional HSI dataset is a VNIR cube of a riveted aluminum panel found on the island of Nikumaroro – an uninhabited Pacific island near where Amelia Earhart disappeared in 1937.

Microscene data is a new addition to the HSI literature. Designed for rapid, iterative, inexpensive testing of HSI algorithms, microscenes are researcher-engineered scenes containing small, representative examples of natural and manmade materials. Rather than contract an expensive aircraft to collect HSI data or pay for previously collected, suboptimal HSI data, an HSI researcher can model the scene of interest by arranging and imaging representative scene materials in the lab. For example, to test an HSI edge detection algorithm's ability to delineate the boundary of a rare target within a vegetation and soil background, a researcher could assemble and image in the lab with grass clippings, sticks, sand, gravel and the target material. Such microscenes can serve as reliable analogs for real, complex earth remote sensing scenes. Microscenes also have the advantage of allowing for significant control over viewing/illumination geometries due to the control of incident light.

This work tests four HSI microscene datasets of varying complexity. The first microscene contains a rare target chemical within a complex vegetation and sand background [258], while the second microscene contains an array of chemicals of interest also on a sand background [110]. The third and fourth microscenes contain a variety of overlapping thread samples.

Overhead – Reno, Nevada USA

Table 3 summarizes the first and most traditional HSI dataset that this dissertation tests, a ProSpecTIR overhead VNIR/SWIR image of a mixed urban and vegetation scene in Reno, Nevada USA [96]. The scene contains common urban features such as sharp-cornered buildings of various roof type, asphalt roadways, vehicles and concrete parking

lots. Additionally, the scene contains a strong sampling of natural features such as trees, grassy open areas, a waterway, and bare earth.

Table 3: Overhead HSI Dataset #1 - VNIR/SWIR Reno, Nevada USA [96]

Sensor Name	ProSpecTIR
Dataset	Urban and Mixed Environment
Location	Reno, Nevada USA
Date of Collect	Unknown
Data Type	Reflectance
Spectral Range	0.4 μ m - 2.5 μ m
Spectral Resolution	356 bands
Spatial Resolution	~8m
Columns x Rows	320 x 600
Radiometric Resolution	16-bit
Cloud Cover	0%
Noise	Minimal
Scene Description	Urban, Vegetation and Water Features; Daytime; No Apparent Slant Angle
Source	http://www.spectir.com/free-data-samples/

As seen in Figure 72, the Reno hypercube contains roll anomalies common to overhead imagery. Attributable to aircraft roll, the roll anomalies do not present a material barrier to spatial-spectral edge detection testing, although some of the most linear scene features such as roadways and building edges will alarm slightly less strongly against traditional edge detection methods that are sensitive to vertical and horizontal edges. Additionally, Figure 73 contains several sample reflectance spectra extracted from the Reno scene, including vegetation, asphalt and aluminum roofing; the reflectance scale has been scaled by 10,000, as well. Note the high-quality reflectance data obtainable from the ProSpecTIR imager.



Figure 72: Overhead VNIR/SWIR Hypercube, Reno, NV USA - Color Infrared Bands 34, 55, 99 [96]

The Reno dataset supports one of the most traditional HSI applications, urban feature mapping. The Background section detailed several urban feature mapping endeavors, most of which used overhead HSI data similar to the Reno hypercube. By placing the Reno data first among those presented here, this study intends to establish a rigorous link to the HSI urban feature mapping literature with which researchers are most familiar, and which will allow interested readers to quickly compare this work's edge detection performance to the performance of established edge detectors.

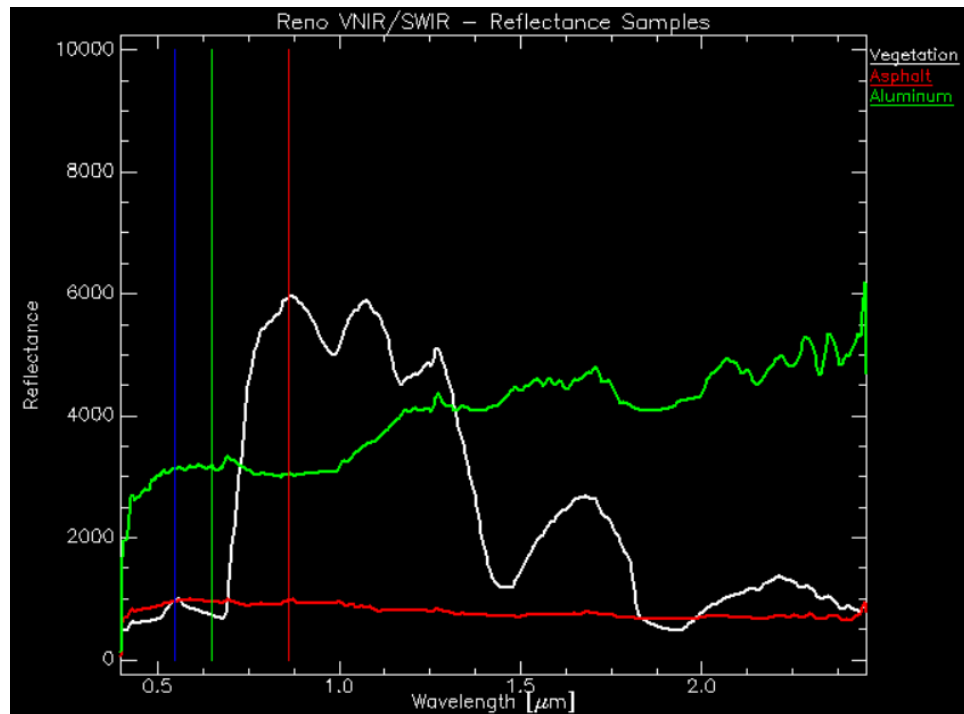


Figure 73: Sample VNIR/SWIR Reflectance Spectra from Reno, NV Hypercube

Overhead – Cuprite, Nevada USA

Table 4 summarizes the second traditional overhead HSI dataset analyzed: a ProSpecTIR VNIR/SWIR image of Cuprite, Nevada USA [96]. A commonly imaged area, the Cuprite hypercube contains a variety of minerals such as alunite, kaolinite and buddingtonite. The minerals are present in a range of conditions, from relatively homogeneous deposits to complex assemblages. Additionally, the scene contains a small sampling of manmade features such as small buildings and long, straight, narrow roadways.

Table 4: Overhead VNIR/SWIR Hypercube - Cuprite, NV USA [96]

Sensor Name	ProSpecTIR VS-1
Dataset	Cuprite
Location	Cuprite, Nevada USA
Date of Collect	June 14, 2008
Data Type	Reflectance
Spectral Range	0.39 μ m - 2.45 μ m
Spectral Resolution	178 bands
Spatial Resolution	4m
Columns x Rows	320 x 2703; 320 x 2729; 320 x 2557; 320 x 2601
Radiometric Resolution	16-bit
Cloud Cover	0%
Noise	Minimal
Scene Description	Mineralogy landscape; two-lane highways; daytime; no apparent slant angle
Source	http://www.spectir.com/free-data-samples/

As seen in Figure 74, the full ProSpecTIR dataset consists of four separate flight lines. While there is some overlap among the four, each flight line captures generally different parts of the Cuprite area. For example, Flight Line #1 contains primarily complex mineral assemblages spread amongst a few unimproved roadways. A large kaolinite deposit is present towards the top of the image. Flight Line #2 contains primarily open desert landscapes interspersed with improved roadways and small buildings. A few vehicles are present in the scene.

Flight Line #3 is characterized by a large, bright playa towards the top of the scene along with a few unimproved roadways. Finally, Flight Line #4 contains several instances of relatively pure alunite deposits. Flight Line #4 also contains a range of shadow intensities, including significant terrain shadowing along the bottom of the

image. A few unimproved roads and small, bright patches are present, as well. Additionally, Figure 75 contains several sample radiance spectra extracted from the Cuprite scene, including dark, medium and light toned materials. Note the high-quality radiance data obtainable from the ProSpecTIR sensor.

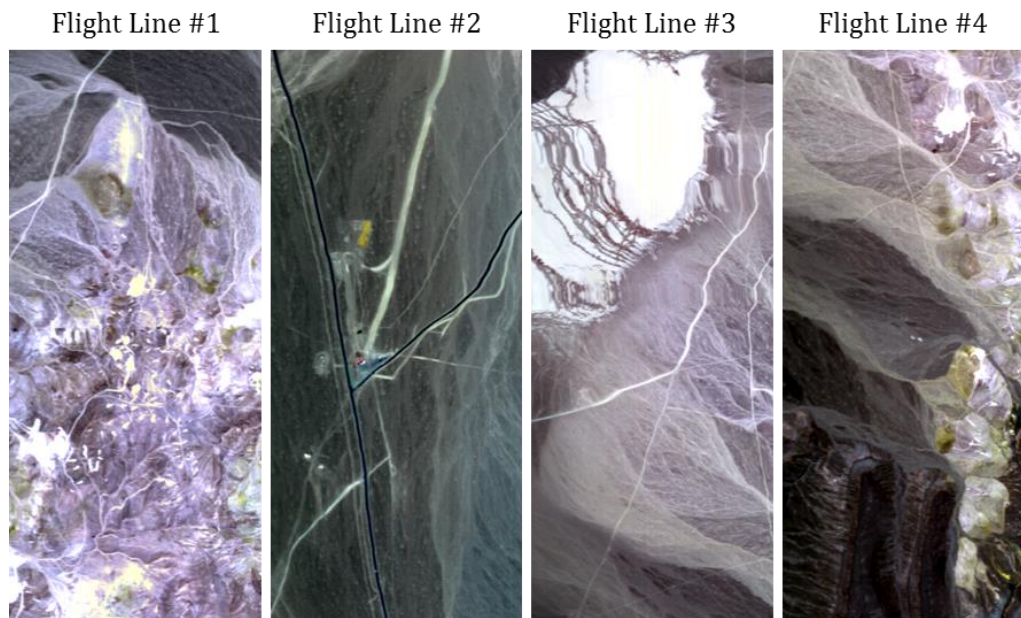


Figure 74: Overhead VNIR/SWIR Hypercube, Cuprite, NV USA - Color Infrared Bands 17, 28, 50 [96]

The Cuprite dataset directly supports another common HSI application, mineral mapping. Indeed, as discussed at length in the Background section, the Cuprite area is the most well-understood and frequently acquired HSI (and other modalities) scene of geologic significance in the HSI literature. This study executes a test of the traditional HSI Cuprite dataset based on the same reasoning behind testing the Reno hypercube first

– to establish an initial sense of how the edge detection algorithms compare to traditional edge detection algorithms as applied to a traditional HSI application like mineral mapping.

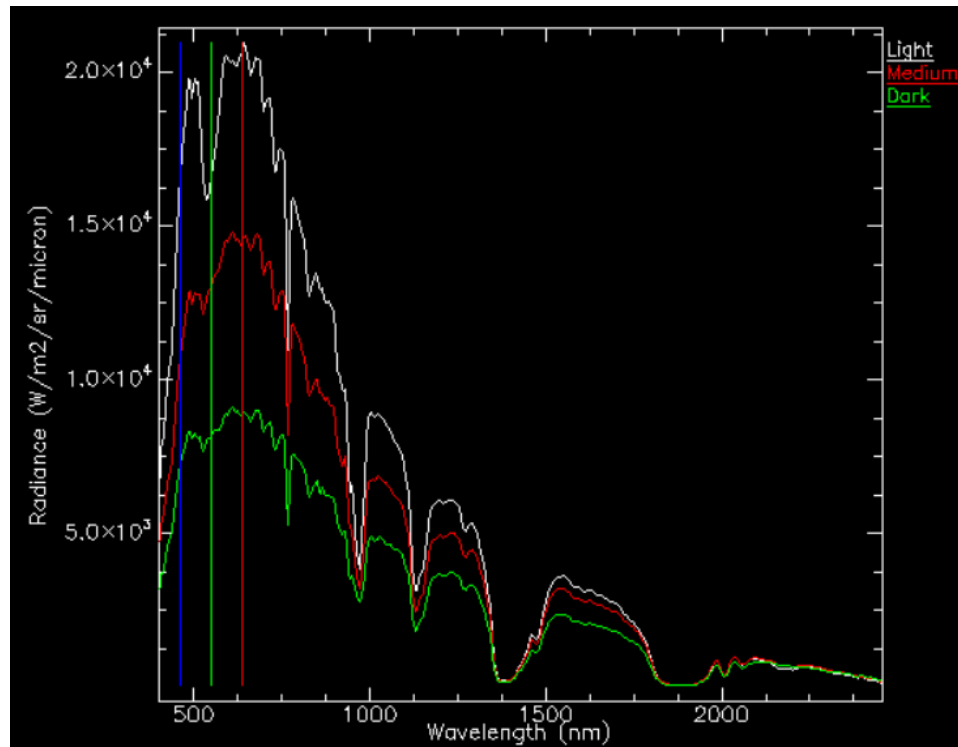


Figure 75: Sample VNIR/SWIR Radiance Spectra from Cuprite, NV Hypercube

Overhead – Indian Pines, Indiana USA

Table 5 summarizes the third and final traditional overhead hypercube tested: an overhead agricultural scene widely used in studies of the traditional HSI application of crop mapping. AVIRIS's 224-band VNIR/SWIR Indian Pines hypercube is the most extensively studied HSI agricultural dataset in the literature due to its accompanying

ground-truth data, which provides pixel-level ground truth for the 16 crop types present within the field of view [259]. Additionally, Figure 76 contains several sample radiance spectra extracted from the Indian Pines scene, including radiance spectra of hay, forest, and soybeans. Note the high-quality radiance data obtainable from the AVIRIS imager.

Table 5: Overhead VNIR/SWIR Hypercube - Indian Pines Agriculture [259]

Sensor Name	AVIRIS
Dataset	Indian Pines Agriculture
Location	Indian Pines, Indiana USA
Date of Collect	June 12, 1992
Data Type	Radiance
Spectral Range	0.40 μ m – 2.50 μ m
Spectral Resolution	224 bands
Spatial Resolution	~20m
Columns x Rows	145 x 145
Radiometric Resolution	10-bit
Cloud Cover	0%
Noise	Minimal
Scene Description	Agricultural fields broken by roadways; daytime; no apparent slant angle
Source	aviris.jpl.nasa.gov/data/free_data.html

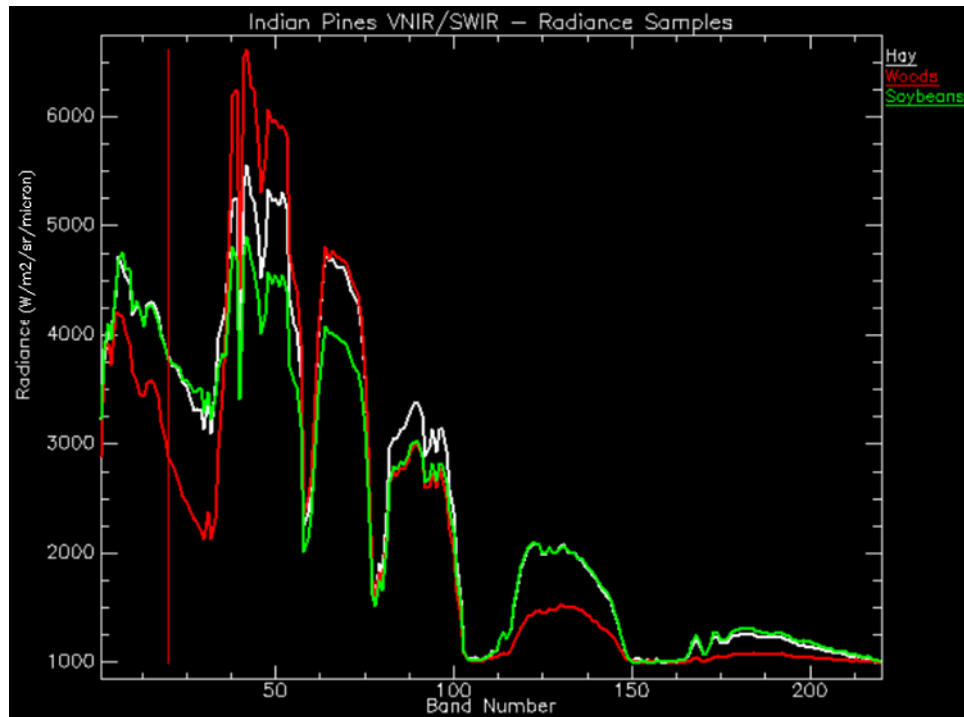


Figure 76: Sample VNIR/SWIR Radiance Spectra from Indian Pines, IN Hypercube

As seen in Figure 77, the Indian Pines hypercube is dominated by agricultural fields containing a variety of crops, including corn, soybean, wheat, hay, and oats. Several grass fields and woodland stands are also visible in the scene, along with a handful of buildings and roadways [259]. The limited GSD (~20m) also lends the scene a fuzzier texture than most of the datasets tested herein, but is generally sufficient for vegetation and crop mapping studies.



Figure 77: Overhead VNIR/SWIR Hypercube, Indian Pines, IN USA - Color Infrared Bands 16, 26, 50 [259]

The Indian Pines data set is the final data set designed to establish a clear link between HSI edge detection and the broader HSI literature addressing airborne data in support of traditional HSI applications. At the conclusion of the Indian Pines testing, this dissertation will have established a clear sense of how its algorithms compare to existing edge techniques with respect to urban feature mapping, mineral mapping and vegetation mapping – three of the most extensively researched applications in the literature on hyperspectral remote sensing. The remaining ten HSI datasets are non-traditional in different ways, and are included in order to extend scientific knowledge into more challenging, less understood areas.

Overhead – Deepwater Horizon Oil Spill, Gulf of Mexico

Table 6 summarizes the first non-traditional HSI dataset that this dissertation tests, an overhead ProSpecTIR VNIR/SWIR image of the 2010 Deepwater Horizon oil spill in the Gulf of Mexico [96]. The Deepwater Horizon scene is non-traditional in the sense that it does not contain any terrestrial materials, only open ocean, sea foam, petroleum and shadow. Consequently, the Deepwater Horizon dataset is likely to challenge algorithm performance in unexpected ways.

Specifically, the implications of an ocean, only, HSI scene are likely to appear during the QUAC atmospheric compensation step, which relies on common terrestrial materials to generate the gains and offsets necessary for atmospheric correction. In order to understand how effectively the edge detection algorithms perform against open ocean HSI data, this study will test each algorithm against both a QUAC-corrected reflectance cube as well as the at-aperture radiance cube. Additionally, the general darkness of the Deepwater Horizon dataset will stress edge detection performance due to the relatively limited intensity range in which discontinuities can be detected.

Table 6: Overhead VNIR/SWIR Hypercube - Deepwater Horizon Oil Spill [96]

Sensor Name	ProSpecTIR VS-1
Dataset	Deepwater Horizon Oil Spill
Location	Gulf of Mexico
Date of Collect	June 6, 2010
Data Type	Radiance
Spectral Range	0.39 μ m - 2.45 μ m
Spectral Resolution	360 bands
Spatial Resolution	2.2m
Columns x Rows	320 x 1160
Radiometric Resolution	16-bit
Cloud Cover	0%
Noise	Minimal
Scene Description	Open ocean; daytime; no apparent slant angle
Source	http://www.spectir.com/free-data-samples/

As seen in Figure 78, the Deepwater Horizon hypercube is an open ocean scene containing petroleum horizons of various thickness floating on seawater. Wave action is noticeably visible as bright, elongated frontiers of wave fronts passing from roughly lower-right to upper-left across the scene. A vessel's wake is also visible running along the bottom of the scene from left to right, and cloud cover is negligible. Sea foam is also present in the scene, and shadowing is present but minor due to the lack of vertical features in the scene able to cast shadows. Overall, the scene is fairly complex despite its low population of distinct materials, and is characterized by overlapping, highly mixed features. Several high-contrast edges are visible within the scene, which is dominated by the dark seawater background. Additionally, Figure 79 contains several sample radiance spectra, including dark sea water, lighter sea water and petroleum. Note that the surface petroleum is clearly distinguishable from seawater in the radiance data.

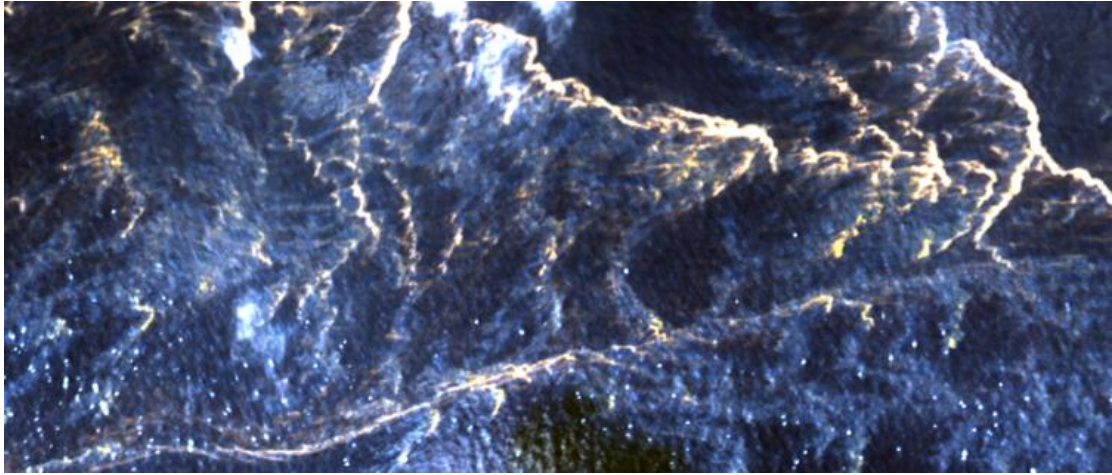


Figure 78: Overhead VNIR/SWIR Hypercube, Deepwater Horizon - Color Infrared Bands 36, 57, 101 [96]

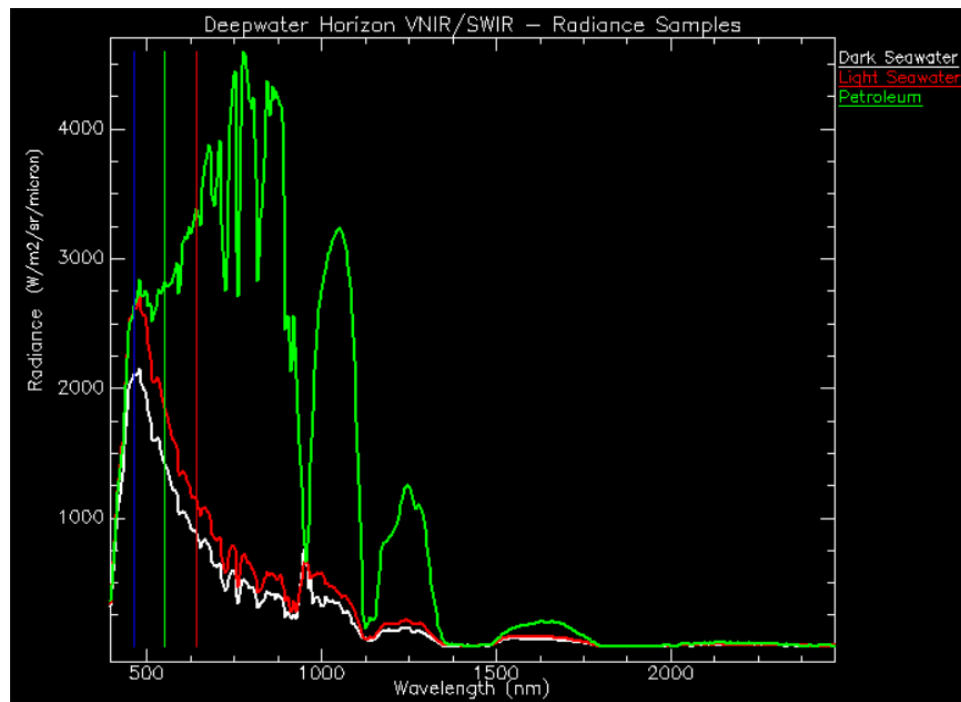


Figure 79: Sample VNIR/SWIR Radiance Spectra from Deepwater Horizon Hypercube

The Deepwater Horizon hypercube supports the first challenging, non-traditional HSI application to be examined here: oil spill mapping. As discussed in the Background section, the HSI literature's dozen or so peer-reviewed HSI efforts to support oil spill detection from a continuity-based, image classification perspective are dominated by band-ratio techniques. None of them attempt a faster, more generalizable discontinuity-based approach to simply delineating the boundary between oil and sea water. Consequently, testing edge detection algorithms against the challenging, non-traditional Deepwater Horizon VNIR/SWIR data presents a unique opportunity to advance HSI science as applied to oil mapping applications.

Ground-Based – Larkhaven

The first ground-based HSI datacube to be considered is the VNIR Larkhaven dataset containing mixed urban features such as metal, plastic, rubber, paint, glass, asphalt and vegetation. Several calibration panels, both dark and light, are also present in the scene. Analogous to the Reno overhead dataset, the Larkhaven dataset begins the ground-based experiments by using a traditional HSI application such as urban feature mapping to establish a link between this work and the broader HSI literature. Table 7 summarizes the Larkhaven dataset, which was collected by Dr. Ron Resmini and Mr. Cary Cox in March 2011 using GMU/GGS's SOC 700 VNIR imager.

Table 7: Ground-Based VNIR Hypercube - Larkhaven

Sensor Name	Surface Optics Corporation (SOC) 700 Series Hyperspectral Imager
Dataset	Urban and Mixed Environment
Location	Larkhaven Terrace, Fairfax Station, VA USA
Date of Collect	March 5, 2011
Data Type	Radiance
Spectral Range	0.4 μ m - 1.0 μ m
Spectral Resolution	128 bands
Spatial Resolution	~5cm
Columns x Rows	640 x 640
Radiometric Resolution	12-bit
Cloud Cover	0%
Noise	Minimal
Scene Description	Urban and vegetation; imaged on a cloudy day; no sky; slant angle level with the ground
Source	Dr. Ron Resmini, George Mason University

The mosaic in Figure 80 presents the full Larkhaven dataset, which consists of seven adjacent samples spanning the front of a colonial style single family home. The most notable edge features in the scene are the linear boundaries between grout and brick, the boundaries between vegetation and brick, and the various complex boundaries among steel, paint, glass and plastics on the motor vehicle in the scene. Also, note the minor misalignment between mosaicked image planes.

A traditional ground-based HSI dataset, the Larkhaven hypercube was collected on a mostly cloudy day and does not contain the sky. Compared to the Reno VNIR/SWIR cube, the Larkhaven dataset enjoys a superior spatial resolution, approximately 5cm, compared to 8m for the Reno dataset. Similarly, the Larkhaven dataset does not contain the aircraft roll errors present in the Reno dataset, meaning that

the truly linear features appear undistorted within the scene. Additionally, Figure 81 contains several sample radiance spectra extracted from the Larkhaven scene, including vegetation, a bright calibration panel and a dark calibration panel. Note the high-quality radiance data obtainable from the SOC710 imager.



Figure 80: Ground-Based VNIR Hypercube, Larkhaven - Color Infrared Bands 35, 60, 109

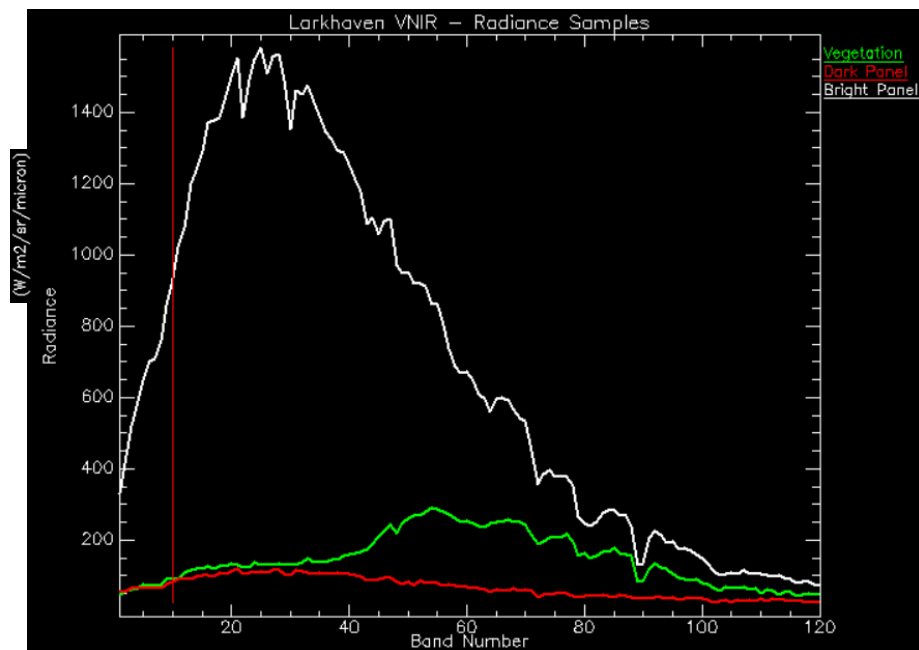


Figure 81: Sample VNIR Radiance Spectra from Larkhaven Hypercube

The Larkhaven scene is also much simpler than the Reno mixed urban scene with respect to the variety of complex materials, although it has a significantly smaller spectral range. Ultimately, the complementary Reno and Larkhaven datasets provide reliable insight into how effectively this study's spatial-spectral edge detection algorithms can inform the traditional HSI application of urban feature mapping.

Ground-Based – Granite VNIR

Table 8 summarizes the first non-traditional ground-based dataset under consideration, a very-high spatial resolution VNIR hypercube of a granite slab. The sample is a commercially-obtained cut-and-polished slab of coarse-grained pink granite from the Fujian Province of China, a large and well-known region of granitic magmatism [260]. Additionally, Figure 83 contains several sample radiance spectra extracted from the cube, including a white region, a black region and a pink region. Note the somewhat noisy, single-pixel reflectance data produced by the 72-band SOC 710 imager.

Table 8: Ground-Based VNIR Hypercube - Granite Slab

Sensor Name	Surface Optics Corporation (SOC) 710 Series Hyperspectral Imager
Dataset	Granite Slab - VNIR
Location	Fujian Province, China
Date of Collect	Unknown
Data Type	Reflectance
Spectral Range	0.45 μ m - 0.88 μ m
Spectral Resolution	72 bands
Spatial Resolution	~2mm
Columns x Rows	605 x 960
Radiometric Resolution	12-bit
Cloud Cover	0%
Noise	Minimal
Scene Description	Large quartz crystals; feldspar; cut and polished; imaged at nadir
Source	Dr. Ron Resmini, The MITRE Corporation; Dr. David Allen, National Institute of Standards and Technology

As seen in Figure 82, the sample is typical of granite; it contains recognizable moderately-toned feldspar and lightly-toned quartz regions. This HSI datacube is traditional in the sense that it contains mineral samples imaged at high spectral resolution, but it is non-traditional in the sense that it complements the high-spectral resolution with very high ground sampling distance (GSD) on the order of 2mm.

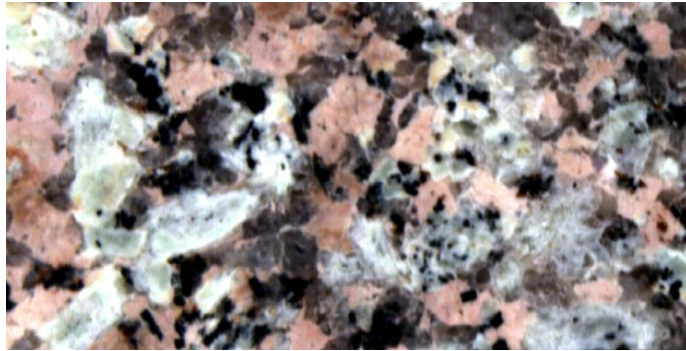


Figure 82: Ground-Based VNIR Hypercube, Granite Slab - True Color Bands 10, 25, 40

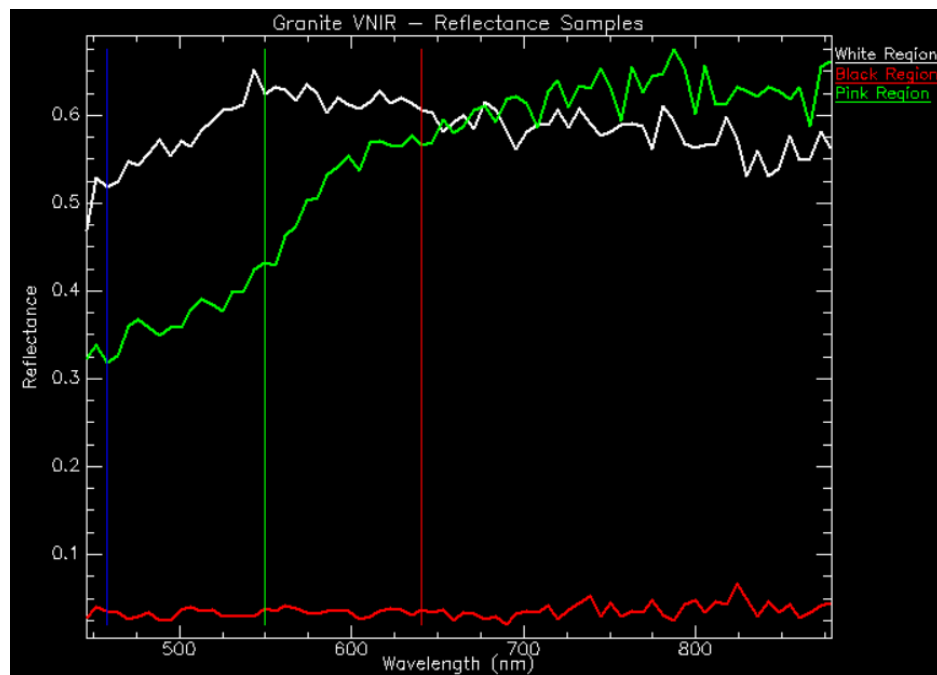


Figure 83: Sample VNIR Reflectance Spectra from Granite Hypercube

By testing a high spatial resolution, high spectral resolution HSI mineralogy scene, this work seeks to measure algorithm dependencies on spatial resolution and spectral resolution. For example, testing the overhead Cuprite data at varying spectral resolutions would provide insight into an algorithm's spectral dependencies, but would

say little about how superior spatial resolutions can affect the algorithm's ability to inform mineral mapping applications. The true spatial-spectral character of the algorithm would remain unknown.

Testing the algorithms' performance against the high spatial and spectral resolution granite dataset, however, will measure the true spatial-spectral nature of each algorithm. For example, by holding the high spatial resolution constant and rigorously decrementing the spectral resolution, this study will measure each algorithm's spectral dependency. Ultimately, the granite VNIR dataset is an attractive choice for this dissertation because its high spatial resolution approaches mineral mapping applications from a unique, challenging perspective – a guiding principle for this dissertation.

Ground-Based – Granite NIR/SWIR

Table 9 summarizes the second non-traditional ground-based dataset under examination – a very-high spatial resolution VNIR/SWIR hypercube of the same pink granite sample detailed in the previous section. The primary difference between the previous VNIR sample and this NIR/SWIR sample is wavelength: the previous sample spans 0.45 μm to 0.88 μm , while the NIR/SWIR sample spans 0.92 μm to 2.50 μm . The broader bandpass of the NIR/SWIR sample also has more channels, 164 compared to 72. As seen in Figure 84, the NIR/SWIR pink granite sample contains the same mineral assemblage as the VNIR sample – clearly recognizable moderately-toned feldspar and lightly-toned quartz regions dominate the scene. Additionally, Figure 85 contains three reflectance spectra extracted from the data. Note the smooth reflectance spectra

produced by the 164-band Headwall Photonics, Inc., HYPERSPEC imager compared to the 72-band Resonon Pika II data from the NIR sample.

Table 9: Ground-Based NIR/SWIR Hypercube - Granite Slab

Sensor Name	Headwall Photonics HYPERSPEC SWIR Imaging Spectrometer
Dataset	Granite Slab - NIR/SWIR
Location	Fujian Province, China
Date of Collect	Unknown
Data Type	Reflectance
Spectral Range	0.92 μ m - 2.50 μ m
Spectral Resolution	164 bands
Spatial Resolution	~2mm
Columns x Rows	324 x 322
Radiometric Resolution	16-bit
Cloud Cover	0%
Noise	Minimal
Scene Description	Large quartz crystals; feldspar; cut and polished; imaged at nadir
Source	Dr. Ron Resmini, The MITRE Corporation; Dr. David Allen, National Institute of Standards and Technology

By including nearly identical granite samples that vary in wavelength, this dissertation measures how different wavelengths affect algorithm performance in the presence of very high spatial sampling. Specifically, each sample's approximately 2mm GSD establishes control between the two measurements, which allows for differences in edge detection performance to be attributable only to spectral characteristics. This approach is analogous to the two urban feature mapping datasets (i.e., Reno and Larkhaven), but supports mineral mapping and is more robust since the two samples are

derived from the same slab sample. The objective is the same, however. By controlling for two of either target material, GSD, or wavelength range, the experiments can begin shedding light on the true spatial-spectral behavior of the new edge detection algorithms.

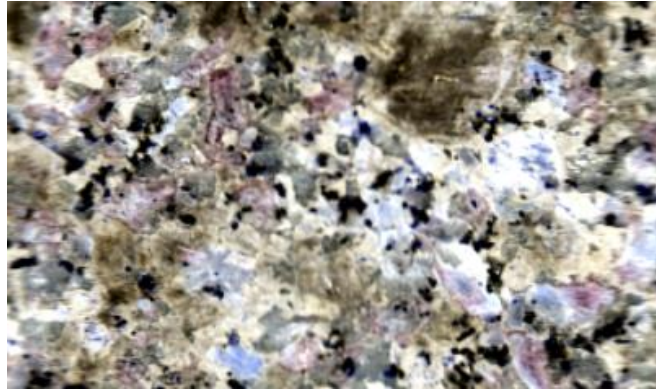


Figure 84: Ground-Based NIR/SWIR Hypercube. Granite Slab - False Color Bands 15, 31, 73

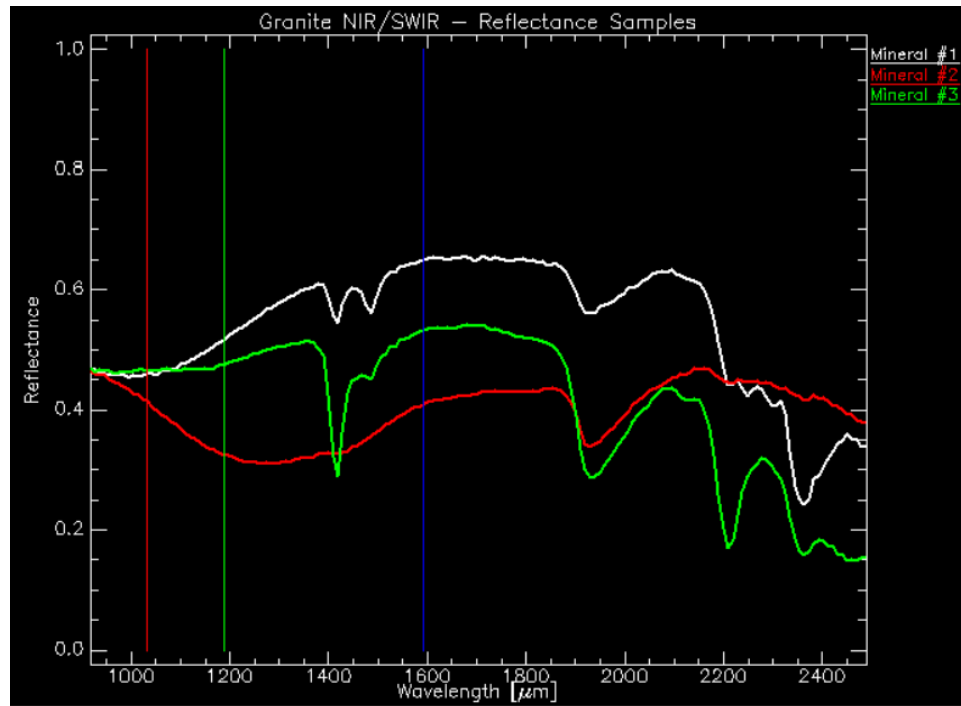


Figure 85: Sample NIR/SWIR Reflectance Spectra from Granite Hypercube

Ground-Based – South African Core Samples

The third non-traditional ground-based HSI dataset is particularly unconventional. The dataset consists of six geologic core samples arranged within the same image plane and separated by a black background. As seen in Table 10, the core samples were imaged with a NIR/SWIR spectrometer. The South African core sample dataset is the fourth and final hypercube directly supporting mineral mapping, and offers a third unique perspective on how effectively the new edge detection algorithms can support one of the most important remote sensing applications.

Table 10: Ground-Based NIR/SWIR Hypercube - South African Core Samples

Sensor Name	Unknown
Dataset	South African Geologic Core Sample
Location	South Africa
Date of Collect	Unknown
Data Type	Reflectance
Spectral Range	1.00 μ m - 2.51 μ m
Spectral Resolution	72 bands
Spatial Resolution	~1cm
Columns x Rows	320 x 724
Radiometric Resolution	12-bit
Cloud Cover	0%
Noise	Minimal
Scene Description	Vertically stacked mineral horizons; several clear edges at various angles
Source	Prof. Michael Sears, University of the Witwatersrand, South Africa

As seen in Figure 86, the core samples contain a variety of minerals arranged in roughly vertical fashion (which appear horizontally in Figure 86 due to image rotation), just as one would expect from core samples of layered rock. The black background on which the samples are arranged appears both around the samples as well as at scattered locations within the samples. Additionally, Figure 87 contains three mineral reflectance spectra extracted from the cube.

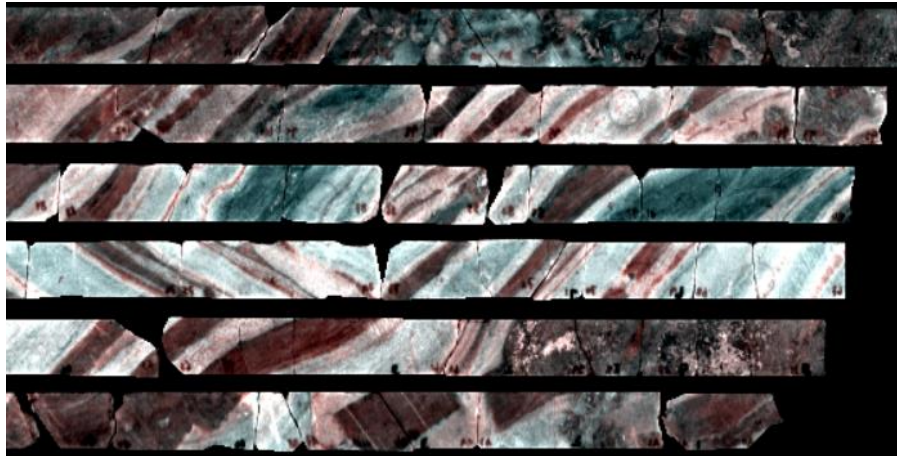


Figure 86: Ground-Based NIR/SWIR Hypercube. South African Core Samples - False Color Bands 47, 50, 98

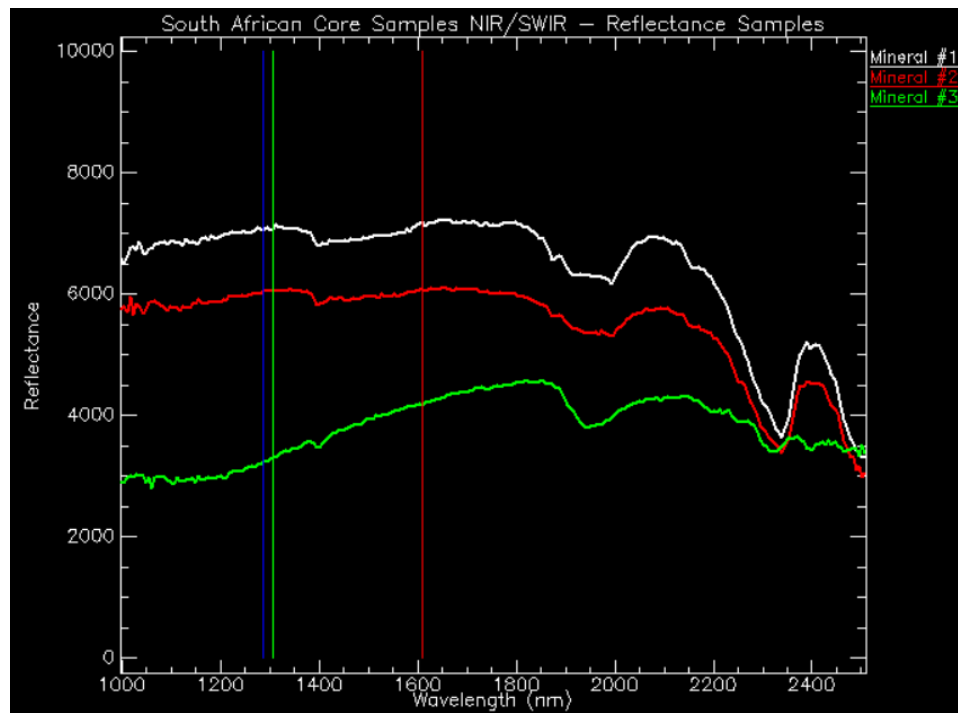


Figure 87: Sample NIR/SWIR Reflectance Spectra from South African Core Sample Hypercube

Ground-Based – Aluminum Panel

Attempting to circumnavigate the globe in a twin-engined Lockheed Elektra, Amelia Earhart and her co-pilot Fred Noonan disappeared over the Pacific Ocean on July 2, 1937 [261]. The ensuing search covered the vast extent of the southern Pacific Ocean, but searchers found no sign of Earhart, Noonan, or the Elektra, which ushered in an era of speculation that continues to this day.

For the last 28 years, the non-profit International Group for Historic Aircraft Recovery (TIGHAR) has endeavored to solve the Amelia Earhart mystery through forensic image science, field investigations, and undersea reconnaissance [262]. Specifically, TIGHAR hypothesizes that Amelia Earhart and Fred Noonan landed, and eventually died, on Gardner Island, now known as Nikumaroro in the Republic of Kiribati [262]. Figure 88 presents a partial map of the South Pacific covering Earhart's planned flight path, TIGHAR's estimated flight path, and the Island of Nikumaroro.

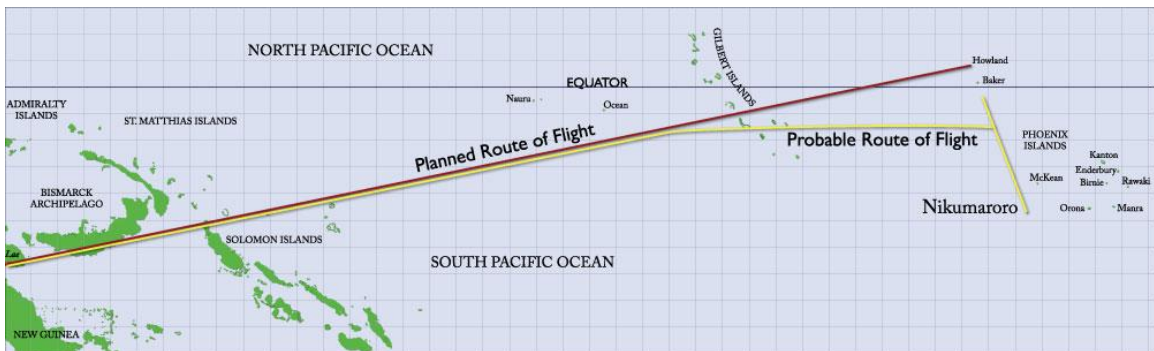


Figure 88: Amelia Earhart's Planned and Hypothesized South Pacific Flight Paths [262]

TIGHAR cites compelling evidence to support their hypothesis, including co-temporal radio distress calls emanating from the vicinity of Nikumaroro, July 1937, a US Navy search plane reporting that Nikumaroro showed “signs of habitation” despite being an uninhabited island, and the dimensional similarity between Amelia Earhart and the skeletal remains of a Nikumaroro castaway found in 1940 [262], [263]; DNA comparison was not available due to the absence of Earhart’s DNA. TIGHAR’s research is not conclusive, but is highly suggestive that Earhart and Noonan landed on or very near Nikumaroro. TIGHAR continues to actively research several lines of investigation as they seek to support their Nikumaroro hypothesis.

Most relevant to this dissertation is TIGHAR’s analysis of an aluminum aircraft panel recovered on Nikumaroro in 1991 [264]. TIGHAR hypothesizes that the aluminum panel is a piece of wreckage from Earhart’s Elektra, and cites as supporting evidence the affixion of an aluminum patch to the Elektra in Miami in early 1937 and the multiple material, dimensional, and alignment similarities between the patch and the aluminum panel recovered on Nikumaroro in 1991 [264]. Figure 89 presents Earhart’s Elektra with the “Miami Patch” in Miami in 1937 (with the yellow arrow pointing to the patch), while Figure 90 presents the aluminum panel recovered on Nikumaroro in 1991.

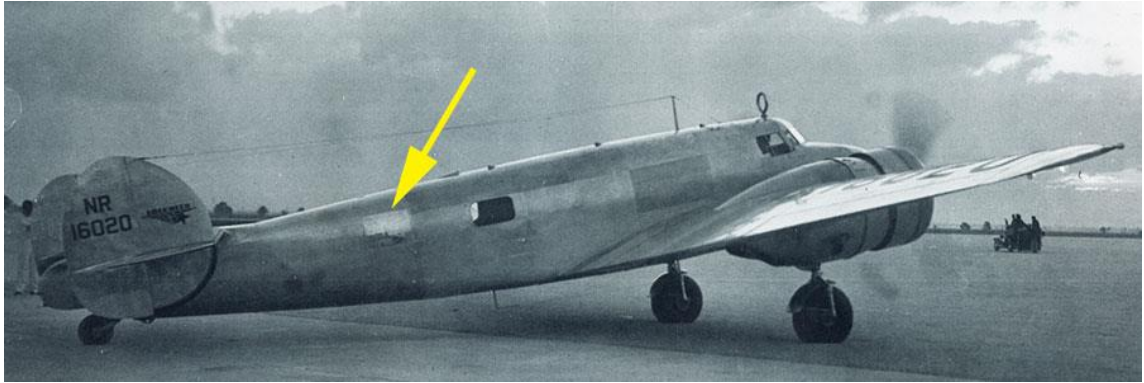


Figure 89: Amelia Earhart's Lockheed Elektra Affixed with the "Miami Patch" in 1937 [264]



Figure 90: Aluminum Aircraft Panel Recovered on the Island of Nikumaroro in 1991 [264]

In August 2014, TIGHAR used a SOC710 hyperspectral imager to collect VNIR data of the recovered aluminum panel in search of sub-visual heat damage indicative of an airplane crash and subsequent fire [265]. Upon request, Mr. Jeff Glickman of

TIGHAR graciously provided the aluminum panel VNIR radiance data for use with the HSI edge detection methods which would hopefully reveal evidence of linearly banded heat damage on the panel. Table 11 summarizes the full-extent VNIR image seen in Figure 90.

Table 11: Ground-Based NIR Hypercube - Aluminum Aircraft Panel

Sensor Name	Surface Optics Corporation (SOC) 710 Series Hyperspectral Imager
Dataset	Aluminum Aircraft Panel
Location	The Island of Nikumaroro, South Pacific Ocean
Date of Collect	August 2014
Data Type	Radiance
Spectral Range	0.4 μ m – 1.0 μ m
Spectral Resolution	128 bands
Spatial Resolution	~5mm
Columns x Rows	696 x 520
Radiometric Resolution	12-bit
Cloud Cover	0%
Noise	Minimal
Scene Description	Uneven aluminum panel with rivet holes and large areas rust; crenellation along right side
Source	The International Group for Historic Aircraft Recovery

As seen in Figure 91, the aluminum panel recovered on Nikumaroro contains five rows of rivet holes, multiple areas of rust and large expanses of well-preserved aluminum. The panel is uneven along both the vertical and horizontal axes, and is crenelated along the right side by samples extracted for metallurgical analysis [264].

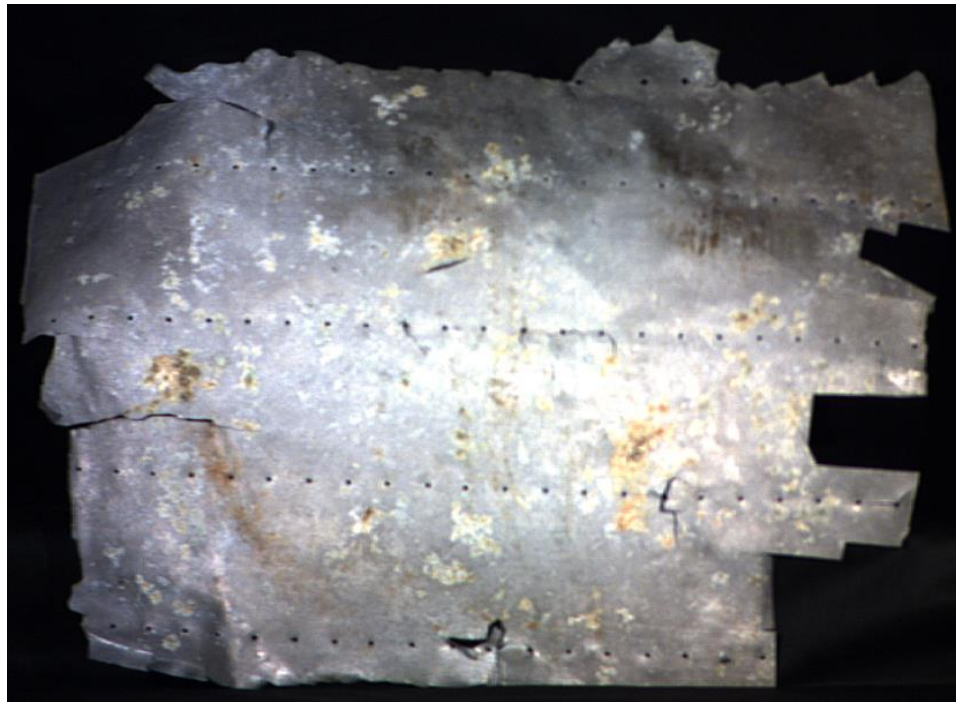


Figure 91: Aluminum Aircraft Panel VNIR Data - True Color Bands 18, 35, 53

Additionally, Figure 92 contains several sample reflectance spectra extracted from the aluminum aircraft panel scene, including an area of bright aluminum, and area of darker aluminum and an area weathered by rust.

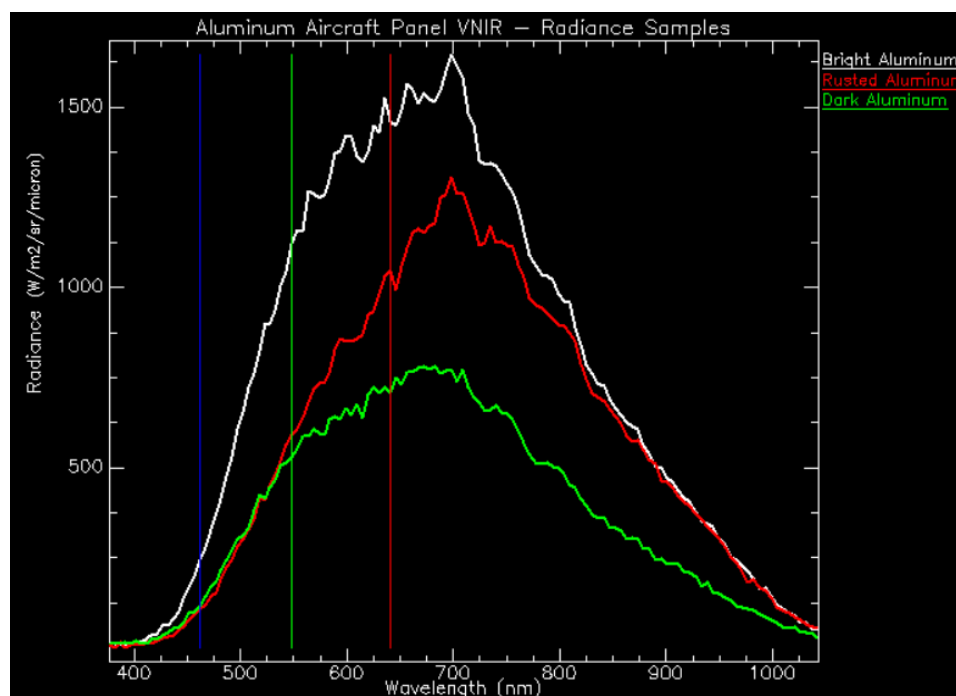


Figure 92: Sample VNIR Radiance Spectra from Aluminum Aircraft Panel Hypercube

The VNIR aluminum aircraft panel data is the most unconventional, challenging data addressed in this study. Except for the edges around the rivet holes, the data's potential, sought-for edge characteristics are complex, faint, and sub-visual. Including this hyperspectral data supports one of the guiding principles of this work: advance the spatial-spectral edge detection science with experiments against challenging, non-traditional HSI datasets.

Microscene – Rare Target on Sand

Table 12 summarizes the first microscene dataset to be considered here, a very-high spatial resolution VNIR hypercube of a complex scene containing a variety of

natural and manmade materials [258]. This microscene models a common problem in HSI remote sensing: find the rare target among the dominant natural background. This microscene is appropriate for this dissertation because it offers an array of complex, overlapping materials that challenge the new edge detection methods.

Table 12: Ground-Based VNIR Hypercube - Rare Targets on Sand Microscene

Sensor Name	Pika II VNIR Hyperspectral Imaging Camera
Dataset	Microscene, Rare Targets on Sand - VNIR
Location	Laboratory
Date of Collect	October 23, 2013
Data Type	Reflectance
Spectral Range	0.44 μ m - 0.88 μ m
Spectral Resolution	72 bands
Spatial Resolution	~2mm
Columns x Rows	640 x 700
Radiometric Resolution	12-bit
Cloud Cover	0%
Noise	Minimal
Scene Description	Rare targets on a sand and vegetation background; highly distinguishable chemicals
Source	Dr. Ron Resmini, The MITRE Corporation; Dr. David Allen, National Institute of Standards and Technology

As seen in Figure 93, the microscene contains sand, grass clippings, paprika, neodymium (III) oxide, hematite, and the pigment aquamarine blue. The GSD (~2mm) is sufficiently high that fine textural details are evident on several materials within the scene, such as striations along the primary axis of the grass clippings, subtle shadowing within the neodymium (III) oxide powder and fine detail within the paprika deposit. To

achieve high performance, the edge detection methods studied here need to accurately delineate those fine details as highly localized, unbroken edges.

One of the more challenging aspects of this microscene is the overlapping nature of several scene constituents. For example, the grass clippings overlapping the paprika and neodymium (III) oxide model how a vegetation canopy can conceal materials on the ground. This microscene will challenge the edge detectors' abilities to coherently delineate materials occluded by another substance.



Figure 93: Ground-Based VNIR Hypercube, Rare Targets on Sand Microscene - Color Infrared Bands 25, 41, 76

Additionally, Figure 94 contains several sample reflectance spectra extracted from the microscene, including grass clippings, neodymium (III) oxide, sand, and a mixed pixel extracted from a grass clipping extending directly over the neodymium (III) oxide sample. Note that several key neodymium (III) oxide absorption features are present within the occluding grass clipping, which will challenge the edge detectors to align that pixel with the grass clipping, the neodymium (III) oxide or a new class of mixed pixel.

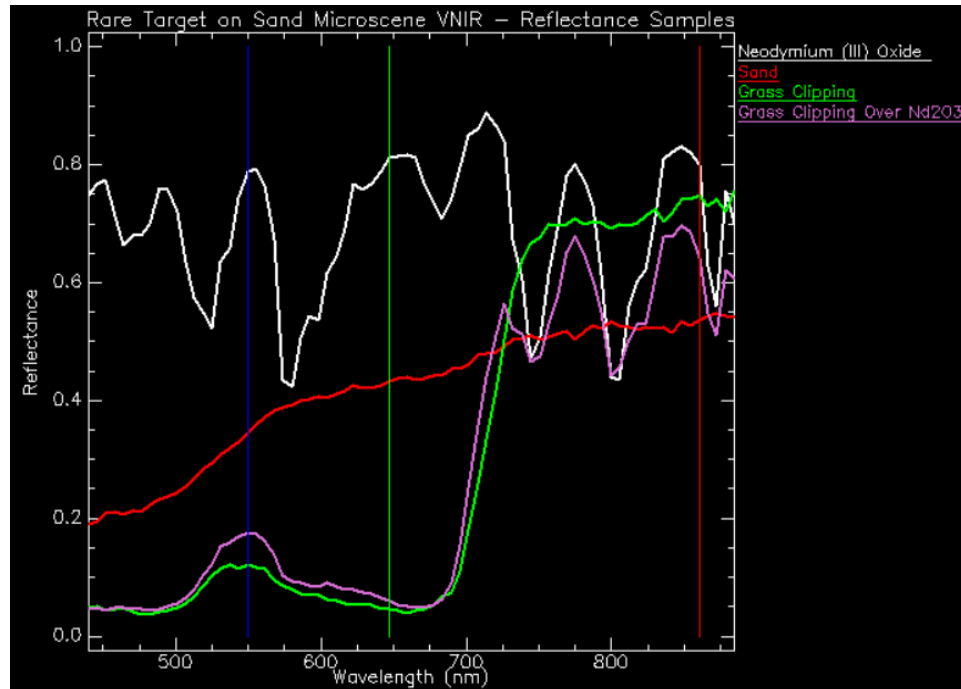


Figure 94: Sample VNIR Reflectance Spectra from Rare Target on Sand Microscene

Microscene – Chemical Array on Sand

Table 13 summarizes the second microscene dataset under examination, a very-high spatial resolution NIR/SWIR hypercube of a chemical array. This microscene

models a test array of chemicals or materials of interest – a reliable and efficient model for a significantly more expensive and time-consuming real-world test array. Similar to the previous microscene, the chemical array microscene is an ideal dataset for image classification, but works well for edge detection due to the texture and shadowing evident in the scene.

Table 13: Ground-Based NIR/SWIR Hypercube - Chemical Array Microscene

Sensor Name	Headwall Photonics HYPERSPEC SWIR Imaging Spectrometer
Dataset	Microscene, Chemical Array - VNIR
Location	Laboratory
Date of Collect	October 23, 2013
Data Type	Reflectance
Spectral Range	0.90 μ m - 2.51 μ m
Spectral Resolution	168 bands
Spatial Resolution	~2mm
Columns x Rows	290 x 335
Radiometric Resolution	16-bit
Cloud Cover	0%
Noise	Minimal
Scene Description	Array of highly distinguishable chemicals on a gravel/sand background
Source	Dr. Ron Resmini, The MITRE Corporation; Dr. David Allen, National Institute of Standards and Technology

As seen in Figure 95 and Table 14, the chemical array microscene contains a wide range of chemicals, including ammonium nitrate and potassium chlorate, two chemicals that play a prominent role in the growing HSI application of trace materials detection

discussed at length in the Background section. The GSD (~2mm) is sufficiently high that fine textural details are evident on several materials within the scene, including subtle shadowing within the powder samples and complex shadowing amongst the fine-grained background substrate. To achieve high performance, the edge detection methods need to accurately delineate those fine details as highly localized, unbroken edges.

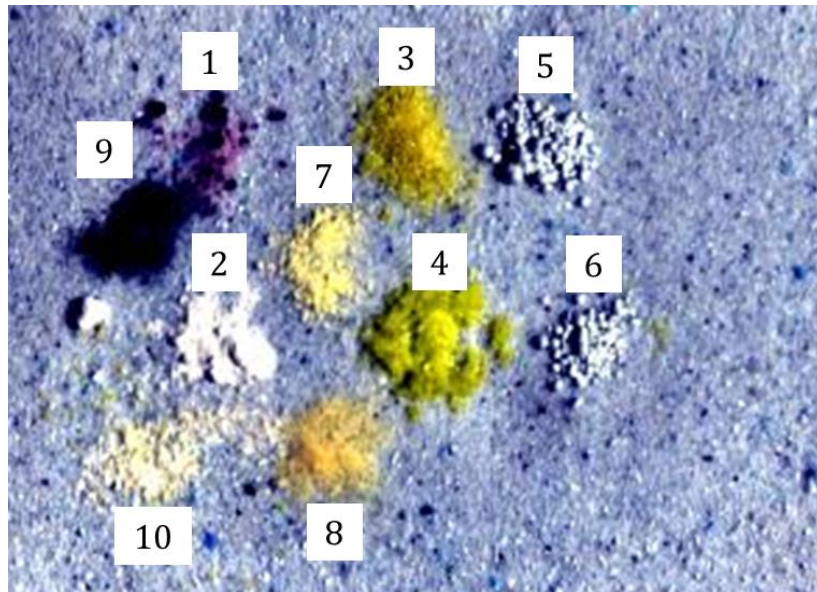


Figure 95: Ground-Based NIR/SWIR Hypercube, Chemical Array Microscene – False Color Bands 15, 31, 73

Table 14: Key to Chemicals in Chemical Array Microscene

Key	Chemical
1	Cobalt chloride/sodium chloride mix
2	Potassium chlorate
3	Ferric ammonium sulfate
4	Ammonium nitrate
5	Garden lime prills
6	Garden lime prills
7	Sodium carbonate
8	Borax
9	Iron filings
10	Sodium polyacrylate

Additionally, Figure 96 contains several sample reflectance spectra extracted from the chemical array microscene, including reflectance spectra of ammonium nitrate, potassium chlorate and sand background. Note the easily recognizable diagnostic absorption features in the ammonium nitrate reflectance spectrum compared to the dearth of diagnostic absorption features in the potassium chlorate spectrum – a relationship that makes ammonium nitrate more easily delineated with NIR/SWIR data than is potassium chlorate, which appears very similar to the background sand substrate in the NIR/SWIR.

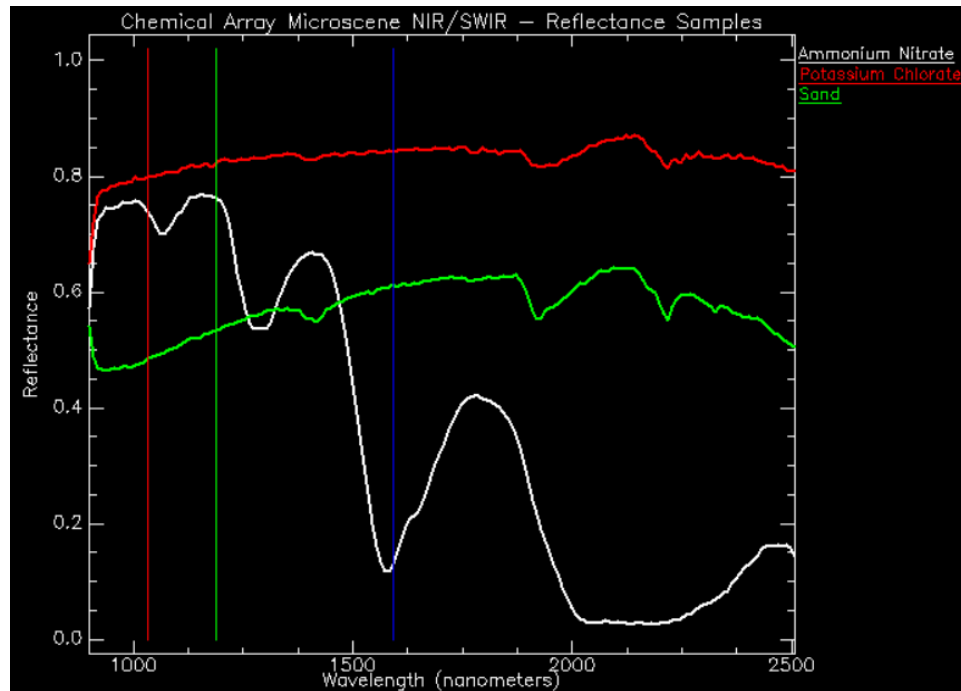


Figure 96: Sample NIR/SWIR Reflectance Spectra from Chemical Array Microscene

Microscene – Cloth Threads on Sand

Table 15 summarizes the third and final microscene dataset under examination, a very-high spatial resolution VNIR hypercube of a scene containing a seven varieties of cloth thread arrayed on a sand background. For much of the field of view, this dataset is the most edge detection-friendly microscene under test due to the long, unbroken edge features attributable to materials that are easily distinguishable from their background.

Table 15: Ground-Based VNIR Hypercube - Threads on Sand Microscene

Sensor Name	Pika II VNIR Hyperspectral Imaging Camera
Dataset	Microscene, Cloth Threads Sand - VNIR
Location	Laboratory
Date of Collect	October 23, 2013
Data Type	Reflectance
Spectral Range	0.40 μ m - 0.85 μ m
Spectral Resolution	80 bands
Spatial Resolution	~2mm
Columns x Rows	640 x 500
Radiometric Resolution	12-bit
Cloud Cover	0%
Noise	Minimal
Scene Description	Cloth threads on a sand background
Source	Dr. Ron Resmini, The MITRE Corporation; Dr. David Allen, National Institute of Standards and Technology

As seen in Figure 97, however, the microscene contains challenging edge pixels at the intersections of the crossing threads. For example, several pixels contain edge information for two or more threads, background material and microshadowing. For the new edge detection methods to achieve high performance, they must properly render these complex edge pixels. Additionally, Figure 98 contains several sample reflectance spectra extracted from the microscene, including reflectance spectra of the following cloth threads: white, blue, green, red (left), red (right), yellow and black. Note the shared spectral features among several threads, including the tight correlation between the two red threads, the closeness between the blue thread and the black thread, and the similarities in the NIR for all threads.

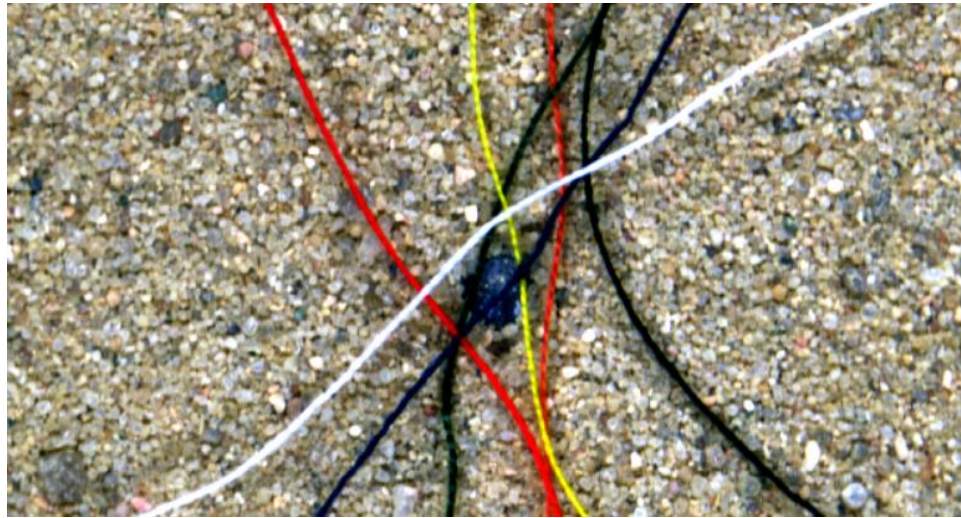


Figure 97: Ground-Based VNIR Hypercube, Threads on Sand Microscene – True Color Bands 10, 25, 40

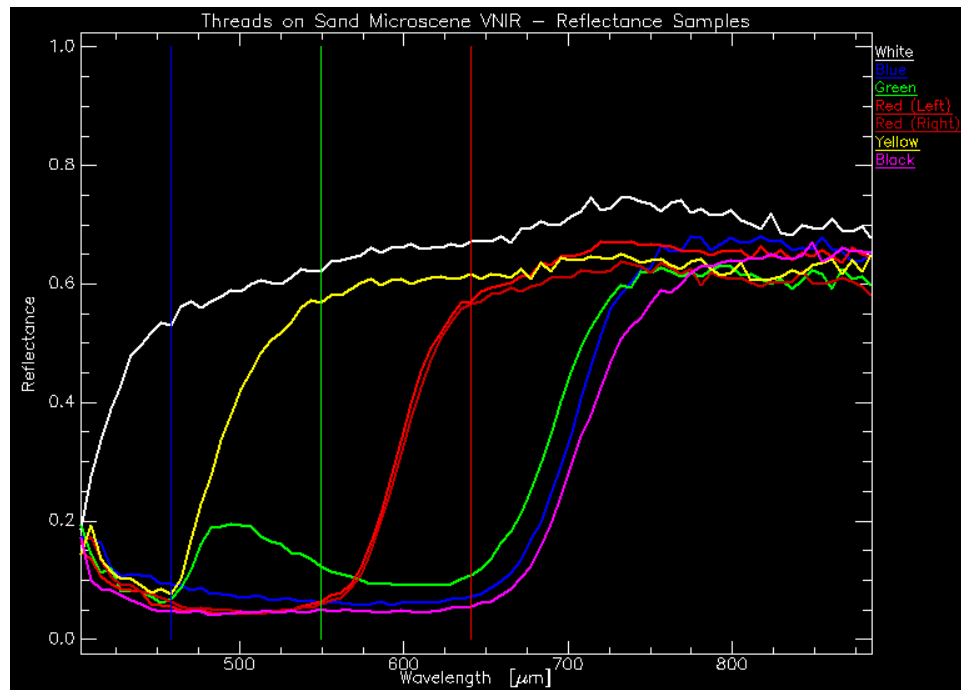


Figure 98: Sample VNIR Reflectance Spectra from Cloth Threads on Sand Microscene

METHODOLOGY

This dissertation tests three algorithms: a Di Zenzo tensor gradient approach for HSI data, a new HySPADE method whose edge detection engine combines Euclidean distance and spectral angle mapper, and a level set-based edge detection algorithm modified to use Euclidean distance for HSI data. While these approaches differ in how they map discontinuities within an image, understanding their commonalities is critical for understanding how the existing literature connects to this study and how it shapes directions follow-on research. For the gradient-based edge detector a three-band gradient MATLAB code [266] was obtained from open source and modified to accept hyperspectral data. The new HySPADE code was premised on Resmini's previous C++ HySPADE [249]. The original MATLAB level set code was obtained from an open source MSI version, which was subsequently modified to accept HSI data [267].

First, and keeping with this work's guiding principles, each algorithm is fully generalizable to all HSI datasets regardless of bandpass, spatial resolution, spectral resolution, radiometric resolution, scene content, atmospheric conditions, data format (i.e., radiance or reflectance), view/illumination angles and noise characteristics. Importantly, none of the algorithms is scene-dependent, none of them require prior knowledge of scene materials and all of them work on both reflectance and radiance data.

Second, each algorithm addresses under-represented (with respect to HSI) but clearly established (edge detection) areas in the scientific literature. As demonstrated in the Background section, gradient-based algorithms abound in the panchromatic and multispectral literature – this work stands on that research as it extends gradient-based edge detection methods into hyperspectral space. HySPADE’s SAM-based approach to spatial-spectral edge detection within conventional HSI scenes is some of the most influential work in the HSI edge detection literature – this study remains grounded on HySPADE’s pioneering research as it extends HySPADE’s capabilities both algorithmically and with respect to more challenging, unconventional HSI datasets and applications.

Level set techniques constitute a major field within both mathematics, computer vision and image analysis. This dissertation borrows heavily from both fields as it advances level set-based edge techniques within the HSI literature. Indeed, the corpus of computer vision research appears to have a stronger understanding of level-set methods than does the remote sensing literature, which affords this dissertation ample insights to apply to HSI data. The upshot of this strategy is that while each algorithm and its associated experiments constitutes new science, each is sufficiently grounded within existing science so as to be accessible by a broad range of researchers across several fields of study. This dissertation endeavors to avoid an all too common scenario of an incremental scientific contribution trapped beyond the confines of established or ongoing scientific research directions.

Third, this study addresses its algorithms' maximum effective range, meaning that each algorithm is tested against challenging, non-traditional datasets traceable to emerging HSI applications like trace chemical detection, oil spill mapping and material analysis. Experiments relevant to conventional applications such as mineral mapping, urban feature mapping and vegetation analysis are useful as a link to the existing literature, but they do little provide insight into more challenging, less understood HSI applications.

As seen in Figure 99, the methodologies for the Di Zenzo, HySPADE and Level-Set experiments encompass four distinct components: preprocessing, compression, edge detection, and algorithm evaluation. Identical for each of the three algorithms, the preprocessing component's key objectives are to configure the HSI data into a format suitable for edge detection, to provide a sense of data quality, to highlight primary scene features that the edge detection algorithm should be expected to delineate, and to identify unusual or suboptimal data behavior that could present a barrier to optimal edge detection processing.

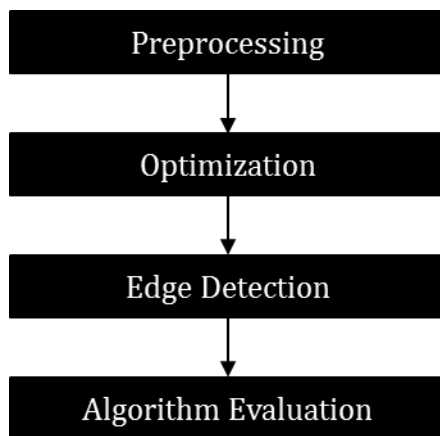


Figure 99: General Methodology Components

The specific compression steps vary by edge detection algorithm, but pursue the same objective of leveraging HSI processing techniques to maximize the likelihood of accurately detecting edges within the scene. The edge detection component executes the specific edge detection algorithms advanced by this work, namely the Di Zenzo's multidimensional gradient method applied to HSI, the new HySPADE algorithm combining Euclidean distance and spectral angle metrics, and the level set-based edge detection algorithm for HSI data.

Additionally, this dissertation establishes scientific control by applying standardized histogram stretches to all grayscale edge planes in order to avoid heuristically thresholding each grayscale edge plane, as commonly seen in the HSI literature. Specifically, this dissertation uses an Otsu threshold as the default histogram stretching method for all grayscale edge planes [268]. A nonparametric and unsupervised automatic histogram thresholding technique, the Otsu threshold has several advantages including simplicity, global stability across the histogram, and generalizability to a broad

range of histogram shapes [268]. Otsu's generalizability and global stability (i.e., its insensitivity to local histogram variations), in particular, make it an attractive choice for this dissertation's broad range on challenging, non-traditional HSI data. For circumstances where the Otsu threshold generates unexpected results (e.g., if the edge plane histogram is highly skewed, highly bimodal, etc.) this dissertation identifies an alternate, standardized threshold method to apply against the relevant edge planes.

The Otsu thresholding method's objective is to establish an optimal histogram threshold that maximizes the between-class variance between the background class and the object class (i.e., foreground class, target class or in this case, edge pixel class) [268]. Put another way, the Otsu method attempts to establish a threshold at the gray scale value that optimally separates background pixels from edge pixels according to their respective variances. Practical instantiations of the Otsu method, such as the "graythresh" functionality in MATLAB [269], tend to pursue an optimal Otsu threshold such that the weighted sum of the background and foreground variances is minimized, which is mathematically equivalent to Otsu's 1979 approach but computationally faster. Both implementations are similar: the constituent pixels in a unique class should behave as similarly as possible (i.e., with minimal within-class variance) and should be optimally separated from other classes according to maximum between-class variance.

As implemented here, the Otsu method employs a sequential search that iterates a six-step process over all possible thresholds in order to find the optimal threshold defined as the lowest weighted sum of background pixel and edge pixel variances. This work adopts the computationally efficient Otsu implementation that iteratively searches for the

threshold that minimizes within-class variance. Note that the volume of all possible thresholds is equivalent to the number of possible grayscale values in the plane.

First, the method selects an initial threshold to test (usually working from grayscale value 1 to n for n grayscale values), thereby dividing the edge plane's pixels into two classes: background pixels and edge pixels. Next, the method calculates each classes' weight according to Equation 23 where ω_B is the background pixel class weight, N_B is the number of background class pixels, N_T is the total number of scene pixels, ω_E is the edge pixel class weight and N_E is the number of edge class pixels. Specifically, Otsu's weighting procedure measures the fraction of edge plane pixels binned into the background and edge pixel classes. Note that this study's use of the term "weight" is equivalent to Otsu's term "probability," both of which speak to the likelihood of a pixel aligning to either the background or edge pixel class. The method then calculates the mean pixel value of each class according to Equation 24, where μ_B is the background class mean, i is grayscale value, k is the grayscale value for the threshold under testing, N_i is the number of pixels at grayscale value i , N_B is the number of background class pixels, N_E is the number of edge pixel class pixels and L is the image's total number of unique grayscale values.

$$\omega_B = \frac{N_B}{N_T}$$

$$\omega_E = \frac{N_E}{N_T}$$

Equation 23: Otsu's Class Weight Calculation [268]

$$\mu_B = \frac{\sum_{i=1}^k iN_i}{N_B}$$

$$\mu_E = \frac{\sum_{i=k+1}^L iN_i}{N_E}$$

Equation 24: Otsu's Mean Calculation [268]

The Otsu method next measures the variance of each class at the given threshold according to Equation 25, where σ_B^2 is the background class variance, σ_E^2 is the edge pixel class variance, i is grayscale value, k is the grayscale value for the threshold under testing, μ_B is the background class mean, μ_E is the edge pixel class mean, N_i is the number of pixels at grayscale value i , N_B is the number of background class pixels and N_E is the number of edge pixel class pixels.. At this point in the process, the Otsu method has separately characterized the background class histogram and the edge pixel class histogram according to a single threshold, but it must generate a combined measure of class separability in order to evaluate threshold "goodness" as determined by both the background class variance and the foreground class variance.

$$\sigma_B^2 = \frac{\sum_{i=1}^k (i - \mu_B)^2 N_i}{N_B}$$

$$\sigma_E^2 = \frac{\sum_{i=k+1}^L (i - \mu_E)^2 N_i}{N_E}$$

Equation 25: Otsu's Class Variance Calculation [268]

Otsu proposed several discriminant criterion measures to evaluate threshold goodness, including the within-class variance criterion whose minimum would correlate to the optimal threshold (i.e. distinctly separable classes should be as homogeneous as possible within themselves). To calculate the within-class variance for the given threshold, the Otsu method multiplies each class variance by its respective weight, and sums the products according to Equation 26, where σ_W^2 is Otsu's within-class variance criterion, ω_B is background pixel weight, ω_E is edge pixel weight, σ_B^2 is background class variance and σ_E^2 is edge pixel class variance. Finally, the method iterates the same process at all other possible thresholds and establishes the optimal threshold at the grayscale value associated with the minimum within-class variance.

$$\sigma_W^2 = \omega_B \sigma_B^2 + \omega_E \sigma_E^2$$

Equation 26: Otsu's Within-Class Variance Calculation [268]

This work's final step, algorithm evaluation, measures the performance of each edge detection algorithm with respect to the performance of existing edge detection methods. The evaluation procedures are both qualitative and quantitative in nature and are founded on Canny's criteria for a good edge detection algorithm. Finally, this dissertation executes all image processing in MATLAB, Microsoft Visual Studio Visual C++, and the Environment for Visualizing Images (ENVI) image processing software [270], [271], [272].

Preprocessing

The preprocessing component is identical for each of the three edge detection algorithms. The preprocessing component's first step, as seen in Figure 100, is to explore the data in order to get a sense of how it compares to similar datasets with respect to noise, scene constituents, etc. This step examines several spectra (radiance or reflectance, depending on the data format) sampled from various scene materials to ensure that they are behaving as expected. For example, radiance data should evidence key atmospheric absorption features (e.g., the $0.76\mu\text{m}$ oxygen feature) at the correct wavelengths and at the right intensities. Radiance data curvature for non-vegetation materials should appear roughly Planckian but with atmospheric absorption features, while radiance data for vegetation often contain recognizable spectral features across the VNIR bands. Note that all of the outdoor data are initially in radiance and that all of the lab data, as provided for this dissertation, are in reflectance.

Reflectance spectra of known materials should appear as expected with respect to intensity and key absorption features. For example, healthy vegetation spectra should contain a clear red edge across the NIR, water spectra should appear dark and featureless, and bare earth spectra should appear roughly concave. In the event that the data exploration step identifies spectral irregularities, they will be noted and considered during the algorithm evaluation component within the Analysis section.

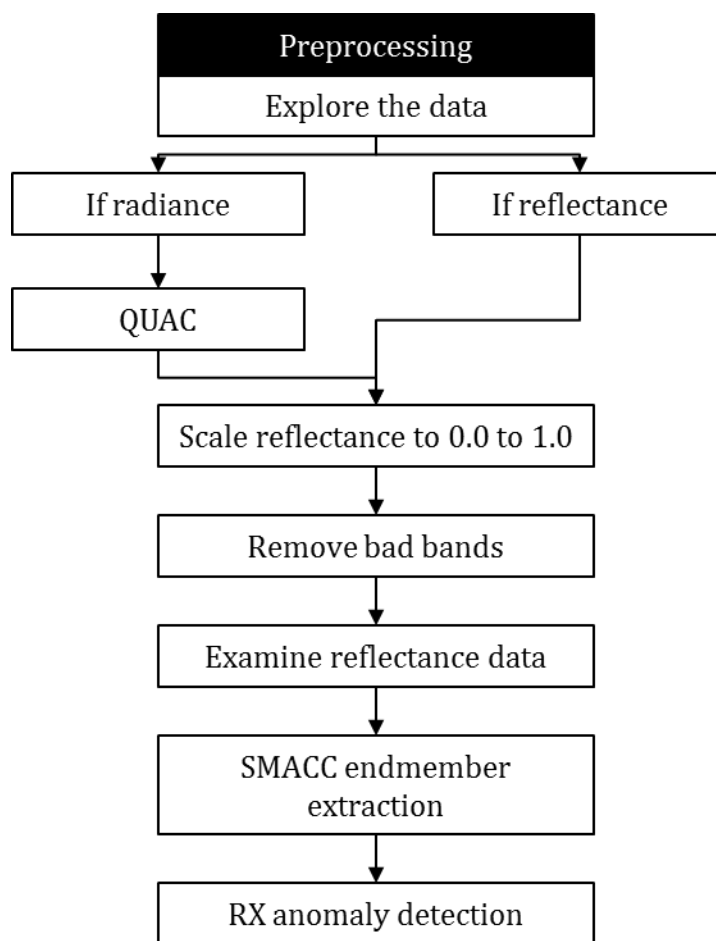


Figure 100: Preprocessing Component

The preprocessing component's second step identifies the HSI data as either reflectance or radiance data, depending on the findings of the data exploration step. For the majority of HSI data sets, discriminating radiance data from reflectance data is a simple task due to the unique characteristics of each, and the datasets tested herein are no exception. The third preprocessing step converts at-aperture radiance data to apparent reflectance via the QUAC atmospheric correction algorithm. The QUAC atmospheric correction algorithm, as detailed in the Background section, uses in-scene information to

estimate scene reflectance – a processing step critical to separating the atmospheric signal from the ground material signals. Once QUAC converts the radiance data to reflectance, a quality check is necessary to determine that the correction executed as expected. Specifically, the newly-generated reflectance spectra of common materials should appear as expected for materials such as vegetation, water and bare earth.

In the unlikely event that QUAC fails to generate useful reflectance data, a few courses of action are available. First, a series of spectral subsets could be derived from the radiance data and run independently through QUAC in the hope that a few noisy or artifact-containing radiance channels (or some pixels within such bands) are distorting the QUAC processing. Second, sometimes a spatial subset can improve QUAC results due to the removal of earth materials (typically unusual materials) that distort the QUAC results. Finally, the researcher can choose to execute the remaining processing and edge detection steps against the radiance data – a suboptimal but viable approach for HSI applications characterized by materials distinguishable by their radiance spectra, such as oil spill mapping applications.

The preprocessing component's fourth step scales the newly-generated reflectance data to 0.0 to 1.0, which is the scale most commonly expected the edge detection algorithms applied here. Many radiance datasets are scaled from 0 to 10,000 as a space-saving measure, but a 0.0 to 1.0 scale is more appropriate for reflectance data.

The fifth preprocessing step requires the removal of bad (i.e., noisy) bands that often remain after the QUAC atmospheric correction process. Although this dissertation uses [10]'s latest version of QUAC that attempts to remove noisy atmospheric bands,

residual noisy channels frequently remain along the edges of the 1.4 μm and 1.9 μm atmospheric water vapor bands. QUAC also often fails to remove noisy bands at the very beginning and at the very end of the spectral range, necessitating a manual redaction of those noisy bands. The researcher must visually determine at which band noise ends and high signal-to-noise ratio reflectance data begins. This process typically involves a detailed, band-by-band examination of noisy regions defined by bands similar in reflectance values. Most of the time, the researcher errs on the side of caution by preferring to risk removing one or two reflectance bands as opposed to risk including noise. This is the preferred approach implemented here, as well, since the likelihood of distorting the edge detection process by removing a few bands is remote. Finally, the bad band removal process usually is scene-dependent and thus the researcher must remove different bands for each scene.

Figure 101 contains an example of a post-QUAC reflectance spectrum containing several bad bands and their underlying causes. Note that for the 0.98 μm atmospheric water absorption feature, QUAC failed to remove any of the channels, as opposed to its nearly complete removal of the atmospheric information around the 1.4 μm and 1.9 μm atmospheric water bands. Also note the sensor noise at the end of the focal plane near 2.44 μm . Ultimately, the bad band removal preprocessing step redacts the residual spectral bands that are dominated by information not attributable to ground materials, thereby maximizing the traceability between actual ground materials and the reflectance spectra representing them in hyperspectral space.

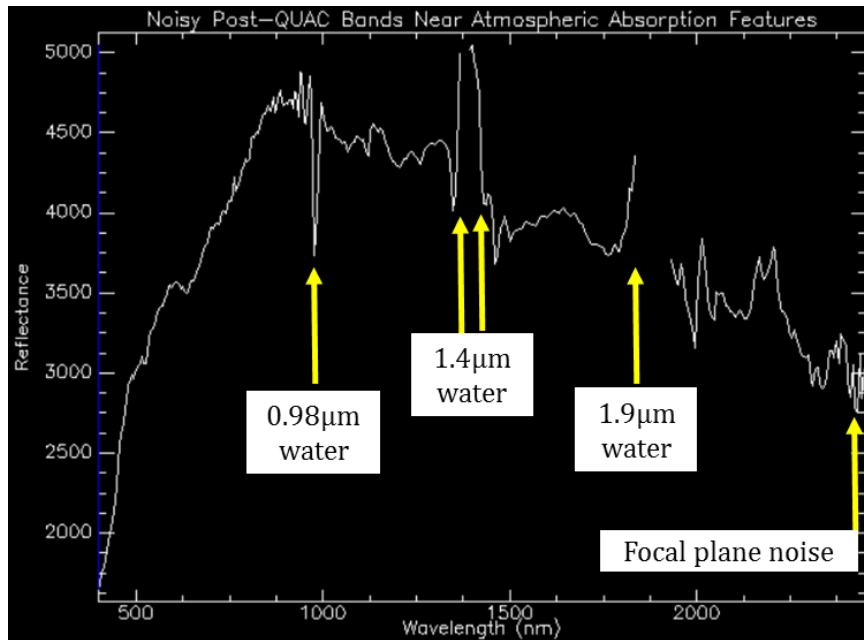


Figure 101: Post-QUAC Bad Bands Requiring Removal

The sixth preprocessing step is another data examination step intended to ensure that the reflectance data is free of atmospheric and sensor artifacts, behaving as expected for common materials, and is behaving properly with respect to the rescaling. Occasionally, additional bad bands will require removal or a common material will contain irregularities (e.g., unusual spiking in the positive and/or negative direction) that have implications for edge detection accuracy.

The seventh preprocessing step executes a SMACC endmember extraction process intended to identify primary scene constituents, and by extension, the primary boundaries that the new edge detection algorithms should be expected to delineate. Although not a true edge detection ground truth datum, the SMACC results are a step in the same direction in the sense that SMACC should capture the primary scene materials.

Importantly, the SMACC abundance planes are generated for reference only – this dissertation does not execute edge detection algorithms against the SMACC abundance planes, only against radiance and reflectance data.

Consider Figure 102, which presents six SMACC abundance planes from the cloth threads on sand VNIR hypercube. Most SMACC abundance planes reinforce the primary scene constituents evident from a routine visual inspection of the scene, but they often reveal subtle features that can go unnoticed by a visual examination. For example, the #6 abundance plane reveals subtle shadowing along the boundaries of several threads. While not immediately visible to the naked eye, the SMACC algorithm as well as this dissertation's new edge detection algorithms will recognize those pixels as distinct from their immediate neighbors. SMACC abundance planes also can help explain irregularities within an edge plane, such as broken or poorly localized edges. For example, the subtle shadowing features in SMACC abundance plane #6 might interfere with an edge detection algorithm's ability to generate accurately localized edges due to their close proximity to the thread edge – a limitation that probably would go unexplained without the SMACC abundance planes. Finally, it is worth noting that the benefit of HSI data, in the form of SMACC and similar HSI algorithms, extends beyond just the edge detection process itself to include the preprocessing and Analysis components.

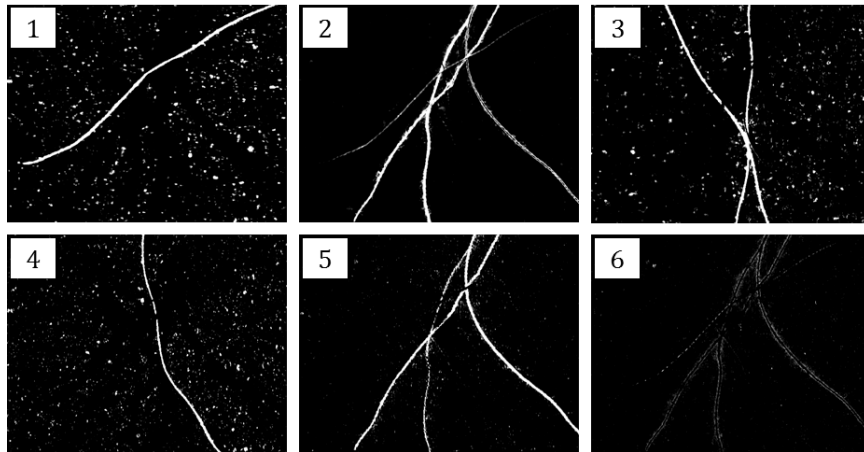


Figure 102: SMACC Abundance Planes from Cloth Threads on Sand Microscene Data

The eighth and final preprocessing step serves a purpose similar to the SMACC endmember extraction step. Specifically, the final preprocessing step generates an RX anomaly plane in order to identify any unusual behavior or materials within the scene. Since the RX anomaly detection algorithm is a discontinuity-based approach, its results directly inform the expected discontinuity-based edge detection methods developed in this study.

For example, consider Figure 103, which presents an RX anomaly plane derived from the aluminum aircraft panel recovered on Nikumaroro Island. The RX anomaly plane indicates that there are multiple anomalies centered roughly within the aluminum panel's brightest part, which is nearly a specular reflection. The upshot is that the RX anomaly plane gives the researcher a sense of the most unusual pixels within the scene and therefore, the anomalous pixels most likely to be flagged as edge pixels.

At the conclusion of the preprocessing component, the researcher should have a sense of the HSI data's structure, scene constituents and irregularities. The chief output

of the preprocessing component is either a radiance hypercube or, more optimally, a reflectance hypercube configured for edge detection.

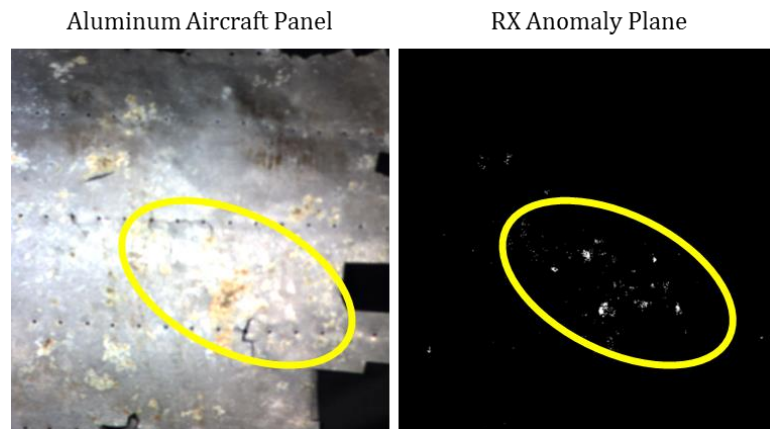


Figure 103: RX Anomaly Plane for the Aluminum Aircraft Panel VNIR Hypercube

Edge Detection: Di Zenzo-Based Gradient Approach for HSI

The first edge detection algorithm applies Di Zenzo's computer vision-inspired multidimensional gradient approach to hyperspectral data. A multispectral, three-band gradient algorithm [266] was obtained from open source MATLAB code and modified to accept hyperspectral data. The new algorithm advances remote sensing science in several ways. First, the new algorithm uses Di Zenzo's multidimensional gradient method to generate edge planes from hyperspectral data – a heretofore untried approach. Second, the method is applied to a variety of datasets spanning multiple HSI applications in order to assess its generalizability as well as its performance against a range of challenging datasets.

Third, and most important, the application of Di Zenzo to HSI endeavors to maximize HSI data's unique spectral character by first executing a PCA transform or an MNF transform prior to executing the gradient-based edge detection methodology. Researchers typically use PCA and its noise-ordered cousin, MNF, to reduce the dimensionality of HSI data in pursuit of improved computational speed, but this work introduces an approach to PCA and MNF preprocessing by treating the two transforms as critical data isolation or spectral information compression procedures designed to emphasize the most meaningful spectral information in the data.

For example, as PCA and MNF attempt to compress data dimensionality, they compress most of the HSI data's variance into as few PCA or MNF bands as possible, which improves computational speed at the cost of identifying reflectance information. The resulting PCA or MNF cube lacks the unique reflectance information that enables image classification, but it maximizes the overall contrast among scene materials while simultaneously concentrating them into a small number of discrete bands – an output that lends itself well to non-supervised, generalizable edge detection experiments. Consequently, this work hypothesizes that the gradient-based edge detection algorithm will generate superior results with PCA and MNF cubes compared to the results obtainable from a reflectance cube.

Figure 104 presents the compression component for the Di Zenzo multidimensional gradient edge detector. For any single iteration of the algorithm, one must choose to compress with either a PCA transform, an MNF transform, or to not compress and simply execute with the full radiance or reflectance hypercube. While the

PCA or MNF compressions directly inform one of the central contributions of this study, the algorithm results obtained from the radiance and reflectance cubes are important for comparing how much PCA and MNF improve edge detection results.

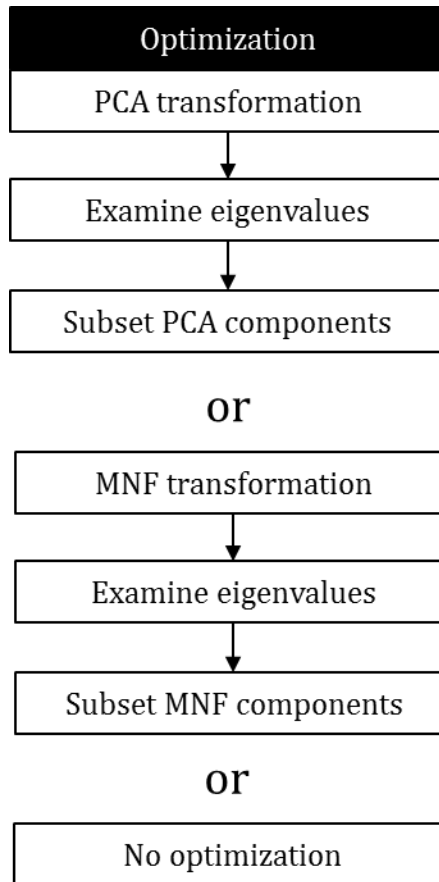


Figure 104: Compression Component for the Di Zenzo HSI Edge Detection Algorithm

After executing the PCA or MNF transform, the second step of the compression component requires the researcher to measure the transform's results by examining the eigenvalue plot corresponding to the dataset under examination. For example, Figure 105

presents a sample from the first PCA component and the corresponding eigenvalue plot derived from the Reno VNIR/SWIR hypercube. The plot indicates that the eigenvalues decrease down to band 4, meaning that the top four PCA components contain the majority of spectral variability within the scene – an expected outcome from the PCA transform. Note the high contrast texture of the first PCA image, which corroborates the eigenvalue plot, as well.

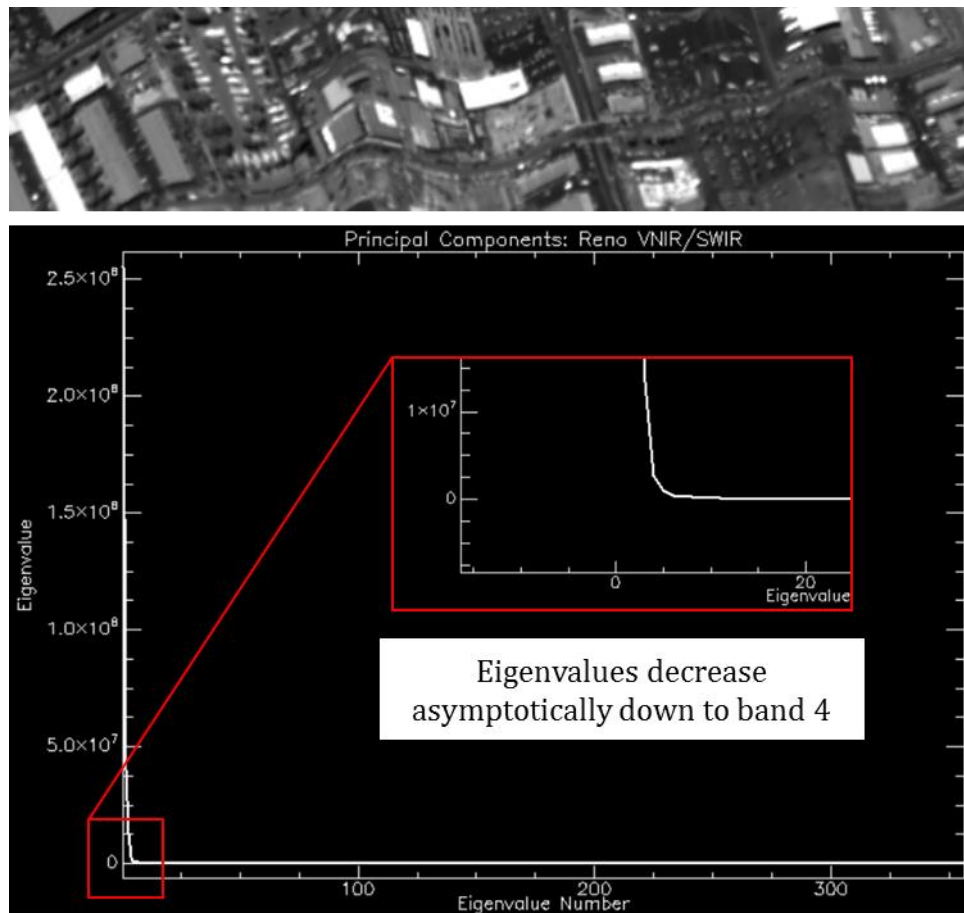


Figure 105: PCA Transform Results Obtained from the Reno VNIR/SWIR Cube

The final step for both the PCA and MNF compressions is to subset the PCA or MNF cube according to what the eigenvalue plot reveals about the concentration of spectral information. For example, in the case of Figure 105, a four-band or five-band subset of the PCA cube would capture the majority of spectral variability in the data, thereby enabling the Di Zenzo multidimensional gradient edge detector to execute almost exclusively against the most meaningful spectral content in the scene. For a similar MNF iteration, the edge detector would execute against a denoised dataset containing the most meaningful spectral content. The result of the PCA and MNF compressions is a key contribution of this dissertation – by compressing and denoising hyperspectral information, HSI edge detection algorithms are likely to produce results superior to MSI and HSI edge detection methods executing against full radiance and reflectance hypercubes.

Following the compression component is the component most central to this dissertation: the actual edge detection process for the Di Zenzo multidimensional gradient edge detector as presented in Figure 106. When provided as input, either a full radiance or reflectance cube, or a PCA or MNF cube, the edge detector first convolves separately across each spectral band, applying Sobel operators to approximate the partial derivatives in the x- and y-directions for each pixel. An approximation is necessary since the precise functions for every pixel and its eight neighbors within every band are unknown within the construct of a rasterized image. The Sobel operator, as previously detailed in Equation 10 and Figure 36, provides an excellent approximation of partial derivatives by virtue of its kernels' ability to isolate and accurately estimate changes in the x-direction

and y-direction. The end result of the first step is to generate two measurements for each pixel at each band: the x-direction Sobel return and the y-direction Sobel return as estimates of the partial derivatives (i.e., edge magnitude) in the x-direction and y-direction, respectively. For example, for a given pixel in a 256-band HSI cube, the second step will generate 512 measurements – 256 in the x-direction and 256 in the y-direction.

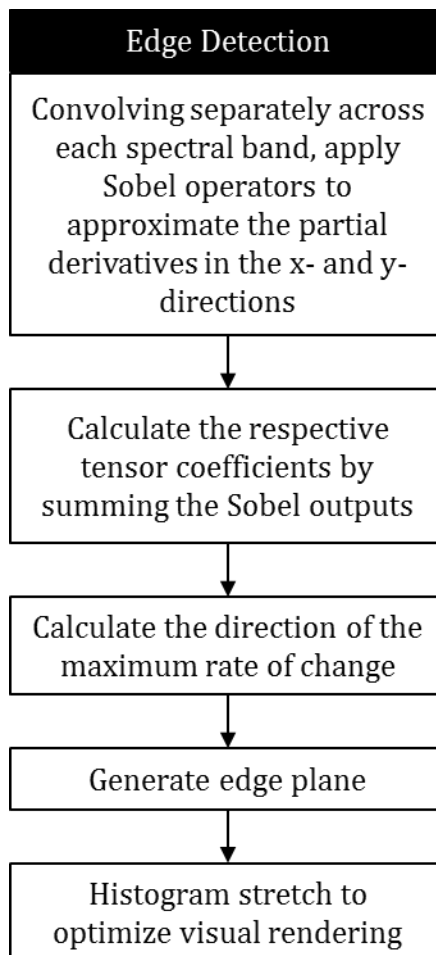
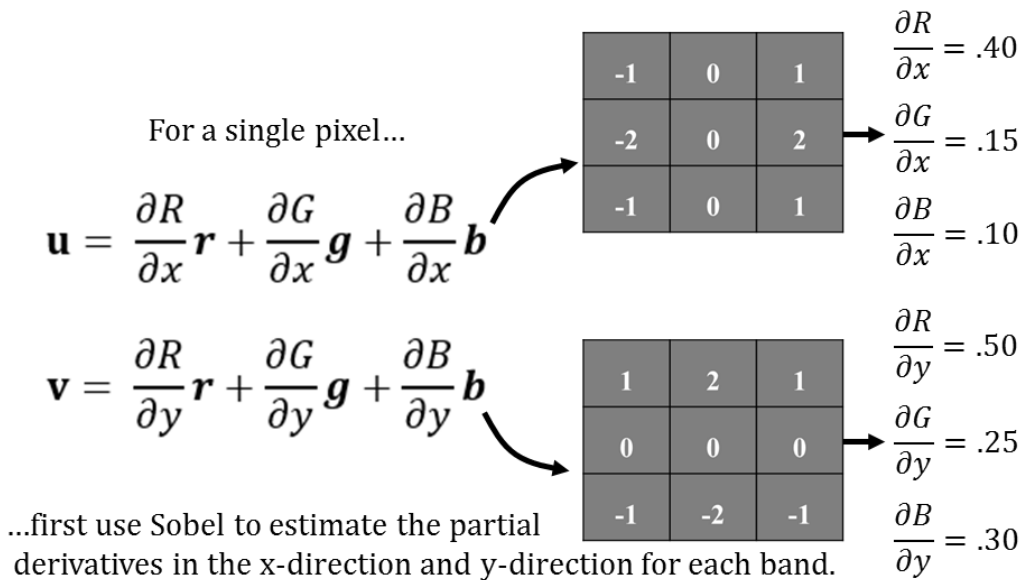


Figure 106: The Di Zenzo Multidimensional Gradient Edge Detection Process for HSI

Using Di Zenzo's Equation 14 detailed in the Background section, the second edge detection step sums the band-respective Sobel partials to obtain the respective tensor components (i.e., the coefficients for g_{xx} , g_{yy} , and g_{xy}) for each pixel. For example, at pixel (10,10) in a 256-band HSI cube, the second step would sum the x-direction partial derivatives from each of the 256 bands at pixel (10,10) to obtain a single x-direction partial derivative estimate (i.e., g_{xx}) for pixel (10,10). The second step then would sum the y-direction partial derivatives from each of the 256 bands at pixel (10,10) to obtain a single y-direction partial derivative estimate (i.e., g_{yy}) for pixel (10,10). At this point in the execution, the algorithm has an aggregate partial derivative estimate on a per-pixel basis for both the x-direction and y-direction, but it does not yet know the maximum magnitude or direction of maximum change for any given pixel.

Using Di Zenzo's Equation 13 as detailed in the Background section, Step 3 ingests the tensor coefficients derived in Step 2 to calculate the direction of the maximum rate of change at that pixel. As a final step, the algorithm combines the magnitude and directional information within Equation 15 to generate a panchromatic edge plane wherein the digital number for each pixel is the value of the maximum rate of change at that pixel along the direction of maximum change. Di Zenzo appropriately refers to this value as "edge strength" [194]. The edge plane typically requires a post-processing histogram stretch to render the optimal visual representation, as well. Figure 107 presents the precise Di Zenzo-based algorithm workflow as it would execute against a single pixel in the Figure 48 example.



To calculate the tensor coefficients...

$$g_{xx} = \mathbf{u} \times \mathbf{u} = \left| \frac{\partial R}{\partial x} \right|^2 + \left| \frac{\partial G}{\partial x} \right|^2 + \left| \frac{\partial B}{\partial x} \right|^2 = |.40|^2 + |.15|^2 + |.10|^2 = .3225$$

$$g_{yy} = \mathbf{v} \times \mathbf{v} = \left| \frac{\partial R}{\partial y} \right|^2 + \left| \frac{\partial G}{\partial y} \right|^2 + \left| \frac{\partial B}{\partial y} \right|^2 = |.50|^2 + |.25|^2 + |.30|^2 = .3625$$

$$g_{xy} = \mathbf{u} \times \mathbf{v} = \frac{\partial R}{\partial x} \frac{\partial R}{\partial y} + \frac{\partial G}{\partial x} \frac{\partial G}{\partial y} + \frac{\partial B}{\partial x} \frac{\partial B}{\partial y} = .40 \cdot .50 + .15 \cdot .25 + .10 \cdot .30 = .2675$$

...calculate cross products in the x-direction, y-direction and the xy direction.

Next, calculate the direction of maximum change.

$$\theta = \frac{1}{2} \tan^{-1} \left(\frac{2g_{xy}}{(g_{xx} - g_{yy})} \right) = \theta = \frac{1}{2} \tan^{-1} \left(\frac{2 \cdot .2675}{.3225 - .3625} \right) = 42.86^\circ$$

Finally, use the direction of maximum change and the tensors to calculate the magnitude along the direction of maximum change, $F(\theta)$. Output the magnitude as the DN to the corresponding pixel in the edge plane.

$$F(\theta) = \sqrt{\{(g_{xx} + g_{yy}) + \cos 2\theta(g_{xx} - g_{yy}) + 2g_{xy} \sin 2\theta\}}$$

Figure 107: The Di Zenzo-Based Algorithm as Applied against an Example

Additionally, Figure 108 presents a graphical representation of the example detailed in Figure 107. Figure 108 is a three-band (red, green and blue), single-pixel example of how the algorithm constructs the overall pixel gradient from the intensity changes within each band at this pixel. For a hyperspectral cube, Figure 108's concepts simply scale to accommodate the additional bands.

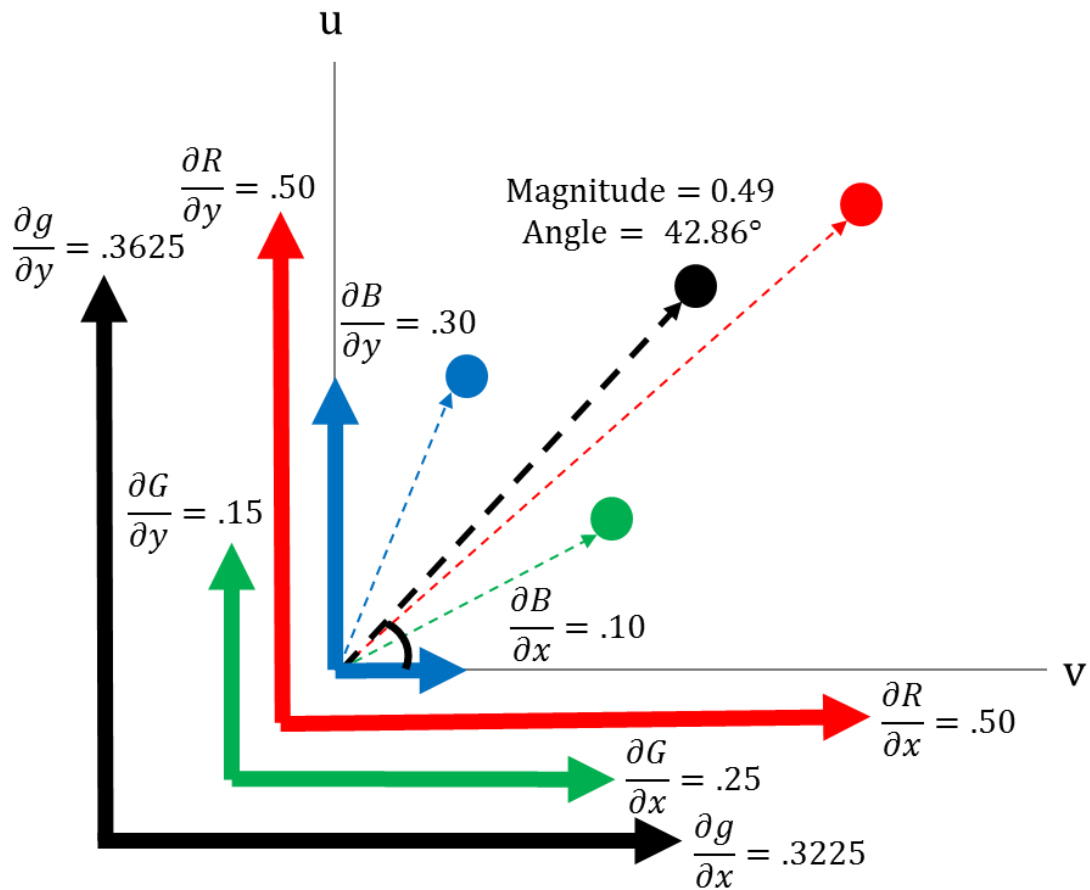


Figure 108: Geometric Outputs of the Di Zenzo-Based Edge Detection Algorithm Workflow

Additionally, this study decrements its PCA and MNF cubes to specific, natural intervals in order to rigorously measure algorithm sensitivity. For example, all three algorithms' methodologies test PCA and MNF cubes at interval depths of all bands and the reduced number of bands (usually 4 to 5) as indicated by the PCA and MNF eigenvalue plots.

The tests measure how effectively PCA and MNF transforms can compress a hypercube's spectral information content into a smaller, more efficient format. Importantly, the PCA and MNF transforms are not intended to sacrifice meaningful spectral information in order to achieve speed or simplicity – they are intended to optimize the data by efficiently separating the meaningful spectral signal from degrading noise. This dissertation thus executes the Di Zenzo-based edge detection algorithm against each radiance or reflectance data as well as a range of PCA and MNF cubes.

Figure 110 presents a demonstration of the gradient-based edge detector as tested against a noise-injected synthetic 420-band VNIR/SWIR dataset. The synthetic dataset is comprised of two mineral features interspersed with noise features. Significant noise added to the mineral spectra, and edges increase in difficulty from right to left. Figure 109 presents sample spectra from each feature, where the first noise block is in white, the first mineral feature is in red, the second noise block is in green and the second noise block is in blue. As seen in Figure 110, the reflectance test generated noisy, broken boundaries between the materials while the gradient-based algorithm generated thin, unbroken edges accurately along the feature boundaries for the compressed PCA test – a useful demonstration of the utility of using compressed HSI data to improve results.

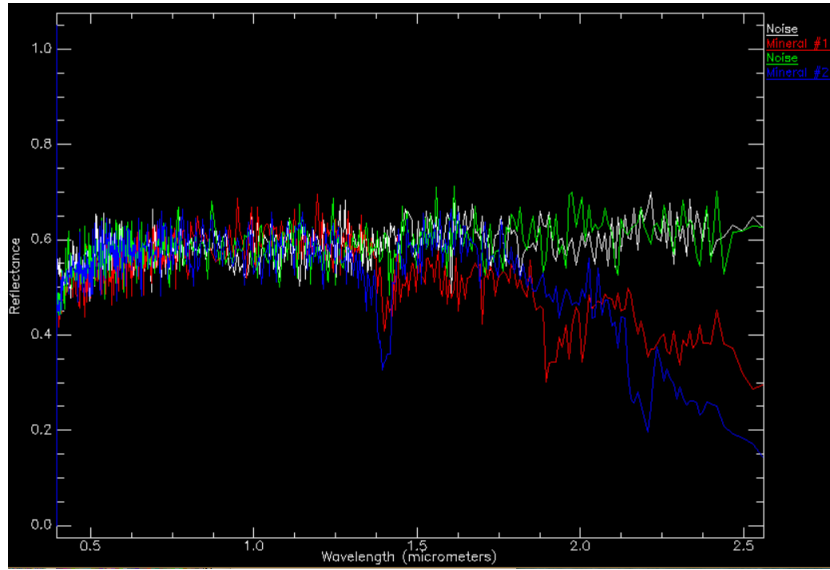


Figure 109: Sample Spectra from Synthetic Dataset

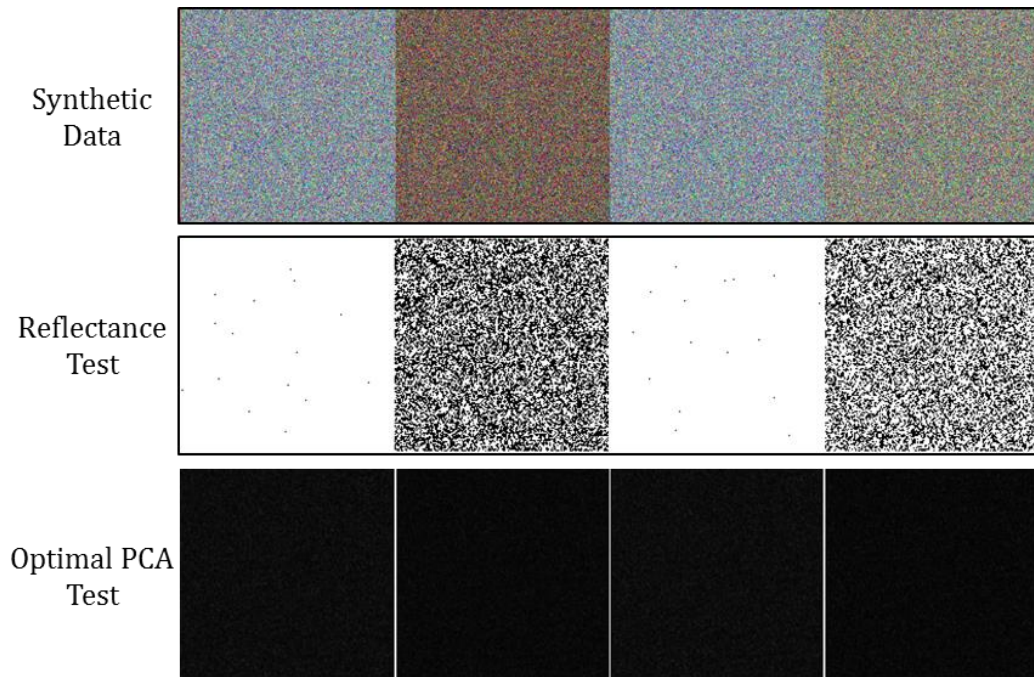


Figure 110: Gradient Demonstration against Synthetic HSI Dataset

Figure 111 presents the gradient-based edge detector as executed against a 145-band 0.4 μm to 0.7 μm subset of the full reflectance cube tested in Figure 110. Compared to the full VNIR/SWIR test in Figure 110, the VIS-only cube generated suboptimal results due to the loss of the NIR/SWIR bands. As expected, VIS-only data is more challenging to HSI edge detectors than VNIR/SWIR data.

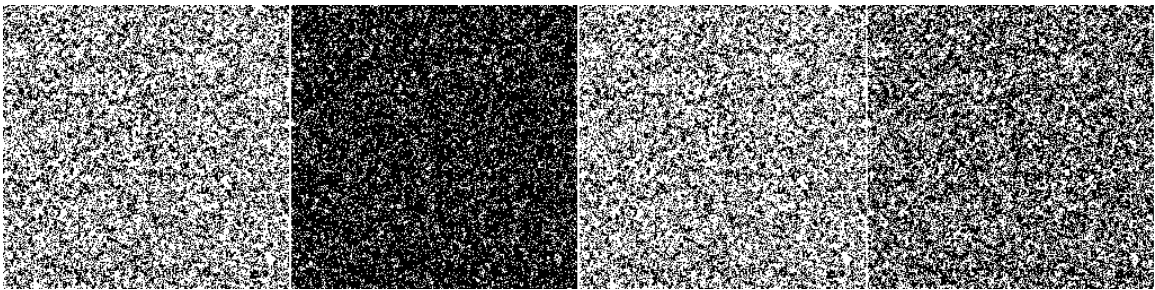


Figure 111: Gradient Test against Synthetic HSI Data, VIS Bands Only

Edge Detection: A New HySPADE Approach Combining ED and SAM

This work's second new edge detection algorithm improves Resmini's HySPADE edge detection algorithm for hyperspectral data. The new algorithm advances the capability in several ways. First, by combining a spectral distance measure (i.e., magnitude) and a spectral shape measure (i.e., correlation), it improves upon previous instantiations of HySPADE that implemented only Euclidean distance or Spectral Angle Mapper [219], [250], [249]. Specifically, this dissertation develops a novel version of HySPADE that integrates the Spectral Similarity Scale as developed by Sweet et al [273] into the spatial-spectral processing framework unique to the original HySPADE algorithm [219].

Sweet et al.'s Spectral Similarity Scale generates a measurement of hyperspectral image quality by combining a spectral magnitude measurement with a spectral shape measurement to generate a single similarity metric. Sweet et al used Euclidean distance as a measure of spectral (i.e., vector) magnitude as implemented in Equation 27, and they used a correlation measurement as implemented in Equation 28 wherein r^2 is the square of the correlation coefficient for vectors x and y , Nb is the number of bands in the hypercube, and σ is the standard deviation [273]. Equation 29 presents Sweet et al.'s spectral similarity metric that constitutes a two-element vector called the "difference vector" wherein d_e is the Euclidean distance measurement and r^2 is the square of the correlation coefficient [273]. Small Spectral Similarity measurements suggest a discontinuity between pixels and therefore are indicative of edge strength. Large scores indicate strong similarity between pixels and therefore a strong likelihood that the underlying physical materials are continuous.

$$\|x - y\| = \sqrt{\sum_{k=1}^K (x_k - y_k)^2}$$

Equation 27: Euclidean Distance Calculation for Improved HySPADE

$$r^2 = \left(\frac{\frac{1}{Nb - 1} \sum_{i=1}^{Nb} (x_i - \mu_x)(y_i - \mu_y)}{\sigma_x \sigma_y} \right)^2$$

Equation 28: Sweet et al's Correlation Measurement [273]

$$\text{Spectral Similarity} = \sqrt{d_e^2 + \hat{r}^2}$$

Equation 29: The Spectral Similarity Metric [273]

This dissertation's methodology integrates Sweet et al's spectral similarity metric into the HySPADE spatial-spectral processing framework first by replacing the legacy SAM or ED score with the output from Equation 29. First, the improved HySPADE algorithm implements the Euclidean distance measurement as seen in Equation 3. Second, the algorithm implements Equation 28 to calculate the correlation coefficient. Finally, the ED and correlation coefficients are squared, summed and square rooted to achieve the Spectral Similarity score of Equation 29.

The pixel values in the final HySPADE edge plane reflect a tally, on a pixel-by-pixel basis, of the number of times a given pixel alarms as an edge according to a one-dimensional edge detection process applied to each SSS spectrum [249]. This methodology flags a pixel as an edge pixel if the value of the first-order finite-difference process generates a value exceeding a threshold. The HySPADE threshold implementation in this study generates a final two-dimensional HySPADE edge plane by combining the outputs of 40 intermediate edge planes, each of which represents a unique threshold from 0.10σ to 4.0σ by 0.10σ . For example, the final edge strength for a given pixel reflects the number of times, among the 40, that the pixel exceeded a threshold. Edge pixels that exceed 35-40 thresholds will be the strongest edge pixels in the edge plane, while edge pixels that exceed the thresholds in one to five planes will be among the weakest. Pixels that exceed the thresholds in none of the 40 intermediate edge planes receive a DN of zero, meaning that they carry no edge information.

This dissertation tested several volumes of intermediate edge planes in order to determine how they affect edge detection results and to identify the optimal volume for experimental control. As seen in the Cuprite Flight Line #4 VNIR/SWIR image tests in Figure 112, nearly identical edge detection results are achieved for 20, 30 and 40 intermediate edge planes. Consequently, this work uses 40 intermediate edge planes to balance performance against too few intermediate edge planes.

Additionally, as seen in Figure 113, this dissertation tested several standard deviation thresholds in order to determine how they affect edge detection results and to identify the optimal spread. As seen in the Cuprite Flight Line #4 VNIR/SWIR image tests, the optimal spread is 0.1σ to 4.0σ compared to 0.2σ to 8.0σ and 0.3σ to 12.0σ . The 0.2σ to 8.0σ and 0.3σ to 12.0σ tests generated a suboptimal volume of false alarms. Therefore, this dissertation establishes the threshold at 0.1σ to 4.0σ for each HySPADE test.

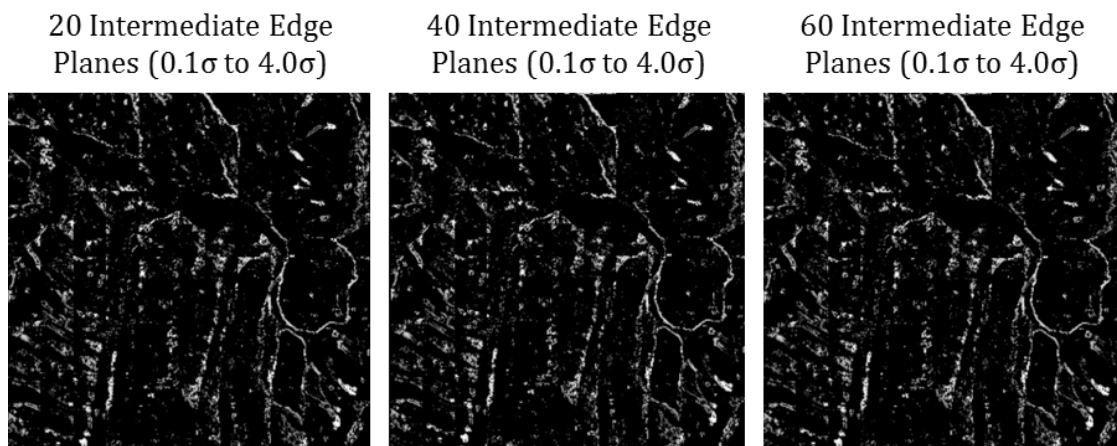


Figure 112: HySPADE Intermediate Edge Plane Testing against Cuprite Flight Line #4 VNIR/SWIR Data

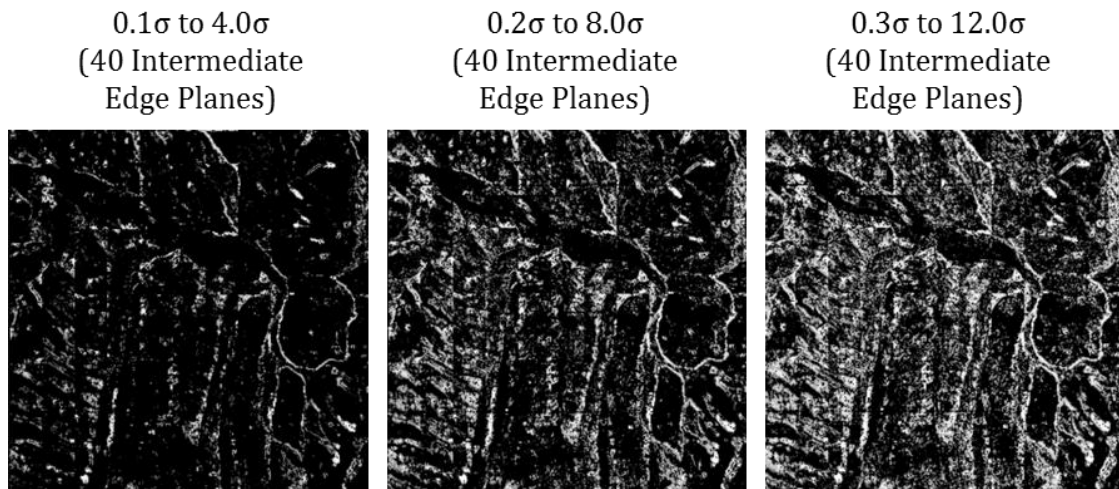


Figure 113: HySPADE Intermediate Edge Plane Testing against Cuprite Flight Line #4 VNIR/SWIR Data

The second way in which this work advances the capability of the HySPADE approach is by testing it against non-traditional datasets spanning a variety of traditional and emerging HSI applications. Specifically, the available HySPADE research focuses on robust, well-behaved VNIR/SWIR HSI data for urban feature mapping and mineral mapping applications, while this dissertation will test HySPADE’s ability to support a much broader range of HSI applications and its performance against challenging, non-traditional datasets and emerging HSI applications. For example, Resmini’s flagship HySPADE publication used the VNIR/SWIR ProSpecTIR Reno dataset also addressed by this dissertation, which is a traditional, edge detection-friendly urban feature mapping dataset [249]. Similarly, Cox’s 2009 HySPADE publication used VNIR/SWIR AVIRIS data of Cuprite, which is a traditional, edge-detection friendly mineral mapping dataset. This dissertation seeks to extend this baseline understanding by testing HySPADE’s

ability to delineate challenging features within non-traditional datasets like the Deepwater Horizon ocean data and Aluminum Aircraft Panel data.

The third manner in which this dissertation advances HySPADE is by expanding the scientific understanding of HySPADE's sensitivity to spatial and spectral resolutions. Specifically, the Resmini and Cox HySPADE work considered only modest spatial resolution VNIR/SWIR HSI data, but this study expands the breadth of spatial and spectral resolution mix in order to measure HySPADE's performance against various combinations of spatial and spectral resolutions. For example, this study tests HySPADE's edge detection capability against very-high spatial resolution data sets (e.g., the microscene HSI data), VNIR only data sets (e.g., the SOC700 Larkhaven HSI data) and against NIR/SWIR data sets (e.g., the chemical array HSI data).

Following the preprocessing component described in the preprocessing section, Figure 114 presents the compression component for the improved HySPADE algorithm edge detector, which is identical to the Di Zenzo-based edge detection compression component. Consequently, the HySPADE experiments leverage the compression results achieved during the Di Zenzo-based edge detection experiments.

For any single iteration of the algorithm, this dissertation compresses with either a PCA transform, the MNF transform, or to not compress and simply execute with the full radiance or reflectance hypercube. While the PCA or MNF compressions directly inform one of the central contributions of this work, the algorithm results obtained from the uncompressed radiance and reflectance cubes are important for measuring how much the compressions improve edge detection results.

After executing the PCA or MNF transform, the second step of the compression component requires the researcher to measure the transform's results by examining the eigenvalue plot corresponding to the dataset under examination. Optimal PCA and MNF thresholds are determined by first locating the PCA and MNF eigenvalue plot "knee in the curve" after which little diagnostic spectral information is expected; in this manner, each test executes against at least 99% of spectral information (i.e., variance) in the scene. Second, the researcher confirms the threshold by visually examining the PCA and MNF planes to confirm that the post-threshold bands are noise dominated.

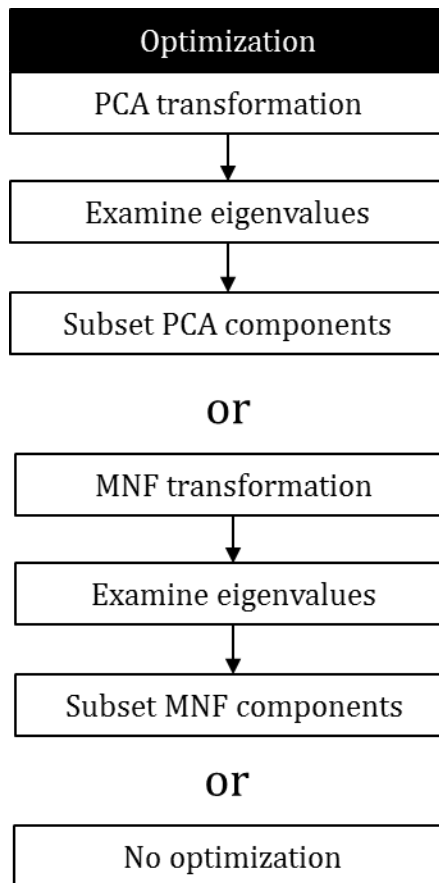


Figure 114: Compression Component for the Improved HySPADE HSI Edge Detection Algorithm

The final step for both the PCA and MNF compressions is to subset the PCA and MNF cubes according to what the eigenvalue plot reveals about the concentration of spectral information (i.e., data variance). Specifically, the PCA and MNF thresholds are used to subset their respective parent cubes such that the improved HySPADE edge detector executes against a denoised dataset containing the most meaningful spectral content. The result of the PCA and MNF compressions is a key contribution of this dissertation – by concentrating and denoising hyperspectral data, HSI edge detection

algorithms can produce results superior to MSI and HSI edge detection methods executing against uncompressed radiance and reflectance hypercubes.

Following the compression component is the edge detection process with the improved HySPADE edge detector as presented in Figure 115. Taking input either a radiance or reflectance cube, or a PCA or MNF cube, the edge detector first begins generating Spectral Similarity measurements between each pixel in the sliding window and every other pixel in the window to build an intermediate HySPADE cube spatially bounded to the window's footprint. For example, the edge detector's first Spectral Similarity measurement uses Equation 29 to generate the combined ED and SAM score between the spectrum at input cube pixel (1,1) and input cube pixel (1,2) within the first window position. That measurement is then assigned to band 1, pixel (1,2) in a new HySPADE output cube which ultimately will be an intermediate n -band cube for an n -pixel hypercube (i.e., a 20 pixel x 20 pixel window of any spectral resolution always will produce a 400-band intermediate HySPADE cube). Note that the HySPADE cube's band 1, pixel (1,1) has already been populated with the maximum Spectral Similarity measurement of 1.0 due to the maximum similarity between a pixel and itself.

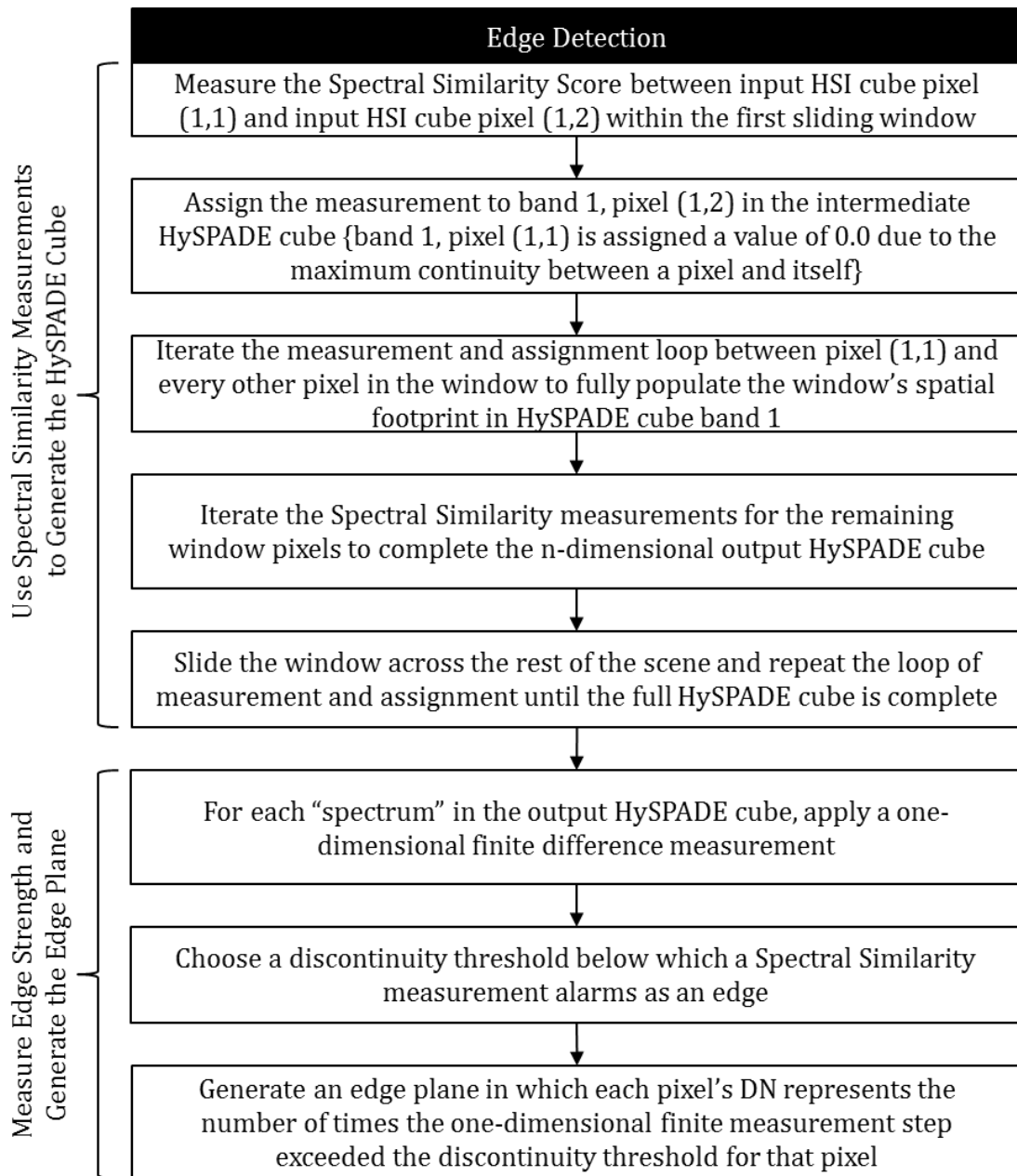


Figure 115: The Improved HySPADE Edge Detection Process for HSI

The improved HySPADE edge detector then iterates the Spectral Similarity pairwise measurements for pixel (1,1) against the remaining input pixels in the window in order to fully populate band 1 of the HySPADE cube at that window's spatial footprint.

For example, the algorithm will populate HySPADE band 1, pixel (10,10) with the Spectral Similarity measurement between the HSI spectra at input pixel (1,1) and (10,10). Next, the algorithm simply repeats the process for every remaining pixel in the window to fully populate the intermediate n -band HySPADE cube for an n -pixel HSI cube. For example, the algorithm will populate HySPADE cube band 10 with the Spectral Similarity measurements between the input HSI cube pixel (1,10) and every other pixel in the window. The window then slides to the adjacent spatial footprint and repeats until the full scene is reflected in a series of intermediate HySPADE cubes. The intermediate cubes are then spatially joined to create a single HySPADE output cube. The result is a fully populated HySPADE cube in which each “HySPADE spectrum” reflects the edge behavior (i.e., shape) and strength (i.e., magnitude) in the window.

Next, the algorithm applies a one-dimensional finite difference measurement to identify discontinuities exceeding the discontinuity threshold within each pixel “spectrum” in the output HySPADE cube. The algorithm keeps a running tally based on each time the Spectral Similarity score alarms against the threshold, resulting in a single score for each pixel. That score is a direct reflection of how frequently HySPADE declared that pixel as an edge pixel and therefore translates directly to edge map generation.

The improved HySPADE algorithm then begins measuring edge strength in order to generate the final edge plane. To measure edge strength, the algorithm establishes a user-defined discontinuity threshold below which a spectral similarity score will alarm as an edge – recall that the low Spectral Similarity measurements are indicative of

discontinuities due to the small ED and correlation scores consistent with a boundary between dissimilar physical materials. Initial thresholds typically are established as a multiple of the standard deviation and adjusted according to HySPADE results. Keep in mind that much of hyperspectral remote sensing is an iterative process requiring constant adjustments depending on how particular data sets respond to processing. For this work, the initial threshold is established at a single standard deviation based on the population of Spectral Similarity scores measured across the full hypercube. Single standard deviation threshold produced satisfactory results in previous HySPADE research and therefore provide a reliable starting point for comparing the improved HySPADE algorithm to the legacy algorithm. If necessary, the threshold will be adjusted up or down to achieve interpretable results.

For example, recall Figure 64 which presented a HySPADE pixel spectrum characterized by step functions correlating to edge behavior between high contrast materials. By substituting the Spectral Similarity score for either ED or SAM, the improved HySPADE algorithm generates similar spectra in which step functions correlate to the boundary between one material and another. As the one-dimensional finite difference filter is passed across the spectrum, it will increment the “edge tally” according to how many step functions exceed the user-defined discontinuity threshold. In this construct, HySPADE spectra with many step functions are more likely to be edge pixels than HySPADE spectra with fewer step functions.

Recall that a HySPADE spectrum communicates edge behavior when the combined ED and correlation scores exceed a user-defined threshold due to the spatial-

spectral discontinuity between adjacent pixels. Another way to think about the step function behavior is to envision pixel (1,1) executing against 10 adjacent pixels of material A, which will generate 10 very similar Spectral Similarity scores at, for example, 0.90. As HySPADE encounters the edge between material A and material B, the Spectral Similarity measurement will abruptly change due to the difference between pixel (1,1) versus Material A scores and pixel (1,1) versus Material B scores. When the pixel (1,1) versus Material B scores begin appearing at, for example, 0.20, edge behavior will appear in the HySPADE spectrum between band 10 and band 11. The magnitude of the edge behavior is directly correlated to the spectral discontinuity between the adjacent materials and therefore is appropriately constructed for a thresholded edge detection operations.

The improved HySPADE's final step generates an edge plane in which each pixel's DN represents the number of times the one-dimensional finite measurement step exceeded the discontinuity threshold for that pixel. HySPADE pixels that frequently exceeded the threshold will appear more strongly in the edge plane than pixels that alarmed less frequently – an optimal output for an edge detector.

To summarize the improved HySPADE's edge detection process, the algorithm accepts as input the output from the preprocessing and compression components. The input takes the form of either a radiance cube, a reflectance cube, a full PCA cube, a full MNF cube, a compressed PCA cube or a compressed MNF cube. The algorithm then applies an $n \times n$ pixel window to the n -pixel input data to generate an n -band HySPADE cube in which each pixel spectrum is comprised of Spectral Similarity measurements between itself and every other pixel in the scene. Each HySPADE spectrum is then

scored according to how many times it alarms as an edge according to a discontinuity threshold and a one-dimensional finite difference measurement. The final single-band edge plane consist of n pixels with DNs corresponding to edge strength as measured by above-threshold Spectral Similarity scores.

Figure 116 presents a demonstration of the HySPADE edge detector as tested against the synthetic 420-band VNIR/SWIR dataset. As shown, the reflectance test generated largely accurate, unbroken boundaries between the materials while false alarming on several noisy pixels within each of the blocks. HySPADE generated thin, unbroken edges accurately along the feature boundaries for the compressed PCA test – a useful demonstration of how compressed HSI data can improve HySPADE edge detection results. Also note that the compressed PCA test significantly reduced false alarms.

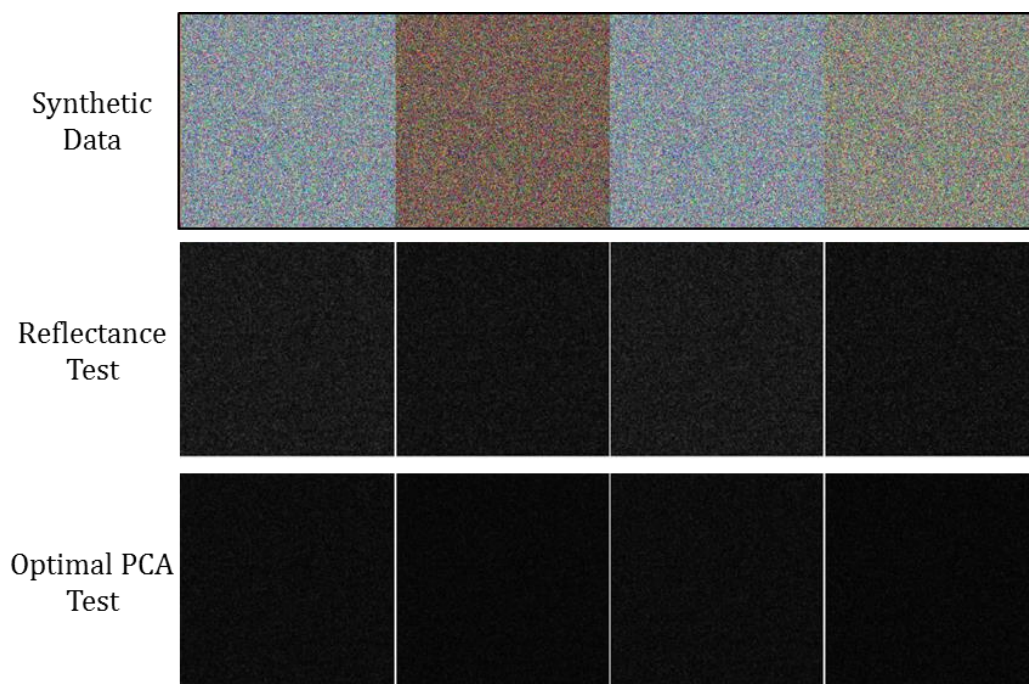


Figure 116: HySPADE Demonstration against Synthetic HSI Dataset

Edge Detection: A Level Set Edge Detection Approach for HSI

This work's third new edge detection algorithm develops a level set-based approach to hyperspectral edge detection. The original MATLAB level set code was obtained from an open source MSI version, which was subsequently modified to accept HSI data [267]. An extension of Lu et al's level set approach [211] to hyperspectral data, the new algorithm advances the edge detection capability in several ways. First and most importantly, it extends level set methods to hyperspectral imagery— a largely unexplored intersection of methods, as demonstrated in the background section. Secondly, this approach tests the level set edge detection approach against a variety of spatial and spectral resolutions with the intent of measuring the algorithm's sensitivity to spatial and spectral resolutions. Thirdly, this dissertation tests the performance of level set edge

detection methods against HSI data sets aligned to a broad range of HSI applications, including traditional applications as well as emerging applications. In sum, the present approach intends to advance a level set-based edge detection method into hyperspectral remote sensing, test its performance against a range of spatial and spectral resolutions, and demonstrate its applicability against a broad set of HSI applications.

Adopting Lu et al's level set approach to HSI data requires three steps: initial curve selection, initial level set calculation and level set evolution. First, an initial circular curve is placed at the center of an i by j image, according to Equation 30, where x, y is the center coordinate of the image, the initial time ($n\Delta t$) is zero and the radius is set to $\frac{1}{8}$ of the image's longest dimension. The initial curve could theoretically be placed at any location within the image and could be assigned a radius of any dimension, but Lu et al recommend placing it at the center of the image and to initialize it with a small initial radius. In this way, the level set initial curve operates much like a seed in traditional image processing.

$$\varphi_{i,j}^n = \varphi(x_i, y_j, n\Delta t)$$

Equation 30: Level Set Initial Curve

This research tested Lu et al's hypothesis regarding locating the initial curve at the image center by testing how locating the initial curve at different starting locations affected edge detection results. As seen in the Cuprite Flight Line #4 VNIR/SWIR image tests in Figure 117, nearly identical edge detection results are achieved regardless of

where the initial curve is located. Consequently, this dissertation locates the initial curve at the center of the image.

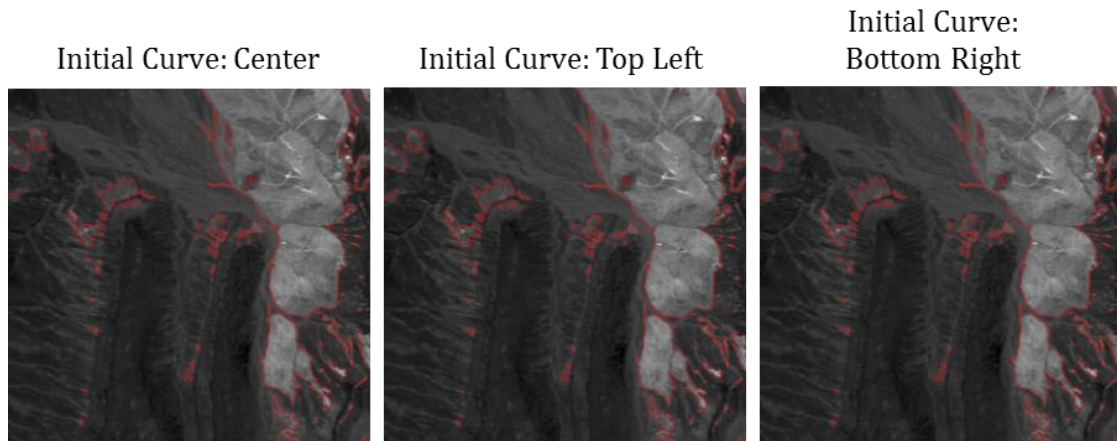


Figure 117: Level Set Initial Curve Testing against Cuprite Flight Line #4 VNIR/SWIR Data

The second step assigns initial distance values to each pixel and calculate the initial level set function. Once positioned at the center of the image, the initial level set function is calculated as a signed distance function $\varphi(x, y, t)$ generated from the distance between every point in the image and the initial contour [211]. According to Equation 31, the algorithm assigns zero values to pixels falling along the initial curve, negative values to pixels falling within the initial curve, and positive values to pixels falling outside the initial curve. In this manner, the positions and distances of the scene pixels determine the level set function $\varphi(x, y, t)$. Now, the interface between the region where $\varphi(x, y, t) > 0$ and the region where $\varphi(x, y, t) < 0$ is identified as the zero level set because $\varphi = 0$ at all points along the curve. Finally, this zero level set defines the two-

dimensional, closed contour or set of closed contours C , which will evolve in the next step to solve the traditional level set energy minimization problem.

$$\varphi(x, y, t) = \begin{cases} 0 & \text{if Pixel Intersects Level Set} \\ + & \text{if Pixel is Outside Level Set} \\ - & \text{if Pixel Inside Level Set} \end{cases}$$

Equation 31: The Zero Level Set of a Function

The third and final step evolves the initial level set to solve the level set energy minimization equation, thereby establishing the level set curve C along the edge of scene features. To discretize the level set evolution, the algorithm uses an explicit finite difference scheme to control evolution timing and spacing. First, the algorithm establishes the contour space step as a single pixel, meaning that the contour will evolve by only a single pixel in any direction for any given evolution, thereby avoiding sinks, contour overlaps and unnecessary complexity. Specifically, the algorithm denotes the space step as $h = 1$.

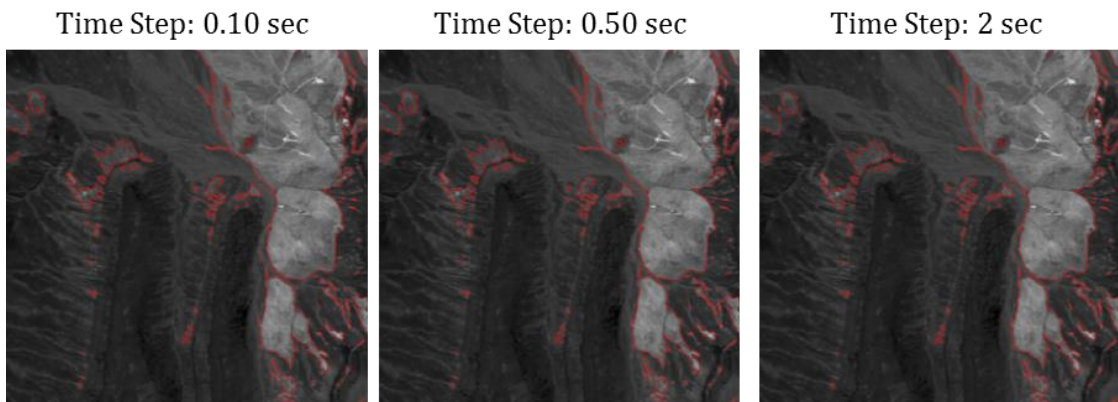


Figure 118: Level Set Time Step Testing against Cuprite Flight Line #4 VNIR/SWIR Data

Next, the algorithm establishes the evolving contour's time step as Δt to control how long the surface has to evolve for any given evolution. This research tested several time steps to determine how they affect edge detection results. As seen in the Cuprite Flight Line #4 VNIR/SWIR image tests in Figure 118, nearly identical edge detection results are achieved for 0.1s, 0.5s and 2.0s time steps. Consequently, this work uses a Δt of 0.1 seconds to maximize performance. To formalize the discretization, let $(x_i, y_j) = (ih, jh)$ for $1 \leq i \leq M, 1 \leq j \leq N$ where $Nh \times Mh$ is the image size [211]. Within this construct, Equation 32 presents the discretized approximation of $\varphi(x, y, t)$ for $n \geq 0$ where n represents the n th iteration.

$$\varphi_{i,j}^n = \varphi(x_i, y_j, n\Delta t)$$

Equation 32: Discretization of the Level Set Function [211]

$$\varphi_{i,j}^{n+1} = \varphi_{i,j}^n + \Delta t \times |\nabla \varphi_{i,j}^n| \left[-\lambda_1 \left(u_{0,i,j} - c_1(\phi^n) \right)^2 + \lambda_2 \left(u_{0,i,j} - c_2(\phi^n) \right)^2 \right]$$

Equation 33: Level Set Evolution [211]

Finally, Equation 33 presents the computation for the level set evolution, where $u_{0,i,j}$ is image pixel value, and $c_1(\phi^n)$ and $c_2(\phi^n)$ are the averages of vector magnitude values inside and outside the curve C in the n th iteration, respectively [211]. The

algorithm will continue iterating until either it reaches the maximum number of user-defined iterations or $\varphi_{i,j}^n = \varphi_{i,j}^{n+1}$. For this dissertation, the maximum number of iterations is set to 15 in order to maintain consistency among tests.

The 15 iteration threshold was determined by testing the algorithm's sensitivity to the number of iterations. Specifically, using the Cuprite Flight Line #4 VNIR/SWIR image, this dissertation conducted several iteration tests in order to determine the optimal number of iterations to execute. As seen in Figure 119, iterations of five, 15, and 20 generated nearly identical results around the most important features of the scene (e.g., the large kaolinite deposits to the east and the silica outcroppings along the western edges).

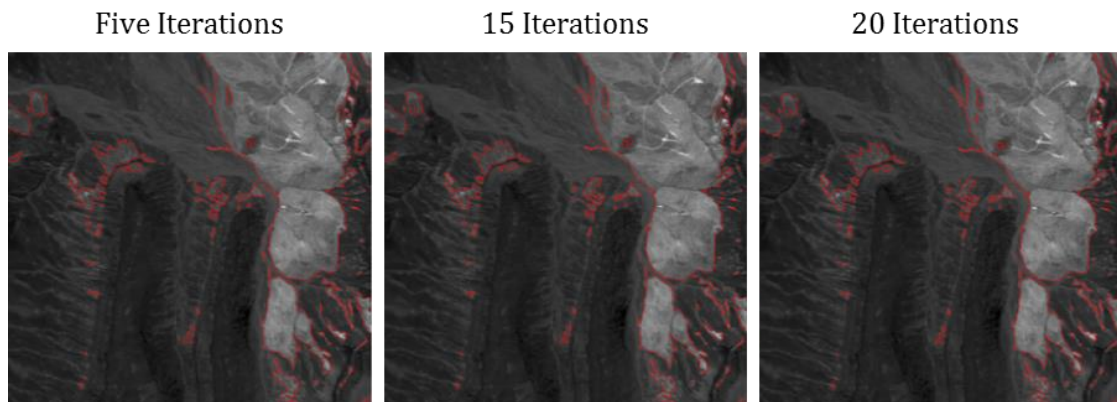


Figure 119: Level Set Iteration Testing against Cuprite Flight Line #4 VNIR/SWIR Data

The most significant difference among the tests is that, in a handful of minor cases, the five-iteration test delineated a single line around closely-spaced features while the 15-iteration and 20-iteration tests accurately captured the narrow gap between the

features. Additionally, the five-iteration test occasionally missed minor details along the edges of the kaolinite features, while the 15-iteration and 20-iteration tests accurately delineated the detail. Also note that the 15-iteration test and the 20-iteration tests are nearly identical. Since the five-iteration test lacked sufficient iterations to capture minor edge details, and the 20-iteration did not improve upon the 15-iteration test, each level set test will be executed (i.e., controlled) with 15 iterations.

At the algorithm's conclusion, the satisfaction of Equation 33 represents the satisfaction of the central level set challenge: minimize the energy of an active contour along the discontinuous pixels delineating an object. Specifically, when the value of $\varphi_{i,j}^n$ equals (or in most circumstances, approaches very closely) the value of $\varphi_{i,j}^{n+1}$, the algorithm is declaring that additional level set evolutions only increase the variance (i.e., energy) between subsequent evolutions, meaning that the evolutions have reached their minimum and satisfied the level set objective. The final output for this study's level set algorithm is an image plane overlaid with the level set contours indicated in single-pixel width red curves.

As also seen in the Gradient and HySPADE methodologies, the Level Set methodology applies PCA and MNF transforms to compress the hypercubes. Both full PCA and MNF cubes are tested as well as PCA and MNF cubes compressed to contain only the most diagnostic spectral information in the original hypercube.

Figure 120 presents a demonstration of the level set edge detector as tested against the synthetic 420-band VNIR/SWIR dataset. As shown, the reflectance test generated largely accurate, unbroken edges between the first mineral and its noisy

neighbors, but missed the low-spectral contrast boundary between the second mineral and its noisy neighbor. The compressed PCA results were nearly identical, suggesting that the level set algorithm is subject to suboptimal false negative performance between low-spectral contrast features.

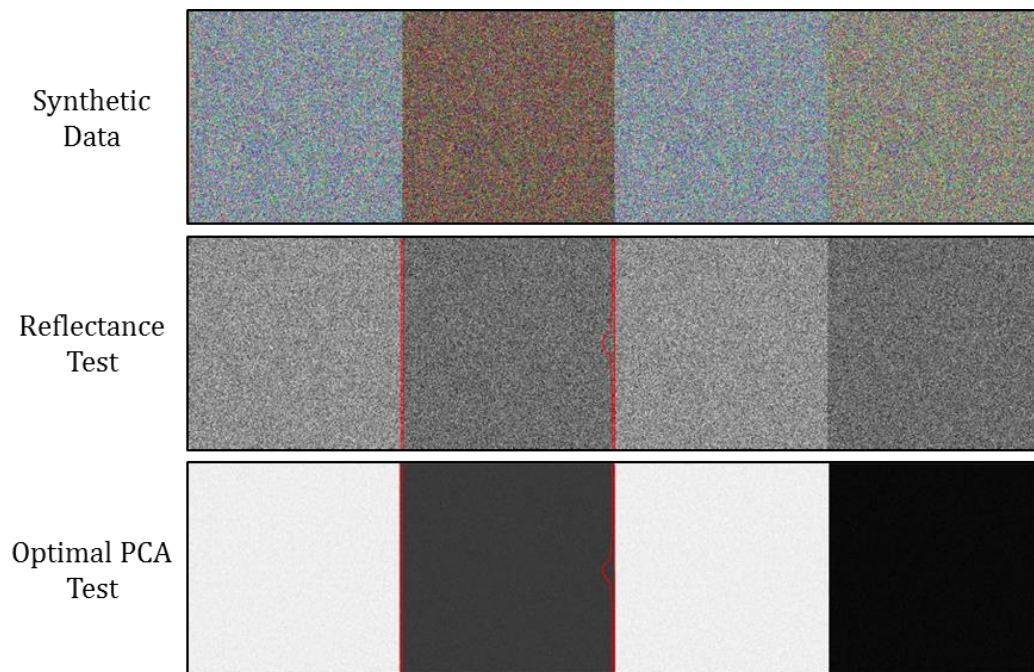


Figure 120: Level Set-Based Algorithm Demonstration against Synthetic HSI Dataset

Algorithm Evaluation

This dissertation's primary evaluation methodology measures algorithm performance against Canny's optimal edge detection criteria: low false positive rates, low false negative rates, accurate localization of edges and single-point response of edge pixels. Additionally, the evaluation includes Canny's secondary edge detection criteria:

robustness in the presence of noise and unbroken edge generation. In most of the literature, the secondary criteria are ignored in favor of the primary criteria, but this study explicitly considers them in order to derive the most complete possible understanding of algorithm performance against challenging, non-traditional HSI datasets. By using Canny's criteria for a good edge detector, this work grounds its evaluation methodology within the construct of empirical, widely accepted image processing traditions.

The primary evaluation vehicle structures the Canny criteria and edge detection experiments into simple, ordinal rank-based matrices as seen in the example in Table 16. Each matrix record corresponds to an input dataset (e.g., a reflectance cube, a compressed PCA cube, etc.) and each field corresponds to a specific Canny criterion. Using a mix of quantitative and qualitative evaluation techniques, this methodology applies a five-point Likert scoring system to rate performance against the Canny criteria. As seen in Table 16, each record's Likert scores are summed and normalized in the final field, which provides an aggregate score for each input dataset as measured across the full suite of Canny criteria.

Different evaluation techniques measure an experiment's performance against a Canny criterion depending on the optimal measurement for the criterion, the availability of ground truth data, and the suitability of the underlying HSI dataset for an evaluation technique. Quantitative measurements are given primacy to qualitative techniques wherever possible, and qualitative techniques are used when quantitative techniques are insufficient. Specifically, this dissertation relies on a blend of techniques including Ground Truth Evaluation, Interest Point Evaluation, Visual Inspection, localization

Accuracy and Pairwise Image Subtraction, each of which is treated in detail in a later section.

Table 16: Notional Ordinal Rank Metric – Single Algorithm, Single Dataset

Notional Evaluation: Gradient Algorithm Reno VNIR/SWIR Dataset	False Positives	False Negatives	Localization	Single-Point Response	Robustness to Noise	Unbroken Edges	Normalized Score
Reflectance	1	3	5	4	5	4	3.7
Optimal PCA	4	2	5	3	2	4	3.3
Optimal MNF	4	2	1	5	4	1	2.8
Full PCA	3	2	1	3	2	1	2.0
Full MNF	1	4	2	3	1	4	2.5
Roberts	2	3	5	2	2	2	2.7
Sobel	5	2	4	5	2	4	3.7

Likert Scale Scoring

The evaluation techniques provide the underlying scientific insight for the broader evaluation superstructure. Specifically, the various quantitative and qualitative evaluation measurements generate five-point Likert scale scorings that populate the discrete matrix scores. In this manner, the discrete matrix scores reflect the performance of specific edge tests against specific Canny criteria. Low scores correspond to stronger performance, as the Likert scale proceeds in ascending order from one to five where one corresponds to the strongest performance and five corresponds to the weakest performance.

The Likert scales vary according to the specific image processing behavior dictated by each Canny criterion. For example, Figure 121 presents the Likert scale for

measuring Canny’s false positive criterion. Figure 121 contains visualizations for what each rating would look like for a 100 x 100 image. For example, a Likert 1 rating (i.e., a Rare rating) would have fewer than 100 false alarms, which corresponds to less than 1% of the 10,000 total image pixels. As false alarms increase, Likert ratings correspondingly degrade to reflect the increasing barrier false alarms present to reliable edge detection performance.

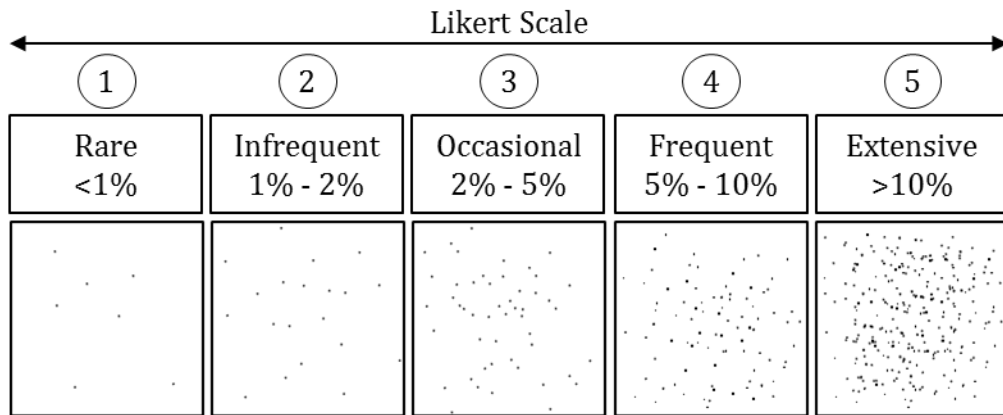


Figure 121: Likert Scale for Canny's False Positive Criterion

The percentage bounds for each false alarm Likert rating were chosen at natural breaks in how false alarm behavior affects edge detection performance. For example, there is a meaningful difference between 50 possible false edge pixels in a 100 x 100 scene (a Likert rating of 1) and 200 possible false edges within the same scene (a Likert rating of 2). There also is a natural break between the Likert ratings of 4 and 5 compared to the Likert ratings of 1, 2 and 3. Specifically, Likert ratings of 4 and 5 (frequent and extensive false alarms, respectively) generally present an obstacle to reliable edge

detection processing. This framework aligns to the work of image scientists, who for most HSI applications would prefer to encounter rare or infrequent false alarms, can manage occasional false alarms, but cannot reliably execute in the presence of frequent or extensive false alarms. Additionally, a Likert score of 3 corresponds to a 95% performance interval for most Canny criteria, which is consistent with the typical application of performance intervals in applied science and statistics [274], [275], [276], [277]. With respect to this dissertation's hypotheses, the 95% performance threshold establishes the boundary between average or below-average performance (i.e., the null hypothesis) and superior performance. For additional detail on this dissertation's Likert scale methodology, please refer to Appendix B.

Ground Truthing

To generate discrete Likert scores, this methodology employs a cascade of evaluation techniques tuned to the unique properties of each criterion and HSI dataset. For example, measuring localization evaluation requires a different technique than the unbroken edges evaluation. Similarly, quantitative methods can empirically evaluate some Canny criteria (e.g., false positives), while other criteria (e.g., robustness to noise) require quantitative techniques informed by qualitative methods. Consequently, this methodology uses a range of well-known evaluation techniques (e.g., ground truthing) and adopts several traditional image processing evaluation techniques (e.g., information content) to the unique attributes of the challenging, non-traditional HSI data and experiments conducted here.

In remote sensing, ground truthing is the standard for results evaluation.

Wherever possible, this study relies on ground truth data to measure experimental performance against the five Canny criteria. Specifically, ground truth data is available for six of the 12 HSI datasets tested in this study: Cuprite, Indian Pines, Larkhaven, Rare Target on Sand, Chemical Array on Sand and Cloth Threads on Sand. Figure 122 presents the ground truth map for the Cuprite, NV area as determined by the United States Geological Survey [278]. Figure 123 presents the ground truth map for the Indian Pines data set as determined by Baumgardner et al. [259].

Although no pixel-based ground truth map is available for the Larkhaven dataset, the data was collected by Cox and Resmini and the home itself is the property of Resmini. Hence, the scene features are well known to Cox and Resmini, whose personal knowledge of the image features, the collection method and the collection environment serve as a reliable ground truth reference.

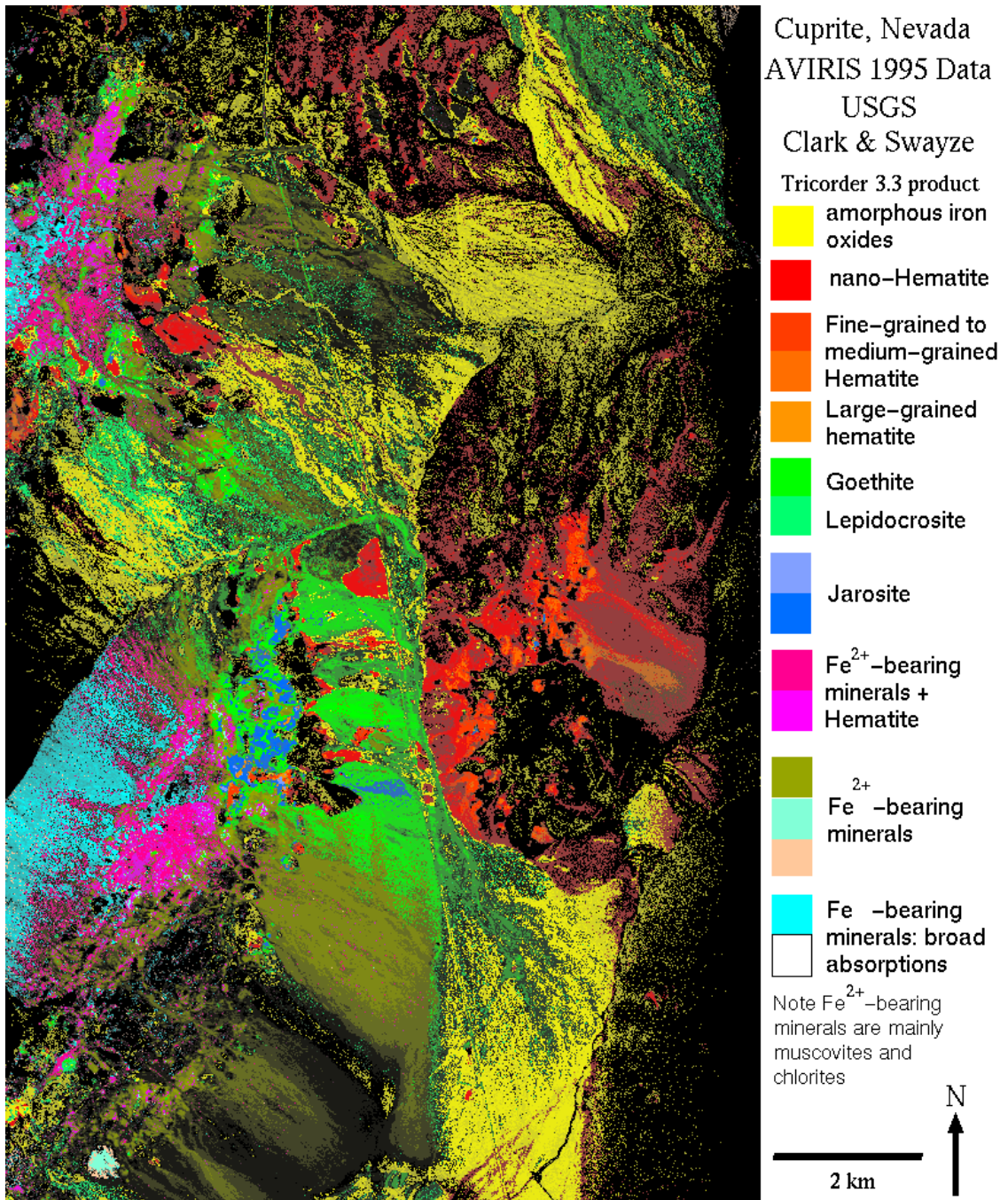


Figure 122: Cuprite, NV USA Ground Truth Map [278]



Figure 123: Indian Pines, IN USA Ground Truth Map [259]

The microscene data are naturally suited to ground truthing since they are imaged at very high spatial resolutions and are manually constructed with precisely known materials. Figure 124 presents the sequential construction and ground truth information for the Rare Target on Sand dataset as determined by Resmini et al [258], Figure 125 presents the ground truth for the Chemical Array dataset and Figure 126 presents the ground truth information for the Cloth Threads on Sand dataset.

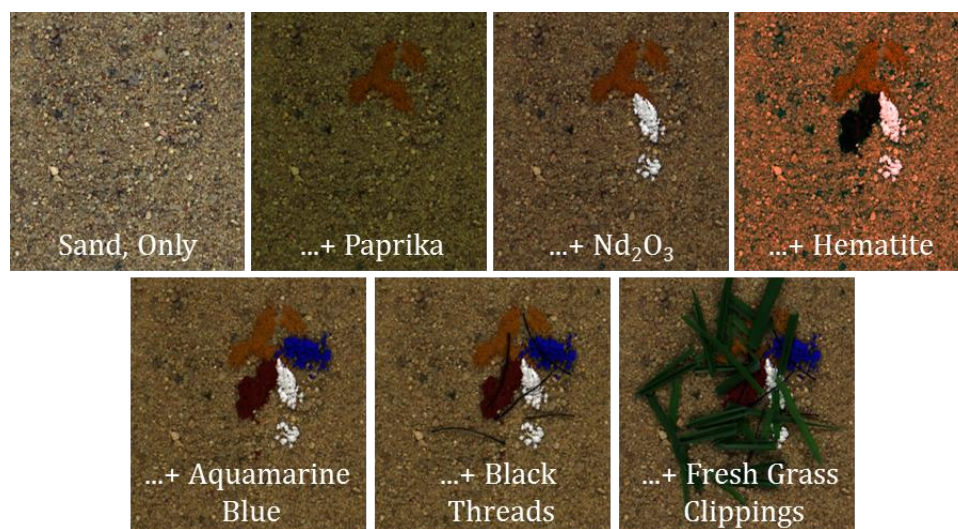


Figure 124: Rare Target on Sand Ground Truth Information [258]

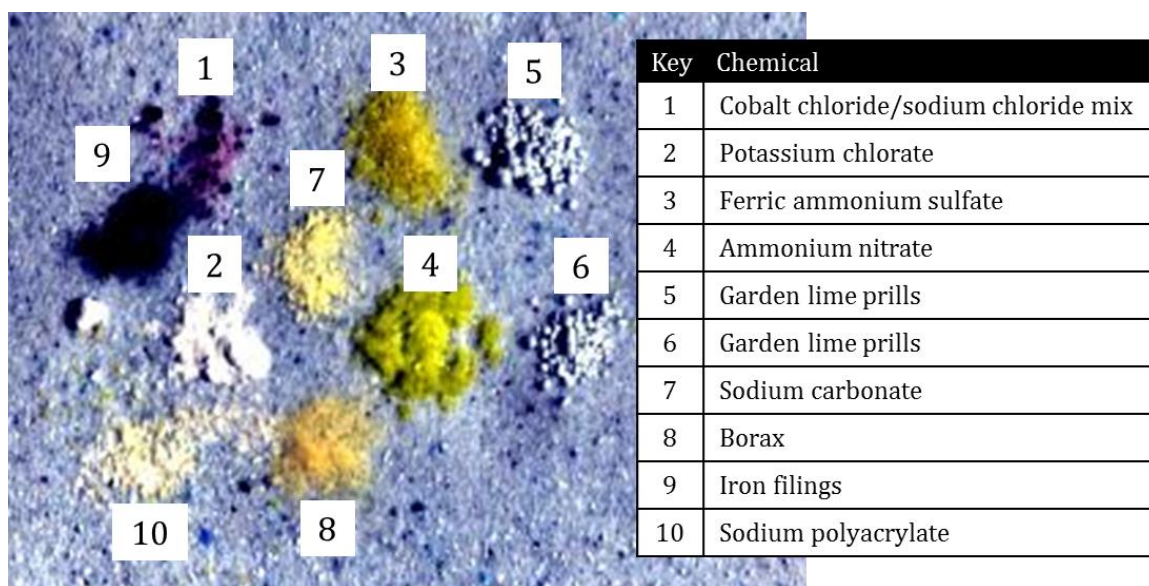


Figure 125: Chemical Array Ground Truth Information

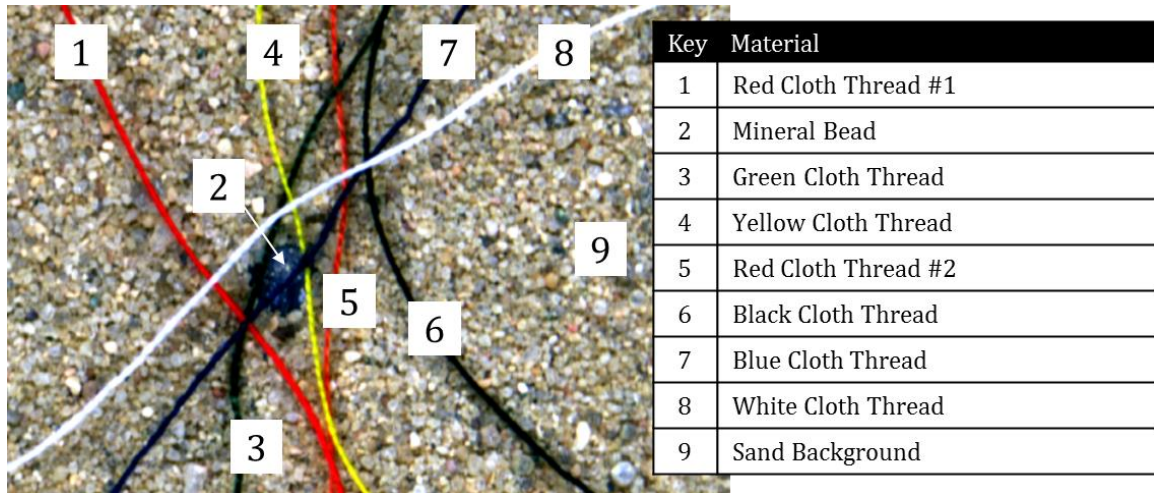


Figure 126: Cloth Threads on Sand Ground Truth Information

Information Content at Interest Points

The image processing literature offers many evaluation criteria that can be extended to hyperspectral remote sensing. One such criterion involves measuring the information content at interest points within the scene, as proposed by Schmid et al [279]. In [279], an image's interest points are the set of points at which the signal changes two dimensionally, a set which includes conventional "corners" as well as single black pixels on a white background.

For example, consider Figure 127, which presents a subset of interest points that Schmid et al extracted from a gray-scale image of Van Gogh's sower painting. Note that the authors thresholded the interest points to include only the strongest interest points in the scene. Thought of from an edge detection perspective, the set of interest points within an image should include all edge points, which represent n -dimensional discontinuities within a hyperspectral scene. Specifically, this dissertation extends the

traditional image processing concept of interest points into hyperspectral space by defining hyperspectral interest points as all points with the scene that are detected as edge points as defined by this study's edge model.



Figure 127: Interest Points Detected on Van Gogh's Sower Painting [279]

Additionally, interest points can be derived by a variety of interest point detectors, including intensity-based methods, contour-based methods and parametric model-based methods [279]. Intensity-based interest point detectors identify edge points by measuring the gray scale differences among adjacent pixels, and contour-based detectors use a surface's changes in curvature to identify interest points within a scene [279]. Importantly, there is a clear conceptual link between intensity-based interest point detection methods and this dissertation's gradient-based and improved HySPADE edge

detection methods, just as there is a conceptual link between contour-based interest point detectors and this dissertation's level set-based edge detection method.

For example, intensity-based interest point detectors use a gradient-based approach to identify interest points, just as the gradient-based edge detection algorithm uses gradient methods to extract edge points. Similarly, just as contour-based intensity point detectors use curved surfaces to identify interest points, the level set-based algorithm evolves a surface to extract edge points along the intersection of the surface and the image plane. The link between interest point detection methods and edge detection methods indicate evaluation criteria used to measure the former can reasonably be extended to measure the latter. Here, edge pixels are interest points for the purpose of measuring information content.

Once the edge detectors extract edge pixels/interest points from a scene, the evaluation methodology proceeds to evaluate their information content as implemented in Schmid et al. Schmid et al state that an interest point's information content is the measure of its distinctiveness, and that an interest point's information content is inversely related to its probability [279]. This work borrows these concepts in their pure form. That is, this study measures an edge pixel's information content as a function of how unique the pixel is among its immediate edge pixel neighbors.

Proceeding to the precise means of measurement for a specific scene, Schmid et al use an entropy metric to evaluate interest point information content as measured across thousands of samples imaged at various illuminations, rotations, scales, viewpoints and noise levels [279]. Each interest point is then measured for how much information

content it transmits across the various collection environments, where low entropy (i.e. optimal) scores indicate high information content, and high entropy scores are associated with lower information content [279].

This methodology is extremely effective for evaluating algorithm performance within a highly controlled and robust test environment (i.e., when the researchers control the sensors, the collection environment, the collection execution and the final data output), however it is not directly translatable to this work's small sampling of diversely sourced HSI datasets, each of which aligns to only a single unique earth remote sensing scene. Therefore, this dissertation's methodology adapts Schmid et al's entropy-based, high volume information content measurement by developing an in-scene metric based on the unique edge strength of fundamental edge points.

Fundamental edge points are defined as the key diagnostic edge pixels for primary scene features, such as a large building, a rare target or the advancing front of an oil slick. The fundamental edge crossing points can be visualized by imagining a wire diagram delineating a major feature, and extracting the vertices marking a significant angular change in the delineating framework. Importantly, these fundamental edge points occur at major angular changes in the feature and do not reflect every minor angular change, which would include a suboptimal volume of non-critical edge pixels. In this manner, the fundamental edge points are analogous to Schmid et al's highly thresholded interest points as seen in the Van Gogh image in Figure 127, but are more meaningful from an edge mapping perspective in that the fundamental edge crossing points represent the minimum number of key pixels sufficient to delineate a key feature's major contours.

Specifically, Figure 128 presents this dissertation's novel workflow for identifying and evaluating a scene's fundamental edge points. Note that the HSI-optimized Schmid et al workflow blends qualitative expert judgment (i.e., determining the scene's key features and interest points) with quantitative measures based on traditional image processing evaluation criteria for edge detector performance (i.e., empirically measuring the statistical uniqueness of fundamental edge points), which creates an optimal balance between HSI applications-focused research and a basic science approach to image processing.

As seen in Figure 128, the first step requires the researcher to identify prominent scene features, such as key buildings, roadways, mineral deposits, chemicals, oil spills, crops or other key features that have direct bearing on the underlying HSI application. For example, the prominent oil spills fronts in the Deepwater Horizon VNIR/SWIR data represent the key features in the data since their positioning directly addresses the underlying HSI application, oil spill mapping. In contrast, the multiple surface vessels in the scene would not be key features since they do not directly inform oil spill mapping. Consequently, the edge detectors' abilities to delineate the surface vessels are not evaluated in this workflow but instead are considered in a separate evaluation workflow.

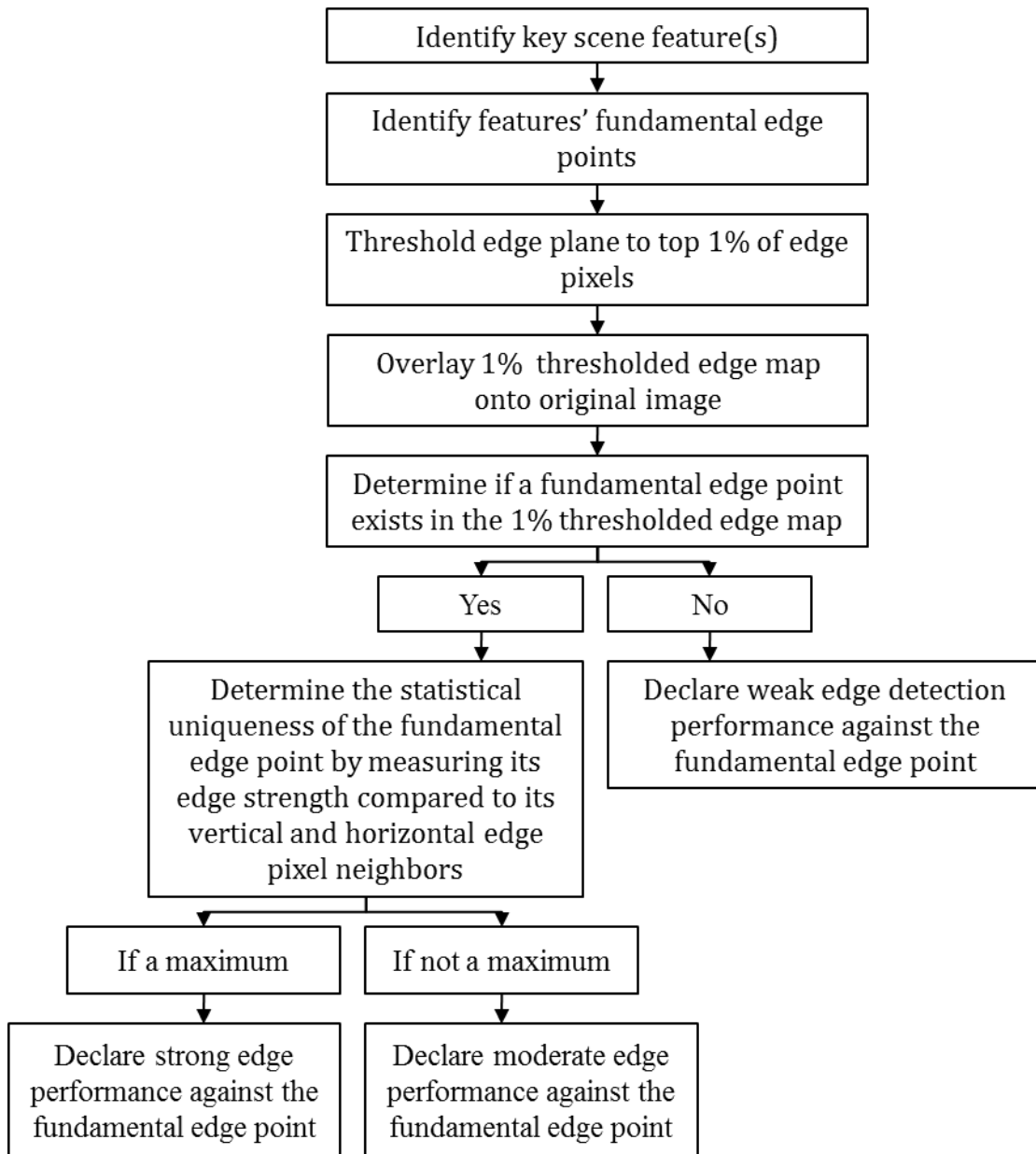


Figure 128: Evaluation Workflow for Fundamental Edge Point Information Content

After identifying the scene’s prominent features, the workflow proceeds to identifying which pixels along the features’ edges most closely define the overall spatial and spectral characteristics of the features. Specifically, this step establishes a baseline

for future edge plane measurements by identifying which edge pixels contain the most significant information content – a key direct extension of the Schmid et al approach to information content measurements. For example, the corners of the U-shaped building in Figure 129 represent the key pixels from which the building can be characterized with respect to both its shape (i.e., spatial character) and its physical composition (i.e., spectral character).

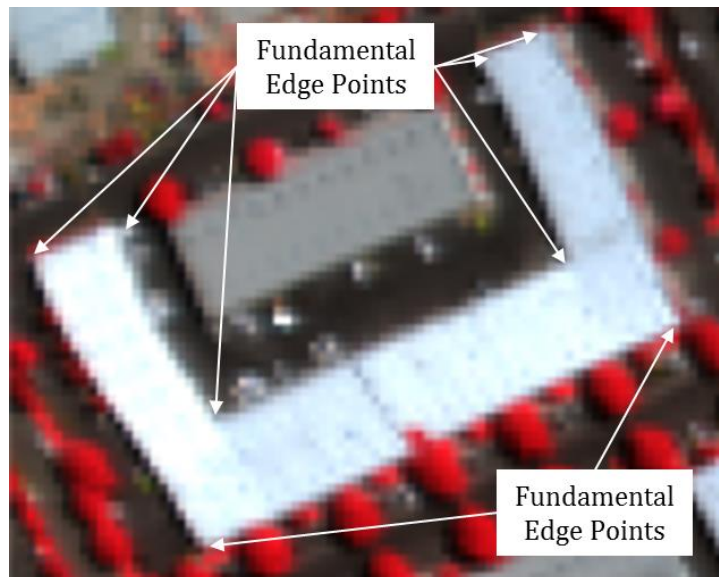


Figure 129: Fundamental Edge Point Identification

In practice, this portion of the workflow considers very small clusters of pixels centered on the fundamental edge points in order to avoid skewing the evaluation due to a single-pixel misidentification of the true fundamental edge point. Picking the one true fundamental pixel from a small set of two to three pixels is unlikely to be repeatable,

easily agreed upon and sufficiently rigorous, and there is usually no diagnostic difference between those two to three pixels that often span a fundamental edge point – any one of those two to three pixels would suitably anchor the delineation of the feature and therefore are treated equally in the absence of a clear, singularly recognizable fundamental edge point.

Histogram	DN	Npts	Total	Percent	Acc Pct
Band 1	0.000000	22142	22142	11.5323	11.5323
Bin=28.2352	28.235294	961	23103	0.5005	12.0328
	56.470588	715	23818	0.3724	12.4052
	84.705882	565	24383	0.2943	12.6995
	112.941176	524	24907	0.2729	12.9724
Top ~1% threshold	6974.117647	1318	182959	0.6865	95.2911
of edge strength,	7002.352941	1177	184136	0.6130	95.9042
constituting a 2725-	7030.588235	1189	185325	0.6193	96.5234
pixel subset of the	7058.823529	1312	186637	0.6833	97.2068
192,000-pixel Reno	7087.058824	1296	187933	0.6750	97.8818
hypercube	7115.294118	1342	189275	0.6990	98.5807
→	7143.529412	1583	190858	0.8245	99.4052
	7171.764706	1102	191960	0.5740	99.9792
	7200.000000	40	192000	0.0208	100.0000

Figure 130: Isolating the Top 1% of Edge Pixels in the Edge Plane

In order to isolate the strongest edge pixels in the scene, the third step in the information content evaluation workflow subsets the edge plane to approximately the top 1% of edge pixels according to DN's. For example, Figure 130 presents the statistical summary from the HySPADE edge plane derived from the Reno VNIR/SWIR hypercube. Note that the very strongest edge pixels rate a DN of 7200.00, and that there are only 40 of those pixels across the entire 192,000-pixel scene. Adjusting the threshold to capture approximately 1% (an exact 1% is often unobtainable due to binning) facilitates the isolation of the strongest edge pixels in the scene, in this case 2725 edge pixels with a DN

of 7143.53 or higher. The output from this step is a highly thresholded edge plane containing only those edge pixels that alarmed most strongly against the respective edge detection algorithm.

The fourth step generates an overlay of the highly thresholded edge plane against the original image. A simple flickering technique accomplishes this step, which enables the fifth step, determining if a fundamental edge point exists in the 1% thresholded edge map. Flickering between the edge plane and the original image quickly identifies whether the edge detector alarmed sufficiently (i.e., very strongly, within the top 1%) against the high information content within the fundamental edge point. If the edge detector failed to alarm sufficiently, the workflow makes a declaration that the edge detector performed weakly against the fundamental edge point. This declaration is consistent with a natural interpretation of edges in the sense that if an edge detector fails to identify the most important edge pixels in a scene, it is unlikely to support the underlying HSI application in a reliable, robust manner.

If the fifth step determines that a fundamental edge point is present within the highly thresholded edge plane, a statistical determination is made to measure the information content of the pixel compared to its neighboring edge pixel. Specifically, the fifth step determines if the fundamental edge point represents a point of maximum spatial-spectral information content by measuring its DN against its neighboring edge pixels. If the fundamental edge pixel represents the local edge strength maximum, the workflow declares a strong edge detector performance against the point – a rating consistent with an optimal performance against a key diagnostic pixel. Alternatively, if

the edge detector incorrectly indicates that one or more neighboring edge pixels contains more information content (i.e., a larger DN), then the workflow declares a moderate edge detector performance against the point. In the moderate declaration, the edge detector adequately returned an appropriate absolute information content value (i.e., it measured the edge strength at a level exceeding the top 1% threshold), but it returned an undervalued relative edge strength compared to the neighboring edge pixels, which contain less information content. Therefore, the performance rates a moderate assignment.

At the conclusion of the HSI-compressed information content workflow, the evaluation empirically informs a Likert rating consistent with edge detection performance. Experiments that accurately translate a hypercube's information content into an accurate edge plane are more likely to satisfy the high standards for Canny's evaluation criteria, particularly the localization and single-point response criteria. For example, in the case single-point response, very high scoring fundamental edge points will increase the likelihood of statistical separation for the top 1% compared to its below-threshold neighbors, meaning that very strongly scoring edge pixels are less likely to invite near-peer multi-pixel responses.

Global Measures of Coherence

In the absence of ground truth data, traditional approaches to evaluating edge detection performance often rely on comparing hundreds (or thousands) of same-scene images collected from a variety of conditions, view angles, etc. Although this dissertation does not test multiple images of the same scene, it adapts traditional

grayscale measures of performance to the HSI datasets tested herein. Specifically, Baker and Nayer [280] developed edge detection benchmarks useful in the absence of ground truth data: collinearity of edges and single-point intersections between two edges. Although Baker and Nayer advanced these two global measures of coherence by testing them against large volumes of grayscale images, this dissertation extends their basic principles to measure edge detection performance within single-sample HSI data.

For example, Baker and Nayer's collinearity measure of performance stipulates that a reliable edge detector should map edge pixels along the same line. For example, all edge pixels should map to a single row on the edge plane for a straight horizontal edge feature. Baker and Nayer referred to this approach as a "global coherence" evaluative measure because it measures alignment across the entire scene - a theme that this study adopts in full by identifying benchmark edges throughout the scene. By doing so, the evaluative methodology will capture the full range of edge performance, both strong and weak. Additionally, this simple metric supports several Canny criteria, including single-point edge response, localization, false positives and false negatives.

This dissertation adapts Baker and Nayer's collinearity constraint to single-sample HSI data by the five step process detailed in Figure 131. First, benchmark vertical and horizontal edges are identified within each HSI dataset. Vertical and horizontal edges are preferred to diagonal edges for evaluation because their collinearity is more easily measured in image rows and columns; diagonal edges tend to wander left and right or up and down a single pixel as the edge detector tries to map a diagonal edge onto square pixels. Consequently, evaluating vertical and horizontal edges is a more

robust and reliable approach for measuring collinearity. Next, the collinearity evaluation counts the number of pixels comprising the benchmark edges in the original image. For example, if a vertical edge along the western side of a building spans 10 pixels, that benchmark edge is assigned a reference value of 10. The sum of the benchmark edges for a given image provides the baseline (i.e., the denominator) against which the collinear edge pixels (i.e., the numerator) are compared.

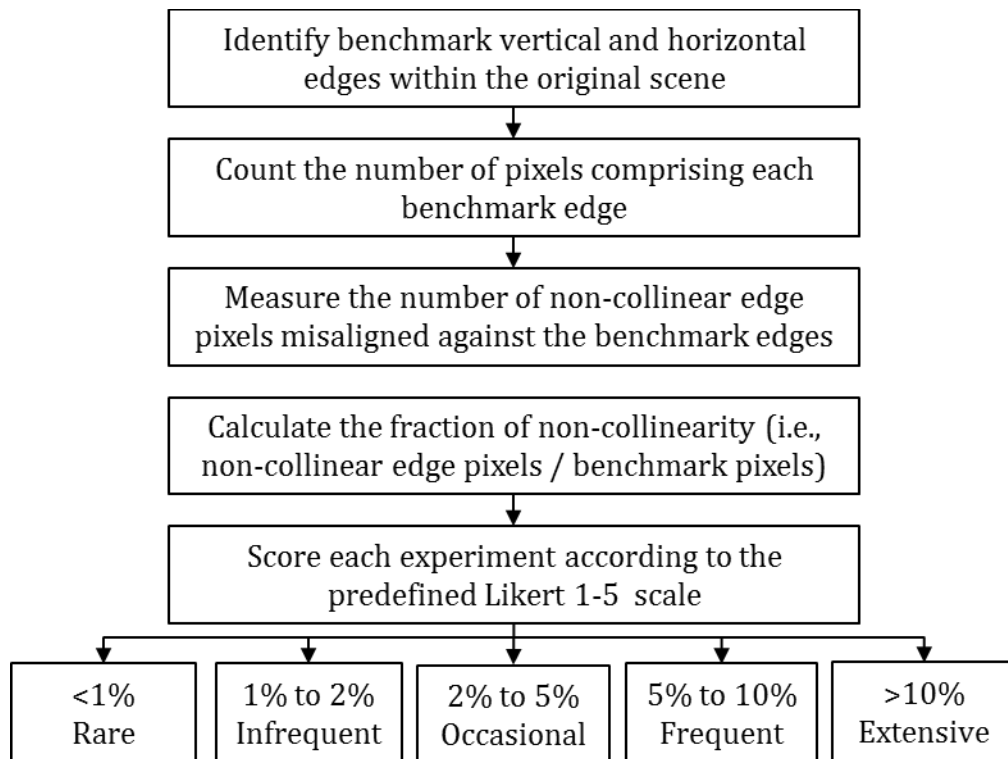


Figure 131: Edge Pixel Collinearity Evaluation Methodology

After measuring the collinearity baseline, the evaluation methodology proceeds to measure the collinearity between the baseline and the edge plane under evaluation. This

measurement is achieved by a simple overlay of the edge map onto the original image's benchmark edges and counting the number of non-collinear edge plane pixels. Finally, collinearity is evaluated by calculating the fraction of non-collinearity, where small non-collinearity fractions suggest strong edge detection performance in accordance with the conventional one to five Likert scale used in this study. The fraction of non-collinearity is calculated by dividing the volume of non-collinear edge pixels by the volume of benchmark collinear pixels, thereby generating the fraction reflecting the volume of non-collinear edge pixels. This fraction is then binned in a way that reflects the Likert scales it informs. For example, a fraction of less than one percent non-collinearity would align to a Likert score of 1, Rare, which is consistent with very strong edge detection performance. Similarly, a large volume of non-collinear edge pixels (e.g., greater than 10% of benchmark pixels) indicates poor performance and would align to a Likert score of 5, the weakest level of performance.

This study also adapts to HSI imagery Baker and Nayer's global measure of coherence for single-point intersections between two edges. Similarly to their development of the collinearity measure of coherence, Baker and Nayer developed the single-point intersection criterion by testing its performance against hundreds of same-scene images collected under varying conditions – a precondition that is not replicated here given its focus on single-collect samples of natural scenes. Instead, Baker and Nayer's approach is applied by identifying benchmark intersections within each tested scene when possible. For example, identifying benchmark intersections in the Larkhaven

data is more straightforward (and therefore more reliable) than choosing benchmark intersections in the granite VNIR data composed entirely of naturally-formed minerals.

Similarly to the approach taken for evaluating collinearity, this work evaluates an edge plane's benchmark single-point intersections to support the Canny criteria of localization and single-point response. As seen in Figure 132, the evaluation methodology first identifies benchmark single-pixel intersections within the original scene, the sum of which serves as the denominator in the single-point intersection fraction. Where possible, single-pixel intersections between horizontal edges and vertical edges are selected for benchmark intersections since they are more accurately evaluated than multi-point intersections between diagonal or curvilinear edges.

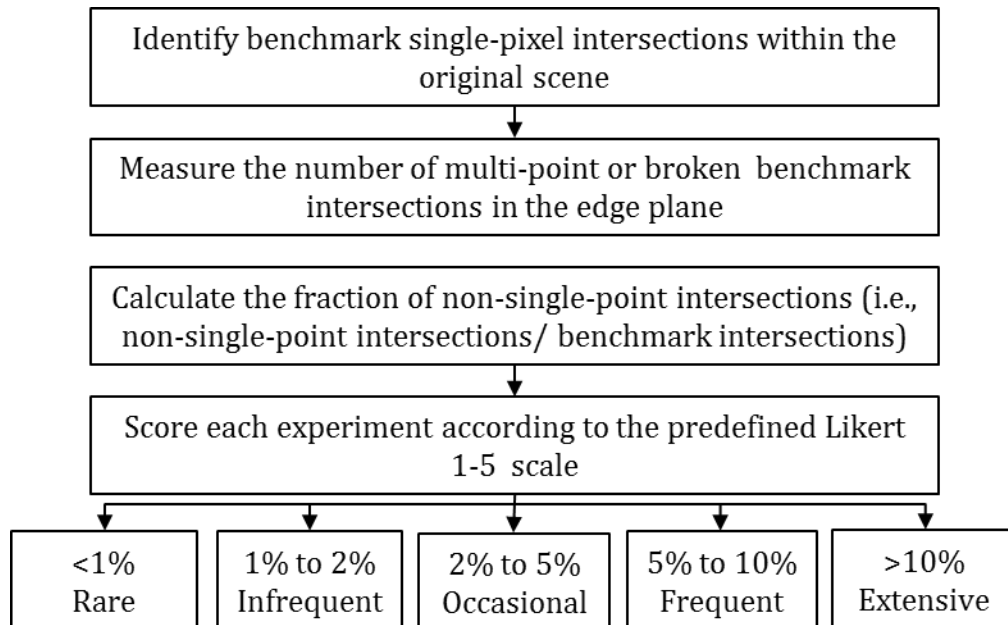


Figure 132: Edge Pixel Single-Point Intersection Evaluation Methodology

Next, the evaluation methodology measures the number of multi-point or broken benchmark intersections in the edge plane, which will serve as the numerator in the single-point intersection fraction. This measurement is achieved by either an overlay of the edge plane onto the original image or through traditional flickering image interpretation techniques. Multi-point or broken benchmark intersections in the edge plane then are simply counted and summed.

The evaluation next generates the single-point intersection fraction for each experiment by dividing the number of multi-point or broken benchmark intersections in the edge plane by the number of benchmark single-pixel intersections within the original scene. This fraction is then binned in a way that reflects the Likert scales it informs. For example, a fraction of less than one percent multi-pixel or broken pixel edges would align to a Likert score of 1, rare, which is consistent with very strong edge detection performance. Similarly, a large volume of multi-pixel or broken intersections (e.g., greater than 10% of benchmark intersections) indicates poor performance and would align to a Likert score of 5, the weakest level of performance.

The adaptation of Baker and Nayer global measures of coherence to this work further grounds its evaluation measures within accepted practices while optimizing them for HSI data. This study borrows as appropriate from traditional remote sensing evaluation techniques and extends them as necessary to accommodate the unique characteristics of HSI data and the small sample size of this dissertation's test datasets.

Image Subtraction

Another evaluation measure used within traditional grayscale image evaluation is image subtraction, which is most commonly used for change detection [281]. Image subtraction methods simply subtract one image from another in order to measure the difference between the two images, usually a reference or ground truth image compared to a test image. The objective is to identify pixel behavior that deviates from expected behavior as indicated by a ground truth image.

This dissertation uses image subtraction techniques to evaluate relative edge detection performance between similar experiments, such as different PCA tests of the same image, different MNF tests of the same image or for comparing radiance to reflectance edge results obtained from the same image. Specifically, this dissertation uses image subtraction techniques to evaluate several Canny criteria, including false positives, false negatives, localization and robustness to noise.

For example, an image subtraction between an experiment's full MNF edge detection results and the experiment's compressed MNF results can indicate how successfully the compressed MNF dataset improved an edge detector's robustness to noise. Similarly, an image subtraction between an experiment's reflectance results and the experiment's PCA results can indicate the extent to which the PCA compression improved edge performance against the false positive and false negative criteria.

Intuitive Interpretation

Finally, this dissertation makes a place for the "art" of remote sensing during the evaluation process. The empirical methods described above provide much of the heavy lifting for the evaluation process, but they must be paired with intuitive interpretation to

provide a complete sense of edge detection performance. By combining empirical and intuitive evaluation measures, this study seeks to fully evaluate each experiment both from a quantitative approach as well as from an applications-oriented practical approach.

For example, false negative evaluation measures can cue the researcher to areas of weak edge detection and provide a quantitative measure of performance, but they could not recognize a scenario in which the weak performance is confined to scene materials secondary or irrelevant to the application under study. Perhaps the edge detector failed to reliably delineate clouds obscuring a scene, or perhaps the edge detector failed to detect edges reflected on a window pane but successfully mapped the original feature.

Final Evaluation Matrices

The first evaluation uses an ordinal-ranked based approach to measure algorithm performance against Canny's primary optimal edge detection criteria: low false positive and false negative rates, accurate localization and single-point response. Additionally, the ordinal ranking metric will include Canny's secondary edge detection criteria, robustness in the presence of noise and unbroken edge generation. In most of the literature, the secondary criteria are ignored in favor of the primary criteria, but this work explicitly considers them in order to derive the most complete possible understanding of algorithm performance.

As seen in the notional example previously shown in Table 16, the first execution of the ordinal rank metric considers only one algorithm on a per dataset basis. For example, in order to measure the strengths and weaknesses of the improved HySPADE algorithm, its performance against each dataset is measured independently of the other

algorithms. All six Canny criteria are included in the evaluation, and the scores are aggregated in order to measure relative performance across each test. The key advantage of this evaluation approach is that it allows the researcher to see specific areas of strength and weaknesses with respect to the input data types (e.g., reflectance, compressed PCA, etc.). For example, this ordinal rank metric might allow the researcher to see that an algorithm excels at localization, but only after a PCA or MNF transform. Similarly, this metric might show that gradient executions against reflectance datasets tend to generate more false positives than the compressed PCA and MNF cubes. Ultimately, this metric allows the researcher to measure how effectively HSI data and HSI data compression improve edge detection performance as measured by Canny's edge detection criteria.

Table 17: Notional Ordinal Rank Metric – All Algorithms, Single Dataset

Notional Evaluation: All Algorithms, Single Dataset	False Positives	False Negatives	Localization	Single-Point Response	Robustness to Noise	Unbroken Edges	Normalized Score
Gradient: Reflectance	4	11	9	10	7	11	8.7
Gradient: Optimal PCA	1	10	13	9	11	6	8.3
Gradient: Optimal MNF	7	9	10	4	3	7	6.7
Gradient: Full PCA	9	3	4	11	12	1	6.7
Gradient: Full MNF	2	8	11	1	4	17	7.2
HySPADE: Reflectance	12	4	6	2	8	14	7.7
HySPADE: Optimal PCA	8	1	8	7	5	5	5.7
HySPADE: Optimal MNF	11	2	3	3	13	15	7.8
HySPADE: Full PCA	5	5	2	6	2	10	5.0
HySPADE: Full MNF	13	6	7	5	1	4	6.0
Level Set: Reflectance	14	7	17	12	10	9	11.5
Level Set: Optimal PCA	15	12	1	17	17	3	10.8
Level Set: Optimal MNF	3	13	5	15	9	8	8.8
Level Set: Full PCA	6	4	12	14	6	2	7.3
Level Set: Full MNF	10	17	15	8	15	12	12.8
Canny	16	15	14	13	16	13	14.5
Sobel	17	16	16	16	14	16	15.8

The second execution of the ordinal rank metric compares the performance of all algorithms against a single dataset, as shown in the notional table in Table 17. This metric builds upon the single algorithm, single dataset ordinal rank metric by allowing the researcher to compare performance across algorithms and input datatypes. Specifically, the all algorithms, single dataset ordinal rank metric allows the researcher to measure relative performance of each algorithm as a function of data input (e.g., compressed PCA, compressed MNF, etc.).

For example, this metric allows the researcher to identify trends such as how well the compressed PCA cubes improve edge localization, how well the improved HySPADE

algorithm generates single-point edge responses compared to the gradient-based algorithm, how the level set-based edge detection algorithm performed to the gradient-based algorithm, etc. The final output from the all algorithms, single dataset ordinal rank metric is a clear sense of which algorithms are performing most strongly against Canny’s criteria, and what, if any, dependencies they have on HSI data compression procedures.

Table 18 presents the third ordinal rank metric, which is a notional roll-up of algorithm performance across all Canny criteria as measured against a single dataset. This metric allows the researcher to measure overall algorithm performance on a single dataset – a useful tool for answering simple questions about which algorithm “worked the best” against a single dataset.

Similarly, Table 19 presents a notional fourth ordinal rank roll-up that measures the influence of data input on algorithm performance. This metric addresses how effectively a data type performed across algorithms, thereby answering key questions such as what improvement is derived from PCA and MNF compressions unique to spectral processing.

Table 18: Notional Final Ordinal Rank Metric – Criteria Aggregation, Single Dataset

Notional Final Evaluation All Algorithms, Single Dataset	Normalized Score
Gradient	7.5
HySPADE	6.4
Level Set	10.3
Canny	14.5
Sobel	15.8

Table 19: Notional Final Ordinal Rank Metric – Data Input Aggregation, Single Dataset

Notional Final Evaluation All Data Inputs, Single Dataset	Normalized Score
Reflectance	9.3
Optimal PCA	8.3
Optimal MNF	7.8
Full PCA	6.3
Full MNF	8.7

Table 20 and Table 21 present notional versions of the two ordinal rank evaluation metrics addressing overall algorithm performance across all HSI datasets and overall data input performance across all HSI datasets, respectively. These metrics attempt to aggregate performance across all HSI datasets in order to measure how well each algorithm performs against an average HSI dataset, and how well each data input affects edge detection performance within an average HSI dataset. These metrics mitigate against the common practice of focusing on the best performance (usually attributable to the author’s algorithm) or on the worst performance (usually attributable to the comparison algorithms).

Table 20: Notional Final Ordinal Rank Metric –All Algorithms, All Datasets

Notional Final Evaluation All Algorithms, All Datasets	Normalized Score
Gradient	7.2
HySPADE	6.7
Level Set	7.0
Canny	15.0
Sobel	14.2

Table 21: Notional Final Ordinal Rank Metric –All Data Inputs, All Datasets

Notional Final Evaluation All Data Inputs, All Datasets	Normalized Score
Reflectance	11.7
Optimal PCA	6.4
Optimal MNF	5.0
Full PCA	8.3
Full MNF	8.1

As seen in Table 22, a final ordinal rank metric is used to evaluate how well each algorithm performed against HSI applications. Underlying the ordinal ranks in Table 22 are the performance data derived from the previous evaluations, which are simply parsed by aligning HSI datasets to HSI applications to derive the metric. This metric provides insight into which edge detection methods perform most optimally in support of various HSI applications. The metric also provides additional insight into overall algorithm performance by measuring performance through the lens of HSI applications.

Table 22: Notional Ordinal Rank Metric – All Algorithms, All HSI Applications

Notional Evaluation: All Algorithms, All HSI Applications	Urban Feature Mapping	Mineral Mapping	Crop Mapping	Oil Spill Mapping	Trace Target Detection	Material Analysis	Normalized Score
Gradient	1	2	3	2	1	3	2.0
HySPADE	3	1	2	3	4	1	2.3
Level Set	2	3	1	1	2	2	1.8
Canny	4	5	5	5	3	4	4.3
Sobel	5	4	4	4	5	5	4.5

EXPERIMENTS

This section presents only experimental findings and observations about data quality, irregularities, patterns, etc. The Analysis section contains detailed examination and evaluation of each test along with discussion about results that support or do not support specific hypotheses. The experiments section is divided into three sections aligning to each of the three new edge detection algorithms: the Di Zenzo-based gradient edge detection method, the new HySPADE method and the level set-based edge detection method.

Di Zenzo-Based Gradient Findings

This work tests the Di Zenzo-based gradient edge detection algorithm against all 12 HSI datasets, including tests against reflectance and/or radiance cubes, PCA cubes of varying depth and MNF cubes of varying depth. This section presents samples from each test, the Analysis section examines key sections and draws scientific conclusions and evaluations for each dataset, and Appendix A presents the full spatial extent of each experiment. Experimental observations from the Di Zenzo-based gradient edge detection algorithm are as follows.

Importantly, one of the initial findings was the surprising observation that the Otsu threshold failed to produce an optimal histogram stretch for the gradient-based edge planes, as seen in the Reno hypercube example in Figure 133 and Figure 134. In Figure

133, note the significant increase in false negatives within the Otsu-stretched edge plane compared to the unstretched edge plane, particularly along the bottom half of the image.

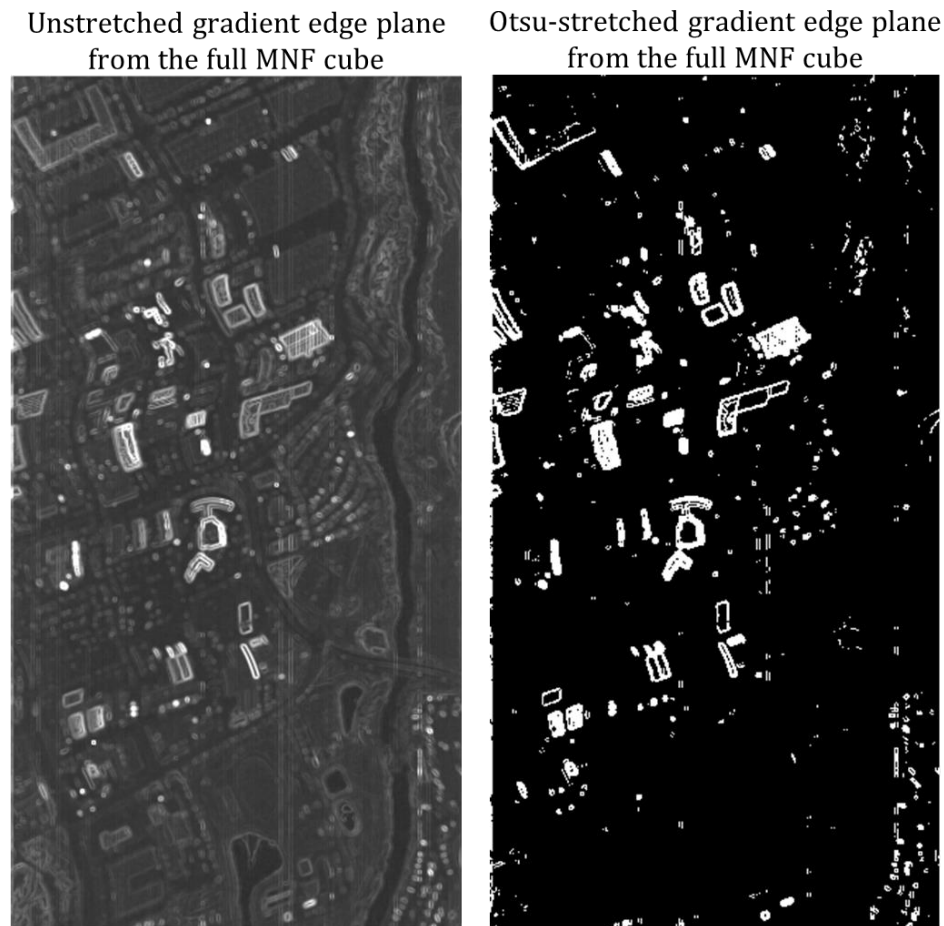
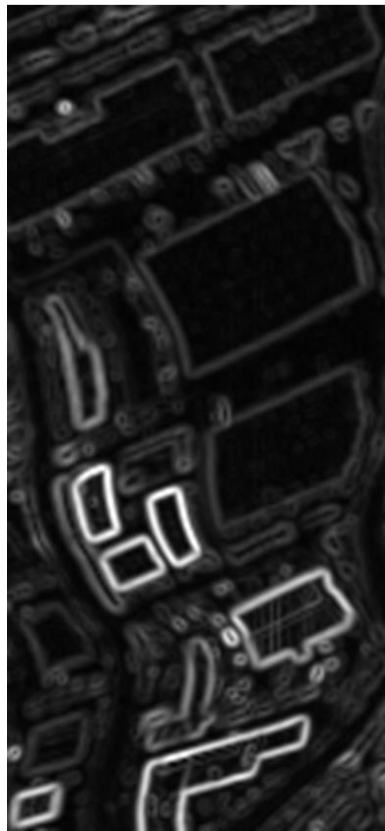


Figure 133: Suboptimal Gradient-Based Edge Planes from Otsu Thresholding

Figure 134 provides a detailed comparison of the histogram stretching performance against the key buildings towards the top of the image. Specifically, notice how the Otsu thresholding artificially injects broken edges around the two structures along the top of the image, while the unstretched edge plane accurately delineates the two

buildings with unbroken edges – a key Canny criterion underpinning the evaluated results. Additionally, the Otsu thresholding injected significant false negatives, particularly around the two large warehouses in the center of the image. Note that the unstretched edge plane demonstrates fully delineated, unbroken edges while the Otsu-thresholded edge plane fails to suggest even the possible presence of the large structures.

Unstretched gradient
edge plane from the
optimal MNF cube



Otsu-stretched gradient
edge plane from the
optimal MNF cube



Figure 134: Otsu-Injected False Positives, False Negatives and Broken Edges

Also, note how the Otsu-thresholding artificially increases the width of the edges in the unstretched edge plane. This suboptimal result weakens the gradient-based edge detector's performance against the Canny criteria of localization and single-point response, clearly indicating that the unstretched edge plane provides superior results. The Otsu-stretched edge planes also exhibit choppier edges than the unstretched edge planes, further decreasing algorithm performance against the Canny criteria of localization and single-point response.

Given the surprisingly suboptimal results obtained from using the Otsu threshold against the gradient-based edge planes, this dissertation evaluates edge detection performance against the unstretched gradient-based edge plane. Specifically, since the Otsu thresholding of gradient-based edge plane artificially degrades algorithm performance against the Canny criteria of false positives, false negatives, localization, single-point response and unbroken edges, unstretched gradient-based edge planes are more likely to support a broad range of HSI applications.

The unexpected Otsu thresholding results are likely attributable to the unique behavior of hyperspectral data compared to the panchromatic imagery on which Otsu thresholding has built its esteemed reputation. Specifically, the suboptimal Otsu results could be explained by low spectral contrast between adjacent ground materials (e.g., concrete of two different types on a roof and the adjacent sidewalk). Spectral contrast is not a barrier to optimally thresholding single-band imagery, but it certainly exists within hyperspectral data. Since the grayscale edge planes are derived from hyperspectral data, they inherently reflect the character of the underlying hyperspectral data, even though

their appearance suggests that they should behave like traditional grayscale imagery. The unexpected Otsu findings also reinforce the general observation that traditional grayscale image processing techniques must be optimized for HSI data rather than simply applied in their original form. Ultimately, this dissertation proceeds with the superior results obtained from unstretched gradient-based edge planes and identifies optimal thresholding for HSI edge planes as a topic for further research.

Overhead – Reno, Nevada USA

The first gradient-based edge detection experiment uses the VNIR/SWIR Reno, NV USA hypercube. Specifically, this experiment tests the algorithm against five distinct datasets: a 356-band reflectance cube, a four-band compressed PCA cube, the full 356-band PCA cube, an eight-band compressed MNF cube, and the full 356-band MNF cube.

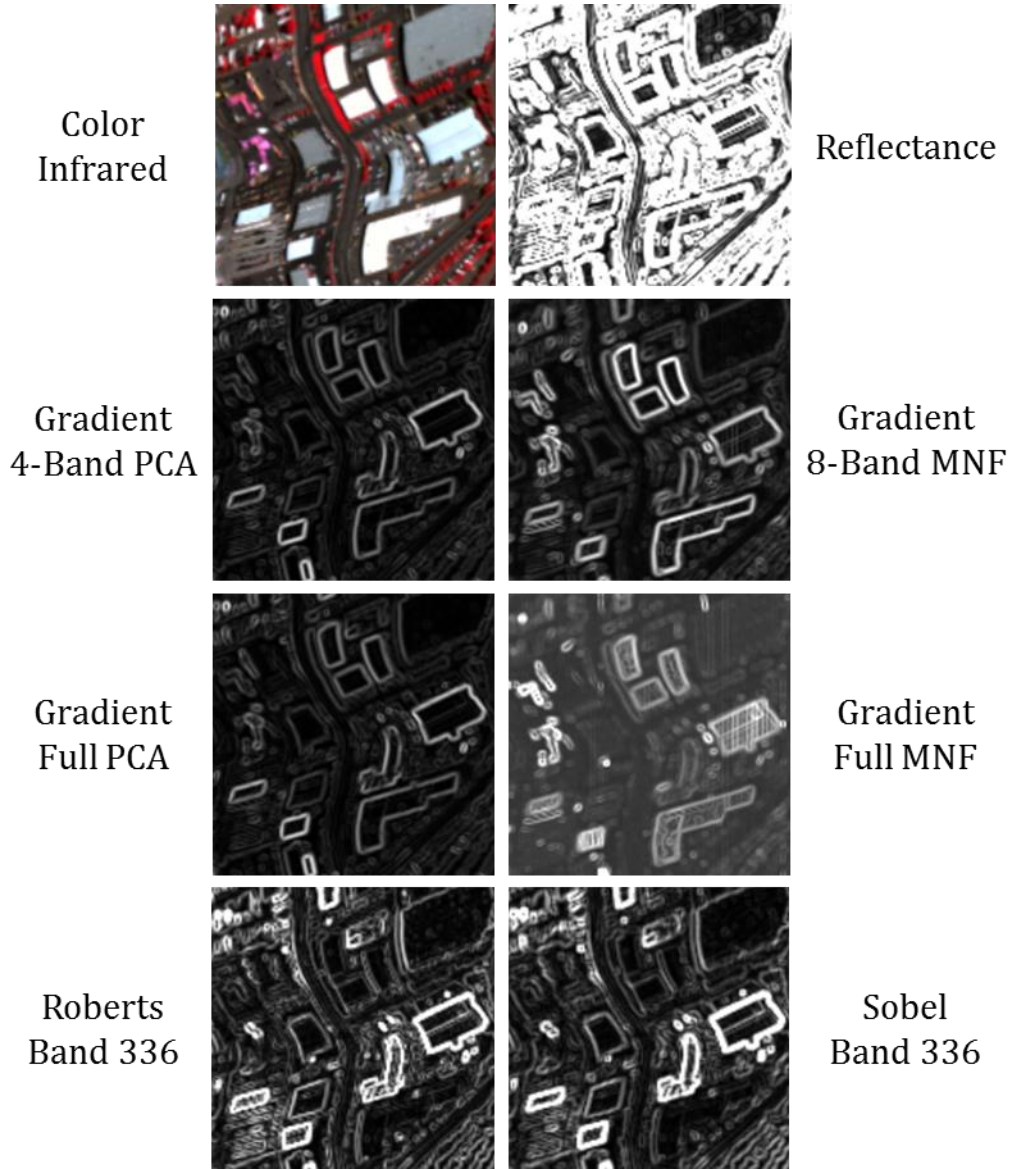


Figure 135: Gradient Experiment for Reno, NV Overhead VNIR/SWIR Data, Unstretched

For comparison, this test also executes the Roberts operator and the Sobel operator against the full reflectance cube. Figure 135 presents samples of each of the seven tests, and Appendix A contains the full spatial extent for each test.

The methodology's first step, data exploration, indicates that the ProSpecTIR data is well-calibrated and of good quality across all channels, and is already converted to reflectance. Figure 136 presents the data exploration results, which indicate that similar materials (e.g., vegetation, water, aluminum, etc.) are rendered similarly in reflectance space. Specifically, note how closely clustered the pixels are for manmade materials like roofs and for dark materials like water. The vegetation spectra are spaced normally, as well, with the healthy vegetation spectra presenting a strong reflectance increases in the NIR.

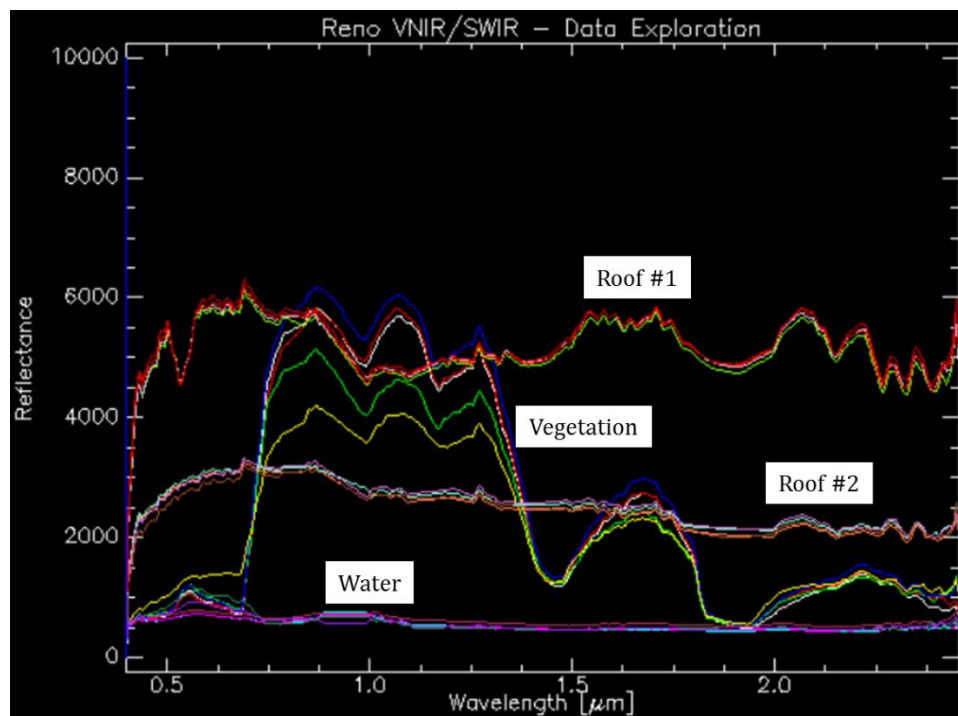


Figure 136: Data Exploration for the Reno, NV USA Hypercube

The second step requires a determination as to whether the HSI data are in reflectance or in radiance. As seen in Figure 136, ProSpecTIR provides the data in reflectance, therefore QUAC is unnecessary for this dataset. Step 3 scales the Reno reflectance dataset from 0.0 to 1.0. Step 4, bad band removal, is unnecessary since ProSpecTIR removed bad bands prior to making the data available, and Step 5, examine the reflectance data, is also unnecessary given the analysis in Figure 136.

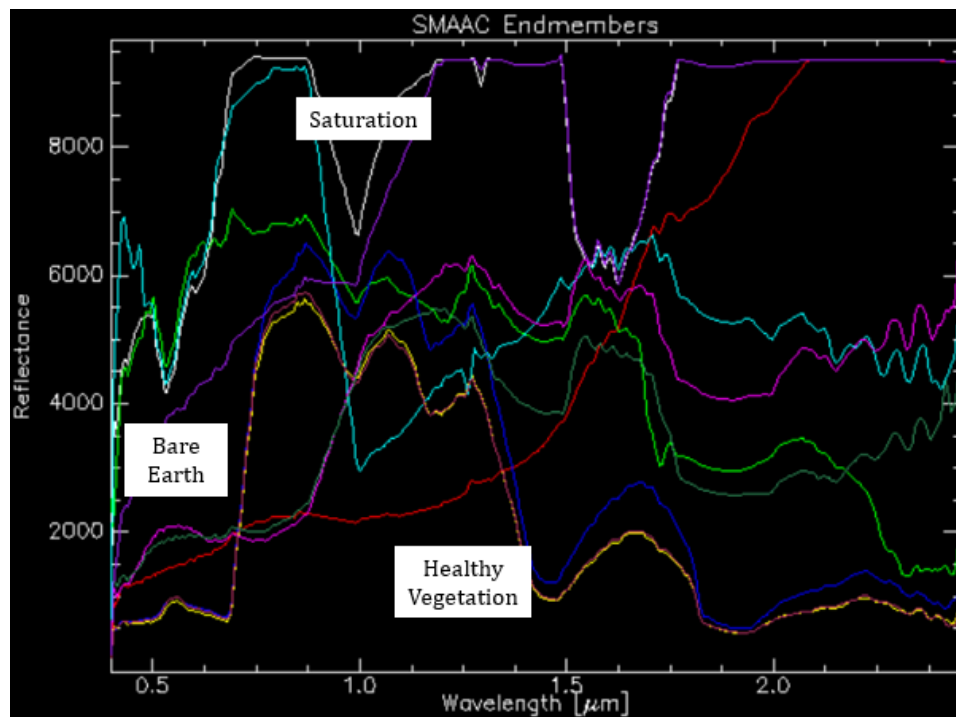


Figure 137: SMAAC Endmembers for the Reno, NV USA Hypercube

Figure 137 presents the results of Step 6, SMAAC endmember extraction. The SMAAC results indicates that routine materials like bare earth and healthy vegetation are easily distinguishable in reflectance space – a key indicator of a healthy reflectance

dataset. Also, note that SMACC indicates the presence of saturation within the scene as evidenced by the very bright and highly irregular spectra at the top of the plot.

In order to determine the extent to which saturation is present within the scene and a barrier to reliable edge detection experiments, this study extracted SMACC's first saturation endmember and generated a spectral angle mapper (SAM) plane to identify the extent and locations of saturation. As seen in Figure 138, saturation appears within only a handful of pixels at three areas within the scene, and it is traceable to specular reflections off metal materials in every case. Consequently, saturation is not a barrier to edge detection.

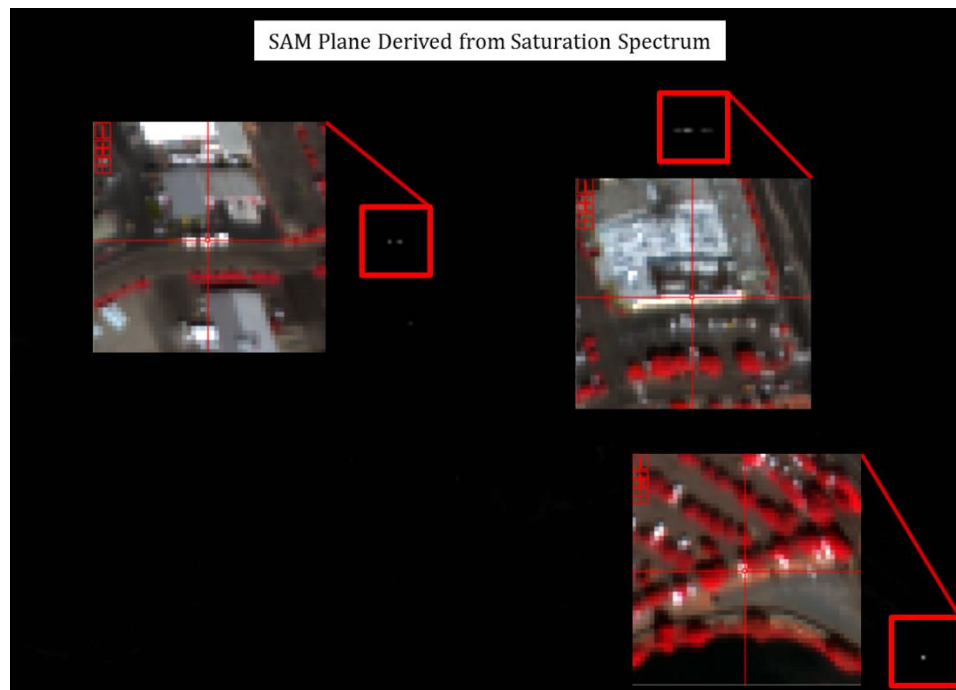


Figure 138: Saturation within the Reno, NV Hypercube - Color Infrared Bands 34, 55 and 99

The preprocessing component's final step generates an RX anomaly plane as a final check on data quality and scene behavior. As seen in Figure 139 and Figure 140, the RX processing detected minimal anomalies, all of which appear to be attributable to saturation or atmospheric correction anomalies, neither of which are expected to affect edge detection processing.

Ultimately, the preprocessing component indicates that the Di Zenzo-based edge detection algorithm experiment executes against a high-quality reflectance dataset relevant to urban feature mapping.



Figure 139: RX Anomaly Plane for Reno, NV USA Hypercube

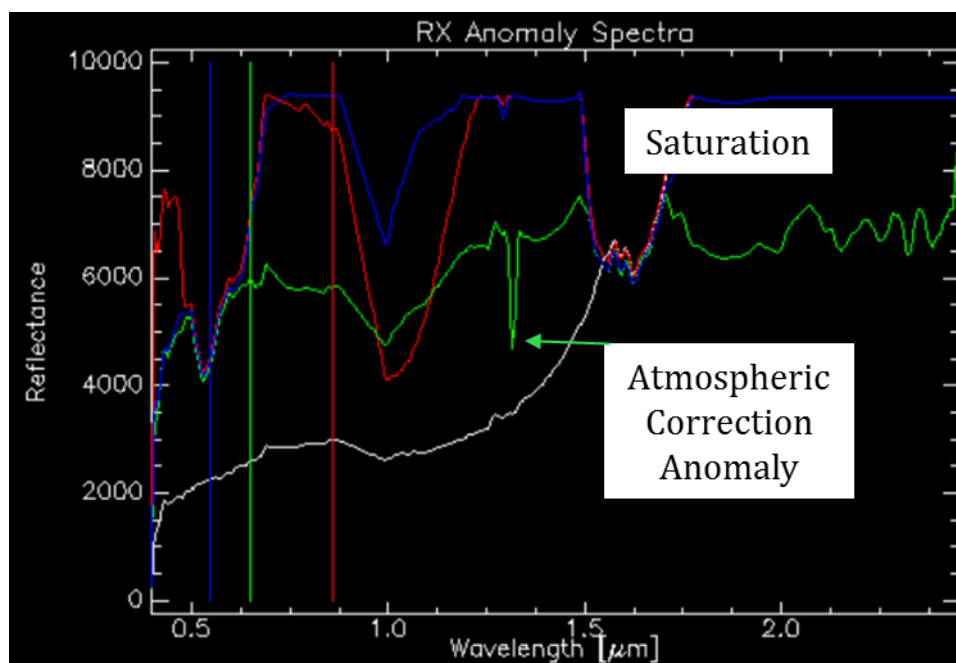


Figure 140: RX Anomaly Spectra for Reno, NV USA Hypercube

With the preprocessing component complete, the compression component begins with both a PCA and an MNF transformation. Figure 141 and Figure 142 present Step 1 and 2 of the compression component, a plot of the key PCA bands and MNF bands, respectively. As shown, the optimal PCA threshold occurs at PCA band 4, after which very little diagnostic spectral information is available. Therefore, Step 3 of the PCA compression establishes the optimal threshold at PCA band 4. Similarly, the optimal MNF threshold occurs at MNF band 8, after which the bands contain mostly noise.

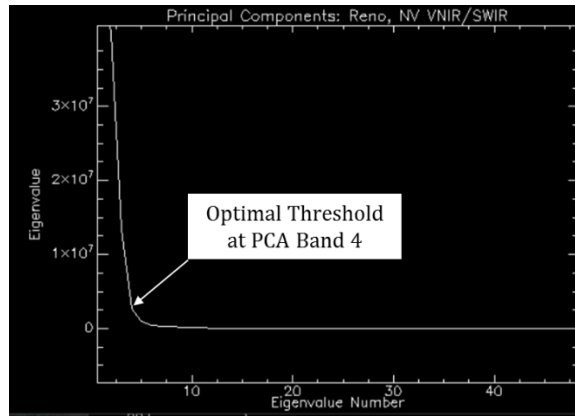


Figure 141: Optimal Threshold for PCA Cube, Reno, NV VNIR/SWIR

At the conclusion of the preprocessing and compression components, the reflectance, full PCA, compressed PCA, full MNF and compressed MNF cubes are ready for the edge detection component. The reflectance cube also is ready for the Roberts and Sobel comparison tests. As seen in Figure 135, the preprocessing and compression components yielded high-quality HSI data from which the Di Zenzo-based gradient edge detector generated consistent, interpretable results.

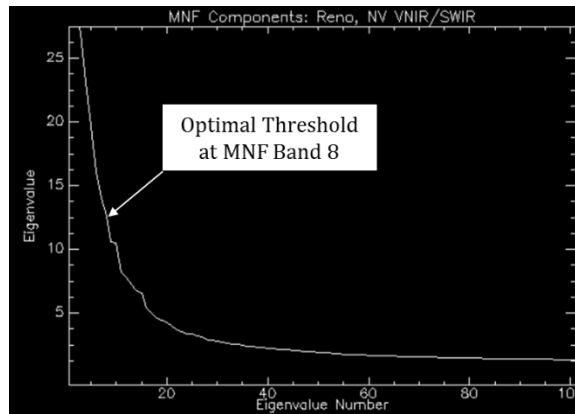


Figure 142: Optimal Threshold for MNF Cube, Reno, NV VNIR/SWIR

Overhead – Cuprite, Nevada USA

The second gradient-based edge detection experiment uses the four VNIR/SWIR flight lines covering Cuprite, NV USA. Specifically, this experiment tests the algorithm against five distinct datasets for each flight line: the full reflectance cube, a compressed PCA cube, the full PCA cube, a compressed MNF cube, and the full MNF cube. For comparison, this test also executes the Roberts operator and the Sobel operator against the full reflectance cube for each flight line. Figure 143, Figure 144, Figure 145 and Figure 146 present samples of the seven experiments for each flight line, and Appendix A contains the full spatial extent for each test.

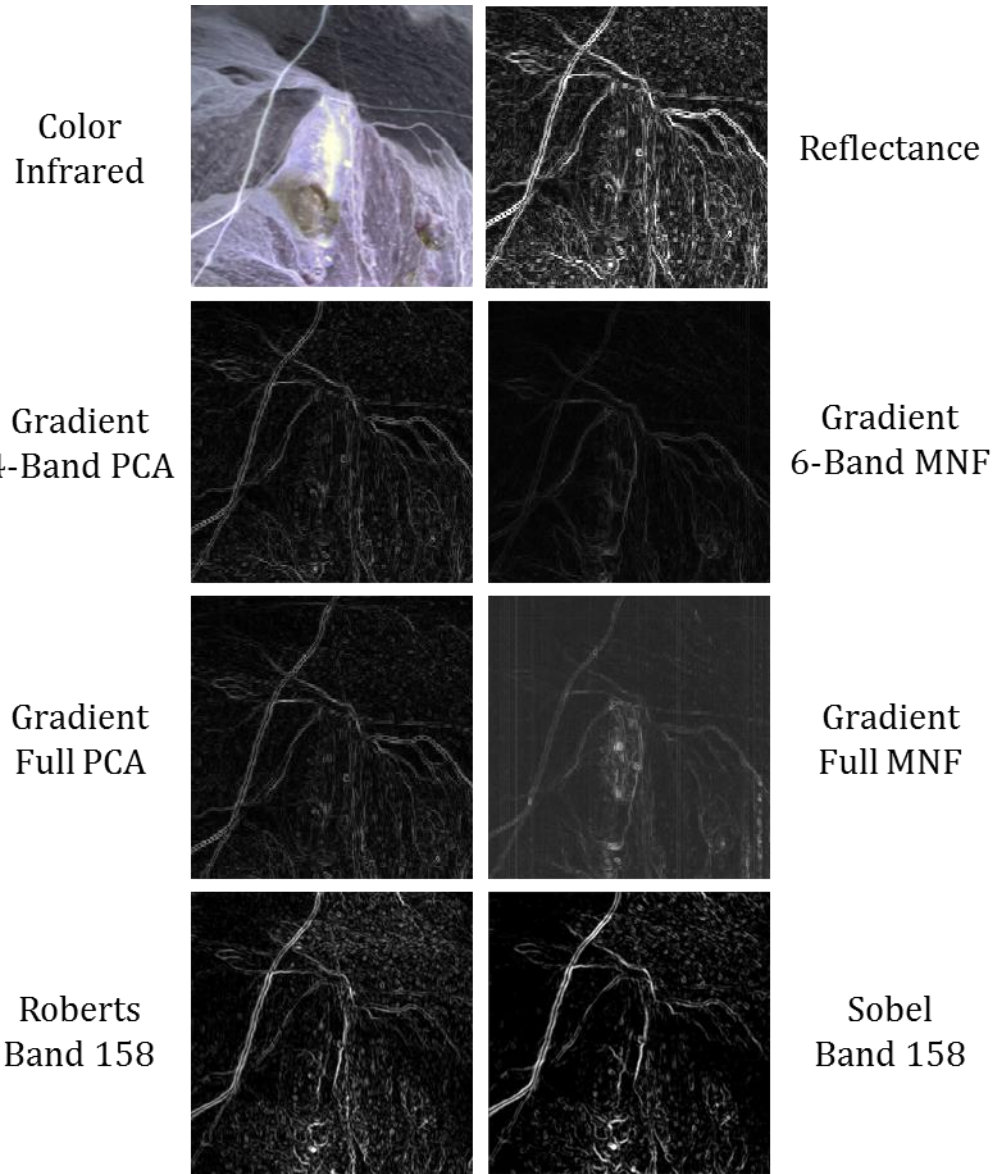


Figure 143: Gradient Experiment for Cuprite Overhead VNIR/SWIR Data, Flight Line #1, Unstretched

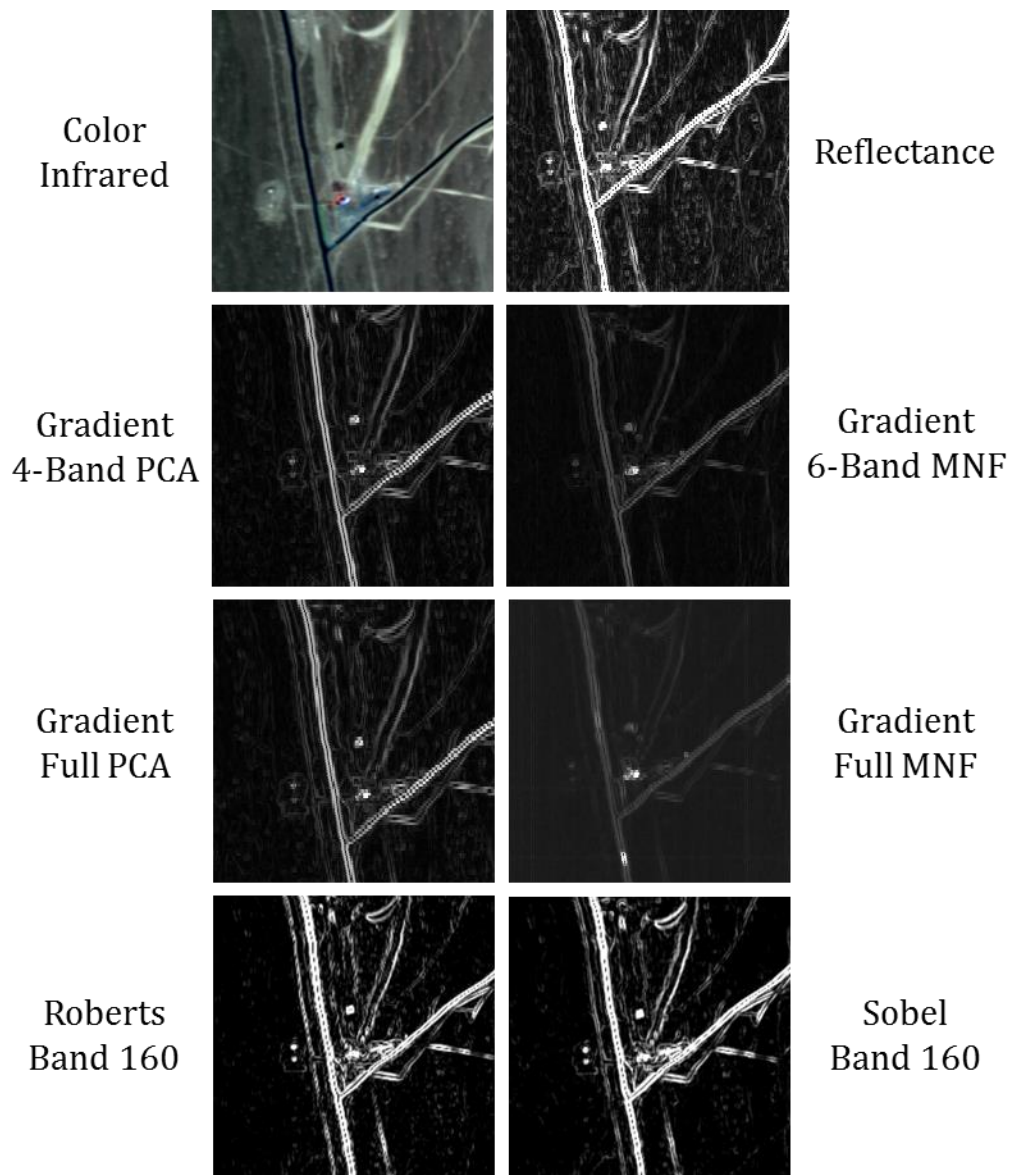


Figure 144: Gradient Experiment for Cuprite Overhead VNIR/SWIR Data, Flight Line #2, Unstretched

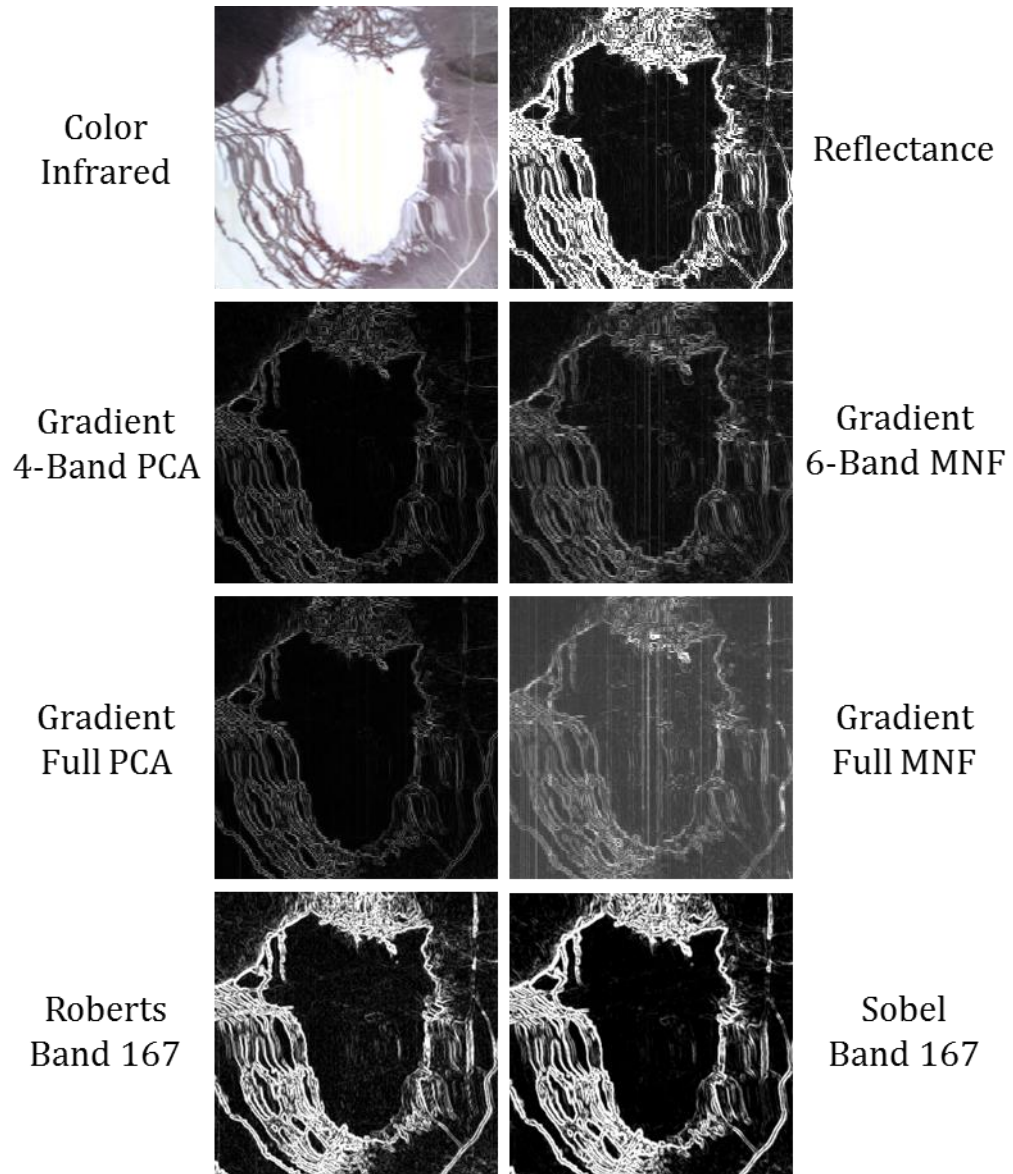


Figure 145: Gradient Experiment for Cuprite Overhead VNIR/SWIR Data, Flight Line #3, Unstretched

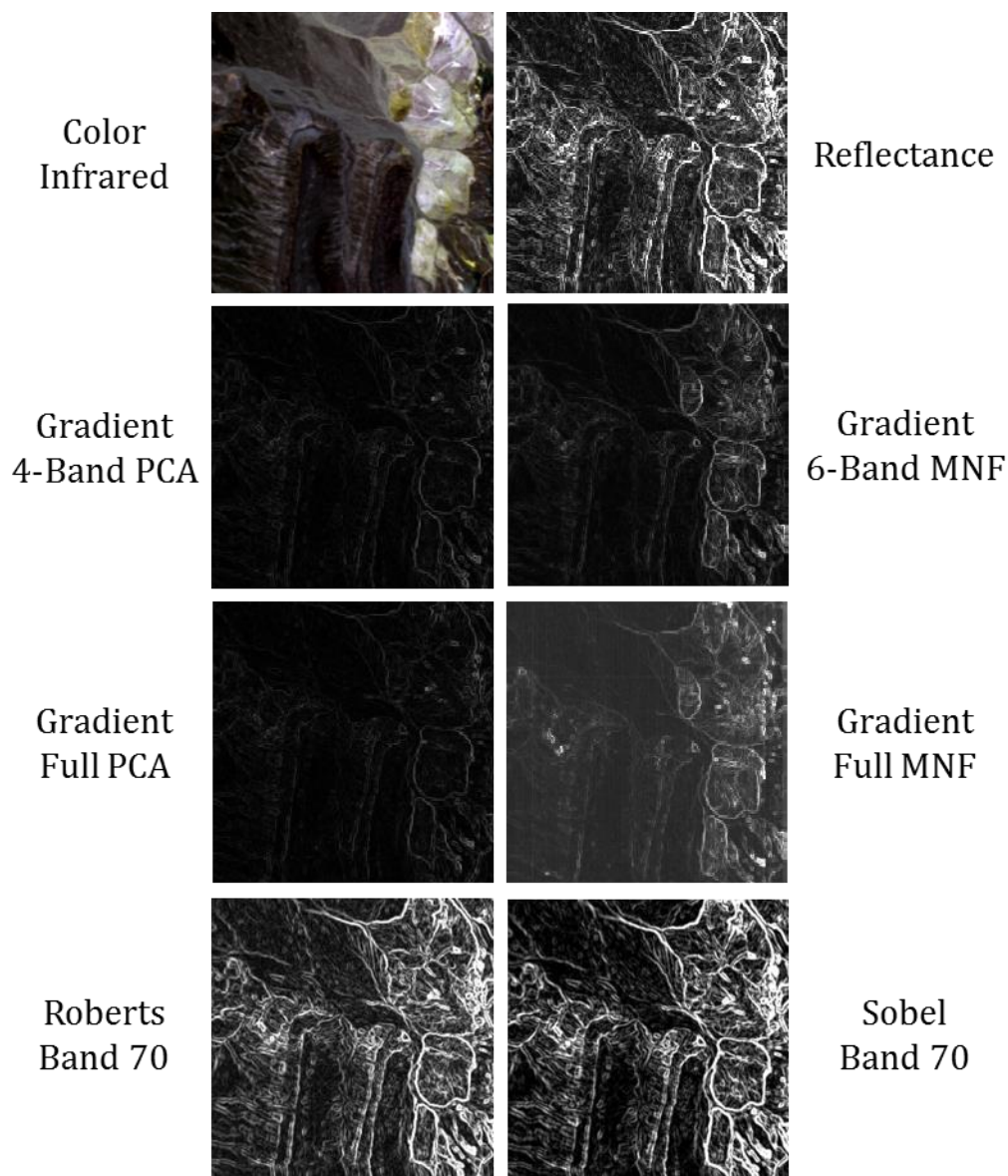


Figure 146: Gradient Experiment for Cuprite Overhead VNIR/SWIR Data, Flight Line #4, Unstretched

The preprocessing methodology's first step, data exploration, indicates that the ProSpecTIR data for all four flight lines is well-calibrated and of good quality across all channels, and is already converted to reflectance. Figure 147, Figure 148, Figure 149 and Figure 150 present the data exploration results from all four flight lines, which indicate

that similar materials (e.g., bare earth, roadways, homogeneous mineral deposits, etc.) are rendered similarly in reflectance space. Specifically, note how closely clustered the pixels are for roadway surfaces in Flight Line #1, and the similarity among spectra derived from the same mineral. The tight spectral clustering among similar materials suggest that an edge detection algorithm should be able to delineate the boundary among disparate materials characterized by similar spectra.

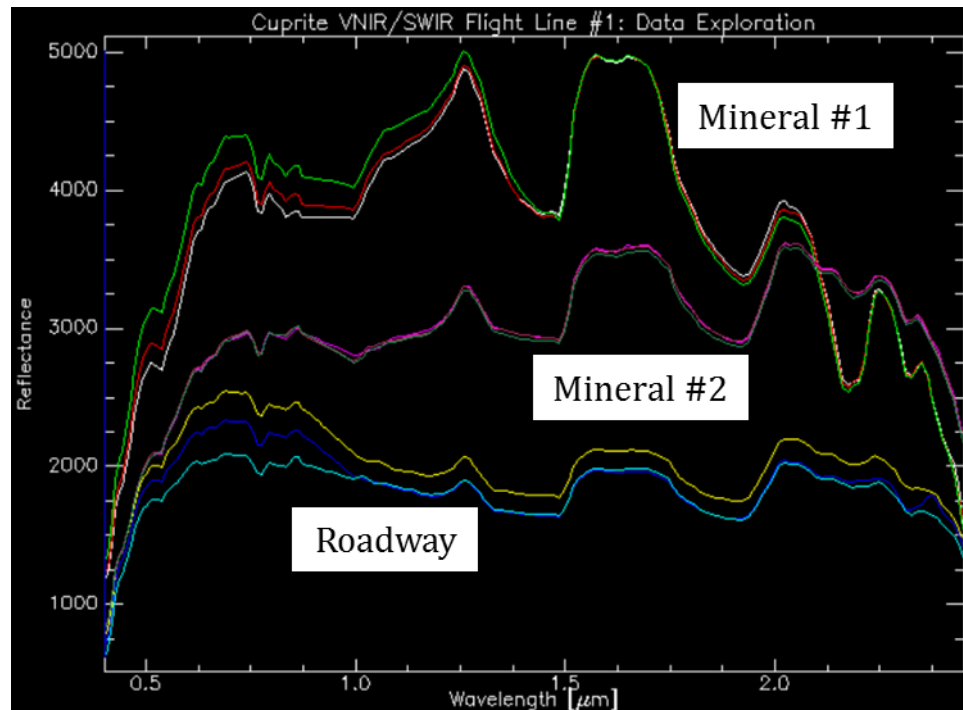


Figure 147: Data Exploration for the Cuprite Hypercube, Flight Line #1

Data exploration for Flight Line #2 yields similar results, as seen in Figure 148. Roof materials (likely metal) cluster closely, while the roadway pixels are tightly

clustered and distinct. This pattern is similar to that seen in Flight Line #1 and also suggests that the data is well-suited for edge detection operations.

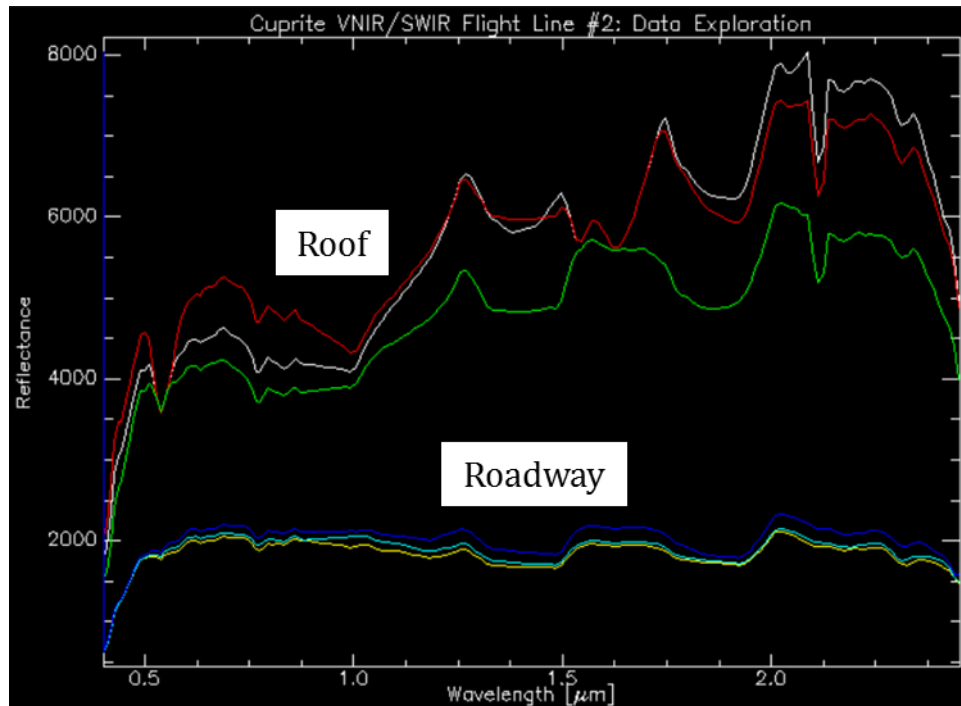


Figure 148: Data Exploration for the Cuprite Hypercube, Flight Line #2

As seen in Figure 149 and Figure 150, Flight Lines # 3 and #4 are similarly well-behaved. The playa at Cuprite is a bright, spectrally distinct area that should be clearly distinguishable by an edge detector. Other minerals in Flight Line #3 and Flight Line #4 are also spectrally similar. Additionally, many areas across all four flight lines are characterized by highly mixed mineral assemblages, which are significantly more challenging features for an edge detector. Shadows are prevalent throughout the scenes, as well.

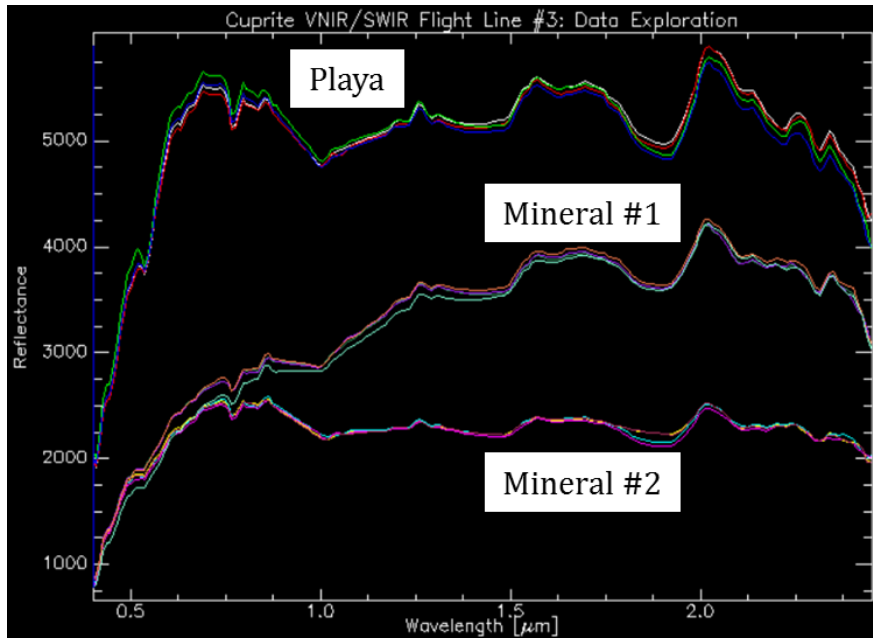


Figure 149: Data Exploration for the Cuprite Hypercube, Flight Line #3

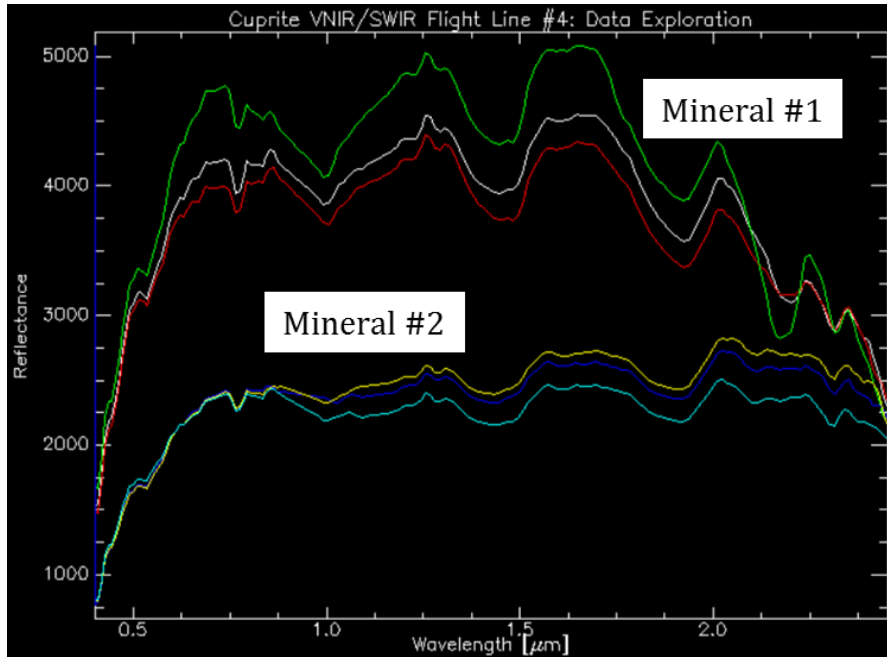


Figure 150: Data Exploration for the Cuprite Hypercube, Flight Line #4

Figure 151, Figure 152, Figure 153 and Figure 154 present Step 6's SMAAC endmember extraction results for Flight Line #1, Flight Line #2, Flight Line #3 and Flight Line #4, respectively. Given the similar of results of the four SMAAC results, they are treated as one discussion. Specifically, the SMAAC results are as expected for a mineralogy scene – minerals are the primary scene constituents. Key diagnostic absorption features are clearly distinguishable within the SWIR bands for all four flight lines, indicating that the Cuprite scenes are healthy reflectance datasets that can reliably support edge detection experiments. The key materials in the scene are readily distinguishable, suggesting that the boundaries among them will be recognizable by an edge detection algorithm. Also, no saturation was observed within any of the four flight lines.

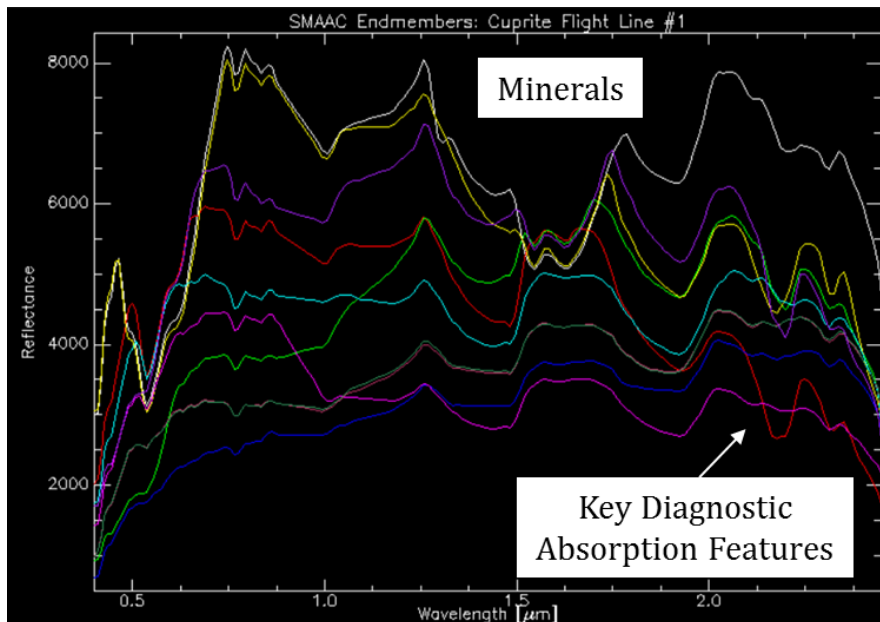


Figure 151: SMAAC Endmembers for the Cuprite Hypercube, Flight Line #1

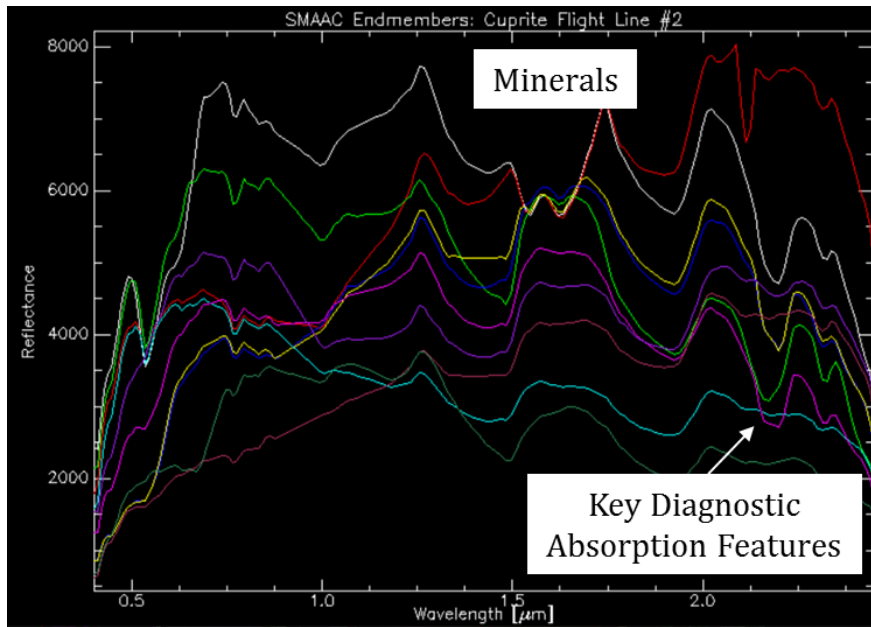


Figure 152: SMAAC Endmembers for the Cuprite Hypercube, Flight Line #2

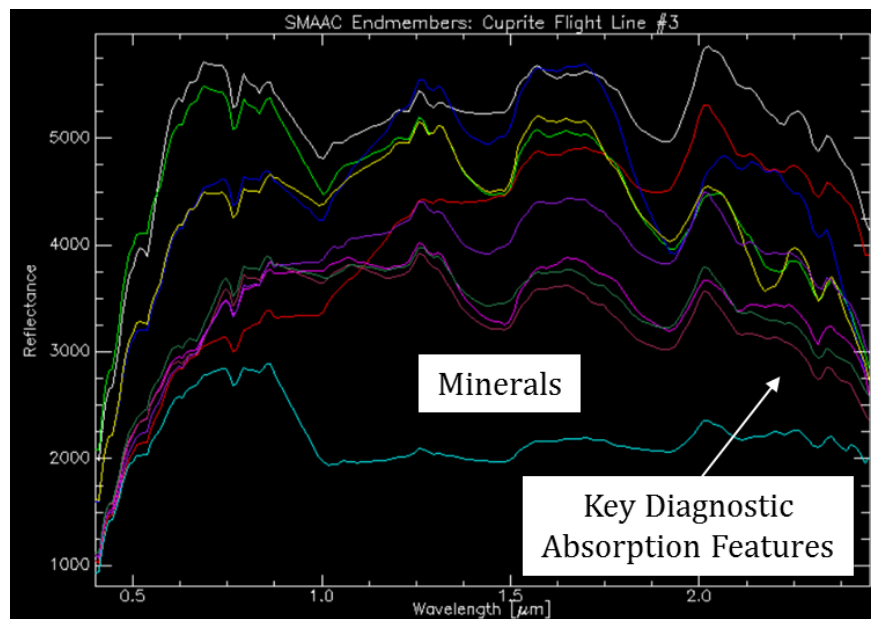


Figure 153: SMAAC Endmembers for the Cuprite Hypercube, Flight Line #3

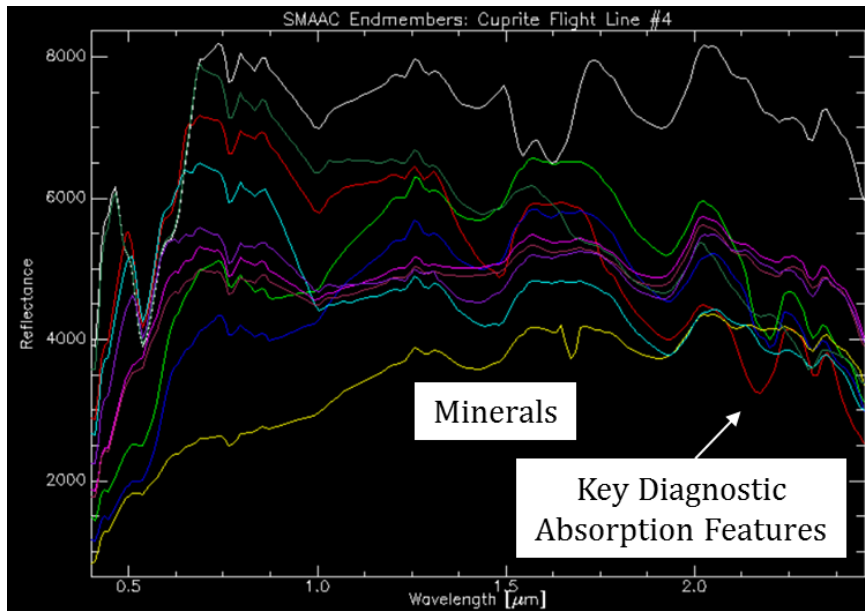


Figure 154: SMAAC Endmembers for the Cuprite Hypercube, Flight Line #4

The methodology’s final step generates an RX anomaly plane as a final check on data quality and scene behavior. Figure 155, Figure 156, Figure 157 and Figure 158 present the RX anomaly planes for Flight Line #1, Flight Line #2, Flight Line #3 and Flight Line #4, respectively. All four RX anomaly planes are consistent with a mineralogy scene whose primary constituents are relatively similar, indicating that the data is behaving as expected; the handful of scattered positive returns within the RX planes result from the absence of highly unusual (with respect to the background statistics) materials in the scene. For natural landscapes, RX often will generate noisy results because there simply is not a meaningful statistical separation between the “anomalous” pixels in the scene and the background pixels. The result is that even very high thresholding still captures pixels that actually belong in the background. Simply

stated, nearly all of the scene is background, which is the optimal condition for a dataset intended to support edge detection experiments for HSI mineral mapping applications.

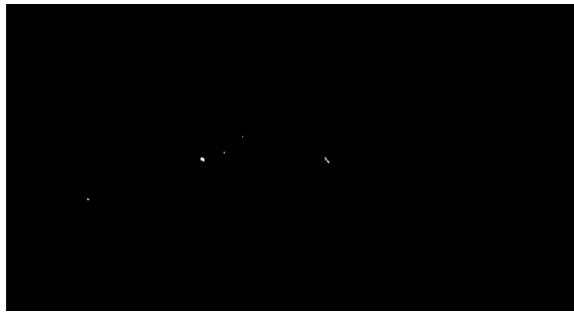


Figure 155: RX Anomaly Plane for Cuprite Hypercube, Flight Line #1

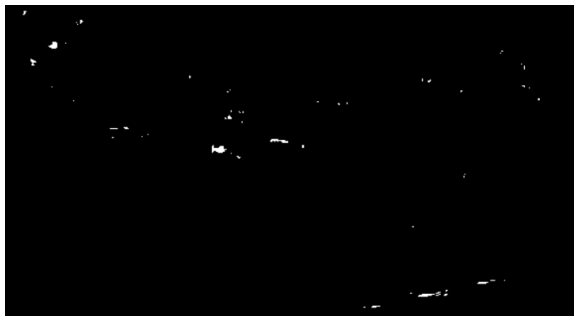


Figure 156: RX Anomaly Plane for Cuprite Hypercube, Flight Line #2

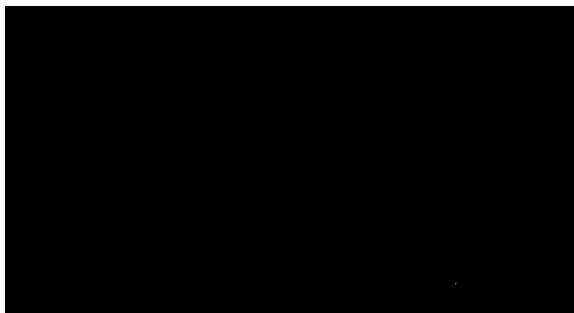


Figure 157: RX Anomaly Plane for Cuprite Hypercube, Flight Line #3

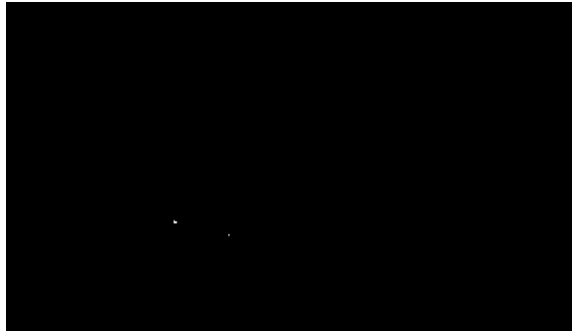


Figure 158: RX Anomaly Plane for Cuprite Hypercube, Flight Line #4

With the preprocessing component complete, the compression component begins with both a PCA and an MNF transformation for each flight line. For Flight Line #1, Figure 159 and Figure 160 present the PCA eigenvalue plot and the MNF eigenvalue plot, respectively. As shown, the optimal PCA threshold occurs at PCA band 4, after which very little diagnostic spectral information is available. Similarly, the optimal MNF threshold occurs at MNF band 6, after which the bands contain a suboptimal amount of noise.

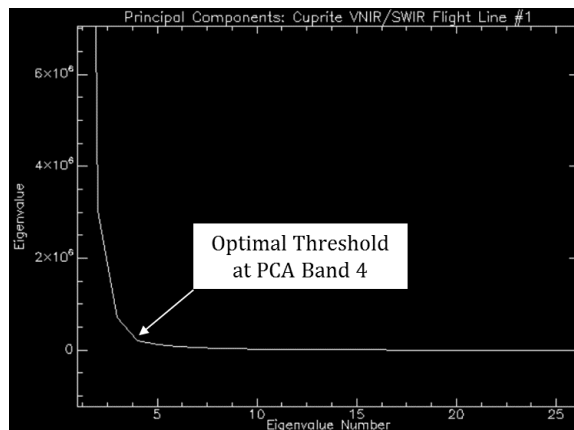


Figure 159: Optimal Threshold for PCA Cube, Cuprite Flight Line #1

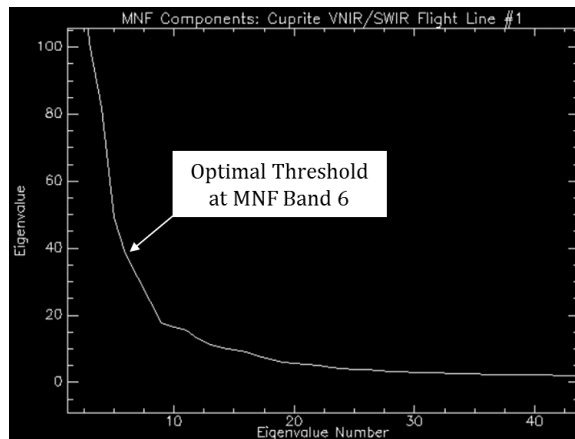


Figure 160: Optimal Threshold for MNF Cube, Cuprite Flight Line #1

For Flight Line #2, Figure 161 and Figure 162 present the PCA eigenvalue plot and the MNF eigenvalue plot, respectively. As shown, the optimal PCA threshold occurs at PCA band 4, after which very little diagnostic spectral information is available. Similarly, the optimal MNF threshold occurs at MNF band 6, after which the bands contain a suboptimal amount of noise. Note that the thresholds for Flight Line #2 are identical to Flight Line #1's thresholds – an unsurprising, but not guaranteed, result given that the spatially adjacent flight lines were collected under identical conditions.

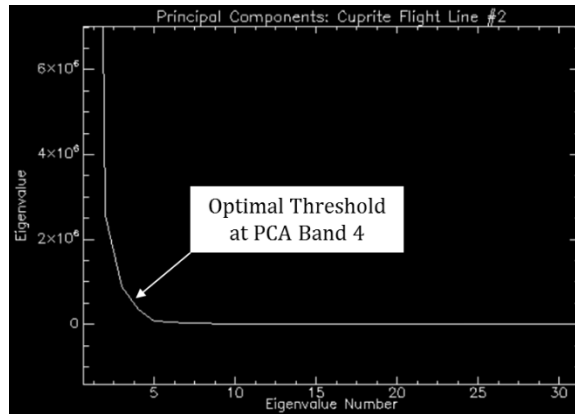


Figure 161: Optimal Threshold for PCA Cube, Cuprite Flight Line #2

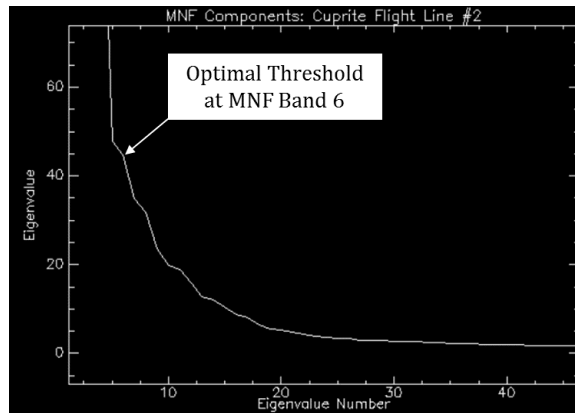


Figure 162: Optimal Threshold for MNF Cube, Cuprite Flight Line #2

For Flight Line #3, Figure 163 and Figure 164 present the PCA eigenvalue plot and the MNF eigenvalue plot, respectively. As shown, the optimal PCA threshold occurs at PCA band 3, after which very little diagnostic spectral information is available. Similarly, the optimal MNF threshold occurs at MNF band 5, after which the bands contain a suboptimal amount of noise. Note that the optimal MNF threshold falls at a higher band than the thresholds for Flight Line #1 and Flight Line #2.

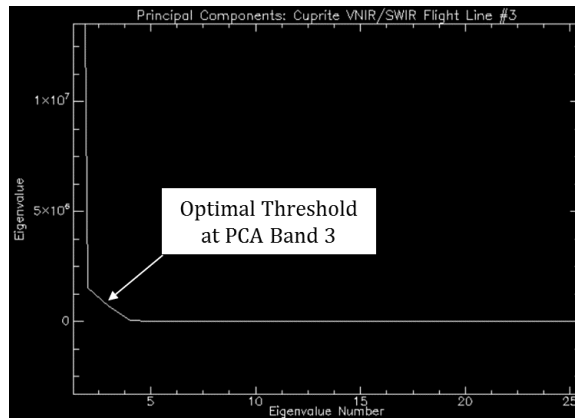


Figure 163: Optimal Threshold for PCA Cube, Cuprite Flight Line #3

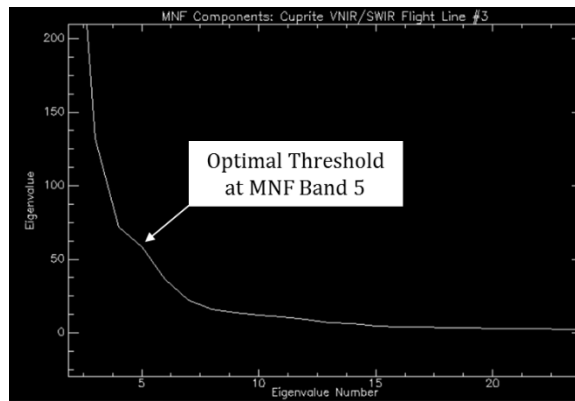


Figure 164: Optimal Threshold for MNF Cube, Cuprite Flight Line #3

For Flight Line #4, Figure 165 and Figure 166 present the PCA eigenvalue plot and the MNF eigenvalue plot, respectively. As shown, the optimal PCA threshold occurs at PCA band 3, after which very little diagnostic spectral information is available. Similarly, the optimal MNF threshold occurs at MNF band 7, after which the bands contain a suboptimal amount of noise.

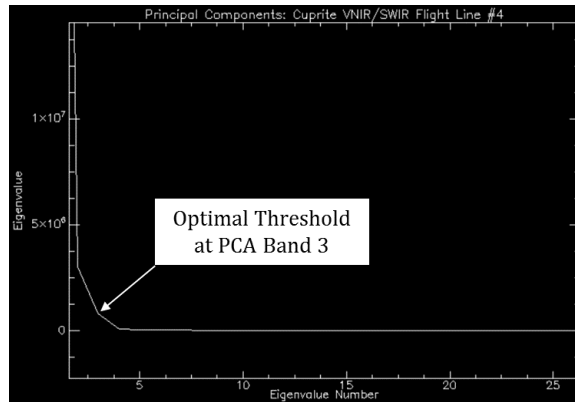


Figure 165: Optimal Threshold for PCA Cube, Cuprite Flight Line #4

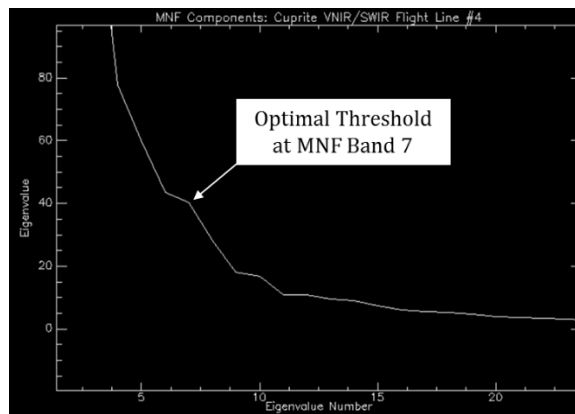


Figure 166: Optimal Threshold for MNF Cube, Cuprite Flight Line #4

At the conclusion of the preprocessing and compression components, the reflectance, full PCA, compressed PCA, full MNF and compressed MNF cubes for each flight line are ready for the edge detection component. The reflectance cubes also are ready for the Roberts and Sobel comparison tests. As seen in Figure 143, Figure 144, Figure 145 and Figure 146, the preprocessing and compression components yielded high-

quality HSI data from which the Di Zenzo-based gradient edge detector generated consistent, interpretable results for each flight line.

Overhead – Indian Pines, Indiana USA

The third gradient-based edge detection experiment uses the VNIR/SWIR Indian Pines, IN USA hypercube. Specifically, this experiment tests the algorithm against five distinct datasets: a 256-band reflectance cube, a 4-band compressed PCA cube, the full 256-band PCA cube, a 4-band compressed MNF cube, and the full 256-band MNF cube. For comparison, this test also executes the Roberts operator and the Sobel operator against the full Indian Pines reflectance cube. Figure 167 presents samples of the seven experiments for the Indian Pines data, and Appendix A contains the full spatial extent for each test.

The methodology's first step, data exploration, indicates that the VNIR/SWIR AVIRIS data is well-calibrated and of good quality across all channels, and is provided in radiance. Figure 168 presents the data exploration results, which indicate that similar materials (e.g., vegetation, bare earth, etc.) are rendered similarly in radiance space. Specifically, note how closely clustered the pixels are for bare earth, and note the consistently lower VNIR channels for the vegetation spectra.

The second methodological step requires a determination as to whether the HSI data are in reflectance or in radiance. As seen in Figure 168, ProSpecTIR provides the data in high-quality radiance, therefore QUAC is necessary to derive estimated reflectance. To prepare the radiance data for QUAC, specific wavelengths had to be assigned to each band (not the "Band Number" x-axis in Figure 168). This task was

accomplished by parsing the center wavelength field out of the AVIRIS-provided calibration text file, uploading the center wavelength file to the ENVI header, and designating the bands in nanometers. The result is a reflectance file configured for QUAC ingestion.

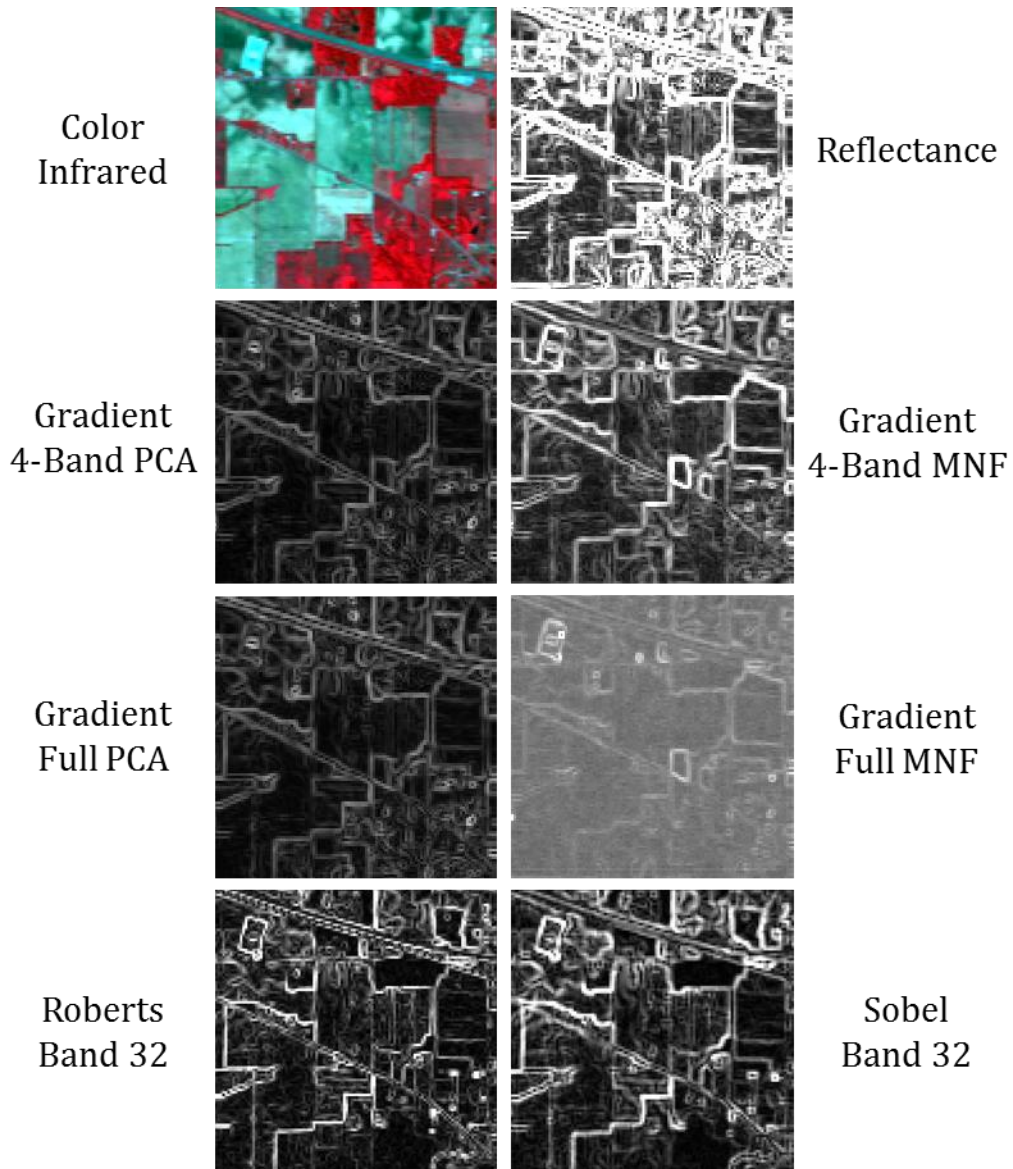


Figure 167: Gradient Experiment for Indian Pines Overhead VNIR/SWIR Data, Unstretched

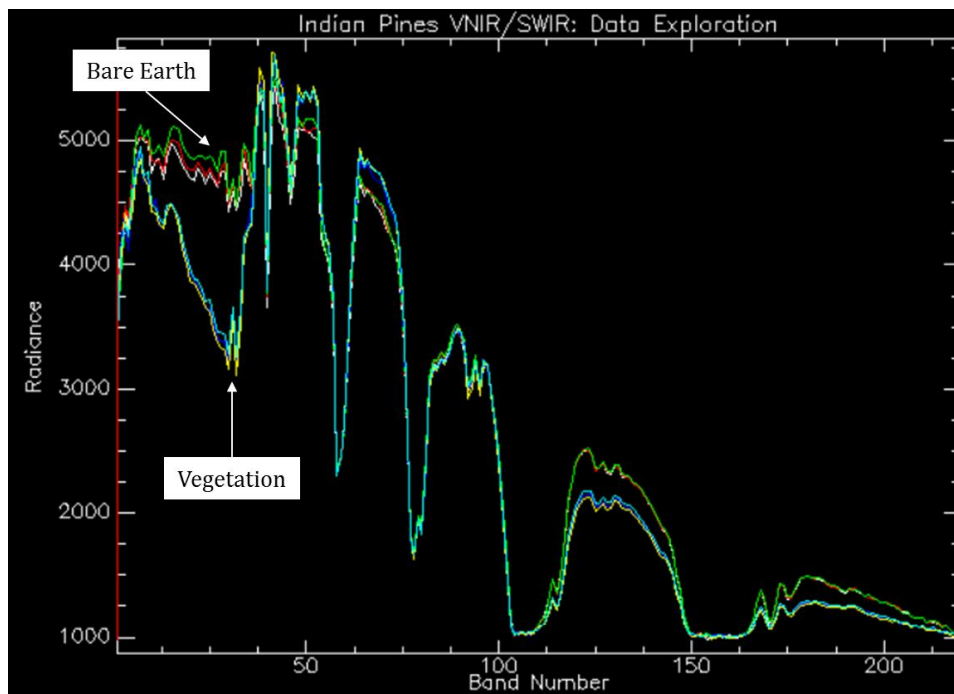


Figure 168: Radiance Data Exploration for the Indian Pines Hypercube

Figure 169 presents vegetation spectra derived from the 220-band QUAC results. As indicated by the well-behaved and closely-clustered red edge samples, QUAC generated high-quality estimated reflectance. Additionally, the green reflectance peak is properly distinguished from the other visible bands, which is also a reliable sign of quality reflectance data. Also, note that QUAC did not attempt to remove bad bands, as seen in the very noisy bands within the $1.4\mu\text{m}$ and $1.9\mu\text{m}$ atmospheric water absorption features. Noisy bands also appear at the edges of the focal plane.

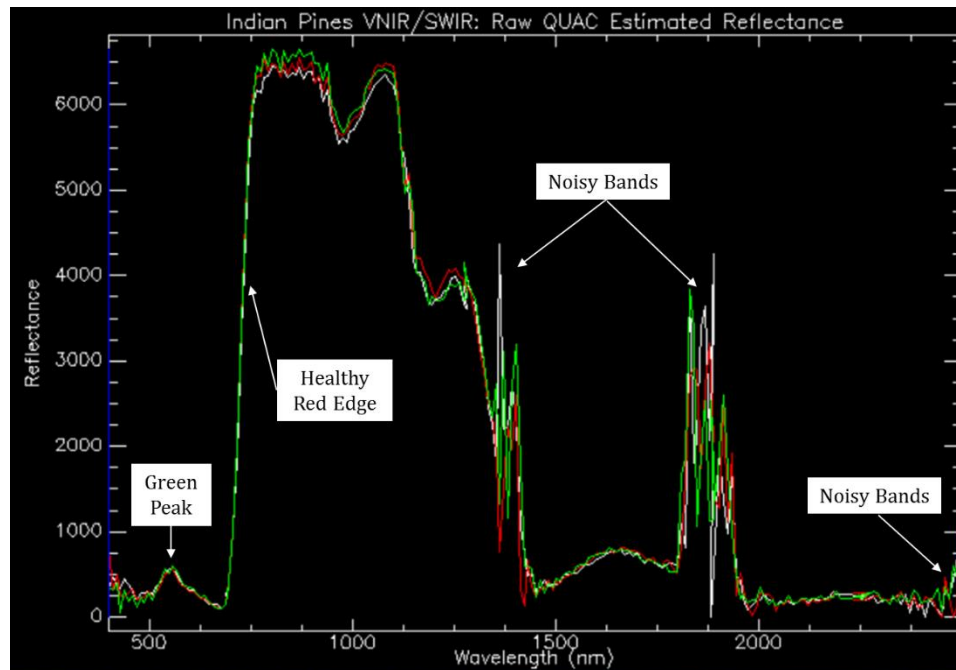


Figure 169: Indian Pines QUAC Results

After the third methodological step scales the reflectance values from 0.0 to 1.0, the fourth step removes the remnant bad bands. 61 bands were removed, including 20 bands near the 1.4 μ m water absorption feature, 24 bands near the 1.9 μ m water absorption feature, seven bands at the beginning of the focal plane and five near its end. Additionally, bad bands likely due to AVIRIS calibration errors were removed at channels 32, 95, 96, 191 and 192. The final reflectance cube contains 159 bands. Figure 170 presents a sample vegetation spectrum from the final 159-band reflectance cube with the bad bands removed.

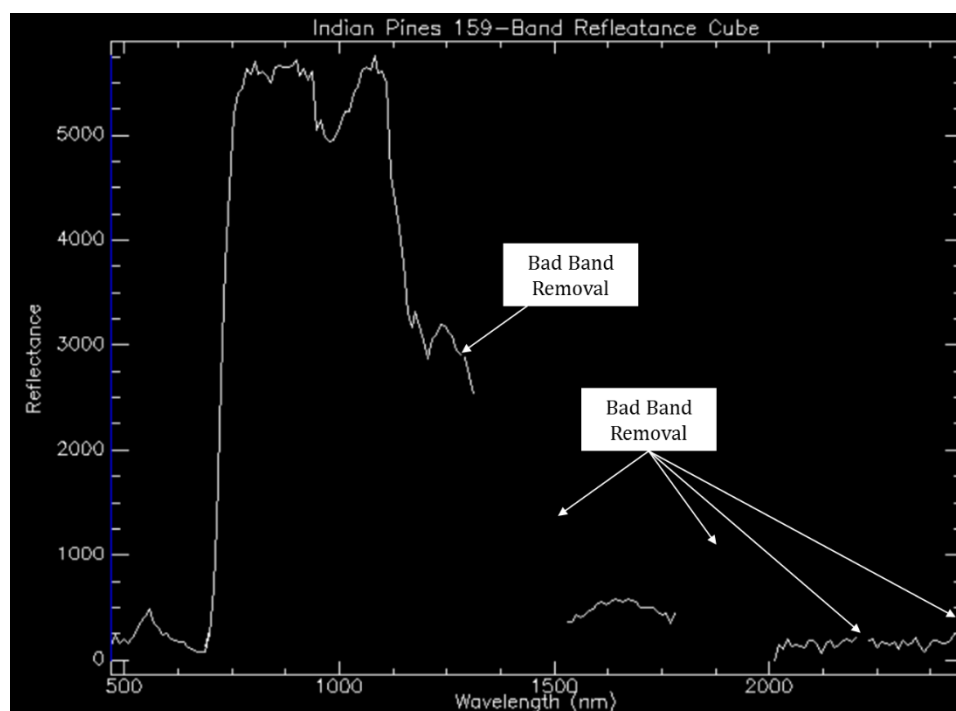


Figure 170: Indian Pines Bad Band Removal

After converting to reflectance and removing additional bad bands, the fifth step calls for a final examination of the reflectance data prior to edge detection. Figure 171 presents several sample reflectance spectra derived from common scene materials such as vegetation and roadway material. Note the expected behavior across all channels for each material, indicating that the data is optimally configured for edge detection. Intensity differences also appear as expected, and noise with the darker roadway spectra is manageable. The NIR bands within the vegetation spectra contain some noise, as well, but overall the noise profile of the final reflectance cube does not present a barrier to edge detection testing.

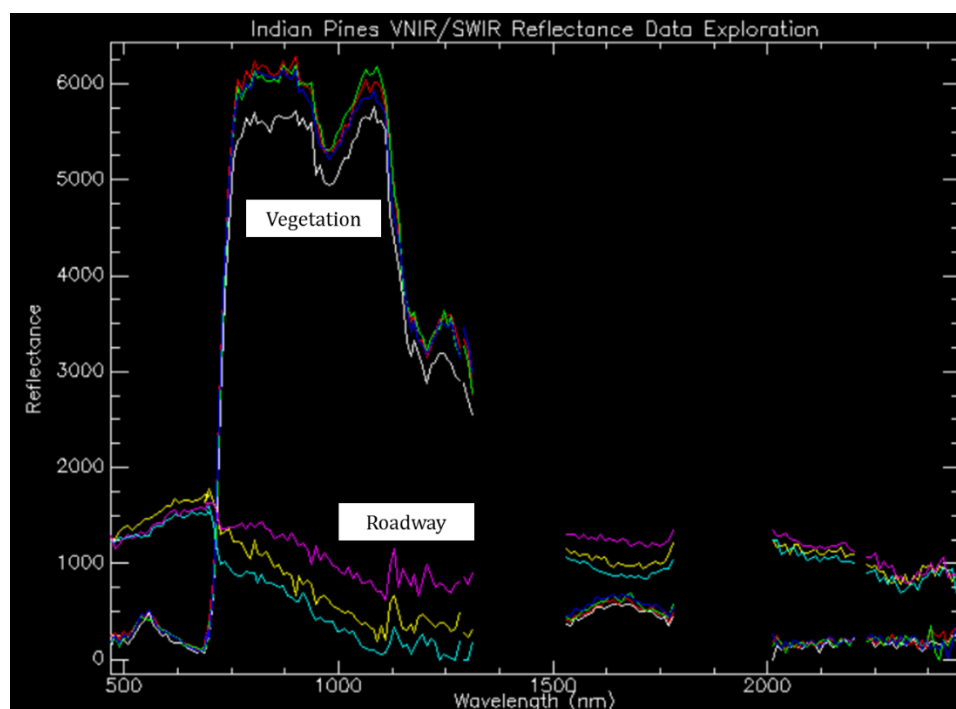


Figure 171: Reflectance Data Exploration for the Indian Pines Hypercube

Figure 172 presents the results of Step 6, SMACC endmember extraction. The SMACC results indicates that the healthy vegetation endmembers are easily distinguishable in reflectance space – a key indicator of a healthy reflectance dataset, particularly a dataset dominated by vegetation. Also, note that SMACC indicates the likely presence of saturation within the scene as evidenced by the very bright and highly irregular spectra. An alternative explanation for the unusual spectra is a QUAC failure on manmade materials, which occasionally occurs when QUAC does not have a sufficient diversity of natural endmembers to generate a high-quality mean spectrum for the scene. Most likely, however, the AVIRIS sensor was calibrated to optimize the

collection of vegetation, which is quite different from the optimal calibration for bright manmade objects. The result of which is an increased probability of saturation on metal.

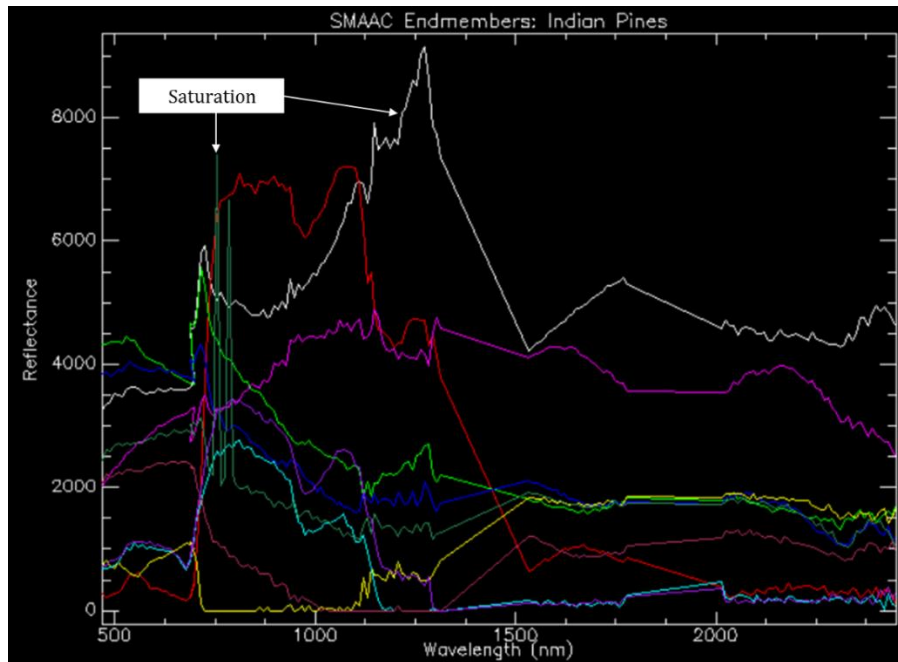


Figure 172: SMAAC Endmembers for the Indian Pines Hypercube

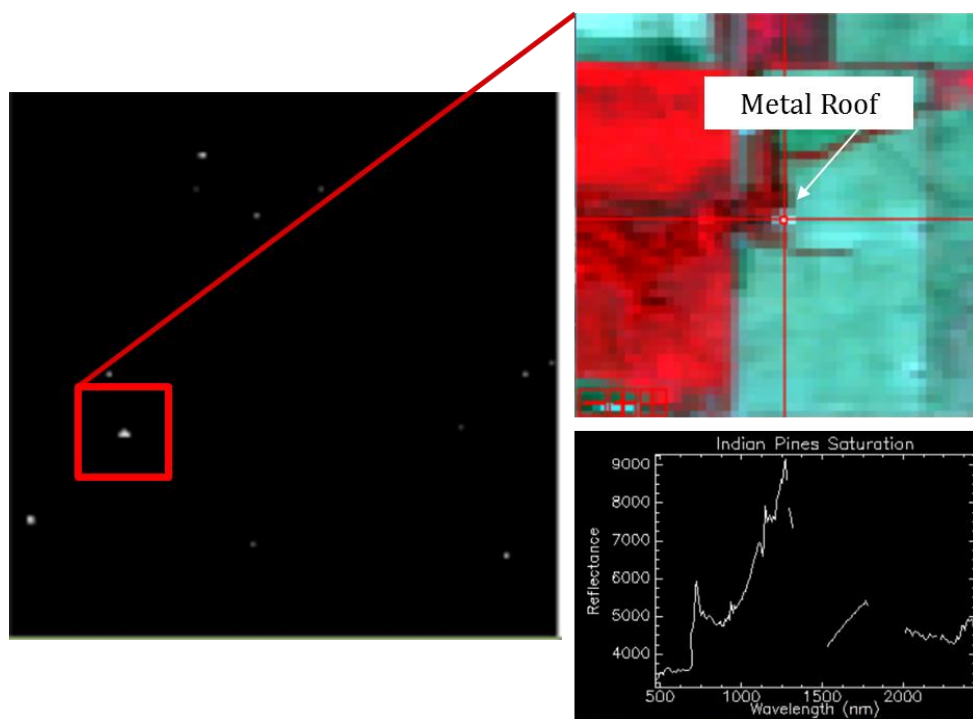


Figure 173: RX Anomaly Plane and Saturation Source for Indian Pines Hypercube - Color Infrared Bands 16, 26, 50

Step 7's RX anomaly plane presented in Figure 173 confirms that the anomalous saturation pixels are attributable to specular reflections off the tops of metal buildings. AVIRIS's ground truth data also corroborates the visual and spectral analysis that the source of saturation is specular reflections off metal objects. Also seen in the RX plane is that the saturated pixels constitute a very small fraction of the overall dataset, meaning that the saturation does not present a barrier to edge detection analysis in support of crop mapping applications. Additionally, the edge detection performance around the saturated pixels should be strong given the strong spectral contrast between the saturated pixels and their natural backgrounds. The RX analysis concludes the preprocessing component for the Indian Pines dataset.

With the preprocessing component complete, the compression component begins with both a PCA and an MNF transformation. Figure 174 and Figure 175 present Step 1 and 2 of the compression component, a plot of the key PCA bands and MNF bands, respectively. As shown, the optimal PCA threshold occurs at PCA band 4, after which very little diagnostic spectral information is available. Therefore, Step 3 of the PCA compression establishes the optimal threshold at PCA band X. Similarly, the optimal MNF threshold occurs at MNF band 4, after which the bands contain mostly noise.

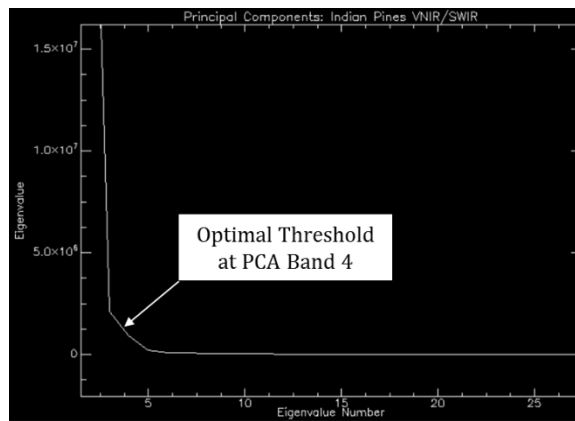


Figure 174: Optimal Threshold for PCA Cube, Indian Pines VNIR/SWIR

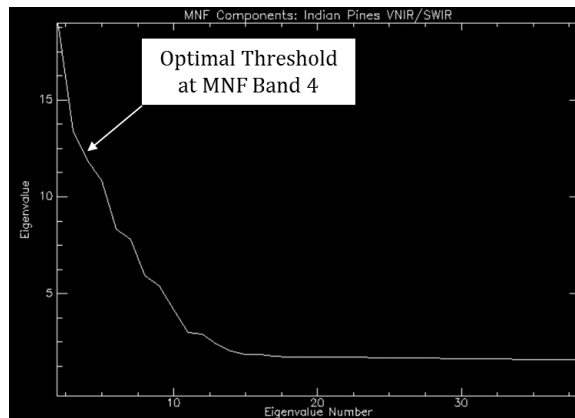


Figure 175: Optimal Threshold for MNF Cube, Indian Pines VNIR/SWIR

At the conclusion of the preprocessing and compression components, the reflectance, full PCA, compressed PCA, full MNF and compressed MNF cubes are ready for the edge detection component. The reflectance cube also is ready for the Roberts and Sobel comparison tests. As seen in Figure 167, the preprocessing and compression components yielded high-quality HSI data from which the Di Zenzo-based gradient edge detector generated consistent, interpretable results.

Overhead – Deepwater Horizon Oil Spill, Gulf of Mexico

The fourth and final gradient-based edge detection experiment for overhead imagery uses ProSpecTIR’s VNIR/SWIR hypercube of the 2010 Deepwater Horizon oil spill in the Gulf of Mexico – the first challenging, non-traditional dataset in this study. The Deepwater Horizon dataset is expected to present a challenge to the Di Zenzo-based gradient algorithm given the dark (i.e., noisy) background, the lack of terrestrial features and the curvilinear nature of the scene’s dominant features.

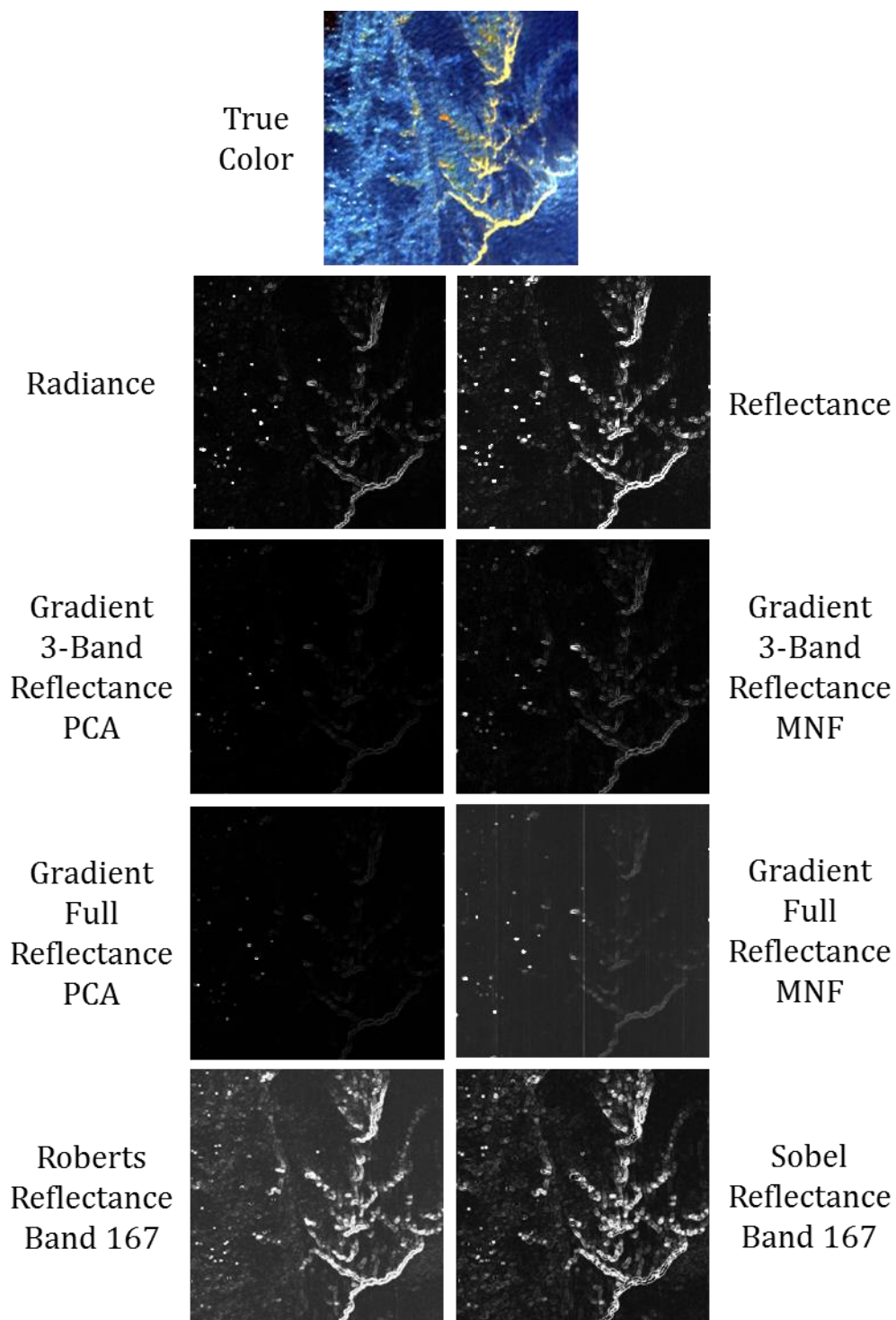


Figure 176: Gradient Experiment for Deepwater Horizon Overhead VNIR/SWIR Data, Unstretched

Specifically, this experiment tests the algorithm against six distinct datasets: a 360-band radiance cube, a 320-band reflectance cube, a 3-band compressed PCA cube, the full 320-band PCA cube, a 3-band compressed MNF cube, and the full 320-band MNF cube. For comparison, this test also executes the Roberts operator and the Sobel operator against the full Deepwater Horizon reflectance cube. Figure 176 presents samples of the seven experiments for the Deepwater Horizon data, and Appendix A contains the full spatial extent for each test.

The methodology's first step, data exploration, indicates that the VNIR/SWIR ProSpecTIR data is well-calibrated and of good quality across all channels, and is provided in radiance. Figure 177 presents the data exploration results, which indicate that similar materials (e.g., open ocean, petroleum, etc.) are rendered similarly in radiance space. Specifically, note how closely clustered the pixels are for water pixels, and note the significantly brighter, closely clustered petroleum spectra.

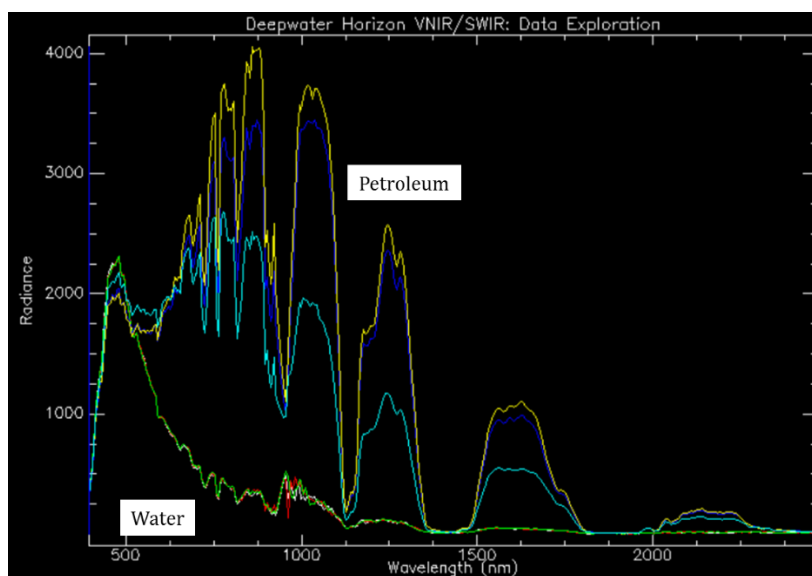


Figure 177: Data Exploration for the Deepwater Horizon Hypercube

The second methodological step requires a determination as to whether the HSI data are in reflectance or in radiance. As seen in Figure 177, ProSpecTIR provides the data in high-quality radiance, therefore QUAC is necessary to derive estimated reflectance. As opposed to the AVIRIS radiance data that required band assignment, ProSpecTIR provides radiance data with bands already assigned, which allows QUAC to run on the as-provided data. However, as discussed in the Background section, QUAC estimates reflectance by generating a mean spectrum from in-scene terrestrial materials, none of which are present within the Deepwater Horizon VNIR/SWIR data. Therefore, this work will make a close examination of the QUAC-generated reflectance data with the objective of determining whether QUAC estimated reflectance data of sufficient quality so as to spectroscopically render petroleum's key absorption features – a necessary achievement for delineating the oil features from within the water features.

For Step 5, Figure 178 presents a petroleum spectrum derived from the 360-band QUAC results, which appear to contain significant quantities of residual atmospheric information, indicating that QUAC did indeed struggle to generate high-quality reflectance data in the absence of terrestrial materials. However, a close examination of a petroleum pixel's reflectance estimate indicates that sufficient reflectance data may be present to distinguish petroleum from water, and thereby be sufficient for oil spill mapping applications. Specifically, as indicated by the color gun alignment in Figure 178, several modest reflectance features align to petroleum absorption features, suggesting that the petroleum reflectance signature is present, albeit not as strongly as it would be under optimal conditions. In line with one of the central themes of this work, the suboptimal Deepwater Horizon reflectance data will undergo testing. This work also will test radiance data as a second attempt at deriving meaningful edges from a challenging, non-traditional hyperspectral dataset. Finally, note that QUAC satisfactorily removed bad bands at the primary atmospheric absorption features as well as from the noisy areas at the beginning and end of the focal plane, obviating the need for the preprocessing component's fourth step, bad band removal.

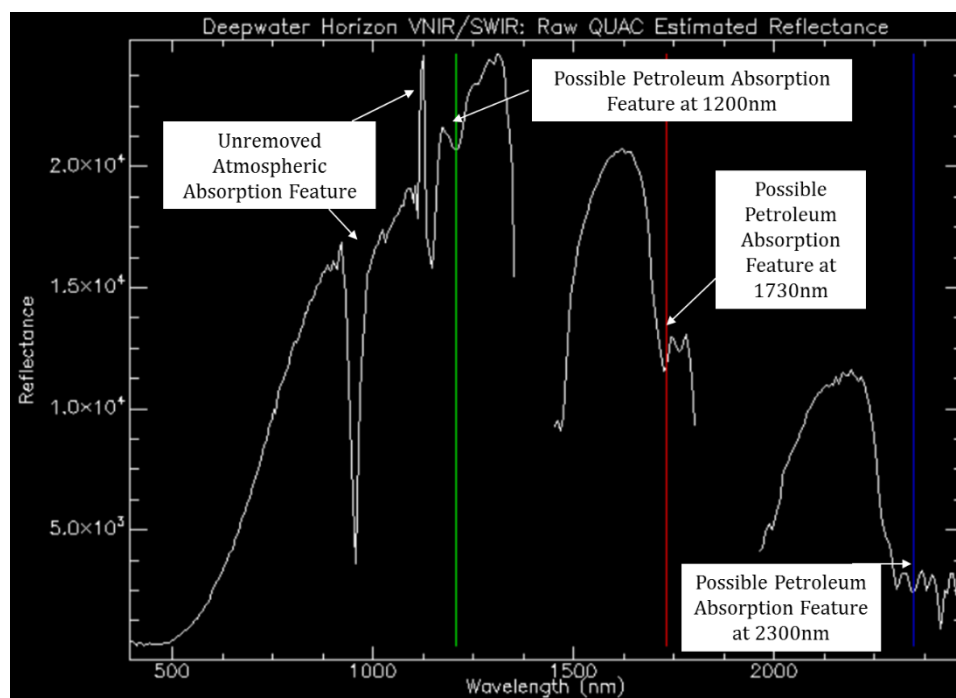


Figure 178: Deepwater Horizon QUAC Results

Figure 179 presents the results of Step 6, SMACC endmember extraction. As seen, the SMACC results corroborate the previous low-quality assessment for the reflectance data. SMACC was challenged to overcome the residual atmospheric information to distill meaningful endmembers, which is unsurprising given the challenging nature of the dataset. Interestingly, the saturation endmembers present within the SMACC results suggest the possible presence of surface ships or other floating equipment (i.e. metal objects) within the scene, which can generate specular reflections and the ensuing saturation.

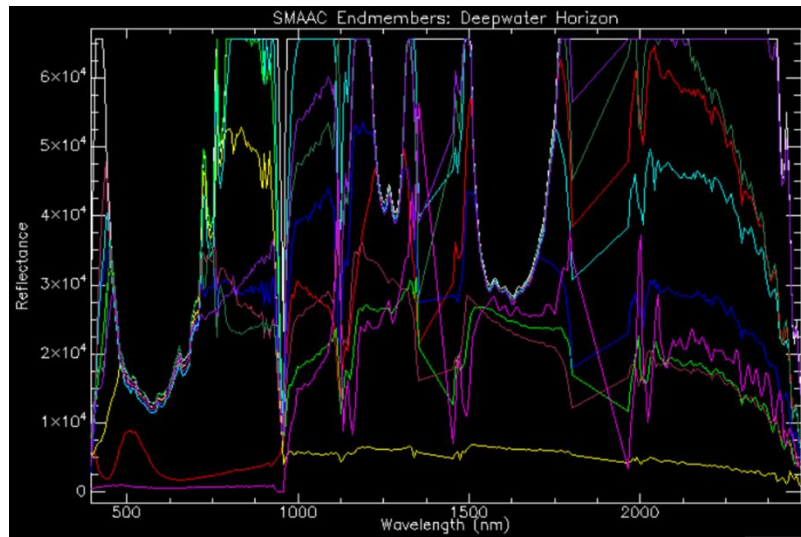


Figure 179: SMAAC Endmembers for the Deepwater Horizon Hypercube



Figure 180: RX Anomaly Plane for Deepwater Horizon Hypercube

Figure 180 presents the Deepwater Horizon RX anomaly plane, the final step in the preprocessing component. The RX plane is characterized by low noise and a cluster of anomalies along the bottom of the data in the area characterized by the choppy seas. Single-pixel anomalies appear to be consistent with the chop.

Additionally, a few multi-pixel anomalies are present within the scene. Examination of the multi-pixel anomalies, as seen in Figure 181, indicates that they are the sources of saturation and therefore likely surface ships. Edge behavior around the saturated pixels is likely to be inconsistent. Finally, note that the RX plane does not indicate the presence of oil slicks within the scene – no linear anomalies are present within the scene. The RX analysis concludes the preprocessing component for the Deepwater Horizon dataset.

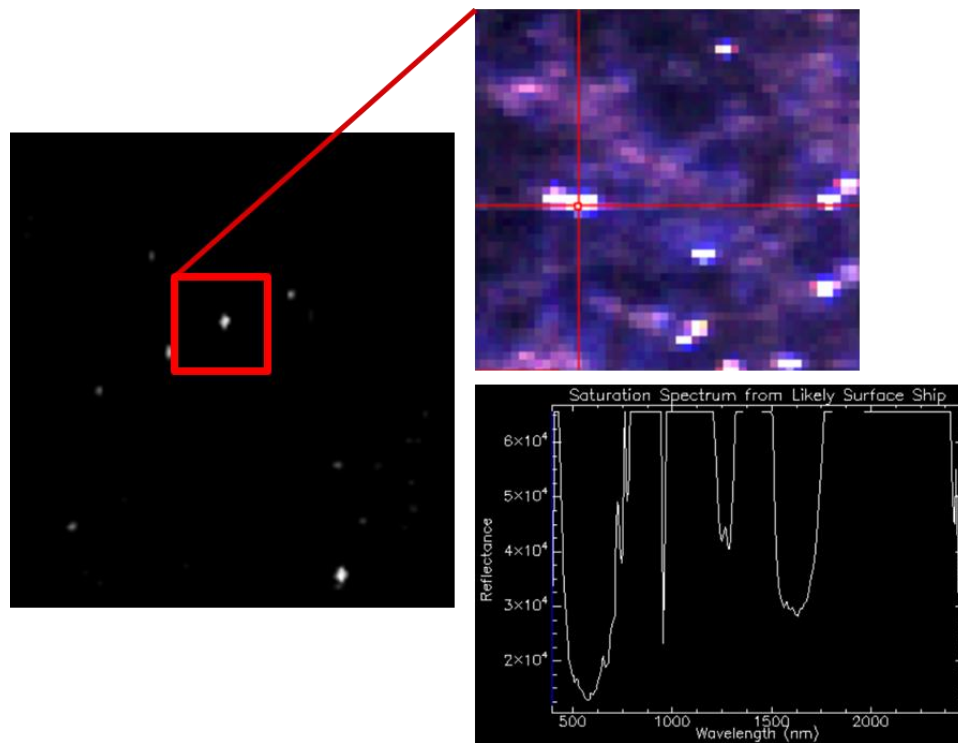


Figure 181: RX Anomaly Plane and Saturation Source for Deepwater Horizon Hypercube - Color Infrared Bands 36, 57, 101

With the preprocessing component complete, the compression component begins with both a PCA and an MNF transformation. Figure 182 and Figure 183 present Step 1 and 2 of the compression component, a plot of the key PCA bands and MNF bands, respectively. As shown, the optimal PCA threshold occurs at PCA band 3, after which very little diagnostic spectral information is available. Therefore, Step 3 of the PCA compression establishes the optimal threshold at PCA band 3. Similarly, the optimal MNF threshold occurs at MNF band 3, after which the bands contain mostly noise.

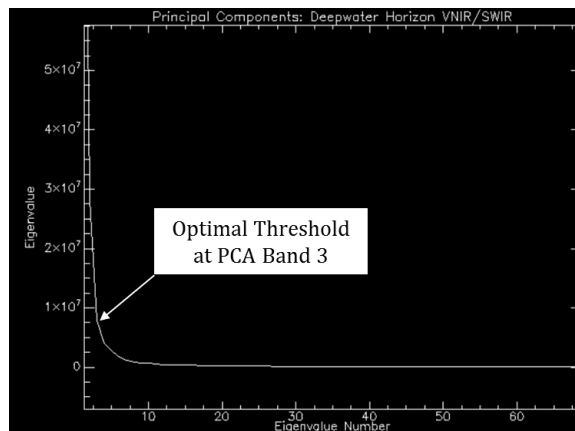


Figure 182: Optimal Threshold for PCA Cube, Deepwater Horizon VNIR/SWIR

At the conclusion of the preprocessing and compression components, the reflectance, full PCA, compressed PCA, full MNF and compressed MNF cubes are ready for the edge detection component. The reflectance cube also is ready for the Roberts and Sobel comparison tests. As seen in Figure 176, the preprocessing and compression

components yielded high-quality HSI data from which the Di Zenzo-based gradient edge detector generated consistent, interpretable results.

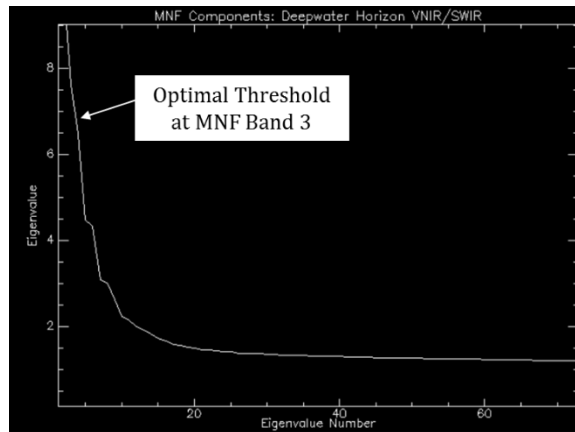


Figure 183: Optimal Threshold for MNF Cube, Deepwater Horizon VNIR/SWIR

Ground-Based – Larkhaven

The first gradient-based edge detection experiment on ground-based hyperspectral data uses SOC710 VNIR imagery of a residential home in Fairfax Station, Virginia. This test is analogous to the Reno, NV overhead data in the sense that it also supports urban feature mapping applications. Specifically, this experiment tests the algorithm against five distinct datasets: a 120-band reflectance cube, a 4-band compressed PCA cube, the full 120-band PCA cube, a 3-band compressed MNF cube, and the full 120-band MNF cube. For comparison, this test also executes the Roberts operator and the Sobel operator against the full Larkhaven reflectance cube. Figure 184 presents samples of the seven experiments for the Larkhaven data, and Appendix A contains the full spatial extent for each test.

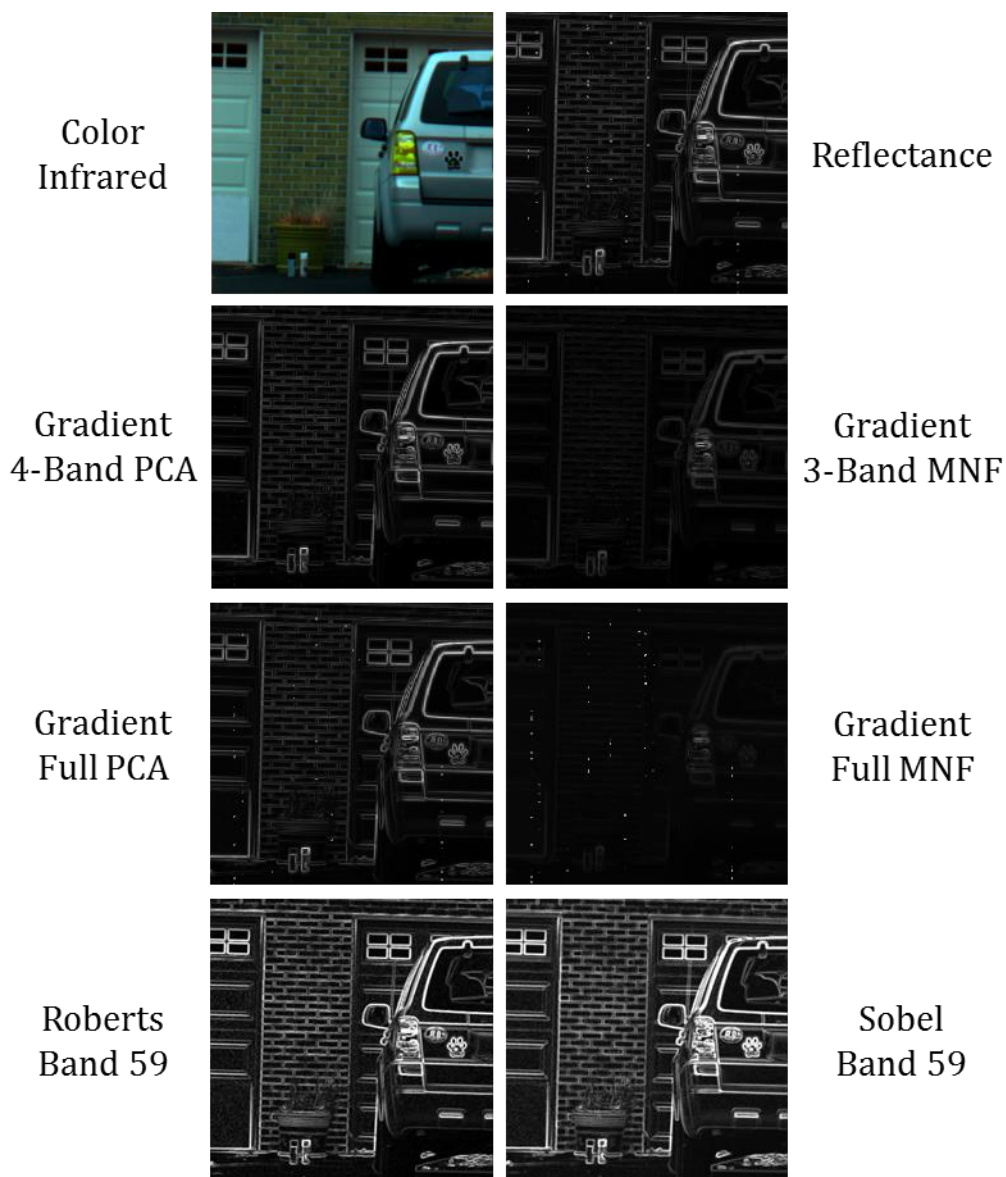


Figure 184: Gradient Experiment for Larkhaven Ground-Based VNIR Data, Unstretched

The methodology's first step, data exploration, indicates that the VNIR SOC710 data is well-calibrated and of good quality across all channels, and is provided in radiance. Figure 185 presents the data exploration results, which indicate that similar materials (e.g., vegetation, calibration panels, etc.) are rendered similarly in radiance

space. Specifically, note how closely clustered the pixels are for white calibration panel and for the black calibration panel. Both appear at the proper intensities and with an acceptable amount of noise. Also, note the characteristic behavior for the vegetation radiance spectra. Ultimately, the SOC710 Larkhaven data appear to be high-quality data free of significant radiance-based anomalies.

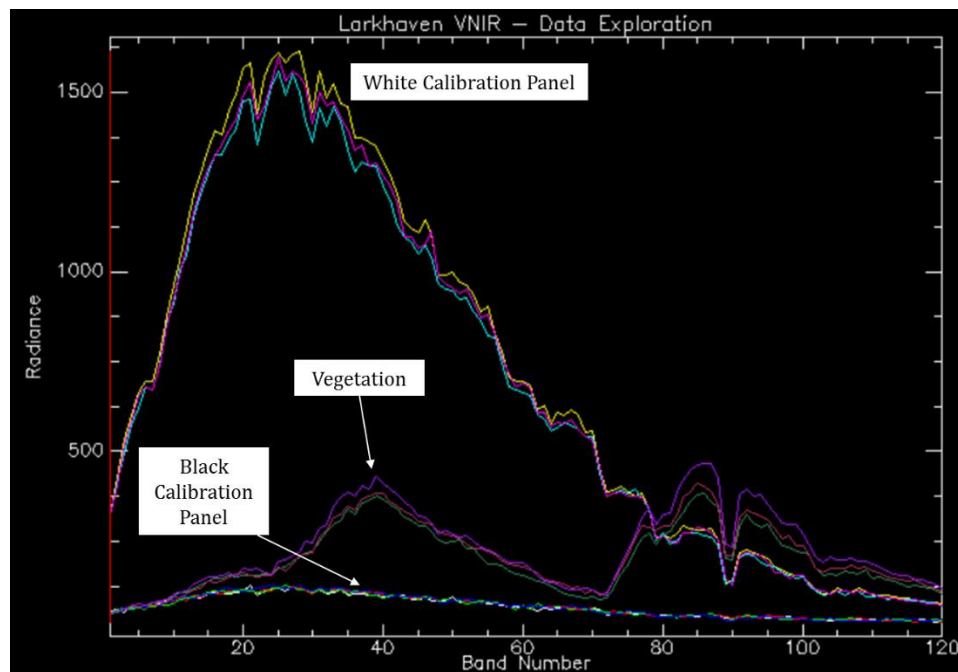


Figure 185: Radiance Data Exploration for the Larkhaven Hypercube

The second methodological step requires a determination as to whether the HSI data are in reflectance or in radiance. As seen in Figure 185, the SOC generates high-quality radiance data, therefore QUAC is necessary to derive estimated reflectance. To prepare the radiance data for QUAC, several preprocessing steps were necessary to

optimize the data for visualization and QUAC execution. First, specific wavelengths were assigned to each SOC710 band (not the “Band Number” x-axis in Figure 185). This task was accomplished by parsing the center wavelength field out of the SOC710-provided calibration text file, uploading the center wavelength file to the ENVI header, and designating the bands in nanometers.

Next, the seven constituent SOC710 HSI cubes were rotated horizontally to the ground plane for optimal visualization (the SOC710 collects imagery -90° to the horizontal). Then the seven cubes were mosaicked together to generate a single HSI cube. Finally, the mosaicked cube was spatially cropped to remove the black background pixels which would distort the QUAC radiance to reflectance conversion. The result is a reflectance file configured for QUAC ingestion, as seen in Figure 186.



Figure 186: Larkhaven VNIR Radiance Data Optimized for QUAC and Visualization - Color Infrared Bands 35, 60, 109

Step 3 scales the Larkhaven reflectance dataset from 0.0 to 1.0. Step 4, bad band removal, is unnecessary since the dataset contains no bad bands. Step 5, examine the reflectance data, is presented in Figure 187. Note the consistent behavior within material

classes. The vehicle paint spectra align closely and contain all expected diagnostic absorption features. The vegetation spectra are expectedly weaker given the early spring collection date, and the black calibration panel spectra appear consistent and featureless, as expected. Ultimately, QUAC generated high-quality VNIR reflectance data that is well-suited for edge detection experiments.

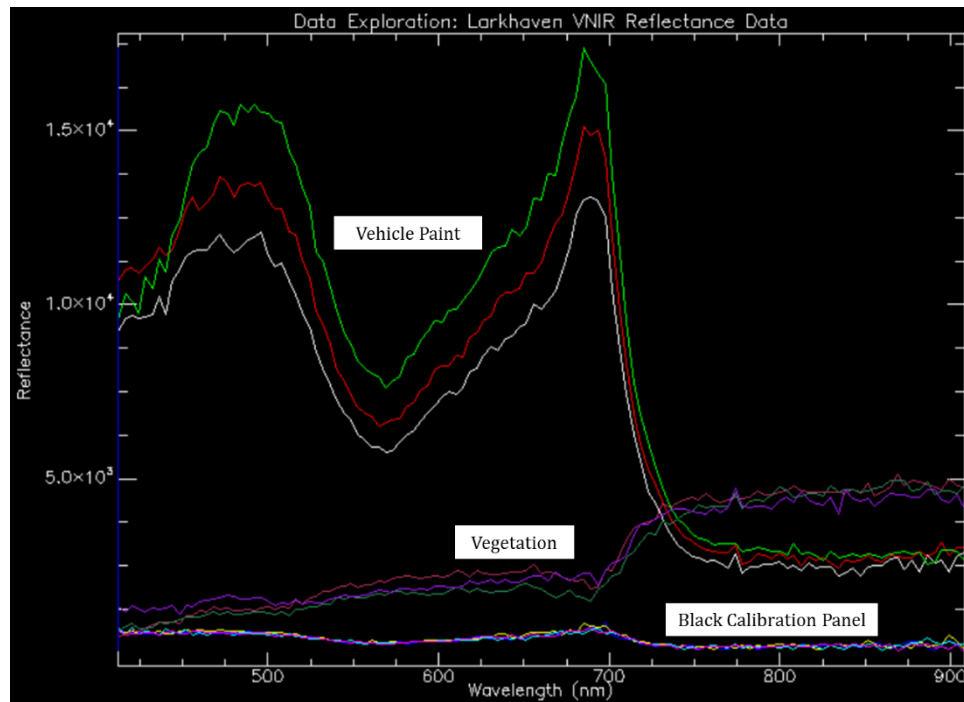


Figure 187: Reflectance Data Exploration for the Larkhaven Hypercube

Figure 188 presents the results of Step 6, SMACC endmember extraction. The SMACC results indicates that routine materials like brick and vegetation are easily distinguishable in reflectance space – a key indicator of a healthy reflectance dataset. Also, note that SMACC indicates the presence of sensor anomalies and mosaic anomalies

within the scene as evidenced by the highly irregular spectra throughout the SMACC plot. Sensor anomalies are not unusual within SOC710 data, and while they appear disruptive with the SMACC results, they typically are not sufficiently widespread so as to present a barrier to analysis. The mosaic anomalies are typical in mosaicked data and occur due to the imperfect alignment along the seams of overlapping imagery. The mosaic anomalies occur only along the seams of mosaicked imagery and therefore do not present a general barrier to edge detection experiments.

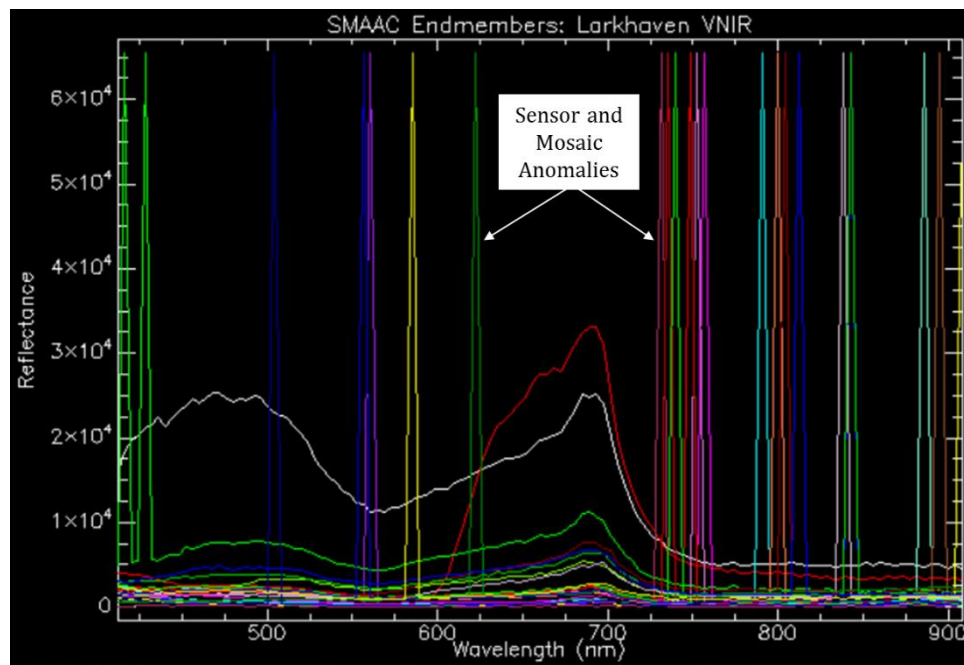


Figure 188: SMAAC Endmembers for the Larkhaven Hypercube

Step 7's RX anomaly plane presented in Figure 189 confirms that many anomalous pixels are attributable to scattered sensor anomalies and mosaic anomalies

along the seams of overlapping imagery. Anomalous pixels also are evident along the some of the horizontal window frame components, and on the plastic housing covering the vehicle's taillights – both of which are not unwanted anomalies in the sense that they truly are unusual materials in the scene and therefore are features that the edge detectors should delineate.

Also seen in the RX plane is that the unwanted anomalous pixels attributable to mosaicking and sensor anomalies constitute a very small fraction of the overall dataset, meaning that they do not present a barrier to edge detection analysis in support of urban feature mapping applications. The RX analysis concludes the preprocessing component for the Larkhaven dataset.

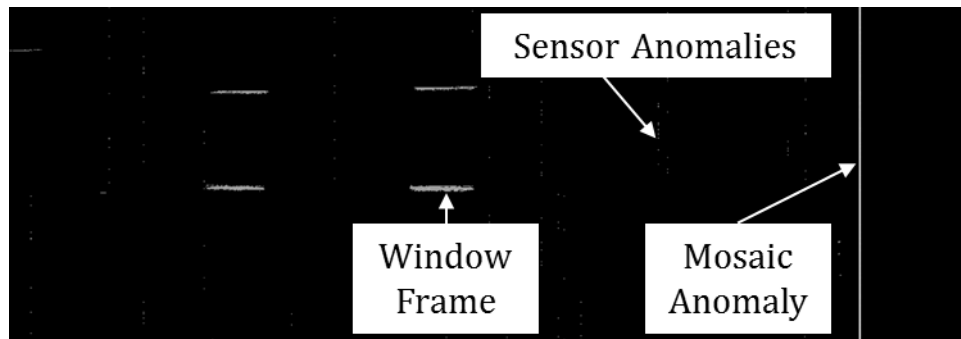


Figure 189: RX Anomaly Plane for Larkhaven Hypercube

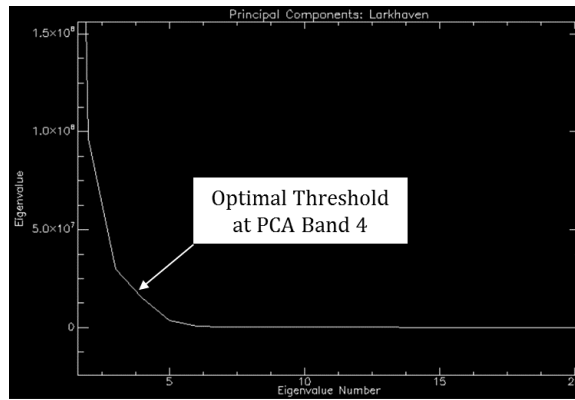


Figure 190: Optimal Threshold for PCA Cube, Larkhaven VNIR

With the preprocessing component complete, the compression component begins with both a PCA and an MNF transformation. Figure 190 and Figure 191 present Step 1 and 2 of the compression component, a plot of the key PCA bands and MNF bands, respectively. As shown, the optimal PCA threshold occurs at PCA band 4, after which very little diagnostic spectral information is available. Therefore, Step 3 of the PCA compression establishes the optimal threshold at PCA band 4. Similarly, the optimal MNF threshold occurs at MNF band 3, after which the bands contain mostly noise.

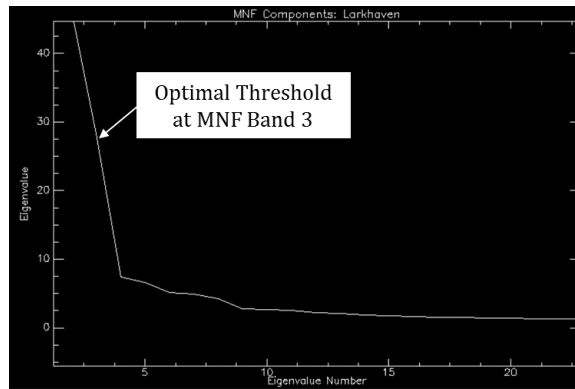


Figure 191: Optimal Threshold for MNF Cube, Larkhaven VNIR

At the conclusion of the preprocessing and compression components, the reflectance, full PCA, compressed PCA, full MNF and compressed MNF cubes are ready for the edge detection component. The reflectance cube also is ready for the Roberts and Sobel comparison tests. As seen in Figure 184, the preprocessing and compression components yielded high-quality HSI data from which the Di Zenzo-based gradient edge detector generated consistent, interpretable results.

Ground-Based – Granite VNIR

The second gradient-based edge detection experiment on ground-based hyperspectral data uses Pika II VNIR imagery of a high-spatial resolution granite sample. This test is analogous to the Cuprite, NV overhead data in the sense that it also supports mineral mapping applications. Specifically, this experiment tests the algorithm against five distinct datasets: a 72-band reflectance cube, a 2-band compressed PCA cube, the full 72-band PCA cube, a 2-band compressed MNF cube, and the full 72-band MNF cube. For comparison, this test also executes the Roberts operator and the Sobel operator

against the full Granite VNIR reflectance cube. Figure 192 presents samples of the seven experiments for the Granite VNIR data, and Appendix A contains the full spatial extent for each test.

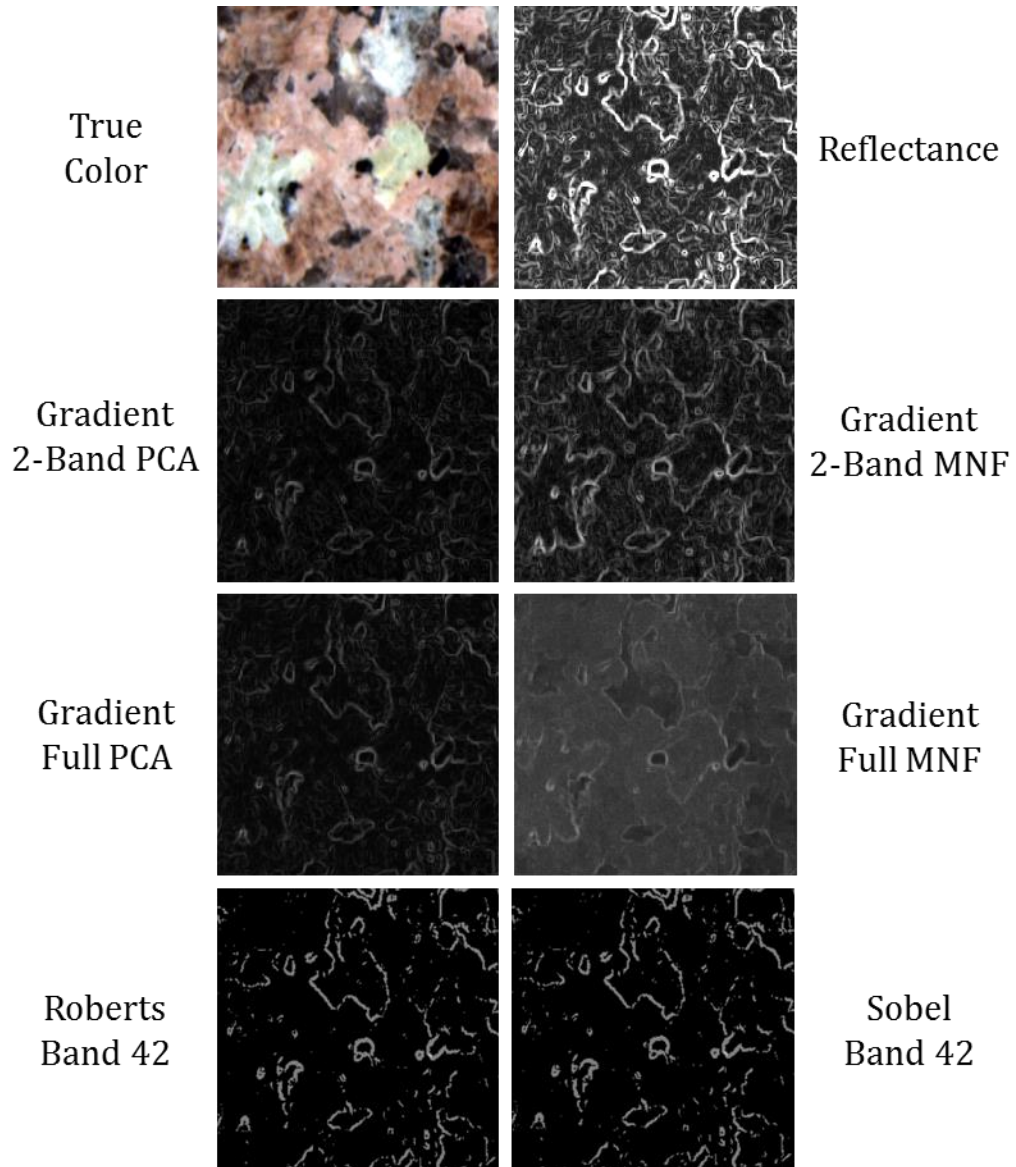


Figure 192: Gradient Experiment for Granite Ground-Based VNIR Data, Unstretched

The methodology's first step, data exploration, indicates that the VNIR SOC710 data is of acceptable quality across all channels, but has a higher noise floor than the previously tested datasets. The VNIR data is provided in reflectance, as well. Figure 193 presents the data exploration results, which indicate that similar materials (e.g., white region, pink region, etc.) are rendered similarly in reflectance space, but are not closely knit, even for adjacent pixels. Specifically, note the intensity differences among the pink region spectra. Additionally, note the absence of diagnostic absorption features in the VNIR data – a limiting characteristic of minerals imaged in the VNIR, which is why most traditional HSI mineral applications rely on SWIR data to identify or delineate minerals. Ultimately, the SOC710 Granite VNIR data will present a challenge to the edge detection algorithms due to its high noise floor and the limited VNIR spectral contrast among scene features.

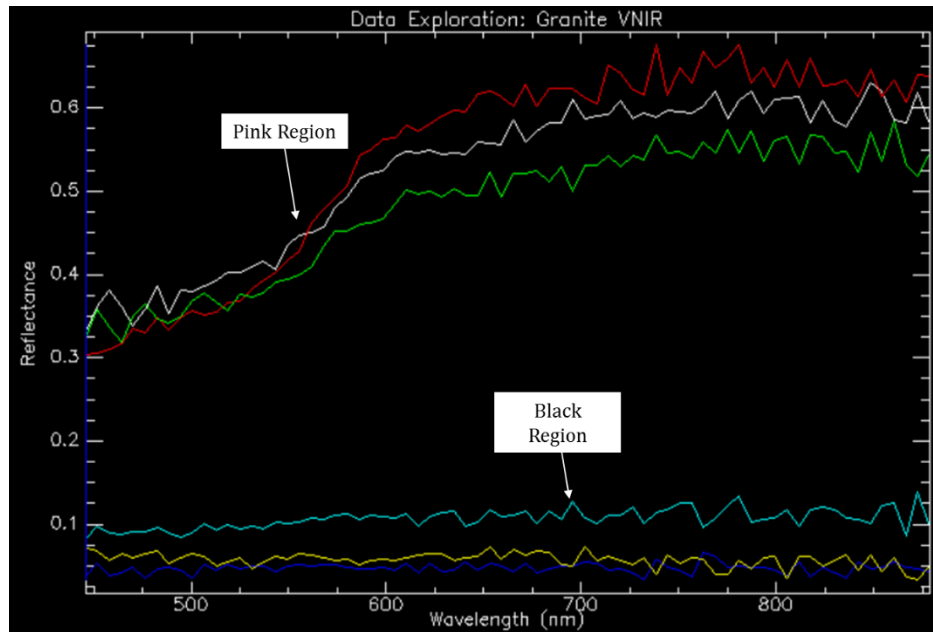


Figure 193: Data Exploration for the Granite VNIR Hypercube

The second methodological step requires a determination as to whether the HSI data are in reflectance or in radiance. As seen in Figure 193, the Granite VNIR is already in reflectance, therefore QUAC is unnecessary for this dataset. Step 3 scales the reflectance dataset from 0.0 to 1.0. Step 4, bad band removal, is unnecessary since the dataset contains no bad bands, and Step 5, examine the reflectance data, is also unnecessary given the reflectance analysis in Figure 193.

Figure 194 presents the results of Step 6, SMACC endmember extraction. The SMACC results indicate that minerals dominate the scene, as expected. No saturation is evident in the scene, and no unusual spectra appear in the SMACC endmembers. Overall, the SMACC processing indicates that the Granite VNIR dataset is well-behaved and free of irregularities that could distort edge detection testing.

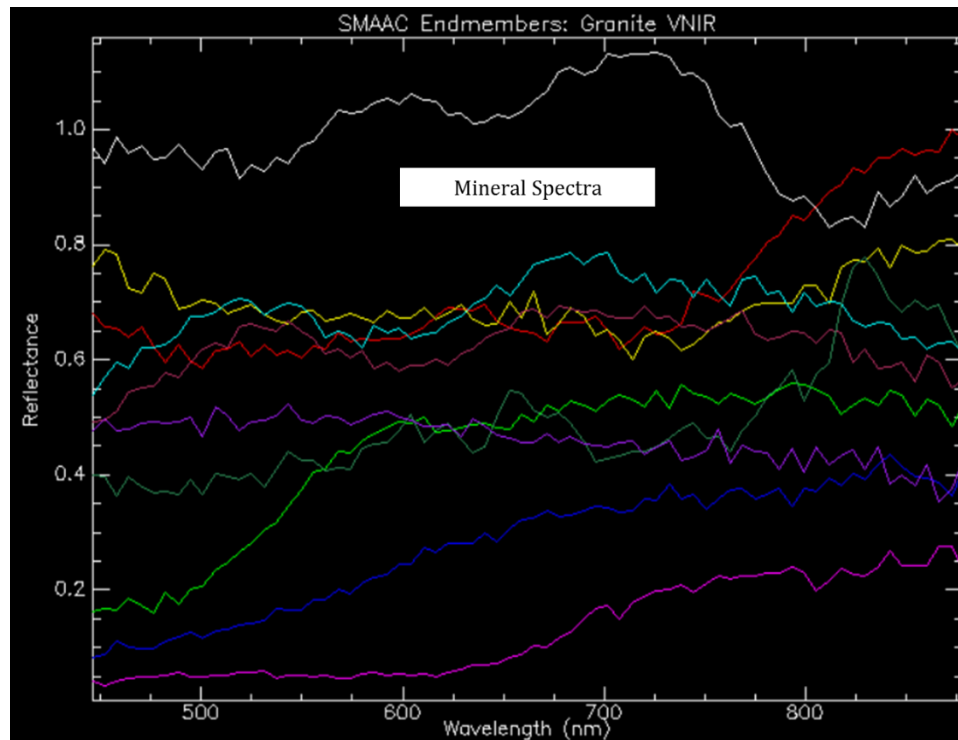


Figure 194: SMAAC Endmembers for the Granite VNIR Hypercube

The preprocessing component's final step generates an RX anomaly plane as a final check on data quality and scene behavior. As seen in Figure 195, the RX processing detected no meaningful anomalies. The scattered weak anomalies along the left side of the image are likely attributable to sensor anomalies since they are so heavily skewed towards one side of an image with proportionally arrayed features. Also supporting this conclusion is the abrupt end to the weak anomalies along a vertical line extending across the scene from top to bottom. Ultimately, these light anomalies present no barrier to rigorous edge detection testing.

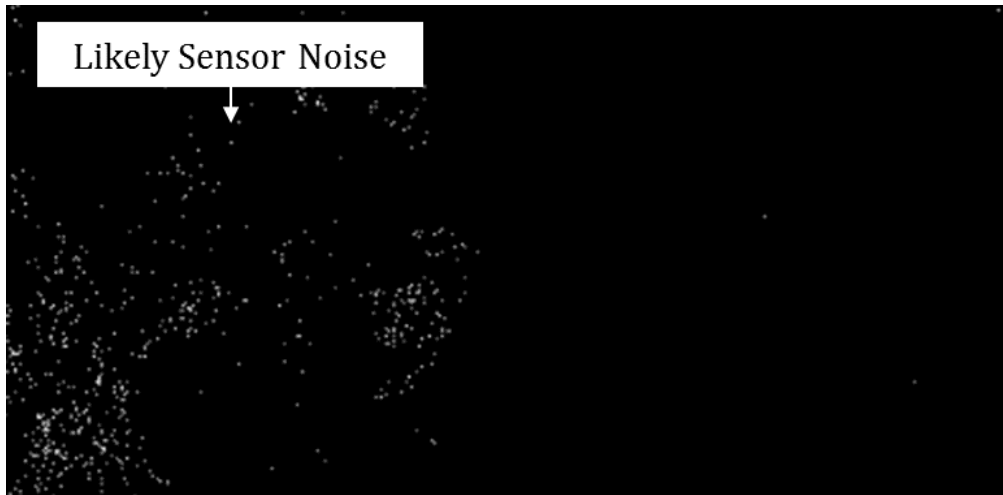


Figure 195: RX Anomaly Plane for Granite VNIR Hypercube

With the preprocessing component complete, the compression component begins with both a PCA and an MNF transformation. Figure 196 and Figure 197 present Step 1 and 2 of the compression component, a plot of the key PCA bands and MNF bands, respectively. As shown, the optimal PCA threshold occurs at PCA band 2, after which very little diagnostic spectral information is available. Therefore, Step 3 of the PCA compression establishes the optimal threshold at PCA band 2. Similarly, the optimal MNF threshold occurs at MNF band 2, after which the bands contain mostly noise. Also, note that the optimal PCA and MNF thresholds appear at higher-order bands (i.e., Band 2 as opposed to Band 4 or Band 5, etc.) than more diverse scenes, an expected outcome given the relative homogeneity of a mineral mapping scene comprised of similar minerals.

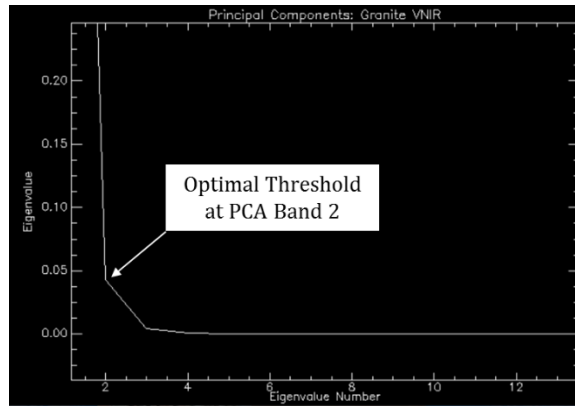


Figure 196: Optimal Threshold for PCA Cube, Granite VNIR

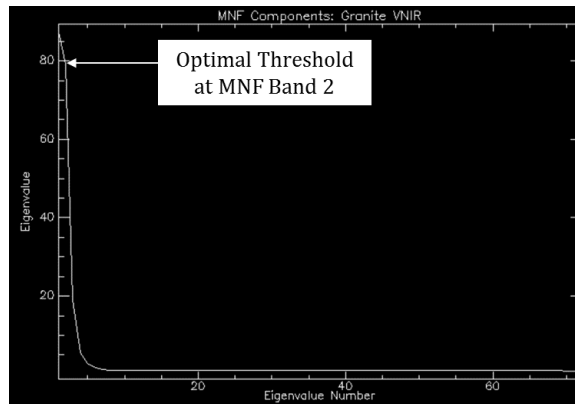


Figure 197: Optimal Threshold for MNF Cube, Granite VNIR

At the conclusion of the preprocessing and compression components, the reflectance, full PCA, compressed PCA, full MNF and compressed MNF cubes are ready for the edge detection component. The reflectance cube also is ready for the Roberts and Sobel comparison tests. As seen in Figure 192, the preprocessing and compression components yielded HSI data from which the Di Zenzo-based gradient edge detector generated consistent, interpretable results.

Ground-Based – Granite NIR/SWIR

The third gradient-based edge detection experiment on ground-based hyperspectral data is a close cousin to the previous Granite VNIR test. This experiment uses high-spatial resolution Pika II NIR/SWIR imagery of a different area from the same granite sample as the previous test. The primary difference is the wavelength and sampling rate – this test includes the SWIR bands so important to accurate mineral mapping applications, excludes the VIS bands and has 162 bands as opposed to 72. This test also is analogous to the Cuprite, NV overhead data in the sense that it supports mineral mapping applications.

Specifically, this experiment tests the algorithm against five distinct datasets: a 164-band reflectance cube, a 3-band compressed PCA cube, the full 164-band PCA cube, a 5-band compressed MNF cube, and the full 162-band MNF cube. For comparison, this test also executes the Roberts operator and the Sobel operator against the full Granite NIR/SWIR reflectance cube. Figure 198 presents samples of the seven experiments for the Granite NIR/SWIR data, and Appendix A contains the full spatial extent for each test.

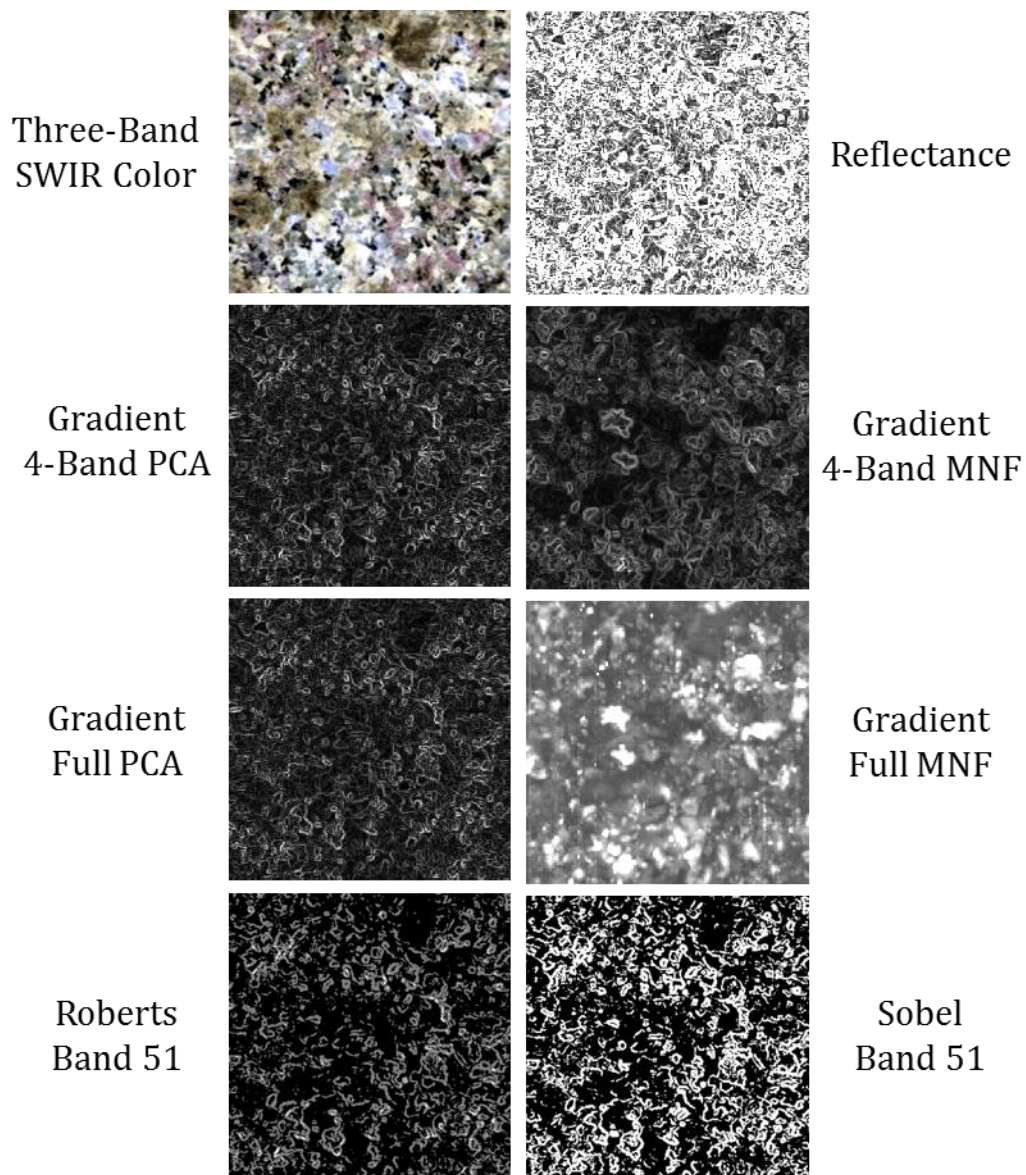


Figure 198: Gradient Experiment for Granite Ground-Based NIR/SWIR Data, Unstretched

The methodology's first step, data exploration, indicates that the Pika II data is of high quality across all channels, with very little noise. In this manner, the Pika II NIR/SWIR data is superior to the SOC710 VNIR data, which contains significantly more noise. The spatial resolutions of the two granite datasets are identical, however. The

NIR/SWIR data is provided in reflectance, as well. Figure 199 presents the data exploration results, which indicate that similar mineral samples are rendered similarly in reflectance space across all bands. Note the clearly recognizable diagnostic absorption features in the SWIR data – a key advantage to imaging minerals in the SWIR, which is why most traditional HSI mineral applications rely on SWIR data to identify or delineate minerals. Diagnostic absorption features appear in the NIR for some minerals, as well. Ultimately, the Pika II Granite NIR/SWIR data is a high-quality data set optimized for supporting edge detection experiments aligned to mineral mapping HSI applications.

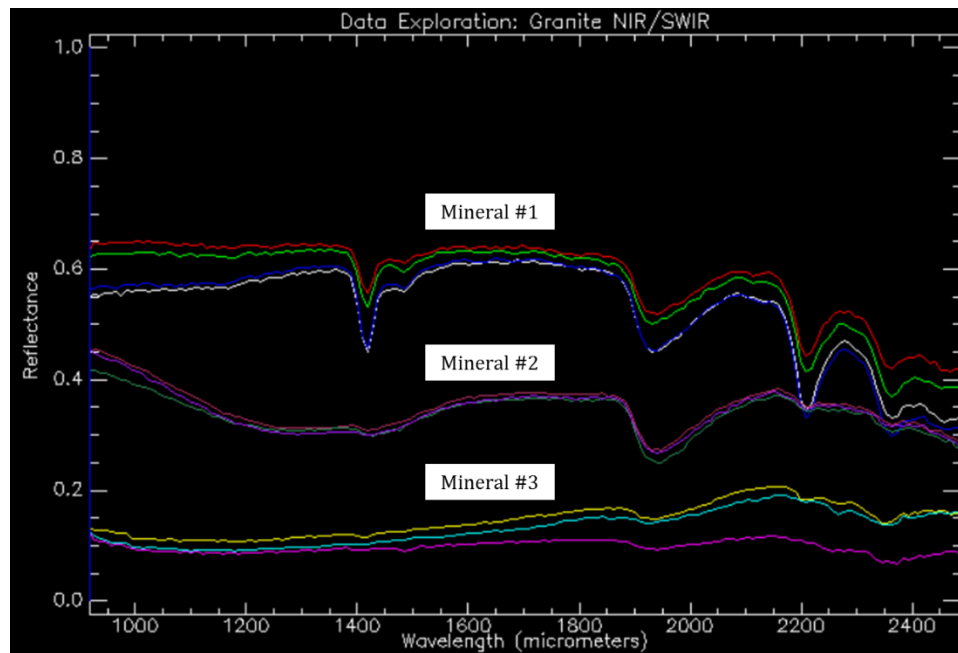


Figure 199: Data Exploration for the Granite NIR/SWIR Hypercube

The second methodological step requires a determination as to whether the HSI data are in reflectance or in radiance. As seen in Figure 199, the Granite NIR/SWIR is already in reflectance, therefore QUAC is unnecessary for this dataset. Step 3 scales the reflectance dataset from 0.0 to 1.0, which is unnecessary for this dataset since it is already properly scaled. Step 4, bad band removal, also is unnecessary since the dataset contains no bad bands, and Step 5, examine the reflectance data, is unnecessary as well, given the reflectance analysis in Figure 199.

Figure 200 presents the results of Step 6, SMACC endmember extraction. The SMACC results indicate that minerals dominate the scene, as expected. No saturation is evident in the scene, and no unusual spectra appear in the SMACC endmembers. Overall, the SMACC processing indicates that the Granite VNIR dataset is well-behaved and free of irregularities that could distort edge detection testing. The results also corroborate the reflectance assessment which concluded that the dataset is highly optimized for mineral mapping in the sense that it clearly renders and separates different minerals. Again, note the concentration of diagnostic absorption features in the SWIR.

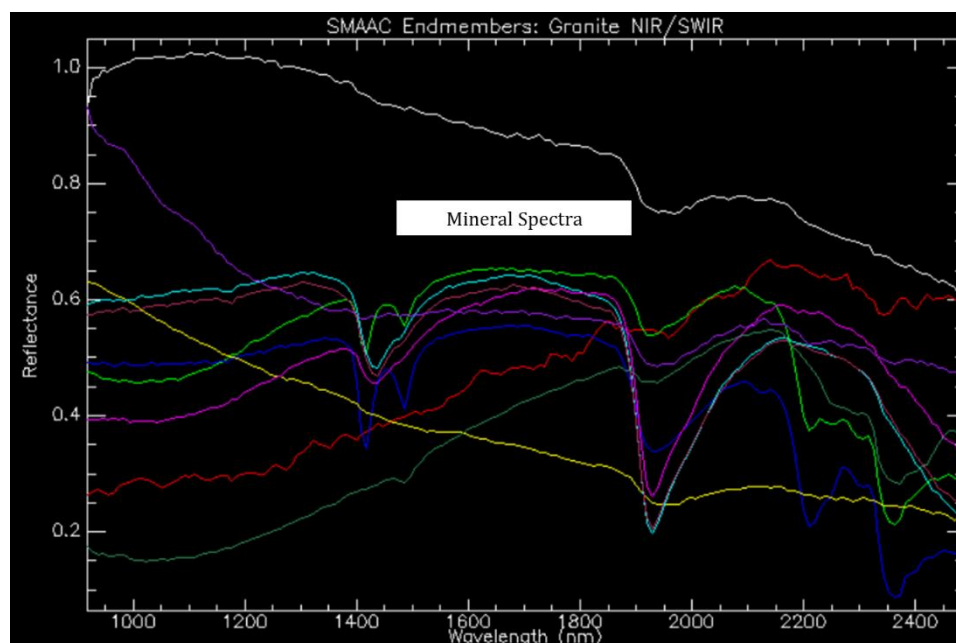


Figure 200: SMAAC Endmembers for the Granite NIR/SWIR Hypercube

The preprocessing component's final step generates an RX anomaly plane as a final check on data quality and scene behavior. As seen in Figure 201, the RX processing anomalies, many of which are strong, throughout the scene. Investigation into the anomalies yielded mixed results. The strong, multi-pixel anomalies appear to be fine grains of a mineral rare within the scene, and their spectra contained no unusual behavior. These pixels present no barrier to edge detection experiments and should, in fact, be accurately delineated.

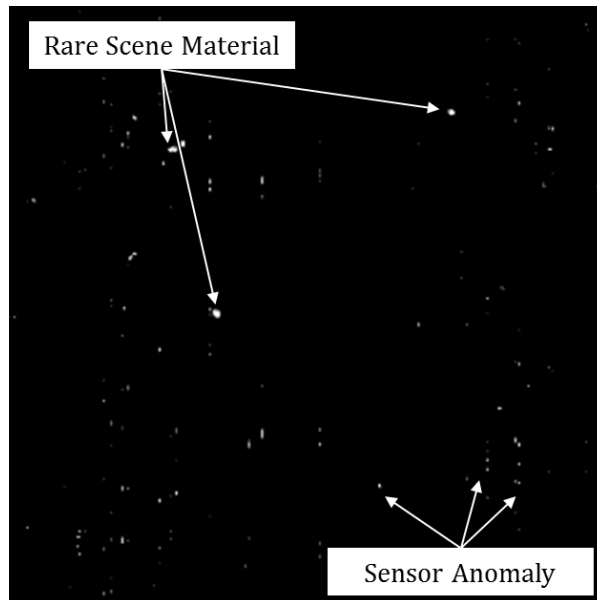


Figure 201: RX Anomaly Plane for Granite NIR/SWIR Hypercube

The RX plane reveals hundreds of sensor anomalies throughout the scene, however. Most sensor anomalies appear as single pixels or vertically linear arrangements of two to five pixels, and contain obvious flaws in their estimated reflectance curves. For example, consider Figure 202, which presents a series of anomalous spectra characterized by erroneous spiky behavior affecting only a single band at a time – spectral behavior that is inconsistent with all natural materials and most manmade materials in the NIR/SWIR. Notice that in every case, the spectral anomaly affects only a single band at a time but that it can occur at various wavelengths, as well, which is characteristic of HSI focal plane anomalies. The most likely source of the anomalies is intermittent element failure along the focal plane, an affliction common to HSI sensors. The upshot of the widespread sensor anomalies is that this dissertation’s discontinuity-based edge detectors likely will generate false alarms at these pixels, which presents a manageable barrier to

accuracy measurements since anomalies' positions are known. Ultimately, since the spectral anomalies are confined to only one band per 162-band spectrum, however, they do not present a material barrier to the edge detection experiments.

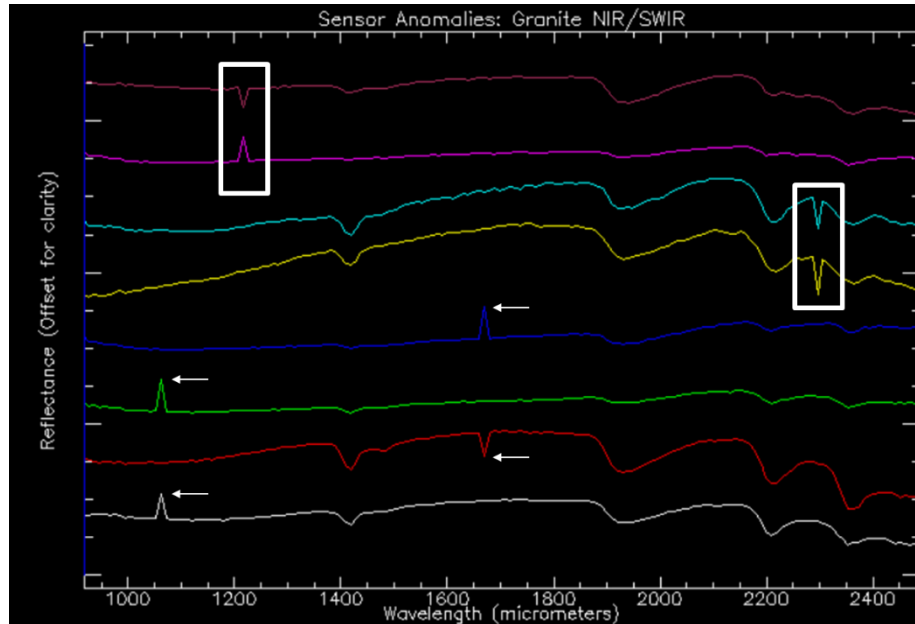


Figure 202: Single-Band Sensor Anomalies in Granite NIR/SWIR Hypercube

With the preprocessing component complete, the compression component begins with both a PCA and an MNF transformation. Figure 203 and Figure 204 present Step 1 and 2 of the compression component, a plot of the key PCA bands and MNF bands, respectively. As shown, the optimal PCA threshold occurs at PCA band 3, after which very little diagnostic spectral information is available. Therefore, Step 3 of the PCA compression establishes the optimal threshold at PCA band 3. Similarly, the optimal MNF threshold occurs at MNF band 5, after which the bands contain mostly noise.

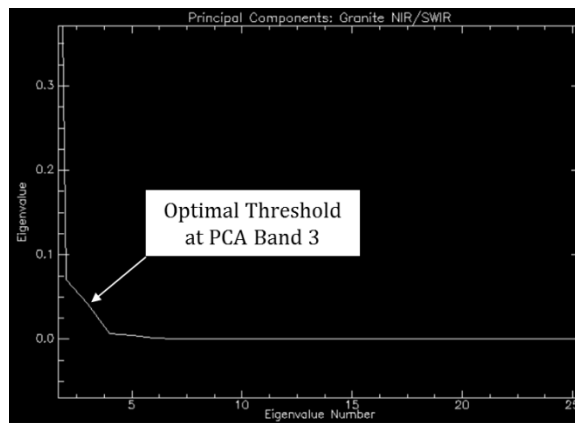


Figure 203: Optimal Threshold for PCA Cube, Granite NIR/SWIR

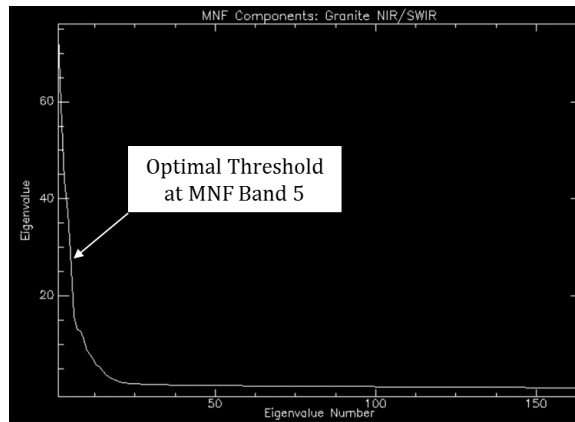


Figure 204: Optimal Threshold for MNF Cube, Granite NIR/SWIR

At the conclusion of the preprocessing and compression components, the reflectance, full PCA, compressed PCA, full MNF and compressed MNF cubes are ready for the edge detection component. The reflectance cube also is ready for the Roberts and Sobel comparison tests. As seen in Figure 198, the preprocessing and compression components yielded high-quality HSI data from which the Di Zenzo-based gradient edge detector generated consistent, interpretable results.

Ground-Based – South African Core Samples

The fourth gradient-based edge detection experiment on ground-based hyperspectral data also aligns to mineral mapping applications. This experiment uses high-spatial resolution NIR/SWIR imagery of six South African geologic core samples arranged within the same image plane. Specifically, this experiment tests the algorithm against five distinct datasets: a 234-band reflectance cube, a 3-band compressed PCA cube, the full 234-band PCA cube, a 5-band compressed MNF cube, and the full 234-band MNF cube. For comparison, this test also executes the Roberts operator and the Sobel operator against the full South African NIR/SWIR reflectance cube. Figure 205 presents samples of the seven experiments for the South African Core Sample NIR/SWIR data, and Appendix A contains the full spatial extent for each test.

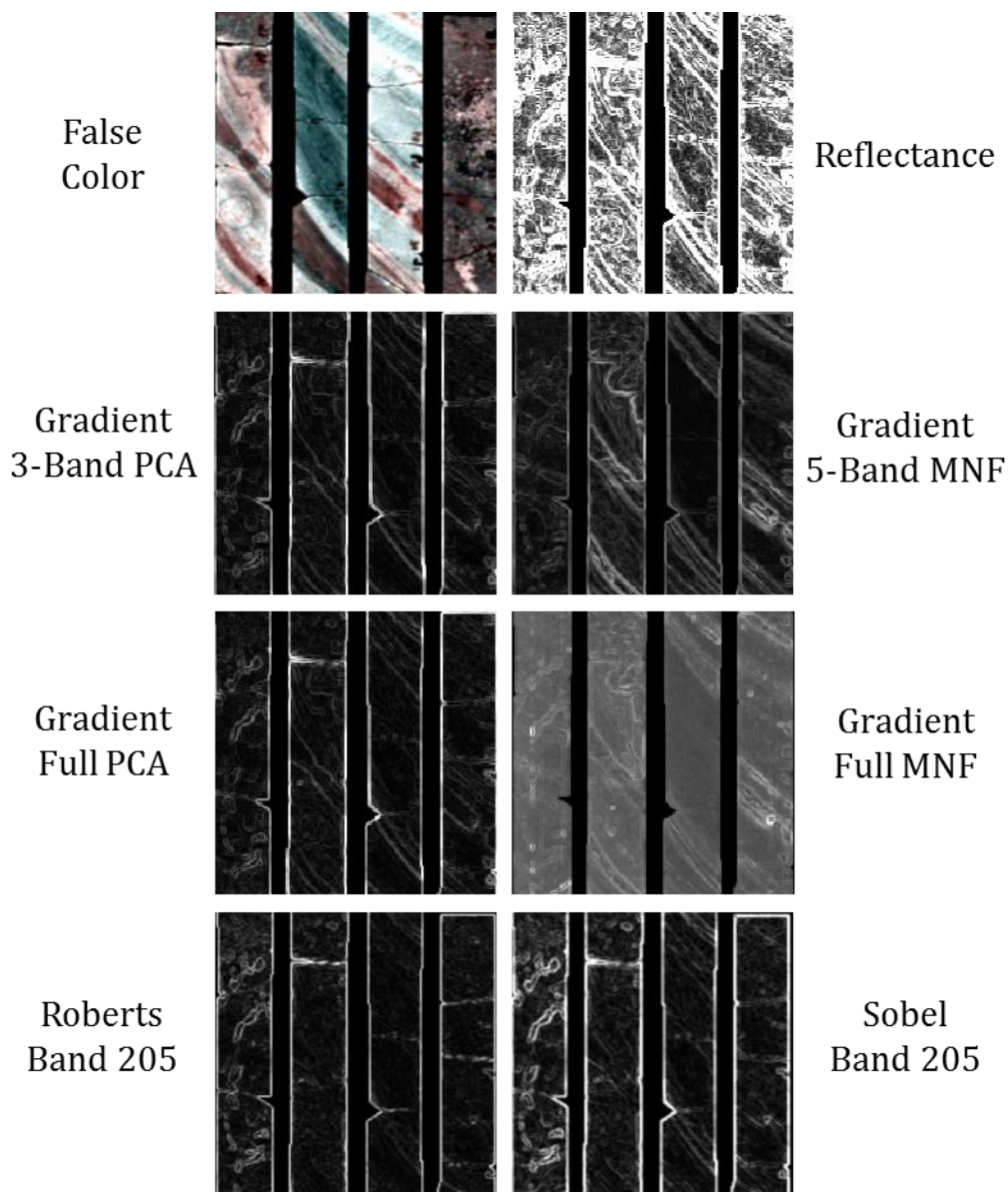


Figure 205: Gradient Experiment for South African Core Sample Ground-Based NIR/SWIR Data, Unstretched

The methodology's first step, data exploration, indicates that the South African core data is well-calibrated and of good quality across all channels, and is already converted to reflectance. Figure 206 presents the data exploration results, which indicate that similar minerals are rendered similarly in reflectance space. Specifically, note how

closely clustered the pixels are for specific mineral types. Also, note that low grade noise is present throughout the data, and note the noisy bands between 1000nm and 1100nm. While the noise is pervasive, it likely is not strong enough to present a meaningful barrier to edge detection experiments.

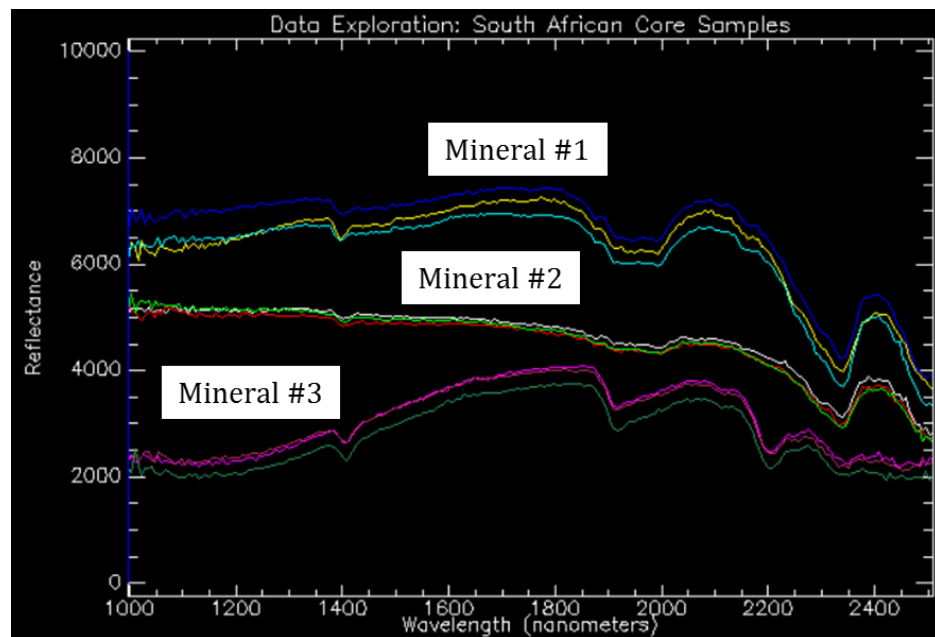


Figure 206: Data Exploration for the South African Core Sample Hypercube

The second methodological step requires a determination as to whether the HSI data are in reflectance or in radiance. As seen in Figure 206, the South African Core Sample data is already in reflectance, therefore QUAC is unnecessary for this dataset. Step 3 scales the reflectance dataset from 0.0 to 1.0. Step 4, bad band removal, also is unnecessary since the dataset contains no bad bands, and Step 5, examine the reflectance data, is also unnecessary given the reflectance analysis in Figure 193.

Figure 207 presents the results of Step 6, SMACC endmember extraction. The SMACC results indicate that various minerals dominate the scene, as expected. No saturation is evident in the scene, and no unusual spectra appear in the SMACC endmembers. The successful SMACC endmember extraction also reinforces the assessment that the low-grade noise across all channels is unlikely to disrupt the edge detection experiments, most likely because the noise is equally distributed across all channels and materials and is therefore not falsely unique to any region, material or wavelength subset. Overall, the SMACC processing indicates that the South African Core Sample dataset is well-behaved and free of irregularities that could significantly distort edge detection testing.

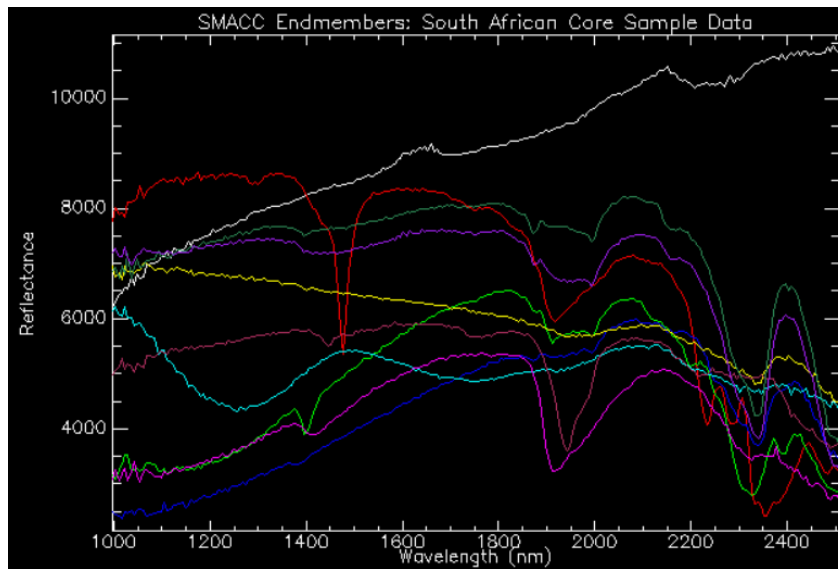


Figure 207: SMACC Endmembers for the South African Core Sample NIR/SWIR Hypercube

The preprocessing component's final step generates an RX anomaly plane as a final check on data quality and scene behavior. As seen in Figure 208, the RX processing detected no disruptive anomalies. The scattered weak anomalies along the lower side of the image are likely attributable to sensor anomalies since they are arrayed linearly along the edge of a core sample and are characterized by single-band spike anomalies similar to those seen in Figure 202 for the Granite NIR/SWIR hypercube. RX also identified rare minerals relative to the scene, as expected. Ultimately, the minor sensor anomalies and scattered rare minerals present no barrier to rigorous edge detection testing.

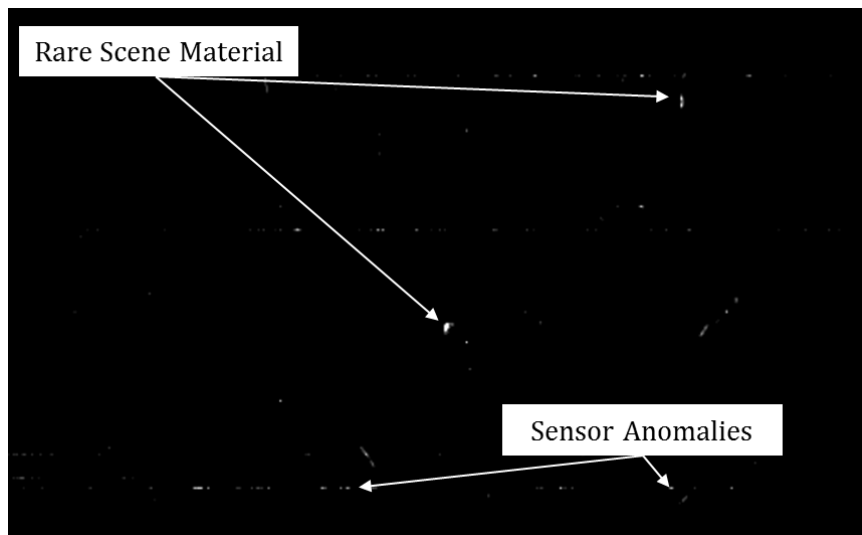


Figure 208: RX Anomaly Plane for South African Core Sample NIR/SWIR Hypercube

With the preprocessing component complete, the compression component begins with both a PCA and an MNF transformation. Figure 209 and Figure 210 present Step 1 and 2 of the compression component, a plot of the key PCA bands and MNF bands,

respectively. As shown, the optimal PCA threshold occurs at PCA band 3, after which very little diagnostic spectral information is available. Therefore, Step 3 of the PCA compression establishes the optimal threshold at PCA band 3. Similarly, the optimal MNF threshold occurs at MNF band 5, after which the bands contain mostly noise.

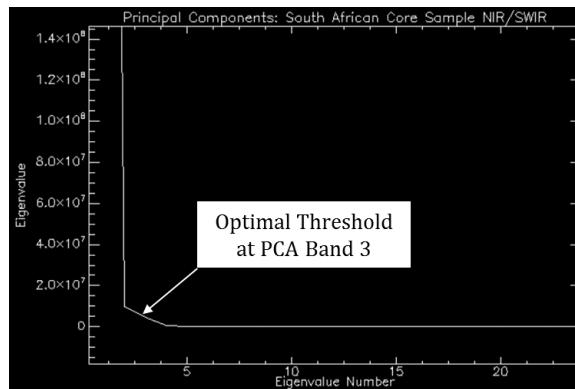


Figure 209: Optimal Threshold for PCA Cube, South African Core Sample NIR/SWIR

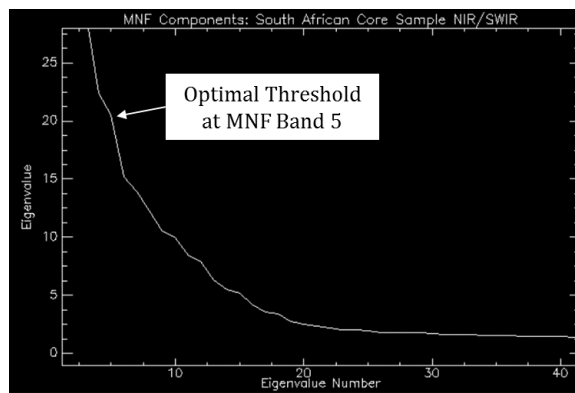


Figure 210: Optimal Threshold for MNF Cube, South African Core Sample NIR/SWIR

At the conclusion of the preprocessing and compression components, the reflectance, full PCA, compressed PCA, full MNF and compressed MNF cubes are ready for the edge detection component. The reflectance cube also is ready for the Roberts and Sobel comparison tests. As seen in Figure 205, the preprocessing and compression components yielded high-quality HSI data from which the Di Zenzo-based gradient edge detector generated consistent, interpretable results.

Ground-Based – Aluminum Panel

The fifth and final gradient-based edge detection experiment on ground-based hyperspectral data addresses the aluminum aircraft panel possibly traceable to Amelia Earhart's Lockheed Electra. This experiment aligns to the growing field of using HSI instruments for material analysis, and uses high-spatial resolution VNIR imagery of a riveted aluminum aircraft panel recovered on the Pacific island of Nikumaroro in 1991. Specifically, this experiment tests the algorithm against five distinct datasets: a 103-band reflectance cube, a 2-band compressed PCA cube, the full 103-band PCA cube, a 3-band compressed MNF cube, and the full 103-band MNF cube. For comparison, this test also executes the Roberts operator and the Sobel operator against the full Aluminum Aircraft Panel VNIR reflectance cube. Figure 211 presents samples of the seven experiments for the Aluminum Aircraft Panel data, and Appendix A contains the full spatial extent for each test.

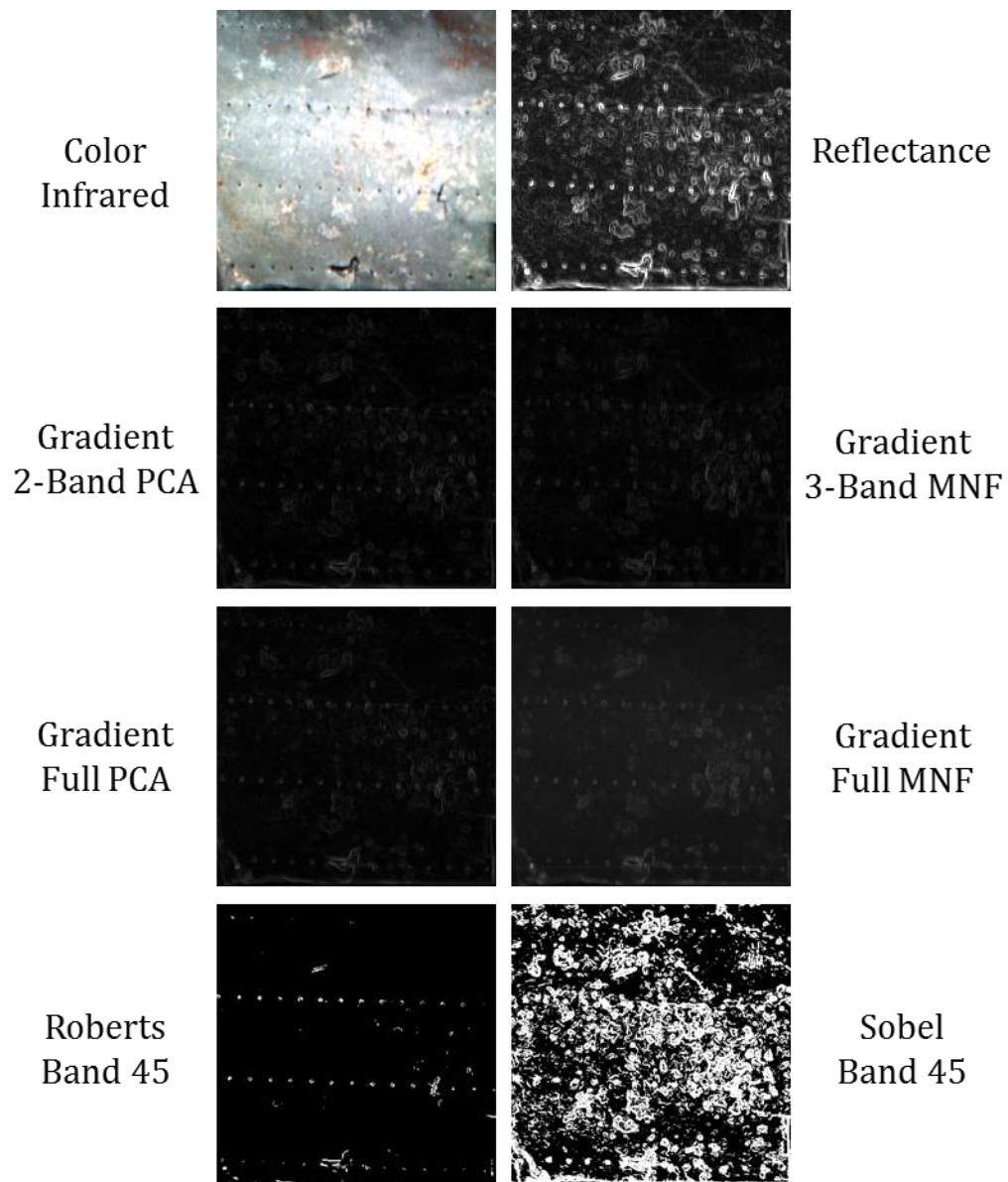


Figure 211: Gradient Experiment for Aluminum Aircraft Panel Ground-Based VNIR Data, Unstretched

The methodology's first step, data exploration, indicates that the SOC710 VNIR data is well-calibrated and of good quality across most channels, and is already converted to reflectance. Figure 212 presents the data exploration results, which indicate that similar regions are rendered similarly in reflectance space. Specifically, note how closely

clustered the pixels are for rusted areas, brightly illuminated areas and the regions on the panel. Also, note that the SOC710 generated significant sensor noise between 377nm and 437nm and between 982nm and 1043nm. The noise is pervasive and strong and would likely present a barrier to accurate edge detection experiments, indicating that Step 4 of the preprocessing component should remove the bad bands.

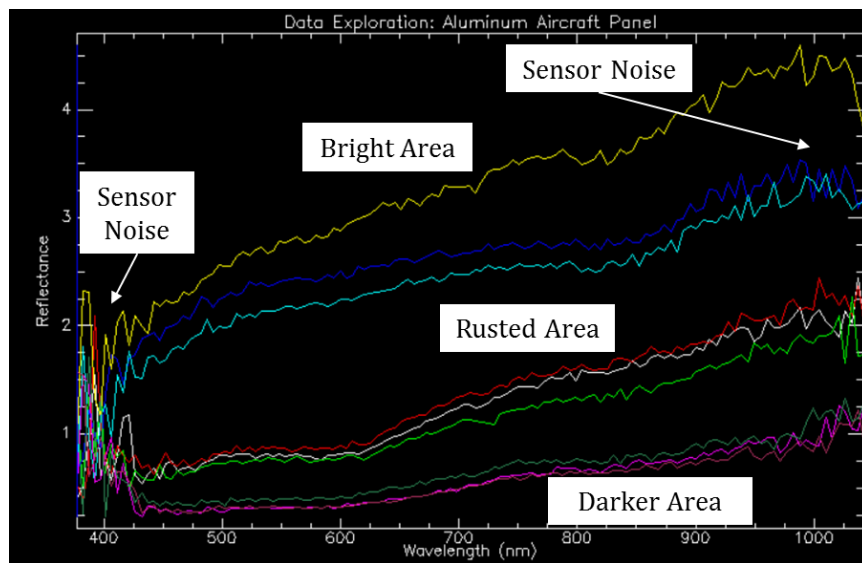


Figure 212: Data Exploration for the Aluminum Aircraft Panel Hypercube

The second methodological step requires a determination as to whether the HSI data are in reflectance or in radiance. As seen in Figure 212, the Aluminum Aircraft Panel data is already in reflectance, therefore QUAC is unnecessary for this dataset. Step 3 scales the reflectance dataset from 0.0 to 1.0. Step 4, bad band removal, also is necessary to remove the bad bands at the edges of the focal plane. Specifically, 13 bad bands were removed between 377nm and 437nm, and 12 bad bands were removed

between 982nm and 1043nm, resulting in a reflectance cube comprised of 103 bands spanning the wavelengths between 442 and 977nm. Figure 213 presents sample spectra from the resulting 103-band reflectance cube. Note the smoother consistency among the shortest and longest wavelengths retained in the bad band-removed reflectance cube, which results in a reflectance cube optimized for edge detection experiments.

Finally, Step 5, examine the reflectance data, has already been accomplished given the reflectance analysis in Figure 212.

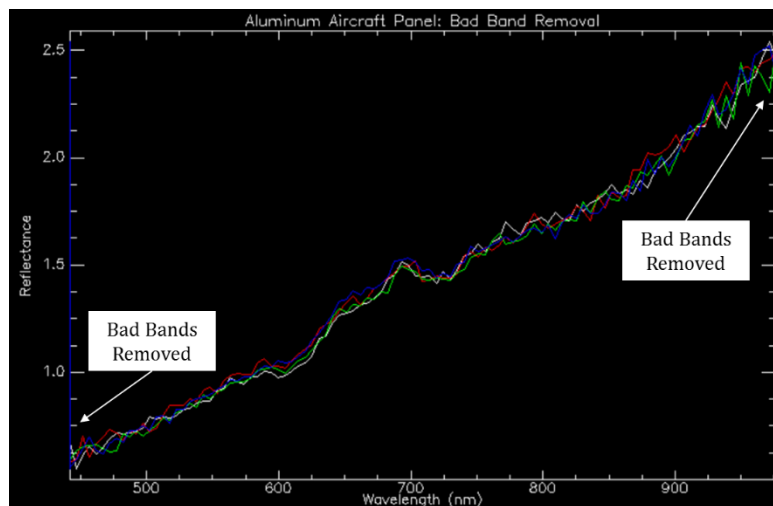


Figure 213: Aluminum Aircraft Panel Bad Band Removal

Figure 214 presents the results of Step 6, SMACC endmember extraction, as executed against the compressed 103-band reflectance cube. The SMACC results indicate that metal spectra dominate the scene, as expected. No saturation is evident in the scene, and no unusual spectra appear in the SMACC endmembers. Overall, the

SMACC processing indicates that the Aluminum Aircraft Panel dataset is well-behaved and free of irregularities that could disrupt edge detection testing.

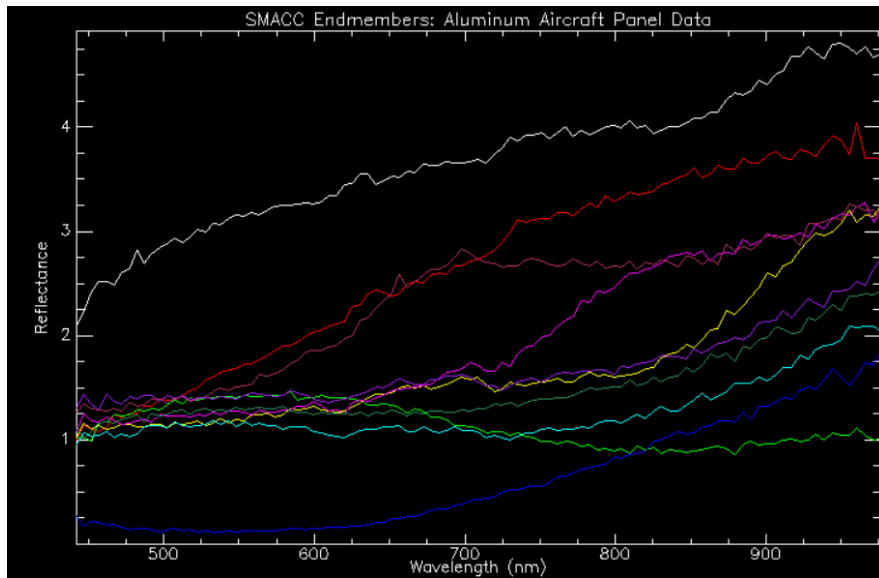


Figure 214: SMACC Endmembers for the Aluminum Aircraft Panel VNIR Hypercube

The preprocessing component's final step generates an RX anomaly plane as a final check on data quality and scene behavior. As seen in Figure 215, the RX processing detected hundreds of anomalous pixels, most of which are concentrated within a brightly illuminated portion of the panel. An examination of the anomalous pixels indicated that they are illumination anomalies attributable to the uneven illumination across the parabolic surface of the panel. The RX plane's anomalous pixels are not materially different from their non-anomalous neighbors and only appear as such due to the irregular illumination of the incident light. Additionally, a few scattered unusual pixels are present within the scene, but they do not appear in disruptive volumes or patterns.

Ultimately, the minor illumination anomalies and scattered unusual pixels present no barrier to rigorous edge detection testing.

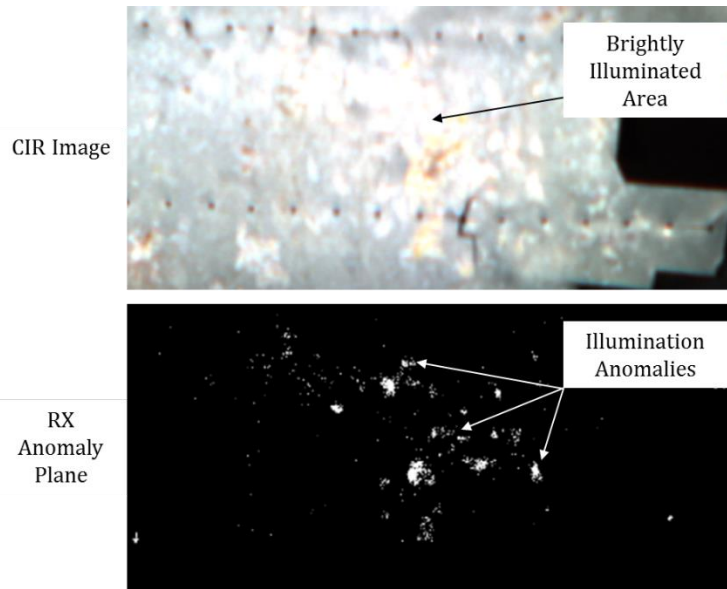


Figure 215: RX Anomaly Results for Aluminum Aircraft Panel VNIR Hypercube - True Color Bands 18, 35, 53

With the preprocessing component complete, the compression component begins with both a PCA and an MNF transformation. Figure 216 and Figure 217 present Step 1 and 2 of the compression component, a plot of the key PCA bands and MNF bands, respectively. Both PCA and MNF transforms used the 103-band compressed reflectance cube as input. As shown, the optimal PCA threshold occurs at PCA band 2, after which very little diagnostic spectral information is available. Therefore, Step 3 of the PCA compression establishes the optimal threshold at PCA band 2. Similarly, the optimal MNF threshold occurs at MNF band 3, after which the bands contain mostly noise.

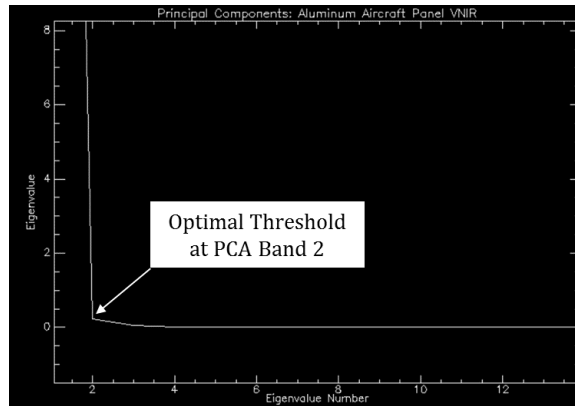


Figure 216: Optimal Threshold for PCA Cube, Aluminum Aircraft Panel VNIR

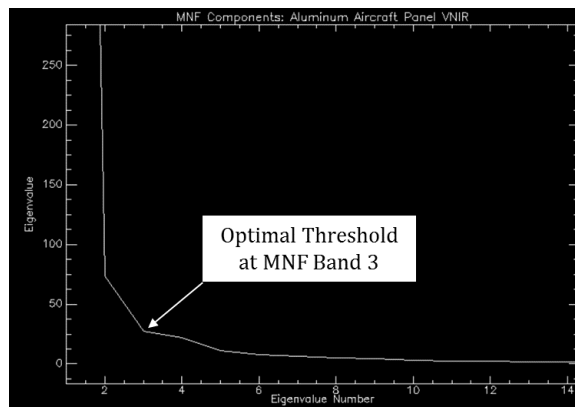


Figure 217: Optimal Threshold for MNF Cube, Aluminum Aircraft Panel VNIR

At the conclusion of the preprocessing and compression components, the reflectance, full PCA, compressed PCA, full MNF and compressed MNF cubes are ready for the edge detection component. The reflectance cube also is ready for the Roberts and Sobel comparison tests. As seen in Figure 211, the preprocessing and compression

components yielded high-quality HSI data from which the Di Zenzo-based gradient edge detector generated consistent, interpretable results.

Microscene – Rare Target on Sand

The first gradient-based edge detection experiment on microscene hyperspectral data uses Pika II VNIR imagery of a complex microscene on sand. This test supports trace chemical detection HSI applications due to the presence of a rare target in a complex background. Specifically, this experiment tests the algorithm against five distinct datasets: a 74-band reflectance cube, a 3-band compressed PCA cube, the full 74-band PCA cube, a 5-band compressed MNF cube, and the full 74-band MNF cube. For comparison, this test also executes the Roberts operator and the Sobel operator against the full Rare Target on Sand reflectance cube. Figure 218 presents samples of the seven experiments for the Rare Target on Sand data, and Appendix A contains the full spatial extent for each test.

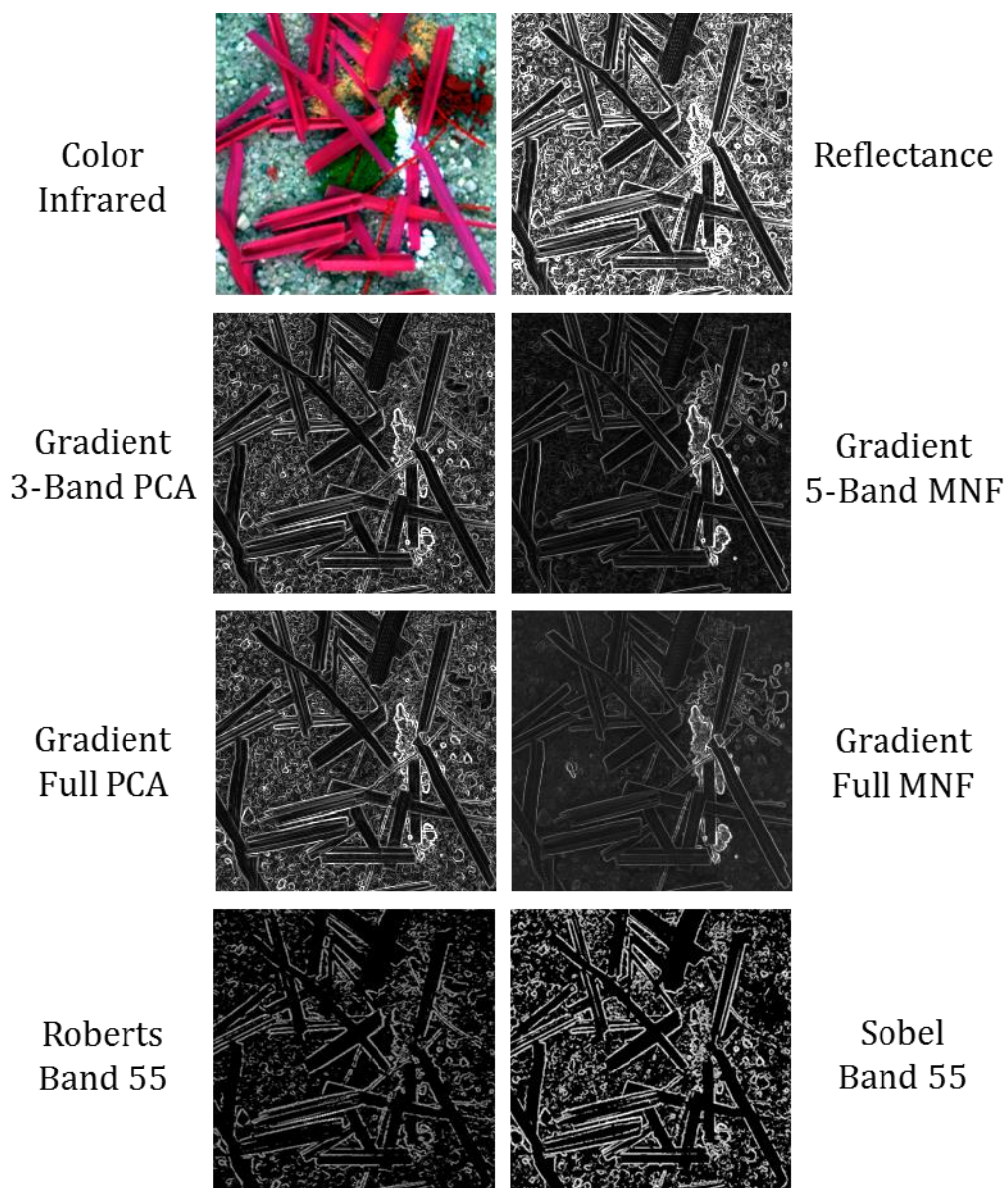


Figure 218: Gradient Experiment for Rare Target on Sand VNIR Data, Unstretched

The methodology's first step, data exploration, indicates that the Pika II VNIR data is well-calibrated and of good quality across all channels, and is already converted to reflectance. Figure 219 presents the data exploration results, which indicate that similar materials (e.g., vegetation, sand, rare target, etc.) are rendered similarly in reflectance

space. Specifically, note how closely clustered the pixels are for the rare target. The vegetation spectra are spaced normally, as well, with the grass clipping spectra presenting a strong reflectance increases in the NIR. Additionally, note the tight spacing among mixed pixels containing rare target occluded by vegetation, which appear as a spectral mixture of vegetation absorption features and absorption features attributable to the rare target.

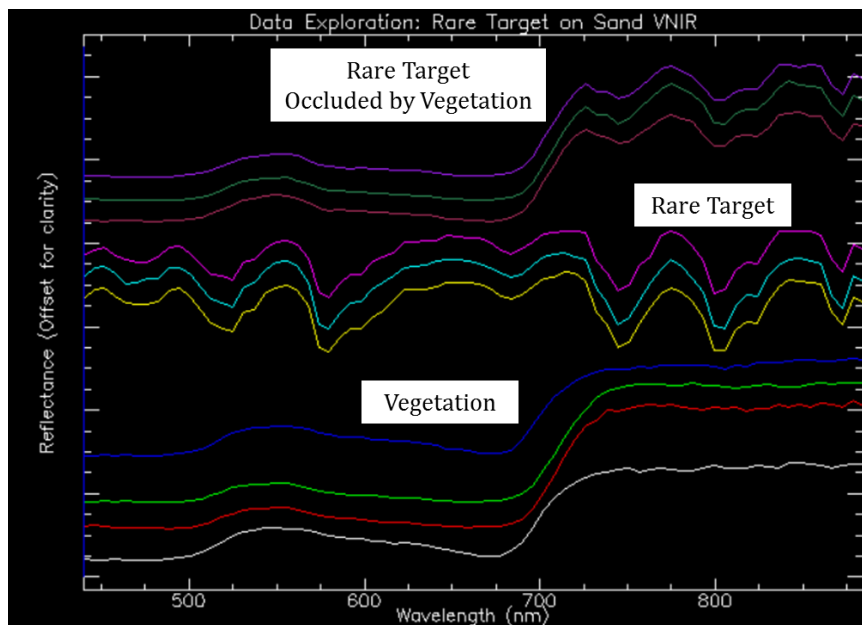


Figure 219: Data Exploration for the Rare Target on Sand Hypercube

The second methodological step requires a determination as to whether the HSI data are in reflectance or in radiance. As seen in Figure 219, the Pika II data has already been converted to high-quality estimated reflectance, therefore QUAC is unnecessary for this dataset. Step 3 scales the Rare Target on Sand reflectance dataset from 0.0 to 1.0.

Step 4, bad band removal, is unnecessary since the dataset contains no bad bands, and Step 5, examine the reflectance data, is also unnecessary given the reflectance analysis in Figure 219.

Figure 220 presents the results of Step 6, SMACC endmember extraction. The SMACC results indicates that routine materials like bare earth and healthy vegetation are easily distinguishable in reflectance space – a key indicator of a healthy reflectance dataset. Also, note that SMACC extracted the rare target spectra, the mixed rare target-vegetation pixels and other unique materials in the scene. Ultimately, the SMACC results indicate a healthy, well-behaved dataset free of saturation and disruptive irregularities.

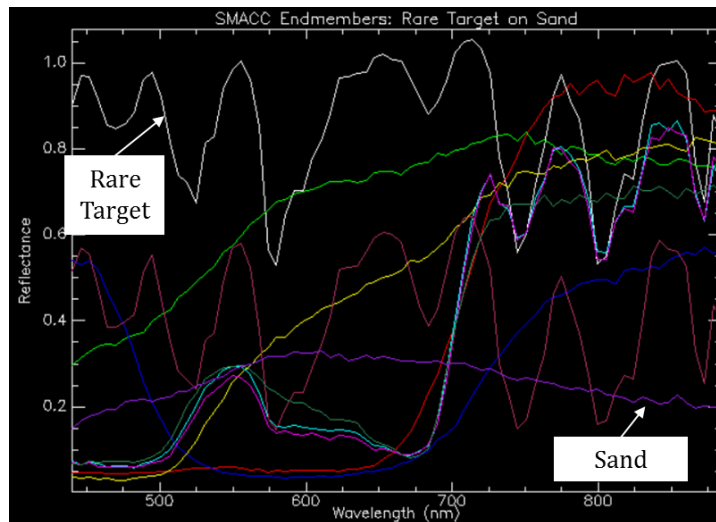


Figure 220: SMACC Endmembers for the Rare Target on Sand Hypercube

The preprocessing component's final step generates an RX anomaly plane as a final check on data quality and scene behavior. As seen in Figure 221, the RX processing detected few anomalies beyond the rare target pixels. No saturation or sensor noise was observed, and the RX results corroborate the exploration finding indicating that the data is high quality and well-suited for edge detection experiments.

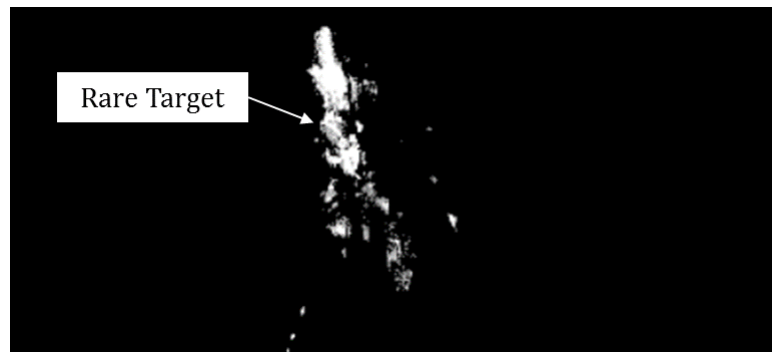


Figure 221: RX Anomaly Plane for Rare Target on Sand Hypercube

With the preprocessing component complete, the compression component begins with both a PCA and an MNF transformation. Figure 222 and Figure 223 present Step 1 and 2 of the compression component, a plot of the key PCA bands and MNF bands, respectively. As shown, the optimal PCA threshold occurs at PCA band 3, after which very little diagnostic spectral information is available. Therefore, Step 3 of the PCA compression establishes the optimal threshold at PCA band 3. Similarly, the optimal MNF threshold occurs at MNF band 5, after which the bands contain mostly noise.

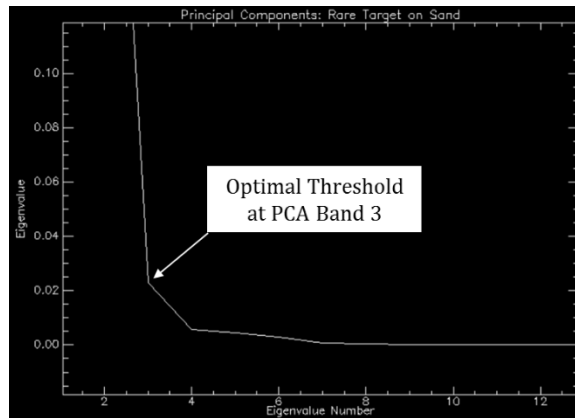


Figure 222: Optimal Threshold for PCA Cube, Rare Target on Sand VNIR

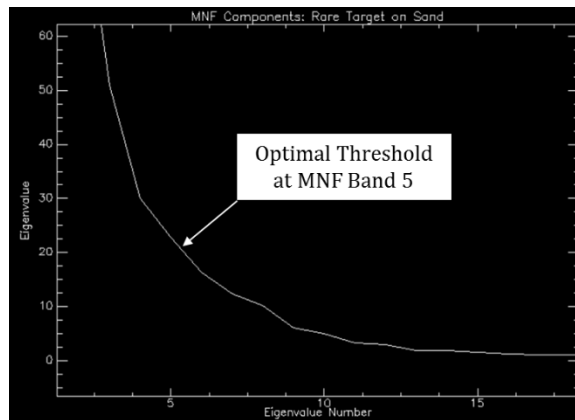


Figure 223: Optimal Threshold for MNF Cube, Rare Target on Sand VNIR

At the conclusion of the preprocessing and compression components, the reflectance, full PCA, compressed PCA, full MNF and compressed MNF cubes are ready for the edge detection component. The reflectance cube also is ready for the Roberts and Sobel comparison tests. As seen in Figure 218, the preprocessing and compression components yielded high-quality HSI data from which the Di Zenzo-based gradient edge detector generated consistent, interpretable results.

Microscene – Chemical Array

The second gradient-based edge detection experiment on microscene hyperspectral data uses 168-band HYPERSPEC NIR/SWIR imagery of a chemical array on sand. This test supports trace chemical detection HSI applications due to the presence of several rare targets on a simple background. Specifically, this experiment tests the algorithm against five distinct datasets: a 168-band reflectance cube, a 3-band compressed PCA cube, the full 168-band PCA cube, a 5-band compressed MNF cube, and the full 168-band MNF cube. For comparison, this test also executes the Roberts operator and the Sobel operator against the full Rare Target on Sand reflectance cube. Figure 224 presents samples of the seven experiments for the Chemical Array data, and Appendix A contains the full spatial extent for each test.

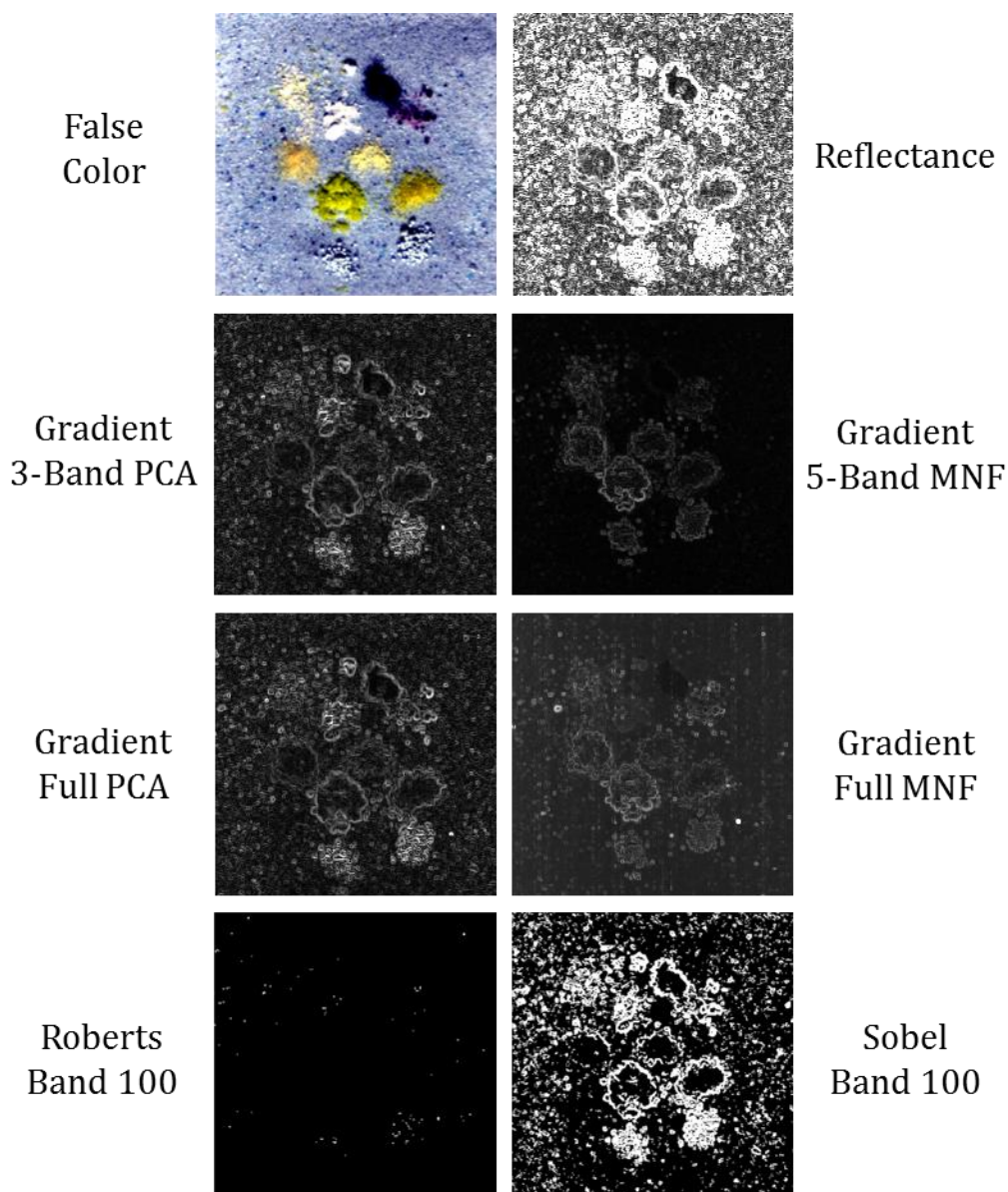


Figure 224: Gradient Experiment for Chemical Array NIR/SWIR Data, Unstretched

The methodology's first step, data exploration, indicates that the HYPERSPEC NIR/SWIR data is well-calibrated and of good quality across all channels, and is already converted to reflectance. Figure 225 presents the data exploration results, which indicate that similar materials (e.g., ammonium nitrate, iron, sand, etc.) are rendered similarly in

reflectance space. Specifically, note how closely clustered the pixels are for the chemicals. The background (i.e., sand) spectra are spaced normally, as well. Ultimately, data exploration indicates that the data is well-behaved and suitable for edge detection experiments. The significant spectral contrast between targets and the sand background also presents strong edges that should be readily discernable by the edge detectors.

The second methodological step requires a determination as to whether the HSI data are in reflectance or in radiance. As seen in Figure 225, the HYPERSPEC data has already been converted to high-quality estimated reflectance, therefore QUAC is unnecessary for this dataset. Step 3 scales the Chemical Array reflectance dataset from 0.0 to 1.0. Step 4, bad band removal, is unnecessary since the dataset contains no bad bands, and Step 5, examine the reflectance data, is also unnecessary given the reflectance analysis in Figure 225.

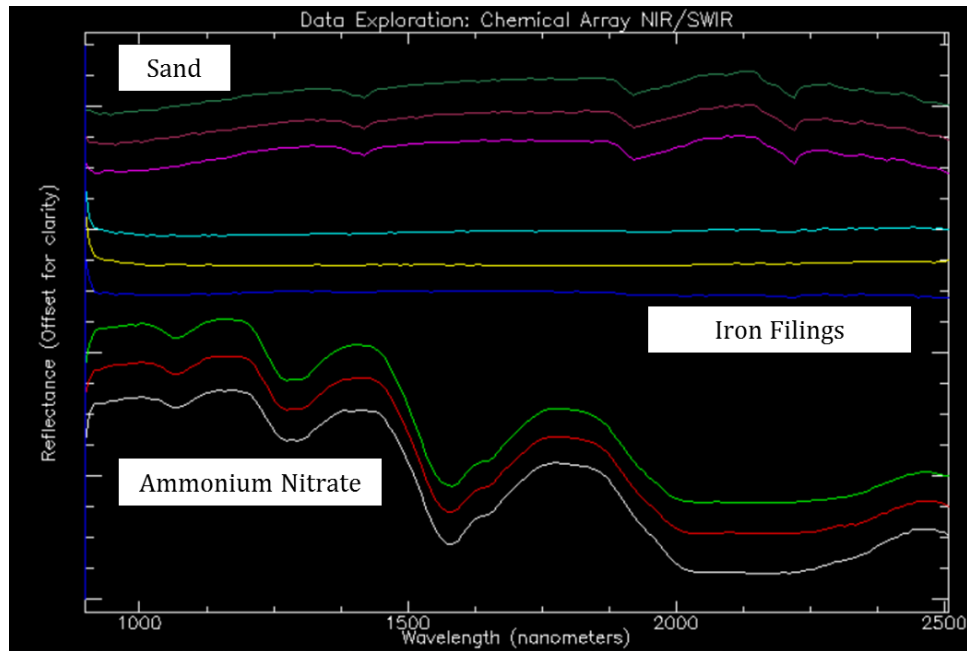


Figure 225: Data Exploration for the Chemical Array Hypercube

Figure 226 presents the results of Step 6, SMACC endmember extraction. The SMACC results indicate that the target chemicals are clearly distinguishable within hyperspace. Also, note that SMACC extracted irregular spectra possibly attributable to sensor anomalies or the etalon effect [282]. The sensor anomalies appear as sinusoidal curves of increasing brightness and are easily recognizable as sensor errors due to the regular error pattern. As long as the errors are confined to a small volume of scene pixels and do not appear along key edges of array chemicals, they will not disrupt the edge detection experiments. Given that only two sensor anomaly spectra appear in the top ten SMACC results, the irregularities are unlikely to be widespread. Ultimately, the SMACC results indicate a healthy, well-behaved dataset with a scattering of non-disruptive sensor anomalies.

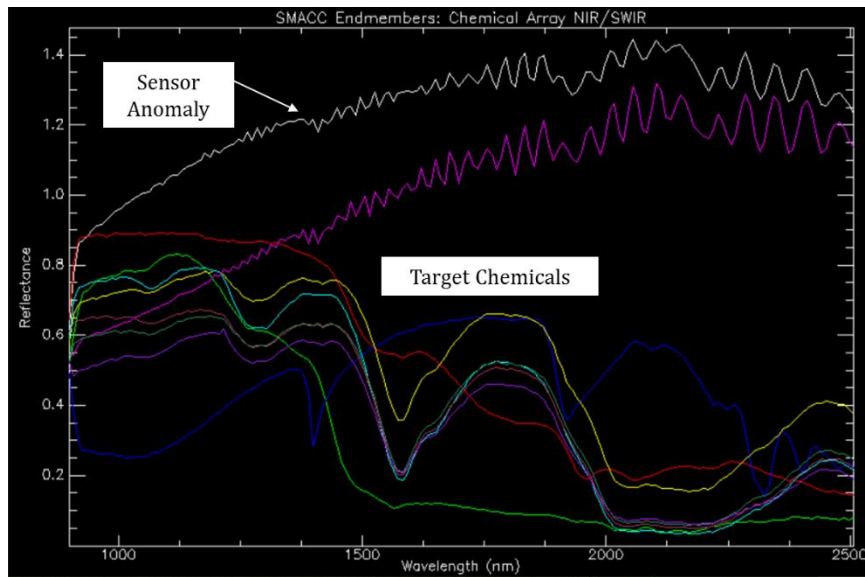


Figure 226: SMACC Endmembers for the Chemical Array Hypercube

The preprocessing component's final step generates an RX anomaly plane as a final check on data quality and scene behavior. As seen in Figure 227, the RX processing detected several anomalies, including the possible sensor anomalies or etalon effects identified in the SMACC processing, a few single-band sensor anomalies and several anomalies attributable to stray chemical grains that likely were inadvertently dropped during the construction of the microscene. As seen in Figure 227, the sensor anomalies are few and scattered and do not present a barrier to edge detection experiments. Additionally, the stray chemical grains present small, challenging targets for the edge detectors. Finally, note that unlike the RX results from the Rare Target on Sand dataset, RX did not alarm against the primary chemical deposits. This is most likely because the chemicals constitute a significant part of the scene and therefore are statistically part of the background. Ultimately, the RX results corroborate the data exploration and SMACC

results indicating that the data is of high quality with only a handful of non-disruptive sensor anomalies.

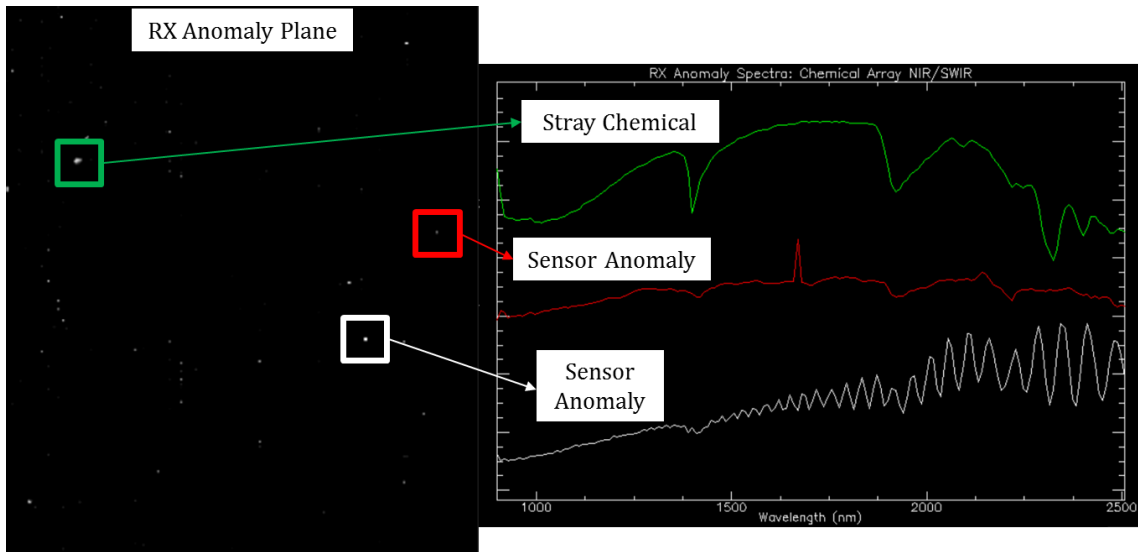


Figure 227: RX Anomaly Plane and Spectra for Chemical Array Hypercube

With the preprocessing component complete, the compression component begins with both a PCA and an MNF transformation. Figure 228 and Figure 229 present Step 1 and 2 of the compression component, a plot of the key PCA bands and MNF bands, respectively. As shown, the optimal PCA threshold occurs at PCA band 3, after which very little diagnostic spectral information is available. Therefore, Step 3 of the PCA compression establishes the optimal threshold at PCA band 3. Similarly, the optimal MNF threshold occurs at MNF band 5, after which the bands contain mostly noise.

At the conclusion of the preprocessing and compression components, the reflectance, full PCA, compressed PCA, full MNF and compressed MNF cubes are ready

for the edge detection component. The reflectance cube also is ready for the Roberts and Sobel comparison tests. As seen in Figure 224, the preprocessing and compression components yielded high-quality HSI data from which the Di Zenzo-based gradient edge detector generated consistent, interpretable results.

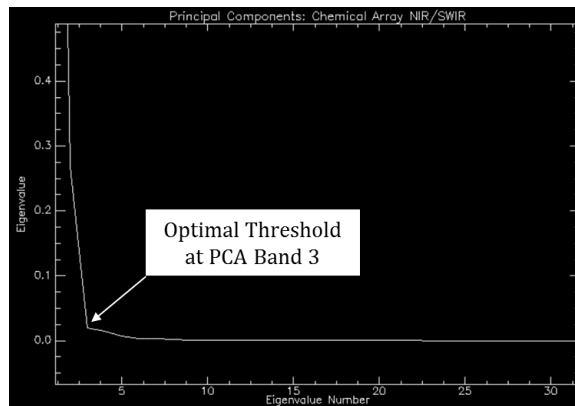


Figure 228: Optimal Threshold for PCA Cube, Chemical Array NIR/SWIR

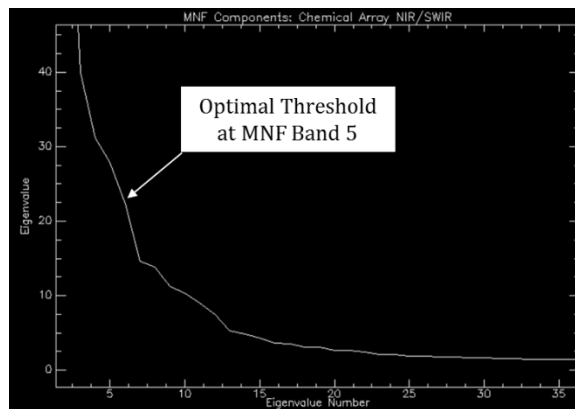


Figure 229: Optimal Threshold for MNF Cube, Chemical Array NIR/SWIR

Microscene – Cloth Threads

The third and final gradient-based edge detection experiment on microscene hyperspectral data uses 80-band Pika II VNIR imagery of a series of different color cloth threads arrayed on a sand background. Specifically, this experiment tests the algorithm against five distinct datasets: an 80-band reflectance cube, a 3-band compressed PCA cube, the full 80-band PCA cube, a 5-band compressed MNF cube, and the full 80-band MNF cube. For comparison, this test also executes the Roberts operator and the Sobel operator against the full Rare Target on Sand reflectance cube. Figure 230 presents samples of the seven experiments for the Cloth Thread data, and Appendix A contains the full spatial extent for each test.

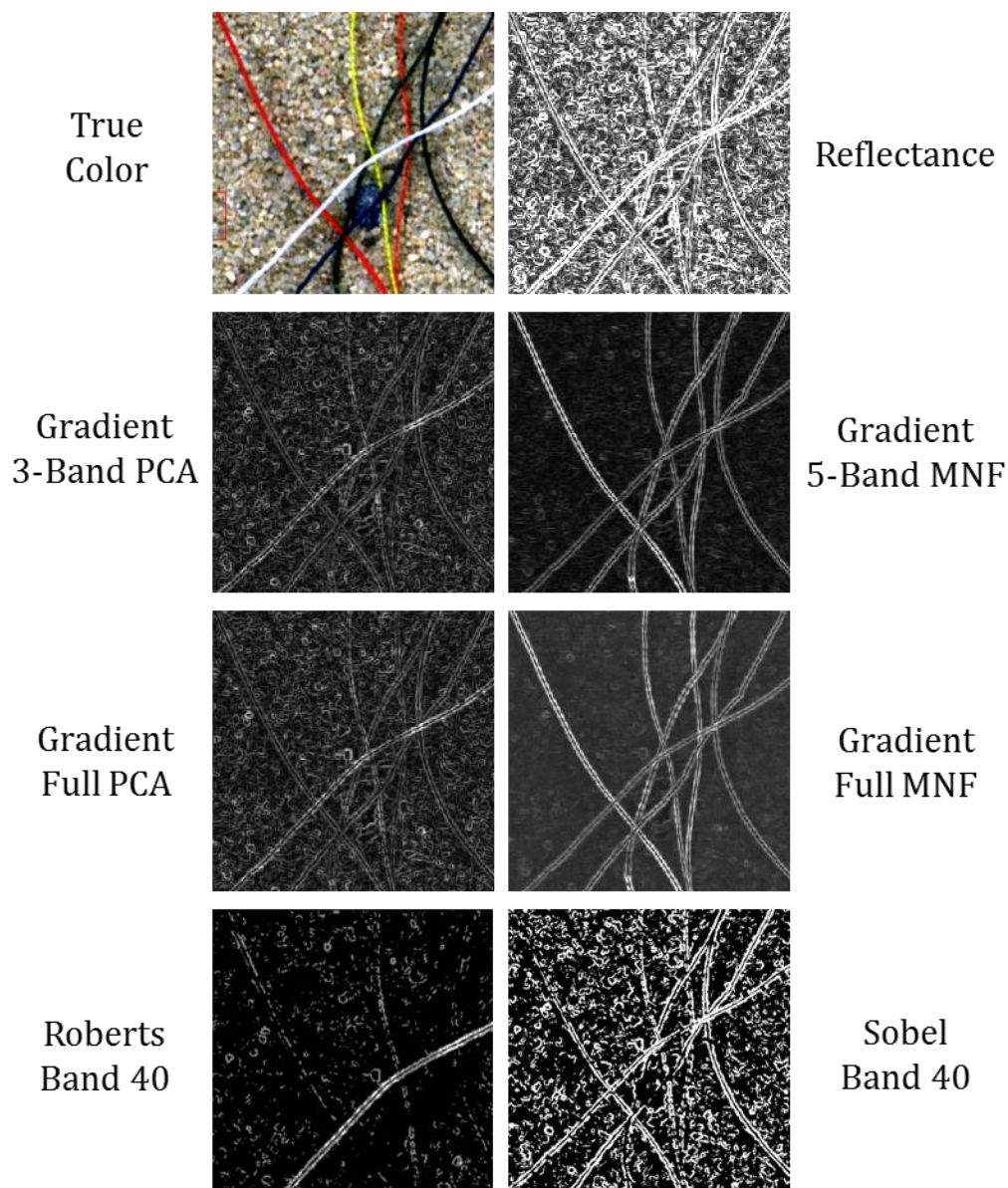


Figure 230: Gradient Experiment for Cloth Threads VNIR Data, Unstretched

The methodology's first step, data exploration, indicates that the Pika II VNIR data is well-calibrated and of good quality across all channels, and is already converted to reflectance. Figure 231 presents the data exploration results, which indicate that similar materials (e.g., red thread, yellow thread, sand, etc.) are rendered similarly in reflectance

space. Specifically, note how closely clustered the pixels are for each thread type. The background (i.e., sand) spectra are spaced normally, as well. Ultimately, data exploration indicates that the data is well-behaved and suitable for edge detection experiments. The significant spectral contrast between colored threads and the sand background also presents strong edges that should be readily discernable by the edge detectors.

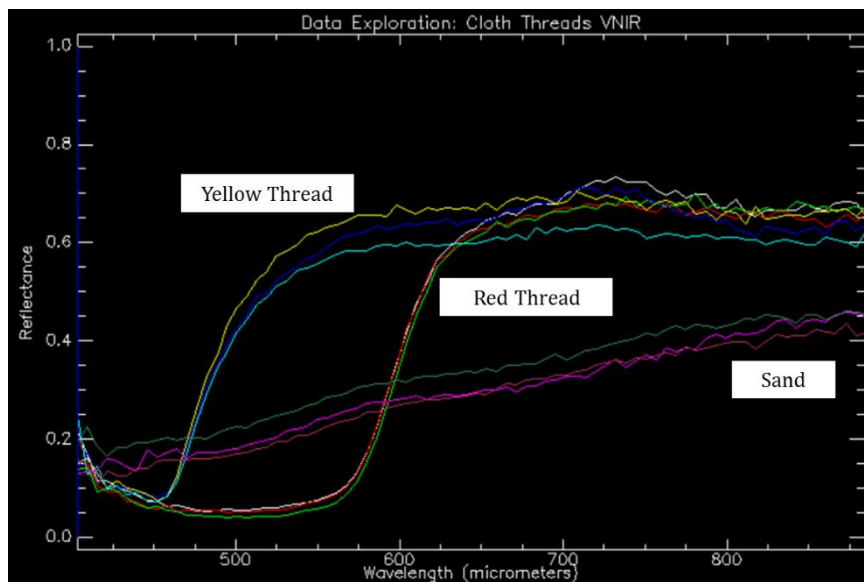


Figure 231: Data Exploration for the Cloth Thread Hypercube

The second methodological step requires a determination as to whether the HSI data are in reflectance or in radiance. As seen in Figure 231, the HYPERSPEC data has already been converted to high-quality estimated reflectance, therefore QUAC is unnecessary for this dataset. Step 3 scales the Cloth Thread reflectance dataset from 0.0 to 1.0. Step 4, bad band removal, is unnecessary since the dataset contains no bad bands,

and Step 5, examine the reflectance data, is also unnecessary given the reflectance analysis in Figure 231.

Figure 232 presents the results of Step 6, SMACC endmember extraction. The SMACC results indicate that the cloth threads are clearly distinguishable from the sand background, and that there is no saturation or irregular behavior evident within the scene. Ultimately, the SMACC results indicate a healthy, well-behaved dataset free of sensor anomalies.

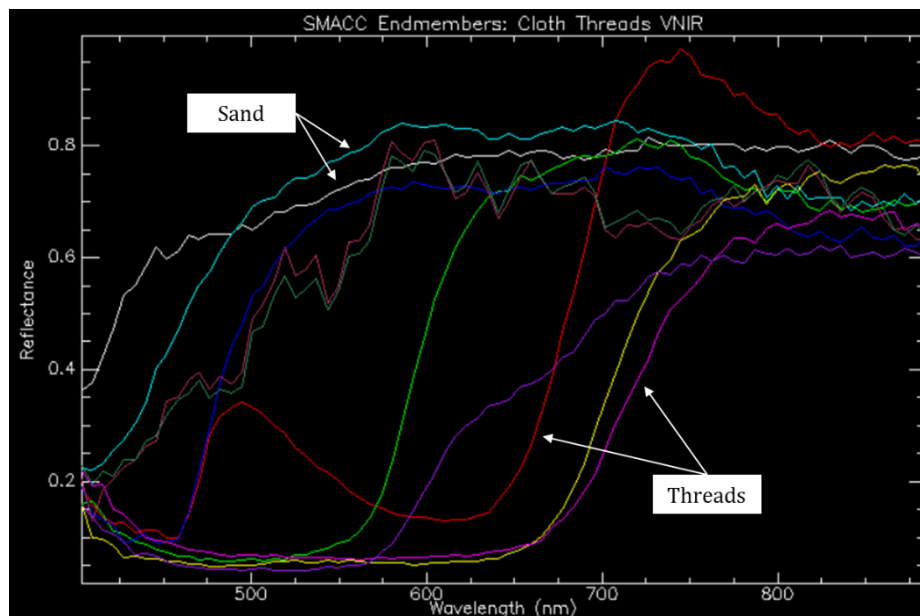


Figure 232: SMACC Endmembers for the Cloth Threads Hypercube

The preprocessing component's final step generates an RX anomaly plane as a final check on data quality and scene behavior. As seen in Figure 233, the RX processing detected very few anomalies, all of which are minor irregularities along the dark green

thread. No sensor anomalies or saturation was observed in the RX plane. Consistent with the data exploration and SMACC findings, the RX findings suggest a high-quality, well-behaved hyperspectral dataset suitable for edge detection testing.

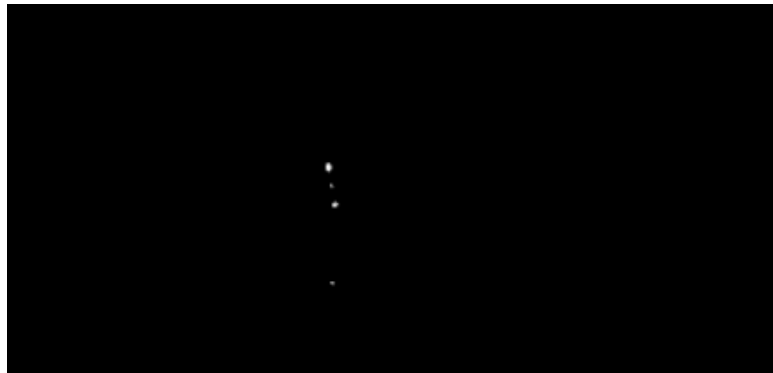


Figure 233: RX Anomaly Plane for Cloth Thread Hypercube

With the preprocessing component complete, the compression component begins with both a PCA and an MNF transformation. Figure 234 and Figure 235 present Step 1 and 2 of the compression component, a plot of the key PCA bands and MNF bands, respectively. As shown, the optimal PCA threshold occurs at PCA band 3, after which very little diagnostic spectral information is available. Therefore, Step 3 of the PCA compression establishes the optimal threshold at PCA band 3. Similarly, the optimal MNF threshold occurs at MNF band 5, after which the bands contain mostly noise.

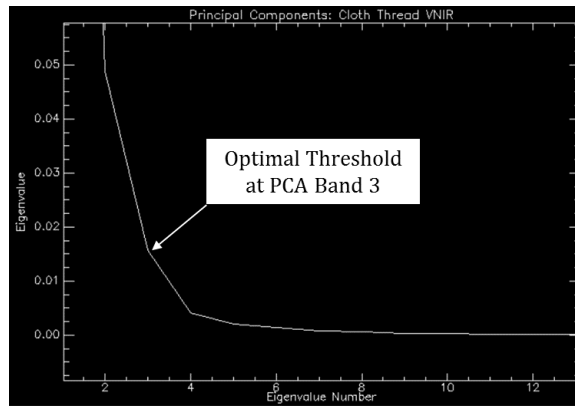


Figure 234: Optimal Threshold for PCA Cube, Cloth Threads VNIR

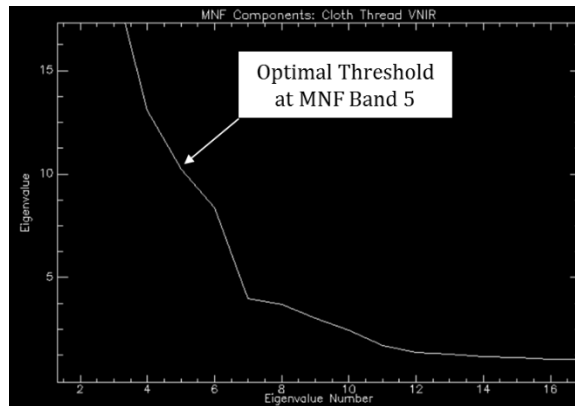


Figure 235: Optimal Threshold for MNF Cube, Cloth Threads VNIR

At the conclusion of the preprocessing and compression components, the reflectance, full PCA, compressed PCA, full MNF and compressed MNF cubes are ready for the edge detection component. The reflectance cube also is ready for the Roberts and Sobel comparison tests. As seen in Figure 230, the preprocessing and compression components yielded high-quality HSI data from which the Di Zenzo-based gradient edge detector generated consistent, interpretable results.

HySPADE Findings

This dissertation tests the new HySPADE edge detection algorithm against all 12 HSI datasets, including tests against reflectance and/or radiance cubes, PCA cubes of full and compressed depths and MNF cubes of full and compressed depths. The Experiments section presents samples from each test, the Analysis section examines key sections and draws scientific conclusions for each dataset and Appendix A presents the full spatial extent of each experiment.

Importantly, one of the initial findings was that the Otsu threshold failed to produce an optimal histogram stretch for the new HySPADE edge planes, as seen in the Reno hypercube example in Figure 236. The Otsu method produced suboptimal results against HySPADE edge planes due to the strongly bimodal distribution between HySPADE's background pixels (assigned a grayscale value of zero) and HySPADE's strong edge pixels as seen in Figure 237. This bimodal distribution forces the Otsu method to establish a threshold at a very low number in order to minimize the variance between the background pixel class and the edge pixel class, thereby resulting in the washed-out edge plane seen in Figure 236.

The washed-out appearance occurs because the Otsu threshold properly bins all background pixels into a zero grayscale value but cannot discriminate between the weakest HySPADE edge pixels and the strongest HySPADE edge pixels. In the Reno reflectance edge plane example, Otsu bins approximately 21,000 pixels into a grayscale value of zero, and approximately 171,000 edge pixels into a grayscale value of 255. This has the effect of binning any pixel containing any edge strength whatsoever into a grayscale value of 255, meaning that the weakest HySPADE edge pixels are rendered

identically to the strongest HySPADE edge pixels – a clearly suboptimal result.

Therefore, the new HySPADE edge planes require an alternate standardized stretching method to achieve optimal visualization.

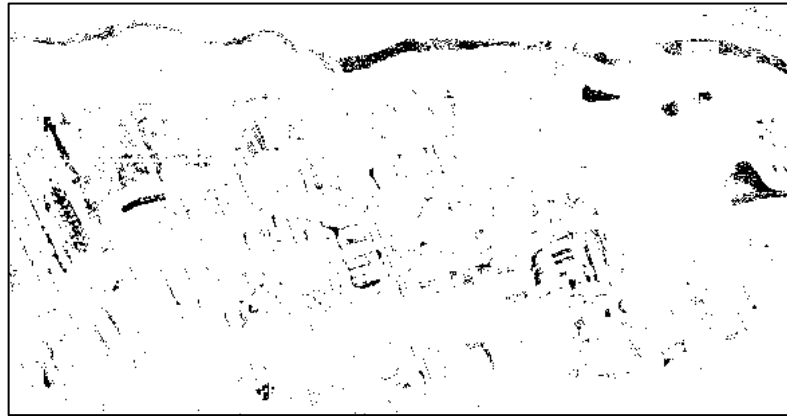


Figure 236: Suboptimal Results from Otsu Histogram Thresholding of the Reno Reflectance Edge Plane

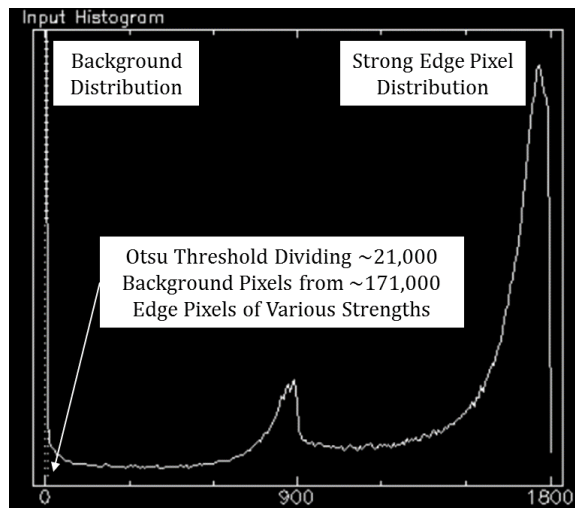


Figure 237: A Strong Bimodal Distribution Explains Suboptimal Otsu Thresholding Performance

In order to maintain rigor, each HySPADE edge plane's histogram is stretched by the same method that isolates the strongest edge pixels and binning them into a narrow range of grayscale values. This stretching method was chosen because it isolates only the strongest edge pixels while maintaining a sense of edge pixel strength within the strongest class of edge pixels. Specifically, each HySPADE edge plane histogram is linearly stretched with the minimum value established at the peak of the strong edge pixel distribution and the maximum value placed at the maximum grayscale value as seen in Figure 238. As seen in Figure 239, the optimized histogram stretch produces significantly improved results for the HySPADE edge planes.

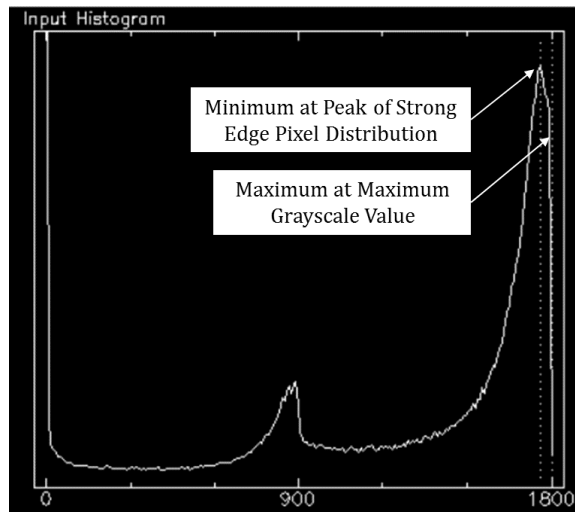


Figure 238: Optimal Histogram Stretch for HySPADE Edge Planes



Figure 239: Improved Results from Optimized Histogram Thresholding of the Reno Reflectance Edge Plane

Overhead – Reno, Nevada USA

The first HySPADE edge detection experiment uses the VNIR/SWIR Reno, NV USA hypercube. Specifically, this experiment tests the algorithm against five distinct datasets: a 356-band reflectance cube, a four-band compressed PCA cube, the full 356-band PCA cube, an eight-band compressed MNF cube, and the full 356-band MNF cube. The Results along with Sobel and Roberts comparison edge planes are shown in Figure 240.

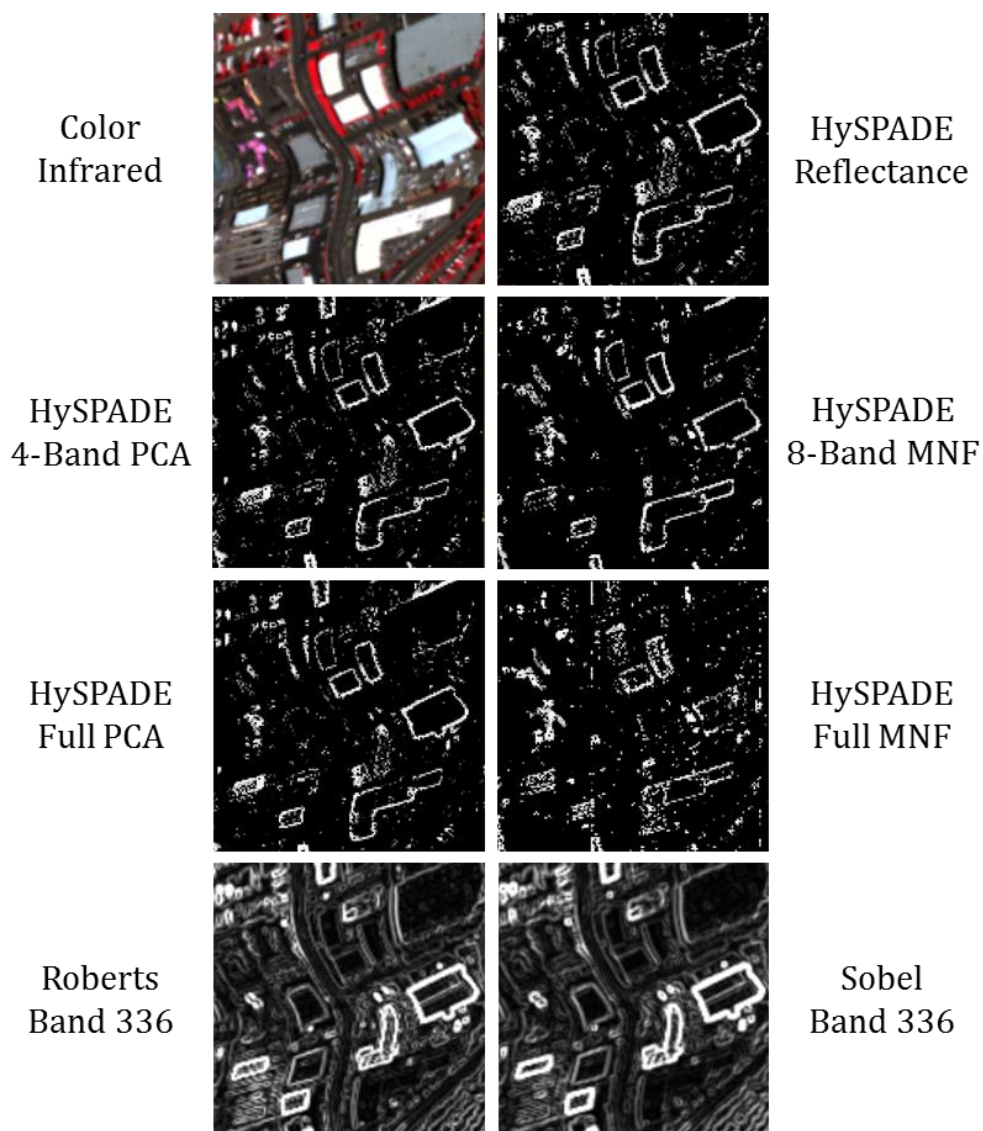


Figure 240: HySPADE Experiment for Reno, NV Overhead VNIR/SWIR Data, Linear Stretch of Strong Edge Pixels, Threshold at 40 Intermediate Planes from 0.10σ to 4.0σ

Overhead – Cuprite, Nevada USA

The second HySPADE edge detection experiment tests the four VNIR/SWIR flight lines covering Cuprite, NV USA. Specifically, this experiment tests the algorithm against five distinct datasets for each flight line: the full reflectance cube, a compressed

PCA cube, the full PCA cube, a compressed MNF cube, and the full MNF cube. For comparison, this test also executes the Roberts operator and the Sobel operator against the full reflectance cube for each flight line. Figure 241, Figure 242, Figure 243 and Figure 244 present samples of the seven experiments for each flight line, and Appendix A contains the full spatial extent for each test.

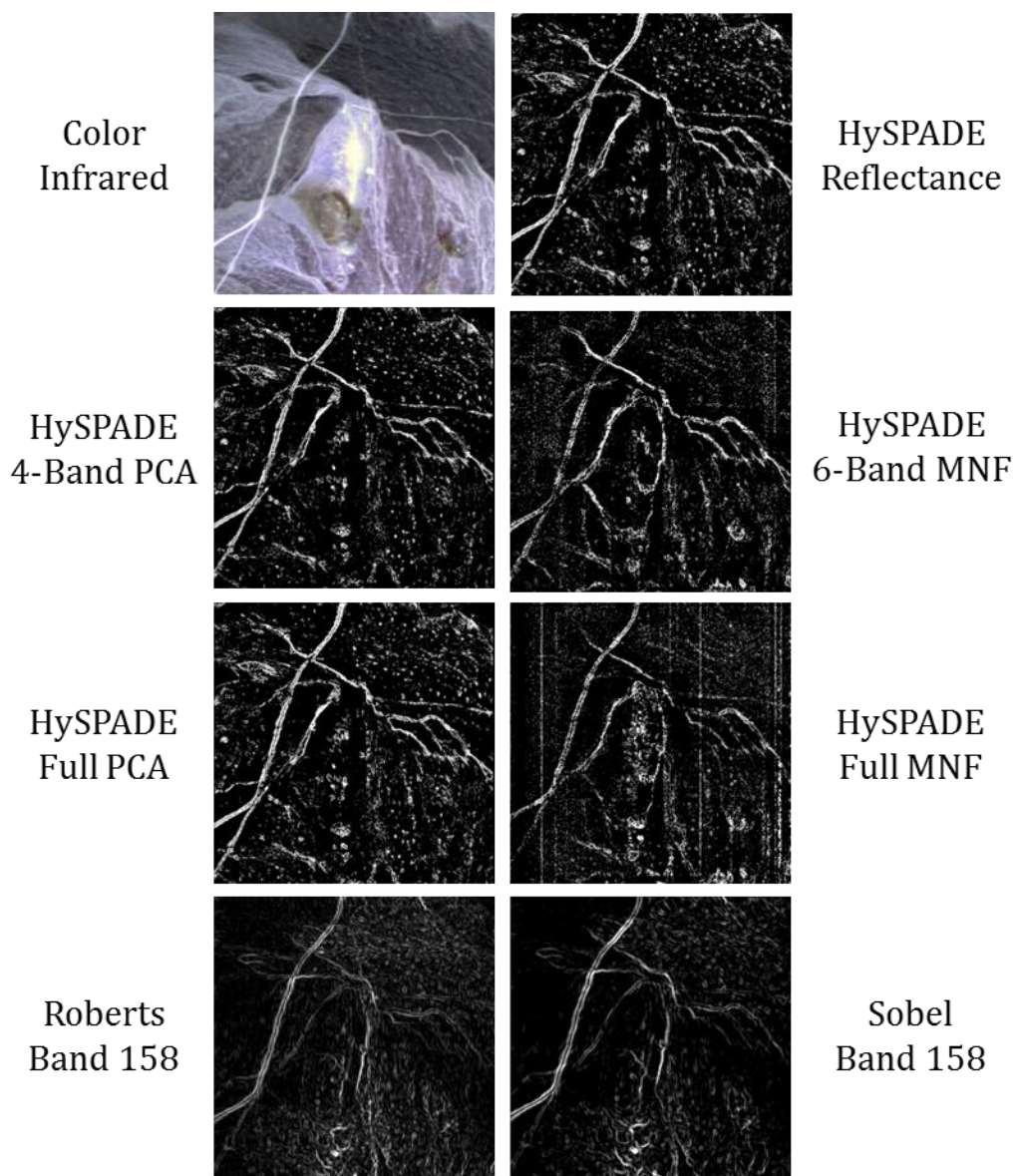


Figure 241: HySPADE Experiment for Cuprite Overhead VNIR/SWIR Data, Flight Line #1, Linear Stretch of Strong Edge Pixels, Threshold at 40 Intermediate Planes from 0.10σ to 4.0σ

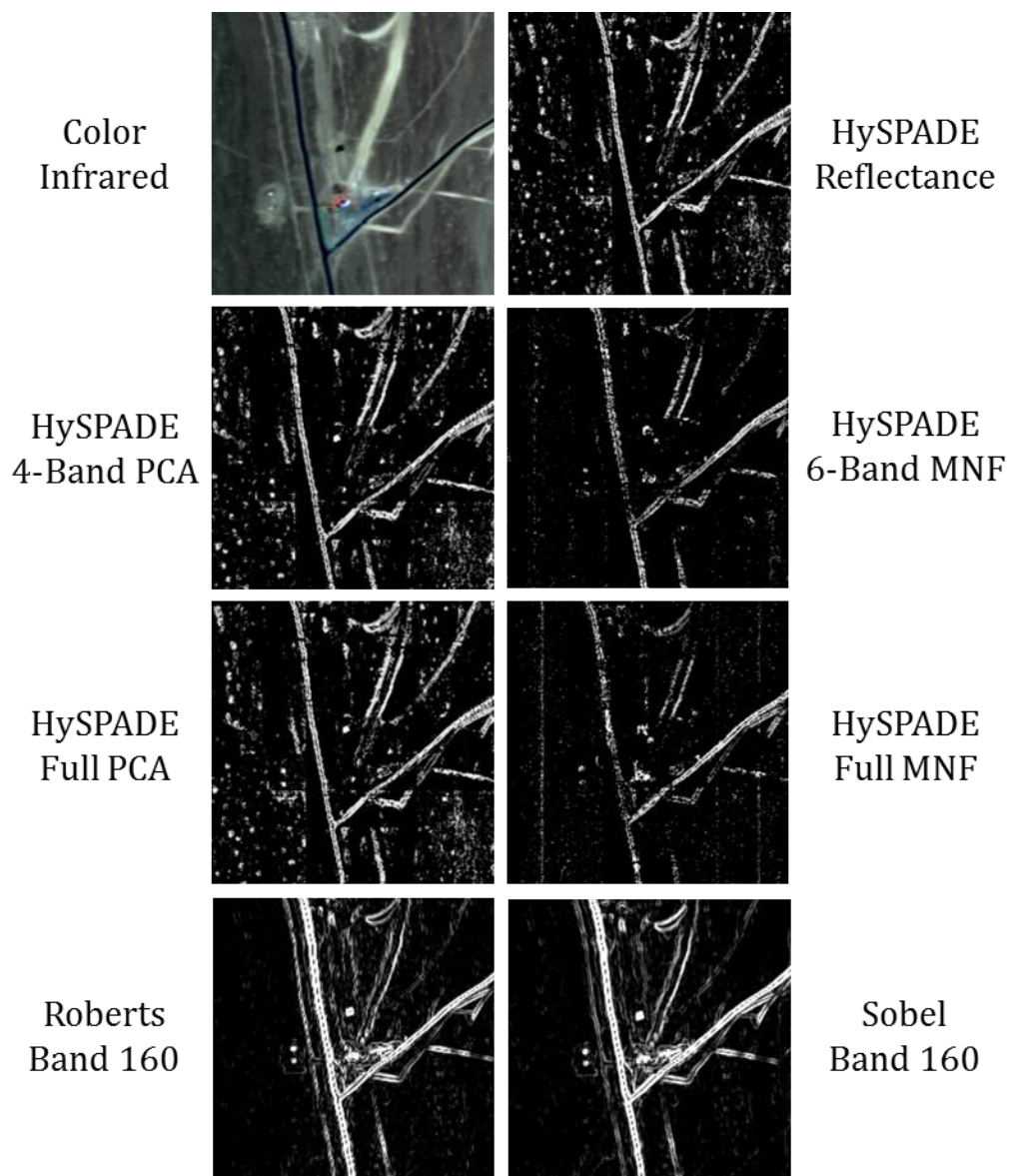


Figure 242: HySPADE Experiment for Cuprite Overhead VNIR/SWIR Data, Flight Line #2, Linear Stretch of Strong Edge Pixels, Threshold at 40 Intermediate Planes from 0.10σ to 4.0σ

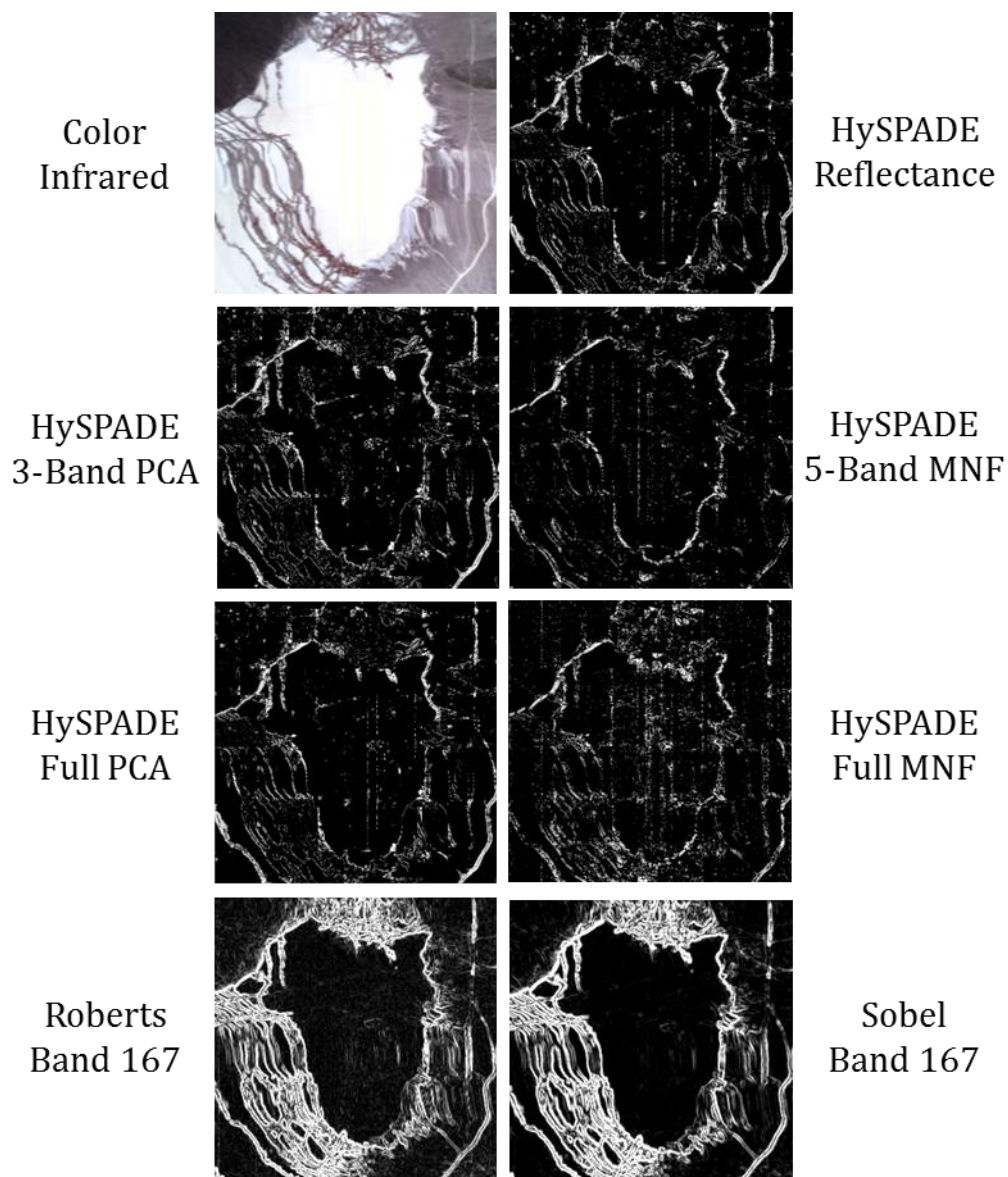


Figure 243: HySPADE Experiment for Cuprite Overhead VNIR/SWIR Data, Flight Line #3, Linear Stretch of Strong Edge Pixels, Threshold at 40 Intermediate Planes from 0.10σ to 4.0σ

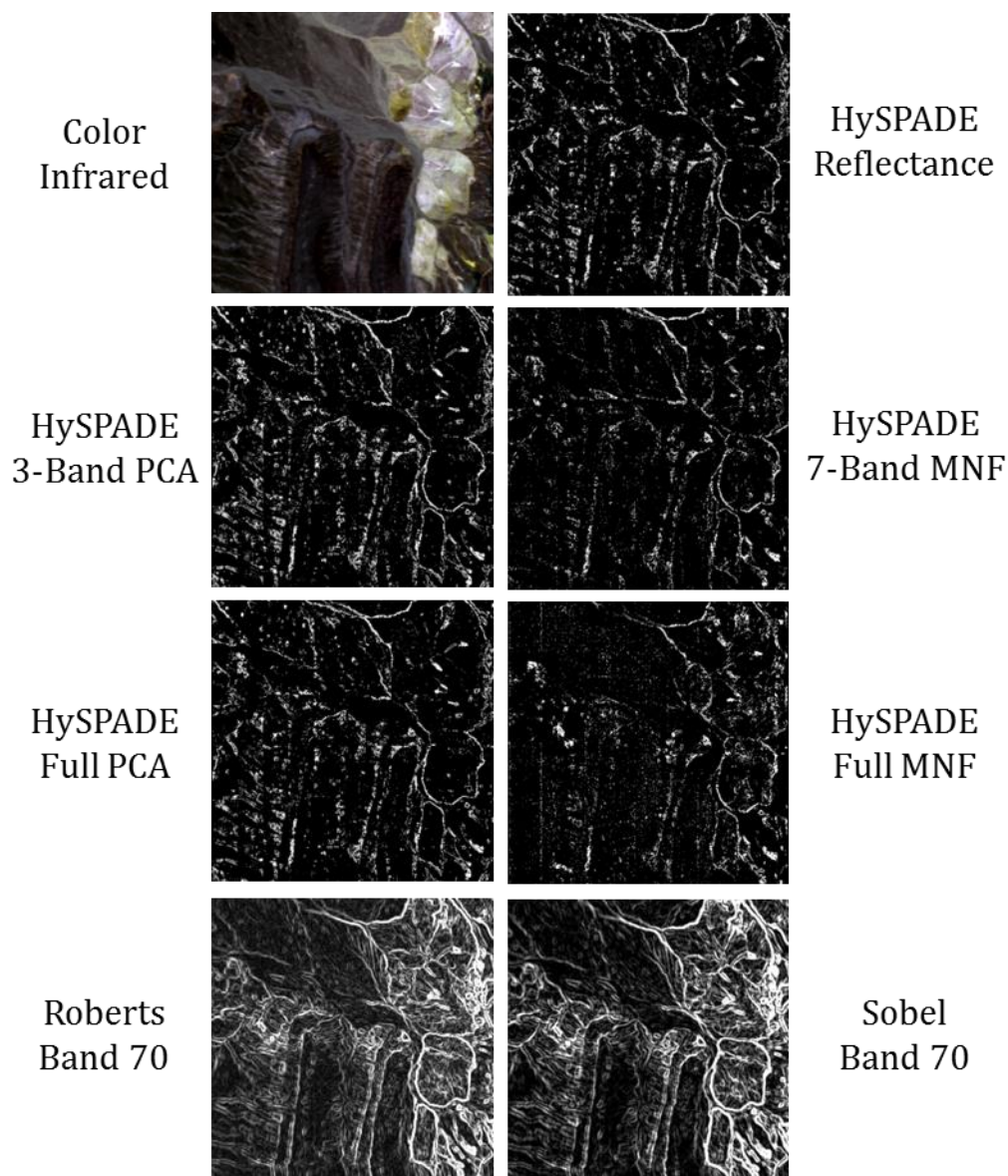


Figure 244: HySPADE Experiment for Cuprite Overhead VNIR/SWIR Data, Flight Line #4, Linear Stretch of Strong Edge Pixels, Threshold at 40 Intermediate Planes from 0.10σ to 4.0σ

Overhead – Indian Pines, Indiana USA

The third HySPADE edge detection experiment uses the VNIR/SWIR Indian Pines, IN USA hypercube. Specifically, this experiment tests the algorithm against five distinct datasets: a 256-band reflectance cube, a 4-band compressed PCA cube, the full

256-band PCA cube, a 4-band compressed MNF cube, and the full 256-band MNF cube. For comparison, this test also executes the Roberts operator and the Sobel operator against the full Indian Pines reflectance cube. Figure 245 presents samples of the seven experiments for the Indian Pines data, and Appendix A contains the full spatial extent for each test.

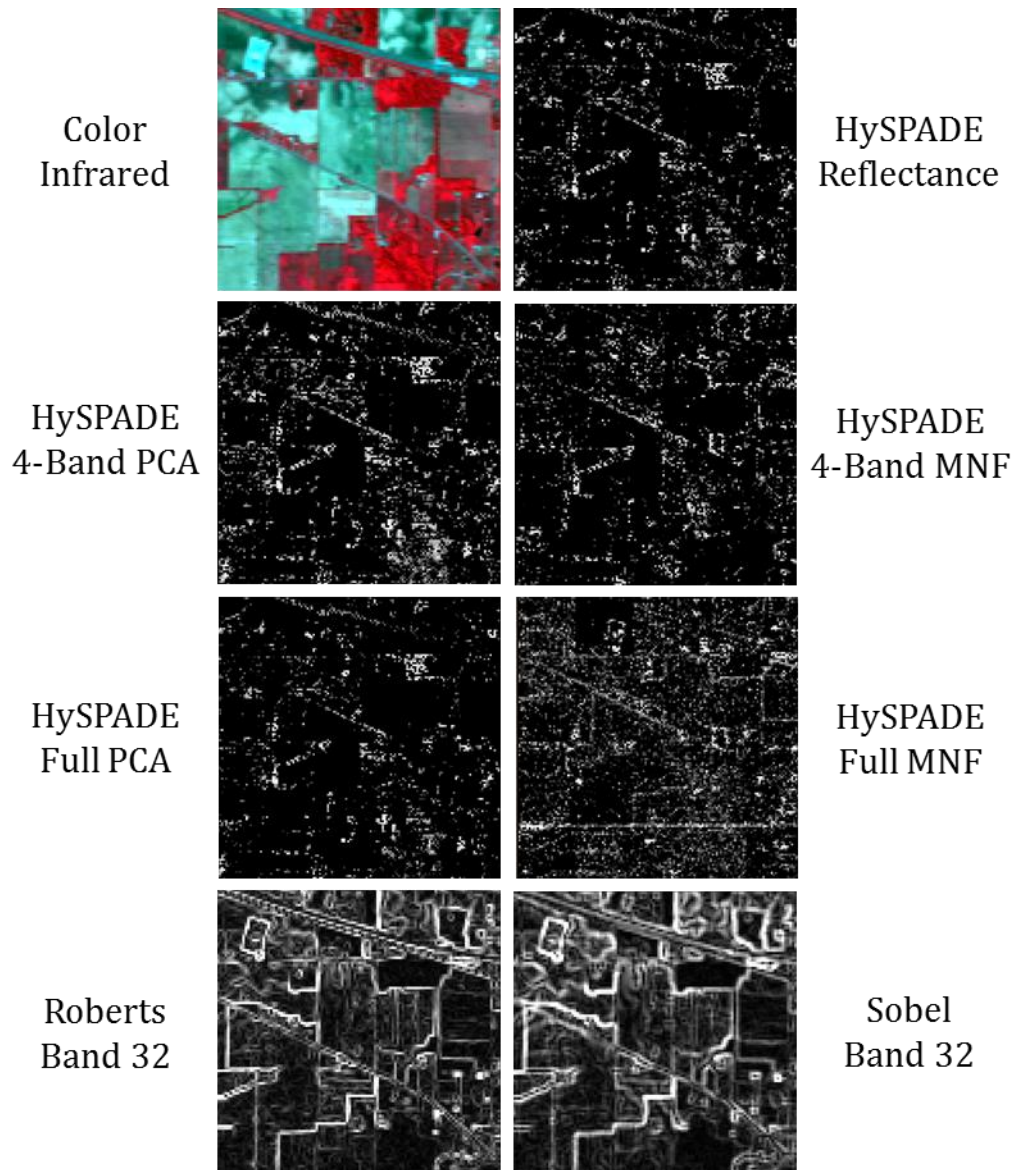


Figure 245: HySPADE Experiment for Indian Pines Overhead VNIR/SWIR Data, Linear Stretch of Strong Edge Pixels, Threshold at 40 Intermediate Planes from 0.10σ to 4.0σ

Overhead – Deepwater Horizon Oil Spill, Gulf of Mexico

The fourth and final HySPADE edge detection experiment for overhead imagery uses ProSpecTIR's VNIR/SWIR hypercube of the 2010 Deepwater Horizon oil spill in

the Gulf of Mexico – a challenging, non-traditional dataset. The Deepwater Horizon dataset is expected to present a challenge to the HySPADE algorithm given the dark (i.e., noisy) background, the lack of terrestrial features and the curvilinear nature of the scene’s dominant features. Specifically, this experiment tests the algorithm against six distinct datasets: a 360-band radiance cube, a 320-band reflectance cube, a 3-band compressed PCA cube, the full 320-band PCA cube, a 3-band compressed MNF cube, and the full 320-band MNF cube. For comparison, this test also executes the Roberts operator and the Sobel operator against the full Deepwater Horizon reflectance cube. Figure 246 presents samples of the seven experiments for the Deepwater Horizon data, and Appendix A contains the full spatial extent for each test.

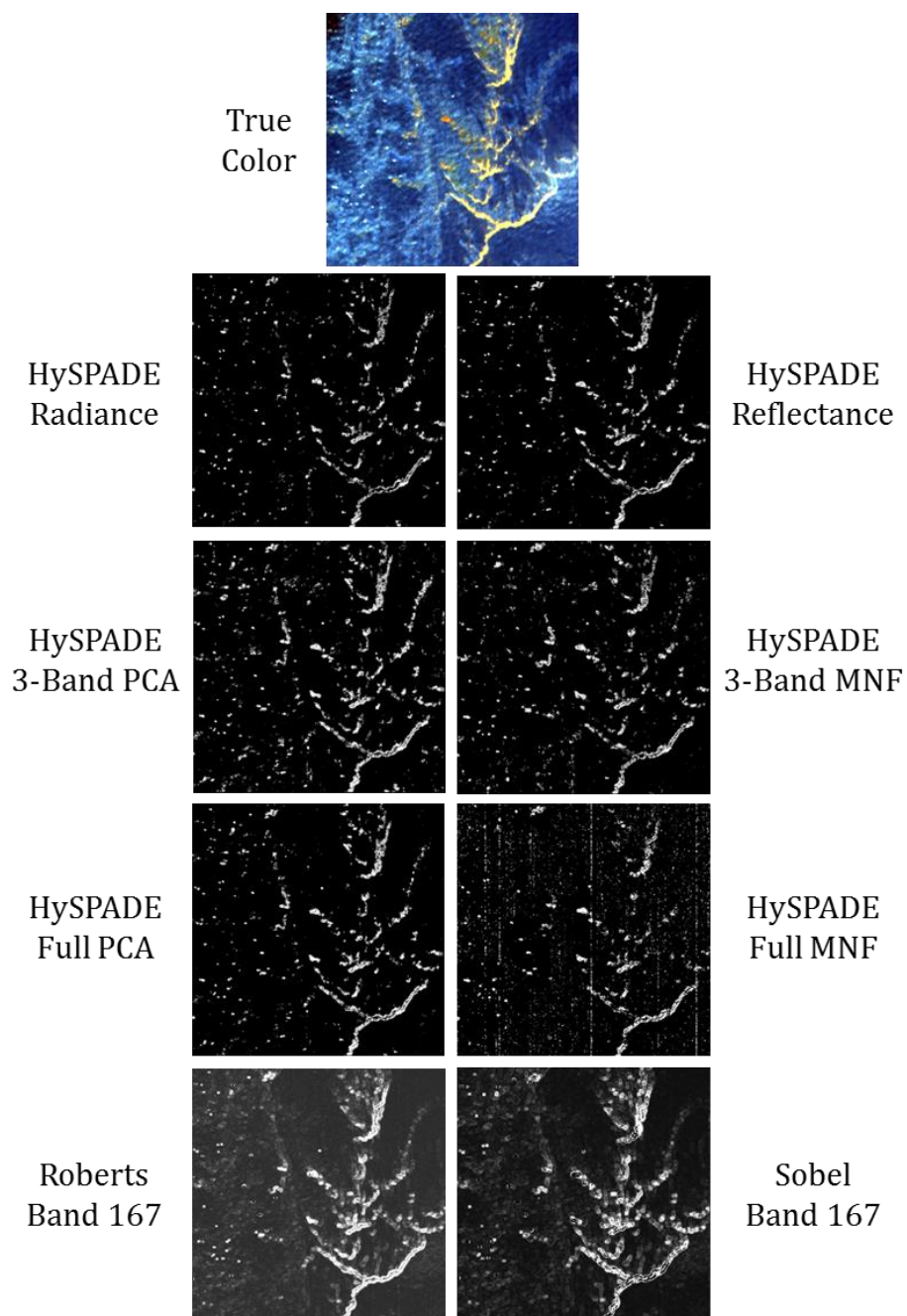


Figure 246: HySPADE Experiment for Deepwater Horizon Overhead VNIR/SWIR Data, Linear Stretch of Strong Edge Pixels, Threshold at 40 Intermediate Planes from 0.10σ to 4.0σ

Ground-Based – Larkhaven

The first HySPADE edge detection experiment on ground-based data uses VNIR imagery of a residential home in Fairfax Station, Virginia. Specifically, this experiment tests the algorithm against five distinct datasets: a 120-band reflectance cube, a 4-band compressed PCA cube, the full 120-band PCA cube, a 3-band compressed MNF cube, and the full 120-band MNF cube. Sobel and Roberts are also tested against the reflectance cube. Figure 247 presents samples of the seven experiments for the Larkhaven data.

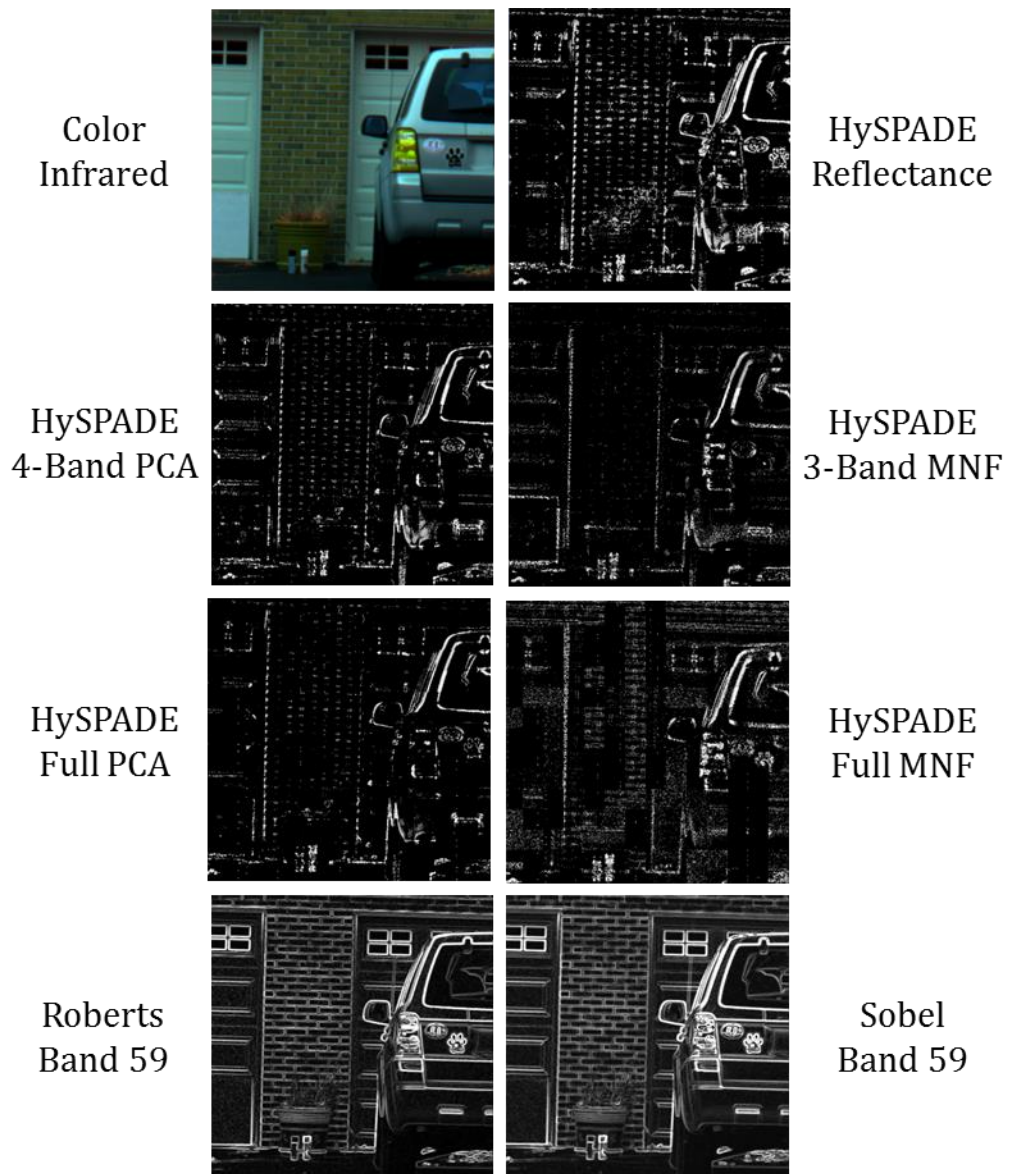


Figure 247: HySPADE Experiment for Larkhaven VNIR Data, Linear Stretch of Strong Edge Pixels, Threshold at 40 Intermediate Planes from 0.10σ to 4.0σ

Ground-Based – Granite VNIR

The second HySPADE edge detection experiment on ground-based hyperspectral data uses Pika II VNIR imagery of a high-spatial resolution granite sample. Specifically, this experiment tests the algorithm against five distinct datasets: a 72-band reflectance

cube, a 2-band compressed PCA cube, the full 72-band PCA cube, a 2-band compressed MNF cube, and the full 72-band MNF cube. For comparison, this test also executes the Roberts operator and the Sobel operator against the full Granite VNIR reflectance cube. Figure 248 presents samples of the seven experiments for the Granite VNIR data, and Appendix A contains the full spatial extent for each test.

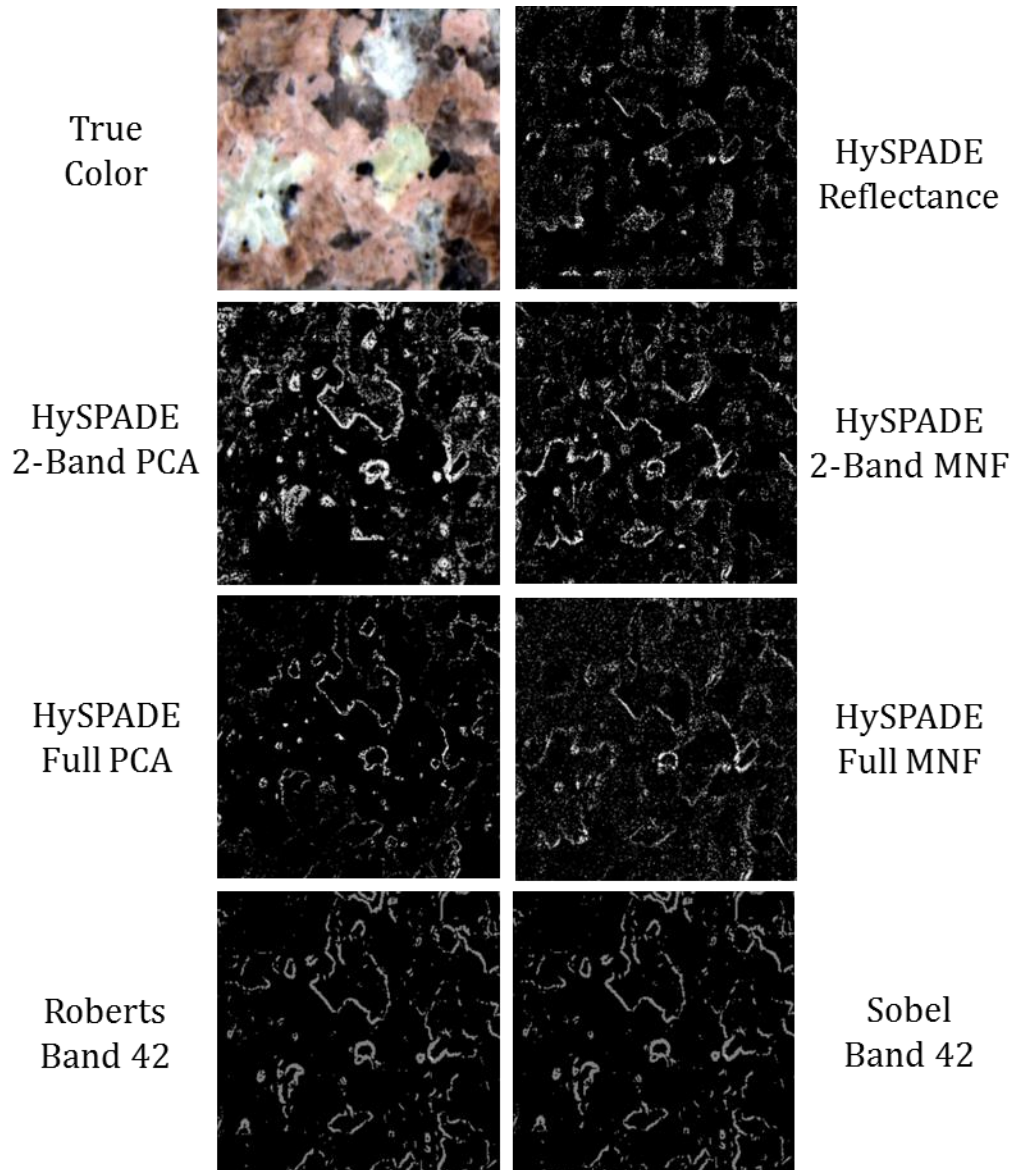


Figure 248: HySPADE Experiment for Granite Ground-Based VNIR Data, Linear Stretch of Strong Edge Pixels, Threshold at 40 Intermediate Planes from 0.10σ to 4.0σ

Ground-Based – Granite NIR/SWIR

The third HySPADE edge detection experiment on ground-based hyperspectral data is a close cousin to the previous Granite VNIR test. This experiment uses high-

spatial resolution Pika II NIR/SWIR imagery of a different area from the same granite sample as the previous test. The primary difference is the wavelength and sampling rate – this test includes the SWIR bands so important to accurate mineral mapping applications, excludes the VIS bands and has 162 bands as opposed to 72. This test also is analogous to the Cuprite, NV overhead data in the sense that it supports mineral mapping applications.

Specifically, this experiment tests the algorithm against five distinct datasets: a 164-band reflectance cube, a 3-band compressed PCA cube, the full 164-band PCA cube, a 5-band compressed MNF cube, and the full 162-band MNF cube. For comparison, this test also executes the Roberts operator and the Sobel operator against the full Granite NIR/SWIR reflectance cube. Figure 249 presents samples of the seven experiments for the Granite NIR/SWIR data, and Appendix A contains the full spatial extent for each test.

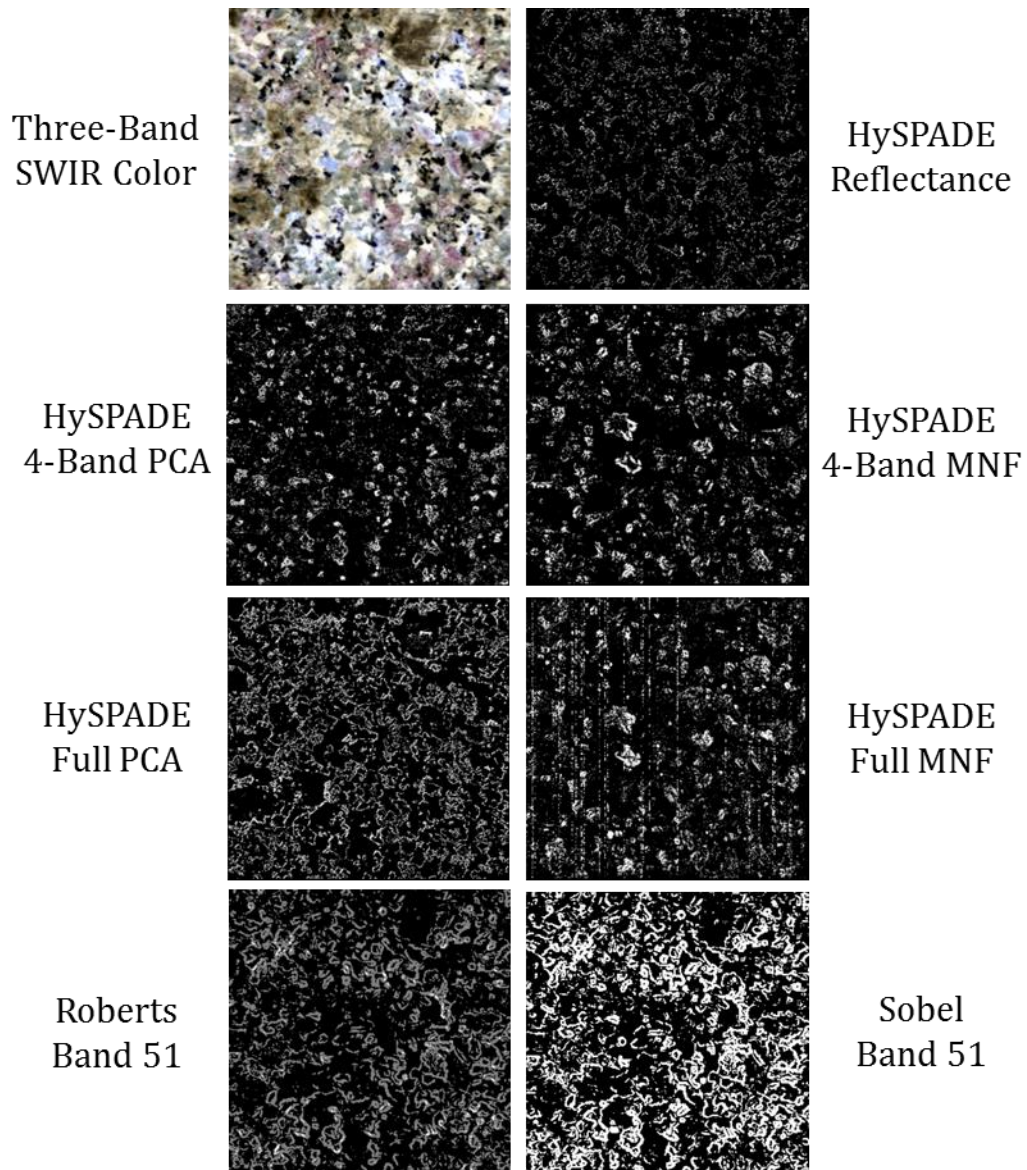


Figure 249: HySPADE Experiment for Granite Ground-Based NIR/SWIR Data, Linear Stretch of Strong Edge Pixels, Threshold at 40 Intermediate Planes from 0.10σ to 4.0σ

Ground-Based – South African Core Samples

The fourth HySPADE detection experiment on ground-based hyperspectral data also aligns to mineral mapping applications. This experiment uses high-spatial resolution NIR/SWIR imagery of six South African geologic core samples arranged within the same

image plane. Specifically, this experiment tests the algorithm against five distinct datasets: a 234-band reflectance cube, a 3-band compressed PCA cube, the full 234-band PCA cube, a 5-band compressed MNF cube, and the full 234-band MNF cube. For comparison, this test also executes the Roberts operator and the Sobel operator against the full South African NIR/SWIR reflectance cube. Figure 250 presents samples of the seven experiments for the South African Core Sample NIR/SWIR data.

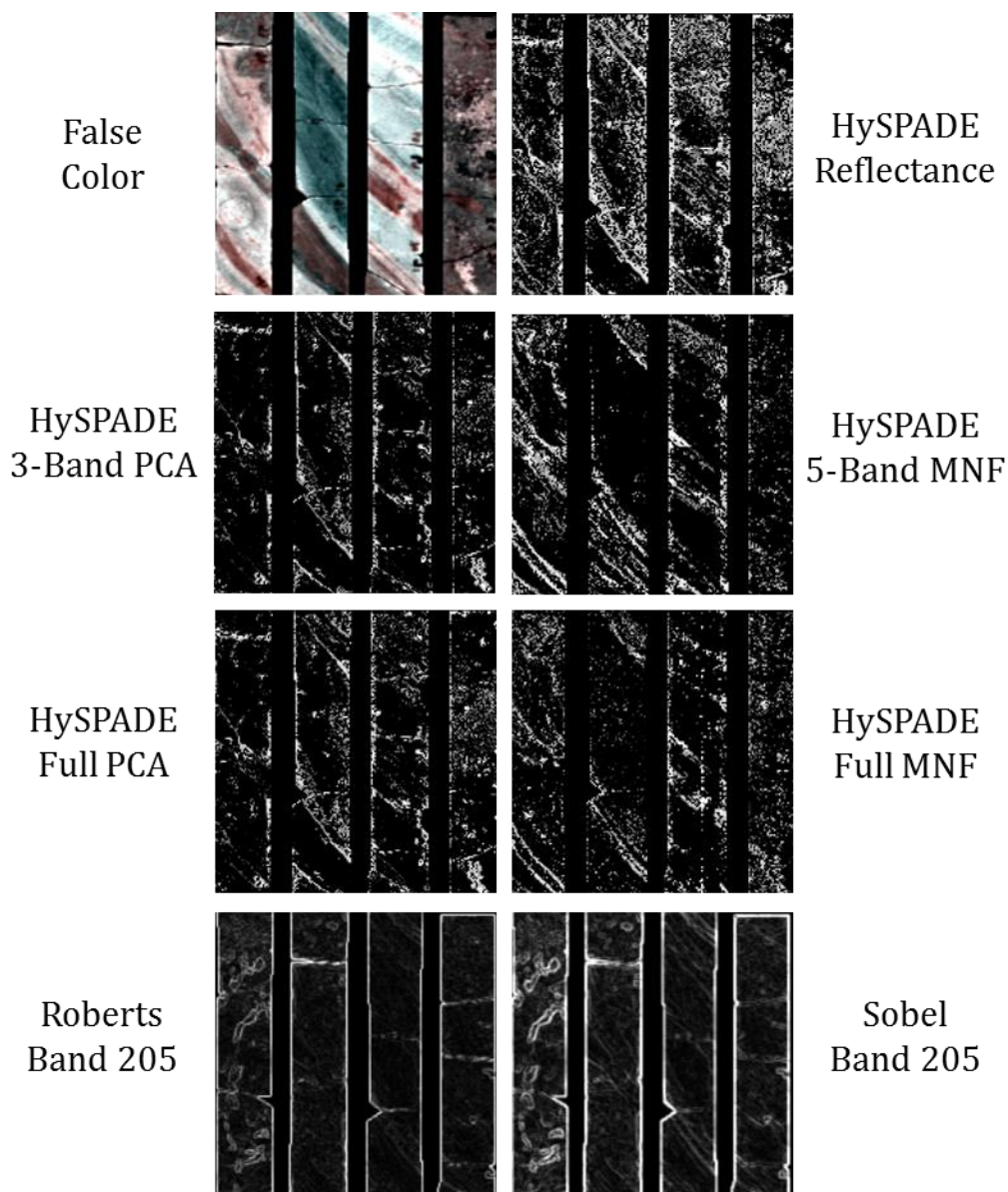


Figure 250: HySPADE Experiment for South African Core Sample Ground-Based NIR/SWIR Data, Linear Stretch of Strong Edge Pixels, Threshold at 40 Intermediate Planes from 0.10σ to 4.0σ

Ground-Based – Aluminum Panel

The fifth and final HySPADE edge detection experiment on ground-based hyperspectral data addresses the aluminum aircraft panel possibly traceable to Amelia

Earhart's Lockheed Electra. Specifically, this experiment tests the algorithm against five distinct datasets: a 103-band reflectance cube, a 2-band compressed PCA cube, the full 103-band PCA cube, a 3-band compressed MNF cube, and the full 103-band MNF cube. For comparison, this test also executes the Roberts operator and the Sobel operator against the full Aluminum Aircraft Panel VNIR reflectance cube. Figure 251 presents samples of the seven experiments for the Aluminum Aircraft Panel data.

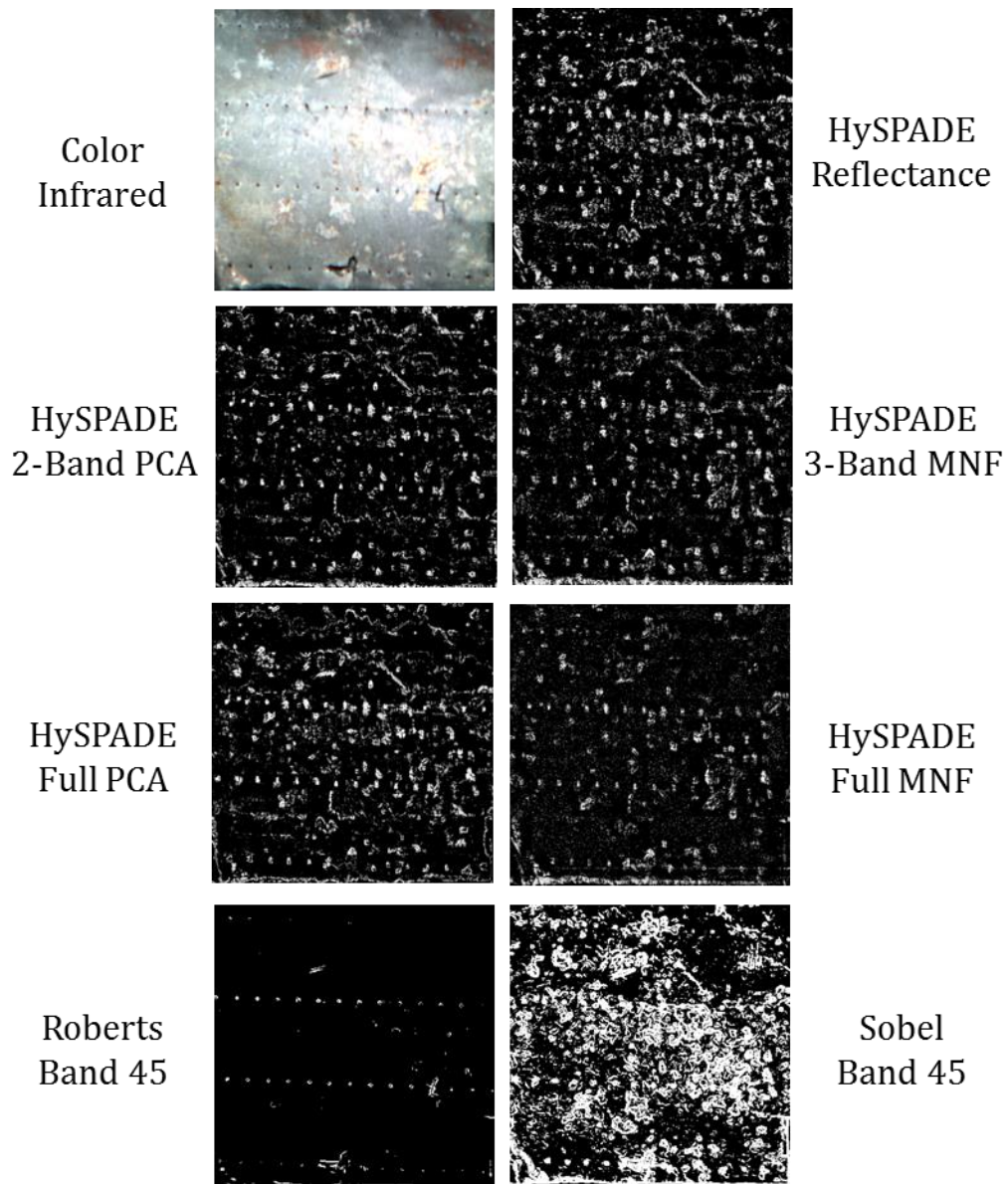


Figure 251: HySPADE Experiment for Aluminum Aircraft Panel Ground-Based VNIR Data, Linear Stretch of Strong Edge Pixels, Threshold at 40 Intermediate Planes from 0.10σ to 4.0σ

Microscene – Rare Target on Sand

The first HySPADE edge detection experiment on microscene hyperspectral data uses Pika II VNIR imagery of a complex microscene on sand. This test supports trace

chemical detection HSI applications due to the presence of a rare target in a complex background. Specifically, this experiment tests the algorithm against five distinct datasets: a 74-band reflectance cube, a 3-band compressed PCA cube, the full 74-band PCA cube, a 5-band compressed MNF cube, and the full 74-band MNF cube. For comparison, this test also executes the Roberts operator and the Sobel operator against the full Rare Target on Sand reflectance cube. Figure 252 presents samples of the seven experiments for the Rare Target on Sand data.

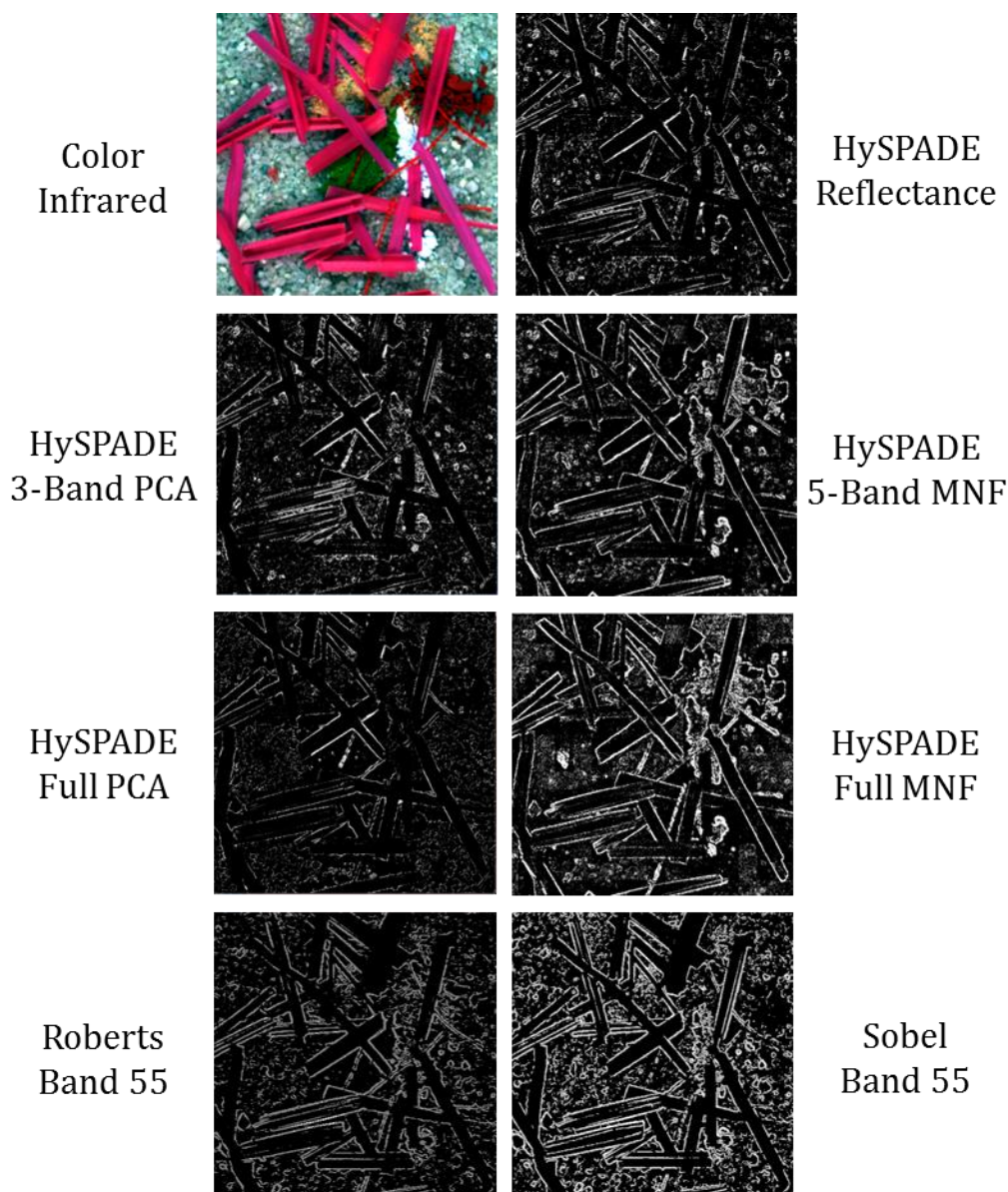


Figure 252: HySPADE Experiment for Rare Target on Sand VNIR Data, Linear Stretch of Strong Edge Pixels, Threshold at 40 Intermediate Planes from 0.10σ to 4.0σ

Microscene – Chemical Array

The second HySPADE experiment on microscene hyperspectral data uses 168-band HYPERSPEC NIR/SWIR imagery of a chemical array on sand. This test supports

trace chemical detection HSI applications due to the presence of several rare targets on a simple background. Specifically, this experiment tests the algorithm against five distinct datasets: a 168-band reflectance cube, a 3-band compressed PCA cube, the full 168-band PCA cube, a 5-band compressed MNF cube, and the full 168-band MNF cube. For comparison, this test also executes the Roberts operator and the Sobel operator against the full Rare Target on Sand reflectance cube. Figure 253 presents samples of the seven experiments for the Chemical Array data.

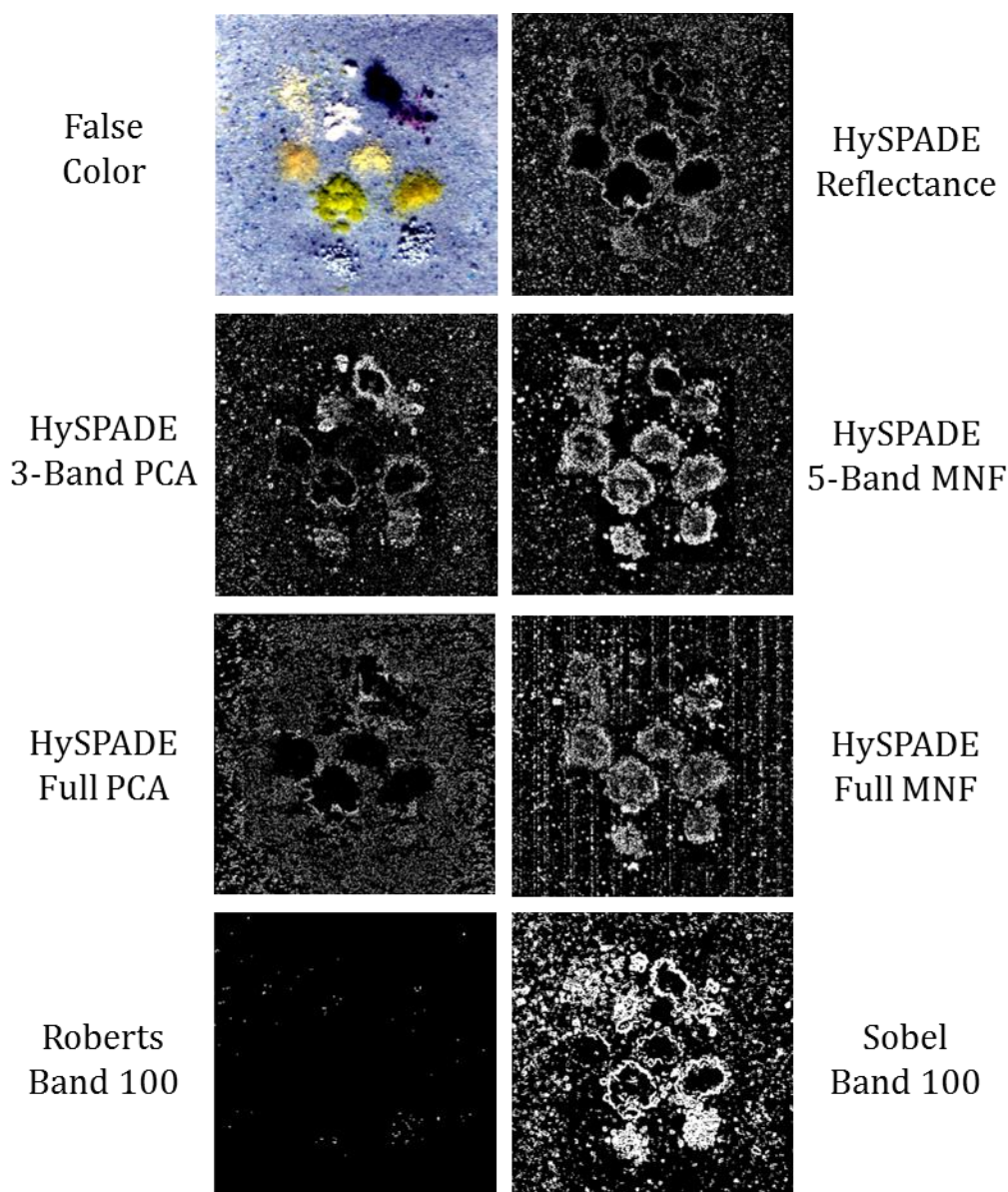


Figure 253: HySPADE Experiment for Chemical Array NIR/SWIR Data, Linear Stretch of Strong Edge Pixels, Threshold at 40 Intermediate Planes from 0.10σ to 4.0σ

Microscene – Cloth Threads

The third and final HySPADE experiment on microscene hyperspectral data uses 80-band Pika II VNIR imagery of a series of different color cloth threads arrayed on a

sand background. Specifically, this experiment tests the algorithm against five distinct datasets: an 80-band reflectance cube, a 3-band compressed PCA cube, the full 80-band PCA cube, a 5-band compressed MNF cube, and the full 80-band MNF cube. For comparison, this test also executes the Roberts operator and the Sobel operator against the full Rare Target on Sand reflectance cube. Figure 254 presents samples of the seven experiments for the Cloth Thread data.

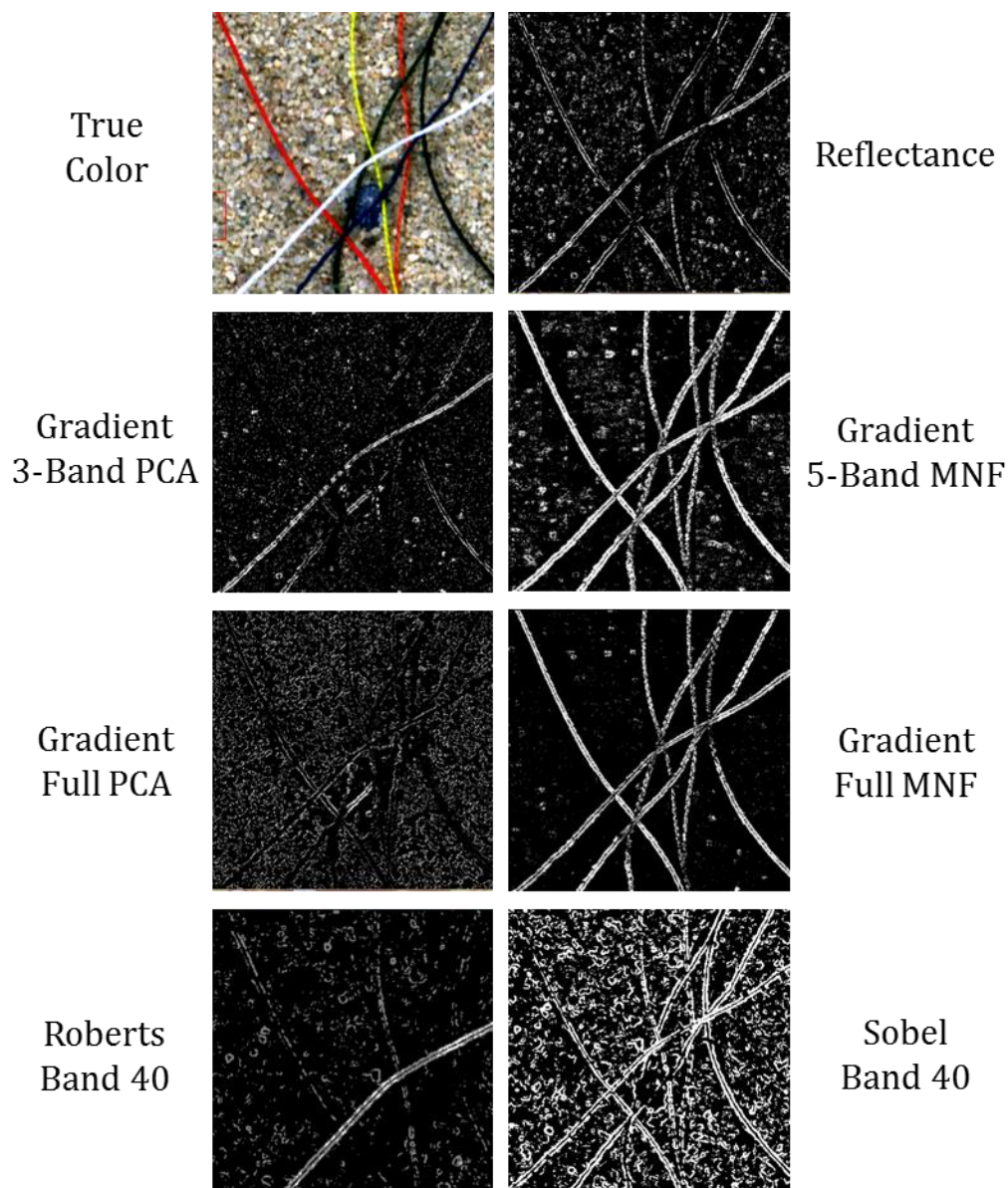


Figure 254: HySPADE Experiment for Cloth Threads VNIR Data, Linear Stretch of Strong Edge Pixels, Threshold at 40 Intermediate Planes from 0.10σ to 4.0σ

Level Set Edge Detection Findings

This dissertation tests the level set-based edge detection algorithm against all 12 HSI datasets, including tests against reflectance and/or radiance cubes, PCA cubes of

varying depth and MNF cubes of varying depth. The Experiments section presents samples from each test, the Analysis section examines key sections and draws scientific conclusions for each dataset and Appendix A presents the full spatial extent of each experiment. Experimental observations from the level set-based edge detection algorithm are as follows.

Overhead – Reno, Nevada USA

The first level set edge detection experiment uses the VNIR/SWIR Reno, NV USA hypercube. Specifically, this experiment tests the algorithm against five distinct datasets: a 356-band reflectance cube, a four-band compressed PCA cube, the full 356-band PCA cube, an eight-band compressed MNF cube, and the full 356-band MNF cube. The Results along with Sobel and Roberts comparison edge planes are shown in Figure 255.

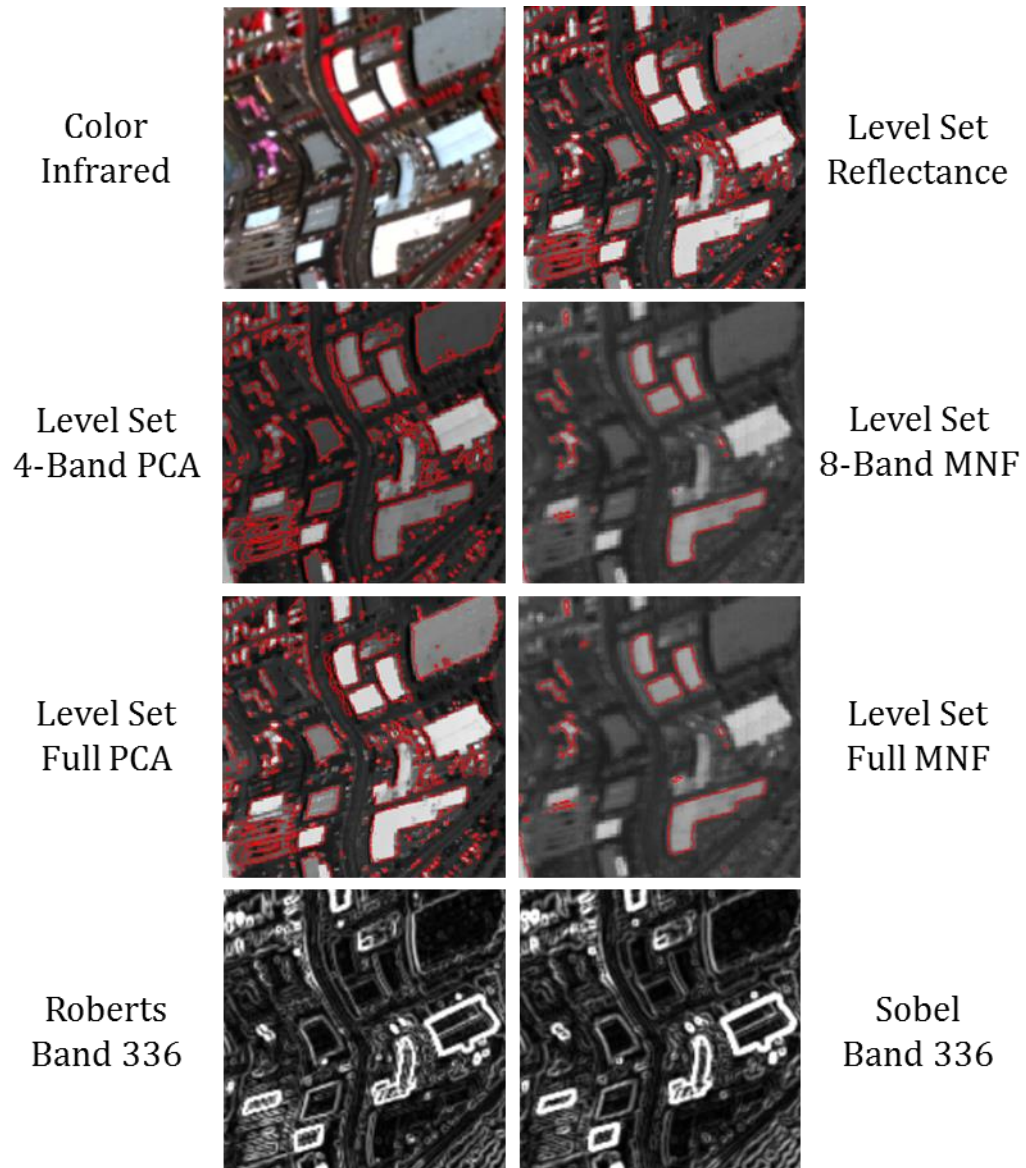


Figure 255: Level Set Experiment for Reno, NV Overhead VNIR/SWIR Data, Initial Curve at Image Center, Initial Radius 1/8 Longest Dimension, Single-Pixel Stepping, 0.1 Second Time Step, Maximum 20 Iterations

Overhead – Cuprite, Nevada USA

The second level set edge detection experiment tests the four VNIR/SWIR flight lines covering Cuprite, NV USA. Specifically, this experiment tests the algorithm against five distinct datasets for each flight line: the full reflectance cube, a compressed-

band PCA cube, the full PCA cube, a compressed MNF cube, and the full MNF cube. For comparison, this test also executes the Roberts operator and the Sobel operator against the full reflectance cube for each flight line. Figure 256, Figure 257, Figure 258 and Figure 259 present samples of the seven experiments for each flight line, and Appendix A contains the full spatial extent for each test.

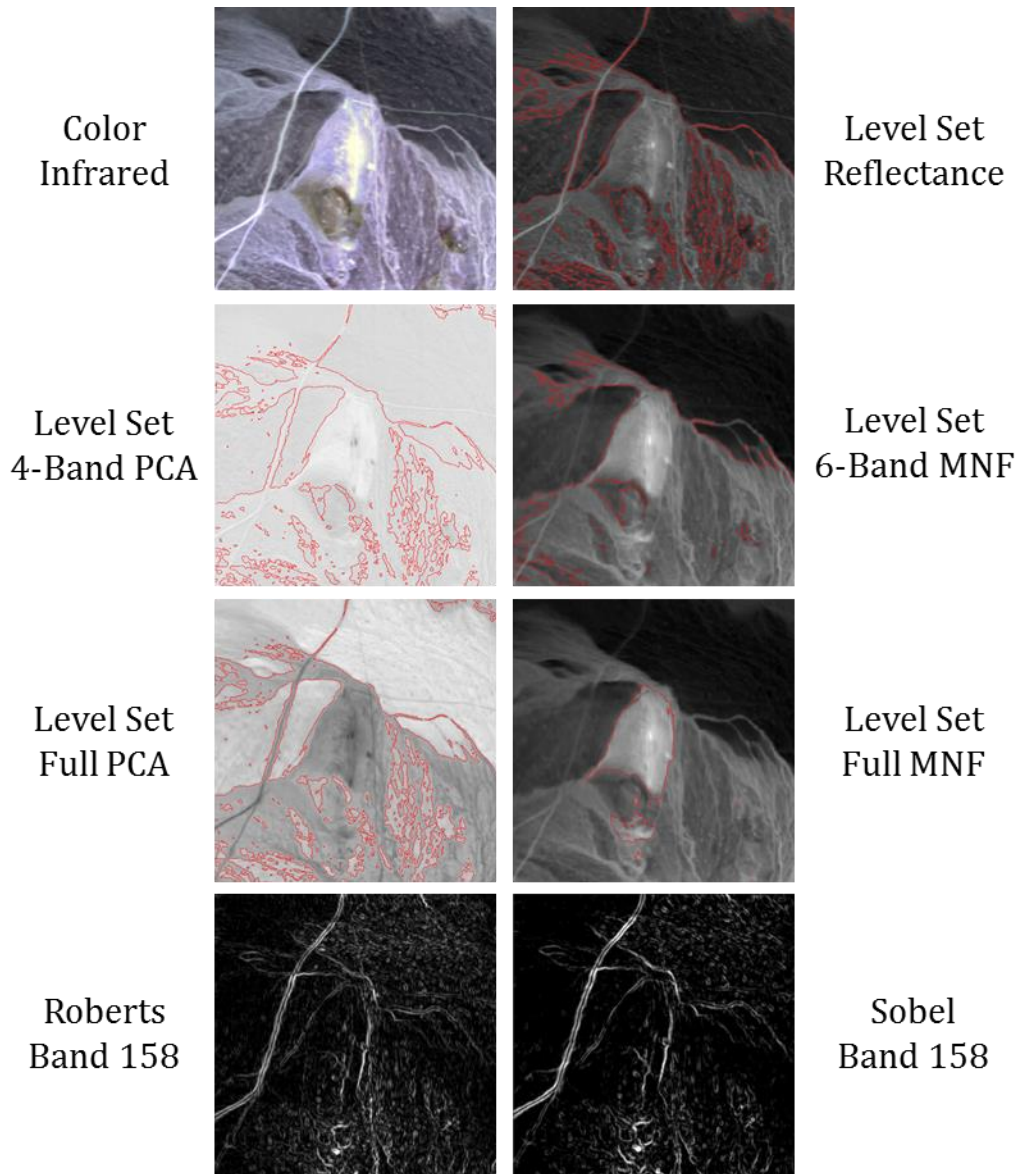


Figure 256: Level Set Experiment for Cuprite Overhead VNIR/SWIR Data, Flight Line #1, Initial Curve at Image Center, Initial Radius 1/8 Longest Dimension, Single-Pixel Stepping, 0.1 Second Time Step, Maximum 20 Iterations

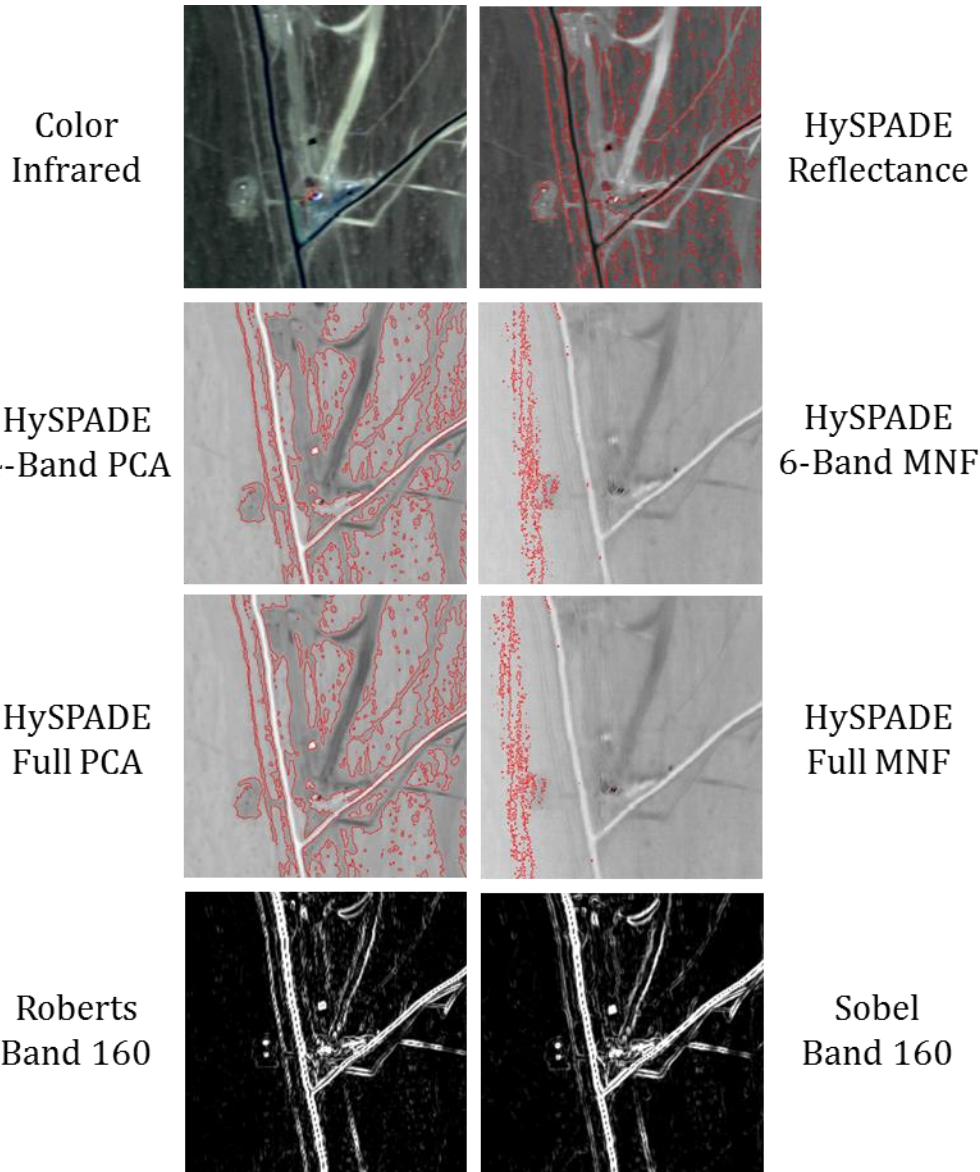


Figure 257: Level Set Experiment for Cuprite Overhead VNIR/SWIR Data, Flight Line #2, Initial Curve at Image Center, Initial Radius 1/8 Longest Dimension, Single-Pixel Stepping, 0.1 Second Time Step, Maximum 20 Iterations

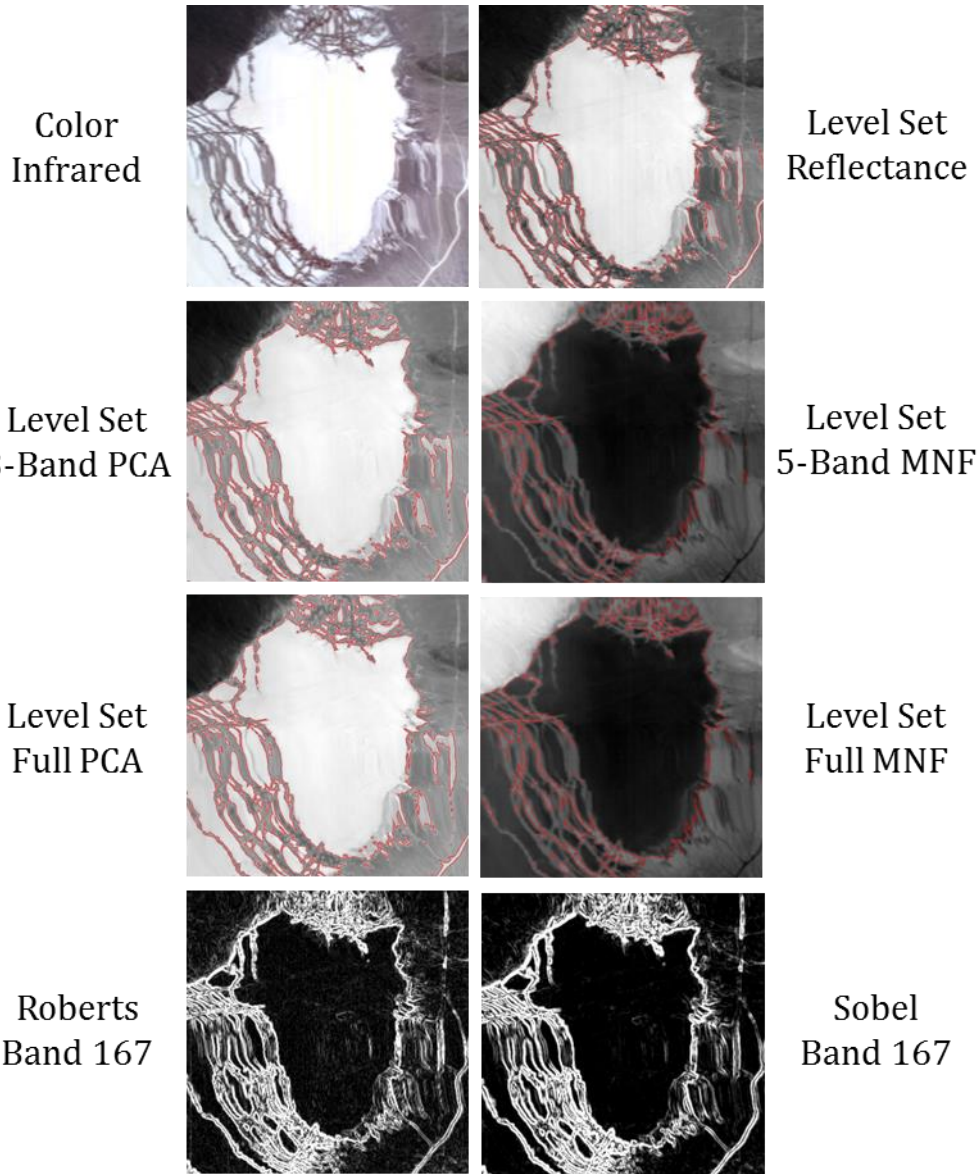


Figure 258: Level Set Experiment for Cuprite Overhead VNIR/SWIR Data, Flight Line #3, Initial Curve at Image Center, Initial Radius 1/8 Longest Dimension, Single-Pixel Stepping, 0.1 Second Time Step, Maximum 20 Iterations

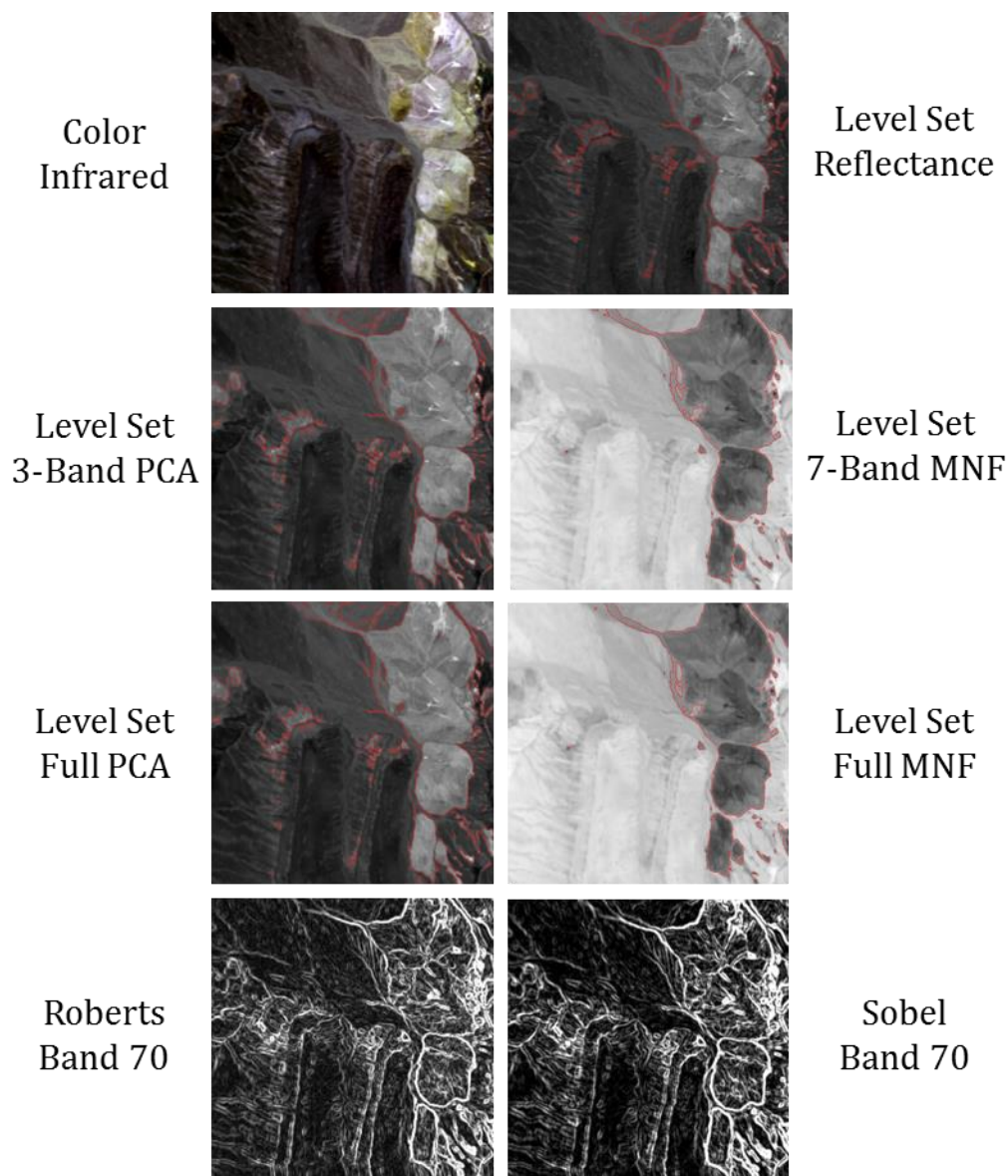


Figure 259: Level Set Experiment for Cuprite Overhead VNIR/SWIR Data, Flight Line #4, Initial Curve at Image Center, Initial Radius 1/8 Longest Dimension, Single-Pixel Stepping, 0.1 Second Time Step, Maximum 20 Iterations

Overhead – Indian Pines, Indiana USA

The third level set edge detection experiment uses the VNIR/SWIR Indian Pines, IN USA hypercube. Specifically, this experiment tests the algorithm against five distinct

datasets: a 256-band reflectance cube, a 4-band compressed PCA cube, the full 256-band PCA cube, a 4-band compressed MNF cube, and the full 256-band MNF cube. For comparison, this test also executes the Roberts operator and the Sobel operator against the full Indian Pines reflectance cube. Figure 260 presents samples of the seven experiments for the Indian Pines data, and Appendix A contains the full spatial extent for each test.

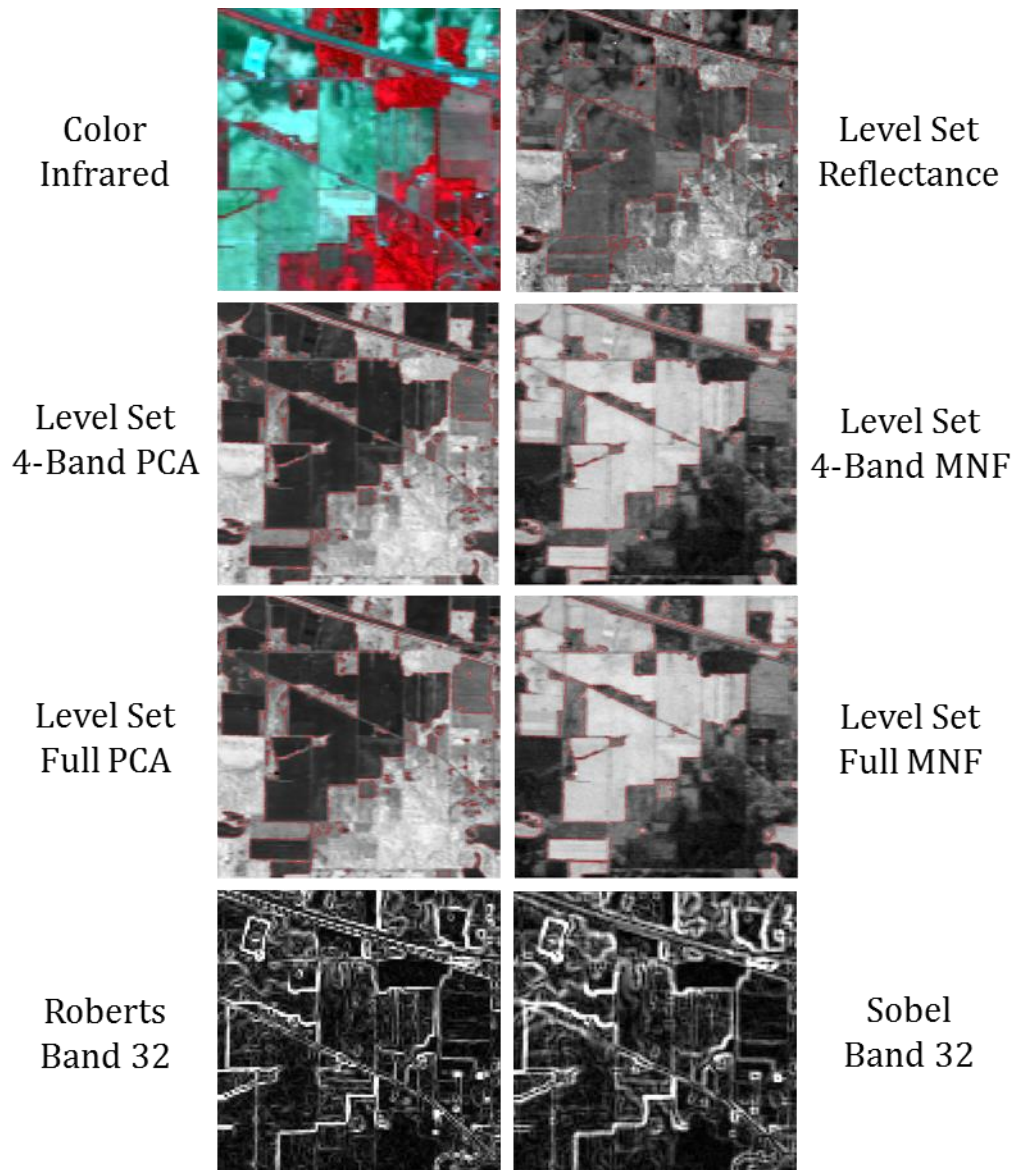


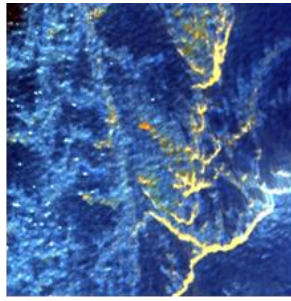
Figure 260: Level Set Experiment for Indian Pines Overhead VNIR/SWIR Data, Initial Curve at Image Center, Initial Radius 1/8 Longest Dimension, Single-Pixel Stepping, 0.1 Second Time Step, Maximum 20 Iterations

Overhead – Deepwater Horizon Oil Spill, Gulf of Mexico

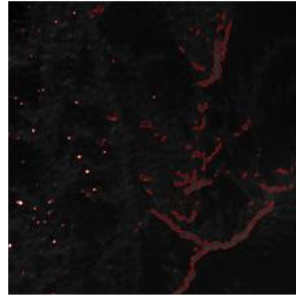
The fourth and final level set edge detection experiment for overhead imagery uses ProSpecTIR’s VNIR/SWIR hypercube of the 2010 Deepwater Horizon oil spill in the Gulf of Mexico. Specifically, this experiment tests the algorithm against six distinct

datasets: a 360-band radiance cube, a 320-band reflectance cube, a 3-band compressed PCA cube, the full 320-band PCA cube, a 3-band compressed MNF cube, and the full 320-band MNF cube. For comparison, this test also executes the Roberts operator and the Sobel operator against the full Deepwater Horizon reflectance cube. Figure 261Figure 246 presents samples of the seven experiments for the Deepwater Horizon data.

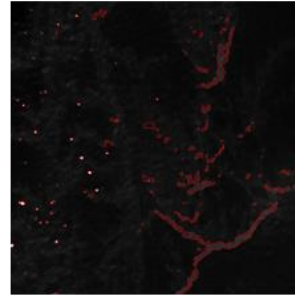
True
Color



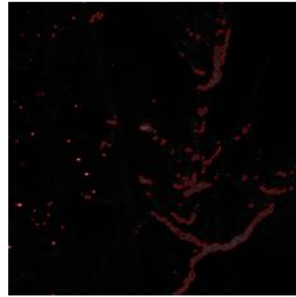
Level Set
Radiance



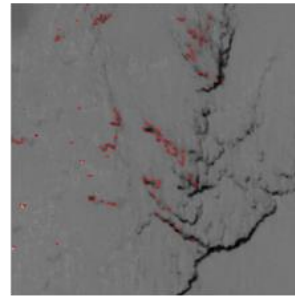
Level Set
Reflectance



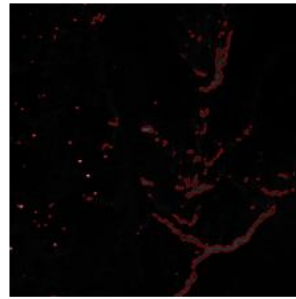
Level Set
3-Band PCA



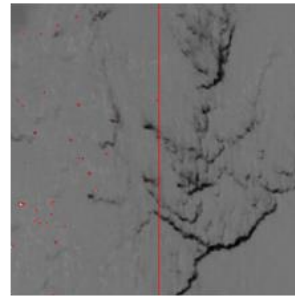
Level Set
3-Band MNF



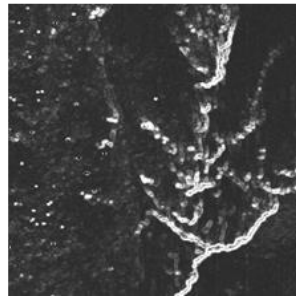
Level Set
Full PCA



Level Set
Full MNF



Roberts
Band 167



Sobel
Band 167

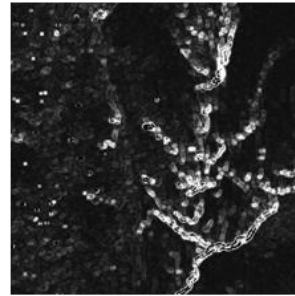


Figure 261: Level Set Experiment for Deepwater Horizon Overhead VNIR/SWIR Data, Initial Curve at Image Center, Initial Radius 1/8 Longest Dimension, Single-Pixel Stepping, 0.1 Second Time Step, Maximum 20 Iterations

Ground-Based – Larkhaven

The first level set edge detection experiment on ground-based data uses VNIR imagery of a residential home in Fairfax Station, Virginia. Specifically, this experiment tests the algorithm against five distinct datasets: a 120-band reflectance cube, a 4-band compressed PCA cube, the full 120-band PCA cube, a 3-band compressed MNF cube, and the full 120-band MNF cube. Sobel and Roberts are also tested against the reflectance cube. Figure 262 presents samples of the seven experiments for the Larkhaven data.

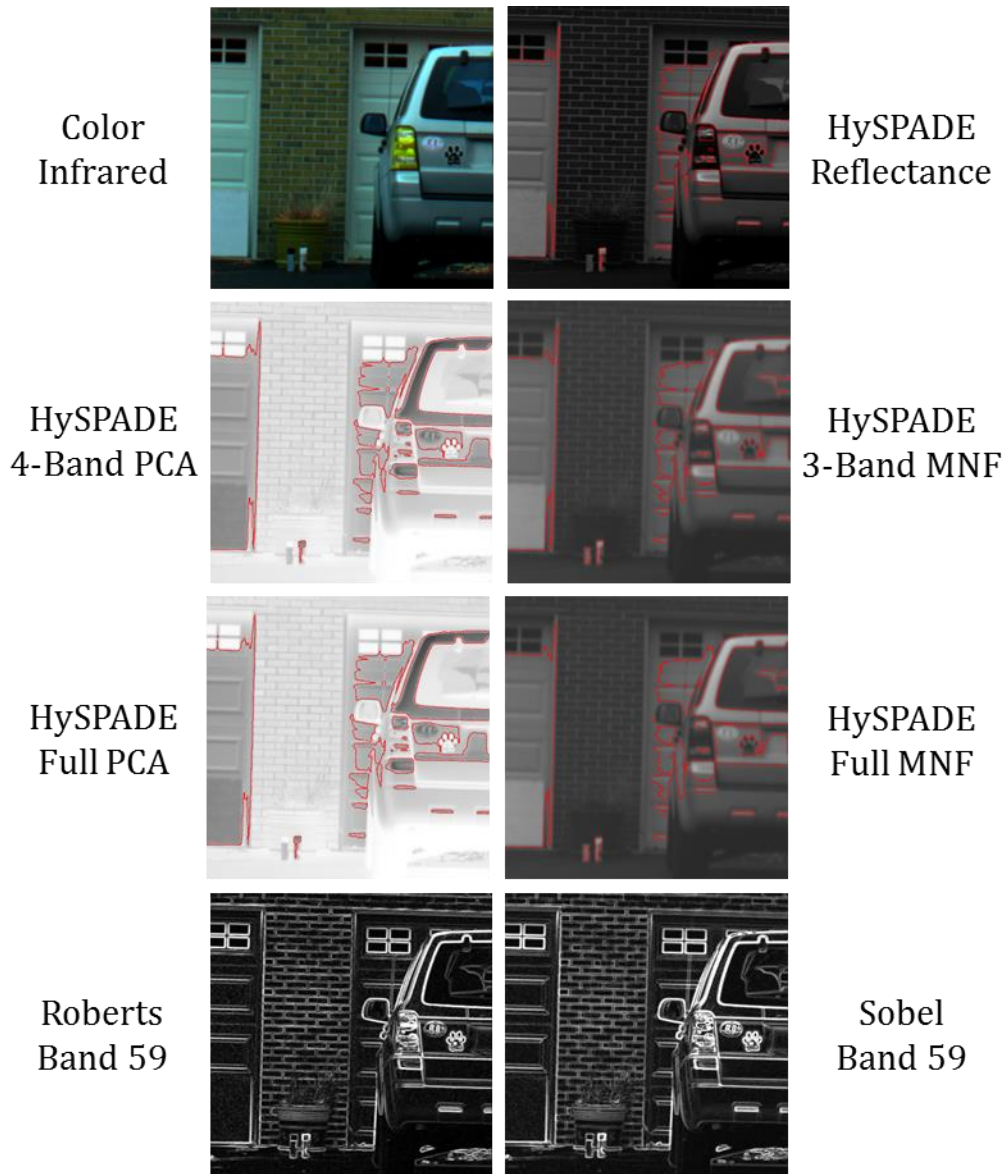


Figure 262: Level Set Experiment for Larkhaven VNIR Data, Initial Curve at Image Center, Initial Radius 1/8 Longest Dimension, Single-Pixel Stepping, 0.1 Second Time Step, Maximum 20 Iterations

Ground-Based – Granite VNIR

The second level set edge detection experiment on ground-based hyperspectral data uses Pika II VNIR imagery of a high-spatial resolution granite sample. Specifically, this experiment tests the algorithm against five distinct datasets: a 72-band reflectance

cube, a 2-band compressed PCA cube, the full 72-band PCA cube, a 2-band compressed MNF cube, and the full 72-band MNF cube. For comparison, this test also executes the Roberts operator and the Sobel operator against the full Granite VNIR reflectance cube. Figure 263 presents samples of the seven experiments for the Granite VNIR data.

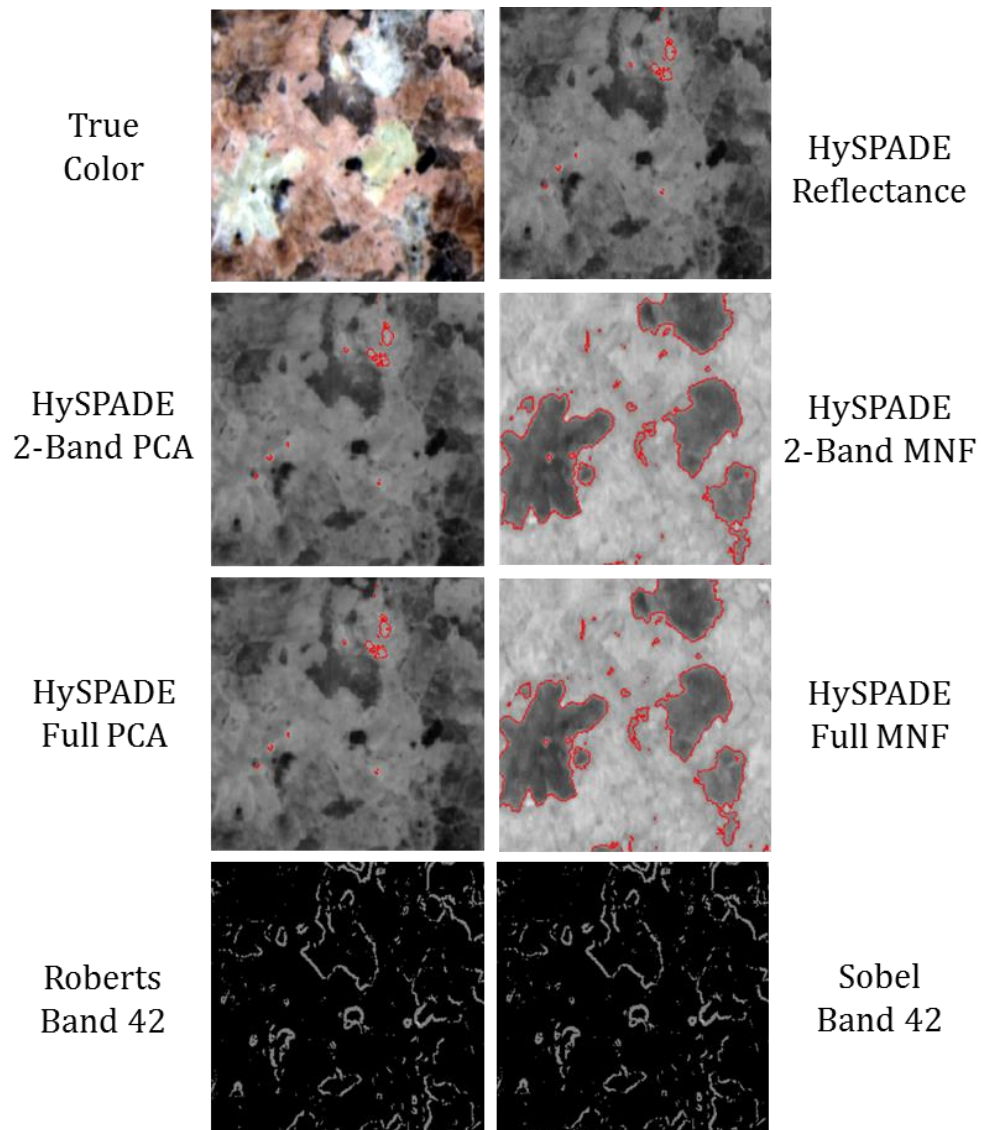


Figure 263: Level Set Experiment for Granite Ground-Based VNIR Data, Initial Curve at Image Center, Initial Radius 1/8 Longest Dimension, Single-Pixel Stepping, 0.1 Second Time Step, Maximum 20 Iterations

Ground-Based – Granite NIR/SWIR

The third level set edge detection experiment on ground-based hyperspectral data uses high-spatial resolution Pika II NIR/SWIR imagery of a different area from the same granite sample as the previous test. Specifically, this experiment tests the algorithm

against five distinct datasets: a 164-band reflectance cube, a 3-band compressed PCA cube, the full 164-band PCA cube, a 5-band compressed MNF cube, and the full 162-band MNF cube. For comparison, this test also executes the Roberts operator and the Sobel operator against the full Granite NIR/SWIR reflectance cube. Figure 264 presents samples of the seven experiments for the Granite NIR/SWIR data.

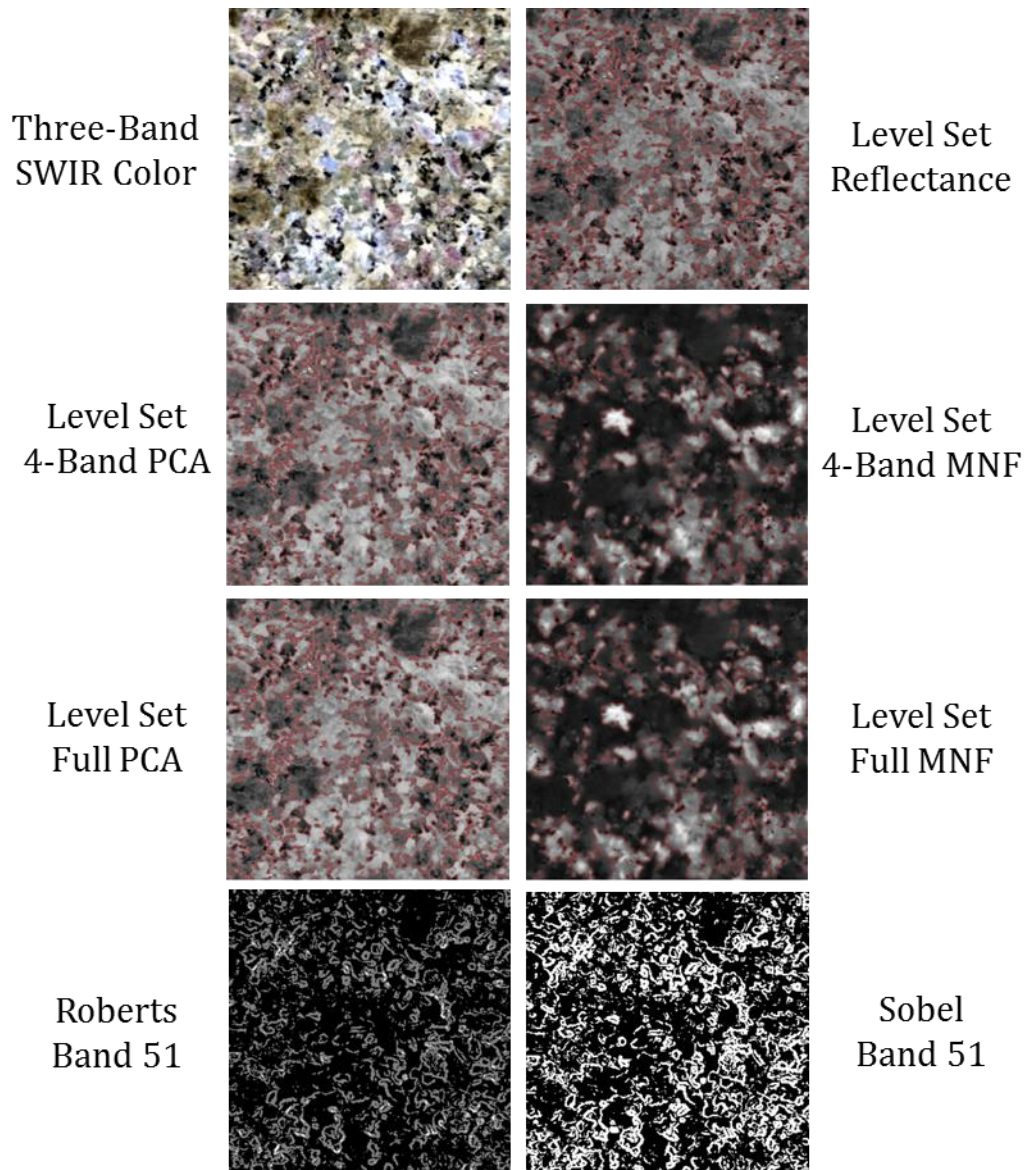


Figure 264: Level Set Experiment for Granite Ground-Based NIR/SWIR Data, Initial Curve at Image Center, Initial Radius 1/8 Longest Dimension, Single-Pixel Stepping, 0.1 Second Time Step, Maximum 20 Iterations

Ground-Based – South African Core Samples

The fourth level set detection experiment on ground-based hyperspectral data also aligns to mineral mapping applications. This experiment uses high-spatial resolution NIR/SWIR imagery of six South African geologic core samples arranged within the same

image plane. Specifically, this experiment tests the algorithm against five distinct datasets: a 234-band reflectance cube, a 3-band compressed PCA cube, the full 234-band PCA cube, a 5-band compressed MNF cube, and the full 234-band MNF cube. For comparison, this test also executes the Roberts operator and the Sobel operator against the full South African NIR/SWIR reflectance cube. Figure 265 presents samples of the seven experiments for the South African Core Sample NIR/SWIR data.

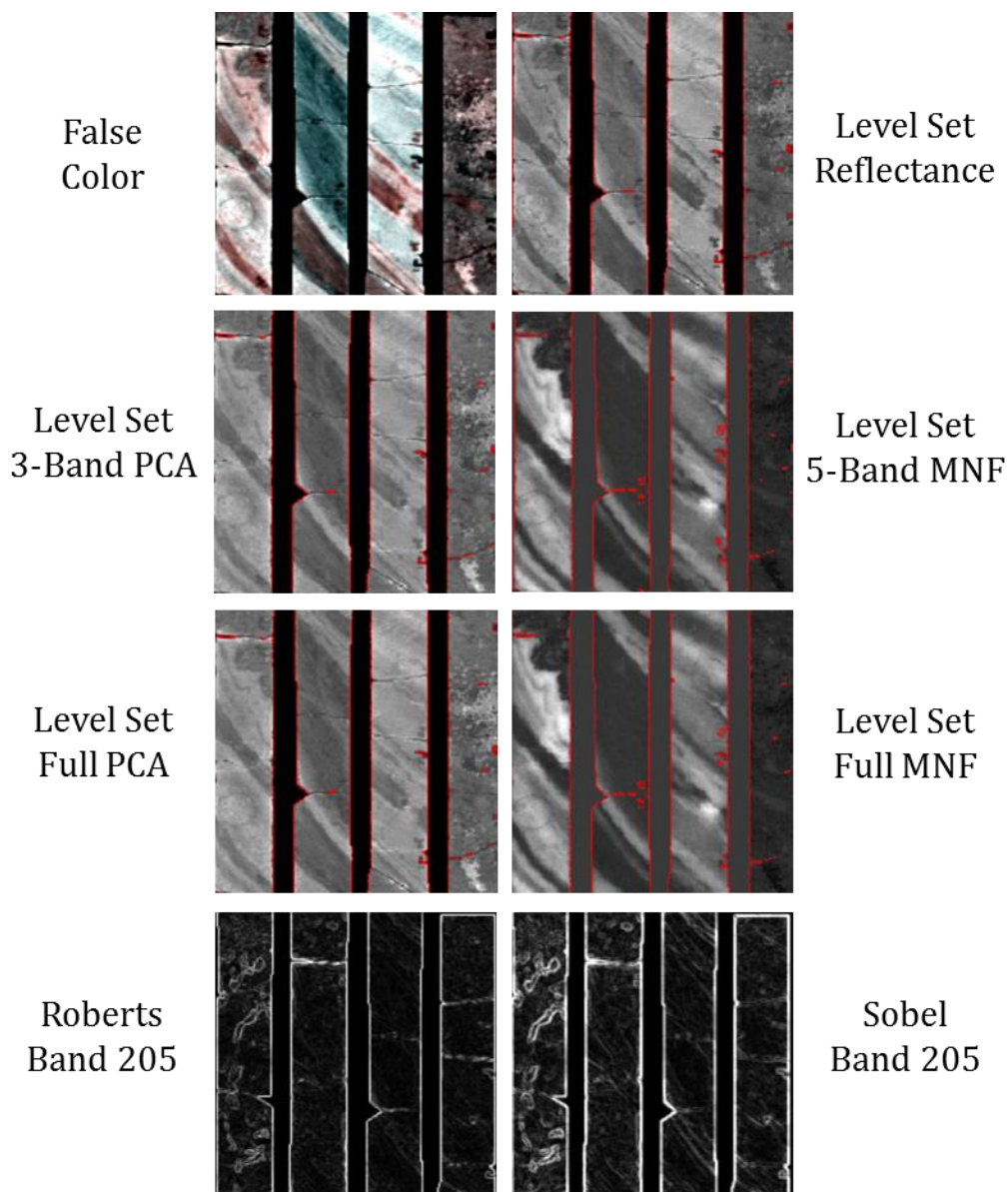


Figure 265: Level Set Experiment for South African Core Sample Ground-Based NIR/SWIR Data, Initial Curve at Image Center, Initial Radius 1/8 Longest Dimension, Single-Pixel Stepping, 0.1 Second Time Step, Maximum 20 Iterations

Ground-Based – Aluminum Panel

The fifth and final level set edge detection experiment on ground-based hyperspectral data addresses the aluminum aircraft panel possibly traceable to Amelia

Earhart's Lockheed Electra. Specifically, this experiment tests the algorithm against five distinct datasets: a 103-band reflectance cube, a 2-band compressed PCA cube, the full 103-band PCA cube, a 3-band compressed MNF cube, and the full 103-band MNF cube. For comparison, this test also executes the Roberts operator and the Sobel operator against the full Aluminum Aircraft Panel VNIR reflectance cube. Figure 266 presents samples of the seven experiments for the Aluminum Aircraft Panel data.

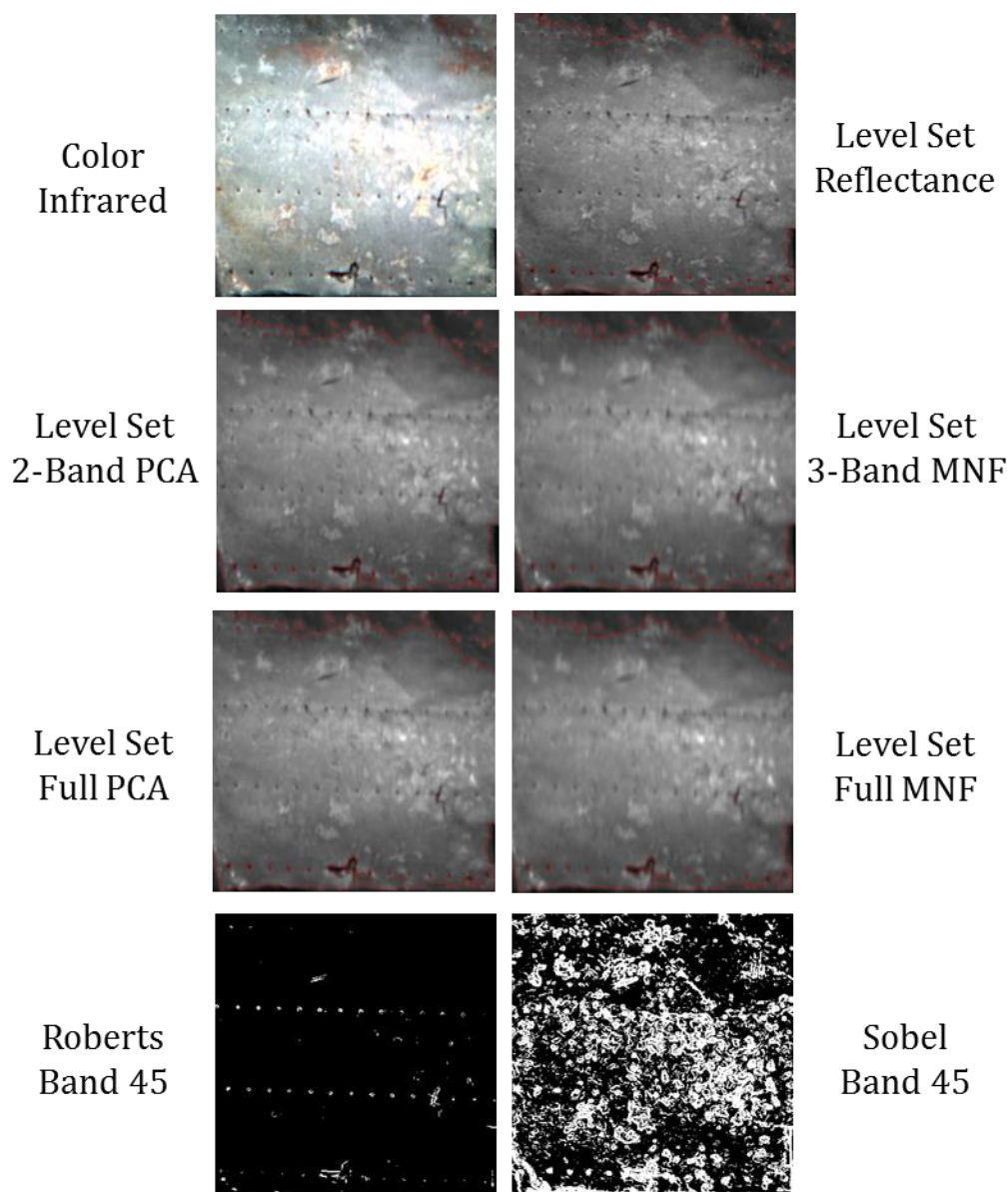


Figure 266: Level Set Experiment for Aluminum Aircraft Panel Ground-Based VNIR Data, Initial Curve at Image Center, Initial Radius 1/8 Longest Dimension, Single-Pixel Stepping, 0.1 Second Time Step, Maximum 20 Iterations

Microscene – Rare Target on Sand

The first level set edge detection experiment on microscene hyperspectral data uses Pika II VNIR imagery of a complex microscene on sand. This test supports trace

chemical detection HSI applications due to the presence of a rare target in a complex background. Specifically, this experiment tests the algorithm against five distinct datasets: a 74-band reflectance cube, a 3-band compressed PCA cube, the full 74-band PCA cube, a 5-band compressed MNF cube, and the full 74-band MNF cube. For comparison, this test also executes the Roberts operator and the Sobel operator against the full Rare Target on Sand reflectance cube. Figure 267 presents samples of the seven experiments for the Rare Target on Sand data.

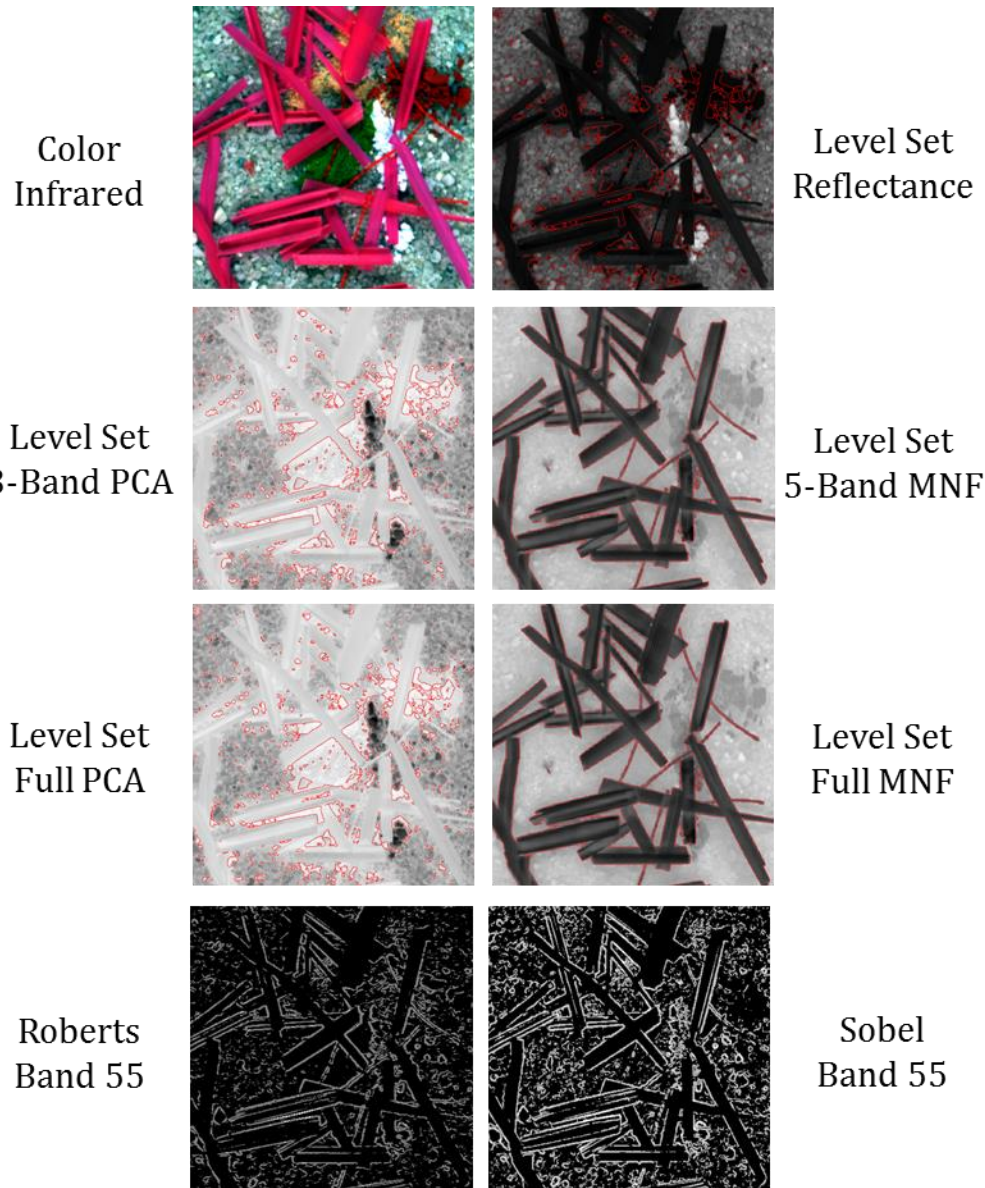


Figure 267: Level Set Experiment for Rare Target on Sand VNIR Data, Initial Curve at Image Center, Initial Radius 1/8 Longest Dimension, Single-Pixel Stepping, 0.1 Second Time Step, Maximum 20 Iterations

Microscene – Chemical Array

The second level set experiment on microscene hyperspectral data uses 168-band HYPERSPEC NIR/SWIR imagery of a chemical array on sand. This test supports trace

chemical detection HSI applications due to the presence of several rare targets on a simple background. Specifically, this experiment tests the algorithm against five distinct datasets: a 168-band reflectance cube, a 3-band compressed PCA cube, the full 168-band PCA cube, a 5-band compressed MNF cube, and the full 168-band MNF cube. For comparison, this test also executes the Roberts operator and the Sobel operator against the full Rare Target on Sand reflectance cube. Figure 268 presents samples of the seven experiments for the Chemical Array data.

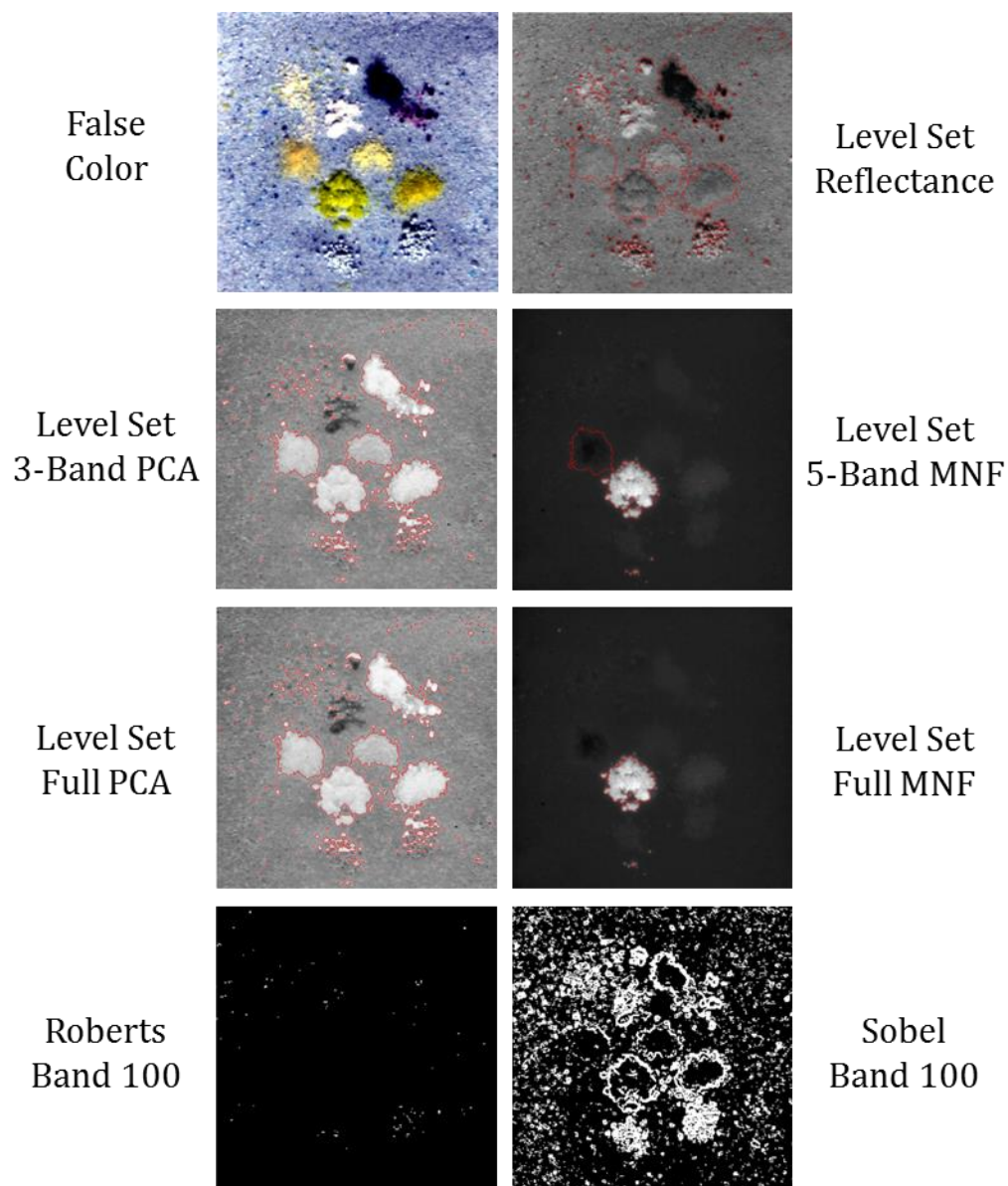


Figure 268: Level Set Experiment for Chemical Array NIR/SWIR Data, Initial Curve at Image Center, Initial Radius 1/8 Longest Dimension, Single-Pixel Stepping, 0.1 Second Time Step, Maximum 20 Iterations

Microscene – Cloth Threads

The third and final level set experiment on microscene hyperspectral data uses 80-band Pika II VNIR imagery of a series of different color cloth threads arrayed on a sand

background. Specifically, this experiment tests the algorithm against five distinct datasets: an 80-band reflectance cube, a 3-band compressed PCA cube, the full 80-band PCA cube, a 5-band compressed MNF cube, and the full 80-band MNF cube. For comparison, this test also executes the Roberts operator and the Sobel operator against the full Rare Target on Sand reflectance cube. Figure 269 presents samples of the seven experiments for the Cloth Thread data.

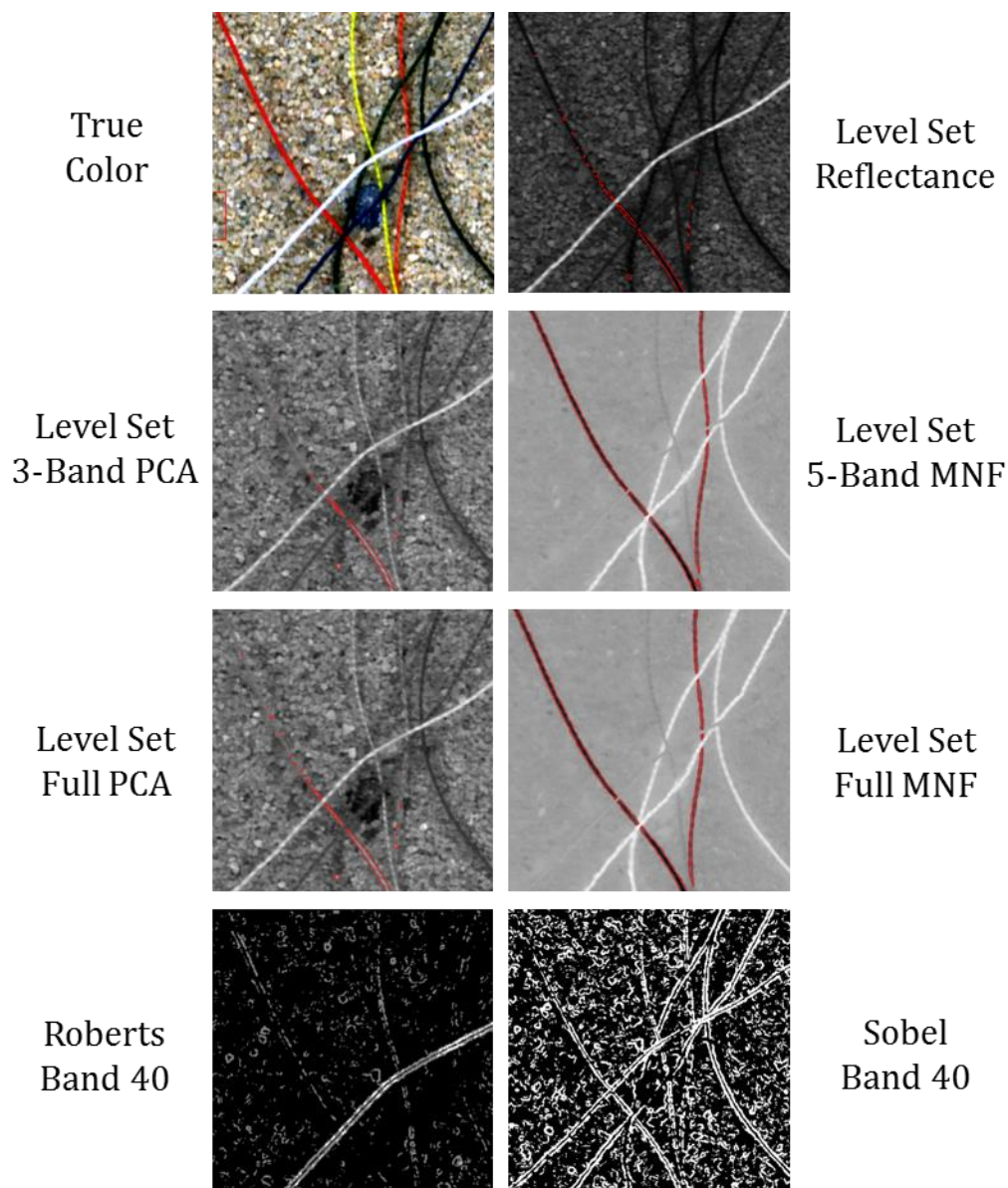


Figure 269: Level Set Experiment for Cloth Threads VNIR Data, Initial Curve at Image Center, Initial Radius 1/8 Longest Dimension, Single-Pixel Stepping, 0.1 Second Time Step, Maximum 20 Iterations

ANALYSIS AND EVALUATION

The Analysis and Evaluation section consists of three sections, each of which corresponds to one of the three new edge detection algorithms.

Di Zenzo-Based Gradient Analysis and Evaluation

This section presents the empirical evaluation of the gradient-based edge detection operator as measured against the six Canny evaluation criteria. For each evaluation criteria, this study presents samples of the strongest measurements, while the complete edge planes are available in Appendix A. Additionally, the precise evaluation measurements are presented in a single table, which enables comparison across data input type and Canny evaluation criteria. Each section also contains the associated interest points, benchmark vertical edge points, benchmark horizontal edge points and benchmark single-point intersections.

Overall, the gradient-based edge detection algorithm produced satisfactory evaluation measurements across a broad range of datasets. The algorithm performed particularly strongly against the false negatives, localization and unbroken edges criteria, while performing most weakly against the false positives criterion. In general, the false positive performance was not a barrier to generating useful edge detection results, however. Additionally, the compressed PCA and compressed MNF data inputs produced

the strongest results, a finding that supports the hypothesis that concentrating spectral information into fewer channels improves edge detection results.

Overhead – Reno, Nevada USA

As seen in Figure 270 and Table 23, the Gradient-based edge detection algorithm produced satisfactory results across several data input types and Canny evaluation criteria. The compressed PCA and MNF cubes produced the strongest normalized Canny criteria scores, measuring strongly against the false positives, false negatives, localization, robustness to noise and unbroken edges criteria. The reflectance cube measured strongly against all Canny criteria except for single-point response criterion, against which is produced suboptimal multi-pixel edges as seen in Appendix A. Note that for most evaluation criteria, the compressed PCA and MNF cubes outperformed their full PCA and full MNF counterparts, which supports the hypothesis that concentrating spectral information into fewer channels improves edge detection results.

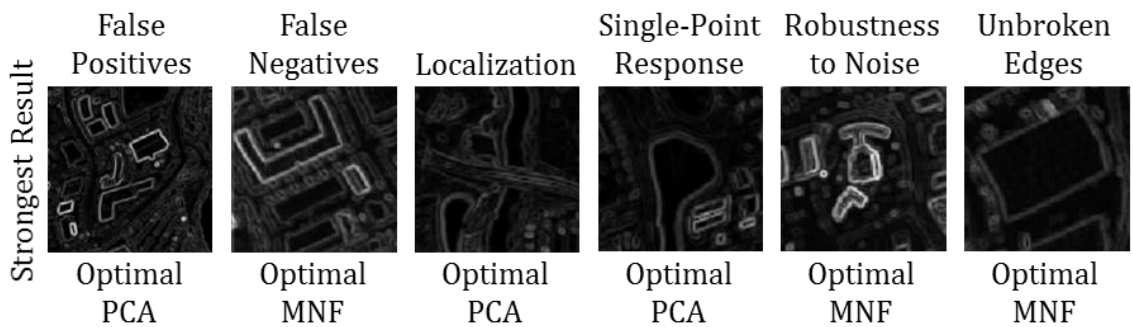


Figure 270: Strongest Gradient Evaluation Results for Reno, NV Overhead VNIR/SWIR Data, Unstretched

For the Reno VNIR/SWIR data, Table 24, Table 25, Table 26, and Table 27 present the evaluation interest points, benchmark vertical edge points, benchmark horizontal edge points and benchmark single-point intersections, respectively. Each interest point and benchmark point was chosen according to the criteria detailed in the Methodology component and apply to all three algorithm evaluations.

Table 23: Gradient Evaluation Measurements for Reno, NV Overhead VNIR/SWIR Data

Gradient Algorithm Reno	False Positives	False Negatives	Localization	Single-Point Response	Robustness to Noise	Unbroken Edges	Normalized Score
Reflectance	2	2	1	5	2	1	2.2
Optimal PCA	1	2	1	2	1	1	1.3
Optimal MNF	1	1	1	2	1	1	1.2
Full PCA	2	2	1	3	2	1	1.8
Full MNF	3	2	1	3	3	1	2.2
Roberts	4	3	2	4	3	3	3.2
Sobel	2	3	2	3	2	4	2.7

A variety of evaluation methods were used to assess the Gradient-based edge detection algorithm’s performance against the dataset, including interest points, collinearity of edges, single-point intersections and image subtraction. For example, the algorithm successfully delineated edges through all interest points within the compressed MNF cube, including all benchmark edge points and benchmark single-point intersections. Additionally, edge collinearity techniques indicated that the algorithm

accurately localized edges across all five HSI input data sets and produced unbroken edges across all five inputs.

Table 24: Interest Points for Reno VNIR/SWIR Data

Interest Point	Position (x,y)	Feature
1	4, 2170	U-shaped building
2	12, 2167	U-shaped building
3	24, 2189	U-shaped building
4	64, 2171	U-shaped building
5	55, 2147	U-shaped building
6	61, 2145	U-shaped building
7	75, 2177	U-shaped building
8	23, 2201	U-shaped building
9	151, 2409	Major intersection
10	161, 2405	Major intersection
11	167, 2414	Major intersection
12	157, 2418	Major intersection
13	279, 2280	River bend with vegetation
14	276, 2292	River bend with vegetation
15	276, 2310	River bend with vegetation
16	292, 2280	River bend with vegetation
17	289, 2292	River bend with vegetation
18	292, 2311	River bend with vegetation
19	272, 2547	Bridge
20	285, 2549	Bridge
21	284, 2559	Bridge
22	272, 2557	Bridge

Table 25: Benchmark Vertical Edge Points for Reno VNIR/SWIR Data

Vertical Edge Point	Position (x,y)	Feature
1	175, 2375	L-shaped building
2	175, 2376	L-shaped building
3	175, 2377	L-shaped building
4	175, 2378	L-shaped building
5	175, 2379	L-shaped building
6	175, 2380	L-shaped building
7	175, 2381	L-shaped building
8	175, 2382	L-shaped building
9	175, 2383	L-shaped building
10	175, 2384	L-shaped building
11	175, 2385	L-shaped building
12	175, 2386	L-shaped building
13	175, 2387	L-shaped building
14	175, 2388	L-shaped building
15	233, 2570	Vegetation around pond
16	233, 2571	Vegetation around pond
17	233, 2572	Vegetation around pond
18	233, 2573	Vegetation around pond
19	233, 2574	Vegetation around pond
20	233, 2575	Vegetation around pond
21	233, 2576	Vegetation around pond
22	233, 2577	Vegetation around pond
23	233, 2578	Vegetation around pond
24	233, 2579	Vegetation around pond
25	233, 2580	Vegetation around pond

Table 26: Benchmark Horizontal Edge Points for Reno VNIR/SWIR Data

Horizontal Edge Point	Position (x,y)	Feature
1	137, 2437	Convex building extension
2	138, 2437	Convex building extension
3	139, 2437	Convex building extension
4	140, 2437	Convex building extension
5	141, 2437	Convex building extension
6	142, 2437	Convex building extension
7	143, 2437	Convex building extension
8	144, 2437	Convex building extension
9	145, 2437	Convex building extension
10	240, 2565	Vegetation around pond
11	241, 2565	Vegetation around pond
12	242, 2565	Vegetation around pond
13	243, 2565	Vegetation around pond
14	244., 2565	Vegetation around pond
15	245, 2565	Vegetation around pond
16	246, 2565	Vegetation around pond
17	247, 2565	Vegetation around pond
18	248, 2565	Vegetation around pond

Table 27: Benchmark Single-Point Intersections for Reno VNIR/SWIR Data

Single-Point Intersection	Position (x,y)	Feature
1	181, 2717	Water and concrete
2	30, 2723	Concrete and asphalt
3	23, 2718	Roof and vegetation
4	115, 2545	Roof and vehicle
5	65, 2581	Different roofing materials
6	163, 2188	Roof and vehicle
7	267, 2370	Vegetation and water
8	288, 2310	Earth and water
9	306, 2199	Vegetation and bare earth
10	188, 2391	Asphalt and concrete

Overhead – Cuprite, Nevada USA

As seen in Figure 271 and Table 28 for Cuprite Flight Line #1, the Gradient-based edge detection algorithm produced satisfactory results across only the compressed PCA and compressed MNF data input types. Results indicate that the dataset is particularly challenging for the false negatives criterion, against which each input data type performed no better than average.

The compressed PCA and MNF cubes produced the strongest normalized Canny criteria scores, measuring strongly against the false positives, localization, robustness to noise and unbroken edges criteria. The reflectance cube measured strongly against only the localization criteria and weakly against the remaining criteria. Except for the compressed MNF cube, all input data types performed weakly against the single-point response criterion as seen in Appendix A. False positives were particularly challenging for the algorithm against this dataset, as well. Note that for most evaluation criteria, the compressed PCA and MNF cubes outperformed their full PCA and full MNF counterparts, which supports the hypothesis that concentrating spectral information into fewer channels improves edge detection results.

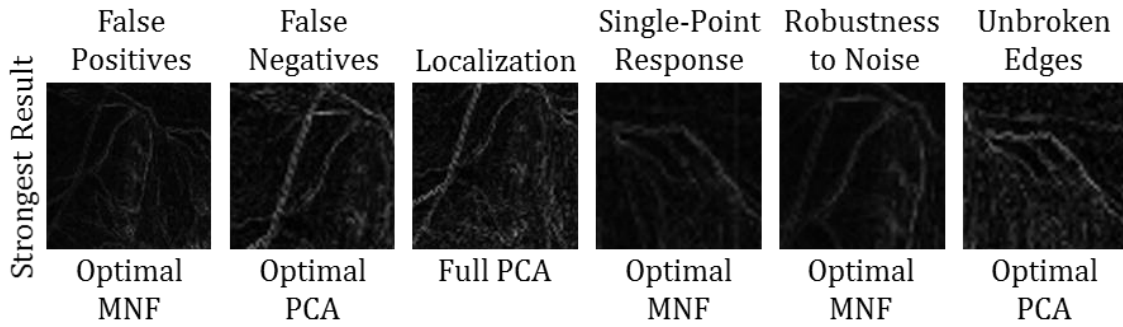


Figure 271: Strongest Gradient Evaluation Results for Cuprite FL #1 Overhead VNIR/SWIR Data, Unstretched

Table 28: Gradient Evaluation Measurements for Cuprite FL #1 Overhead VNIR/SWIR Data

Gradient Algorithm Cuprite Flight Line #1	False Positives	False Negatives	Localization	Single-Point Response	Robustness to Noise	Unbroken Edges	Normalized Score
Reflectance	4	3	1	4	3	3	3.0
Optimal PCA	2	3	1	3	2	2	2.2
Optimal MNF	2	4	1	2	2	2	2.2
Full PCA	3	3	1	4	2	2	2.5
Full MNF	5	3	1	4	4	3	3.3
Roberts	5	3	2	3	4	2	3.2
Sobel	5	3	2	3	4	2	3.2

For the Cuprite VNIR/SWIR Flight Line #1 data, Table 29, Table 30, Table 31, and Table 32 present the evaluation interest points, benchmark vertical edge points, benchmark horizontal edge points and benchmark single-point intersections, respectively. Each interest point and benchmark point were chosen according to the criteria detailed in the Methodology component and apply to all three algorithm evaluations.

Table 29: Interest Points for Cuprite VNIR/SWIR Flight Line #1 Data

Interest Point	Position (x,y)	Feature
1	79, 1180	Mineral salient
2	100, 1156	Mineral salient
3	108, 1128	Mineral salient
4	134, 1097	Mineral salient
5	141, 1086	Mineral salient
6	166, 1082	Mineral salient
7	181, 1186	Mineral salient
8	182, 1212	Mineral salient
9	2, 1233	SW-NE running road
10	47, 1206	SW-NE running road
11	67, 1145	SW-NE running road
12	87, 1084	SW-NE running road
13	106, 1052	SW-NE running road
14	134, 1020	SW-NE running road

Table 30: Benchmark Vertical Edge Points for Cuprite VNIR/SWIR Flight Line #1 Data

Vertical Edge Point	Position (x,y)	Feature
1	171, 1315	High-reflectance feature
2	171, 1316	High-reflectance feature
3	171, 1317	High-reflectance feature
4	171, 1318	High-reflectance feature
5	171, 1319	High-reflectance feature
6	171, 1320	High-reflectance feature
7	171, 1321	High-reflectance feature

Table 31: Benchmark Horizontal Edge Points for Cuprite VNIR/SWIR Flight Line #1 Data

Horizontal Edge Point	Position (x,y)	Feature
1	224, 1101	W-E running linear feature
2	225, 1101	W-E running linear feature
3	226, 1101	W-E running linear feature
4	227, 1101	W-E running linear feature
5	228, 1101	W-E running linear feature
6	229, 1101	W-E running linear feature
7	230, 1101	W-E running linear feature

Table 32: Benchmark Single Point Intersections for Cuprite VNIR/SWIR Flight Line #1 Data

Single-Point Intersection	Position (x,y)	Feature
1	45, 1209	Road intersection
2	166, 1093	Road intersection
3	96, 1065	Road intersection
4	179, 1323	Mineral intersection
5	267, 1353	Mineral intersection

A variety of evaluation methods were used to assess the Gradient-based edge detection algorithm's performance against the Cuprite Flight Line #1 dataset, including interest points, collinearity of edges, single-point intersections and ground truthing. For example, the algorithm was challenged to delineate edges through all interest points for most data types, particularly along the large triangular kaolinite deposit. Additionally, edge collinearity techniques indicated that the algorithm accurately localized edges across all five HSI input data sets and produced satisfactorily unbroken edges across the compressed MNF cube, the compressed PCA cube and the full PCA cube.

As seen in Figure 272 and Table 33 for Cuprite Flight Line #2, the Gradient-based edge detection algorithm produced satisfactory results across all four data input types and

most strongly against the compressed PCA and compressed MNF cubes. Results indicate that the algorithm generated strong results with respect to single-point response and unbroken edges. Localization measurements also were strong, and the gradient operator appears to be consistently generating strong localization performance across datasets.

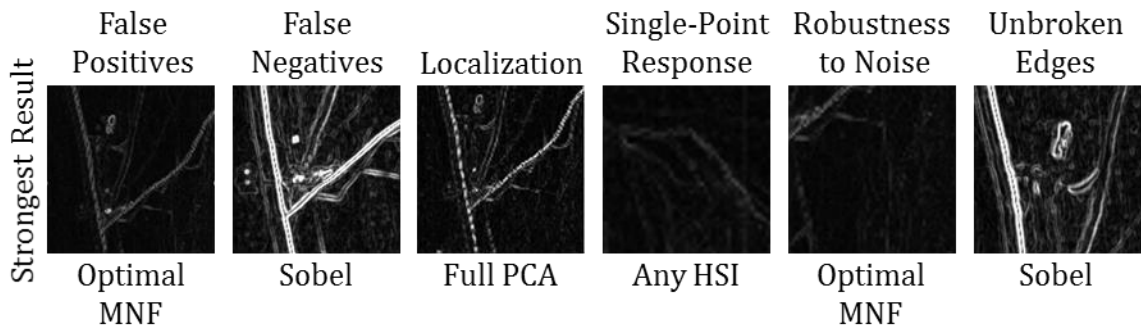


Figure 272: Strongest Gradient Evaluation Results for Cuprite FL #2 Overhead VNIR/SWIR Data, Unstretched

The compressed PCA and MNF cubes produced the strongest normalized Canny criteria scores, measuring strongly all six evaluation criteria except for the compressed MNF cube's average false positive performance. The reflectance cube measured nominally against the false positives and robustness to noise criteria, but performed above average for the remaining criteria. As seen in Appendix A, for all data types the edge operator accurately delineated all major interest points and features within the scene. Note that for most evaluation criteria, the compressed PCA and MNF cubes outperformed or equaled their full PCA and full MNF counterparts, which provides

additional support to the hypothesis that concentrating spectral information into fewer channels improves edge detection results.

Table 33: Gradient Evaluation Measurements for Cuprite FL#2 Overhead VNIR/SWIR Data

Gradient Algorithm Cuprite Flight Line #2	False Positives	False Negatives	Localization	Single-Point Response	Robustness to Noise	Unbroken Edges	Normalized Score
Reflectance	3	2	1	2	3	2	2.2
Optimal PCA	2	2	1	2	1	2	1.7
Optimal MNF	2	3	1	2	1	2	1.8
Full PCA	2	2	1	2	2	2	1.8
Full MNF	3	4	1	2	4	3	2.8
Roberts	5	2	1	3	4	2	2.8
Sobel	4	2	1	4	3	2	2.7

For the Cuprite VNIR/SWIR Flight Line #2 data, Table 34, Table 35, Table 36, and Table 37 present the evaluation interest points, benchmark vertical edge points, benchmark horizontal edge points and benchmark single-point intersections, respectively. Each interest point and benchmark point were chosen according to the criteria detailed in the Methodology component and apply to all three algorithm evaluations.

Table 34: Interest Points for Cuprite VNIR/SWIR Flight Line #2 Data

Interest Point	Position (x,y)	Feature
1	107, 543	Major intersection
2	107, 548	Major intersection
3	103, 550	Major intersection
4	102, 544	Major intersection
5	120, 338	Northern outbuilding
6	129, 336	Northern outbuilding
7	121, 365	Northern outbuilding
8	115, 363	Northern outbuilding

Table 35: Benchmark Vertical Edge Points for Cuprite VNIR/SWIR Flight Line #2 Data

Vertical Edge Point	Position (x,y)	Feature
1	126, 655	Asphalt road
2	126, 656	Asphalt road
3	126, 657	Asphalt road
4	126, 658	Asphalt road
5	126, 659	Asphalt road
6	126, 660	Asphalt road
7	126, 661	Asphalt road
8	126, 662	Asphalt road
9	126, 663	Asphalt road
10	126, 664	Asphalt road
11	126, 665	Asphalt road

Table 36: Benchmark Horizontal Edge Points for Cuprite VNIR/SWIR Flight Line #2 Data

Horizontal Edge Point	Position (x,y)	Feature
1	270, 428	Bend in W-E running road
2	271, 428	Bend in W-E running road
3	272, 428	Bend in W-E running road
4	273, 428	Bend in W-E running road
5	274, 428	Bend in W-E running road
6	275, 428	Bend in W-E running road
7	276, 428	Bend in W-E running road
8	277, 428	Bend in W-E running road
9	278, 428	Bend in W-E running road
10	279, 428	Bend in W-E running road
11	280, 428	Bend in W-E running road

Table 37: Benchmark Single-Point Intersections for Cuprite VNIR/SWIR Flight Line #2 Data

Single-Point Intersection	Position (x,y)	Feature
1	239, 321	Road intersection
2	227, 459	Road intersection
3	139, 467	Road intersection
4	112, 475	Water and earth intersection
5	120, 508	Building and earth intersection
6	126, 650	Road Intersection

A variety of evaluation methods were used to assess the Gradient-based edge detection algorithm's performance against the Cuprite Flight Line #2 dataset, including interest points, collinearity of edges, single-point intersections and ground truthing. For example, the algorithm missed less than 4% of the scene's interest points for all four datasets, meaning that the tests delineated nearly all major features at each interest point. Additionally, edge collinearity techniques indicated that the algorithm accurately localized edges across all five HSI input data sets and produced satisfactorily unbroken

edges across all five data input types. Overall, the gradient algorithm appears perform most strongly against the localization and unbroken edges criteria.

As seen in Figure 273 and Table 38 for Cuprite Flight Line #3, the Gradient-based edge detection algorithm produced satisfactory results with the compressed PCA and full PCA cubes. The reflectance, compressed MNF and full MNF produced unsatisfactory results with respect to false positives, and the reflectance cube struggled against all but the localization criteria. Results indicate that the algorithm generated strong results with respect to single-point response and unbroken edges.

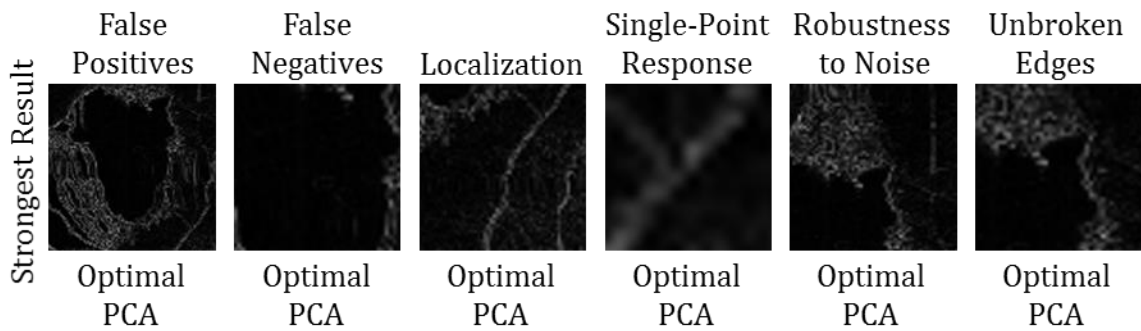


Figure 273: Strongest Gradient Evaluation Results for Cuprite FL #3 Overhead VNIR/SWIR Data, Unstretched

Table 38: Gradient Evaluation Measurements for Cuprite FL #3 Overhead VNIR/SWIR Data

Gradient Algorithm Cuprite Flight Line #3	False Positives	False Negatives	Localization	Single-Point Response	Robustness to Noise	Unbroken Edges	Normalized Score
Reflectance	5	2	2	4	4	4	3.5
Optimal PCA	1	1	1	2	1	2	1.3
Optimal MNF	4	2	1	2	3	3	2.5
Full PCA	2	1	1	2	2	2	1.7
Full MNF	5	2	1	3	5	4	3.3
Roberts	4	2	2	2	3	3	2.7
Sobel	2	1	1	3	2	2	1.8

The compressed PCA and full PCA cube evaluation were particularly strong, with both cubes fully delineating all interest points around the large playa dominating the scene. Where the edges were broken, they were at non-interest point pixels within the scene, and the breaks were few. Note that this is the first test in which the compressed MNF cube test did not generate results comparable to the compressed PCA test. Most likely, this diversion is attributable to the over-selection of MNF bands, which would allow low-information bearing bands to remain in the cube.

For the Cuprite VNIR/SWIR Flight Line #3 data, Table 39, Table 40, Table 41, and Table 42 present the evaluation interest points, benchmark vertical edge points, benchmark horizontal edge points and benchmark single-point intersections, respectively. Each interest point and benchmark point were chosen according to the criteria detailed in the Methodology component and apply to all three algorithm evaluations.

Table 39: Interest Points for Cuprite VNIR/SWIR Flight Line #3 Data

Interest Point	Position (x,y)	Feature
1	107, 1375	Playa Feature
2	156, 1400	Playa Feature
3	236, 1394	Playa Feature
4	225, 1417	Playa Feature
5	241, 1455	Playa Feature
6	228, 1534	Playa Feature
7	207, 1560	Playa Feature
8	201, 1591	Playa Feature
9	164, 1622	Playa Feature
10	119, 1590	Playa Feature
11	101, 1541	Playa Feature
12	52, 1466	Playa Feature
13	62, 1406	Playa Feature

Table 40: Benchmark Vertical Edge Points for Cuprite VNIR/SWIR Flight Line #3 Data

Vertical Edge Point	Position (x,y)	Feature
1	295, 1557	Bend in SE road
2	295, 1558	Bend in SE road
3	295, 1559	Bend in SE road
4	295, 1560	Bend in SE road
5	295, 1561	Bend in SE road
6	295, 1562	Bend in SE road
7	295, 1563	Bend in SE road
8	295, 1564	Bend in SE road

Table 41: Benchmark Horizontal Edge Points for Cuprite VNIR/SWIR Flight Line #3 Data

Horizontal Edge Point	Position (x,y)	Feature
1	303, 1396	Mineral salient
2	304, 1396	Mineral salient
3	305, 1396	Mineral salient
4	306, 1396	Mineral salient
5	307, 1396	Mineral salient
6	308, 1396	Mineral salient
7	309, 1396	Mineral salient
8	310, 1396	Mineral salient
9	311, 1396	Mineral salient
10	312, 1396	Mineral salient
11	313, 1396	Mineral salient
12	314, 1396	Mineral salient
13	315, 1396	Mineral salient
14	316, 1396	Mineral salient

Table 42: Benchmark Single-Point Intersections for Cuprite VNIR/SWIR Flight Line #3 Data

Single-Point Intersection	Position (x,y)	Feature
1	270, 1631	Road intersection
2	306, 1537	Road intersection
3	159, 1406	Mineral intersection
4	282, 1429	Mineral intersection
5	283, 1399	Mineral intersection
6	22, 1674	Mineral intersection

A variety of evaluation methods were used to assess the Gradient-based edge detection algorithm's performance against the Cuprite Flight Line #3 dataset, including interest points, collinearity of edges, single-point intersections and ground truthing. For example, the algorithm accurately mapped all interest points in the scene with almost completely unbroken edges according to the interest points, benchmark vertical and benchmark horizontal points. Additionally, edge collinearity techniques indicated that

the algorithm accurately localized edges for all datasets and produced edge maps with very few false positives.

As seen in Figure 274 and Table 43 for Cuprite Flight Line #4, the Gradient-based edge detection algorithm produced satisfactory for only the compressed MNF cube. For the reflectance, compressed PCA and full PCA cubes, the algorithm generated a suboptimal volume of either false positives or false negatives. The reflectance cube, in particular, generated a very high volume of false positives as seen in Appendix A. Again, edge localization performance was high for the gradient algorithm across all data inputs, and the compressed PCA and compressed MNF performed strongly against the false positive criteria.

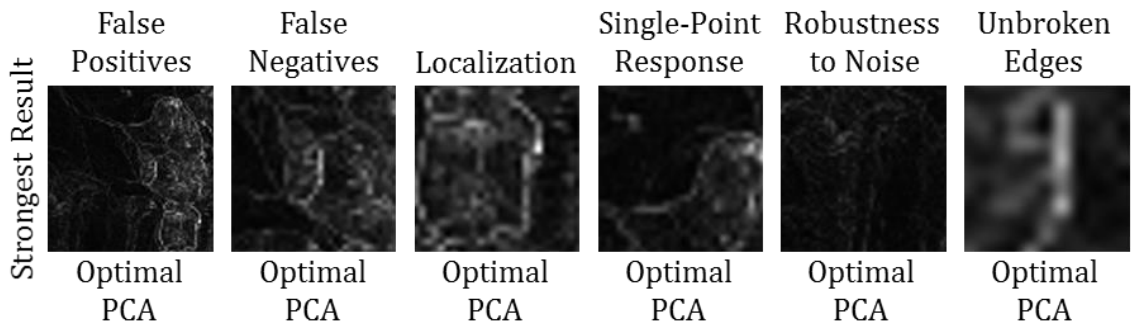


Figure 274: Strongest Gradient Evaluation Results for Cuprite FL #4 Overhead VNIR/SWIR Data, Unstretched

Table 43: Gradient Evaluation Measurements for Cuprite FL #4 Overhead VNIR/SWIR Data

Gradient Algorithm Cuprite Flight Line #4	False Positives	False Negatives	Localization	Single-Point Response	Robustness to Noise	Unbroken Edges	Normalized Score
Reflectance	5	3	1	2	3	3	2.8
Optimal PCA	1	4	1	1	2	3	2.0
Optimal MNF	1	2	1	1	1	2	1.3
Full PCA	1	4	1	1	2	3	2.0
Full MNF	2	2	1	1	4	2	2.0
Roberts	4	3	1	4	3	3	3.0
Sobel	4	3	1	4	3	2	2.8

The algorithm’s performance against the compressed MNF cube was notably strong, including the delineation of subtle silica outcroppings along the western ridges, full delineation of the eastern kaolinite deposits and a very low false alarm rate. The compressed MNF test missed only five interest points along the edge of the southernmost kaolinite deposit, but the overall false negative performance was strong. The compressed MNF cube excelled at generating unbroken edges, as well. The compressed PCA cube performed well against the false positives and single-point response criteria, but generated an unacceptable volume of false negatives, missing a high volume of interest points along the eastern kaolinite deposits.

For the Cuprite VNIR/SWIR Flight Line #4 data, Table 44, Table 45, Table 46, and Table 47 present the evaluation interest points, benchmark vertical edge points, benchmark horizontal edge points and benchmark single-point intersections, respectively.

Each interest point and benchmark point were chosen according to the criteria detailed in the Methodology component and apply to all three algorithm evaluations.

Table 44: Interest Points for Cuprite VNIR/SWIR Flight Line #4 Data

Interest Point	Position (x,y)	Feature
1	204, 2320	Mineral deposit
2	212, 2320	Mineral deposit
3	218, 2315	Mineral deposit
4	225, 2322	Mineral deposit
5	226, 2339	Mineral deposit
6	223, 2339	Mineral deposit
7	220, 2346	Mineral deposit
8	217, 2352	Mineral deposit
9	208, 2354	Mineral deposit
10	203, 2349	Mineral deposit
11	202, 2342	Mineral deposit
12	203, 2325	Mineral deposit

Table 45: Benchmark Vertical Edge Points for Cuprite VNIR/SWIR Flight Line #4 Data

Vertical Edge Point	Position (x,y)	Feature
1	290, 2426	Right edge of mineral deposit
2	290, 2427	Right edge of mineral deposit
3	290, 2428	Right edge of mineral deposit
4	290, 2429	Right edge of mineral deposit
5	290, 2430	Right edge of mineral deposit
6	290, 2431	Right edge of mineral deposit
7	290, 2432	Right edge of mineral deposit
8	290, 2433	Right edge of mineral deposit
9	290, 2434	Right edge of mineral deposit
10	290, 2435	Right edge of mineral deposit

Table 46: Benchmark Horizontal Edge Points for Cuprite VNIR/SWIR Flight Line #4 Data

Horizontal Edge Point	Position (x,y)	Feature
1	183, 2258	Mineral deposit
2	184, 2258	Mineral deposit
3	185, 2258	Mineral deposit
4	186, 2258	Mineral deposit
5	187, 2258	Mineral deposit
6	188, 2258	Mineral deposit
7	189, 2258	Mineral deposit
8	190, 2258	Mineral deposit

Table 47: Benchmark Single-Point Intersections for Cuprite VNIR/SWIR Flight Line #4 Data

Single-Point Intersection	Position (x,y)	Feature
1	243, 2283	Road intersection
2	231, 2464	Mineral intersection
3	254, 2300	Mineral intersection
4	293, 2199	Mineral intersection
5	253, 2505	Mineral intersection
6	116, 2539	Mineral intersection
7	176, 2204	Mineral intersection
8	223, 2346	Mineral intersection

A variety of evaluation methods were used to assess the Gradient-based edge detection algorithm's performance against the Cuprite Flight Line #4 dataset, including interest points, collinearity of edges, single-point intersections and ground truthing. For example, the algorithm accurately mapped all interest points in the scene with almost completely unbroken edges according to the interest points, benchmark vertical and benchmark horizontal points when tested against the compressed MNF cube.

Additionally, edge collinearity techniques indicated that the algorithm accurately localized edges for all datasets and produced edge maps with very few false positives.

Overhead – Indian Pines, Indiana USA

As seen in Figure 275 and Table 48, the Gradient-based edge detection algorithm produced satisfactory results across several data input types and Canny evaluation criteria. The compressed PCA and MNF cubes produced the strongest normalized Canny criteria scores, measuring strongly against the localization and unbroken edges criteria. The reflectance cube measured weakly against the single-point response Canny criteria, which is seen in the suboptimal multi-pixel edges Appendix A. Note that for all six Canny evaluation criteria, the compressed PCA and MNF cubes outperformed their full PCA and full MNF counterparts, which supports the hypothesis that concentrating spectral information into fewer channels improves edge detection results.

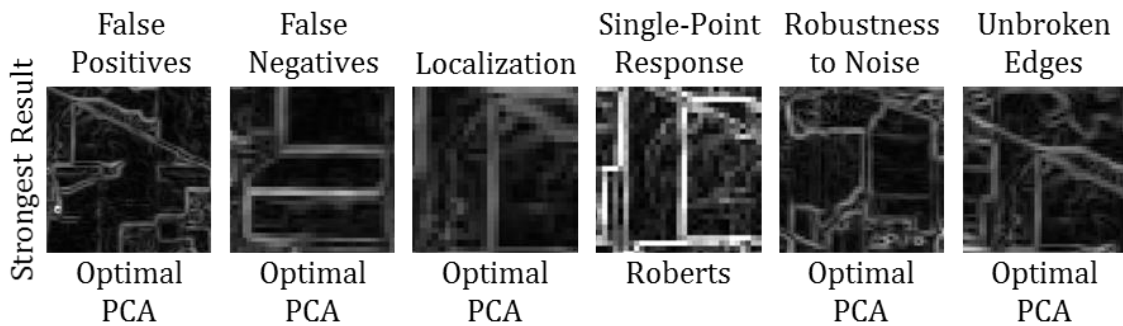


Figure 275: Strongest Gradient Evaluation Results for Indian Pines, IN Overhead VNIR/SWIR Data, Unstretched

Table 48: Gradient Evaluation Measurements for Indian Pines, IN Overhead VNIR/SWIR Data

Gradient Algorithm Indian Pines	False Positives	False Negatives	Localization	Single-Point Response	Robustness to Noise	Unbroken Edges	Normalized Score
Reflectance	3	3	2	4	3	2	2.8
Optimal PCA	2	2	1	3	2	1	1.8
Optimal MNF	3	3	2	3	3	2	2.7
Full PCA	2	2	1	3	2	1	1.8
Full MNF	5	4	3	3	5	4	4.0
Roberts	3	3	1	2	3	2	2.3
Sobel	3	3	1	3	2	2	2.3

For no input data type did the gradient algorithm generate strong results against the single-point response evaluation criteria – throughout the scene, three-pixel and occasionally four-pixel edges prevailed. The most likely explanation for the average to below-average single-point performance is the scene content itself. Namely, the primary edges in the scene are bounded by different vegetation classes which appear quite similar spectrally. Furthermore, many of the planted fields contain very young crops and therefore present spectra containing a substantial volume of soil information. Put simply, the scene contains quite challenging edges bordered by similar materials, which is a likely explanation for the gradient algorithm’s broad edges. For example, consider the sample young crop spectra in Figure 276, which demonstrates that young soybeans (green), hay (red) and corn (white) appear very similar, particularly beyond the visible channels. Also note that the strong presence of soil information in the spectra will present a significant challenge to an edge detection algorithm.

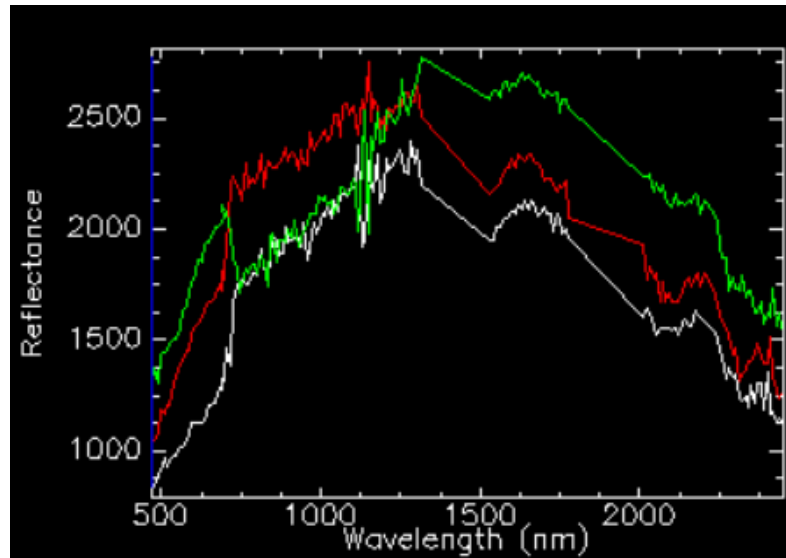


Figure 276: Similarity among Adjacent Vegetation Classes in the Indian Pines VNIR/SWIR Hypercube

The compressed PCA and MNF cubes produced the strongest normalized Canny criteria scores, performing strongly against all Canny criteria except single-point response, against which it produced nominal results. All data input types produced satisfactory results against the localization and unbroken edges criteria as seen in Appendix A. Note that for most evaluation criteria, the compressed PCA and MNF cubes outperformed their full PCA and full MNF counterparts, which provides further support to the hypothesis that concentrating spectral information into fewer channels improves edge detection results.

A variety of evaluation methods were used to assess the Gradient-based edge detection algorithm's performance against the Indian Pines VNIR/SWIR dataset, including interest points, collinearity of edges, single-point intersections and ground truthing. For example, the compressed PCA and compressed MNF cubes missed only

between 1% and 2% of scene interest points and single-point intersections, earning them a strong Likert score of two for the false negatives criterion. Additionally, edge collinearity techniques indicated that the algorithm accurately localized edges across all five HSI input data sets and produced satisfactorily unbroken edges across all data inputs except for the full MNF cube, for which it performed weakly.

For the Indian Pines VNIR/SWIR data, Table 49, Table 50, Table 51, and Table 52 present the evaluation interest points, benchmark vertical edge points, benchmark horizontal edge points and benchmark single-point intersections, respectively. Each interest point and benchmark point were chosen according to the criteria detailed in the Methodology component and apply to all three algorithm evaluations.

Table 49: Interest Points for Indian Pines VNIR/SWIR Data

Interest Point	Position (x,y)	Feature
1	73, 74	L-shaped cornfield
2	95, 74	L-shaped cornfield
3	95, 83	L-shaped cornfield
4	84, 83	L-shaped cornfield
5	84, 94	L-shaped cornfield
6	73, 94	L-shaped cornfield

Table 50: Benchmark Vertical Edge Points for Indian Pines VNIR/SWIR Data

Vertical Edge Point	Position (x,y)	Feature
1	37, 48	Soybeans next to grass and trees
2	37, 49	Soybeans next to grass and trees
3	37, 50	Soybeans next to grass and trees
4	37, 51	Soybeans next to grass and trees
5	37, 52	Soybeans next to grass and trees
6	37, 53	Soybeans next to grass and trees
7	37, 54	Soybeans next to grass and trees
8	37, 55	Soybeans next to grass and trees
9	37, 56	Soybeans next to grass and trees
10	37, 57	Soybeans next to grass and trees
11	37, 58	Soybeans next to grass and trees
12	37, 59	Soybeans next to grass and trees
13	37, 60	Soybeans next to grass and trees
14	37, 61	Soybeans next to grass and trees
15	37, 62	Soybeans next to grass and trees
16	37, 63	Soybeans next to grass and trees
17	37, 64	Soybeans next to grass and trees
18	37, 65	Soybeans next to grass and trees

Table 51: Benchmark Horizontal Edge Points for Indian Pines VNIR/SWIR Data

Horizontal Edge Point	Position (x,y)	Feature
1	18, 125	Cornfield next to pasture
2	19, 125	Cornfield next to pasture
3	20, 125	Cornfield next to pasture
4	21, 125	Cornfield next to pasture
5	22, 125	Cornfield next to pasture
6	23, 125	Cornfield next to pasture
7	24, 125	Cornfield next to pasture
8	25, 125	Cornfield next to pasture
9	26, 125	Cornfield next to pasture
10	27, 125	Cornfield next to pasture
11	28, 125	Cornfield next to pasture
12	29, 125	Cornfield next to pasture
13	30, 125	Cornfield next to pasture
14	31, 125	Cornfield next to pasture
15	32, 125	Cornfield next to pasture
16	33, 125	Cornfield next to pasture
17	34, 125	Cornfield next to pasture
18	35, 125	Cornfield next to pasture

Table 52: Benchmark Single-Point Intersections for Indian Pines VNIR/SWIR Data

Single-Point Intersection	Position (x,y)	Feature
1	73, 64	Vegetation and road
2	96, 75	Vegetation and road
3	73, 30	Vegetation and road
4	26, 41	Vegetation and road
5	3, 29	Road intersection
6	73, 73	Vegetation intersection
7	73, 94	Vegetation intersection
8	48, 73	Vegetation intersection
9	73, 41	Vegetation intersection
10	120, 42	Vegetation intersection

Overhead – Deepwater Horizon Oil Spill

As seen in Figure 277 and Table 53, the Gradient-based edge detection algorithm produced satisfactory results across several data input types and Canny evaluation criteria. In particular, the radiance and compressed MNF cubes produced strong results across all six criteria, and the reflectance cube produced strong results against all criteria except single-point response, against which is scored a respectable average. Indeed, the compressed MNF cube produced one of the most robust edge planes in this work, earning the strongest Likert score for five of the six criteria.

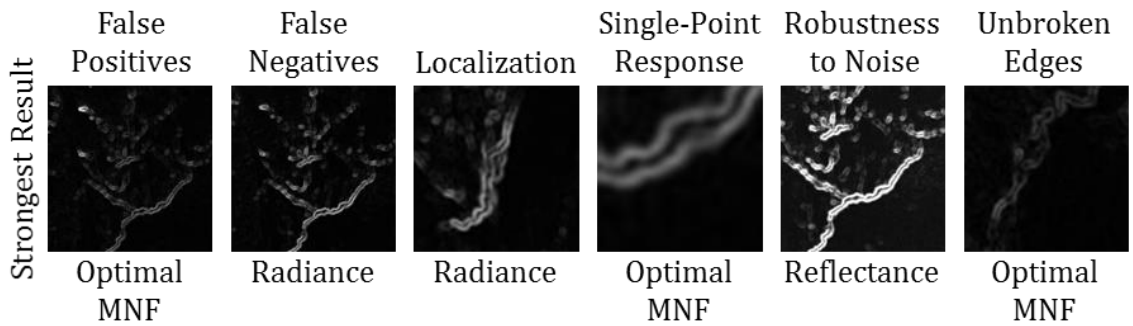


Figure 277: Strongest Gradient Evaluation Results for Deepwater Horizon Overhead VNIR/SWIR Data, Unstretched

Table 53: Gradient Evaluation Measurements for Deepwater Horizon Overhead VNIR/SWIR Data

Gradient Algorithm Deepwater Horizon	False Positives	False Negatives	Localization	Single-Point Response	Robustness to Noise	Unbroken Edges	Normalized Score
Radiance	1	1	1	2	2	1	1.3
Reflectance	2	2	1	3	2	1	1.8
Optimal PCA	2	5	1	2	2	3	2.5
Optimal MNF	1	1	1	1	2	1	1.2
Full PCA	2	5	1	2	3	3	2.7
Full MNF	3	3	1	2	5	2	2.7
Roberts	5	3	1	3	5	2	3.2
Sobel	5	2	1	3	4	1	2.7

The radiance, reflectance and compressed MNF cubes measured strongly against the false positives, false negatives, single-point response and unbroken edges criteria, in each case generating a highly accurate edge plane of oil spill fronts on the ocean surface. As seen in Appendix A, the three tests also accurately delineated several surface ships along the western edge of the image and successfully avoided falsely alarming against the choppy seas throughout the scene. The compressed PCA and full PCA cubes measured weakly against the false negatives Canny criterion, which is seen in the suboptimal volume of missed oil-water edges in Appendix A’s edge planes. The PCA cubes’ underperformances are likely attributable to the significant volume of noise present in the scene – a barrier that the MNF cubes can overcome by virtue of their denoising step prior to the PCA transform.

Additionally, the strong evaluation measurements from the radiance cube test suggest that the Di Zenzo-based edge operator can robustly delineate unique targets on a

uniform background without the benefit of reflectance data. Note that for all six Canny evaluation criteria, the compressed PCA and MNF cubes outperformed their full PCA and full MNF counterparts, which supports the hypothesis that concentrating spectral information into fewer channels improves edge detection results.

A variety of evaluation methods were used to assess the Gradient-based edge detection algorithm's performance against the Deepwater Horizon VNIR/SWIR dataset, including interest points, collinearity of edges and single-point intersections. For example, the compressed MNF and radiance cubes correctly delineated edges through 100% of interest points and single-point intersections, earning them the strongest Likert score for the false negatives criterion. As seen in Figure 277, the algorithm generated clean, unbroken edges along the major oil slicks within the scene – a meaningful finding with respect to oil spill mapping applications. Additionally, edge collinearity techniques indicated that the algorithm accurately localized edges across all five HSI input data sets.

For the Deepwater Horizon VNIR/SWIR data, Table 54, Table 55, Table 56, and Table 57 present the evaluation interest points, benchmark vertical edge points, benchmark horizontal edge points and benchmark single-point intersections, respectively. Each interest point and benchmark point were chosen according to the criteria detailed in the Methodology component and apply to all three algorithm evaluations.

Table 54: Interest Points for Deepwater Horizon VNIR/SWIR Data

Interest Point	Position (x,y)	Feature
1	188, 4772	Front of SE oil slick
2	197, 4765	Front of SE oil slick
3	198, 4763	Front of SE oil slick
4	198, 4759	Front of SE oil slick
5	204, 4755	Front of SE oil slick
6	205, 4750	Front of SE oil slick
7	203, 4744	Front of SE oil slick
8	204, 4739	Front of SE oil slick
9	207, 4736	Front of SE oil slick
10	219, 4725	Front of SE oil slick
11	228, 4724	Front of SE oil slick
12	234, 4722	Front of SE oil slick
13	239, 4723	Front of SE oil slick
14	241, 4722	Front of SE oil slick
15	247, 4720	Front of SE oil slick
16	253, 4715	Front of SE oil slick
17	258, 4714	Front of SE oil slick
18	264, 4707	Front of SE oil slick
19	274, 4692	Front of SE oil slick
20	277, 4690	Front of SE oil slick
21	284, 4684	Front of SE oil slick
22	290, 4680	Front of SE oil slick
23	291, 4672	Front of SE oil slick

Table 55: Benchmark Vertical Edge Points for Deepwater Horizon VNIR/SWIR Data

Vertical Edge Point	Position (x,y)	Feature
1	228, 4517	W edge of oil slick
2	228, 4518	W edge of oil slick
3	228, 4516	W edge of oil slick
4	228, 4517	W edge of oil slick
5	228, 4518	W edge of oil slick
6	228, 4519	W edge of oil slick
7	228, 4520	W edge of oil slick
8	228, 4521	W edge of oil slick
9	228, 4522	W edge of oil slick
10	228, 4523	W edge of oil slick
11	228, 4524	W edge of oil slick
12	228, 4525	W edge of oil slick
13	228, 4526	W edge of oil slick
14	228, 4527	W edge of oil slick
15	228, 4528	W edge of oil slick

Table 56: Benchmark Horizontal Edge Points for Deepwater Horizon VNIR/SWIR Data

Horizontal Edge Point	Position (x,y)	Feature
1	281, 4386	S edge of oil slick
2	282, 4386	S edge of oil slick
3	283, 4386	S edge of oil slick
4	284, 4386	S edge of oil slick
5	285, 4386	S edge of oil slick
6	286, 4386	S edge of oil slick
7	287, 4386	S edge of oil slick
8	288, 4386	S edge of oil slick
9	289, 4386	S edge of oil slick
10	290, 4386	S edge of oil slick

Table 57: Benchmark Single-Point Intersections for Deepwater Horizon VNIR/SWIR Data

Single-Point Intersection	Position (x,y)	Feature
1	193, 4653	Oil and water intersection
2	238, 4478	Oil and water intersection
3	252, 4425	Oil and water intersection
4	211, 4726	Oil and water intersection
5	203, 4743	Oil and water intersection
6	233, 4608	Oil and water intersection
7	115, 4583	Oil and water intersection
8	101, 4467	Oil and water intersection
9	235, 4514	Oil and water intersection
10	310, 4641	Oil and water intersection

Ground-Based – Larkhaven

As seen in Figure 278 and Table 58, the Gradient-based edge detection algorithm produced satisfactory results across several data input types and Canny evaluation criteria. The algorithm generated its strongest Larkhaven results against the compressed PCA and compressed MNF cubes, consistent with tests against other remote sensing scenes in that it performed above average for all six criteria. The reflectance cube also performed strongly against five criteria and all five HSI data types produced strong scores against the unbroken edges criterion. Notably, all five HSI data types measured above average for 28 of the 30 evaluative measures; only the reflectance cube and the full PCA cube merited an average Likert score of 3 with respect to the robustness to noise criterion. Finally, note that the algorithm produced the strongest available localization score across all five HSI data types.

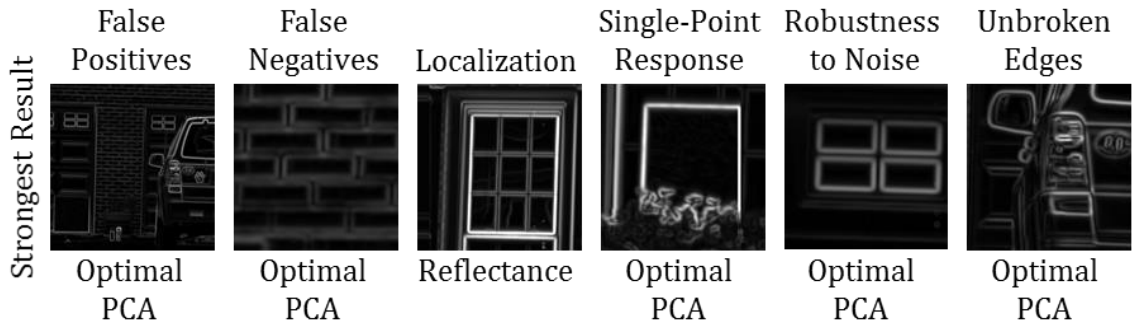


Figure 278: Strongest Gradient Evaluation Results for Larkhaven Ground-Based VNIR Data, Unstretched

Table 58: Gradient Evaluation Measurements for Larkhaven Ground-Based VNIR Data

Gradient Algorithm Larkhaven	False Positives	False Negatives	Localization	Single-Point Response	Robustness to Noise	Unbroken Edges	Normalized Score
Reflectance	2	1	1	2	3	1	1.7
Optimal PCA	1	1	1	2	1	1	1.2
Optimal MNF	1	2	1	2	2	2	1.7
Full PCA	1	1	1	2	3	1	1.5
Full MNF	3	5	1	2	5	2	3.0
Roberts	3	1	1	2	3	1	1.8
Sobel	3	1	1	3	3	1	2.0

The compressed PCA Larkhaven gradient test produced one of the most accurate and complete edge planes in this dissertation, rating a 1.2 normalized score. As seen in Appendix A, the compressed PCA result accurately delineated all major scene constituents and performed strongly against a range of scene materials including vegetation, asphalt, paint, brick, mortar and glass. The gradient’s strong performance against the Larkhaven dataset is suggestive of its potential to support urban mapping applications, as well.

A variety of evaluation methods were used to assess the Gradient-based edge detection algorithm's performance against the Larkhaven VNIR dataset, including interest points, collinearity of edges, single-point intersections and ground truthing. For example, the gradient tests against the reflectance, compressed PCA and full PCA cubes correctly delineated edges through 100% of interest points and single-point intersections, earning them the strongest Likert score for the false negatives criterion. As seen in Figure 278, the algorithm generated clean, unbroken edges along the structure's façade as well as along the vehicle's edges, calibration panel edges and along the boundary between vegetation and manmade material – a meaningful finding with respect to urban feature mapping applications. Additionally, edge collinearity techniques indicated that the algorithm accurately localized edges across all five HSI input data sets.

For the Larkhaven VNIR data, Table 59, Table 60, Table 61, and Table 62 present the evaluation interest points, benchmark vertical edge points, benchmark horizontal edge points and benchmark single-point intersections, respectively. Each interest point and benchmark point were chosen according to the criteria detailed in the Methodology component and apply to all three algorithm evaluations.

Table 59: Interest Points for Larkhaven VNIR Data

Interest Point	Position (x,y)	Feature
1	2320, 592	White calibration panel
2	2409, 594	White calibration panel
3	2408, 684	White calibration panel
4	2317, 683	White calibration panel
5	2618, 501	Plastic tail light
6	2638, 502	Plastic tail light
7	2643, 507	Plastic tail light
8	2648, 562	Plastic tail light
9	2612, 562	Plastic tail light
10	2573, 402	Garage window
11	2600, 403	Garage window
12	2600, 418	Garage window
13	2573, 418	Garage window

Table 60: Benchmark Vertical Edge Points for Larkhaven VNIR Data

Vertical Edge Point	Position (x,y)	Feature
1	1972, 304	Edge between brick and siding
2	1972, 305	Edge between brick and siding
3	1972, 306	Edge between brick and siding
4	1972, 307	Edge between brick and siding
5	1972, 308	Edge between brick and siding
6	1972, 309	Edge between brick and siding
7	1972, 310	Edge between brick and siding
8	1972, 311	Edge between brick and siding
9	1972, 312	Edge between brick and siding
10	1972, 313	Edge between brick and siding
11	1972, 314	Edge between brick and siding
12	1972, 315	Edge between brick and siding
13	1972, 316	Edge between brick and siding
14	1972, 317	Edge between brick and siding
15	1972, 318	Edge between brick and siding
16	1972, 319	Edge between brick and siding

Table 61: Benchmark Horizontal Edge Points for Larkhaven VNIR Data

Horizontal Edge Point	Position (x,y)	Feature
1	2471, 323	Edge between brick and mortar
2	2472, 323	Edge between brick and mortar
3	2473, 323	Edge between brick and mortar
4	2474, 323	Edge between brick and mortar
5	2475, 323	Edge between brick and mortar
6	2476, 323	Edge between brick and mortar
7	2477, 323	Edge between brick and mortar
8	2478, 323	Edge between brick and mortar
9	2479, 323	Edge between brick and mortar
10	2480, 323	Edge between brick and mortar
11	2481, 323	Edge between brick and mortar
12	2482, 323	Edge between brick and mortar
13	2483, 323	Edge between brick and mortar
14	2484, 323	Edge between brick and mortar
15	2485, 323	Edge between brick and mortar

Table 62: Benchmark Single-Point Intersections for Larkhaven VNIR Data

Single-Point Intersection	Position (x,y)	Feature
1	2574, 324	Brick and mortar intersection
2	2534, 533	Brick and mortar intersection
3	2458, 447	Brick and mortar intersection
4	2602, 400	Window frame and glass
5	2649, 562	Tail light and vehicle paint
6	2482, 683	Plastic cap and paint
7	2026, 369	Light fixture and brick intersection
8	1990, 457	Siding intersection
9	1883, 574	Vegetation and brick
10	1885, 711	Vegetation and asphalt

Ground-Based – Granite VNIR

As seen in Figure 279 and Table 63, the Gradient-based edge detection algorithm produced satisfactory results across several data input types and Canny evaluation criteria for the Granite VNIR data. In particular, the compressed MNF cube produced excellent

results, accurately delineating all major scene features with narrow, unbroken edges. The reflectance cube produced a suboptimal volume of false alarms and unbroken edges while the full PCA cube also struggled to produce unbroken edges.

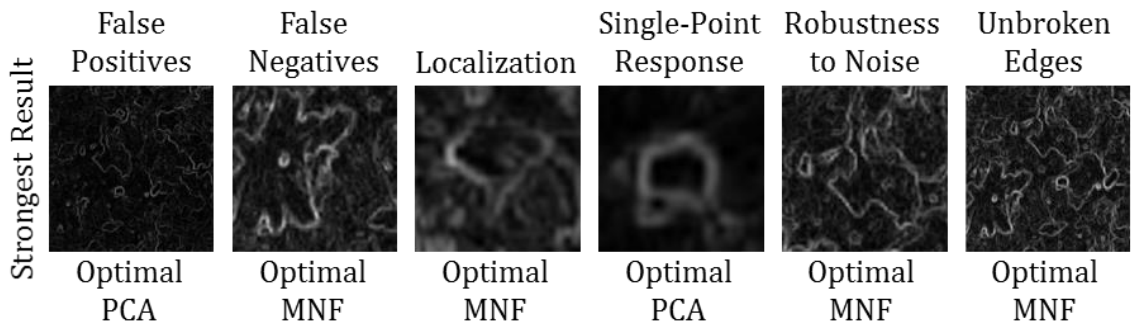


Figure 279: Strongest Gradient Evaluation Results for Granite Ground-Based VNIR Data, Unstretched

Table 63: Gradient Evaluation Measurements for Granite Ground-Based VNIR Data

Gradient Algorithm Granite VNIR	False Positives	False Negatives	Localization	Single-Point Response	Robustness to Noise	Unbroken Edges	Normalized Score
Reflectance	4	3	1	3	3	4	3.0
Optimal PCA	1	2	1	1	2	3	1.7
Optimal MNF	1	1	1	1	2	1	1.2
Full PCA	2	3	1	1	2	4	2.2
Full MNF	2	2	1	1	5	3	2.3
Roberts	3	4	1	2	4	3	2.8
Sobel	2	2	1	3	3	2	2.2

The false positives and unbroken edges criteria were particularly challenging for the gradient algorithm as executed against the Granite VNIR dataset – an unsurprising finding given the complexity and challenging nature of the scene. As seen in Appendix A, the compressed MNF edge plane is the only gradient Granite VNIR test fully delineating all major interest points, most likely due to the combination of its noise mitigation and spectral compression attributes, which is a key hypothesis for this dissertation. The reflectance and full PCA cubes measured weakly against the unbroken edges Canny criterion, and the reflectance cube also generated a suboptimal volume of false positives. Also note in Appendix A that the full MNF cube produced unacceptably noisy results, an output consistent with previous gradient tests against MNF cubes. Also, note that the tests, with the exception of the compressed MNF test, struggled to produce better than average measurements against the false negative criterion. This underperformance is likely attributable to the general absence of strong diagnostic absorption features for minerals in the VNIR wavelengths; most key mineral absorption features are present in the SWIR bands. The absence of VNIR diagnostic absorption features for minerals makes the compressed MNF evaluation performance all the more impressive; the noise reduction and spectral information compression characteristics of the compressed MNF cube were able to overcome the diagnostic absorption feature limitation to produce a high-quality edge plane.

A variety of evaluation methods were used to assess the Gradient-based edge detection algorithm's performance against the Granite VNIR dataset, including interest points, collinearity of edges, and single-point intersections. For example, the gradient

tests against the compressed MNF data type correctly delineated edges through 100% of interest points and single-point intersections, earning the strongest Likert score for the false negatives criterion. As seen in Figure 279, the algorithm generated accurate, unbroken edges around the major minerals within the rock – a meaningful finding with respect to mineral mapping applications. Additionally, edge collinearity techniques indicated that the algorithm accurately localized edges across all five HSI input data sets.

For the Granite VNIR data, Table 64, Table 65, Table 66, and Table 67 present the evaluation interest points, benchmark vertical edge points, benchmark horizontal edge points and benchmark single-point intersections, respectively. Each interest point and benchmark point were chosen according to the criteria detailed in the Methodology component and apply to all three algorithm evaluations.

Table 64: Interest Points for Granite VNIR Data

Interest Point	Position (x,y)	Feature
1	10, 616	Starburst feature
2	21, 628	Starburst feature
3	38, 589	Starburst feature
4	53, 596	Starburst feature
5	44, 625	Starburst feature
6	83, 599	Starburst feature
7	88, 615	Starburst feature
8	54, 640	Starburst feature
9	65, 680	Starburst feature
10	52, 685	Starburst feature
11	47, 671	Starburst feature
12	35, 690	Starburst feature
13	27, 674	Starburst feature
14	15, 696	Starburst feature
15	1, 694	Starburst feature

Table 65: Benchmark Vertical Edge Points for Granite VNIR Data

Vertical Edge Point	Position (x,y)	Feature
1	304,587	E edge of dark mineral
2	304,588	E edge of dark mineral
3	304,589	E edge of dark mineral
4	304,590	E edge of dark mineral
5	304,591	E edge of dark mineral
6	304,592	E edge of dark mineral
7	304,593	E edge of dark mineral
8	304,594	E edge of dark mineral
9	304,595	E edge of dark mineral
10	304,596	E edge of dark mineral
11	304,597	E edge of dark mineral
12	304,598	E edge of dark mineral
13	304,599	E edge of dark mineral

Table 66: Benchmark Horizontal Edge Points for Granite VNIR Data

Horizontal Edge Point	Position (x,y)	Feature
1	118,720	N edge of mineral deposit
2	119,720	N edge of mineral deposit
3	120,720	N edge of mineral deposit
4	121,720	N edge of mineral deposit
5	122,720	N edge of mineral deposit
6	123,720	N edge of mineral deposit
7	124,720	N edge of mineral deposit
8	125,720	N edge of mineral deposit
9	126,720	N edge of mineral deposit
10	127,720	N edge of mineral deposit
11	128,720	N edge of mineral deposit
12	129,720	N edge of mineral deposit
13	130,720	N edge of mineral deposit
14	131,720	N edge of mineral deposit
15	132,720	N edge of mineral deposit
16	133,720	N edge of mineral deposit

Table 67: Benchmark Single-Point Intersections for Granite VNIR Data

Single-Point Intersection	Position (x,y)	Feature
1	63, 187	Mineral intersection
2	214, 193	Mineral intersection
3	234, 89	Mineral intersection
4	74, 253	Mineral intersection
5	418, 741	Mineral intersection
6	553, 867	Mineral intersection
7	539, 684	Mineral intersection
8	397, 246	Mineral intersection
9	471, 124	Mineral intersection
10	575, 252	Mineral intersection

Ground-Based – Granite NIR/SWIR

As seen in Figure 280 and Table 68, the Gradient-based edge detection algorithm produced satisfactory results across a narrow range of data input types and Canny evaluation criteria for the Granite NIR/SWIR data. Only the compressed MNF cube enabled the gradient-based edge detector to generate consistently above-average evaluation measurements. The remaining cubes produced suboptimal results against one or more Canny evaluation criteria.

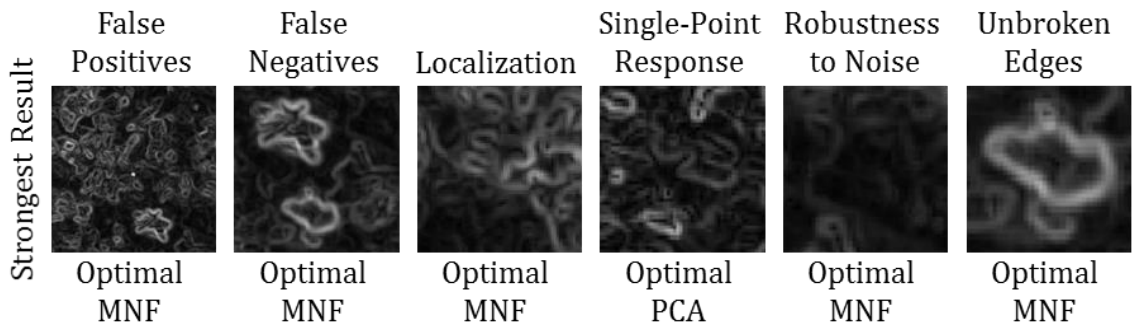


Figure 280: Strongest Gradient Evaluation Results for Granite Ground-Based NIR/SWIR Data, Unstretched

Table 68: Gradient Evaluation Measurements for Granite Ground-Based NIR/SWIR Data

Gradient Algorithm Granite NIR/SWIR	False Positives	False Negatives	Localization	Single-Point Response	Robustness to Noise	Unbroken Edges	Normalized Score
Reflectance	5	1	1	3	4	1	2.5
Optimal PCA	3	4	1	2	2	2	2.3
Optimal MNF	1	1	1	3	1	1	1.3
Full PCA	3	4	1	2	2	2	2.3
Full MNF	5	4	2	5	5	3	4.0
Roberts	5	5	1	2	4	5	3.7
Sobel	4	4	1	3	3	4	3.2

The false positives and false negatives criteria were particularly challenging for the gradient algorithm as executed against the Granite NIR/SWIR dataset – an unsurprising finding given the complexity and challenging nature of the scene, similar to the results seen in the Granite VNIR dataset tests. As seen in Appendix A, the compressed MNF edge plane is the only gradient Granite VNIR test fully delineating all major interest points through unbroken edges, most likely due to the combination of its

noise mitigation and spectral compression attributes, which is a key hypothesis for this dissertation. Again, the strong compressed MNF results are consistent with the observations from the Granite VNIR tests.

The reflectance and full MNF cubes measured most weakly against the false positives Canny criterion, while the compressed PCA and full PCA cubes failed to identify a suboptimal volume of interest points resulting in very weak false negative measurements. Also, note in Appendix A that the full MNF cube produced unacceptably poor results, an output suggesting that optimizing the MNF and PCA cubes is more likely to generate useful edge planes than using the full MNF or PCA cube.

Also, note that the presence of SWIR bands did not improve the false negative rate for the full MNF and full PCA cubes compared to the comparable gradient tests against the Granite VNIR data. The reflectance cube test, however, improved from a Likert 3 to a Likert 1 comparing the VNIR tests to the NIR/SWIR tests, suggesting that the presence of key SWIR diagnostic absorption features for minerals significantly reduces the false negative rate.

A variety of evaluation methods were used to assess the Gradient-based edge detection algorithm's performance against the Granite NIR/SWIR dataset, including interest points, collinearity of edges and single-point intersections. For example, the gradient tests against the compressed MNF data type correctly delineated edges through 100% of interest points and single-point intersections, earning the strongest Likert score for the false negatives criterion. As seen in Figure 280, the algorithm generated accurate, unbroken edges around the major minerals within the rock – a meaningful finding with

respect to mineral mapping applications. Additionally, edge collinearity techniques indicated that the algorithm accurately localized edges across all but the full MNF data set.

For the Granite VNIR data, Table 64, Table 65, Table 66, and Table 67 present the evaluation interest points, benchmark vertical edge points, benchmark horizontal edge points and benchmark single-point intersections, respectively. Each interest point and benchmark point were chosen according to the criteria detailed in the Methodology component and apply to all three algorithm evaluations.

Table 69: Interest Points for Granite NIR/SWIR Data

Interest Point	Position (x,y)	Feature
1	125, 245	Starburst feature
2	129, 247	Starburst feature
3	136, 245	Starburst feature
4	133, 250	Starburst feature
5	148, 254	Starburst feature
6	148, 262	Starburst feature
7	142, 261	Starburst feature
8	143, 267	Starburst feature
9	134, 265	Starburst feature
10	131, 261	Starburst feature
11	117, 264	Starburst feature
12	115, 260	Starburst feature
13	118, 257	Starburst feature
14	114, 255	Starburst feature
15	119, 252	Starburst feature
16	120, 246	Starburst feature

Table 70: Benchmark Vertical Edge Points for Granite NIR/SWIR Data

Vertical Edge Point	Position (x,y)	Feature
1	127, 160	W side of vertical pink feature
2	127, 161	W side of vertical pink feature
3	127, 162	W side of vertical pink feature
4	127, 163	W side of vertical pink feature
5	127, 164	W side of vertical pink feature
6	127, 165	W side of vertical pink feature
7	127, 166	W side of vertical pink feature
8	127, 167	W side of vertical pink feature
9	127, 168	W side of vertical pink feature
10	127, 169	W side of vertical pink feature
11	128, 170	W side of vertical pink feature
12	128, 171	W side of vertical pink feature
13	128, 172	W side of vertical pink feature
14	128, 173	W side of vertical pink feature
15	128, 174	W side of vertical pink feature
16	128, 175	W side of vertical pink feature
17	128, 176	W side of vertical pink feature
18	128, 177	W side of vertical pink feature
19	128, 178	W side of vertical pink feature
20	128, 179	W side of vertical pink feature
21	128, 180	W side of vertical pink feature

Table 71: Benchmark Horizontal Edge Points for Granite NIR/SWIR Data

Horizontal Edge Point	Position (x,y)	Feature
1	128, 293	N edge of elongated gray feature
2	129, 293	N edge of elongated gray feature
3	130, 293	N edge of elongated gray feature
4	131, 293	N edge of elongated gray feature
5	132, 293	N edge of elongated gray feature
6	133, 293	N edge of elongated gray feature
7	134, 293	N edge of elongated gray feature
8	135, 293	N edge of elongated gray feature
9	136, 293	N edge of elongated gray feature
10	137, 292	N edge of elongated gray feature
11	138, 292	N edge of elongated gray feature
12	139, 292	N edge of elongated gray feature
13	140, 292	N edge of elongated gray feature
14	141, 292	N edge of elongated gray feature
15	142, 292	N edge of elongated gray feature
16	143, 293	N edge of elongated gray feature
17	144, 294	N edge of elongated gray feature
18	145, 295	N edge of elongated gray feature
19	146, 296	N edge of elongated gray feature
20	147, 296	N edge of elongated gray feature
21	148, 296	N edge of elongated gray feature
22	149, 296	N edge of elongated gray feature
23	150, 296	N edge of elongated gray feature
24	151, 296	N edge of elongated gray feature

Table 72: Benchmark Single-Point Intersections for Granite NIR/SWIR Data

Single-Point Intersection	Position (x,y)	Feature
1	255, 241	Mineral intersection
2	117, 216	Mineral intersection
3	152, 369	Mineral intersection
4	314, 315	Mineral intersection
5	337, 194	Mineral intersection
6	294, 154	Mineral intersection
7	61, 254	Mineral intersection
8	68, 405	Mineral intersection
9	37, 358	Mineral intersection
10	166, 279	Mineral intersection

Ground-Based – South African Core Samples

As seen in Figure 281 and Table 73, the Gradient-based edge detection algorithm produced satisfactory results across several data input types and Canny evaluation criteria. In particular, the compressed PCA, full PCA and compressed MNF cubes produced satisfactory results across all six criteria, with the compressed MNF cube producing the strongest results, while the compressed PCA and full PCA cubes produced above average results for all Canny criteria except for false negatives, against which they produced an average evaluation measurement. Additionally, all input data types produced above average results for the localization and unbroken edges criteria. Indeed, the overall gradient results for the South African Core Sample dataset were quite strong, with 28 of the 30 measurements scoring average or above average. The combination of spectral contrast and high spatial resolution are likely key enablers for the gradient algorithm’s strong evaluation.

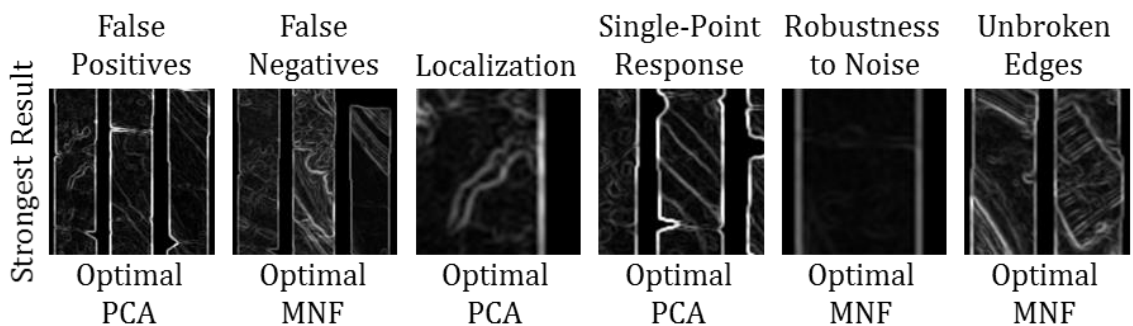


Figure 281: Strongest Gradient Evaluation Results for Core Sample Ground-Based NIR/SWIR Data, Unstretched

Table 73: Gradient Evaluation Measurements for Core Sample Ground-Based NIR/SWIR Data

Gradient Algorithm South African Core Samples	False Positives	False Negatives	Localization	Single-Point Response	Robustness to Noise	Unbroken Edges	Normalized Score
Reflectance	3	3	1	3	3	2	2.5
Optimal PCA	2	3	1	1	2	2	1.8
Optimal MNF	2	1	1	2	2	1	1.5
Full PCA	2	3	1	1	2	2	1.8
Full MNF	4	3	1	2	4	2	2.7
Roberts	3	4	1	2	2	4	2.7
Sobel	2	4	1	3	2	3	2.5

As seen in Appendix A, the compressed MNF and compressed PCA cubes generated reliable edge planes consistent with low false positives, high accuracy and satisfactory single-point response. The false negative criterion appears to be the most challenging evaluative measure for the gradient-based edge detector when applied against mineral mapping datasets. As seen in the Cuprite and Granite datasets, a low false negative rate was more difficult to achieve than the other criteria. For all cases, however, the compressed MNF cube enabled the gradient operator to achieve its strongest results.

A variety of evaluation methods were used to assess the Gradient-based edge detection algorithm's performance against the South Africa Core Sample dataset, including interest points, collinearity of edges and single-point intersections. For example, the gradient tests against the compressed MNF data type correctly delineated edges through 100% of interest points and single-point intersections, earning the strongest Likert score for the false negatives criterion. As seen in Figure 281, the algorithm generated accurate, unbroken edges around the major minerals within the core

samples just as it did for the two Granite datasets – a meaningful finding with respect to mineral mapping applications. Additionally, edge collinearity techniques indicated that the algorithm accurately localized edges across all five HSI input data sets.

For the South African Core Sample NIR/SWIR data, Table 74, Table 75, Table 76, and Table 77 present the evaluation interest points, benchmark vertical edge points, benchmark horizontal edge points and benchmark single-point intersections, respectively. Each interest point and benchmark point were chosen according to the criteria detailed in the Methodology component and apply to all three algorithm evaluations.

Table 74: Interest Points for South African Core Sample NIR/SWIR Data

Interest Point	Position (x,y)	Feature
1	70, 110	NW-SE running brown layer
2	86, 133	NW-SE running brown layer
3	86, 137	NW-SE running brown layer
4	89, 137	NW-SE running brown layer
5	105, 153	NW-SE running brown layer
6	104, 168	NW-SE running brown layer
7	92, 152	NW-SE running brown layer
8	84, 153	NW-SE running brown layer
9	81, 139	NW-SE running brown layer
10	70, 132	NW-SE running brown layer
11	270, 279	Slanting brown banded feature
12	295, 315	Slanting brown banded feature
13	294, 343	Slanting brown banded feature
14	274, 357	Slanting brown banded feature
15	260, 336	Slanting brown banded feature

Table 75: Benchmark Vertical Edge Points for South African Core Sample NIR/SWIR Data

Vertical Edge Point	Position (x,y)	Feature
1	190, 658	NE-SW running thin layer
2	182, 673	NE-SW running thin layer
3	167, 689	NE-SW running thin layer

Table 76: Benchmark Horizontal Edge Points for South African Core Sample NIR/SWIR Data

Horizontal Edge Point	Position (x,y)	Feature
1	167, 97	Dark horizontal feature
2	185, 96	Dark horizontal feature
3	201, 94	Dark horizontal feature
4	124, 449	Light horizontal feature
5	153, 463	Light horizontal feature

Table 77: Benchmark Single-Point Intersections for South African Core Sample NIR/SWIR Data

Single-Point Intersection	Position (x,y)	Feature
1	102, 230	Mineral intersection
2	226, 280	Mineral intersection
3	268, 267	Mineral intersection
4	266, 372	Mineral intersection
5	137, 356	Mineral intersection
6	48, 361	Mineral intersection
7	183, 654	Mineral intersection
8	134, 605	Mineral intersection
9	146, 591	Mineral intersection
10	87, 492	Mineral intersection

Ground-Based – Aluminum Panel

As seen in Figure 282 and Table 78, the aluminum panel VNIR data challenged the Gradient-based edge detection algorithm to produce satisfactory results across

multiple data input types and Canny evaluation criteria. In particular, all five HSI input data sets measured quite weakly against the false positives criterion, as seen in Appendix A. The algorithm also struggled to measure well against the robustness to noise criterion, and only the compressed MNF cube scored average or better in five of the six evaluation categories. Clearly, the aluminum panel VNIR data stretches the gradient edge detection algorithm's ability to generate reliable edge planes.

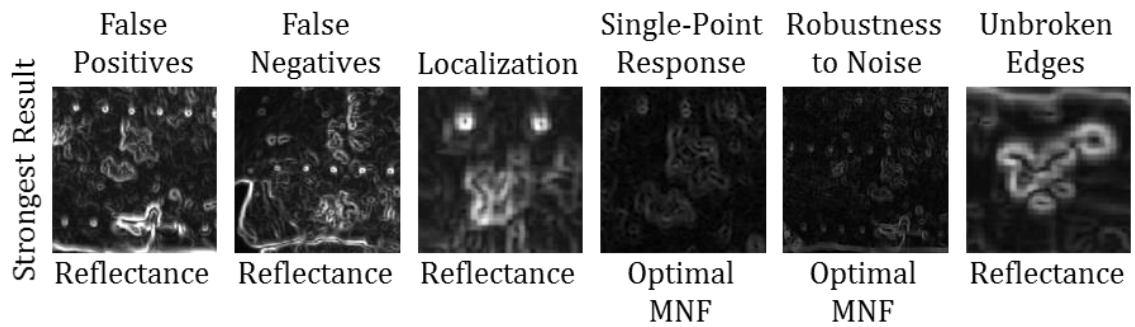


Figure 282: Strongest Gradient Evaluation Results for Aluminum Panel Ground-Based VNIR Data, Unstretched

Table 78: Gradient Evaluation Measurements for Aluminum Panel Ground-Based VNIR Data

Gradient Algorithm Aluminum Panel	False Positives	False Negatives	Localization	Single-Point Response	Robustness to Noise	Unbroken Edges	Normalized Score
Reflectance	5	2	1	3	5	2	3.0
Optimal PCA	5	3	1	3	4	2	3.0
Optimal MNF	5	2	1	2	3	2	2.5
Full PCA	5	2	1	3	4	2	2.8
Full MNF	5	2	1	2	4	2	2.7
Roberts	5	3	1	2	4	5	3.3
Sobel	5	3	1	2	4	5	3.3

As seen in Appendix A, the gradient algorithm generated a suboptimal volume of false alarms across the mottled and rusted surface of the aluminum panel. Figure 282 shows that the algorithm generates strong and accurate edges around the unique rust features, but false alarmed against weathered features that are chemically identical to unweathered aluminum features. The false alarms are weak, but the algorithm appears to false alarm on variations in intensity – a violation of this study’s edge model. The algorithm performed strongly, however, against the false negatives, localization, single-point response and unbroken edges evaluation criteria. The compressed MNF cube yielded the strongest results, although none of the test cubes generated above average results against all criteria.

Overall, the dataset proved to be one of the most challenging tests in this dissertation, as expected. The combination of subtle feature contrast, limited spectral bandwidth and no ground truth made for challenging tests. The generally poor performance against the false positive criterion juxtaposed against the above average

performance against the false negative criterion is suggestive of an algorithm that could benefit from a dataset optimized to reduce false positives (i.e., a weighted band-selection process).

A variety of evaluation methods were used to assess the Gradient-based edge detection algorithm's performance against the Aluminum Panel dataset, including interest points, collinearity of edges and single-point intersections. For example, the gradient tests against the compressed MNF data type correctly delineated edges through 100% of interest points and single-point intersections, earning the strongest Likert score for the false negatives criterion. As seen in Figure 282, the algorithm generated accurate, unbroken edges around the major rust features and rivets. Additionally, edge collinearity techniques indicated that the algorithm accurately localized edges across all five HSI input data sets.

Interest point analysis also indicated that the algorithm generated multiple false positives within the scene, most likely due to intensity variations. Consider Figure 283, which shows a spectrum from bright, un-weathered aluminum (in white) compared to a spectrum from darker, weathered aluminum (in green). Although the gradient delineated these pixels into different features, they belong within the same feature due to their spectral similarity – they differ almost exclusively in brightness (i.e., intensity). The implication is that under certain conditions, such as weathered metal backgrounds, the gradient edge detection method can false alarm at suboptimal volumes.

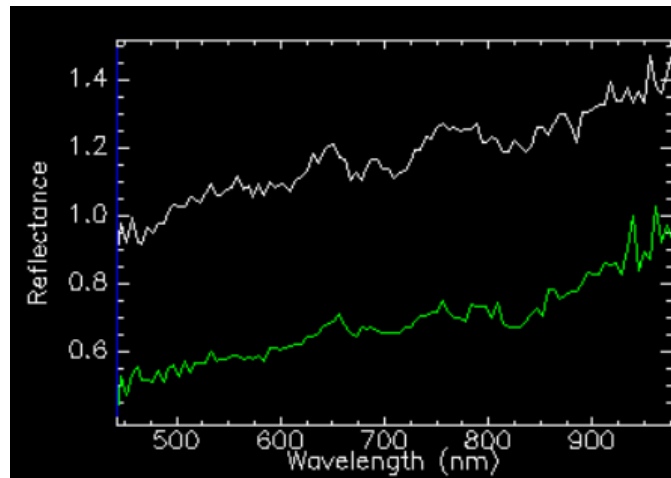


Figure 283: False Positive Spectra from Aluminum Panel VNIR Data

For the Aluminum Panel VNIR data, Table 79, Table 80, Table 81, and Table 82 present the evaluation interest points, benchmark vertical edge points, benchmark horizontal edge points and benchmark single-point intersections, respectively. Each interest point and benchmark point were chosen according to the criteria detailed in the Methodology component and apply to all three algorithm evaluations.

Table 79: Interest Points for Aluminum Panel VNIR Data

Interest Point	Position (x,y)	Feature
1	461, 307	Large rust feature
2	473, 303	Large rust feature
3	490, 308	Large rust feature
4	470, 328	Large rust feature
5	379, 341	Large rust feature
6	466, 351	Large rust feature
7	468, 374	Large rust feature
8	470, 383	Large rust feature
9	460, 380	Large rust feature
10	452, 382	Large rust feature
11	449, 372	Large rust feature
12	453, 364	Large rust feature
13	448, 358	Large rust feature
14	444, 336	Large rust feature
15	450, 321	Large rust feature
16	456, 316	Large rust feature
17	465, 244	Rivet hole
18	467, 244	Rivet hole
19	467, 247	Rivet hole
20	465, 247	Rivet hole

Table 80: Benchmark Vertical Edge Points for Aluminum Panel VNIR Data

Vertical Edge Point	Position (x,y)	Feature
1	335, 369	W side of weathered feature
2	335, 370	W side of weathered feature
3	335, 371	W side of weathered feature
4	335, 372	W side of weathered feature
5	335, 373	W side of weathered feature
6	335, 374	W side of weathered feature
7	335, 384	W side of weathered feature
8	335, 385	W side of weathered feature
9	335, 386	W side of weathered feature
10	335, 387	W side of weathered feature
11	335, 388	W side of weathered feature
12	335, 389	W side of weathered feature

Table 81: Benchmark Horizontal Edge Points for Aluminum Panel VNIR Data

Horizontal Edge Point	Position (x,y)	Feature
1	128, 261	Rust feature along W side
2	129, 261	Rust feature along W side
3	130, 261	Rust feature along W side
4	131, 261	Rust feature along W side
5	132, 261	Rust feature along W side
6	133, 261	Rust feature along W side
7	134, 261	Rust feature along W side
8	135, 261	Rust feature along W side
9	136, 261	Rust feature along W side
10	137, 261	Rust feature along W side
11	138, 261	Rust feature along W side
12	139, 261	Rust feature along W side
13	140, 261	Rust feature along W side
14	141, 261	Rust feature along W side
15	142, 261	Rust feature along W side
16	143, 261	Rust feature along W side
17	144, 261	Rust feature along W side
18	145, 261	Rust feature along W side
19	146, 261	Rust feature along W side

Table 82: Benchmark Single-Point Intersections for Aluminum Panel VNIR Data

Single-Point Intersection	Position (x,y)	Feature
1	204, 96	Aluminum and background
2	266, 132	Rivet hole
3	180, 309	Aluminum and weathered area
4	480, 367	Aluminum and background
5	542, 232	Aluminum and rust
6	425, 348	Aluminum and weathered area
7	498, 143	Aluminum and rust
8	497, 71	Rivet hole
9	380, 135	Aluminum and weathered area
10	337, 167	Aluminum and rust

Microscene – Rare Target on Sand

As seen in Figure 284 and Table 83, the Gradient-based edge detection algorithm produced satisfactory results across several data input types and Canny evaluation criteria. In particular, the compressed MNF and full MNF cubes produced strong results across all six criteria, and the compressed PCA and full PCA cubes produced strong results against all criteria except false alarms, against which is earned an average measurement (i.e., a Likert score of three).

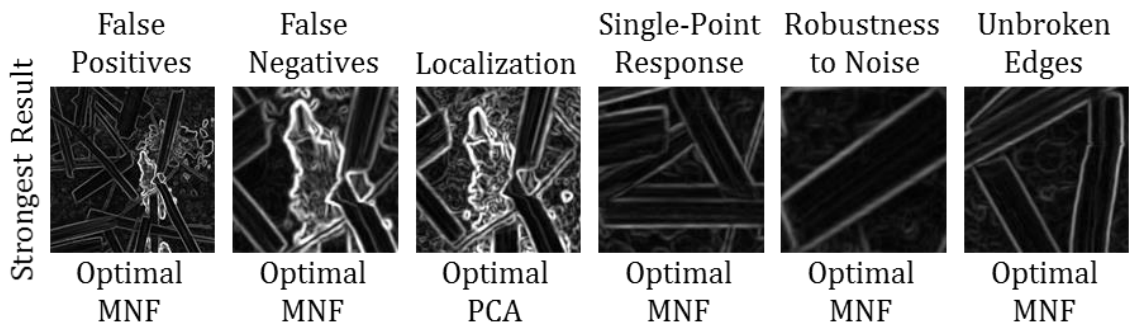


Figure 284: Strongest Gradient Evaluation Results for Rare Target on Sand Microscene VNIR Data, Unstretched

Table 83: Gradient Evaluation Measurements for Rare Target on Sand Microscene VNIR Data

Gradient Algorithm Rare Target on Sand	False Positives	False Negatives	Localization	Single-Point Response	Robustness to Noise	Unbroken Edges	Normalized Score
Reflectance	4	1	1	3	3	1	2.2
Optimal PCA	3	2	1	2	2	1	1.8
Optimal MNF	2	1	1	2	1	1	1.3
Full PCA	3	2	1	2	2	1	1.8
Full MNF	2	2	1	2	2	1	1.7
Roberts	3	4	1	2	4	5	3.2
Sobel	2	4	1	3	3	3	2.7

The compressed MNF and full MNF cubes measured most strongly against Canny evaluation criteria, in each case generating a highly accurate edge plane of the rare target surrounded by vegetation and sand. All of the evaluation measurements for the MNF cubes were above average, while the compressed PCA and full PCA cubes measured above average for all criteria except false positives, against which they measured nominally. As seen in Appendix A, the reflectance cube performed weakly against the false positive criterion, generating a suboptimal volume of false alarms on the sand background. The algorithm also generated narrow, unbroken edges for all data input types except for reflectance, and all data types scored above average against the false negative criterion. All tests generated a strong, narrow edge around the principal feature in the scene, the rare target. Overall, the gradient approach generated high-quality edge planes.

A variety of evaluation methods were used to assess the Gradient-based edge detection algorithm’s performance against the Rare Target on Sand dataset, including

interest points, collinearity of edges, single-point intersections and ground truthing. For example, the gradient tests against the compressed MNF data type correctly delineated edges through 100% of interest points and single-point intersections, earning the strongest Likert score for the false negatives criterion. As seen in Figure 285, the algorithm generated accurate, unbroken edges around the neodymium oxide (i.e., the rare target) – a meaningful finding with respect to trace chemical detection applications. Additionally, edge collinearity techniques indicated that the algorithm accurately localized edges across all five HSI input data sets.

In addition to delineating the primary neodymium oxide pile, the algorithm also neatly delineated single-pixel size deposits as seen in the lower right quadrant of Figure 285. The ability to delineate single-pixel targets indicates that the algorithm is sufficiently sensitive to support trace target applications which require an algorithm to balance low false alarm rates against the ability to detect small traces of target chemicals.



Figure 285: Delineation of Single-Pixel Neodymium Oxide Target

For the Rare Target on Sand VNIR data, Table 84, Table 85, Table 86, and Table 87 present the evaluation interest points, benchmark vertical edge points, benchmark

horizontal edge points and benchmark single-point intersections, respectively. Each interest point and benchmark point were chosen according to the criteria detailed in the Methodology component and apply to all three algorithm evaluations.

Table 84: Interest Points for Rare Target on Sand VNIR Data

Interest Point	Position (x,y)	Feature
1	406, 221	Rare chemical
2	410, 230	Rare chemical
3	416, 238	Rare chemical
4	415, 243	Rare chemical
5	415, 246	Rare chemical
6	422, 247	Rare chemical
7	426, 260	Rare chemical
8	424, 241	Rare chemical
9	425, 240	Rare chemical
10	431, 251	Rare chemical
11	428, 266	Rare chemical
12	427, 273	Rare chemical
13	421, 284	Rare chemical
14	429, 288	Rare chemical
15	432, 294	Rare chemical
16	418, 301	Rare chemical
17	414, 300	Rare chemical
18	412, 306	Rare chemical
19	403, 312	Rare chemical
20	401, 306	Rare chemical
21	409, 298	Rare chemical
22	398, 289	Rare chemical
23	403, 284	Rare chemical
24	398, 281	Rare chemical
25	398, 279	Rare chemical
26	401, 277	Rare chemical
27	401, 268	Rare chemical
28	404, 268	Rare chemical
29	403, 263	Rare chemical
30	394, 246	Rare chemical
31	398, 240	Rare chemical
32	399, 225	Rare chemical

Table 85: Benchmark Vertical Edge Points for Rare Target on Sand VNIR Data

Vertical Edge Point	Position (x,y)	Feature
1	297, 135	N-S running grass blade
2	297, 136	N-S running grass blade
3	297, 137	N-S running grass blade
4	297, 138	N-S running grass blade
5	297, 139	N-S running grass blade
6	297, 140	N-S running grass blade
7	297, 141	N-S running grass blade
8	297, 142	N-S running grass blade
9	297, 143	N-S running grass blade
10	297, 144	N-S running grass blade
11	297, 145	N-S running grass blade
12	297, 146	N-S running grass blade
13	297, 147	N-S running grass blade
14	297, 148	N-S running grass blade
15	297, 149	N-S running grass blade
16	297, 150	N-S running grass blade
17	297, 151	N-S running grass blade
18	297, 152	N-S running grass blade
19	297, 153	N-S running grass blade
20	297, 154	N-S running grass blade
21	297, 155	N-S running grass blade
22	297, 156	N-S running grass blade
23	297, 157	N-S running grass blade
24	297, 158	N-S running grass blade
25	297, 159	N-S running grass blade

Table 86: Benchmark Horizontal Edge Points for Rare Target on Sand VNIR Data

Horizontal Edge Point	Position (x,y)	Feature
1	266, 255	W-E running grass blade
2	267, 255	W-E running grass blade
3	268, 255	W-E running grass blade
4	269, 255	W-E running grass blade
5	270, 255	W-E running grass blade
6	271, 255	W-E running grass blade
7	272, 255	W-E running grass blade
8	273, 255	W-E running grass blade
9	274, 255	W-E running grass blade
10	275, 255	W-E running grass blade
11	276, 255	W-E running grass blade
12	277, 255	W-E running grass blade
13	278, 255	W-E running grass blade
14	279, 255	W-E running grass blade
15	280, 255	W-E running grass blade
16	281, 255	W-E running grass blade
17	282, 255	W-E running grass blade

Table 87: Benchmark Single Point Intersections for Rare Target on Sand VNIR Data

Single-Point Intersection	Position (x,y)	Feature
1	415, 122	Vegetation and cloth thread
2	520, 197	Sand and rare target
3	416, 310	Rare target, thread and vegetation
4	466, 99	Vegetation and sand
5	536, 280	Cloth thread and sand
6	71, 322	Vegetation and sand
7	124, 440	Large sand grain intersection
8	321, 344	Vegetation and cloth thread
9	399, 361	Vegetation, sand and cloth thread
10	435, 448	Rare target and sand

Microscene – Chemical Array

As seen in Figure 286 and Table 88, the Gradient-based edge detection algorithm was challenged to produce satisfactory results across several data input types and Canny evaluation criteria. Only the compressed MNF test consistently measured average or above average performance against the Canny criteria, while the remaining tests performed particularly weakly against the false positives and robustness to noise criteria. The false negative criteria also posed a barrier to superior results, as well. Overall, the Chemical Array dataset was more of a challenge than expected for the gradient-based edge detection algorithm, which has previously performed strongly against unique targets on a sand background.

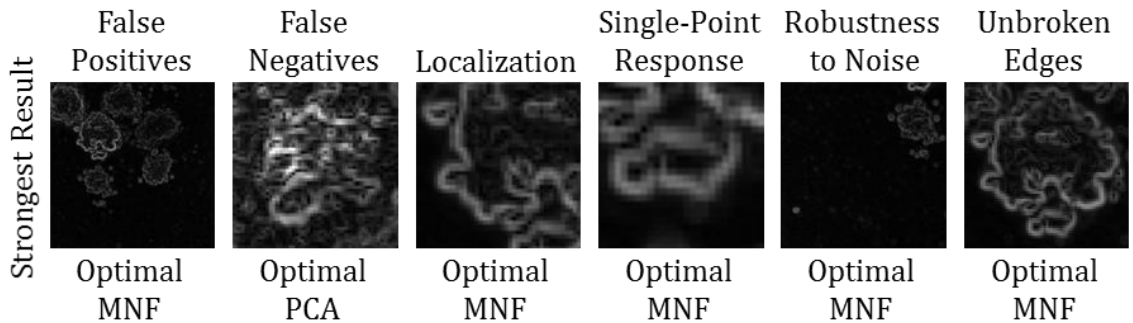


Figure 286: Strongest Gradient Evaluation Results for Chemical Array Microscene NIR/SWIR Data, Unstretched

Table 88: Gradient Evaluation Measurements for Chemical Array Microscene NIR/SWIR Data

Gradient Algorithm Chemical Array on Sand	False Positives	False Negatives	Localization	Single-Point Response	Robustness to Noise	Unbroken Edges	Normalized Score
Reflectance	5	3	2	4	5	2	3.5
Optimal PCA	4	2	1	3	3	2	2.5
Optimal MNF	1	3	1	3	1	1	1.7
Full PCA	4	3	1	3	3	2	2.7
Full MNF	4	3	1	3	5	2	3.0
Roberts	2	4	2	2	5	4	3.2
Sobel	4	3	1	3	4	3	3.0

The operator’s performance against the Chemical Array dataset produced false alarms throughout the scene, including within the sand background and within discrete piles of uniform materials. Similar to the false alarm pattern on the Aluminum Panel tests, the false alarms on the Chemical Array data appear to occur against sand grains of identical chemistry but varying intensity – a suboptimal result according to this study’s edge model that defines an edge as a single-point boundary between chemically distinct features. Figure 287 presents 25 spectra sampled from false alarm features captured during the compressed PCA test. Note that the curves vary mostly according to intensity and that discriminating absorption features are absent, indicating that the materials are chemically homogenous. An optimal edge detector would properly delineate the spatially adjacent spectra within a single unbroken edge.

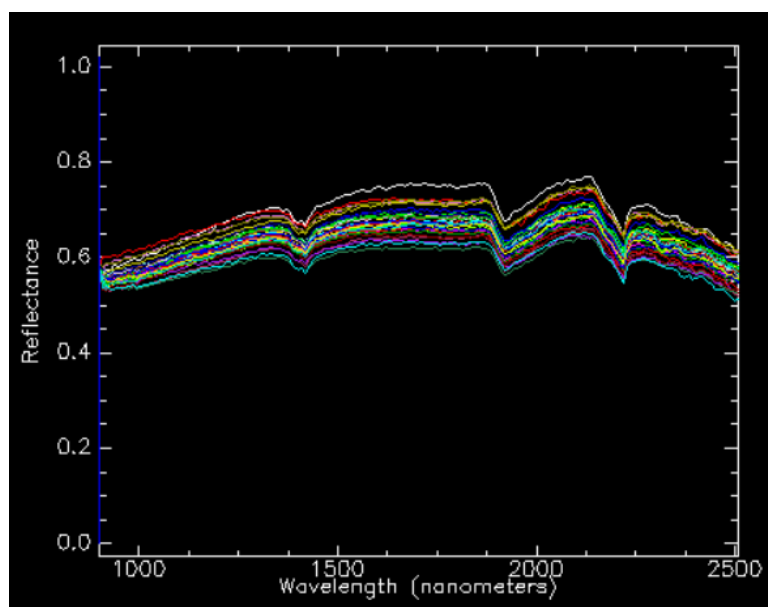


Figure 287: False Alarm Spectra from the Sand Background on the Chemical Array Data

A variety of evaluation methods were used to assess the Gradient-based edge detection algorithm's performance against the Chemical Array dataset, including interest points, collinearity of edges, single-point intersections and ground truthing. For example, the gradient tests against all data types correctly delineated edges through most interest points and single-point intersections, earning the average to above average Likert scores for the false negatives criterion. As seen in Appendix A and Figure 286, the algorithm generated accurate, unbroken edges around the ammonium nitrate sample (shown in the unbroken edges example in Figure 286), meaning that it accurately delineated all interest points for the key feature. Additionally, edge collinearity techniques indicated that the algorithm accurately localized edges across all five HSI input data sets.

Importantly, note that the compressed MNF test measured strongly against the robustness to noise and false positives criteria, which is recognized primarily by the

absence of false alarms on the sand background and within the unique chemical piles. Importantly, the compressed MNF test was the only test to accurately suppress the background and fully delineate the key interest points – another strong performance enabled by the compressed MNF data input type.

For the Chemical Array NIR/SWIR data, Table 89, Table 90, Table 91, and Table 92 present the evaluation interest points, benchmark vertical edge points, benchmark horizontal edge points and benchmark single-point intersections, respectively. Each interest point and benchmark point were chosen according to the criteria detailed in the Methodology component and apply to all three algorithm evaluations.

Table 89: Interest Points for Chemical Array NIR/SWIR Data

Interest Point	Position (x,y)	Feature
1	174, 244	Ammonium nitrate
2	180, 247	Ammonium nitrate
3	182, 251	Ammonium nitrate
4	188, 252	Ammonium nitrate
5	197, 270	Ammonium nitrate
6	194, 276	Ammonium nitrate
7	191, 278	Ammonium nitrate
8	191, 286	Ammonium nitrate
9	187, 288	Ammonium nitrate
10	178, 284	Ammonium nitrate
11	177, 280	Ammonium nitrate
12	170, 279	Ammonium nitrate
13	167, 289	Ammonium nitrate
14	157, 288	Ammonium nitrate
15	152, 281	Ammonium nitrate
16	146, 281	Ammonium nitrate
17	146, 276	Ammonium nitrate
18	152, 274	Ammonium nitrate
19	150, 265	Ammonium nitrate
20	152, 257	Ammonium nitrate
21	159, 254	Ammonium nitrate

Table 90: Vertical Edge Points for Chemical Array NIR/SWIR Data

Vertical Edge Point	Position (x,y)	Feature
1	159, 206	W side of potassium chlorate
2	159, 207	W side of potassium chlorate
3	159, 208	W side of potassium chlorate
4	159, 209	W side of potassium chlorate
5	159, 210	W side of potassium chlorate
6	159, 211	W side of potassium chlorate
7	203, 139	W side of iron filings
8	203, 140	W side of iron filings
9	203, 141	W side of iron filings
10	203, 142	W side of iron filings
11	203, 143	W side of iron filings

Table 91: Horizontal Edge Points for Chemical Array NIR/SWIR Data

Horizontal Edge Point	Position (x,y)	Feature
1	119, 249	S side of borax
2	120, 249	S side of borax
3	121, 249	S side of borax
4	122, 249	S side of borax
5	123, 249	S side of borax
6	124, 249	S side of borax
7	125, 249	S side of borax
8	126, 249	S side of borax
9	127, 249	S side of borax
10	128, 249	S side of borax
11	129, 249	S side of borax
12	130, 249	S side of borax
13	131, 249	S side of borax
14	132, 249	S side of borax
15	133, 249	S side of borax
16	134, 249	S side of borax
17	135, 249	S side of borax
18	136, 249	S side of borax

Table 92: Single-Point Intersections for Chemical Array NIR/SWIR Data

Single-Point Intersection	Position (x,y)	Feature
1	236, 237	Chemical intersection
2	135, 213	Chemical intersection
3	151, 251	Chemical intersection
4	199, 209	Chemical intersection
5	251, 207	Chemical intersection

Microscene - Cloth Threads

As seen in Figure 288 and Table 93, the Gradient-based edge detection algorithm produced satisfactory results across several data input types and Canny evaluation criteria. The compressed MNF test performed quite strongly against all six Canny criteria, while the full MNF, full PCA and compressed PCA cubes also tested above average for all six evaluation criteria. The reflectance cube produced reliable results, as well, with its weakest measurements scoring as average for the single-point response and robustness to noise criteria. Overall, the gradient edge detector performed strongly against the dataset.

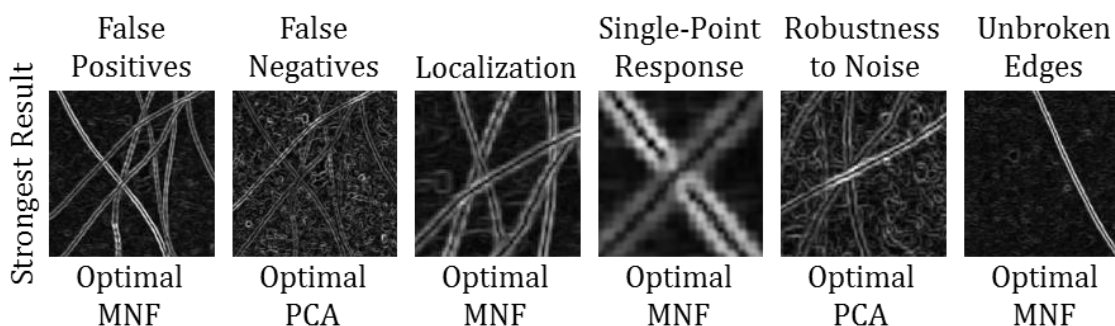


Figure 288: Strongest Gradient Evaluation Results for Cloth Threads Microscene VNIR Data, Unstretched

Table 93: Gradient Evaluation Measurements for Cloth Thread Microscene VNIR Data

Gradient Algorithm Cloth Threads on Sand	False Positives	False Negatives	Localization	Single-Point Response	Robustness to Noise	Unbroken Edges	Normalized Score
Reflectance	2	1	1	3	3	2	2.0
Optimal PCA	2	1	1	2	2	1	1.5
Optimal MNF	1	2	1	1	2	1	1.3
Full PCA	2	1	1	2	2	1	1.5
Full MNF	1	2	1	2	2	1	1.5
Roberts	2	4	1	2	3	5	2.8
Sobel	2	3	1	3	3	3	2.5

The compressed MNF and full MNF tests were the only two tests to earn the maximum score for false positives by virtue of their ability to suppress the noisy sand background on which the other datasets lightly false alarmed. The MNF performance is similar to the compressed MNF and full MNF cube performance on the Chemical Array data, suggesting that the MNF transform’s capacity to improve edge detection performance is robust across datasets and spectral wavelengths. Additionally, note that the gradient algorithm successfully measured above average for the false negatives, localization and unbroken edges criteria for all tests, as seen in Appendix A.

A variety of evaluation methods were used to assess the Gradient-based edge detection algorithm’s performance against the Cloth Threads on Sand dataset, including interest points, collinearity of edges, single-point intersections and ground truthing. For example, the compressed PCA, full PCA and reflectance cubes correctly delineated edges

through 100% of interest points and single-point intersections, earning them the strongest Likert score for the false negatives criterion. As seen in Figure 288, the algorithm generated clean, unbroken edges along scene’s overlapping cloth threads and accurately rendered single-point intersections among the threads. Additionally, edge collinearity techniques indicated that the algorithm accurately localized edges across all five HSI input data sets.

For the Cloth Threads on Sand VNIR data, Table 94, Table 95, Table 96 and Table 97 present the evaluation interest points, benchmark vertical edge points, benchmark horizontal edge points and benchmark single-point intersections, respectively. Each interest point and benchmark point were chosen according to the criteria detailed in the Methodology component and apply to all three algorithm evaluations.

Table 94: Interest Points for Cloth Threads VNIR Data

Interest Point	Position (x,y)	Feature
1	169, 2	W red thread, N portion
2	246, 159	W red thread, N portion
3	276, 202	W red thread, N portion
4	278, 200	W red thread, N portion
5	249, 159	W red thread, N portion
6	173, 2	W red thread, N portion
7	310, 9	Yellow thread, N portion
8	311, 71	Yellow thread, N portion
9	323, 127	Yellow thread, N portion
10	331, 149	Yellow thread, N portion
11	333, 148	Yellow thread, N portion
12	232, 115	Yellow thread, N portion
13	313, 64	Yellow thread, N portion
14	313, 9	Yellow thread, N portion

Table 95: Benchmark Vertical Edge Points for Cloth Threads VNIR Data

Vertical Edge Point	Position (x,y)	Feature
1	359, 8	E red thread, N portion
2	359, 9	E red thread, N portion
3	359, 10	E red thread, N portion
4	359, 11	E red thread, N portion
5	359, 12	E red thread, N portion
6	359, 13	E red thread, N portion
7	359, 14	E red thread, N portion
8	359, 15	E red thread, N portion
9	359, 16	E red thread, N portion
10	359, 17	E red thread, N portion
11	359, 18	E red thread, N portion
12	359, 19	E red thread, N portion
13	359, 20	E red thread, N portion
14	359, 21	E red thread, N portion
15	359, 22	E red thread, N portion
16	359, 23	E red thread, N portion
17	359, 24	E red thread, N portion
18	359, 25	E red thread, N portion
19	359, 26	E red thread, N portion
20	359, 27	E red thread, N portion
21	359, 28	E red thread, N portion
22	359, 29	E red thread, N portion
23	359, 30	E red thread, N portion
24	359, 31	E red thread, N portion
25	359, 32	E red thread, N portion

Table 96: Benchmark Horizontal Edge Points for Cloth Threads VNIR Data

Horizontal Edge Point	Position (x,y)	Feature
1	515, 42	White thread, E portion
2	516, 41	White thread, E portion
3	517, 41	White thread, E portion
4	518, 40	White thread, E portion
5	519, 39	White thread, E portion
6	520, 39	White thread, E portion
7	521, 38	White thread, E portion
8	522, 38	White thread, E portion
9	523, 38	White thread, E portion
10	523, 37	White thread, E portion
11	524, 37	White thread, E portion
12	525, 37	White thread, E portion
13	525, 36	White thread, E portion
14	526, 36	White thread, E portion
15	527, 35	White thread, E portion
16	528, 35	White thread, E portion
17	529, 34	White thread, E portion
18	530, 33	White thread, E portion

Table 97: Benchmark Single-Point Intersections for Cloth Threads VNIR Data

Single-Point Intersection	Position (x,y)	Feature
1	278, 201	Red and white thread intersection
2	333, 149	Black and yellow thread intersection
3	358, 293	Red and yellow thread intersection
4	363, 70	Red and black thread intersection
5	383, 122	Blue and white thread intersection

HySPADE Analysis and Evaluation

This section presents the empirical evaluation of the new HySPADE edge detection operator as measured against the six Canny evaluation criteria. For each evaluation criteria, this study presents samples of the strongest measurements, while the

complete edge planes are available in Appendix A. Additionally, the precise evaluation measurements are presented in a single table, which enables comparison across data input type and Canny evaluation criteria.

Overall, the HySPADE edge detection algorithm produced satisfactory evaluation measurements across a broad range of datasets. The algorithm performed particularly strongly against the localization and single-point response criteria, while performing most weakly against the false positives criterion. In general, the false positive performance was not a barrier to generating useful edge detection results. Additionally, the compressed PCA and compressed MNF data inputs produced the strongest results, a finding that supports the hypothesis that concentrating spectral information into fewer channels improves edge detection results.

Overhead – Reno, Nevada USA

As seen in Figure 289 and Table 98, the HySPADE edge detection algorithm produced satisfactory results across several data input types and Canny evaluation criteria. The compressed MNF cube produced the strongest normalized Canny criteria scores, measuring strongly against the localization and unbroken edges criteria. The reflectance cube measured strongly the localization and single-point response criteria, as well. Only the full MMNF cube produced suboptimal results against the evaluation criteria (i.e., false positives and robustness to noise). Note that for most evaluation criteria, the compressed MNF cube outperformed its full MNF counterpart, which supports the hypothesis that concentrating spectral information into fewer channels improves edge detection results.

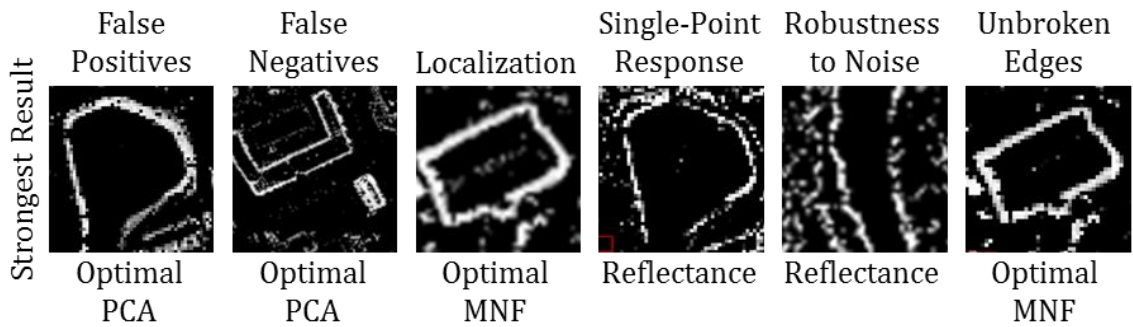


Figure 289: Strongest HySPADE Evaluation Results for Reno VNIR/SWIR Data, Linear Stretch of Strong Edge Pixels, Threshold at 40 Intermediate Planes from 0.10σ to 4.0σ

Table 98: HySPADE Evaluation Measurements for Reno VNIR/SWIR Data

HySPADE Algorithm Reno	False Positives	False Negatives	Localization	Single-Point Response	Robustness to Noise	Unbroken Edges	Normalized Score
Reflectance	3	3	1	1	2	2	2.0
Optimal PCA	2	3	1	2	3	3	2.3
Optimal MNF	2	2	1	3	2	1	1.8
Full PCA	2	3	1	2	3	3	2.3
Full MNF	4	2	1	2	4	3	2.7
Roberts	4	3	2	4	3	3	3.2
Sobel	2	3	2	3	2	4	2.7

Although performing strongly in many areas, none of the discrete tests scored above average across all evaluation categories. The reflectance test produced average results against the false positives and false negatives criteria, the compressed MNF test produced average results against the single-point response criteria, etc. Also note in Figure 289 the high-quality of the reflectance-derived edge plane with respect to single-point response – the thin, single-point edge around the small pond provides a strong sense

of where the water ends and the surrounding vegetation begins. Overall, these results are somewhat weaker than their gradient-based counterparts, but they still support reliable urban feature mapping.

A variety of evaluation methods were used to assess the Gradient-based edge detection algorithm's performance against the Reno VNIR/SWIR dataset, including interest points, collinearity of edges, single-point intersections and image subtraction. For example, the algorithm successfully delineated unbroken edges through all but a few interest points within the compressed MNF cube, particularly around the buildings within the scene; a few interest points were missed around the major intersection and along the river to the east as seen in Appendix A. Additionally, edge collinearity techniques indicated that the algorithm accurately localized edges across all five HSI input data sets.

Overhead – Cuprite, Nevada USA

As seen in Figure 290 and **Error! Reference source not found.** for Cuprite Flight Line #1, the HySPADE edge detection algorithm produced satisfactory results across only the compressed PCA data input type. Results indicate that the dataset is particularly challenging for the false positives criterion, against which only the compressed PCA and compressed MNF cubes performed nominally while the remaining cubes performed weakly.

The compressed PCA and MNF cubes produced the most reliable normalized Canny criteria scores, measuring well against the false negatives, localization, and single-point response criteria. Notably, the compressed MNF cube measured weakly against the unbroken edges criteria while the remaining HSI cubes measured average or better. The

most likely explanation for the under-performance is that the compressed MNF cube lacked the MNF bands carrying sufficient information to produce unbroken edges.

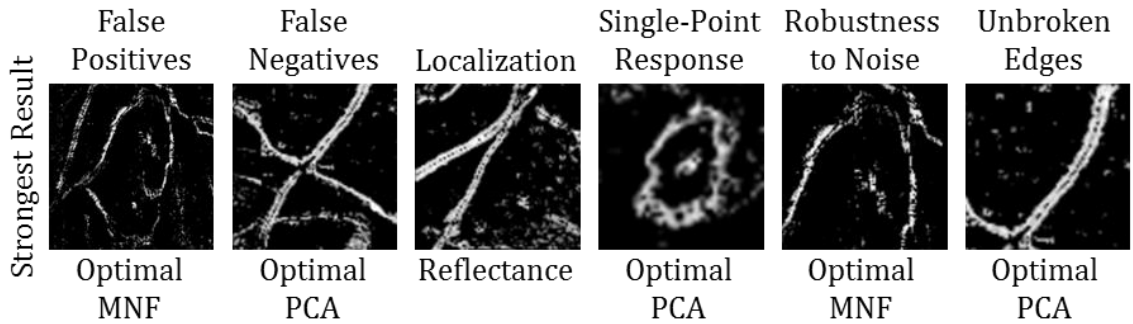


Figure 290: Strongest HySPADE Evaluation Results for Cuprite FL #1 Overhead VNIR/SWIR Data, Linear Stretch of Strong Edge Pixels, Threshold at 40 Intermediate Planes from 0.10σ to 4.0σ

Table 99: HySPADE Evaluation Measurements for Cuprite FL #1 Overhead VNIR/SWIR Data

HySPADE Algorithm Cuprite Flight Line #1	False Positives	False Negatives	Localization	Single-Point Response	Robustness to Noise	Unbroken Edges	Normalized Score
Reflectance	4	2	1	2	3	3	2.5
Optimal PCA	3	2	1	2	3	2	2.2
Optimal MNF	3	2	1	2	2	4	2.3
Full PCA	4	2	1	2	3	3	2.5
Full MNF	5	3	1	3	5	3	3.3
Roberts	5	3	2	3	4	2	3.2
Sobel	5	3	2	3	4	2	3.2

As seen during the gradient-based tests, the Cuprite Flight Line #1 dataset is particularly challenging for the false positives evaluation criteria. Only the compressed

PCA and compressed MNF cubes earned an average evaluation measurement for false positives, while the reflectance, full PCA and full MNF cubes scored quite weakly, missing large sections of the primary kaolinite feature and large sections of improved road. Note that for many evaluation criteria, the compressed PCA and MNF cubes outperformed their full PCA and full MNF counterparts, a finding that provides additional support for the hypothesis that concentrating spectral information into fewer channels improves edge detection results.

A variety of evaluation methods were used to assess the HySPADE edge detection algorithm's performance against the Cuprite Flight Line #1 dataset, including interest points, collinearity of edges, single-point intersections and ground truthing. For example, the algorithm successfully delineated unbroken edges through all but a few interest points within the compressed PCA cube, particularly along the major improved roads and along the edges of the primary kaolinite feature; a few interest points were missed around the minor unimproved roads and around heavily mixed mineral deposits as seen in Appendix A. Additionally, edge collinearity techniques indicated that the algorithm accurately localized edges across all five HSI input data sets.

As seen in Figure 291 and Table 100 for Cuprite Flight Line #2, the HySPADE edge detection algorithm was challenged to produce satisfactory results across the Canny evaluation criteria. Results indicate that the dataset is particularly challenging for the false positive, single-point response and robustness to noise criteria, against which only the compressed PCA test performed average or better while the remaining cubes performed weakly.

Only the compressed PCA test produced satisfactory evaluation scores across all criteria. Only against the false negatives and unbroken edges criteria did the compressed PCA test score above average, however, indicating that the dataset is challenging for the HySPADE algorithm. The most striking result from the tests is the high sensitivity to noise demonstrated by the HySPADE algorithm, which produced multiple false alarms attributable to the noise observed during the preprocessing component. The below-average performance of HySPADE against the two MNF test cubes is notable, as well. Additionally, most data types performed satisfactorily against the false negatives criterion, and overall the results indicate that the HySPADE algorithm can produce results sufficient to support mineral mapping applications.

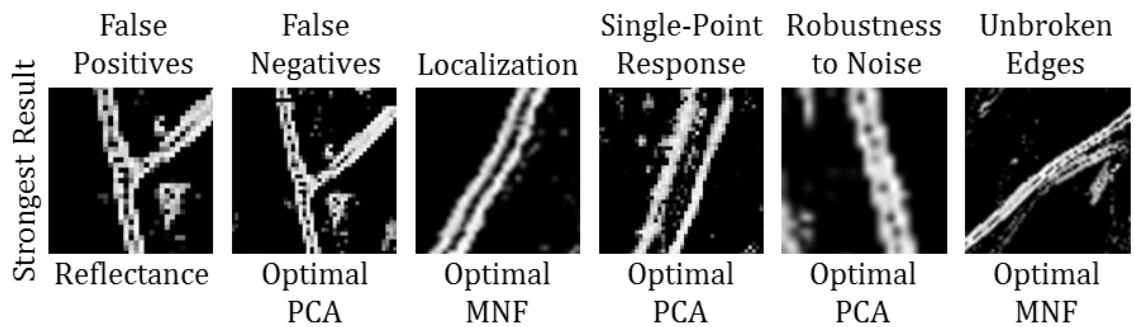


Figure 291: Strongest HySPADE Evaluation Results for Cuprite FL #2 Overhead VNIR/SWIR Data, Linear Stretch of Strong Edge Pixels, Threshold at 40 Intermediate Planes from 0.10σ to 4.0σ

Table 100: HySPADE Evaluation Measurements for Cuprite FL #2 Overhead VNIR/SWIR Data

HySPADE Algorithm Cuprite Flight Line #2	False Positives	False Negatives	Localization	Single-Point Response	Robustness to Noise	Unbroken Edges	Normalized Score
Reflectance	3	3	1	3	4	2	2.7
Optimal PCA	3	2	1	3	3	2	2.3
Optimal MNF	3	2	1	3	4	3	2.7
Full PCA	3	3	1	3	4	2	2.7
Full MNF	4	2	1	3	4	3	2.8
Roberts	5	2	1	3	4	2	2.8
Sobel	4	2	1	4	3	2	2.7

A variety of evaluation methods were used to assess the HySPADE edge detection algorithm’s performance against the Cuprite Flight Line #2 dataset, including interest points, collinearity of edges, single-point intersections and ground truthing. For example, the algorithm successfully delineated unbroken edges through all but a few interest points within the compressed PCA and compressed MNF cubes, the major improved roads and the manmade structures in the center of the image frame; a few interest points were missed around the minor unimproved roads and around heavily mixed mineral deposits as seen in Appendix A. Ground truthing indicated that the algorithm also generated false positives within the open deserts to the east and west, although not at a rate disruptive to mineral mapping applications. Additionally, edge collinearity techniques indicated that the algorithm accurately localized edges across all five HSI input data sets. In general, the HySPADE algorithm appears to accurately localize all edge types contained within this work.

As seen in Figure 292 and Table 101 for Cuprite Flight Line #3, the HySPADE edge detection algorithm was challenged to produce satisfactory results across the Canny evaluation criteria. Results indicate that the dataset is particularly challenging for the false negatives, robustness to noise and unbroken edges criteria, against which only the full PCA test performed average or better while the remaining cubes performed weakly. No test scored better than a Likert score of three against any of the three criteria, indicating that the data set is one of the most challenging encountered for the HySPADE algorithm.

Only the full PCA test produced satisfactory evaluation scores across all criteria, scoring a three of better. All other tests scored at least one Likert score of four while the compressed PCA and full MNF tests measured a Likert score of four across three criteria. False positives also were common within the scene, particularly within the bright playa feature as seen under the false positives header in Figure 292. Overall, the edge planes were quite noisy, as well.

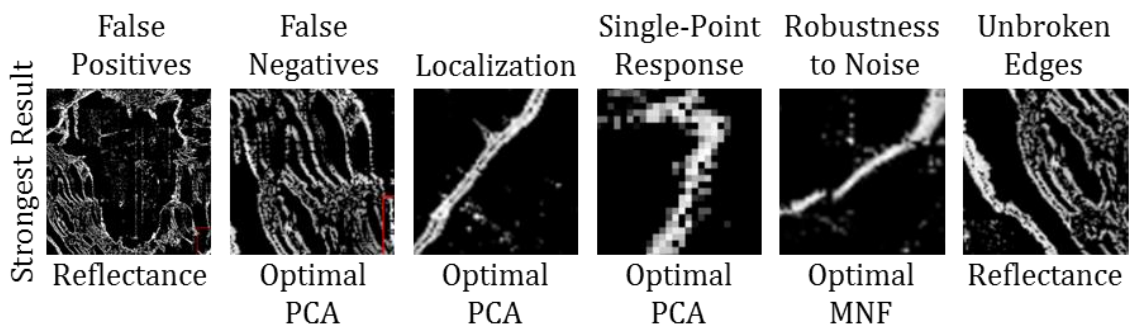


Figure 292: Strongest HySPADE Evaluation Results for Cuprite FL #3 Overhead VNIR/SWIR Data, Linear Stretch of Strong Edge Pixels, Threshold at 40 Intermediate Planes from 0.10σ to 4.0σ

Table 101: HySPADE Evaluation Measurements for Cuprite FL #3 Overhead VNIR/SWIR Data

HySPADE Algorithm Cuprite Flight Line #3	False Positives	False Negatives	Localization	Single-Point Response	Robustness to Noise	Unbroken Edges	Normalized Score
Reflectance	3	2	1	3	4	3	2.7
Optimal PCA	3	4	1	2	4	4	3.0
Optimal MNF	3	4	1	2	3	3	2.7
Full PCA	3	3	1	3	3	3	2.7
Full MNF	3	4	1	2	4	4	3.0
Roberts	4	2	2	2	3	3	2.7
Sobel	2	1	1	3	2	2	1.8

The most likely explanation for the suboptimal results is that the HySPADE algorithm appears to be overly sensitive to intensity under certain conditions such as particularly bright or dark features. Recall that the algorithm incorporates Euclidean distance into its Spectral Similarity Score (SSS), meaning that fully half of the SSS is sensitive to intensity, which would explain the intensity sensitivity.

A variety of evaluation methods were used to assess the HySPADE edge detection algorithm's performance against the Cuprite Flight Line #3 dataset, including interest points, collinearity of edges, single-point intersections and ground truthing. For example, the algorithm was challenged to delineate through all interest points around the primary playa feature; only the reflectance test produced a strong boundary around the feature while the remaining tests missed more than half of the interest points, resulting in poor false negative evaluations. Ground truthing indicated that the algorithm also

generated false positives within the open deserts to the east of the playa, although not at a rate disruptive to mineral mapping applications. Additionally, edge collinearity techniques indicated that the algorithm accurately localized edges across all five HSI input data sets.

As seen in Figure 293 and Table 102 for Cuprite Flight Line #4, the HySPADE edge detection algorithm produced satisfactory results across all Canny evaluation criteria except for false positives, against which three of the five data types produced an unacceptably high volume of false alarms. All data types, however, merited strong evaluation measurements for false negatives, localization, single-point response and unbroken edges. Only the compressed MNF and full MNF tests measured average or better than average for all evaluation criteria, adding additional evidence supporting the hypothesis that HSI datasets optimized for noise reduction and information compression improve edge detection results.

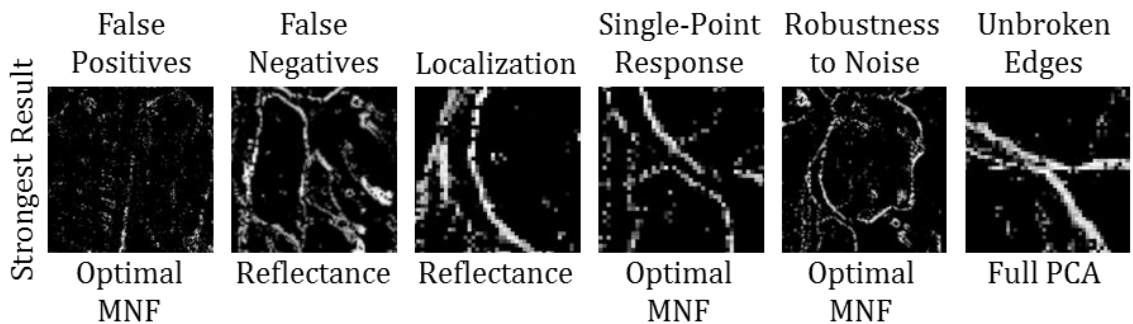


Figure 293: Strongest HySPADE Evaluation Results for Cuprite FL #4 Overhead VNIR/SWIR Data, Linear Stretch of Strong Edge Pixels, Threshold at 40 Intermediate Planes from 0.10σ to 4.0σ

Table 102: HySPADE Evaluation Measurements for Cuprite FL #4 Overhead VNIR/SWIR Data

HySPADE Algorithm Cuprite Flight Line #4	False Positives	False Negatives	Localization	Single-Point Response	Robustness to Noise	Unbroken Edges	Normalized Score
Reflectance	4	2	1	2	3	2	2.3
Optimal PCA	4	2	1	2	3	2	2.3
Optimal MNF	2	2	1	2	2	2	1.8
Full PCA	4	2	1	2	3	2	2.3
Full MNF	2	2	1	2	3	2	2.0
Roberts	4	3	1	4	3	3	3.0
Sobel	4	3	1	4	3	2	2.8

As seen in Figure 293 and Appendix A, the HySPADE accurately delineated the primary kaolinite deposits along the eastern portion of the image despite false alarming within the darker mineral deposits to the west. The algorithm accurately located the kaolinite edges with narrow, largely broken edges. Note that the single-point response example in Figure 293 demonstrates very thin edges between nearby kaolinite deposits. The overall normalized scores are satisfactory for this dataset, although only the compressed MNF and full MNF produced satisfactory results for all criteria, including significant improvement against the false positive criteria.

A variety of evaluation methods were used to assess the HySPADE edge detection algorithm’s performance against the Cuprite Flight Line #4 dataset, including interest points, collinearity of edges, single-point intersections and ground truthing. For example, the algorithm ably delineated through all interest points around the primary kaolinite features, particularly within the compressed MNF and full MNF tests; only the

compressed MNF test produced scores above average against the robustness to noise criteria, successfully suppressing the noisy false alarms within the dark deposits within the western portion of the scene. Ground truthing indicated that the algorithm also generated occasional false positives within the uniform kaolinite deposits, although not at a rate disruptive to mineral mapping applications. Additionally, edge collinearity techniques indicated that the algorithm accurately localized edges across all five HSI input data sets.

Overhead – Indian Pines, Indiana USA

As seen in Figure 294 and Table 103, the HySPADE edge detection algorithm was unable to produce satisfactory results for any HSI data type for the Indian Pines VNIR/SWIR data – a dataset that also challenged the gradient-based algorithm. All five data input types were measured at the weakest Likert score for both false negatives and unbroken edges, as evidenced by the absent or highly interrupted edge planes as seen in Figure 294 and Appendix A. False positives and robustness to noise were also poorly adjudicated, and the localization scores were less than optimal for the first time in the HySPADE results. Only the single-point response results graded out as consistently satisfactory – indeed, one of HySPADE’s strengths appears to be its ability to produce single-point response edge planes.

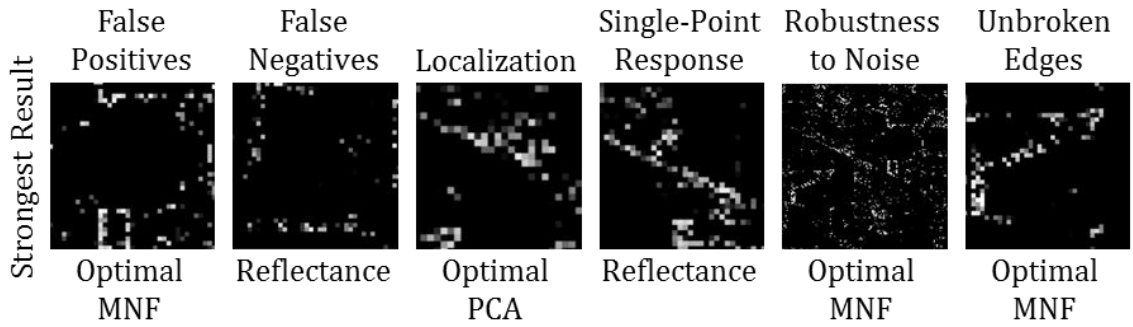


Figure 294: Strongest HySPADE Evaluation Results for Indian Pines Overhead VNIR/SWIR Data, Linear Stretch of Strong Edge Pixels, Threshold at 40 Intermediate Planes from 0.10σ to 4.0σ

Table 103: HySPADE Evaluation Measurements for Indian Pines Overhead VNIR/SWIR Data

HySPADE Algorithm Indian Pines	False Positives	False Negatives	Localization	Single-Point Response	Robustness to Noise	Unbroken Edges	Normalized Score
Reflectance	4	5	3	2	5	5	4.0
Optimal PCA	4	5	2	2	5	5	3.8
Optimal MNF	3	5	2	2	3	5	3.3
Full PCA	4	5	3	2	5	5	4.0
Full MNF	5	5	3	2	5	5	4.2
Roberts	3	3	1	2	3	2	2.3
Sobel	3	3	1	3	2	2	2.3

The Indian Pines results for both the HySPADE and gradient-based algorithms suggest that the combination of limited spatial resolution and low spectral contrast presents a significant barrier to generating high-quality edge planes. While this is an unsurprising result in the abstract, the degree to which the algorithms struggle under these conditions is notable, particularly given the simultaneous weak false positive and false negative rates.

A variety of evaluation methods were used to assess the HySPADE edge detection algorithm's performance against the Indian Pines dataset, including interest points, collinearity of edges, single-point intersections and ground truthing. For example, the algorithm was unable to capture any of the interest points for the scene, resulting in very weak false negative scores. Ground truthing indicated that the algorithm also generated false positives within homogeneous crop fields, resulting in weak false positive evaluations. Additionally, edge collinearity techniques indicated that the algorithm satisfactorily localized edges across all five HSI input data sets, albeit with less accuracy than observed in previous tests. Clearly, the Indian Pines dataset is challenging to HSI edge operators.

Overhead – Deepwater Horizon Oil Spill

As seen in Figure 295 and Table 104, the HySPADE edge detection algorithm produced satisfactory results across several data input types and Canny evaluation criteria. In particular, the reflectance and full PCA cubes produced strong results across all six criteria, and the radiance cube produced satisfactory results across all six criteria. Only the compressed PCA cube underperformed expectations, generating a suboptimal volume of false positives and only average scores for single-point response and robustness to noise. Overall, localization and unbroken edges evaluation measurements were quite strong, with all tests accurately delineating the oil slicks in their proper locations as unbroken features – a positive finding for oil spill mapping applications.

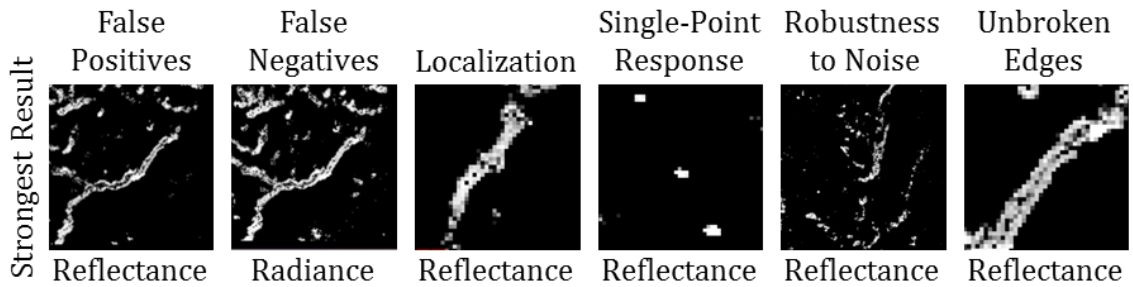


Figure 295: Strongest HySPADE Evaluation Results for Deepwater Horizon Overhead VNIR/SWIR Data, Linear Stretch of Strong Edge Pixels, Threshold at 40 Intermediate Planes from 0.10σ to 4.0σ

Table 104: HySPADE Evaluation Measurements for Deepwater Horizon Overhead VNIR/SWIR Data

HySPADE Algorithm Deepwater Horizon	False Positives	False Negatives	Localization	Single-Point Response	Robustness to Noise	Unbroken Edges	Normalized Score
Radiance	3	2	1	3	3	1	2.2
Reflectance	2	2	1	2	2	1	1.7
Optimal PCA	4	2	1	3	3	2	2.5
Optimal MNF	3	2	1	2	3	1	2.0
Full PCA	2	2	1	2	2	1	1.7
Full MNF	4	3	1	4	4	3	3.2
Roberts	5	2	1	3	4	1	2.7
Sobel	2	1	1	2	3	1	1.7

As seen in Figure 295 and Appendix A, the HySPADE algorithm produced high-quality oil spill edge planes for both the reflectance and full PCA tests. The strong false positive evaluation measurements are particularly notable given the noisy ocean background, and the long, unbroken edges around the broad oil spill features make for an attractive edge plane that could quickly guide oil spill cleanup personnel to the optimal locations for their equipment. Also note that the false negatives evaluation measurements

were strong across all five HSI data input types. Where HySPADE missed oil slick features, the pixels were heavily mixed with oil and water and occurred mostly behind the advancing oil spill fronts, meaning that the false negatives would have minimal bearing on oil spill cleanups designed to inhibit the spill's advance.

A variety of evaluation methods were used to assess the Gradient-based edge detection algorithm's performance against the Deepwater Horizon VNIR/SWIR dataset, including interest points, collinearity of edges and single-point intersections. For example, all five data types correctly delineated edges through over 98% of interest points and 100% of single-point intersections, earning them a strong Likert score for the false negatives criterion. As seen in Figure 295, the algorithm generated clean, unbroken edges along the major oil slicks within the scene – a meaningful finding with respect to oil spill mapping applications. Additionally, edge collinearity techniques indicated that the algorithm accurately localized edges across all five HSI input data sets and produced unbroken edges in the vertical, horizontal and diagonal directions throughout the scene.

Ground-Based – Larkhaven

As seen in Figure 296 and Table 105, the HySPADE edge detection algorithm was unable to produce satisfactory results for any HSI data type for the Larkhaven VNIR data. The algorithm struggled notably with false positives, false negatives and unbroken edges, resulting in the many missing, broken and false edges as seen in Appendix A. The suboptimal edge results were observed throughout the scene rather than within isolated portions. Localization and single-point response performance were areas of strength for

the HySPADE algorithm, which appears to be the case even for the data sets of greatest challenge.

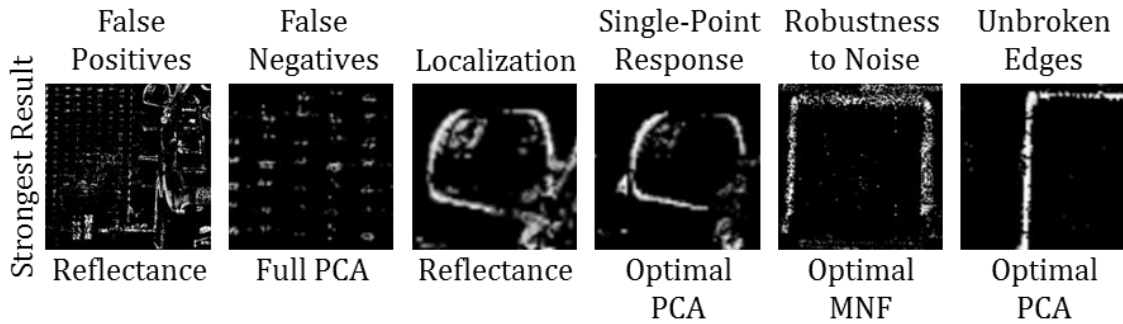


Figure 296: Strongest HySPADE Evaluation Results for Larkhaven Ground-Based VNIR Data, Linear Stretch of Strong Edge Pixels, Threshold at 40 Intermediate Planes from 0.10σ to 4.0σ

Table 105: HySPADE Evaluation Measurements for Larkhaven Ground-Based VNIR Data

HySPADE Algorithm Larkhaven	False Positives	False Negatives	Localization	Single-Point Response	Robustness to Noise	Unbroken Edges	Normalized Score
Reflectance	3	4	1	3	4	4	3.2
Optimal PCA	3	4	1	2	3	3	2.7
Optimal MNF	4	5	1	2	2	4	3.0
Full PCA	3	4	1	3	4	4	3.2
Full MNF	4	4	1	4	4	5	3.7
Roberts	3	1	1	2	3	1	1.8
Sobel	3	1	1	3	3	1	2.0

Consider the false negatives in the HySPADE Larkhaven edge planes. The most obvious false negatives occur between the brick and mortar on the building’s façade. The most likely explanation is the subtle spectral contrast between the brick and mortar,

which HySPADE was evidently unable to discriminate. Additionally, the false positives along the left side of the vehicle appear suboptimal, most likely due to HySPADE's sensitivity to intensity. The MNF cubes also did not provide the noise defeating advantage observed in other tests. Overall, the Larkhaven dataset presented a significant challenge to the HySPADE algorithm, most likely due to sensitivity intensity and an inability to overcome subtle spectral contrast.

A variety of evaluation methods were used to assess the HySPADE edge detection algorithm's performance against the Larkhaven VNIR dataset, including interest points, collinearity of edges, single-point intersections and ground truthing. For example, all five input types missed more than 25% of the scene's interest points, resulting in suboptimal false negative scores. As seen in Figure 296, the algorithm generated noisy, occasionally broken edges along the rearview mirror, the calibration panel edges and along the boundary between vegetation and manmade material. The vast majority of mortar to brick edges also were missed. Consistent with previous HySPADE results, edge collinearity techniques indicated that the algorithm accurately localized edges across all five HSI input data sets.

Ground-Based – Granite VNIR

As seen in Figure 297 and Table 106, the HySPADE edge detection algorithm produced satisfactory Canny evaluation measurements for only the compressed PCA test, thereby providing additional evidence that compressed PCA and MNF cubes offer a measurable advantage over simple reflectance cubes. In particular, the compressed PCA cube produced excellent results against the false positives and false negatives criteria,

against which the remaining data sets measured weakly. Furthermore, the compressed PCA cube was measured significantly stronger against the robustness to noise criteria as seen in the examples in Figure 297. The compressed PCA cube’s single-point response performance was quite strong, as well, delineating thin, unbroken edges through the interest points of key features.

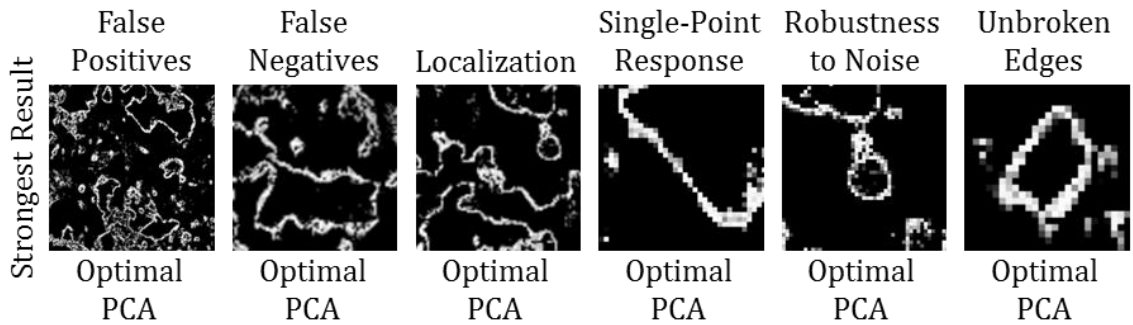


Figure 297: Strongest HySPADE Evaluation Results for Granite Ground-Based VNIR Data, Linear Stretch of Strong Edge Pixels, Threshold at 40 Intermediate Planes from 0.10σ to 4.0σ

Table 106: HySPADE Evaluation Measurements for Granite Ground-Based VNIR Data

HySPADE Algorithm Granite VNIR	False Positives	False Negatives	Localization	Single-Point Response	Robustness to Noise	Unbroken Edges	Normalized Score
Reflectance	4	4	2	2	3	4	3.2
Optimal PCA	2	2	1	2	1	2	1.7
Optimal MNF	4	3	1	2	3	3	2.7
Full PCA	3	3	1	2	3	4	2.7
Full MNF	4	4	1	2	3	3	2.8
Roberts	3	4	1	2	4	3	2.8
Sobel	2	2	1	3	3	2	2.2

The false positives, false negatives and unbroken edges criteria were particularly challenging for the HySPADE algorithm as executed against the Granite VNIR dataset – an unsurprising finding given the complexity and challenging nature of the scene. These results also are consistent with the gradient-based algorithm’s performance against the dataset. As seen in Appendix A, the compressed PCA edge plane is the only gradient Granite VNIR test satisfactorily delineating all major interest points with a low false alarm rate. The compressed PCA cube also significantly outperformed the other tests with respect to robustness to noise, a surprising result given the noise suppression advantages of the MNF cubes. The compressed MNF cube’s uncharacteristically weak performance is likely attributable to the exclusion of too many MNF bands from the cube, which considered only two MNF bands according to the scientific controls established within this dissertation. Including additional bands in the compressed MNF cube would likely improve its results.

A variety of evaluation methods were used to assess the HySPADE edge detection algorithm’s performance against the Granite VNIR dataset, including interest points, collinearity of edges and single-point intersections. For example, the gradient tests against the compressed PCA data type correctly delineated edges through over 98% of interest points, benchmark horizontal edge points, benchmark vertical edge points and single-point intersections, earning a strong Likert score for the false negatives criterion. As seen in Figure 297 and Appendix A, the algorithm generated accurate, unbroken edges around the major minerals within the rock – a meaningful finding with respect to mineral mapping applications. Additionally, edge collinearity techniques indicated that

the algorithm accurately localized edges across all five HSI input data sets except for the reflectance data type, against which the algorithm generated a few broken edges around curvilinear features.

Ground-Based – Granite NIR/SWIR

As seen in Figure 298 and Table 107, the Gradient-based edge detection algorithm produced satisfactory results across a narrow range of data input types and Canny evaluation criteria for the Granite NIR/SWIR data. Only the compressed MNF and compressed PCA cubes enabled the gradient-based edge detector to generate consistently above-average evaluation measurements. The remaining cubes produced suboptimal results against one or more Canny evaluation criteria.

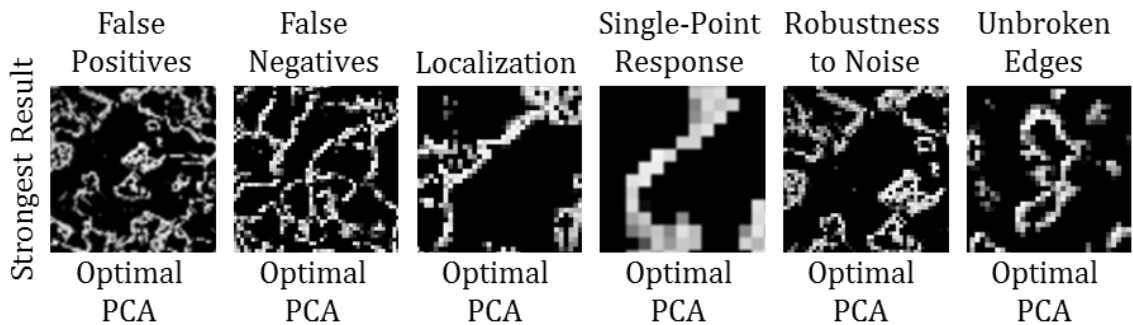


Figure 298: Strongest HySPADE Evaluation Results for Granite Ground-Based NIR/SWIR Data, Linear Stretch of Strong Edge Pixels, Threshold at 40 Intermediate Planes from 0.10σ to 4.0σ

Table 107: HySPADE Evaluation Measurements for Granite Ground-Based NIR/SWIR Data

HySPADE Algorithm Granite NIR/SWIR	False Positives	False Negatives	Localization	Single-Point Response	Robustness to Noise	Unbroken Edges	Normalized Score
Reflectance	4	3	1	2	4	3	2.8
Optimal PCA	2	1	1	2	1	1	1.3
Optimal MNF	3	3	1	2	3	3	2.5
Full PCA	5	4	2	2	4	4	3.5
Full MNF	4	5	1	3	4	3	3.3
Roberts	5	5	1	2	4	5	3.7
Sobel	4	4	1	3	3	4	3.2

The false positives and false negatives criteria were particularly challenging for the HySPADE algorithm as executed against the Granite NIR/SWIR dataset – an unsurprising finding given the complexity and challenging nature of the scene, similar to the results seen in the Granite VNIR dataset tests for both the gradient-based edge detector and the HySPADE edge detector. As seen in Appendix A, the compressed PCA edge plane is the only gradient Granite VNIR test fully delineating 100% of interest points through clean, unbroken edges largely free of false positives. Indeed, the compressed PCA test against the Granite NIR/SWIR data is one of the strongest tests observed in this dissertation, largely due to the cube’s compression of spectral information and HySPADE’s ability to generate thin, unbroken edges.

A variety of evaluation methods were used to assess the HySPADE edge detection algorithm’s performance against the Granite NIR/SWIR dataset, including interest points, collinearity of edges and single-point intersections. For example, the gradient tests against the compressed PCA data type correctly delineated edges through

100% of interest points and single-point intersections, earning the strongest Likert score for the false negatives criterion. As seen in Figure 298, the algorithm generated accurate, unbroken edges around the major minerals within the rock – a meaningful finding with respect to mineral mapping applications. Additionally, edge collinearity techniques indicated that the algorithm accurately localized edges across all but the full PCA data set.

Ground-Based – South African Core Samples

As seen in Figure 299 and Table 108, the HySPADE edge detection algorithm produced satisfactory results across several data input types and Canny evaluation criteria. In particular, the compressed PCA, full PCA and compressed MNF cubes produced satisfactory results across all six criteria, with each test earning a Likert measurement of three for the false positives criterion. Additionally, all input data types except for the full MNF cube produced above average results for the localization, false negatives, single-point response and unbroken edges criteria. The combination of spectral contrast and high spatial resolution are likely key enablers for the HySPADE algorithm’s strong evaluation – advantages also enjoyed by the gradient-based algorithm.

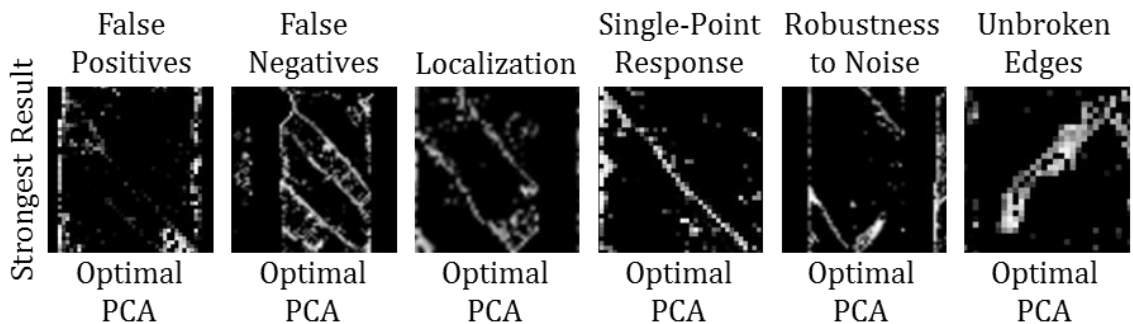


Figure 299: Strongest HySPADE Evaluation Results for Core Sample Ground-Based NIR/SWIR Data, Linear Stretch of Strong Edge Pixels, Threshold at 40 Intermediate Planes from 0.10σ to 4.0σ

As seen in Appendix A, the compressed MNF and compressed PCA cubes generated reliable edge planes consistent with low false positives, high accuracy and satisfactory single-point response. The false positives criterion appears to be the most challenging evaluative measure for the HySPADE edge detector when applied against mineral mapping datasets. As seen in the Cuprite and Granite datasets, a low false positive rate was more difficult to achieve than the other criteria. For all cases, however, the compressed MNF or compressed PCA cube enabled the HySPADE operator to achieve its strongest results.

Table 108: HySPADE Evaluation Measurements for Core Sample Ground-Based NIR/SWIR Data

HySPADE Algorithm South African Core Samples	False Positives	False Negatives	Localization	Single-Point Response	Robustness to Noise	Unbroken Edges	Normalized Score
Reflectance	5	2	1	2	3	2	2.5
Optimal PCA	3	2	1	2	2	2	2.0
Optimal MNF	3	2	1	2	2	2	2.0
Full PCA	3	2	1	2	2	2	2.0
Full MNF	5	3	1	3	4	3	3.2
Roberts	3	4	1	2	2	4	2.7
Sobel	2	4	1	3	2	3	2.5

A variety of evaluation methods were used to assess the HySPADE edge detection algorithm's performance against the South Africa Core Sample dataset,

including interest points, collinearity of edges and single-point intersections. For example, the HySPADE tests against the compressed MNF and compressed PCA data types correctly delineated edges through over 98% of interest points and single-point intersections, earning a strong Likert score for the false negatives criterion. As seen in Figure 299, the algorithm generated accurate, unbroken edges around the major minerals within the core samples just as it did for the two Granite datasets – a meaningful finding with respect to mineral mapping applications. Additionally, edge collinearity techniques indicated that the algorithm accurately localized edges across all five HSI input data sets. Thin, single-point or two-point edges were observed throughout the scene, as well.

Ground-Based – Aluminum Panel

As seen in Figure 300 and Table 109, the HySPADE edge detection algorithm produced satisfactory results across several data input types and Canny evaluation criteria. In particular, the compressed PCA cube yielded strong results for the false positives, localization, robustness to noise and unbroken edges criteria. The full PCA and full MNF cubes also produced reliable results, avoiding suboptimal performance for any evaluation criteria. The Aluminum Panel dataset challenged the HySPADE algorithm with respect to the false negatives and single-point response criteria, against which HySPADE measured no stronger than a Likert rating of three. Overall, however, HySPADE generated useful, accurate edge planes from the Aluminum Panel dataset.

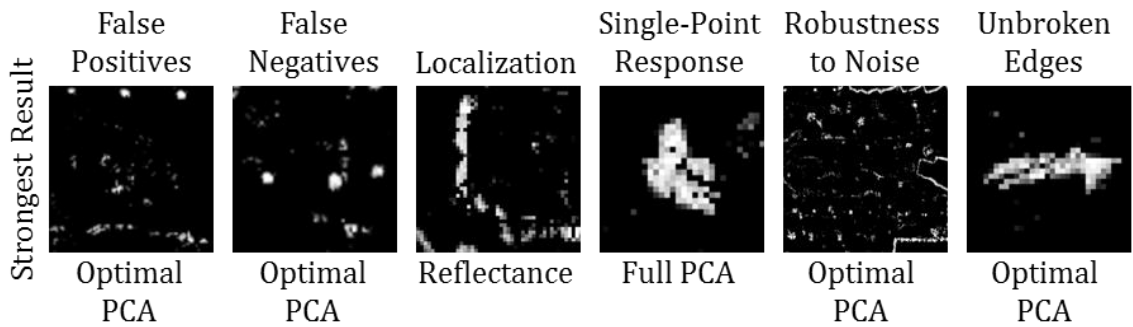


Figure 300: Strongest HySPADE Evaluation Results for Aluminum Panel Ground-Based VNIR Data, Linear Stretch of Strong Edge Pixels, Threshold at 40 Intermediate Planes from 0.10σ to 4.0σ

Table 109: HySPADE Evaluation Measurements for Aluminum Panel Ground-Based VNIR Data

HySPADE Algorithm Aluminum Panel	False Positives	False Negatives	Localization	Single-Point Response	Robustness to Noise	Unbroken Edges	Normalized Score
Reflectance	3	3	1	3	2	4	2.7
Optimal PCA	2	3	1	3	2	2	2.2
Optimal MNF	2	4	1	3	3	3	2.7
Full PCA	3	3	1	3	2	3	2.5
Full MNF	2	3	1	3	3	3	2.5
Roberts	5	3	1	2	4	5	3.3
Sobel	5	3	1	2	4	5	3.3

As seen in Appendix A and Figure 300, the HySPADE algorithm generated a manageable volume of false alarms across the mottled and rusted surface of the aluminum panel for all HSI data types. Figure 300 shows that the algorithm generates strong and accurate edges around the unique rust features from the compressed PCA and full PCA data types with minimal false alarms. Importantly, HySPADE's satisfactory false positive rate against the Aluminum Panel data indicates that it can distinguish

between weathered features that are chemically identical to un-weathered aluminum features – a task that challenged the gradient-based algorithm. The algorithm also performed well against the localization criteria and the robustness to noise criteria, ably avoiding noise-induced errors.

A variety of evaluation methods were used to assess the HySPADE edge detection algorithm's performance against the Aluminum Panel dataset, including interest points, collinearity of edges and single-point intersections. For example, the tests against the compressed PCA data type correctly delineated edges through 98% of interest points and single-point intersections, earning a strong Likert score for the false negatives criterion. As seen in Figure 300, the algorithm generated accurate, unbroken edges around the major rust features and rivets and rarely false alarmed. Additionally, edge collinearity techniques indicated that the algorithm accurately localized edges across all five HSI input data sets.

Microscene – Rare Target on Sand

As seen in Figure 301 and Table 110, the Gradient-based edge detection algorithm produced satisfactory results across several data input types and Canny evaluation criteria, never scoring weaker than a Likert score of three for any of the 30 evaluations spanning the five HSI data type tests. In particular, the compressed PCA cube produced strong results across all six criteria, scoring most strongly against the localization, single-point response and the robustness to noise criteria.

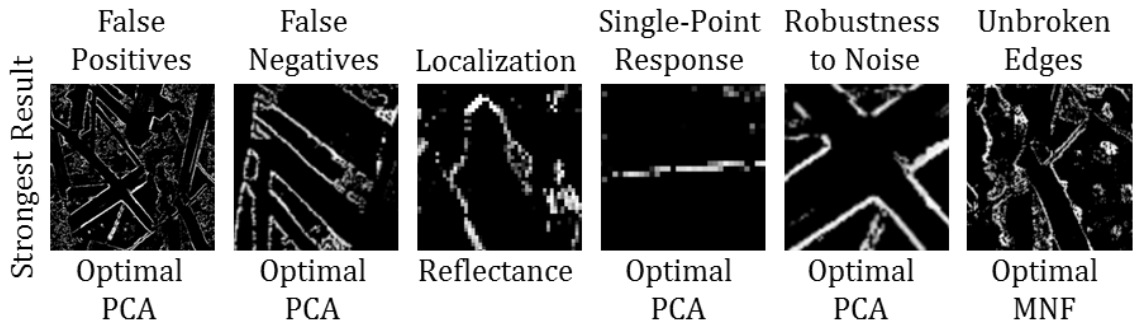


Figure 301: Strongest HySPADE Evaluation Results for Rare Target on Sand Microscene VNIR Data, Linear Stretch of Strong Edge Pixels, Threshold at 40 Intermediate Planes from 0.10σ to 4.0σ

Table 110: HySPADE Evaluation Measurements for Rare Target on Sand Microscene VNIR Data

HySPADE Algorithm Rare Target on Sand	False Positives	False Negatives	Localization	Single-Point Response	Robustness to Noise	Unbroken Edges	Normalized Score
Reflectance	2	3	1	2	2	2	2.0
Optimal PCA	2	2	1	1	1	2	1.5
Optimal MNF	3	3	1	2	2	2	2.2
Full PCA	3	3	1	3	3	3	2.7
Full MNF	3	3	1	3	3	2	2.5
Roberts	3	4	1	2	4	5	3.2
Sobel	2	4	1	3	3	3	2.7

From the compressed PCA cube, HySPADE produced clean, single-pixel response edges around the rare target surrounded by vegetation and sand as well as around the vegetation. Occasional false alarms are observed on the edge planes, but they present at manageable levels. All of the evaluation measurements for the compressed PCA cube were above average, while the reflectance cube measured above average for all criteria except false negatives, against which the cube measured nominally. As seen in

Appendix A, the full PCA cube performed much less strongly against the false positive criterion than did the compressed PCA cube, highlighting the value of optimizing the transformed HSI data. The algorithm also generated narrow, unbroken edges for the reflectance, compressed PCA and compressed MNF data input types, and all data types received the maximum evaluation measurement against the localization criterion. Overall, the HySPADE approach generated high-quality edge planes from the Rare Target on Sand HSI dataset.

A variety of evaluation methods were used to assess the HySPADE edge detection algorithm's performance against the Rare Target on Sand dataset, including interest points, collinearity of edges, single-point intersections and ground truthing. For example, the tests against the compressed PCA data type correctly delineated edges through 98% of interest points and single-point intersections, earning a strong Likert score for the false negatives criterion. As seen in Figure 301, the algorithm generated accurate, mostly unbroken edges around the neodymium oxide (i.e., the rare target) – a meaningful finding with respect to trace chemical detection applications. Additionally, edge collinearity techniques indicated that the algorithm accurately localized edges across all five HSI input data sets.

Microscene – Chemical Array

As seen in Figure 302 and Table 111, the HySPADE edge detection algorithm was challenged to produce satisfactory results across several data input types and Canny evaluation criteria. Only the reflectance test consistently measured average or above average performance against the Canny criteria, while the remaining tests performed

particularly weakly against the false positives, robustness to noise and unbroken edges criteria. The single-point response criterion was a troublesome criterion for many tests, as well. The Chemical Array dataset was more of a challenge than expected for the HySPADE edge detection algorithm, which has previously performed strongly against unique targets on a sand background. Notably, the gradient-based algorithm was similarly challenged by this dataset.

The high false alarm rates for several tests are seen mostly within the sand background, which as evidenced in the gradient evaluation section by Figure 287, is composed on chemically uniform materials varying only in brightness. Only the reflectance and compressed MNF tests generated a manageable number of false alarms, all of which are isolated within the sand background as seen in Appendix A. Importantly, the reflectance and compressed MNF tests produced closed edges around the chemical deposits on the array as seen in the false positives example in Figure 302.

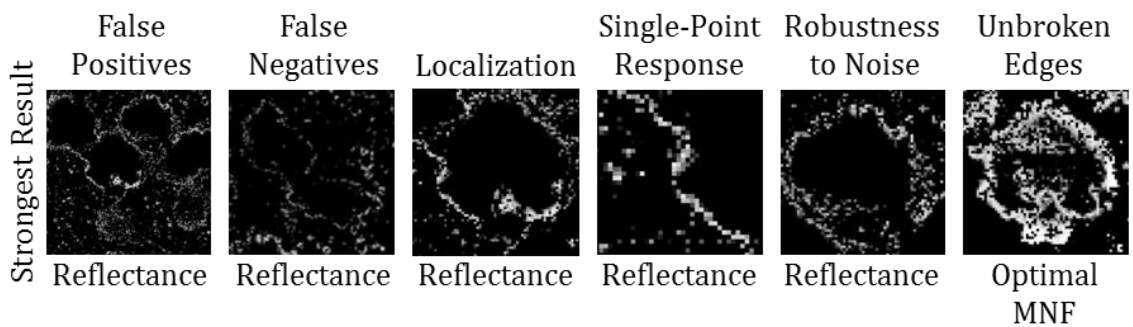


Figure 302: Strongest HySPADE Evaluation Results for Chemical Array Microscene NIR/SWIR Data, Linear Stretch of Strong Edge Pixels, Threshold at 40 Intermediate Planes from 0.10σ to 4.0σ

Table 111: HySPADE Evaluation Measurements for Chemical Array Microscene NIR/SWIR Data

HySPADE Algorithm Chemical Array on Sand	False Positives	False Negatives	Localization	Single-Point Response	Robustness to Noise	Unbroken Edges	Normalized Score
Reflectance	3	2	1	2	2	3	2.2
Optimal PCA	4	3	1	3	4	4	3.2
Optimal MNF	3	2	1	4	3	3	2.7
Full PCA	4	2	1	2	3	3	2.5
Full MNF	5	3	1	4	4	4	3.5
Roberts	2	4	2	2	5	4	3.2
Sobel	4	3	1	3	4	3	3.0

The unbroken edges criterion also presented a challenge to the HySPADE algorithm as applied to the Chemical Array NIR/SWIR data. No test measured better than a Likert score of three and broken edges were common around the key features within the scene. The most likely explanation for the broken edges is heavy spectral mixing along the boundaries.

The HySPADE reflectance test against the chemical array NIR/SWIR data is one of the rare occurrences when the reflectance data consistently outperformed or equaled the evaluation measurements of the compressed PCA and compressed MNF cubes – a result, however isolated, that does not support the hypothesis that optimizing reflectance data improves edge detection performance. The likely explanation for the reflectance outperformance is that the compressed MNF and compressed PCA cubes included too few bands resulting from this study’s scientific controls. Specifically, the compressed PCA cube contained only three bands and the compressed MNF cube contained only five bands. Most likely, PCA bands four and five contain the spectral information sufficient

to improve the performance against false positives and unbroken edges, while MNF bands six and seven contain similar rectifying spectral information. Overall, the reflectance cube's modest outperformance is not sufficient to affirm the null hypothesis concerning reflectance cube compression, but it does shed light on the sensitivity of the compressed PCA and compressed MNF cubes to band thresholding.

A variety of evaluation methods were used to assess the HySPADE edge detection algorithm's performance against the Chemical Array dataset, including interest points, collinearity of edges, single-point intersections and ground truthing. For example, the HySPADE tests against all data type correctly delineated edges through most interest points and single-point intersections, earning the average to above average Likert scores for the false negatives criterion. As seen in Appendix A and Figure 302, the algorithm generated accurate but occasionally broken edges around the ammonium nitrate sample (shown in the localization example in Figure 302), meaning that it accurately delineated all interest points for the key feature. Additionally, edge collinearity techniques indicated that the algorithm accurately localized edges across all five HSI input data sets.

Microscene - Cloth Threads

As seen in Figure 303 and Table 112, the HySPADE edge detection algorithm was challenged to produce satisfactory results across several data input types and Canny evaluation criteria. Only the compressed MNF and full MNF tests performed consistently above a Likert score of three against all six Canny criteria, while the reflectance, full PCA and compressed PCA cubes underperformed against the false positives criterion. Also of note was that the full MNF data type outperformed all others,

including its compressed counterpart, which also performed quite strongly against the VNIR data. The most likely explanation for the full MNF cube outperforming the compressed MNF cube is that the experimental controls limited the spectral information within the compressed MNF cube.

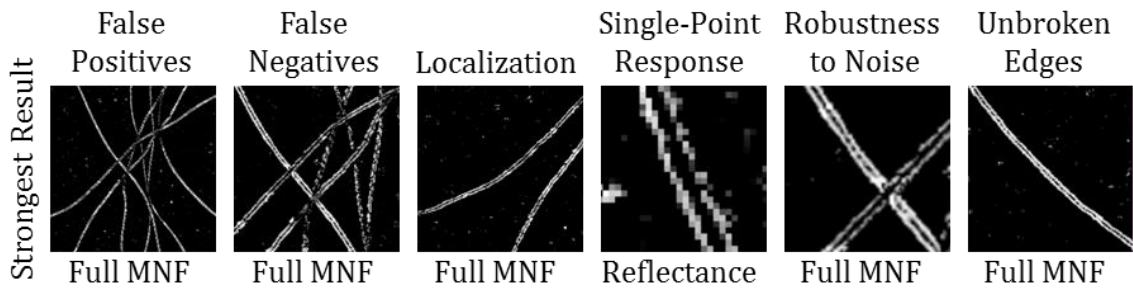


Figure 303: Strongest HySPADE Evaluation Results for Cloth Threads Microscene VNIR Data, Linear Stretch of Strong Edge Pixels, Threshold at 40 Intermediate Planes from 0.10σ to 4.0σ

Table 112: HySPADE Evaluation Measurements for Cloth Threads Microscene VNIR Data

HySPADE Algorithm Cloth Threads on Sand	False Positives	False Negatives	Localization	Single-Point Response	Robustness to Noise	Unbroken Edges	Normalized Score
Reflectance	5	2	1	2	3	3	2.7
Optimal PCA	4	4	1	3	3	5	3.3
Optimal MNF	2	1	1	3	2	3	2.0
Full PCA	5	2	1	3	3	3	2.8
Full MNF	1	1	1	2	1	3	1.5
Roberts	2	4	1	2	3	5	2.8
Sobel	2	3	1	3	3	3	2.5

The compressed MNF and full MNF tests were the only two tests to earn strong evaluation scores for false positives by virtue of their ability to suppress the noisy sand background on which the other datasets significantly false alarmed. The MNF performance is similar to the compressed MNF and full MNF cube performance on the Chemical Array data, suggesting that the MNF transform's capacity to improve edge detection performance is robust across datasets and spectral wavelengths – a finding also observed within the gradient-based tests against the same dataset. Additionally, note that the compressed MNF test scored quite strongly against the false negatives and localization criteria, as seen in Appendix A.

A variety of evaluation methods were used to assess the HySPADE edge detection algorithm's performance against the Cloth Threads on Sand dataset, including interest points, collinearity of edges, single-point intersections and ground truthing. For example, the compressed MNF and full MNF cubes correctly delineated edges through 100% of interest points and single-point intersections, earning them the strongest Likert score for the false negatives criterion. As seen in Figure 303, the algorithm generated clean, unbroken edges along scene's overlapping cloth threads and accurately rendered single-point intersections among the threads. Additionally, edge collinearity techniques indicated that the algorithm accurately localized edges across all five HSI input data sets.

Level Set Edge Detection Analysis and Evaluation

This section presents the empirical evaluation of the level set-based edge detection operator as measured against the six Canny evaluation criteria. For each evaluation criteria, this work presents samples of the strongest measurements, while the

complete edge planes are available in Appendix A. Additionally, the precise evaluation measurements are presented in a single table, which enables comparison across data input type and Canny evaluation criteria.

Overall, the gradient-based edge detection algorithm produced satisfactory evaluation measurements across a broad range of datasets. The algorithm performed particularly strongly against the false positives and single-point response criteria, while performing most weakly against the false negatives criterion. For some HSI datasets, the false negative performance was a barrier to generating useful edge detection results, however. Additionally, the compressed PCA and compressed MNF data inputs produced the strongest results, a finding that supports the hypothesis that concentrating spectral information into fewer channels improves edge detection results.

Overhead – Reno, Nevada USA

As seen in Figure 304 and Table 113, the level set edge detection algorithm produced satisfactory results across several data input types and Canny evaluation criteria. The reflectance, compressed PCA and full PCA cubes produced the strongest normalized Canny criteria scores, measuring very strongly against the false positives, single-point response, localization and unbroken edges criteria. False negatives were somewhat of a challenge for the algorithm against this dataset, as seen by the Likert score of three obtained by the best performing data input types. The compressed MNF and full MNF cubes yielded surprisingly weak results, missing most major features in the scene and rating the weakest Likert score for the false negatives and robustness to noise criteria.

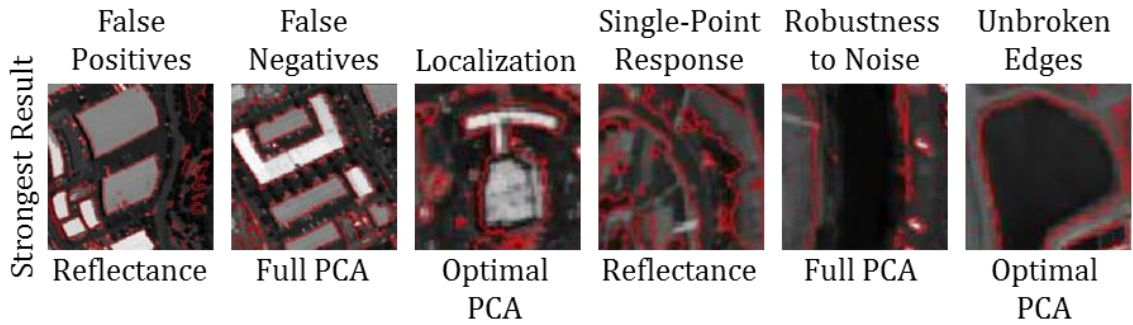


Figure 304: Strongest Level Set Evaluation Results for Reno, NV Overhead VNIR/SWIR Data, Initial Curve at Image Center, Initial Radius 1/8 Longest Dimension, Single-Pixel Stepping, 0.1 Second Time Step, Maximum 20 Iterations

Also of interest are the nearly indistinguishable edge planes and evaluation scores for the reflectance, compressed PCA and full PCA tests – a phenomenon observed consistently across all datasets that clearly supports the null hypothesis that optimizing reflectance data improves edge detection performance for the level set edge operator, thereby rejecting the hypothesis that optimizing reflectance data improves level set edge detection results. A full treatment of this result is provided in the Conclusion section.

Table 113: Level Set Evaluation Measurements for Reno, NV Overhead VNIR/SWIR Data

Level Set Algorithm	False Positives	False Negatives	Localization	Single-Point Response	Robustness to Noise	Unbroken Edges	Normalized Score
Reno							
Reflectance	1	3	1	1	2	1	1.5
Optimal PCA	1	3	1	1	2	1	1.5
Optimal MNF	1	5	1	1	5	1	2.3
Full PCA	1	3	1	1	2	1	1.5
Full MNF	1	5	1	1	5	1	2.3
Roberts	4	3	2	4	3	3	3.2
Sobel	2	3	2	3	2	4	2.7

The level set edge operator performed quite strongly against the false positive criterion, as seen in Figure 304 and Appendix A for all HSI data types. As seen in the edge planes, false alarms were nearly non-existent within both the urban area, on water surfaces and around vegetated areas. Strong localization, single-point response and unbroken edges evaluations combined to produce a clean, highly-accurate edge plane containing solid, narrow edges around key features. The level set edge planes are aesthetically appealing, as well, with single-pixel wide unbroken red edges accurately rendered on a grayscale background.

For the level set tests against the Reno VNIR/SWIR data, none of the data input types yielded better than a Likert score of three for the false negatives criterion – a limitation observed throughout the level set evaluations across data sets. As seen in Appendix A, the algorithm occasionally failed to delineate major buildings, roadways and vegetation features within the reflectance, compressed PCA and full PCA datasets. Large scale, highly disruptive omissions were observed within the compressed MNF and full MNF tests.

A variety of evaluation methods were used to assess the level set edge detection algorithm's performance against the dataset, including interest points, collinearity of edges, single-point intersections and image subtraction. For example, the algorithm successfully delineated edges through 98% of interest points within the reflectance, compressed PCA and full PCA cubes including benchmark edge points and benchmark single-point intersections. Additionally, edge collinearity techniques indicated that the

algorithm accurately localized edges across all five HSI input data sets and produced unbroken edges across all five inputs. Image subtraction confirmed that the reflectance, compressed PCA and full PCA level set edge planes were nearly identical, varying by fewer than ten edge pixels across the full Reno VNIR/SWIR dataset.

Overhead – Cuprite, Nevada USA

As seen in Figure 305 and Table 114 for Cuprite Flight Line #1, the level set edge detection algorithm produced satisfactory results with the reflectance, compressed PCA and full PCA data input types. Results indicate that the dataset is particularly challenging for the false negatives criterion, against the reflectance, compressed PCA and full PCA data input types scored only a Likert measure of three, while the compressed MNF and full MNF cubes yielded weak results.

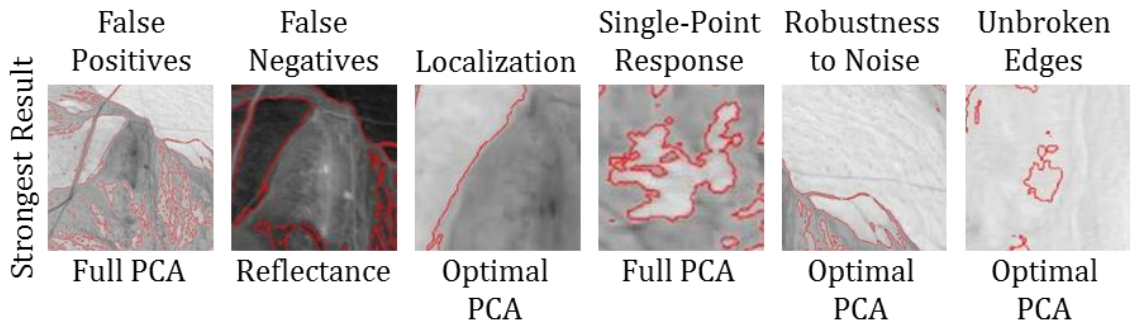


Figure 305: Strongest Level Set Evaluation Results for Cuprite FL #1 Overhead VNIR/SWIR Data, Initial Curve at Image Center, Initial Radius 1/8 Longest Dimension, Single-Pixel Stepping, 0.1 Second Time Step, Maximum 20 Iterations

Table 114: Level Set Evaluation Measurements for Cuprite FL #1 Overhead VNIR/SWIR Data

Level Set Algorithm Cuprite Flight Line #1	False Positives	False Negatives	Localization	Single-Point Response	Robustness to Noise	Unbroken Edges	Normalized Score
Reflectance	1	3	1	1	1	2	1.5
Optimal PCA	1	3	1	1	1	2	1.5
Optimal MNF	2	5	1	1	5	1	2.5
Full PCA	1	3	1	1	1	2	1.5
Full MNF	2	5	1	1	5	1	2.5
Roberts	5	3	2	3	4	2	3.2
Sobel	5	3	2	3	4	2	3.2

All five HSI data input types scored strongly against the false positives criterion, rarely generating false alarms. False negatives were a challenge, with large portions of the improved road to the west being missed. Most data input types produced a reliable, thin edge around the primary kaolinite deposit, however, as seen in Appendix A. Single-point response and localization were strong evaluation criteria, while unbroken edges were typically observed around the scene’s primary features. Similar to the level set results against the Reno dataset, the level set edge operator omitted large swaths of key scene features.

A variety of evaluation methods were used to assess the level set edge detection algorithm’s performance against the Cuprite Flight Line #1 dataset, including interest points, collinearity of edges, single-point intersections and ground truthing. For example, the algorithm successfully delineated unbroken edges through 98% of interest points within the reflectance, compressed PCA and full PCA cubes, particularly along the major improved roads and along the edges of the primary kaolinite feature; a few interest points

were missed around the minor unimproved roads and around heavily mixed mineral deposits as seen in Appendix A. Additionally, edge collinearity techniques indicated that the algorithm accurately localized edges across all five HSI input data sets. Image subtraction methods also confirmed the high correlation among the reflectance, compressed PCA and full PCA cubes.

As seen in Figure 306 and Table 115 for Cuprite Flight Line #2, the level set edge detection algorithm produced satisfactory results across data input types and Canny evaluation criteria. Results indicate that the dataset is most challenging for the false negatives and unbroken edges criteria and that false positives were slightly higher for this Cuprite dataset compared to Cuprite Flight Line #1. Localization results were consistently satisfactory and single-point response evaluations were uniformly strong. Additionally, only the reflectance, compressed PCA and full PCA tests merited a Likert score of three or better across all six Canny evaluation criteria.

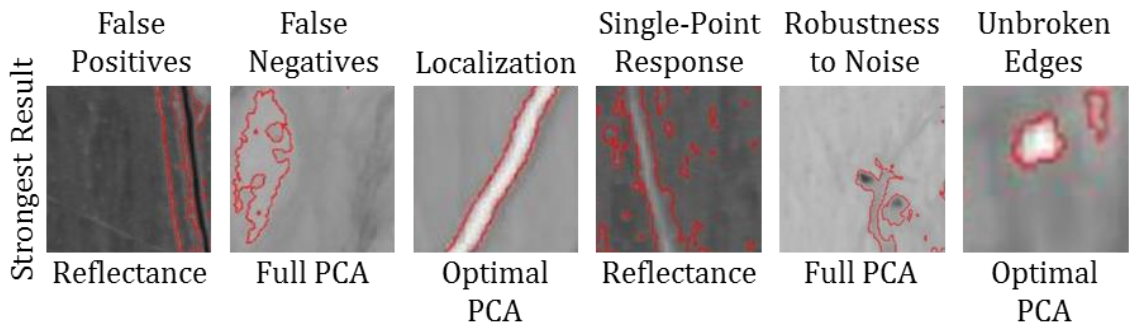


Figure 306: Strongest Level Set Evaluation Results for Cuprite FL #2 Overhead VNIR/SWIR Data

Table 115: Level Set Evaluation Measurements for Cuprite FL #2 Overhead VNIR/SWIR Data

Level Set Algorithm Cuprite Flight Line #2	False Positives	False Negatives	Localization	Single-Point Response	Robustness to Noise	Unbroken Edges	Normalized Score
Reflectance	2	3	2	1	1	3	2.0
Optimal PCA	2	3	2	1	1	3	2.0
Optimal MNF	5	5	3	1	5	5	4.0
Full PCA	2	3	2	1	1	3	2.0
Full MNF	5	5	3	1	5	5	4.0
Roberts	4	2	1	4	3	2	2.7
Sobel	3	2	1	3	4	3	2.7

The localization evaluation scores are slightly depressed compared to other level set results, as seen in the localization example in Figure 306. Note how the level set edge between the improved road and surrounding terrain is slightly off by one to two pixels. Although not a barrier to mineral mapping applications, the inaccuracy is notable for its rarity. Also note that broken edges along the primary improved road and manmade features are more common than desirable.

A variety of evaluation methods were used to assess the level set edge detection algorithm's performance against the Cuprite Flight Line #2 dataset, including interest points, collinearity of edges, single-point intersections and ground truthing. For example, the algorithm successfully delineated unbroken edges through all but a few interest points within the reflectance, compressed PCA and full PCA cubes, the major improved roads and the manmade structures in the center of the image frame; a few interest points were missed around the minor unimproved roads and around heavily mixed mineral deposits as seen in Appendix A. Ground truthing indicated that the algorithm also generated a small volume of false positives within the open deserts to the east and west, although not at a rate disruptive to mineral mapping applications. Additionally, edge collinearity techniques indicated that the algorithm accurately localized edges across all five HSI input data sets.

As seen in Figure 307 and Table 116 for Cuprite Flight Line #3, the level edge detection algorithm produced some of this study's finest results for any algorithm against any dataset. Specifically, the level set edge planes derived from the reflectance, compressed PCA and full PCA data types merited the maximum Likert score for all six Canny criteria, resulting in the optimal normalized score of 1.0 for all three data input types. The compressed MNF and full MNF tests also yielded strong results across all evaluation criteria, and all 30 evaluation measurements for the five HSI input types produced a Likert score of three or better, with fully 26 evaluations ranking a Likert score of two or one.

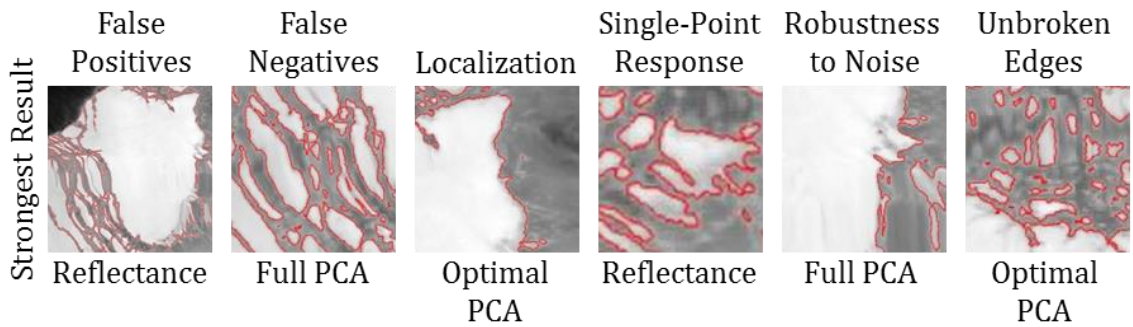


Figure 307: Strongest Level Set Evaluation Results for Cuprite FL #3 Overhead VNIR/SWIR Data

Table 116: Level Set Evaluation Measurements for Cuprite FL #3 Overhead VNIR/SWIR Data

Level Set Algorithm Cuprite Flight Line #3	False Positives	False Negatives	Localization	Single-Point Response	Robustness to Noise	Unbroken Edges	Normalized Score
Reflectance	1	1	1	1	1	1	1.0
Optimal PCA	1	1	1	1	1	1	1.0
Optimal MNF	1	3	2	1	2	3	2.0
Full PCA	1	1	1	1	1	1	1.0
Full MNF	1	3	2	1	2	3	2.0
Roberts	4	2	2	2	3	3	2.7
Sobel	2	1	1	3	2	2	1.8

As seen in Figure 307, the level set edge operator generated thin, unbroken edges around the key features in the scene, most notably the large playa feature dominating the scene. Remarkably, no false alarms were observed for any of the tests. The compressed MNF and full MNF tests omitted a few interest points around the smaller playa features to the west, but delineated a sufficient volume of interest points to support accurate feature mapping.

A variety of evaluation methods were used to assess the HySPADE edge detection algorithm's performance against the Cuprite Flight Line #3 dataset, including interest points, collinearity of edges, single-point intersections and ground truthing. For example, from the reflectance, compressed PCA and full PCA tests, the algorithm accurately mapped all interest points in the scene with unbroken edges according to the interest points, benchmark vertical and benchmark horizontal points. Additionally, edge collinearity techniques indicated that the algorithm accurately localized edges for all datasets and produced edge maps with very few false positives, and in the case of the reflectance, compressed PCA and full PCA tests, no false alarms.

As seen in Figure 308 and Table 117 for Cuprite Flight Line #4, the HySPADE edge detection algorithm produced maximum quality results from the reflectance, compressed PCA and full PCA tests. Like the level set operator's performance against the Cuprite Flight Line #3 dataset, the level set edge planes derived from the reflectance, compressed PCA and full PCA data types merited the maximum Likert score for all six Canny criteria, resulting in the optimal normalized score of 1.0 for all three data input types.

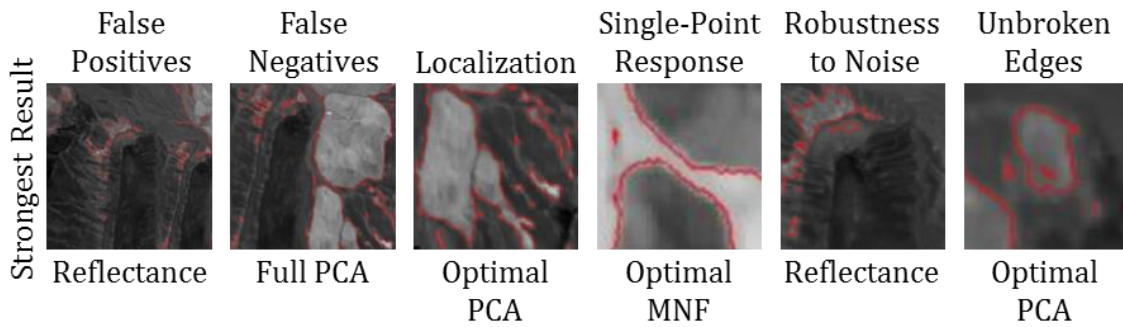


Figure 308: Strongest Level Set Evaluation Results for Cuprite FL #4 Overhead VNIR/SWIR Data

Table 117: Level Set Evaluation Measurements for Cuprite FL #4 Overhead VNIR/SWIR Data

Level Set Algorithm Cuprite Flight Line #4	False Positives	False Negatives	Localization	Single-Point Response	Robustness to Noise	Unbroken Edges	Normalized Score
Reflectance	1	1	1	1	1	1	1.0
Optimal PCA	1	1	1	1	1	1	1.0
Optimal MNF	1	3	1	1	1	1	1.3
Full PCA	1	1	1	1	1	1	1.0
Full MNF	1	3	1	1	1	1	1.3
Roberts	4	3	1	4	3	3	3.0
Sobel	4	3	1	4	3	2	2.8

As seen in Figure 308, the level set edge detection algorithm delineated single-point, unbroken lines through all interest points around the primary kaolinite deposits to the east. Also note in the single-point response example that the algorithm accurately captured the narrow boundary between adjacent piles. In the robustness to noise example in Figure 308 and in Appendix A, note that the level set algorithm accurately delineated the silica outcroppings along the western edges. The level set algorithm's performance against the Cuprite Flight Line #3 dataset is the strongest for any algorithm-dataset

pairing in this dissertation, with 28 of the 30 evaluations measuring at the maximum Likert score of one.

A variety of evaluation methods were used to assess the level set edge detection algorithm's performance against the Cuprite Flight Line #4 dataset, including interest points, collinearity of edges, single-point intersections and ground truthing. For example, the algorithm accurately mapped all interest points in the scene with unbroken edges according to the interest points, benchmark vertical and benchmark horizontal points. Additionally, edge collinearity techniques indicated that the algorithm accurately localized edges for all datasets and produced edge maps with no false positives.

Overhead - Indian Pines, Indiana USA

As seen in Figure 309 and Table 118, the level set edge detection algorithm produced satisfactory results across several data input types and Canny evaluation criteria. Similarly to previous level set operator results, the reflectance, compressed PCA and full PCA tests produced the strongest normalized Canny criteria scores, achieving the strongest Likert score for the false positives, localization and single-point response criteria. All data input types were challenged to score better than an average Likert score for the false negatives and unbroken edges criteria, as seen in Appendix A.

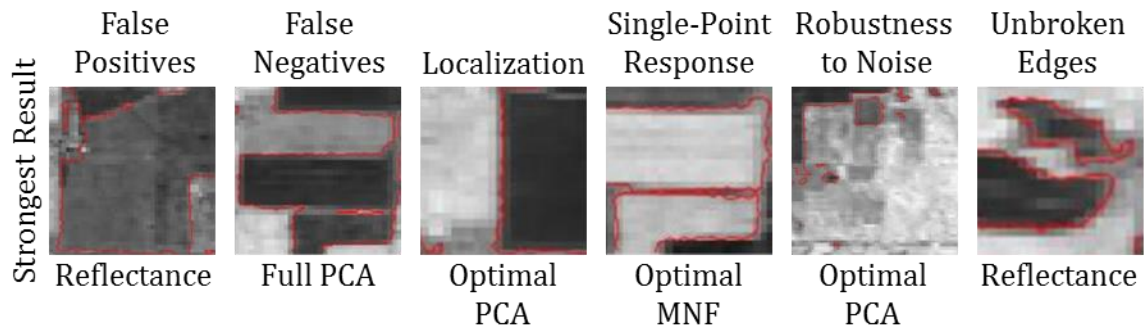


Figure 309: Strongest Level Set Evaluation Results for Indian Pines Overhead VNIR/SWIR Data, Initial Curve at Image Center, Initial Radius 1/8 Longest Dimension, Single-Pixel Stepping, 0.1 Second Time Step, Maximum 20 Iterations

As seen in Table 118, the level set algorithm performed well across all data input types, scoring average or better across all Canny evaluation criteria. The compressed MNF cube produced the weakest results, which were still sufficiently accurate to support vegetation mapping applications. The average (i.e., Likert score of three) false negative performance across all data input types is consistent with the gradient-based and HySPADE tests for this dataset in that the algorithms are challenged to detect discontinuities between adjacent, chemically similar materials such as very young crops.

Table 118: Level Set Evaluation Measurements for Indian Pines Overhead VNIR/SWIR Data

Level Set Algorithm Indian Pines	False Positives	False Negatives	Localization	Single-Point Response	Robustness to Noise	Unbroken Edges	Normalized Score
Reflectance	1	3	1	1	2	3	1.8
Optimal PCA	1	3	1	1	2	3	1.8
Optimal MNF	1	3	2	1	3	3	2.2
Full PCA	1	3	1	1	2	3	1.8
Full MNF	1	3	2	1	3	3	2.2
Roberts	3	3	1	2	3	2	2.3
Sobel	3	3	1	3	2	2	2.3

A variety of evaluation methods were used to assess the level set edge detection algorithm’s performance against the Indian Pines VNIR/SWIR dataset, including interest points, collinearity of edges, single-point intersections and ground truthing. For example, the reflectance, compressed PCA and full PCA cubes missed only 3% of scene interest points and single-point intersections, earning them a Likert score of three for the false negatives criterion. Additionally, edge collinearity techniques indicated that the algorithm accurately localized edges across all five HSI input data sets and produced satisfactorily unbroken edges across all data inputs.

Overhead – Deepwater Horizon Oil Spill

As seen in Figure 310 and Table 119, the level set edge detection algorithm produced high-quality results across several data input types and Canny evaluation criteria. In particular, the radiance, reflectance, compressed PCA and full PCA cubes produced strong results across all six criteria, earning the maximum possible Likert evaluation for all Canny criteria except for false negatives, against which they earned a

strong Likert measurement of two. Indeed, four top-performing Deepwater Horizon level set tests produced some of the most robust edge planes in this dissertation, similarly to the strong performance of the gradient-based algorithm against the Deepwater Horizon dataset.

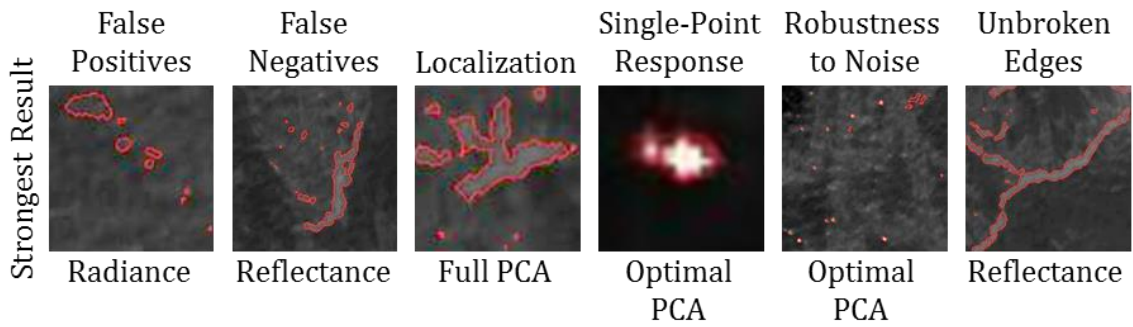


Figure 310: Strongest Level Set Evaluation Results for Deepwater Horizon Overhead VNIR/SWIR Data, Initial Curve at Image Center, Initial Radius 1/8 Longest Dimension, Single-Pixel Stepping, 0.1 Second Time Step, Maximum 20 Iterations

Table 119: Level Set Evaluation Measurements for Deepwater Horizon Overhead VNIR/SWIR Data

Level Set Algorithm Deepwater Horizon	False Positives	False Negatives	Localization	Single-Point Response	Robustness to Noise	Unbroken Edges	Normalized Score
Radiance	1	2	1	1	1	1	1.2
Reflectance	1	2	1	1	1	1	1.2
Optimal PCA	1	2	1	1	1	1	1.2
Optimal MNF	1	5	1	1	4	5	2.8
Full PCA	1	2	1	1	1	1	1.2
Full MNF	1	5	1	1	4	5	2.8
Roberts	5	3	1	3	5	2	3.2
Sobel	5	2	1	3	4	1	2.7

The radiance, reflectance, compressed PCA and full PCA cubes measured strongly against all six Canny evaluation criteria, in each case generating a highly accurate edge plane of oil spill fronts on the ocean surface. As seen in Appendix A and Figure 310, the four tests also accurately delineated several surface ships along the western edge of the image and successfully avoided falsely alarming against the choppy seas throughout the scene. The compressed MNF and full MNF cubes measured weakly against the false negatives Canny criterion, which is seen in the suboptimal volume of missed oil-water edges in Appendix A's edge planes. The MNF cubes' underperformances are likely attributable to an under-sampling of MNF bands according to this study's experimental controls. Additionally, the strong evaluation measurements from the radiance cube test suggest that the level set edge operator, like the gradient-based operator, can robustly delineate unique targets on a uniform background without the benefit of reflectance data.

Note that the slightly elevated false negative evaluation scores are attributable to the algorithm missing edge pixels heavily mixed with oil and water – a challenging target. From the perspective of oil spill mapping applications, these minor false negatives do not present a barrier to using the level set edge operator to guide the rapid deployment of cleanup equipment since the false negatives are confined to the trailing portions of the oil slicks.

A variety of evaluation methods were used to assess the level set detection algorithm's performance against the Deepwater Horizon VNIR/SWIR dataset, including interest points, collinearity of edges and single-point intersections. For example,

radiance, reflectance, compressed PCA and full PCA cubes correctly delineated edges through 100% of interest points and single-point intersections, earning them the strongest Likert score for the false negatives criterion. As seen in Figure 310, the algorithm generated clean, unbroken edges along the major oil slicks within the scene – a meaningful finding with respect to oil spill mapping applications. Additionally, edge collinearity techniques indicated that the algorithm accurately localized edges across all five HSI input data sets.

Ground-Based – Larkhaven

As seen in Figure 311 and Table 120, the level set edge detection algorithm, like the HySPADE algorithm, was unable to produce satisfactory results for any HSI data type for the Larkhaven VNIR data. The algorithm struggled notably with false negatives and unbroken edges, resulting in the many missing and broken edges as seen in Appendix A. The suboptimal edge results were observed throughout the scene rather than within isolated portions. False positives, localization and single-point response performance were areas of strength for the level set algorithm, which appears to be the case even for the data sets of greatest challenge.

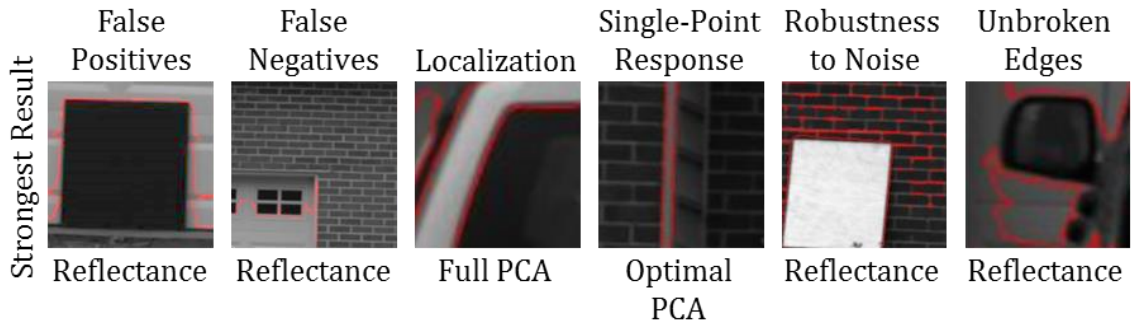


Figure 311: Strongest Level Set Evaluation Results for Larkhaven Ground-Based VNIR Data, Initial Curve at Image Center, Initial Radius 1/8 Longest Dimension, Single-Pixel Stepping, 0.1 Second Time Step, Maximum 20 Iterations

Table 120: Level Set Evaluation Measurements for Larkhaven Ground-Based VNIR Data

Level Set Algorithm	False Positives	False Negatives	Localization	Single-Point Response	Robustness to Noise	Unbroken Edges	Normalized Score
Larkhaven Reflectance	1	5	1	1	3	4	2.5
Larkhaven Optimal PCA	1	5	1	1	3	4	2.5
Larkhaven Optimal MNF	1	5	1	1	4	5	2.8
Larkhaven Full PCA	1	5	1	1	3	4	2.5
Larkhaven Full MNF	1	5	1	1	4	5	2.8
Roberts	3	1	1	2	3	1	1.8
Sobel	3	1	1	3	3	1	2.0

Consider the false negatives in the HySPADE Larkhaven edge planes. The most obvious false negatives occur between the brick and mortar on the building’s façade. The most likely explanation is the subtle spectral contrast between the brick and mortar, which the level set edge operator was evidently unable to discriminate. Additionally, the edges along the vehicle’s rearview mirror appear suboptimal. Overall, the Larkhaven dataset

presented a significant challenge to the level set algorithm, most likely due to an inability to overcome subtle spectral contrast.

A variety of evaluation methods were used to assess the level set edge detection algorithm's performance against the Larkhaven VNIR dataset, including interest points, collinearity of edges, single-point intersections and ground truthing. For example, all five input types missed more than 10% of the scene's interest points, resulting in suboptimal false negative scores. As seen in Figure 311 and Appendix A, the algorithm produced broken edges along the rearview mirror, the window panes on the garage door and along the boundary between vegetation and manmade material. The vast majority of mortar to brick edges also were missed. Consistent with previous level set algorithm results, edge collinearity techniques indicated that the algorithm accurately localized edges across all five HSI input data sets.

Ground-Based – Granite VNIR

As seen in Figure 312 and Table 121, the level set edge detection algorithm was challenged to produce satisfactory Canny evaluation measurements for any of the five HSI data input types. In particular, the algorithm struggled against the false negatives and unbroken edges criteria, missing several key interest points and partially encircling many features within the scene. Localization and single-point response were areas of strength for the algorithm. Notably, the compressed MNF and full MNF tests outperformed the others, scoring average or better against all evaluation criteria except false negatives.

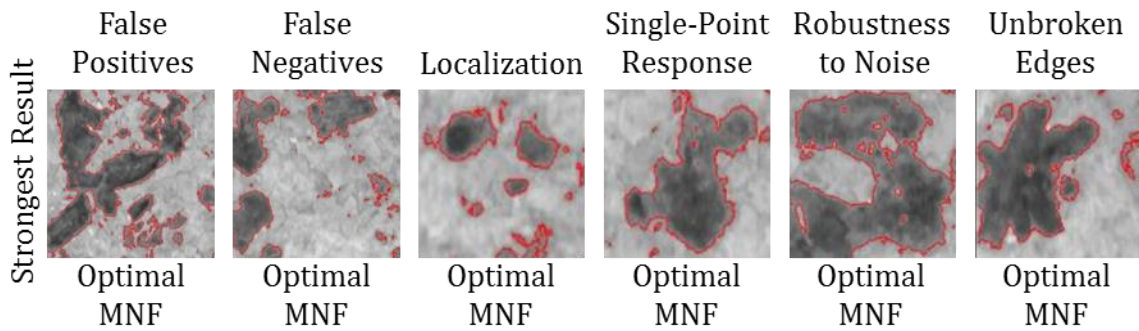


Figure 312: Strongest Level Set Evaluation Results for Granite Ground-Based VNIR Data, Initial Curve at Image Center, Initial Radius 1/8 Longest Dimension, Single-Pixel Stepping, 0.1 Second Time Step, Maximum 20 Iterations

Figure 312 and Appendix A demonstrate the scale of the false negative underperformance, as evidenced by the large swaths of missed features between delineated features. The compressed MNF test nearly measured a satisfactory Likert score of three against the false negatives criterion, but it missed a few too many interest points to justify a three rating. False positives were more stressing for the level set algorithm against this data set than for most others, as well.

Table 121: Level Set Evaluation Measurements for Granite Ground-Based VNIR Data

Level Set Algorithm Granite VNIR	False Positives	False Negatives	Localization	Single-Point Response	Robustness to Noise	Unbroken Edges	Normalized Score
Reflectance	3	5	1	1	4	5	3.2
Optimal PCA	3	5	1	1	4	5	3.2
Optimal MNF	1	4	1	1	2	2	1.8
Full PCA	3	5	1	1	4	5	3.2
Full MNF	1	4	1	1	2	2	1.8
Roberts	3	4	1	2	4	3	2.8
Sobel	2	2	1	3	3	2	2.2

A variety of evaluation methods were used to assess the level set edge detection algorithm's performance against the Granite NIR/SWIR dataset, including interest points, collinearity of edges and single-point intersections. For example, the tests against the compressed MNF data type correctly delineated single-point edges through 92% of interest points and single-point intersections, earning the Likert score of four for the false negatives criterion. As seen in Figure 312, the compressed MNF tests generated accurate, unbroken edges around the major minerals within the rock when the algorithm detected them – a meaningful finding with respect to mineral mapping applications. Additionally, edge collinearity techniques indicated that the algorithm accurately localized edges across all data types.

Ground-Based – Granite NIR/SWIR

As seen in Figure 313 and Table 122, the level set edge detection algorithm was challenged to produce satisfactory results for any data input. All data types performed strongly against the false positives, localization and single-point response criteria, but none was able to measure stronger than a suboptimal Likert score of four for the false negatives – clearly the most challenging criterion for both the HySPADE and level set edge detection algorithms.

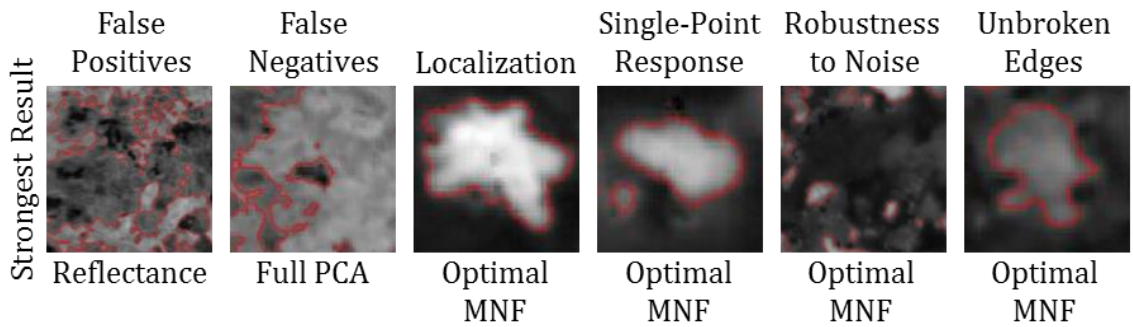


Figure 313: Strongest Level Set Evaluation Results for Granite Ground-Based NIR/SWIR Data, Initial Curve at Image Center, Initial Radius 1/8 Longest Dimension, Single-Pixel Stepping, 0.1 Second Time Step, Maximum 20 Iterations

Table 122: Level Set Evaluation Measurements for Granite Ground-Based NIR/SWIR Data

Level Set Algorithm Granite NIR/SWIR	False Positives	False Negatives	Localization	Single-Point Response	Robustness to Noise	Unbroken Edges	Normalized Score
Reflectance	1	4	1	1	4	3	2.3
Optimal PCA	1	4	1	1	4	3	2.3
Optimal MNF	1	4	1	1	3	2	2.0
Full PCA	1	4	1	1	4	3	2.3
Full MNF	1	4	1	1	3	2	2.0
Roberts	5	5	1	2	4	5	3.7
Sobel	4	4	1	3	3	4	3.2

Similarly to level set tests against the Granite VNIR data, the algorithm missed a significant volume (~9%) of interest points, yielding poor false negative performance. Broken edges were occasionally disruptive but overall scored average or better. The compressed MNF and full MNF tests provided the best overall results, generating suboptimal evaluations only against the false negatives criterion. Overall, the two granite datasets presented a significant challenge to the level set edge detection algorithm.

A variety of evaluation methods were used to assess the level set edge detection algorithm's performance against the Granite NIR/SWIR dataset, including interest points, collinearity of edges and single-point intersections. For example, the tests against the compressed MNF data type correctly delineated single-point edges through 91% of interest points and single-point intersections, earning a suboptimal Likert score for the false negatives criterion. As seen in Figure 313 and Appendix A, the algorithm generated accurate, unbroken edges around the major minerals within the rock when they are detected – a meaningful finding with respect to mineral mapping applications. Additionally, edge collinearity techniques indicated that the algorithm accurately localized edges across data input types.

Ground-Based – South African Core Samples

As seen in Figure 314 and Table 123, the level set edge detection algorithm was challenged to produce satisfactory results for the false negatives and unbroken edges criteria for all input data types. Performance was quite strong for the false positives, localization and single-point response criteria, but the suboptimal false negatives and unbroken edges evaluations precluded the generation of reliable edge planes. Additionally, all five data input types measured identically against the Canny evaluation criteria.

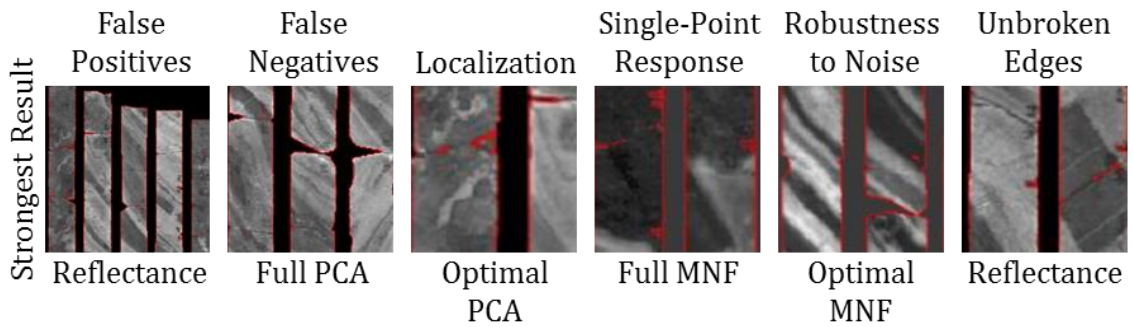


Figure 314: Strongest Level Set Evaluation Results for Core Sample Ground-Based NIR/SWIR Data, Initial Curve at Image Center, Initial Radius 1/8 Longest Dimension, Single-Pixel Stepping, 0.1 Second Time Step, Maximum 20 Iterations

Table 123: Level Set Evaluation Measurements for Core Sample Ground-Based NIR/SWIR Data

Level Set Algorithm South African Core Samples	False Positives	False Negatives	Localization	Single-Point Response	Robustness to Noise	Unbroken Edges	Normalized Score
Reflectance	1	5	1	1	3	5	2.7
Optimal PCA	1	5	1	1	3	5	2.7
Optimal MNF	1	5	1	1	3	5	2.7
Full PCA	1	5	1	1	3	5	2.7
Full MNF	1	5	1	1	3	5	2.7
Roberts	3	4	1	2	2	4	2.7
Sobel	2	4	1	3	2	3	2.5

The false negative poor performance is likely attributable to the level set algorithm's inability to discriminate between subtly different and highly mixed minerals. While the HySPADE algorithm demonstrated a sensitivity to intensity, the level set algorithm appears to be demonstrating occasional insensitivity to spectral contrast.

A variety of evaluation methods were used to assess the level set edge detection algorithm's performance against the South Africa Core Sample dataset, including interest

points, collinearity of edges and single-point intersections. For example, the level set tests against the five HSI data types delineated thin collinear edges throughout the scene, earning a strong Likert score for the single-point response criterion. As seen in Figure 314 and Appendix A, the algorithm generated few false alarms across the scene, as well.

Ground-Based – Aluminum Panel

As seen in Figure 315 and Table 124 the Level Set edge detection algorithm was challenged to produce satisfactory results across all data input types and multiple Canny evaluation criteria. All data input types produced edge planes that were evaluation at the weakest evaluation Likert score for false negatives, robustness to noise and unbroken edges – a combination making for unsatisfactory edge planes. As seen in Appendix A, the false negatives performance was particularly weak, with the algorithm circumscribing a large unbroken edge around the boundary between lightly illuminated and darkly illuminated aluminum – a clear indication that the algorithm is sensitive to intensity under certain conditions, as also observed in the level set Granite VNIR and Granite NIR/SWIR results.

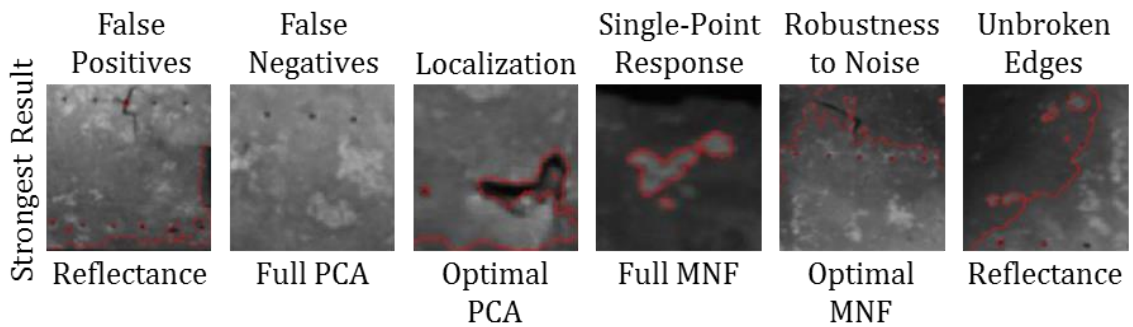


Figure 315: Strongest Level Set Evaluation Results for Aluminum Panel Ground-Based VNIR Data, Initial Curve at Image Center, Initial Radius 1/8 Longest Dimension, Single-Pixel Stepping, 0.1 Second Time Step, Maximum 20 Iterations

Table 124: Level Set Evaluation Measurements for Aluminum Panel Ground-Based VNIR Data

Level Set Algorithm Aluminum Panel	False Positives	False Negatives	Localization	Single-Point Response	Robustness to Noise	Unbroken Edges	Normalized Score
Reflectance	1	5	1	1	4	5	2.8
Optimal PCA	1	5	1	1	4	5	2.8
Optimal MNF	1	5	1	1	4	5	2.8
Full PCA	1	5	1	1	4	5	2.8
Full MNF	1	5	1	1	4	5	2.8
Roberts	5	3	1	2	4	5	3.3
Sobel	5	3	1	2	4	5	3.3

At only a few positions on the aluminum panel did the level set algorithm delineate distinct rust features, but false alarms were quite rare, as well. Edges were thin but frequently broken and incomplete. A variety of evaluation methods were used to assess the level set edge detection algorithm’s performance against the Aluminum Panel dataset, including interest points, collinearity of edges and single-point intersections. For example, the tests against the compressed PCA data type correctly delineated edges through none of the interest points and single-point intersections, earning the weakest available Likert score for the false negatives criterion. As seen in Figure 315, the algorithm generated accurate, unbroken edges around the cuts in the panel and around some of the rivet, but most features were missed. Additionally, edge collinearity

techniques indicated that the algorithm accurately localized edges across all five HSI input data sets.

Microscene – Rare Target on Sand

As seen in Figure 316 and Table 125, the level set edge detection algorithm was challenged to produce satisfactory results for the Rare Target on Sand VNIR data. In particular, false negatives and unbroken edges measured poorly, although false positives, localization and single-point response were criteria of strength for the algorithm. For most tests, the algorithm successfully delineated the grass blades in the scene but missed portions of the neodymium oxide.

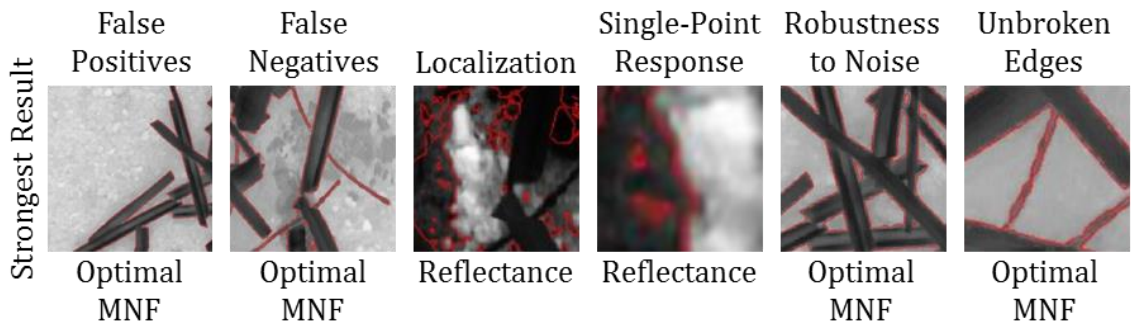


Figure 316: Strongest Level Set Evaluation Results for Rare Target on Sand Microscene VNIR Data, Initial Curve at Image Center, Initial Radius 1/8 Longest Dimension, Single-Pixel Stepping, 0.1 Second Time Step, Maximum 20 Iterations

Table 125: Level Set Evaluation Measurements for Rare Target on Sand Microscene VNIR Data

Level Set Algorithm Rare Target on Sand	False Positives	False Negatives	Localization	Single-Point Response	Robustness to Noise	Unbroken Edges	Normalized Score
Reflectance	2	5	1	1	3	4	2.7
Optimal PCA	2	4	1	1	3	4	2.5
Optimal MNF	2	4	1	1	3	1	2.0
Full PCA	2	4	1	1	3	4	2.5
Full MNF	1	4	1	1	2	1	1.7
Roberts	3	4	1	2	4	5	3.2
Sobel	2	4	1	3	3	3	2.7

Interestingly, the level set algorithm fully and accurately delineated the grass blades for the compressed MNF and compressed PCA tests but missed nearly all of the interest points for the rare target. Given that the reflectance test captured most of the rare target, the likely explanation is that the compressed PCA and compressed MNF cubes were under-sampled with too few bands according to the experimental controls established in the methodology. Note that when the level set algorithm generated edges, they were thin and accurate.

A variety of evaluation methods were used to assess the level set edge detection algorithm's performance against the Rare Target on Sand dataset, including interest points, collinearity of edges, single-point intersections and ground truthing. For example, the tests against the compressed PCA data type missed all but two of the interest points around the rare target and single-point intersections, earning a weak Likert score for the false negatives criterion. As seen in Figure 316, the algorithm generated accurate, mostly unbroken edges around the grass blades and overlapping cloth threads – a meaningful

finding that suggests that band compression would improve the edge detection results. Additionally, edge collinearity techniques indicated that the algorithm accurately localized edges across all five HSI input data sets.

Microscene – Chemical Array

As seen in Figure 317 and Table 126, the level set edge detection algorithm produced satisfactory results across several data input types and Canny evaluation criteria. The reflectance, compressed PCA and full PCA input types evaluated quite strongly across all five Canny criteria, scoring most strongly against the false positives, localization and single-point response criteria. Performance against the unbroken edges and false negatives was also satisfactory for the three cubes. The compressed MNF and full MNF cubes performed well against all criteria except false negatives, against which they were evaluated at a weak Likert score of five.

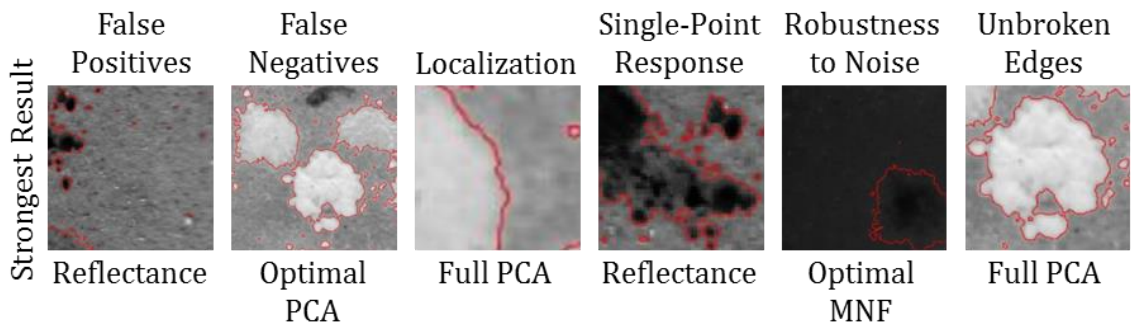


Figure 317: Strongest Level Set Evaluation Results for Chemical Array Microscene NIR/SWIR Data, Initial Curve at Image Center, Initial Radius 1/8 Longest Dimension, Single-Pixel Stepping, 0.1 Second Time Step, Maximum 20 Iterations

Table 126: Level Set Evaluation Measurements for Chemical Array Microscene NIR/SWIR Data

Level Set Algorithm Chemical Array on Sand	False Positives	False Negatives	Localization	Single-Point Response	Robustness to Noise	Unbroken Edges	Normalized Score
Reflectance	1	2	1	1	2	2	1.5
Optimal PCA	1	2	1	1	2	2	1.5
Optimal MNF	1	5	1	1	1	1	1.7
Full PCA	1	2	1	1	2	2	1.5
Full MNF	1	5	1	1	1	1	1.7
Roberts	2	4	2	2	5	4	3.2
Sobel	4	3	1	3	4	3	3.0

The localization performance was particularly strong for this dataset, as seen in the localization example in Figure 317, which demonstrates how the level set algorithm stitched a clean, single-point line along the edge of the ammonium nitrate pile. The algorithm also delineated several single-pixel deposits of stray chemicals, accurately circumscribing unbroken edges around the small targets. Note that the compressed MNF and full MNF cubes earned the strongest evaluation score for five of the six Canny criteria. Only against the false negatives did the compressed MNF and full MNF cubes produce poor results, most likely attributable to over-thresholding of MNF bands within the compressed MNF cube and under-sampling of bands within the full MNF bands.

A variety of evaluation methods were used to assess the level set edge detection algorithm's performance against the Chemical Array dataset, including interest points, collinearity of edges, single-point intersections and ground truthing. For example, the level set tests against the reflectance, compressed PCA and full PCA data type correctly delineated edges through 98% of interest points and single-point intersections, earning

strong Likert scores for the false negatives criterion. As seen in Appendix A and Figure 317, the algorithm generated accurate and mostly unbroken edges around the ammonium nitrate sample (shown in the unbroken edges example in Figure 317), meaning that it accurately delineated all interest points for the key feature. Additionally, edge collinearity techniques indicated that the algorithm accurately localized edges across all five HSI input data sets.

Microscene – Cloth Threads

As seen in Figure 318 and Table 127, the level set edge detection algorithm was challenged to produce satisfactory results across all data input types for the false negatives and against most input types for the unbroken edges criteria. Although performing quite weakly against the false negatives criterion, the algorithm produced maximum quality results for the false positives, localization, single-point response, and robustness to noise criteria.

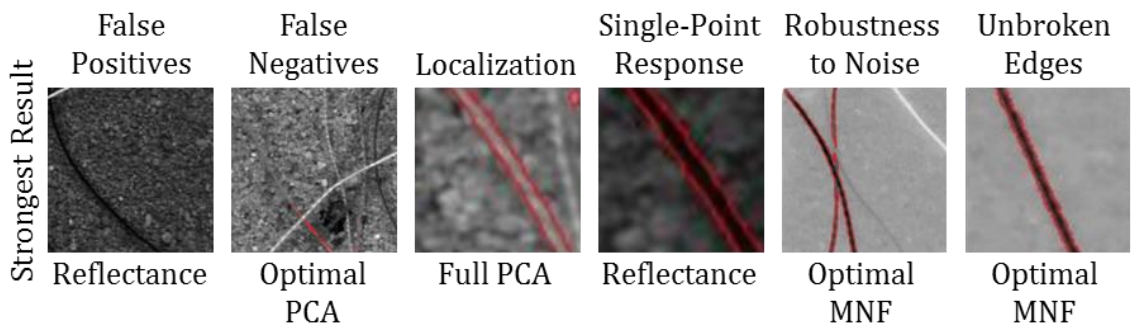


Figure 318: Strongest Level Set Evaluation Results for Cloth Threads Microscene VNIR Data, Initial Curve at Image Center, Initial Radius 1/8 Longest Dimension, Single-Pixel Stepping, 0.1 Second Time Step, Maximum 20 Iterations

Table 127: Level Set Evaluation Measurements for Cloth Threads Microscene VNIR Data

Level Set Algorithm Cloth Threads on Sand	False Positives	False Negatives	Localization	Single-Point Response	Robustness to Noise	Unbroken Edges	Normalized Score
Reflectance	1	5	1	1	1	5	2.3
Optimal PCA	1	5	1	1	1	2	1.8
Optimal MNF	1	5	1	1	1	2	1.8
Full PCA	1	5	1	1	1	5	2.3
Full MNF	1	5	1	1	1	5	2.3
Roberts	2	4	1	2	3	5	2.8
Sobel	2	3	1	3	3	3	2.5

The compressed MNF and compressed PCA tests were the only experiments to produce satisfactory results for the unbroken edges criteria. A variety of evaluation methods were used to assess the level set edge detection algorithm’s performance against the Cloth Threads on Sand dataset, including interest points, collinearity of edges, single-point intersections and ground truthing. For example, the all tests missed at least 20% of interest points and single-point intersections, earning them the weakest Likert score for the false negatives criterion. As seen in Figure 318 and Appendix A for the compressed MNF and compressed PCA tests, the algorithm generated several clean, unbroken edges along scene’s overlapping cloth threads and accurately the edges precisely along the boundary between cloth and sand. Additionally, edge collinearity techniques indicated that the algorithm accurately localized edges across all five HSI input data sets.

CONCLUSIONS AND FURTHER RESEARCH

The Conclusion component examines the experimental results, analysis and evaluations from a variety of perspectives in order to determine the extent to which this work provides support for its hypotheses. Specifically, the Conclusion component addresses each algorithm within the context of the Canny evaluation criteria, HSI data input type, spatial resolution, spectral resolution, HSI applications and hypotheses.

Algorithm Conclusions

Table 128 presents the primary evaluation matrix for the three algorithms within the context of input HSI data type and Canny criteria. Note that for all evaluation matrices in the Conclusion component, the Canny criteria establish the x-axis fields in order to retain emphasis on empirical evaluation methods and to maximize the feasibility of comparisons among the matrices.

As seen in Table 128, the three algorithms have distinct areas of strength and weakness that vary according to data input type – an expected outcome given the markedly different approaches the algorithms take to edge detection. First, observe within the thickly boarded lines that each algorithm produced, on average, satisfactory results across all data types as evidenced by normalized score for each algorithm. Recall that a Likert score of three roughly corresponds to average performance, less than three

indicates varying degrees of strong performance and more than three suggests weak to unusable edge detection performance.

Table 128: Disaggregated Evaluation Matrix for All Algorithms and HSI Data Input Types

Green = Strong Yellow = Average Red = Weak	False Positives	False Negatives	Localization	Single-Point Response	Robustness to Noise	Unbroken Edges	Normalized Score
Gradient	2.7	2.4	1.1	2.4	2.7	1.9	2.2
Reflectance	3.6	2.1	1.2	3.2	3.3	2.1	2.6
Optimal PCA	2.1	2.5	1.0	2.1	1.9	1.9	1.9
Optimal MNF	1.9	1.9	1.1	1.9	1.8	1.5	1.7
Full PCA	2.4	2.5	1.0	2.2	2.3	1.9	2.1
Full MNF	3.5	2.9	1.2	2.5	4.1	2.3	2.7
HySPADE	3.3	2.9	1.1	2.4	3.0	2.9	2.6
Reflectance	3.5	2.8	1.2	2.2	3.1	2.9	2.6
Optimal PCA	3.0	2.7	1.1	2.3	2.7	2.7	2.4
Optimal MNF	2.9	2.8	1.1	2.4	2.6	2.8	2.4
Full PCA	3.4	2.9	1.2	2.4	3.1	3.0	2.7
Full MNF	3.7	3.1	1.1	2.8	3.7	3.3	2.9
Level Set	1.5	4.4	1.3	1.2	2.9	3.4	2.5
Reflectance	1.7	4.7	1.5	1.4	3.0	4.1	2.7
Optimal PCA	1.6	4.3	1.3	1.3	2.8	3.5	2.4
Optimal MNF	1.6	5.1	1.5	1.2	3.5	3.2	2.7
Full PCA	1.4	3.6	1.1	1.1	2.4	3.2	2.1
Full MNF	1.3	4.4	1.3	1.0	3.0	3.0	2.3
Criteria Average	2.5	3.2	1.2	2.0	2.9	2.8	2.4

For example, the gradient-based edge operator performed strongly for all Canny evaluation criteria when the results of all five data input types are averaged. False negatives, unbroken edges and single-point response were particular areas of strength for the algorithm. Localization was also an area of strong performance, as it was for all three algorithms. Importantly, the gradient algorithm generated its strongest results when

operating against the compressed PCA and compressed MNF cubes – a finding that provides support to the hypothesis that compressed HSI datasets will improve edge detection results. Further support for this hypothesis is provided by the notably weaker edge detection results generated by the reflectance data, which was challenged to produce edge planes with satisfactory levels of false alarms and single-point edge responses. Figure 319 provides a Reno edge plane example demonstrating how the compressed MNF cube improved the gradient-based edge detection results, particularly with regard to single-point response and false positives. Overall, the gradient-based algorithm generated satisfactory results according to the Canny evaluation criteria.

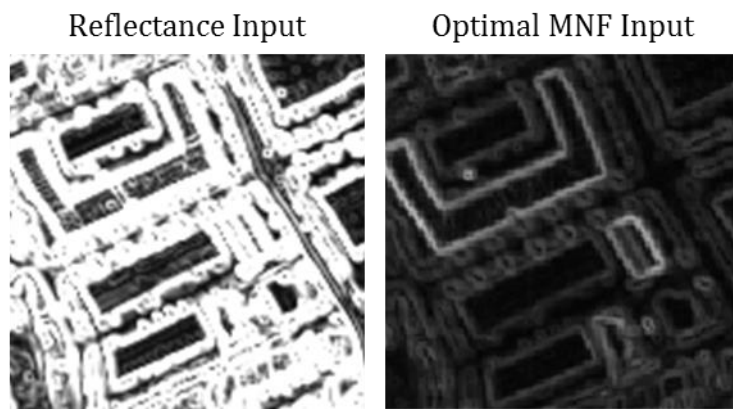


Figure 319: Optimal MNF HSI Data Improving Gradient Edge Detection Performance

As also seen in Table 128, the HySPADE algorithm generated satisfactory results in the aggregate, although it was challenged by false positives for several datasets. Indeed, only the compressed PCA and compressed MNF tests generated satisfactory results across all six evaluation criteria. Single-point response was a consistent source of

strength for HySPADE, which generally produced thin edges around key features. As extensively discussed in the Analysis and Evaluation component, the most likely explanation for modest HySPADE false positives evaluation is that the integrated spectral similarity score places equal weight on Euclidean distance and spectral angle mapper measurements, which obviates much of SAM's chief advantage, insensitivity to intensity. Further research should consider adding a weighting component to the SSS algorithm in manner that overweights SAM and underweights ED. Finally, the outperformance of HySPADE edge planes derived from compressed PCA and compressed MNF cubes corroborates the gradient-based findings providing support to the hypothesis regarding improved edge results derived from compressed HSI data inputs. Figure 320 provides an example of how the compressed MNF data significantly improved HySPADE results compared to the reflectance data, particularly with respect to false positives. Overall, the HySPADE algorithm generated satisfactory results according to the Canny evaluation criteria.

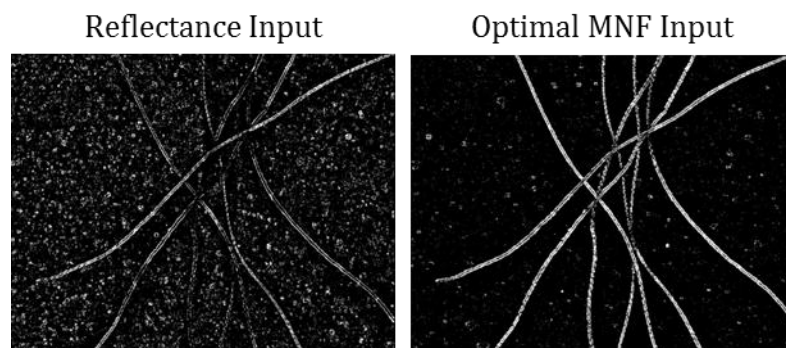


Figure 320: Optimal MNF HSI Data Improving HySPADE Edge Detection Performance

Finally, as seen in Table 128, the level set-based edge detection algorithm generated overall satisfactory results, but was significantly challenged to measure adequately against the false negatives criteria. Areas of strength include false positives, localization and single-point response. Indeed, the level set algorithm demonstrated significantly strong false positives and single-point response performance and produced several of the highest quality edge planes in this study. Interestingly, the level set edge planes tended to produce either high-quality or low-quality edge planes – middle of the road results tended to be the exception, suggesting that the algorithm is sensitive to the specific materials in the scene. Additionally, the algorithm’s false negative challenges are likely attributable to its use of Euclidean distance measurements to calculate energy differences, which would explain why its false negatives frequently align to areas of similar intensity across most channels.

For example, consider Figure 321, which presents an example of poor level set false negative performance against the Indian Pines dataset. Note that the algorithm delineated unbroken, single-point edges mostly along boundaries characterized by large intensity (and in many cases, spectral) differences while missing the boundaries among different crop types that reflect at similar intensities (i.e., equally dark or light). When placed within context of the algorithm’s strong performance on other datasets with more spectral and intensity contrasts, the most likely explanation is clearly Euclidean distance’s sensitivity to intensity.

Indian Pines, Optimal PCA input

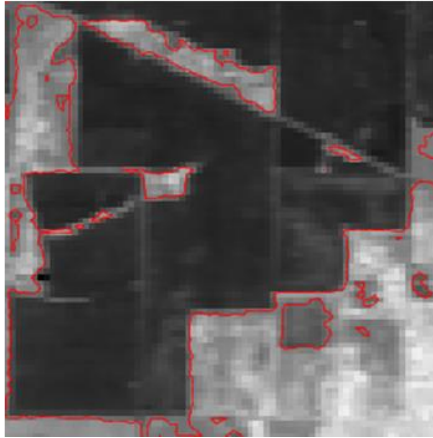


Figure 321: Level Set Edge Detection Algorithm's False Negative Example

Also note that the level set edge operator diverged from the gradient and HySPADE findings in the sense that the compressed PCA and full PCA inputs generated the strongest results, while the compressed MNF tests lagged. Reflectance results were similarly bested by the compressed PCA tests. Overall, the level set compressed PCA and full PCA tests produced satisfactory results and provided an improvement over the reflectance tests, providing additional support to the data compression hypothesis. The most likely reason that the compressed MNF cube underperformed the other datasets, particularly for false negatives, is that the MNF denoising component exacerbated the algorithm's struggle to discriminate between materials of similar brightness and subtle spectral contrast. Even with its false negatives challenge, the level set algorithm produced some of the strongest edge planes in this dissertation, particularly with respect to false positives, which was one of the most challenging criteria for the gradient and HySPADE algorithms.

Table 129: Aggregated Evaluation Matrix for All Algorithms and HSI Data Input Types

Green = Strong Yellow = Average Red = Weak	False Positives	False Negatives	Localization	Single-Point Response	Robustness to Noise	Unbroken Edges	Normalized Score
Reflectance	2.8	2.8	1.2	2.1	2.8	2.6	2.4
Optimal PCA	2.1	2.9	1.0	1.8	2.3	2.5	2.1
Optimal MNF	2.0	3.0	1.1	1.8	2.5	2.4	2.1
Full PCA	2.4	2.9	1.1	1.9	2.6	2.6	2.2
Full MNF	2.8	3.5	1.2	2.1	3.6	2.9	2.7
Criteria Average	2.4	3.0	1.1	1.9	2.8	2.6	2.3

Table 129 presents aggregated algorithm results compared against the Canny evaluation criteria. The intent of Table 129 is to determine to what extent compressed HSI data improves edge detection results. As seen, compressed PCA and compressed MNF input types outperformed reflectance data in every evaluation category, particularly for false positives and single-point response. The superior single-point response of the compressed cubes supports the hypothesis that PCA and MNF cubes can improve upon the results achievable from HSI reflectance data. The full PCA cube also modestly outperformed the reflectance data across most categories, albeit to a lesser degree than its compressed cousin. Only the full MNF cube’s weak false negatives and robustness to noise evaluations breached the average Likert score of three, almost entirely due to the level set algorithm’s weak false negative performance against five of the 15 datasets. Ultimately, Table 129 supports the hypothesis that compressed HSI data improves edge detection results.

Table 130: Aggregated Evaluation Matrix for All Algorithms and HSI Datasets

Green = Strong Yellow = Average Red = Weak	False Positives	False Negatives	Localization	Single-Point Response	Robustness to Noise	Unbroken Edges	Normalized Score
	Reno	1.8	2.7	1.0	2.0	2.6	1.5
Cuprite FL#1	2.8	3.1	1.0	2.2	2.8	2.3	2.4
Cuprite FL#2	2.9	2.9	1.5	2.0	2.9	2.8	2.5
Cuprite FL#3	2.5	2.3	1.2	2.0	2.7	2.7	2.2
Cuprite FL#4	2.1	2.3	1.0	1.4	2.1	1.9	1.8
Indian Pines	2.7	3.6	1.9	2.1	3.3	3.3	2.8
Deepwater Horizon	2.0	2.9	1.0	1.9	2.6	2.1	2.1
Larkhaven	2.0	3.7	1.0	1.9	3.2	3.3	2.5
Granite VNIR	2.5	3.3	1.1	1.5	2.9	3.3	2.4
Granite NIR/SWIR	2.7	3.3	1.1	2.1	3.2	2.4	2.5
South Africa Cores	2.5	3.3	1.0	1.7	2.7	3.0	2.4
Aluminum Panel	2.8	3.5	1.0	2.2	3.5	3.3	2.7
Rare Target	2.4	2.9	1.0	1.8	2.3	2.0	2.1
Chemical Array	2.8	2.8	1.1	2.4	2.7	2.3	2.3
Cloth Threads	2.0	2.8	1.0	1.9	1.9	2.8	2.1
Criteria Average	2.4	3.0	1.1	1.9	2.8	2.6	2.3

Table 130 presents the aggregated evaluation of each test dataset compared to the Canny evaluation criteria. Table 130 is intended to provide a sense of how challenging each dataset is with respect to the evaluation criteria. For example, the Indian Pines and Aluminum panel datasets are clearly the most challenging among the 15, particularly with regard to false negatives and unbroken edges. The commonalities among the datasets suggest scene characteristics most challenging to the three algorithms. Specifically, the Indian Pines and Aluminum Panel data are characterized by adjacent features with low spectral contrast – an expected challenge area for any edge detection algorithm. The young crop pixels in the Indian Pines dataset vary subtly from field to field and contain a substantial degree of soil spectra common to each pixel. Similarly, the Aluminum Panel data is dominated by rust features adjacent to unblemished

aluminum features, which appear quite similar in spectral space. This finding is important in the sense that it provides a sense of the algorithms' maximum effective range (i.e., very challenging, low spectral contrast scenes) and demonstrates that the algorithms' weak performance against the challenging datasets is largely attributable to the nature of the data itself rather than an inherent weakness in the algorithms.

Table 130's evidence of strong performance against specific datasets also indicates that the algorithms are performing consistently with other edge detection algorithms in the scientific literature. Namely, the algorithms perform strongly against high contrast scenes and less strongly against low contrast scenes. For example, the algorithms measured quite strongly against the Reno, Deepwater Horizon, Cuprite Flight Line #4, Rare Target and Cloth Threads datasets. The Cuprite Flight Line #4 and Deepwater Horizon results were particularly strong across all three algorithms. Overall, the average performance against all datasets for all algorithms was generally between Likert scores of two and three, a performance consistent with satisfactory edge planes. Most results were closer to a Likert score of two rather than three, as well, a finding consistent with overall strong performance.

Table 131 presents the disaggregated evaluation of each test dataset compared to the Canny evaluation criteria. This table enables conclusions to be drawn regarding each algorithm through the lens of the test datasets. For example, HySPADE's false positive challenges and the level set operator's false negative challenges can clearly be seen in the table, which also shows that HySPADE's false positives challenges are generally present across all datasets, while the level set's false negative challenges are more scene specific.

Also clear is that the gradient-based edge detector performs admirably across all datasets. The gradient algorithm's weak false positives performance against the difficult Aluminum Panel data is the only blemish on its record, which is otherwise populated with strong to satisfactory performance.

Additionally, Table 131 shows the consistently strong localization performance for all three algorithms across all datasets. The algorithms all accurately geolocate the edges in their proper position, a highly desirable feature of a reliable edge detector. Also striking is the significantly stronger false positives and single-point response performance from the level set operator, which measured fully one to two Likert scores above the HySPADE and gradient algorithm for those criteria. Overall, each algorithm produced satisfactory results for several datasets, a satisfactory result.

Table 131: Disaggregated Evaluation Matrix for All Algorithms and HSI Datasets

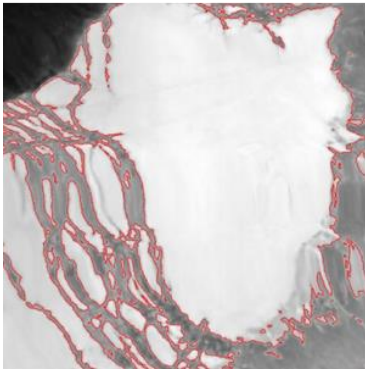
Green = Strong Yellow = Average Red = Weak	False Positives	False Negatives	Localization	Single-Point Response	Robustness to Noise	Unbroken Edges	Normalized Score
Gradient	2.7	2.4	1.1	2.4	2.7	1.9	2.2
Reno	1.8	1.8	1.0	3.0	1.8	1.0	1.7
Cuprite FL#1	3.2	3.2	1.0	3.4	2.6	2.4	2.6
Cuprite FL#2	2.4	2.6	1.0	2.0	2.2	2.2	2.1
Cuprite FL#3	3.4	1.6	1.2	2.6	3.0	3.0	2.5
Cuprite FL#4	2.0	3.0	1.0	1.2	2.4	2.6	2.0
Indian Pines	3.0	2.8	1.8	3.2	3.0	2.0	2.6
Deepwater Horizon	2.0	3.2	1.0	2.0	2.8	2.0	2.2
Larkhaven	1.6	2.0	1.0	2.0	2.8	1.4	1.8
Granite VNIR	2.0	2.2	1.0	1.4	2.8	3.0	2.1
Granite NIR/SWIR	3.4	2.8	1.2	3.0	2.8	1.8	2.5
South Africa Cores	2.6	2.6	1.0	1.8	2.6	1.8	2.1
Aluminum Panel	5.0	2.2	1.0	2.6	4.0	2.0	2.8
Rare Target	2.8	1.6	1.0	2.2	2.0	1.0	1.8
Chemical Array	3.6	2.8	1.2	3.2	3.4	1.8	2.7
Cloth Threads	1.6	1.4	1.0	2.0	2.2	1.2	1.6
HvSPADE	3.3	2.9	1.1	2.4	3.0	2.9	2.6
Reno	2.6	2.6	1.0	2.0	2.8	2.4	2.2
Cuprite FL#1	3.8	2.2	1.0	2.2	3.2	3.0	2.6
Cuprite FL#2	3.2	2.4	1.0	3.0	3.8	2.4	2.6
Cuprite FL#3	3.0	3.4	1.0	2.4	3.6	3.4	2.8
Cuprite FL#4	3.2	2.0	1.0	2.0	2.8	2.0	2.2
Indian Pines	4.0	5.0	2.6	2.0	4.6	5.0	3.9
Deepwater Horizon	3.0	2.2	1.0	2.6	2.8	1.6	2.2
Larkhaven	3.4	4.2	1.0	2.8	3.4	4.0	3.1
Granite VNIR	3.4	3.2	1.2	2.0	2.6	3.2	2.6
Granite NIR/SWIR	3.6	3.2	1.2	2.2	3.2	2.8	2.7
South Africa Cores	3.8	2.2	1.0	2.2	2.6	2.2	2.3
Aluminum Panel	2.4	3.2	1.0	3.0	2.4	3.0	2.5
Rare Target	2.6	2.8	1.0	2.2	2.2	2.2	2.2
Chemical Array	3.8	2.4	1.0	3.0	3.2	3.4	2.8
Cloth Threads	3.4	2.0	1.0	2.6	2.4	3.4	2.5
Level Set	1.3	3.8	1.1	1.0	2.5	2.9	2.1
Reno	1.0	3.8	1.0	1.0	3.2	1.0	1.8
Cuprite FL#1	1.4	3.8	1.0	1.0	2.6	1.6	1.9
Cuprite FL#2	3.2	3.8	2.4	1.0	2.6	3.8	2.8
Cuprite FL#3	1.0	1.8	1.4	1.0	1.4	1.8	1.4
Cuprite FL#4	1.0	1.8	1.0	1.0	1.0	1.0	1.1
Indian Pines	1.0	3.0	1.4	1.0	2.4	3.0	2.0
Deepwater Horizon	1.0	3.2	1.0	1.0	2.2	2.6	1.8
Larkhaven	1.0	5.0	1.0	1.0	3.4	4.4	2.6
Granite VNIR	2.2	4.6	1.0	1.0	3.2	3.8	2.6
Granite NIR/SWIR	1.0	4.0	1.0	1.0	3.6	2.6	2.2
South Africa Cores	1.0	5.0	1.0	1.0	3.0	5.0	2.7
Aluminum Panel	1.0	5.0	1.0	1.0	4.0	5.0	2.8
Rare Target	1.8	4.2	1.0	1.0	2.8	2.8	2.3
Chemical Array	1.0	3.2	1.0	1.0	1.6	1.6	1.6
Cloth Threads	1.0	5.0	1.0	1.0	1.0	3.8	2.1
Criteria Average	2.4	3.0	1.1	1.9	2.8	2.6	2.3

Table 132: Strongest 30 Individual Tests According to Canny Evaluation Results

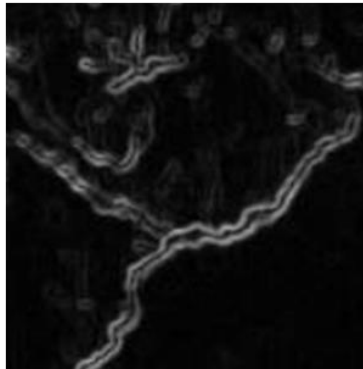
Algorithm	HSI Dataset	HSI Data Input	False Positives	False Negatives	Localization	Single-Point Response	Robustness to Noise	Unbroken Edges	Normalized Score
Level Set	Cuprite 3	Full PCA	1	1	1	1	1	1	1.0
Level Set	Cuprite 4	Full PCA	1	1	1	1	1	1	1.0
Level Set	Cuprite 3	Optimal PCA	1	1	1	1	1	1	1.0
Level Set	Cuprite 4	Optimal PCA	1	1	1	1	1	1	1.0
Level Set	Cuprite 3	Reflectance	1	1	1	1	1	1	1.0
Level Set	Cuprite 4	Reflectance	1	1	1	1	1	1	1.0
Gradient	Granite VNIR	Optimal MNF	1	1	1	1	2	1	1.2
Gradient	Deepwater	Optimal MNF	1	1	1	1	2	1	1.2
Gradient	Reno	Optimal MNF	1	1	1	2	1	1	1.2
Gradient	Larkhaven	Optimal PCA	1	1	1	2	1	1	1.2
Level Set	Deepwater	Full PCA	1	2	1	1	1	1	1.2
Level Set	Deepwater	Optimal PCA	1	2	1	1	1	1	1.2
Level Set	Deepwater	Radiance	1	2	1	1	1	1	1.2
Level Set	Deepwater	Reflectance	1	2	1	1	1	1	1.2
Gradient	Granite N-S	Optimal MNF	1	1	1	3	1	1	1.3
Gradient	Cuprite 3	Optimal PCA	1	1	1	2	1	2	1.3
Gradient	Deepwater	Radiance	1	1	1	2	2	1	1.3
HySPADE	Granite N-S	Optimal PCA	2	1	1	2	1	1	1.3
Gradient	Rare Target	Optimal MNF	2	1	1	2	1	1	1.3
Gradient	Threads	Optimal MNF	1	2	1	1	2	1	1.3
Gradient	Cuprite 4	Optimal MNF	1	2	1	1	1	2	1.3
Gradient	Reno	Optimal PCA	1	2	1	2	1	1	1.3
Level Set	Cuprite 4	Full MNF	1	3	1	1	1	1	1.3
Level Set	Cuprite 4	Optimal MNF	1	3	1	1	1	1	1.3
Gradient	Larkhaven	Full PCA	1	1	1	2	3	1	1.5
Gradient	Threads	Full PCA	2	1	1	2	2	1	1.5
Gradient	South Africa	Optimal MNF	2	1	1	2	2	1	1.5
Gradient	Threads	Optimal PCA	2	1	1	2	2	1	1.5
Gradient	Threads	Full MNF	1	2	1	2	2	1	1.5
HySPADE	Rare Target	Optimal PCA	2	2	1	1	1	2	1.5

Table 132 builds upon Table 131 by presenting the strongest 30 individual tests captured by this study. Optimized HSI data types are bolded in the table in order to emphasize their predominance among the top results. As seen, 25 of the top 30 results are compressed data types. Note the strong performance of the level set algorithm, which constituted 10 of the top 14 results, all of which aligned to either mineral mapping applications or oil spill mapping applications. The level set algorithm also merited all six the perfect 1.0 scores encountered in the research. The gradient-based edge detector also performed strongly, particularly against mineral mapping, oil spill mapping and urban mapping applications. HySPADE's strongest results were aligned to mineral mapping and trace chemical detection applications. Notably absent are any outliers performing strongly against the Indian Pines and Aluminum Panel tests, as well. Indeed, 11 of the weakest 25 tests were attributable to the Indian Pines and Aluminum Panel datasets. Figure 322 presents a sampling of the strongest level set, gradient and HySPADE tests. The thin, unbroken lines are typical of strong level set results, the strong, unbroken edges are typical of gradient results and the single-point response edges are typical of HySPADE edge planes.

Level Set, Optimal PCA,
Cuprite Flight Line #3



Gradient, Optimal MNE,
Deepwater Horizon



HySPADE, Optimal PCA,
Granite NIR/SWIR

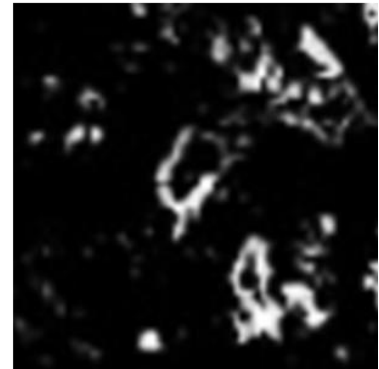


Figure 322: Sample of Top Performing Individual Tests

Table 133: Evaluation Matrix for Spatial Resolution

Green = Strong Yellow = Average Red = Weak	False Positives	False Negatives	Localization	Single-Point Response	Robustness to Noise	Unbroken Edges	Normalized Score
	Gradient	2.6	2.4	1.1	2.4	2.7	1.8
0.002 meters	2.7	2.2	1.1	2.4	2.6	1.8	2.1
0.005	5.0	2.2	1.0	2.6	4.0	2.0	2.8
0.01	2.6	2.6	1.0	1.8	2.6	1.8	2.1
0.05	1.6	2.0	1.0	2.0	2.8	1.4	1.8
2.2	2.0	3.2	1.0	2.0	2.8	2.0	2.2
4	2.2	2.1	0.8	1.8	2.0	2.0	1.8
8	1.8	1.8	1.0	3.0	1.8	1.0	1.7
20	3.0	2.8	1.8	3.2	3.0	2.0	2.6
HySPADE	3.2	3.0	1.2	2.4	3.0	2.9	2.6
0.002	3.4	2.7	1.1	2.4	2.7	3.0	2.5
0.005	2.4	3.2	1.0	3.0	2.4	3.0	2.5
0.01	3.8	2.2	1.0	2.2	2.6	2.2	2.3
0.05	3.4	4.2	1.0	2.8	3.4	4.0	3.1
2.2	3.0	2.2	1.0	2.6	2.8	1.6	2.2
4	2.6	2.0	0.8	1.9	2.7	2.2	2.0
8	2.6	2.6	1.0	2.0	2.8	2.4	2.2
20	4.0	5.0	2.6	2.0	4.6	5.0	3.9
Level Set	1.1	3.9	1.1	1.0	2.8	3.2	2.2
0.002	1.4	4.2	1.0	1.0	2.4	2.9	2.2
0.005	1.0	5.0	1.0	1.0	4.0	5.0	2.8
0.01	1.0	5.0	1.0	1.0	3.0	5.0	2.7
0.05	1.0	5.0	1.0	1.0	3.4	4.4	2.6
2.2	1.0	3.2	1.0	1.0	2.2	2.6	1.8
4	1.3	2.2	1.2	0.8	1.5	1.6	1.4
8	1.0	3.8	1.0	1.0	3.2	1.0	1.8
20	1.0	3.0	1.4	1.0	2.4	3.0	2.0
Criteria Average	2.3	3.1	1.1	1.9	2.8	2.6	2.3

Table 133 presents algorithm performance as a function of descending spatial resolution. One of this dissertation’s hypotheses is that the algorithms would be robust to declining spatial resolution and more sensitive to declining spectral resolution. The

intent behind the hypothesis and the accompanying table is to demonstrate that while spatial resolution is an important determinant of edge detection performance, the strength of this study's edge detector's lies in their ability to leverage high spectral resolution data – the defining feature of hyperspectral remote sensing data.

As seen in Table 133, there is no general pattern of declining algorithm performance against any Canny criteria as spatial resolution weakens. This finding supports the hypothesis by not showing a marked decrease in performance as spatial resolution declines. In fact, the weakest evaluation measurements tended to occur at very high spatial resolutions. This conclusion is not to suggest that high spatial resolution HSI data is a disadvantage. It most certainly is not. Instead, the weak performance against high spatial resolution data is most likely attributable to the low spectral contrast among features (e.g., adjacent similar minerals) in the scenes corresponding to those resolutions.

Note that localization and single-point response performance were particularly resilient across declining spatial resolution for each algorithm. These conclusions speak to the strength of the algorithms' ability to accurately position narrow edges even within low-resolution scenes. Single-point response and localization appear to be strengths for all three algorithms, in general.

Ultimately, the findings in Table 133 support the hypothesis that the algorithms are more likely to be sensitive to declining spectral resolution compare to declining spatial resolution as evidenced by consistently strong, average or weak Canny evaluations as spatial resolution declines.

Table 134: Evaluation Matrix for Spectral Resolution

Green = Strong Yellow = Average Red = Weak	False Positives	False Negatives	Localization	Single-Point Response	Robustness to Noise	Unbroken Edges	Normalized Score
	Gradient	2.5	2.2	1.0	2.4	2.5	1.7
360 bands	2.0	3.2	1.0	2.0	2.8	2.0	2.2
356	1.8	1.8	1.0	3.0	1.8	1.0	1.7
224	1.5	1.4	0.9	1.6	1.5	1.0	1.3
178	2.8	2.6	1.1	2.3	2.6	2.6	2.3
168	3.6	2.8	1.2	3.2	3.4	1.8	2.7
164	3.4	2.8	1.2	3.0	2.8	1.8	2.5
128	3.3	2.1	1.0	2.3	3.4	1.7	2.3
80	1.6	1.4	1.0	2.0	2.2	1.2	1.6
72	2.5	2.1	1.0	1.8	2.5	1.9	2.0
HySPADE	3.1	2.6	1.1	2.3	2.8	2.8	2.5
360	3.0	2.2	1.0	2.6	2.8	1.6	2.2
356	2.6	2.6	1.0	2.0	2.8	2.4	2.2
224	2.0	2.5	1.3	1.0	2.3	2.5	1.9
178	3.3	2.5	1.0	2.4	3.4	2.7	2.5
168	3.8	2.4	1.0	3.0	3.2	3.4	2.8
164	3.6	3.2	1.2	2.2	3.2	2.8	2.7
128	2.9	3.7	1.0	2.9	2.9	3.5	2.8
80	3.4	2.0	1.0	2.6	2.4	3.4	2.5
72	3.3	2.7	1.1	2.1	2.5	2.5	2.4
Level Set	1.1	3.7	1.0	0.9	2.4	2.6	2.0
360	1.0	3.2	1.0	1.0	2.2	2.6	1.8
356	1.0	3.8	1.0	1.0	3.2	1.0	1.8
224	0.5	1.5	0.7	0.5	1.2	1.5	1.0
178	1.7	2.8	1.5	1.0	1.9	2.1	1.8
168	1.0	3.2	1.0	1.0	1.6	1.6	1.6
164	1.0	4.0	1.0	1.0	3.6	2.6	2.2
128	1.0	5.0	1.0	1.0	3.7	4.7	2.7
80	1.0	5.0	1.0	1.0	1.0	3.8	2.1
72	1.7	4.6	1.0	1.0	3.0	3.9	2.5
Criteria Average	2.2	2.9	1.0	1.9	2.6	2.4	2.2

Table 134 presents algorithm performance as a function of descending spectral resolution. Although not consistent across all algorithms and Canny evaluation criteria, there are several trends indicating that the algorithms are sensitive to spectral resolution for some Canny evaluation criteria. For example, with a few exceptions, the gradient algorithm's performance declines as a function of weakening spectral resolution for the false positives, false negatives and robustness to noise criteria. These trends make sense – as spectral contrast declines, so does the algorithm's ability to accurately detect and delineate edges. Surprisingly, the gradient algorithm's localization performance and unbroken edge performance are robust to declining spectral resolution. The sustained accuracy and solid edge performance is likely attributable to the algorithms kernel-based, localized approach to detecting edges, which is in harmony with the general observation that an edge is local within the context of the scene.

Table 134 also indicates that HySPADE performance tends to weaken as spectral resolution declines, particularly for false positives and unbroken edges. The declining unbroken edges performance as a function of declining spectral resolution is likely attributable to the global nature of HySPADE's edge detection process. Namely, since HySPADE considers the spectral relationship between a pixel and all other scene pixels, it is not surprising that generates more broken edges as spectral resolution declines. HySPADE's consideration of global edge relationships is a strength for high spectral resolution data sets but can be a weakness as declining spectral resolution renders all of the scene's pixels more spectrally similar. Overall, the HySPADE's performance evaluations as measured through the lens of spectral resolution provide strong support to

the hypothesis that the algorithms will be more sensitive to spectral resolution than spatial resolution.

Finally, Table 134 demonstrates that the level set algorithm is highly sensitive to declining spectral resolution, most notably for the false negatives and unbroken edges criteria, areas previously identified as challenges for the algorithm. Indeed, declining spectral resolution appears to be the primary explanatory factor for the tests in which the level set algorithm underperformed its typically strong results. For example, for spectral resolutions on the order of 150 bands or more, level set performance against the false negatives criterion ranges from strong to average, but quickly degrades as the spectral resolution approaches 120 bands or below. Clearly, the level set algorithm requires sufficient spectral resolution to support its energy minimization calculations, which rapidly suffer as declining spectral resolution diminishes the spectral contrast (i.e., level set energy) among scene materials.

Similarly, level set performance against the unbroken edges criterion declines for the same reason. As materials lose their separability, the level set algorithm does not detect a meaningful separation between adjacent materials and therefore either misses the edge entirely as a false negative or renders it only partially as a broken edge. The clear conclusion is that the level set algorithm, in particular, is sensitive to declining spectral resolution. Ultimately, the generally weakening performance for all three algorithms as a function of declining spectral resolution provides support for the hypothesis that HSI spatial-spectral edge detection algorithms are more likely to be sensitive to declining spectral resolution than declining spatial resolution.

Table 135: Evaluation Matrix for Spectral Bandpass

Green = Strong Yellow = Average Red = Weak	False Positives	False Negatives	Localization	Single-Point Response	Robustness to Noise	Unbroken Edges	Normalized Score
Gradient	2.9	2.5	1.1	2.5	2.8	1.9	2.3
VNIR/SWIR	2.5	2.6	1.1	2.5	2.5	2.2	2.2
NIR/SWIR	3.5	2.8	1.2	3.1	3.1	1.8	2.6
VNIR	2.6	2.0	1.0	2.0	2.7	1.7	2.0
HySPADE	3.4	2.9	1.1	2.5	3.1	3.0	2.6
VNIR/SWIR	3.3	2.8	1.2	2.3	3.4	2.8	2.6
NIR/SWIR	3.7	2.8	1.1	2.6	3.2	3.1	2.8
VNIR	3.2	2.9	1.0	2.5	2.6	3.0	2.5
Level Set	1.2	3.8	1.1	1.0	2.6	2.8	2.1
VNIR/SWIR	1.4	3.0	1.3	1.0	2.2	2.1	1.8
NIR/SWIR	1.0	3.6	1.0	1.0	2.6	2.1	1.9
VNIR	1.3	4.8	1.0	1.0	2.9	4.1	2.5
Criteria Average	2.5	3.0	1.1	2.0	2.8	2.6	2.3

Table 135 is a companion matrix for Table 134 in the sense that it sheds light on algorithm sensitivity to spectral information. The table is organized to show how algorithm performance relates to declining spectral information as a function of spectral bandpass. For example, generally speaking, there are more diagnostic absorption features in VNIR/SWIR data compared to only VNIR data, suggesting that edge detectors can reasonably be expected to perform more strongly against VNIR/SWIR data compared to VNIR data, all other elements being comparable.

The table corroborates the previous conclusions that the algorithms are more sensitive to less spectral information than less spatial information. For example, the level set performance against the false negatives, robustness to noise and unbroken edges

criteria decline as a function of spectral bandpass. Not all evaluation categories show a decline, however. Level set performance against false positives and localization are robust to declining spectral resolution, a finding that speaks to the algorithm’s strengths. Additionally, HySPADE results modestly decline as a function of bandpass for both false negatives and false positives, while the gradient-based algorithm weakens against false positives and robustness to noise as spectral resolution decreases. Overall, Table 135 is consistent with Table 134’s findings and support to the hypothesis that edge operators are more sensitive to declining spectral resolution than declining spatial resolution.

Table 136: Aggregated Evaluation Matrix for HSI Applications

Green = Strong Yellow = Average Red = Weak	False Positives	False Negatives	Localization	Single-Point Response	Robustness to Noise	Unbroken Edges	Normalized Score
Material Analysis	2.8	3.5	1.0	2.2	3.5	3.3	2.7
Mineral Mapping	2.6	2.9	1.1	1.8	2.7	2.6	2.3
Oil Spill Mapping	2.0	2.9	1.0	1.9	2.6	2.1	2.1
Trace Chemical Detection	2.6	2.8	1.0	2.1	2.5	2.1	2.2
Urban Mapping	1.9	3.2	1.0	2.0	2.9	2.4	2.2
Vegetation Mapping	2.3	3.2	1.5	2.0	2.6	3.1	2.4
Criteria Average	2.4	3.1	1.1	2.0	2.8	2.6	2.3

Table 136 provides an aggregated evaluation of algorithm performance against this dissertation’s six HSI applications. The intent is to provide a sense of which applications were most challenging for the algorithm suite and which applications were more accommodating. Recall that each application does not align to the same number of

datasets, with some applications aligning to only a single dataset (e.g., oil spill mapping and material analysis.)

Overall, material analysis applications, as represented by the difficult Aluminum Panel dataset, were the most challenging. False negatives, robustness to noise and unbroken edges were particularly stressing for the algorithms, most likely due to the low spectral contrast and VNIR bandpass of the Aluminum Panel data. Vegetation mapping also was challenging with respect to false negatives and unbroken edges and urban mapping was stressing with respect to robustness to noise.

Oil spill mapping, urban mapping and trace chemical detection were the most accessible applications, producing strong evaluation scores against the false positives, localization and single-point response criteria. In particular, the algorithms produced high-quality edge planes for oil spill mapping applications from all five HSI datasets, including the radiance and reflectance data. The strong false positive evaluations are particularly notable given the scene complexity, dark background and noise. Mineral mapping results ranged from satisfactory to strong, with false negatives and unbroken edges as the most challenging Canny criteria. Given the heavily mixed nature of many mineral features, average false negative rates represent a relatively strong performance; the spectral mixing of features in a mineral mapping scene make them more easily missed than the mostly spectrally pure features in an urban mapping scene. Overall, the algorithms performed strongly to satisfactorily against all HSI applications except material analysis, against which the average performance was relatively weak.

Table 137: Disaggregated Evaluation Matrix for HSI Applications

Green = Strong Yellow = Average Red = Weak	False Positives	False Negatives	Localization	Single-Point Response	Robustness to Noise	Unbroken Edges	Normalized Score
Gradient	2.8	2.4	1.1	2.4	2.8	1.8	2.2
Material Analysis	5.0	2.2	1.0	2.6	4.0	2.0	2.8
Mineral Mapping	2.7	2.6	1.1	2.2	2.6	2.4	2.3
Oil Spill Mapping	2.0	3.2	1.0	2.0	2.8	2.0	2.2
Trace Chemical Detection	3.2	2.2	1.1	2.7	2.7	1.4	2.2
Urban Mapping	1.7	1.9	1.0	2.5	2.3	1.2	1.8
Vegetation Mapping	2.3	2.1	1.4	2.6	2.6	1.6	2.1
HySPADE	3.1	2.9	1.1	2.5	2.9	2.9	2.6
Material Analysis	2.4	3.2	1.0	3.0	2.4	3.0	2.5
Mineral Mapping	3.4	2.7	1.1	2.3	3.1	2.7	2.5
Oil Spill Mapping	3.0	2.2	1.0	2.6	2.8	1.6	2.2
Trace Chemical Detection	3.2	2.6	1.0	2.6	2.7	2.8	2.5
Urban Mapping	3.0	3.4	1.0	2.4	3.1	3.2	2.7
Vegetation Mapping	3.7	3.5	1.8	2.3	3.5	4.2	3.2
Level Set	1.2	4.0	1.1	1.0	2.6	3.1	2.2
Material Analysis	1.0	5.0	1.0	1.0	4.0	5.0	2.8
Mineral Mapping	1.5	3.5	1.3	1.0	2.5	2.8	2.1
Oil Spill Mapping	1.0	3.2	1.0	1.0	2.2	2.6	1.8
Trace Chemical Detection	1.4	3.7	1.0	1.0	2.2	2.2	1.9
Urban Mapping	1.0	4.4	1.0	1.0	3.3	2.7	2.2
Vegetation Mapping	1.0	4.0	1.2	1.0	1.7	3.4	2.1
Criteria Average	2.4	3.1	1.1	2.0	2.8	2.6	2.3

Table 137 expands upon the high-level conclusions from Table 136 by examining each algorithm’s performance against HSI applications. For example, while material analysis was challenging for all three algorithms, their exhibited varying strengths and weaknesses. The gradient algorithm generated narrow unbroken edges but performed weakly against the false positives and robustness criteria. HySPADE measured well

against the false positives and robustness to noise criteria, but missed several features and produced a suboptimal volume of unbroken edges. The level set algorithm received the highest evaluation scores for false positives, single-point response and localization, but received the weakest evaluation scores for false negatives and broken edges. These findings support the conclusion that material analysis is the most difficult HSI application for the three edge detection algorithms, albeit for different reasons.

The algorithms thrived against different HSI applications, as well. The gradient algorithm performed most strongly in support of urban mapping applications and also demonstrated respectable results against oil spill mapping, vegetation mapping and mineral mapping. Gradient performance against trace chemical detection applications was satisfactory, although false positives were occasionally a concern. The HySPADE algorithm performed most strongly against oil spill mapping applications and also provided satisfactory results against trace chemical detection applications. Vegetation mapping was particularly challenging for the HySPADE algorithm, most likely due to the low spectral contrast among scene features.

The level set algorithm performed most strongly against oil spill mapping, mineral mapping and trace chemical detection applications, producing several of this study's strongest results. False negatives challenged the algorithm across all HSI applications, but as shown previously in Table 132, several individual level set tests significantly outperformed the algorithm's average. The overall conclusion is that different algorithms are suited for different applications according to their strengths and weaknesses. For example, a researcher examining urban mapping applications would

most likely benefit by using the gradient-based edge detector, while environmental cleanup personnel would most likely benefit from the level set edge detector's speed and accuracy in delineating oil spills.

Drawing from the experimental findings, the analyses and evaluations, and the conclusion matrices above, Table 138 presents this study's key conclusions. Specific algorithm strengths and weaknesses are summarized and broader conclusions are provided, as well. Aside from the algorithm strength and weaknesses, one of the most notable conclusions is that compressed HSI data in the form of compressed PCA and MNF cubes enable the strongest edge detection results across all three algorithms, across applications, spectral bandpasses, spatial resolutions and spectral resolutions.

Additionally, material analysis applications were shown to be the most challenging for the three algorithms while oil spill mapping and applications yielded the most satisfying overall results. Trace chemical detection and urban mapping applications also yielded satisfactory results across all three algorithms. The three algorithms also demonstrated more resiliency to declining spatial resolution compared to declining spectral resolution, with edge plane quality gradually declining with reduced spectral resolution.

Across applications, data input types, spatial resolutions and spectral resolutions, the gradient-based edge detector and the level set-based edge detector produced the most reliable and satisfying edge planes. Strong performance was particularly notable against oil spill mapping and trace chemical detection applications, and the algorithms excelled

at producing highly accurate unbroken edges. HySPADE excelled at generating single-point edges with satisfactory false negative rates.

Table 138: Key Conclusions for All Algorithms, Input Data Types and Applications

Key Conclusions	
1	The gradient-based, HySPADE and level set-based edge detection algorithms are more robust to spatial resolution than spectral resolution.
2	Optimized PCA and MNF cubes enable strong gradient operator results across applications, bandpasses, spatial and spectral resolutions
3	The gradient operator's areas of strength are false negatives, localization and unbroken edges. Urban mapping, vegetation mapping and oil spill mapping
4	The gradient operator is occasionally challenged by false positives, robustness to noise, unoptimized reflectance data and material analysis applications
5	Optimized PCA and MNF cubes enable satisfactory HySPADE results across applications, bandpasses, spatial and spectral resolutions
6	HySPADE's areas of strength are localization, single-point response, oil spill mapping and trace chemical detection
7	HySPADE is challenged by false positives, unbroken edges, declining spectral resolution and vegetation mapping
8	Optimized PCA and full PCA cubes enable strong level set results across applications, bandpasses, spatial and spectral resolutions
9	The level set operator's areas of strength are false positives, localization, single-point response, oil spill mapping, mineral mapping and trace chemical detection
10	The level set operator was significantly challenged by false negatives, particularly at high spatial resolutions, urban mapping and vegetation mapping applications
11	Reflectance data tended to underperform compared to optimized HSI data, but produced satisfactory results, including two of the strongest scoring tests
12	Optimal PCA data significantly improved edge detection performance across algorithms, applications, bandpasses, spatial and spectral resolutions
13	Optimal MNF data significantly improved edge detection performance across algorithms, applications, bandpasses, spatial and spectral resolutions
14	Full PCA data generally outperformed reflectance data, and produced the strongest results for the level set algorithm
15	Full MNF data produced the weakest edge detection results of all data types but produced mostly satisfactory results for the level set algorithm
16	Material analysis applications were the most challenging for all algorithms, particularly with respect to false negatives and unbroken edges
17	Mineral mapping applications were generally servicable by the algorithms, of which the level set and gradient algorithms produced high-quality edge planes
18	All three algorithms performed strongly in support of oil spill mapping applications, particularly the level set algorithm
19	Trace chemical detection applications were generally servicable by the algorithms, with the level set and gradient algorithms performing strongly
20	Urban mapping applications were challenging for the HySPADE algorithm, while the gradient algorithm produced some of most satisfactory edge planes
21	Vegetation mapping applications were particularly challenging for the HySPADE algorithm and tended to generate a high volume of false negatives

Table 139: Experiment #1 Hypotheses Evaluation

Experiment #1: Gradient-Based Edge Detection Method	
Hypothesis	Evaluation
H ₀ Null Hypothesis	Not Supported
H ₁ Superior false positive performance	Strongly Supported
H ₂ Superior False negative performance	Strongly Supported
H ₃ Superior localizaton performance	Strongly Supported
H ₄ Superior single-point response performance	Strongly Supported
H ₅ Superior robustness to noise performance	Strongly Supported
H ₆ Superior unbroken edges performance	Strongly Supported
H ₇ Superior optimal PCA and MNF performance	Strongly Supported
H ₈ Robustness to spatial and spectral resolutions	Supported

In accordance with the hypothesis-driven approach pursued herein, this work makes a formal determination regarding the extent to which the experimental findings, evaluations and conclusions support or do not support established hypotheses. Table 139 presents the hypotheses evaluation for the tests aligning to the gradient-based edge detection method. Most importantly, the results and evaluations are sufficiently strong to reject the null hypothesis that the gradient-based edge detection algorithm will demonstrate average performance with respect to the six edge operator evaluation criteria. Specifically, experimental evidence strongly supports H₁ through H₆ aligning to superior performance for the six Canny evaluation criteria. Experimental evidence also

supports H_7 corresponding to superior edge detection performance as enabled by compressed PCA and MNF data input types. Finally, experimental results support the hypothesis that the gradient-based edge detection algorithm will be more robust to declining spatial resolution compared to declining spectral resolution. Overall, the support to the gradient-based edge detector's hypotheses is quite satisfactory.

Table 140: Experiment #2 Hypotheses Evaluation
Experiment #2: HySPADE Edge Detection Method

Hypothesis	Evaluation
H_0 Null Hypothesis	Not Supported
H_1 Superior false positive performance	Supported
H_2 Superior False negative performance	Supported
H_3 Superior localizaton performance	Strongly Supported
H_4 Superior single-point response performance	Strongly Supported
H_5 Superior robustness to noise performance	Supported
H_6 Superior unbroken edges performance	Supported
H_7 Superior optimal PCA and MNF performance	Supported
H_8 Robustness to spatial and spectral resolutions	Supported

Table 140 presents the hypotheses evaluation for the tests aligning to the HySPADE edge detection method. Most importantly, the results and evaluations are sufficiently strong to reject the null hypothesis that the HySPADE edge detection

algorithm will demonstrate average performance with respect to the six edge operator evaluation criteria. Specifically, experimental evidence supports H_1 through H_6 aligning to superior performance for the six Canny evaluation criteria. In particular, evidence strongly supports hypotheses H_3 and H_4 aligning to localization and single-point response, for which HySPADE excelled. Experimental evidence also supports H_7 corresponding to superior edge detection performance as enabled by compressed PCA and MNF data input types. Finally, experimental results for HySPADE support the hypothesis that the HySPADE edge detection algorithm will be more robust to declining spatial resolution compared to declining spectral resolution. Overall, the support to the HySPADE edge detector's hypotheses is satisfactory.

Table 141: Experiment #3 Hypotheses Evaluation

Experiment #3: Level Set Edge Detection Method	
Hypothesis	Evaluation
H ₀ Null Hypothesis	Not Supported
H ₁ Superior false positive performance	Strongly Supported
H ₂ Superior False negative performance	Not Supported
H ₃ Superior localizaton performance	Strongly Supported
H ₄ Superior single-point response performance	Strongly Supported
H ₅ Superior robustness to noise performance	Supported
H ₆ Superior unbroken edges performance	Weakly Supported
H ₇ Superior optimal PCA and MNF performance	Weakly Supported
H ₈ Robustness to spatial and spectral resolutions	Strongly Supported

Table 141 presents the hypotheses evaluation for the tests aligning to the level set-based edge detection algorithm. Most importantly, the results and evaluations are sufficiently strong to reject the null hypothesis that level set-based edge detection algorithm will demonstrate average performance with respect to the six edge operator evaluation criteria. Specifically, experimental evidence strongly supports H₁, H₃, and H₄ aligning to false positives, localization and single-point response performance. Evidence also supports H₅, the hypothesis that the algorithm will generate superior results against the robustness to noise criteria. However, experimental evidence did not support H₂, which hypothesized that the algorithm would generate superior results with respect to

false negatives. Although there are notable exceptions to this conclusion, the general level set false negatives performance was suboptimal. Experimental results also weakly supported H_6 aligning to the unbroken edges criteria. Finally, experimental results for the level set algorithm strongly support the hypothesis that the algorithm will be more robust to declining spatial resolution compared to declining spectral resolution. Overall, the support to the level set edge detector's hypotheses is satisfactory.

The first key science question in this dissertation explores the nature of an edge in hyperspectral space. The experimental results clearly indicate that the concept of an edge assumes material/chemical meaning with hyperspectral space. Namely, the three algorithms demonstrated an ability to use HSI edge detection processes to discriminate among distinct materials. Although sensitivity to intensity was occasionally a barrier for the HySPADE and level set algorithms due to their implementation of Euclidean distance measurements, overall performance indicated that chemical boundaries have meaning in HSI space.

Additionally, the concept of an edge in HSI space varies somewhat according to application. Rather than a precise yes or no answer to a pixel's edge nature, sometimes the answer is yes but weakly, yes, or yes and strongly. The results from the oil spill mapping application tests corroborate this concept, particularly for the gradient-based operator testing. In the gradient tests against the Deepwater Horizon dataset, the gradient algorithm alarmed most strongly along the edges of the mostly purely oil-covered pixels, while delineating weaker, unbroken lines around the more heavily mixed oil and sea water pixels. The key insight is clear: edge strength derived from HSI data has

implications for pixel purity and spectral mixing. The difference is important for an application like oil spill mapping in support of cleanup operations seeking to most optimally emplace their equipment against the most heavily affected seawater.

Similarly, edges in HSI space can be a function of compression procedures such as PCA and MNF. While these cubes sacrifice unique chemical identification properties within their spectra, they demonstrated a highly satisfactory ability to support discontinuity-based edge detection operations. The PCA and MNF cubes give up a capability that really applies more appropriately to continuity-based processes like image classification, while the PCA and MNF cubes are advantaged by their ability to compress spectral information and thereby increasing the spectral contrast among scene materials. The new insight is that edges in PCA and MNF space are more chemically distinct than in reflectance space despite their sacrifice of uniquely identifying spectral information.

This dissertation's second key science question addressed the relative importance of spatial and spectral information to HSI edge detection methods. As previously shown in Table 133, Table 134 and Table 135, experimental results indicate that the algorithms are more sensitive to declining spectral information than declining spatial information. This insight makes sense considering the centrality of spectral resolution to hyperspectral science. Simply stated, as spectral contrast degrades, so does an algorithm's ability to discriminate between materials. Additionally, HSI edge detection methods are fairly robust to declining spatial resolution, particularly for scenes with large features consuming multiple pixels.

Declining spatial resolution in HSI space is really a question of increasing spectral mixing from the perspective of the algorithm math. As spectral mixing increases through declining spatial resolution, spectral contrast declines which in turn degrades an algorithm's ability to discriminate between materials. The net effect is the same as declining spectral resolution leading to weaker spectral contrast. The key insight derived from this question is that rather than thinking through the traditional lenses of spatial resolution and spectral resolution, a researcher will benefit by thinking in terms of spectral purity and spectral impurity. With this new insight in hand, this study concludes that for HSI edge detection methods, spectral resolution is likely to have more bearing on algorithm performance than spatial resolution, but that thinking in terms of spectral purity and spectral impurity is probably a more accurate way of thinking about spatial and spectral relationships for HSI edge detection problems.

Further Research

Several areas of further research are evident from this work's findings and conclusions. First, HySPADE's and the level set-based edge detection algorithm's sensitivity to intensity can be improved. By replacing the agreeably fast but intensity-sensitive Euclidean distance measurement with a metric less sensitive to intensity, one could expect to improve performance. The spectral angle mapper, mixture tuned match filter (MTMF) and adaptive cosine estimator (ACE) algorithms are feasible replacement candidates for the ED.

The gradient-based edge detection method's single-point response performance can be improved. The algorithm's current instantiation uses the Sobel operator to

estimate the partial derivatives in the x- and y-directions, a process that produces gradient measurements in the form of broad edges typical of Sobel edge planes. A variety of alternate measures of differentiation are available and could be explored for improved performance. Similarly, second order differentiation methods such as the Laplacian of the Gaussian should be considered for improved estimation of the gradient.

Also, edge detection research would benefit from a study that measured performance as a function of pixel purity rather than through the traditional constructs of spatial resolution and spectral resolution. This new understanding neatly blends the concepts of spatial and spectral resolution in a way that is uniquely hyperspectral – subpixel target detection via spectral unmixing methods. Integrative spectral unmixing methods for HSI edge detection processes have not been demonstrated in the literature and would forge a new path in the understanding of HSI edge detection methods.

Additionally, further research should investigate optimal histogram stretching methods for HSI edge detection planes. As evidenced by this work's findings, traditional grayscale histogram stretching methods, such as the Otsu histogram stretch, do not translate directly into HSI edge detection space, particularly for the HySPADE algorithm.

Finally, this dissertation considered only terrestrial solids. Additional research into HSI edge detection for gases and atmospheric particulates would be beneficial for broadening the collective understanding of HSI edge detection strengths and weaknesses. Longwave infrared HSI data is the obvious choice for further research into HSI edge detection for gases and atmospheric particulates given LWIR's ability to reliably detect gases and particulates. This dissertation would be particularly beneficial for

understanding how reliably HSI edge detection methods can detect gaseous emissions invisible to the unaided eye.

APPENDIX A: FULL EXPERIMENTAL RESULTS

Gradient-Based Edge Detection Results

1. Gradient-Based Edge Detection Algorithm: Reno

Reflectance



Optimal PCA



Optimal MNF



Full PCA



Full MNF

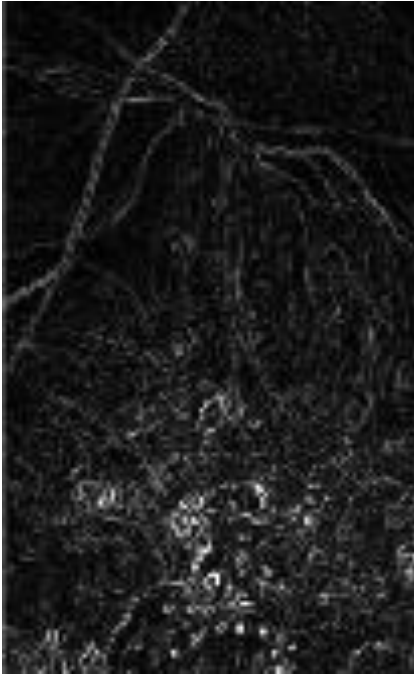


2. Gradient-Based Edge Detection Algorithm: Cuprite Flight Line #1

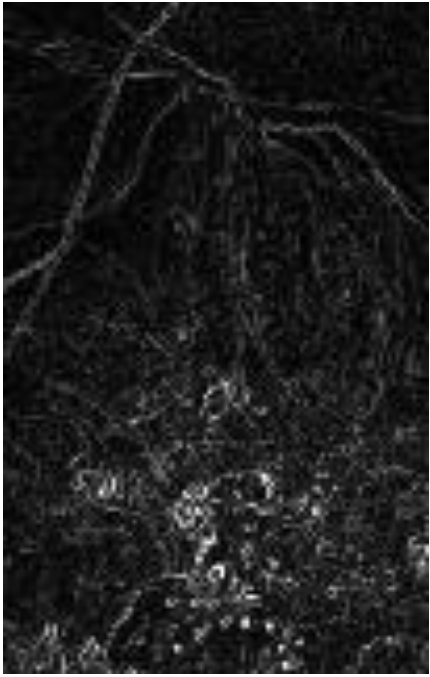
Reflectance



Optimal PCA



Optimal MNF



Full PCA



Full MNF



3. Gradient-Based Edge Detection Algorithm: Cuprite Flight Line #2

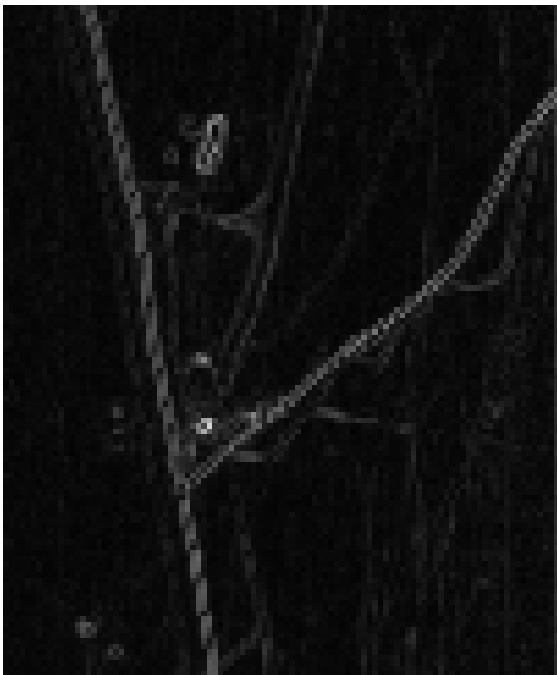
Reflectance



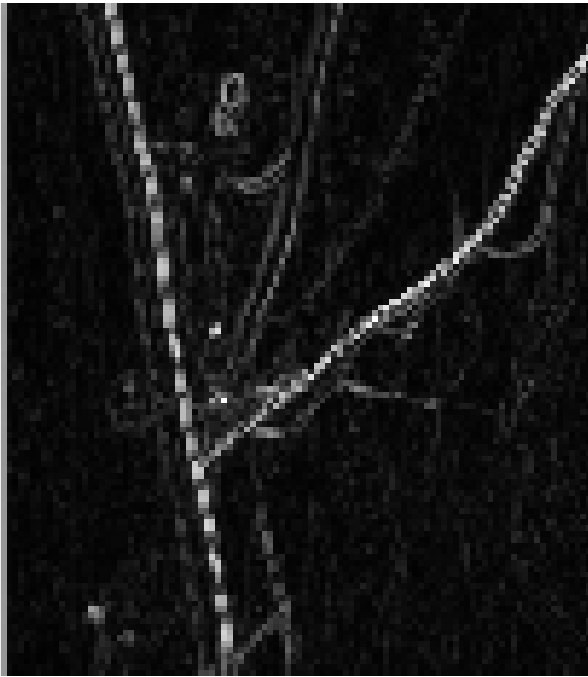
Optimal PCA



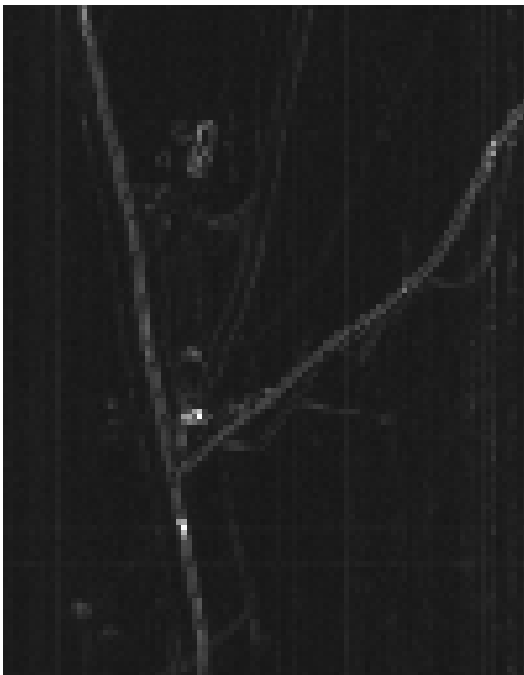
Optimal MNF



Full PCA



Full MNF

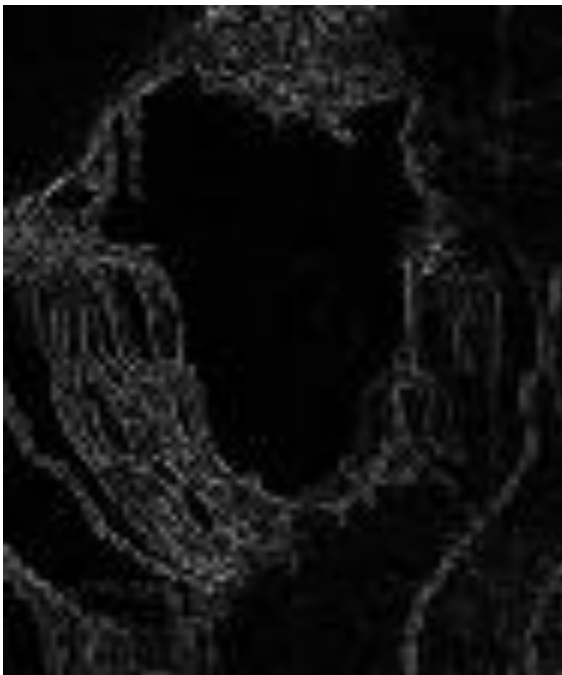


4. Gradient-Based Edge Detection Algorithm: Cuprite Flight Line #3

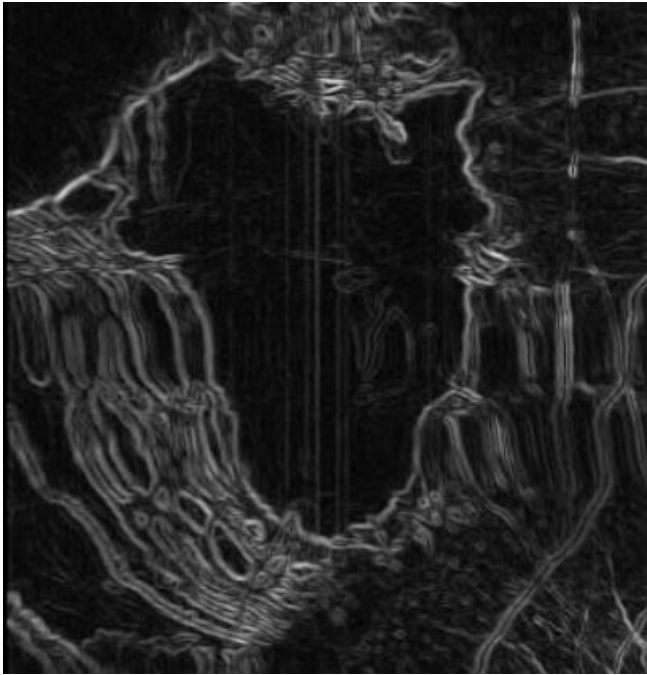
Reflectance



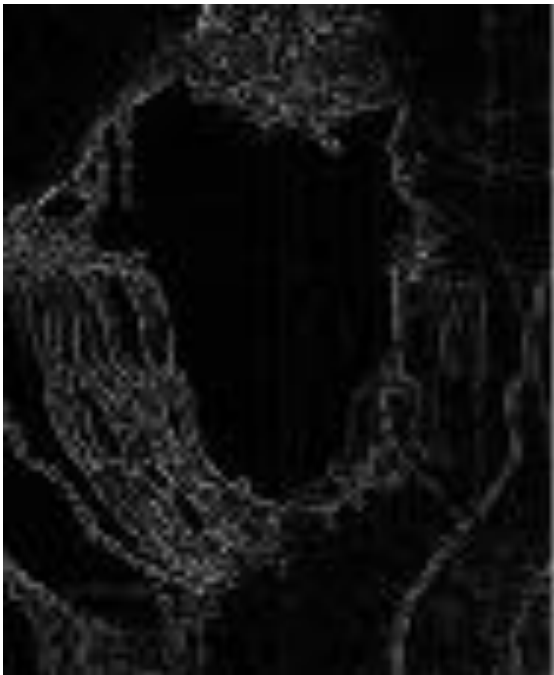
Optimal PCA



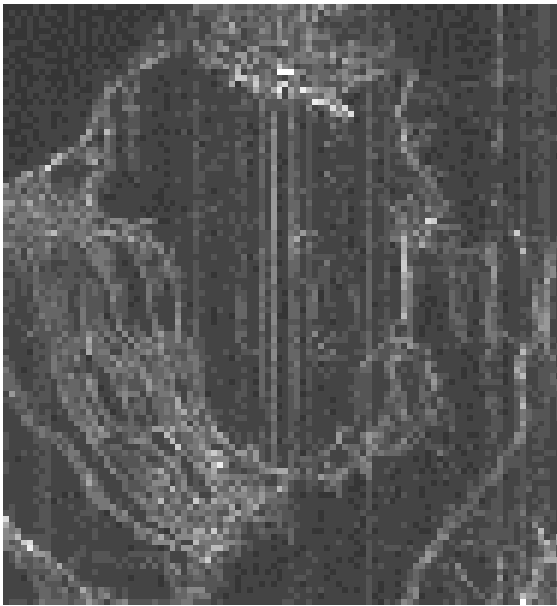
Optimal MNF



Full PCA



Full MNF



5. Gradient-Based Edge Detection Algorithm: Cuprite Flight Line #4

Reflectance



Optimal PCA



Optimal MNF



Full PCA



Full MNF

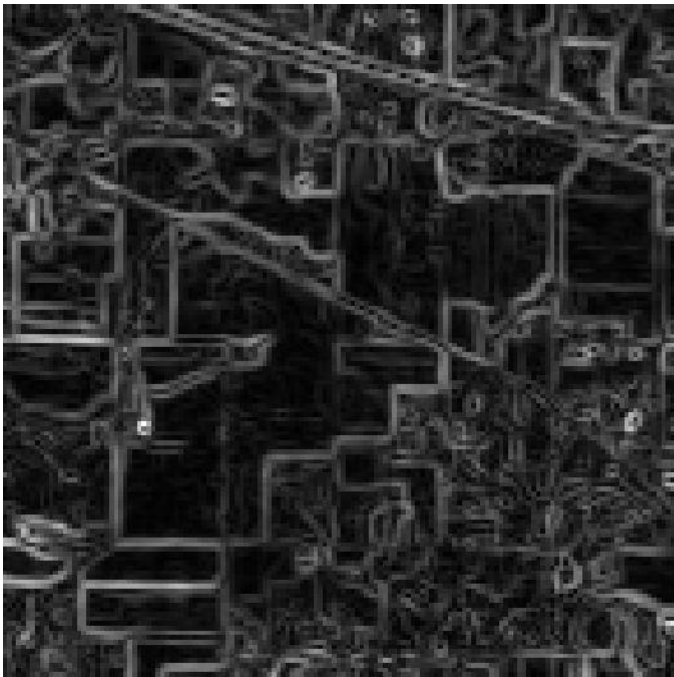


6. Gradient-Based Edge Detection Algorithm: Indian Pines

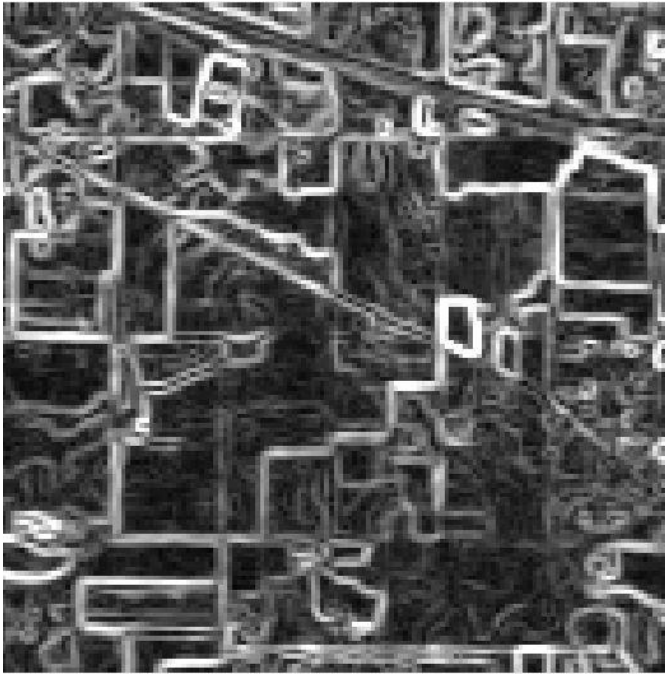
Reflectance



Optimal PCA



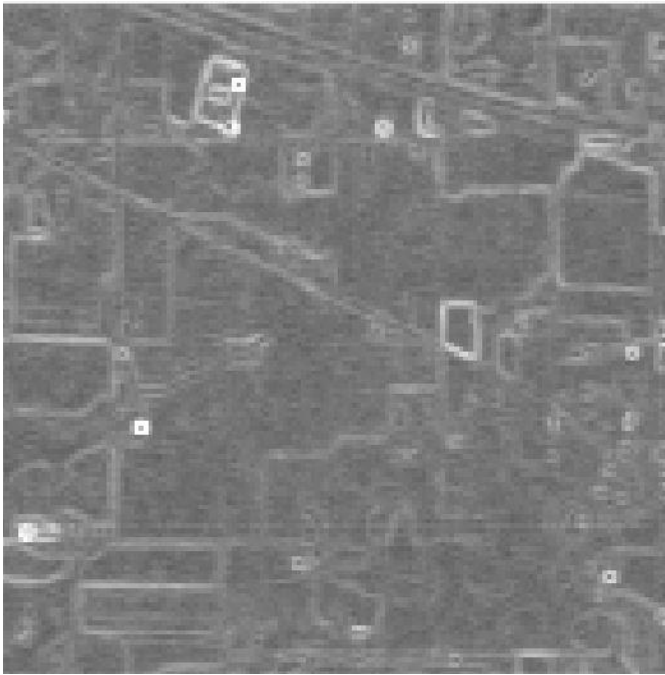
Optimal MNF



Full PCA

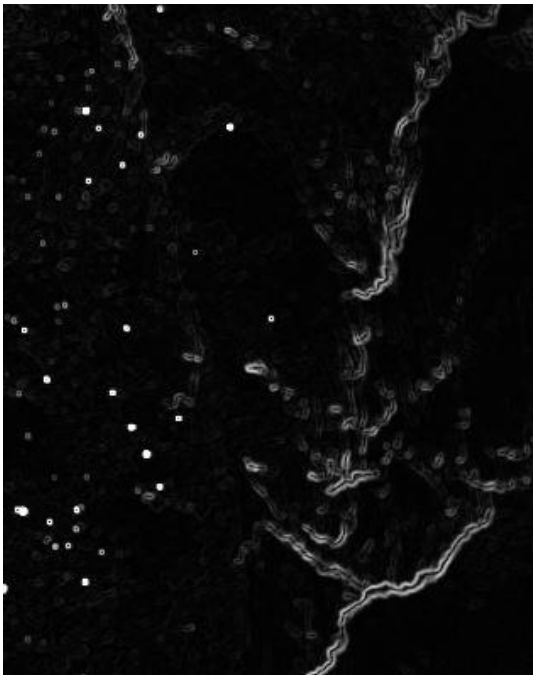


Full MNF

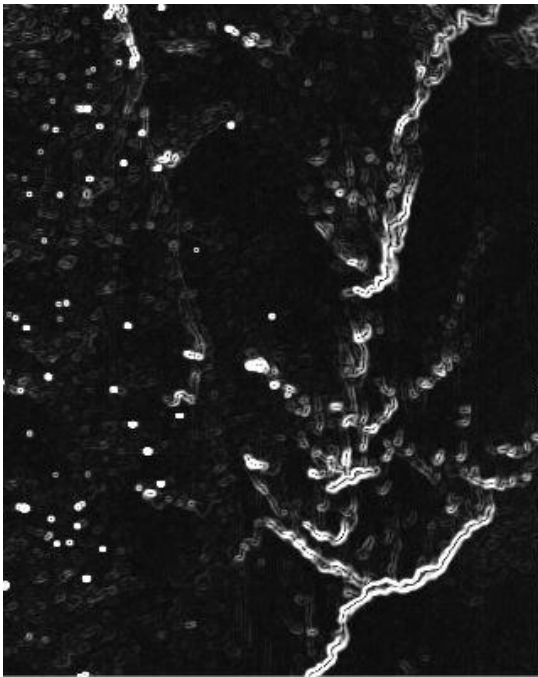


7. Gradient-Based Edge Detection Algorithm: Deepwater Horizon

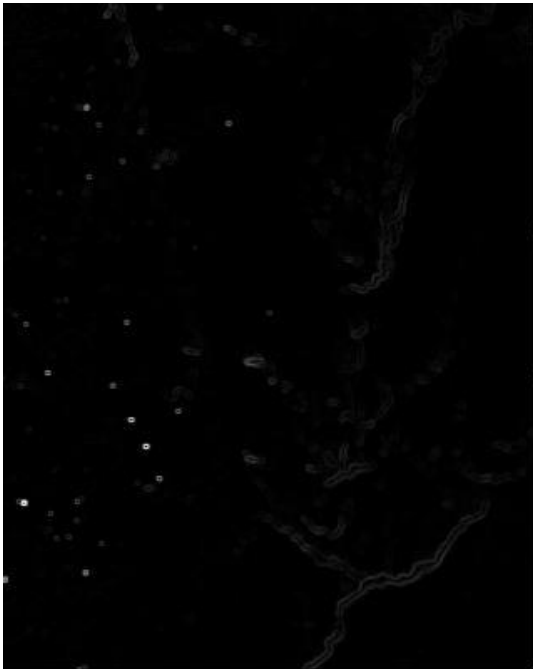
Radiance



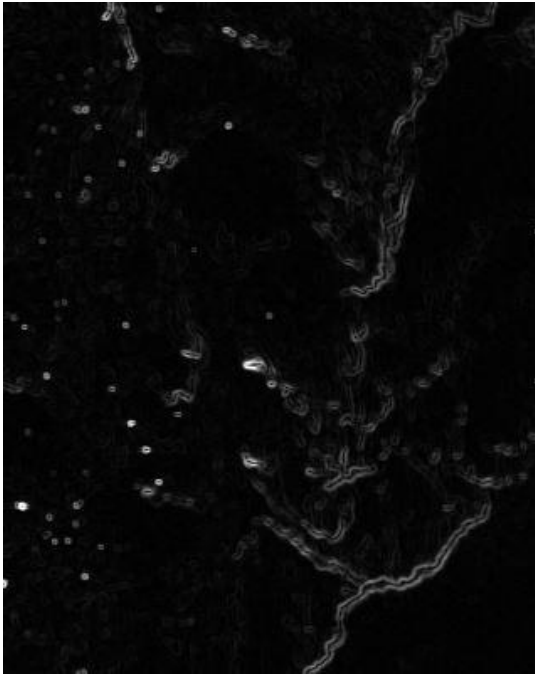
Reflectance



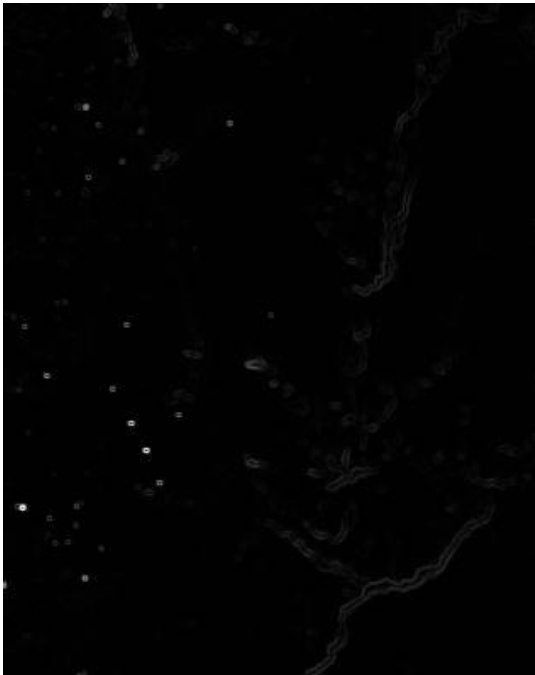
Optimal PCA



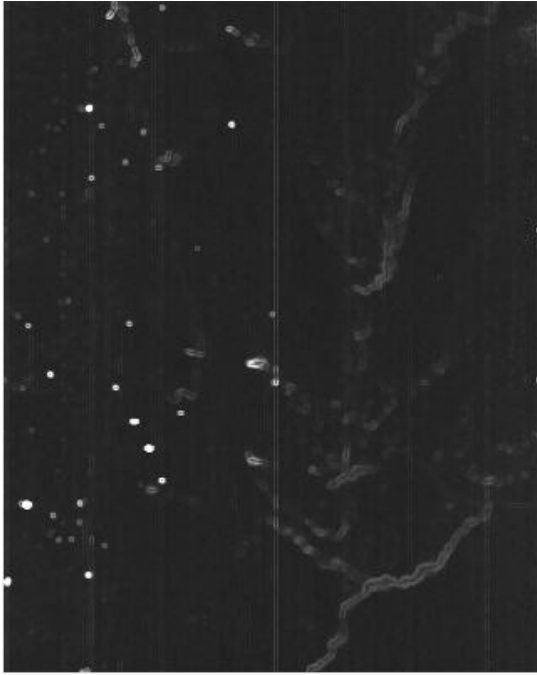
Optimal MNF



Full PCA



Full MNF



8. Gradient-Based Edge Detection Algorithm: Larkhaven

Reflectance



Optimal PCA



Optimal MNF



Full PCA

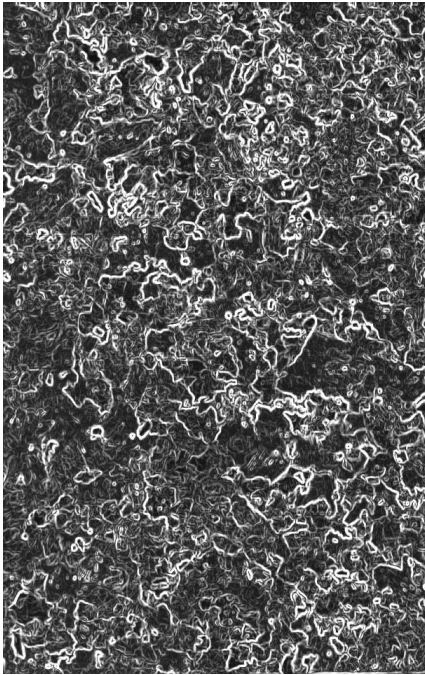


Full MNF

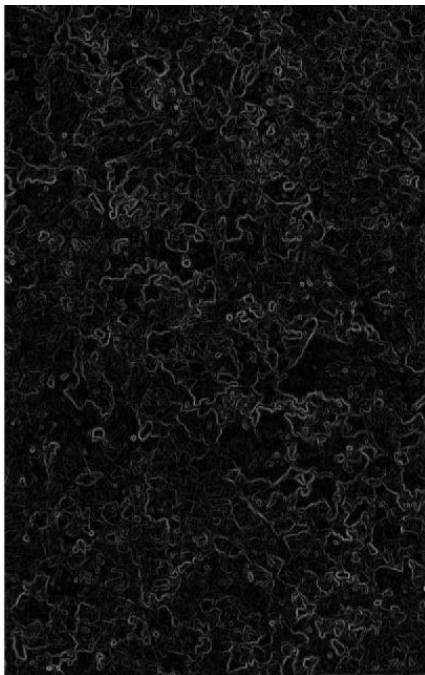


9. Gradient-Based Edge Detection Algorithm: Granite VNIR

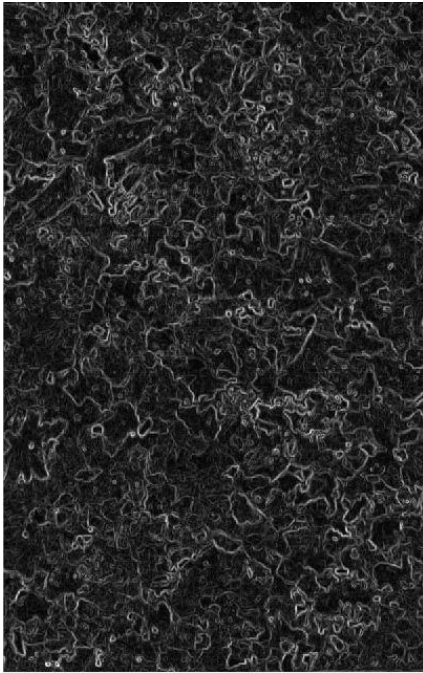
Reflectance



Optimal PCA



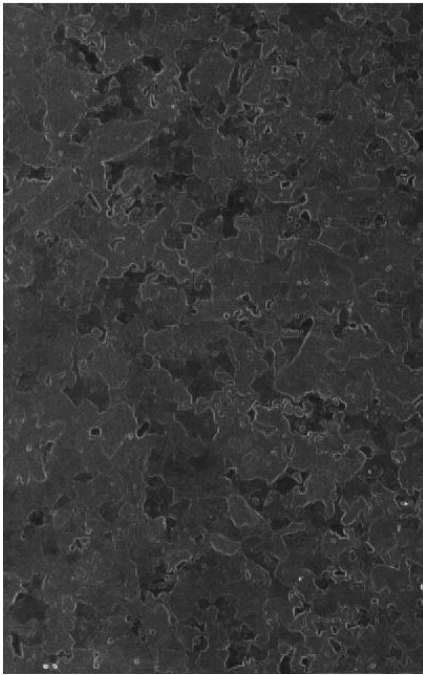
Optimal MNF



Full PCA

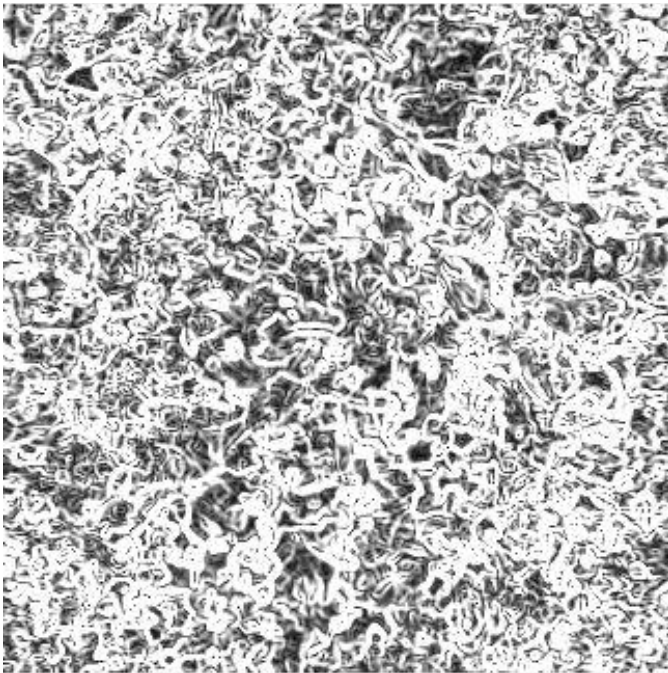


Full MNF

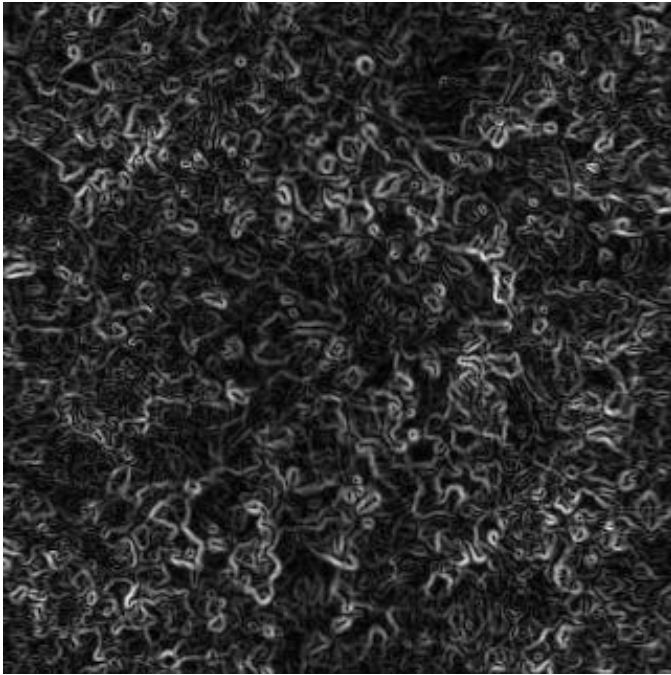


10. Gradient-Based Edge Detection Algorithm: Granite NIR/SWIR

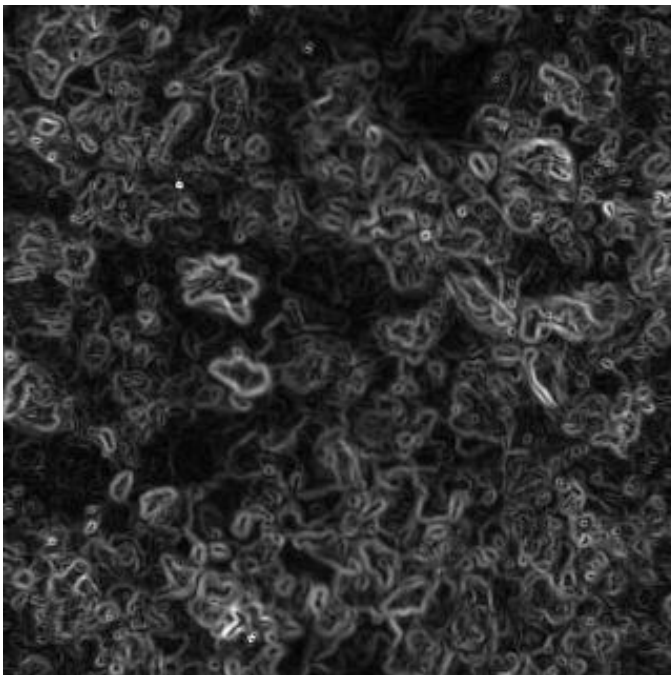
Reflectance



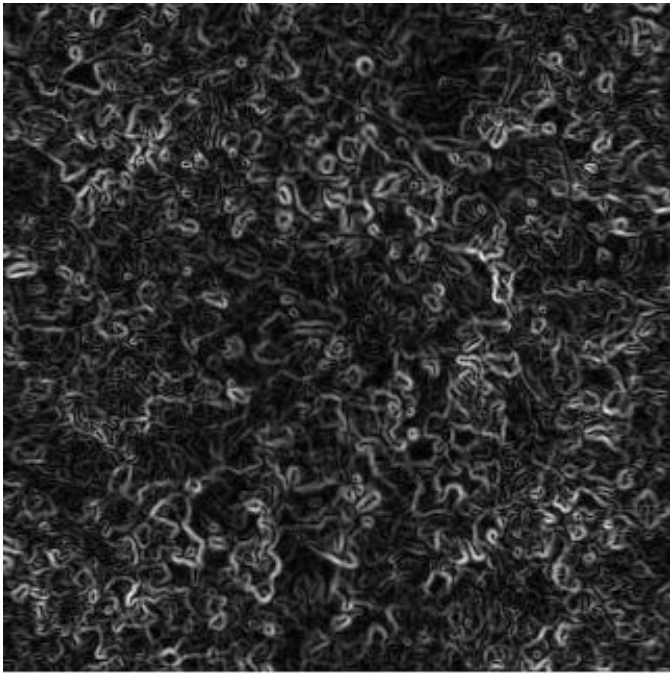
Optimal PCA



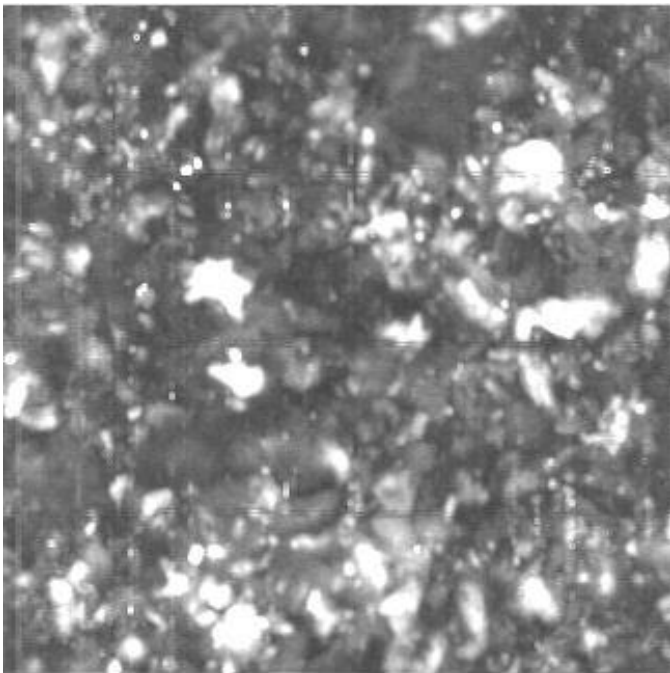
Optimal MNF



Full PCA

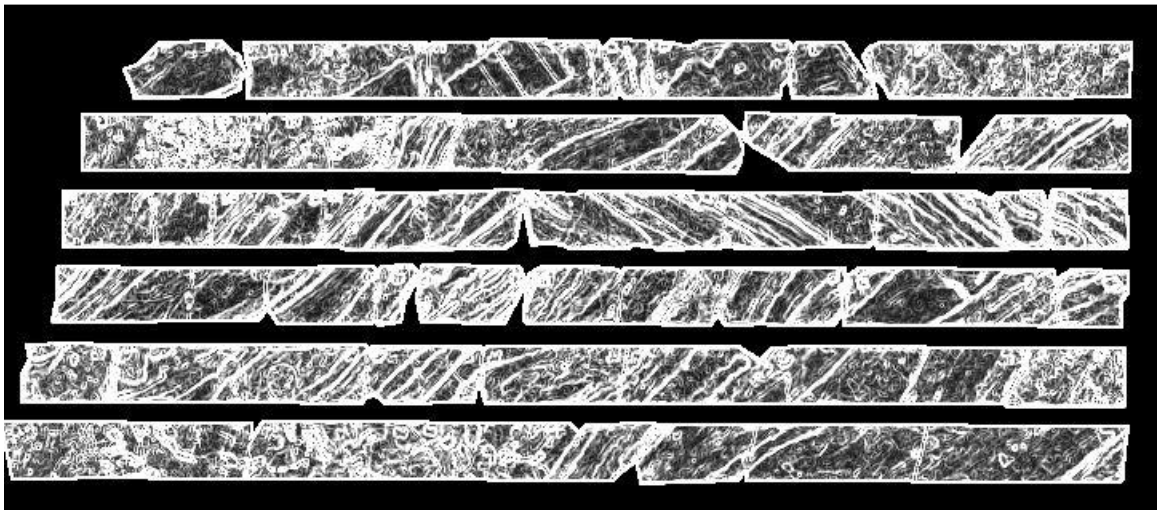


Full MNF

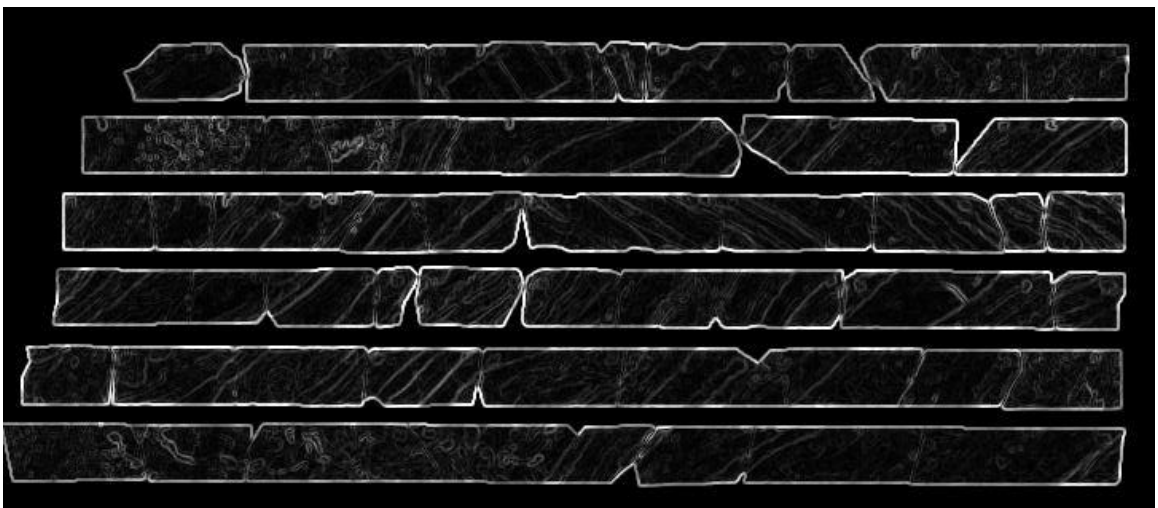


11. Gradient-Based Edge Detection Algorithm: South Africa Core Samples

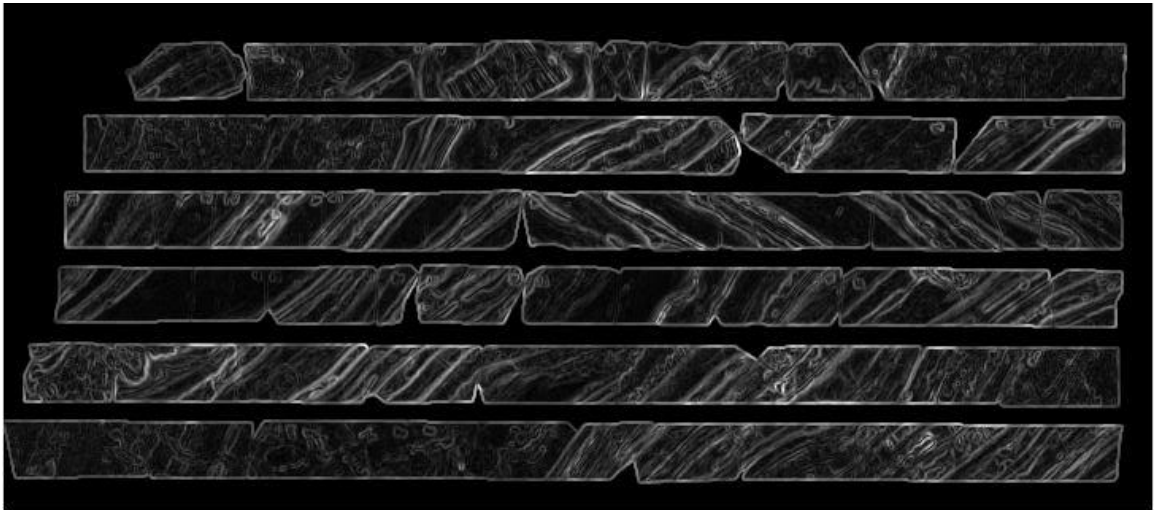
Reflectance



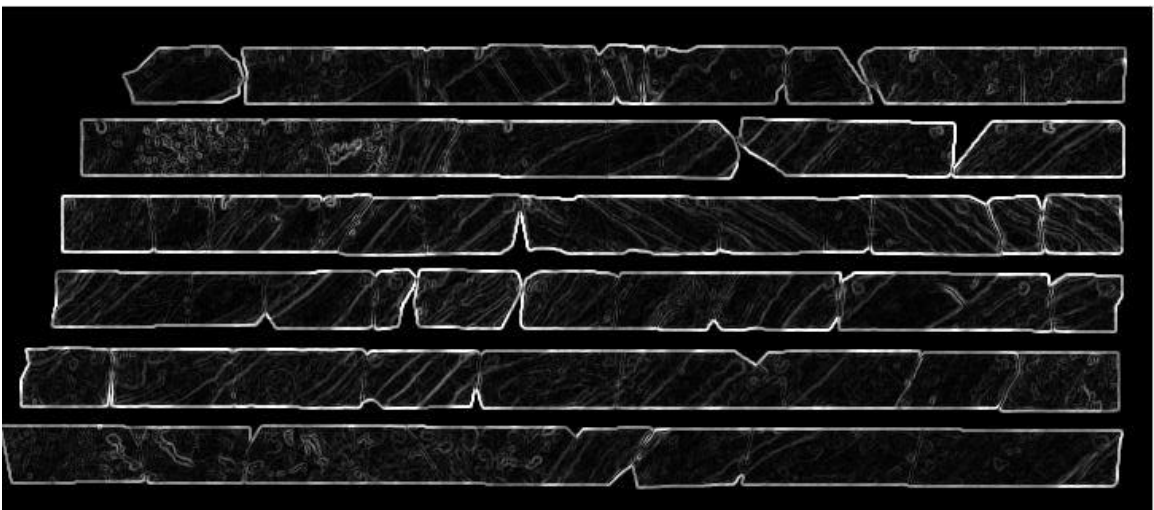
Optimal PCA



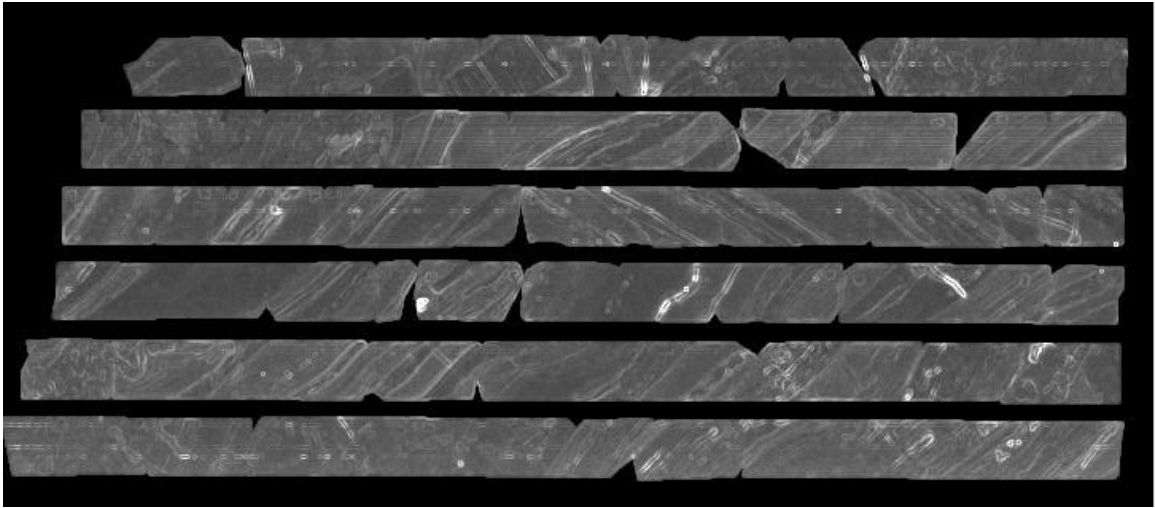
Optimal MNF



Full PCA

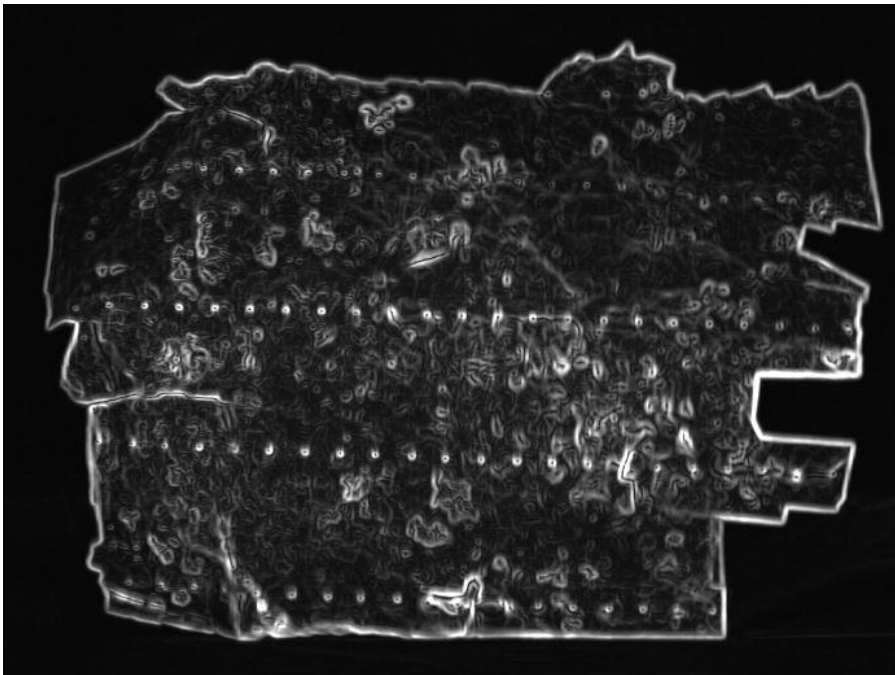


Full MNF

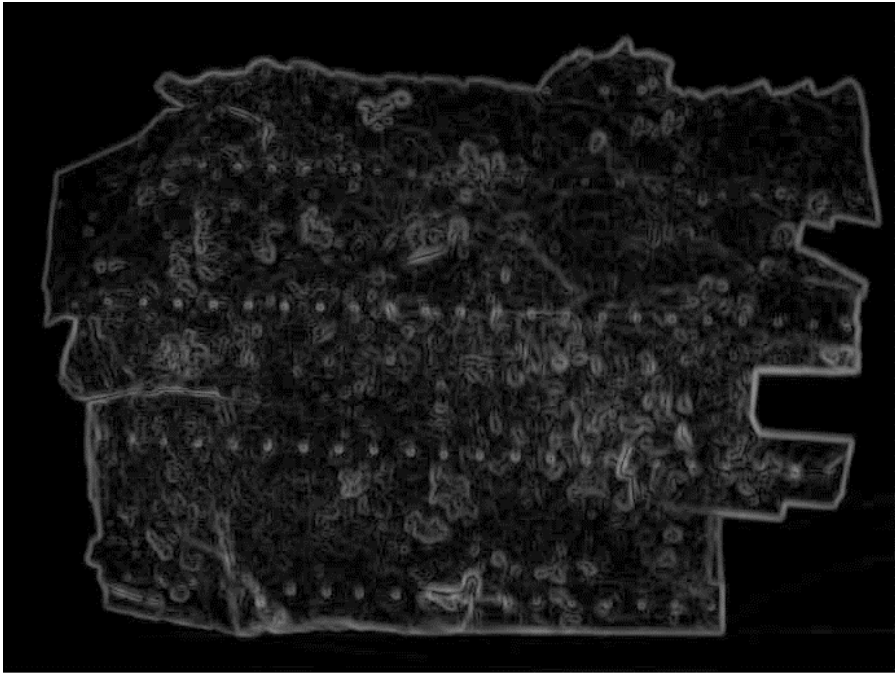


12. Gradient-Based Edge Detection Algorithm: Aluminum Panel

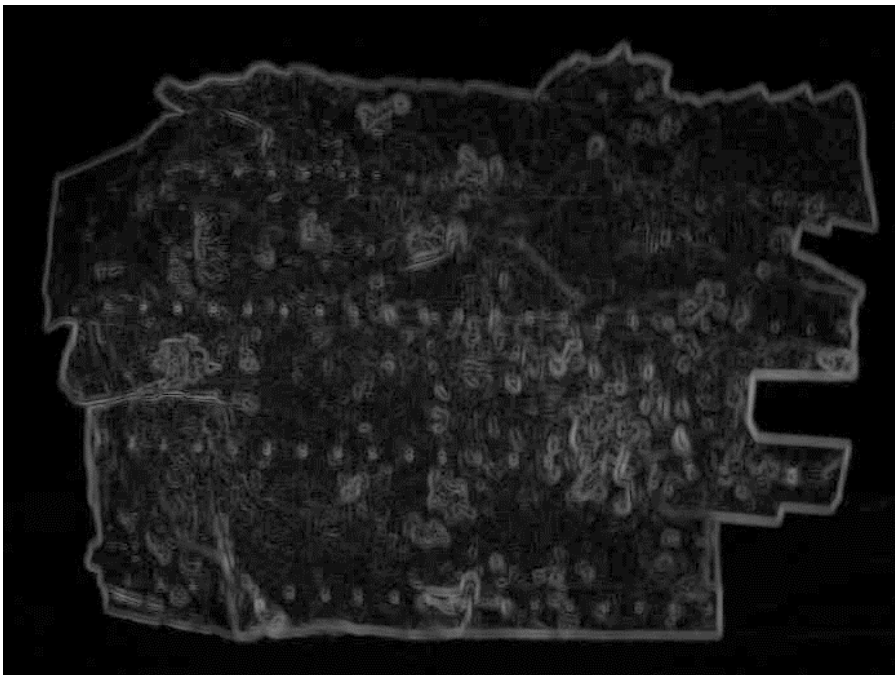
Reflectance



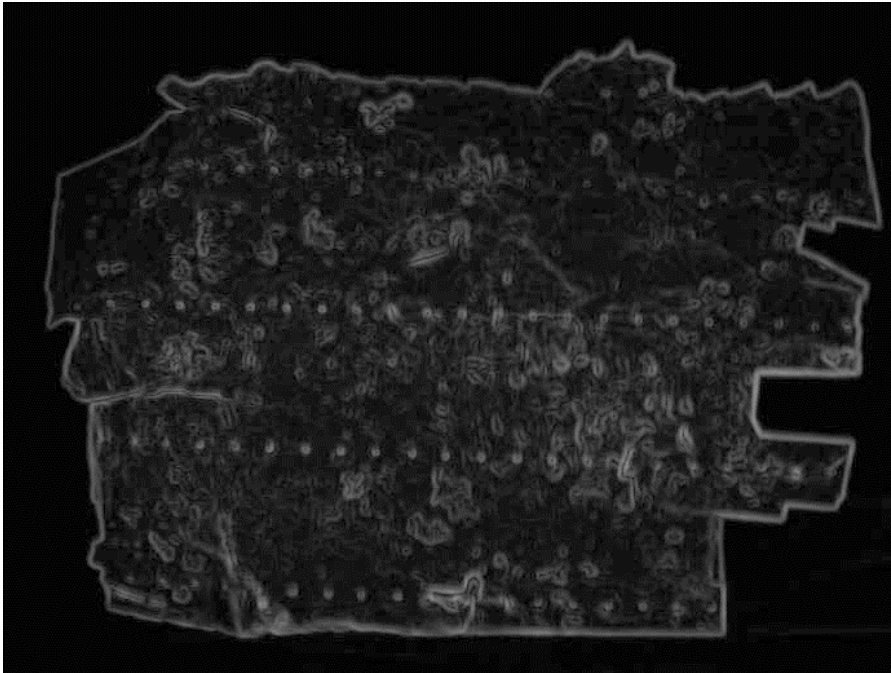
Optimal PCA



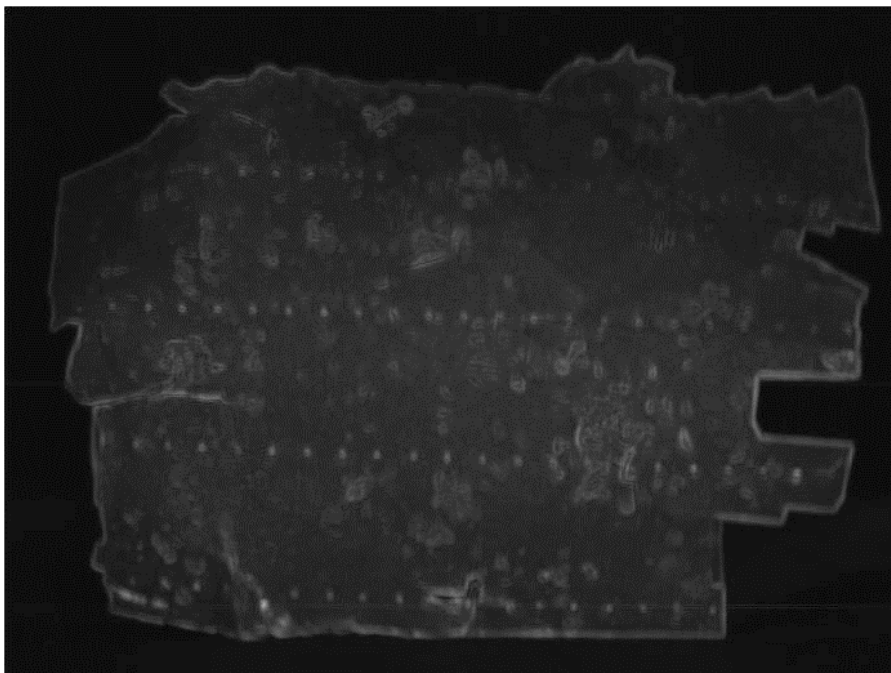
Optimal MNF



Full PCA

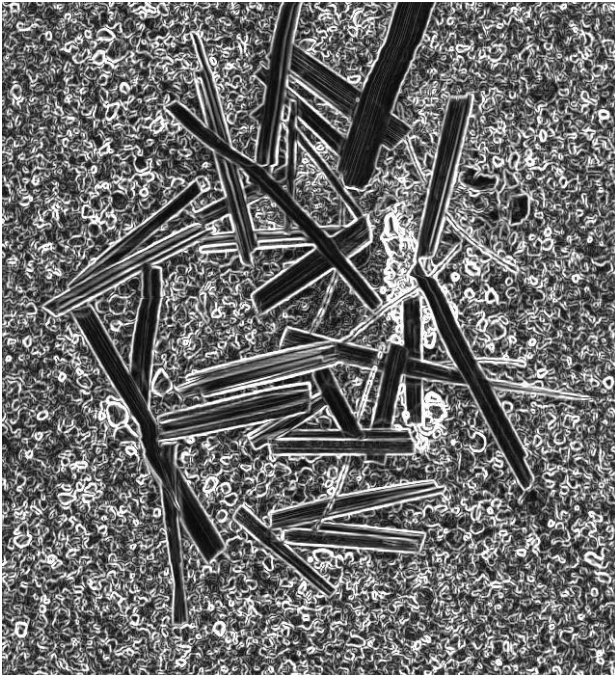


Full MNF

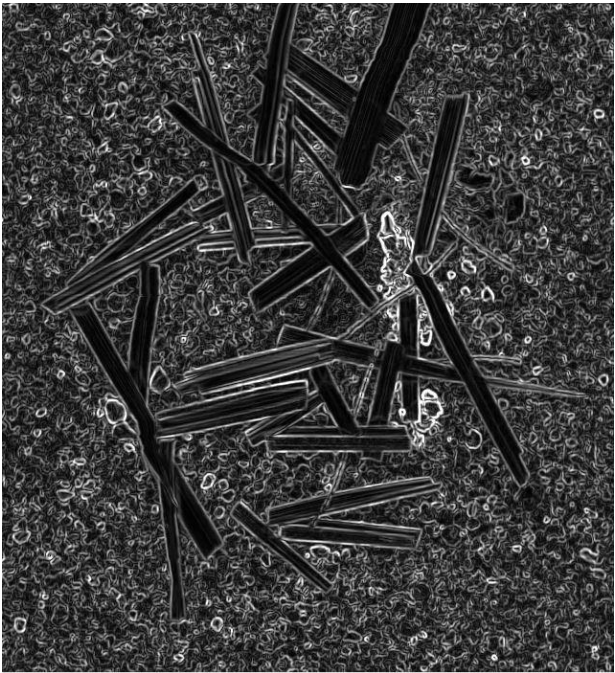


13. Gradient-Based Edge Detection Algorithm: Rare Target on Sand

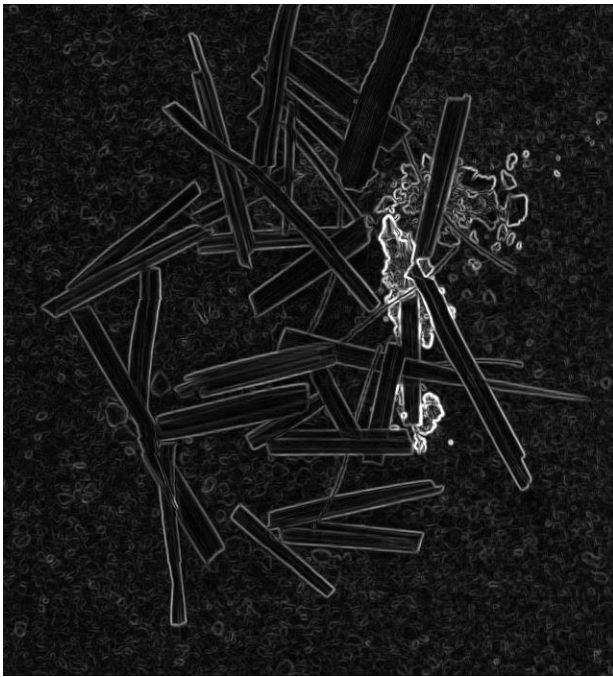
Reflectance



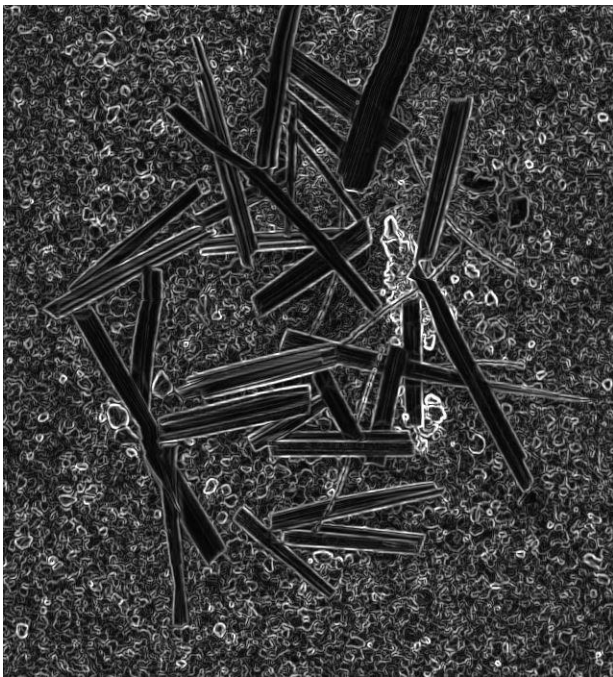
Optimal PCA



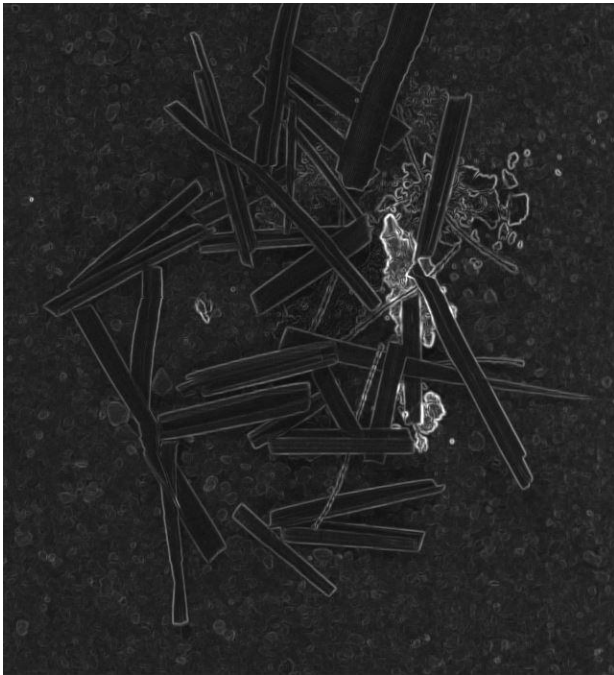
Optimal MNF



Full PCA

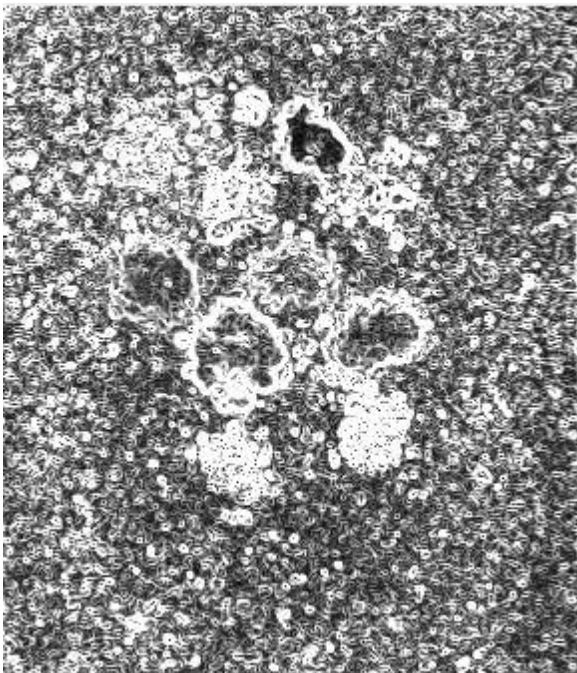


Full MNF

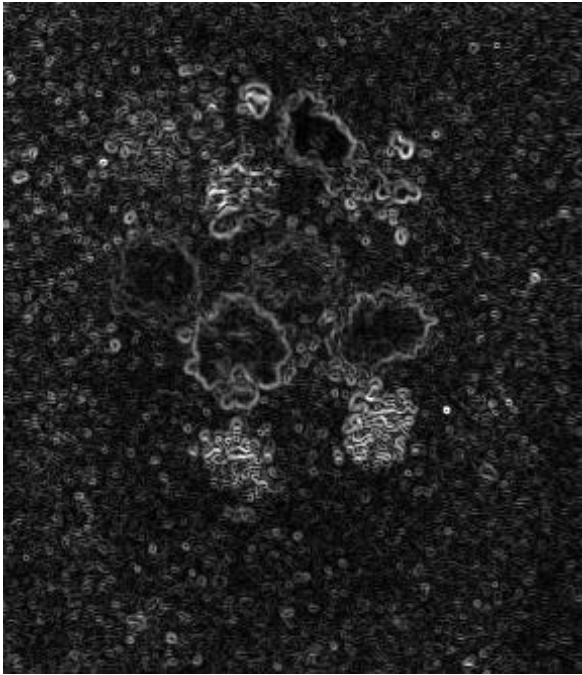


14. Gradient-Based Edge Detection Algorithm: Chemical Array

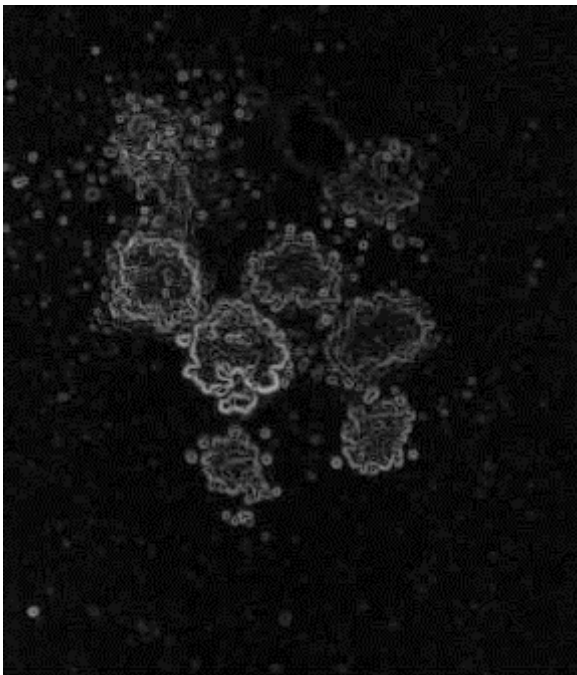
Reflectance



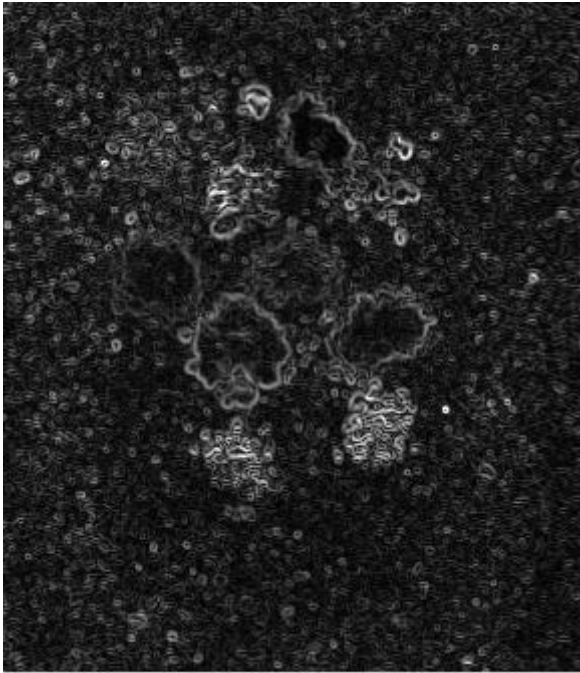
Optimal PCA



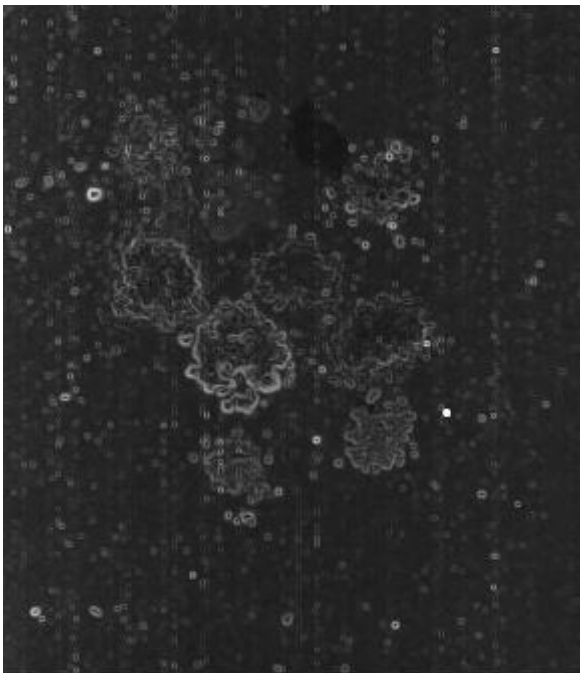
Optimal MNF



Full PCA

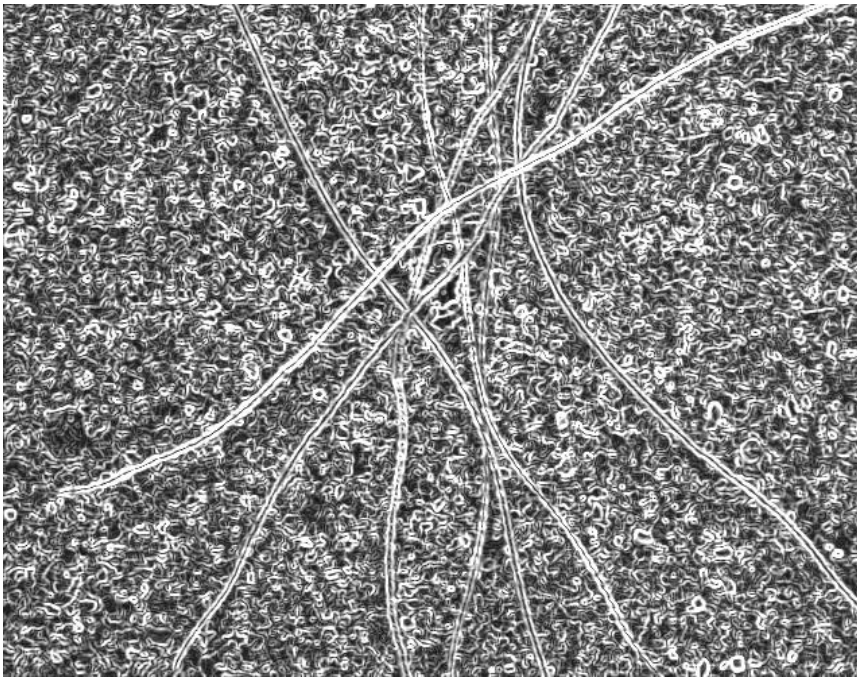


Full MNF

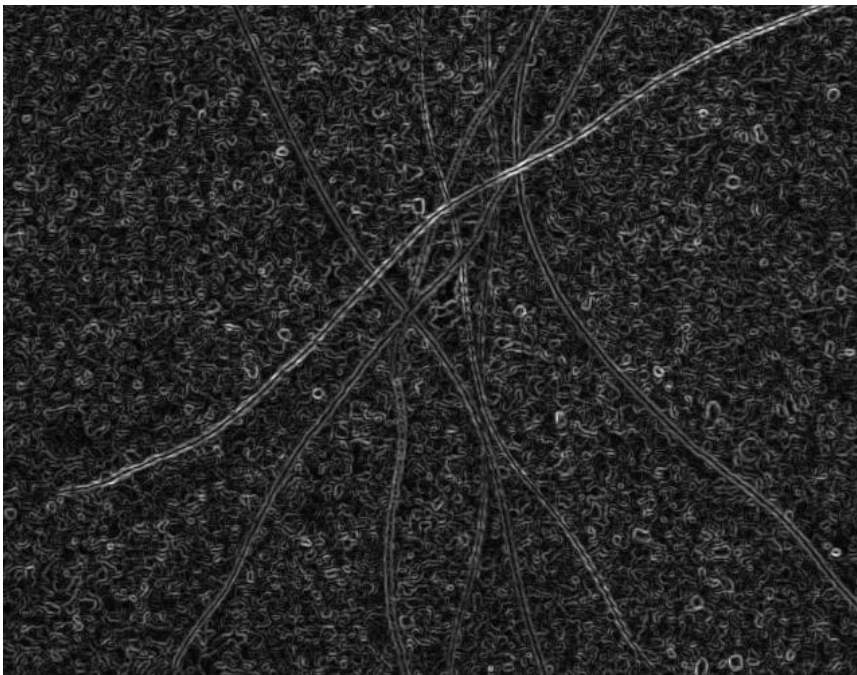


15. Gradient-Based Edge Detection Algorithm: Cloth Threads

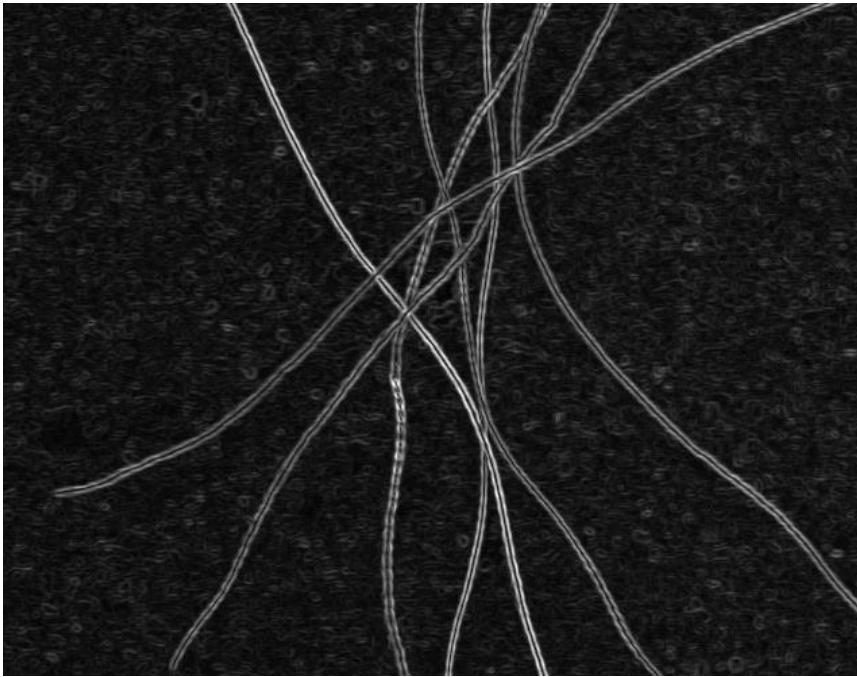
Reflectance



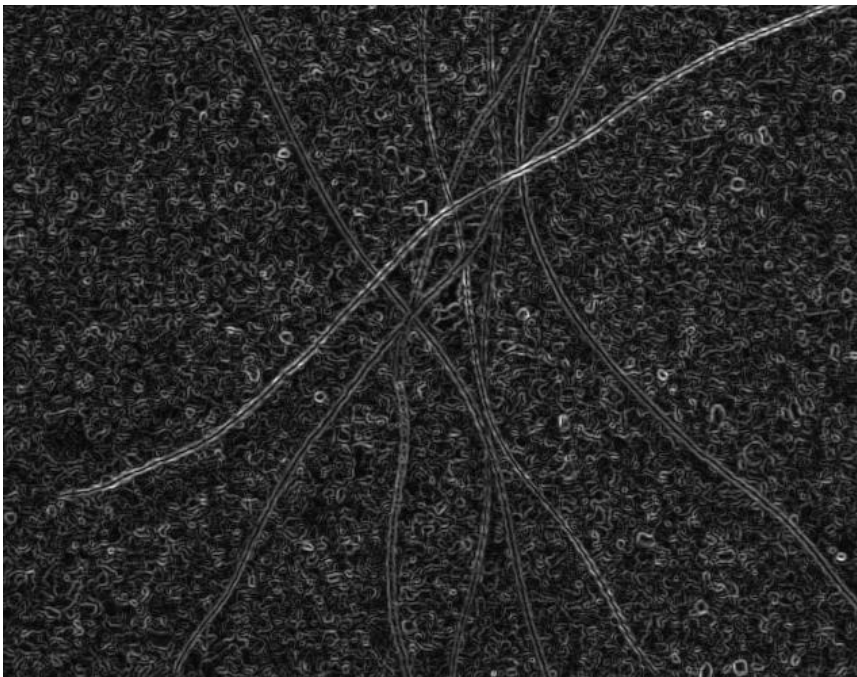
Optimal PCA



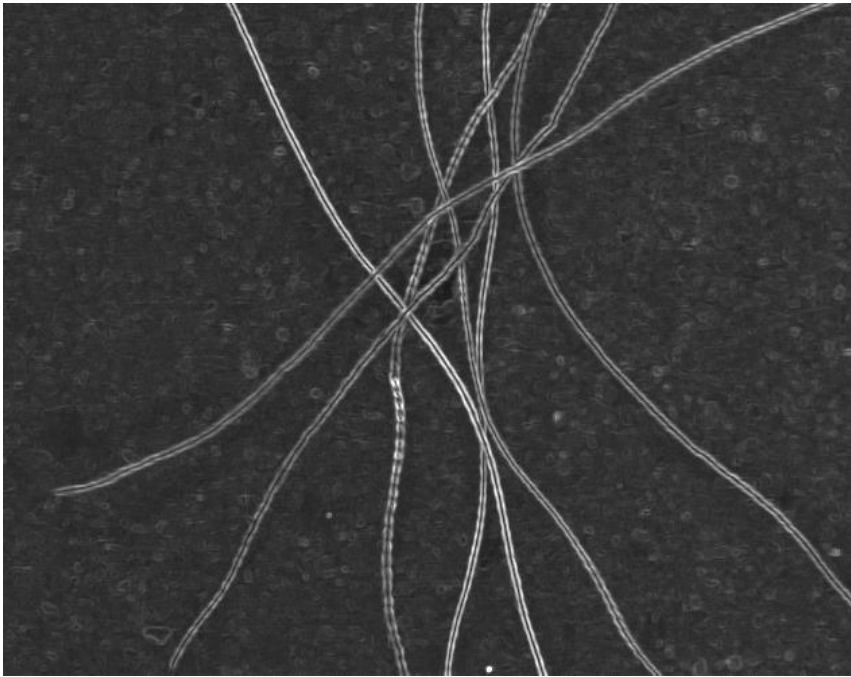
Optimal MNF



Full PCA



Full MNF



HySPADE Edge Detection Results

1. HySPADE Edge Detection Algorithm: Reno

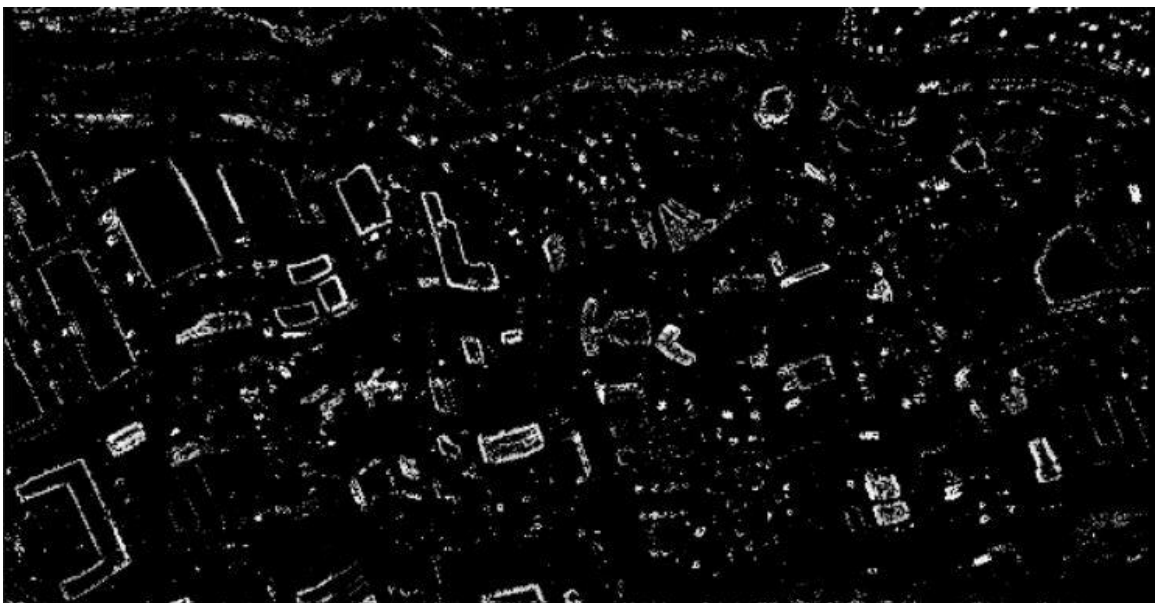
Reflectance



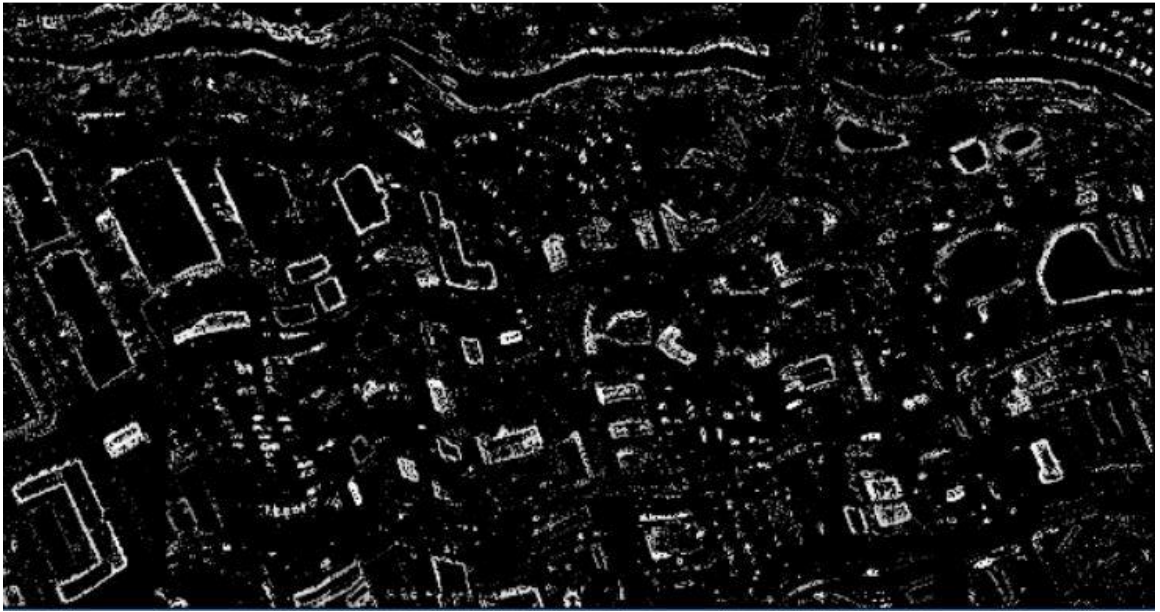
Optimal PCA



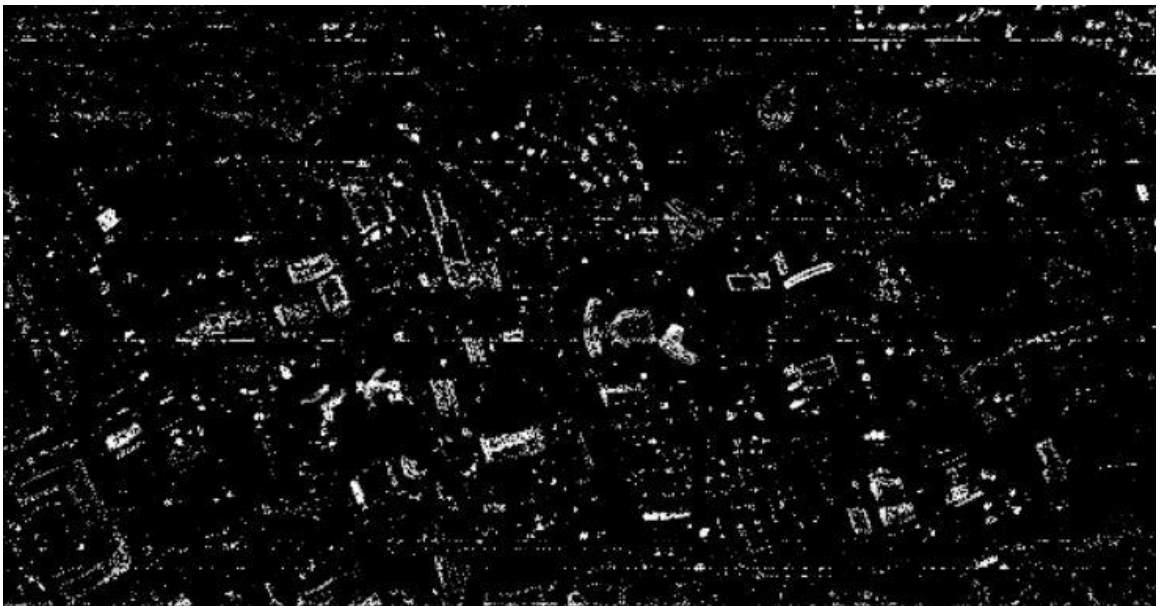
Optimal MNF



Full PCA

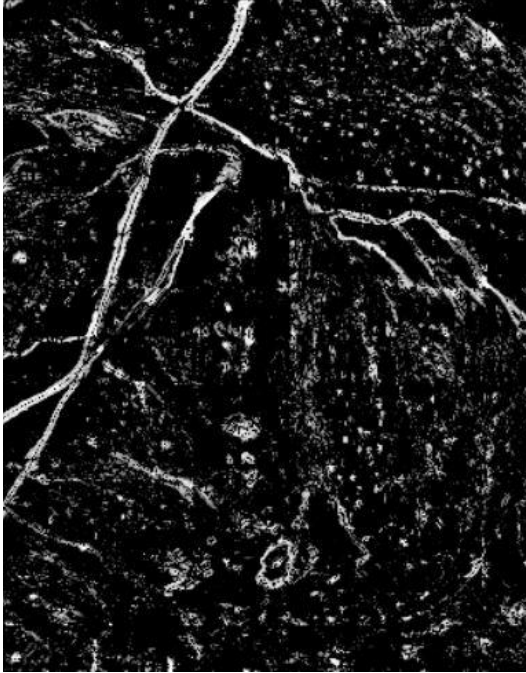


Full MNF

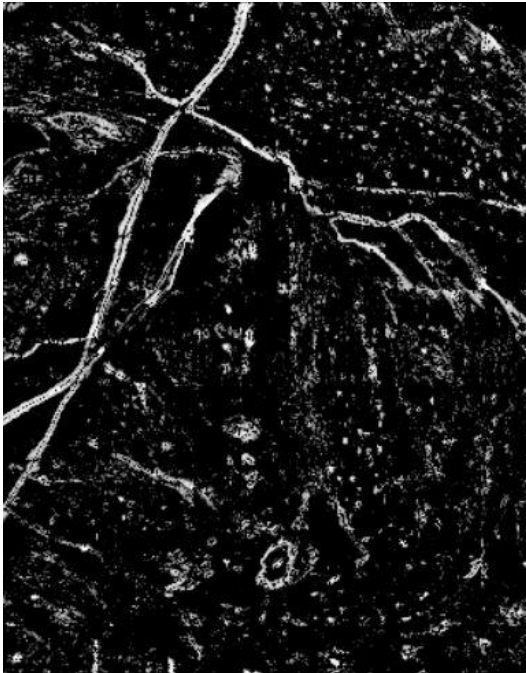


2. HySPADE Edge Detection Algorithm: Cuprite Flight Line #1

Reflectance



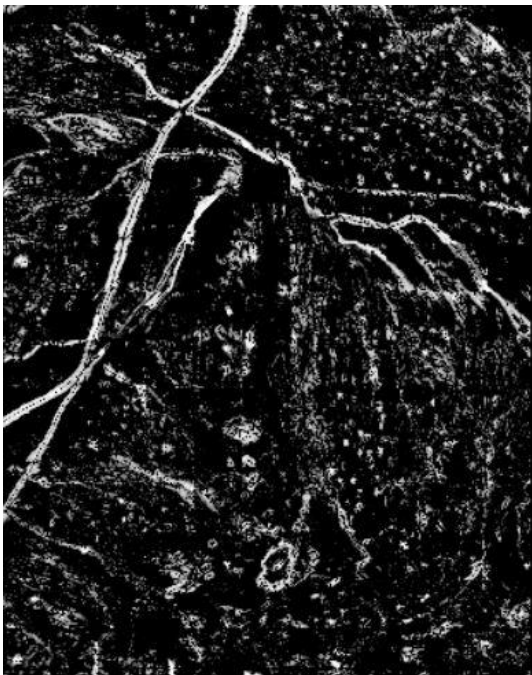
Optimal PCA



Optimal MNF



Full PCA



Full MNF



3. HySPADE Edge Detection Algorithm: Cuprite Flight Line #2

Reflectance



Optimal PCA



Optimal MNF



Full PCA



Full MNF



4. HySPADE Edge Detection Algorithm: Cuprite Flight Line #3

Reflectance



Optimal PCA



Optimal MNF



Full PCA

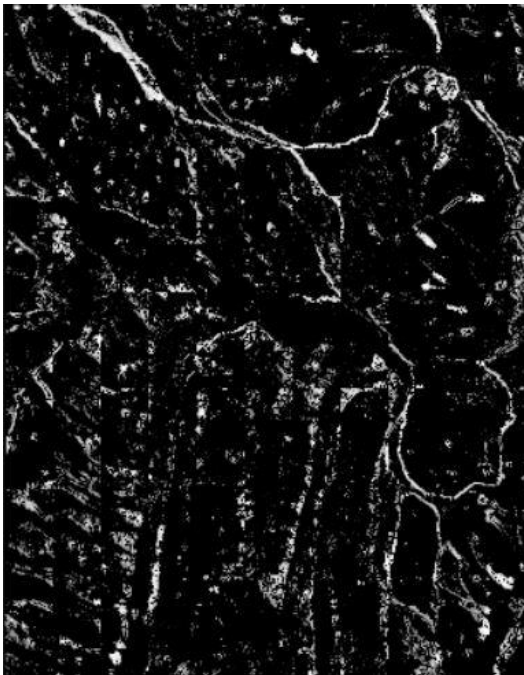


Full MNF

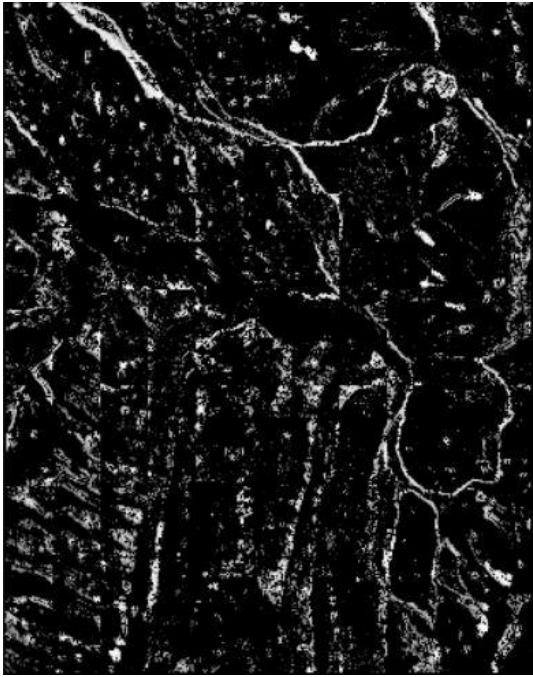


5. HySPADE Edge Detection Algorithm: Cuprite Flight Line #4

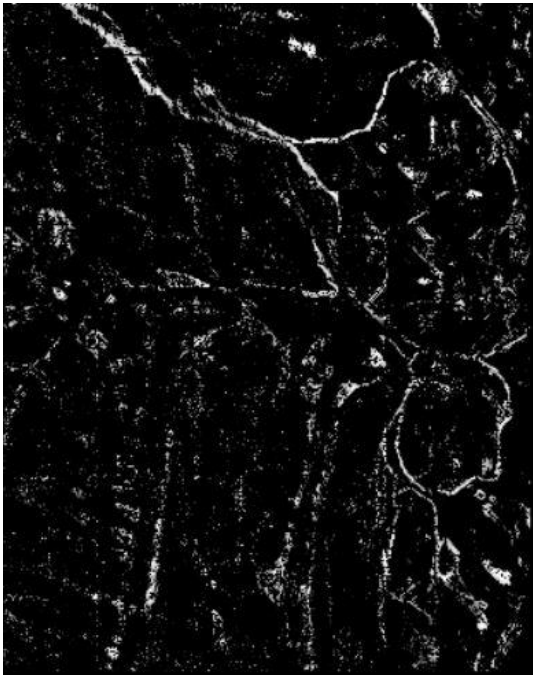
Reflectance



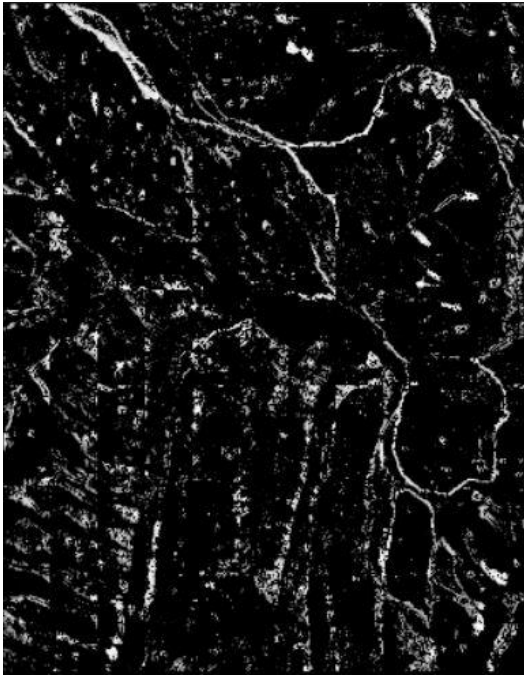
Optimal PCA



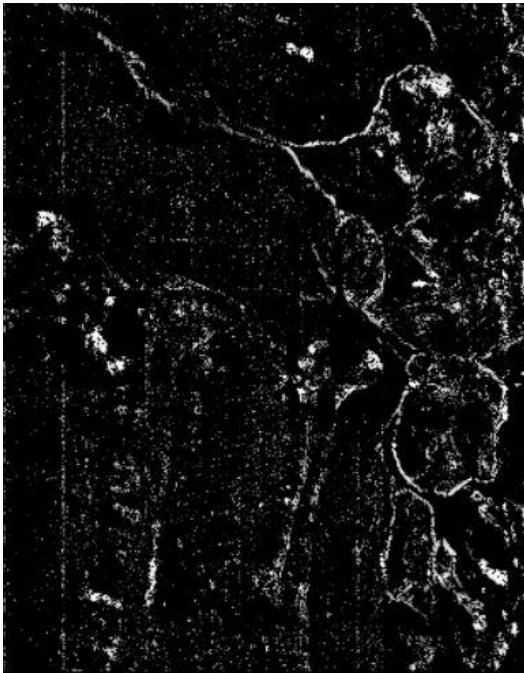
Optimal MNF



Full PCA

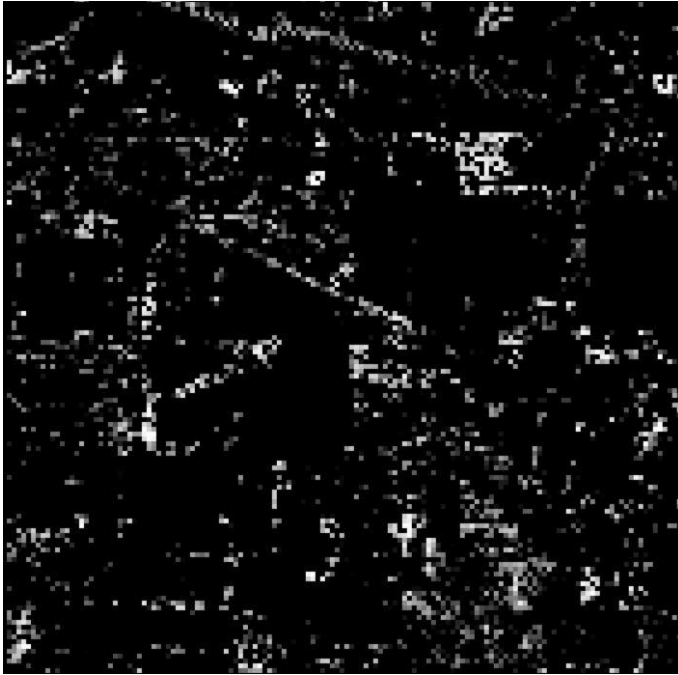


Full MNF



6. HySPADE Edge Detection Algorithm: Indian Pines

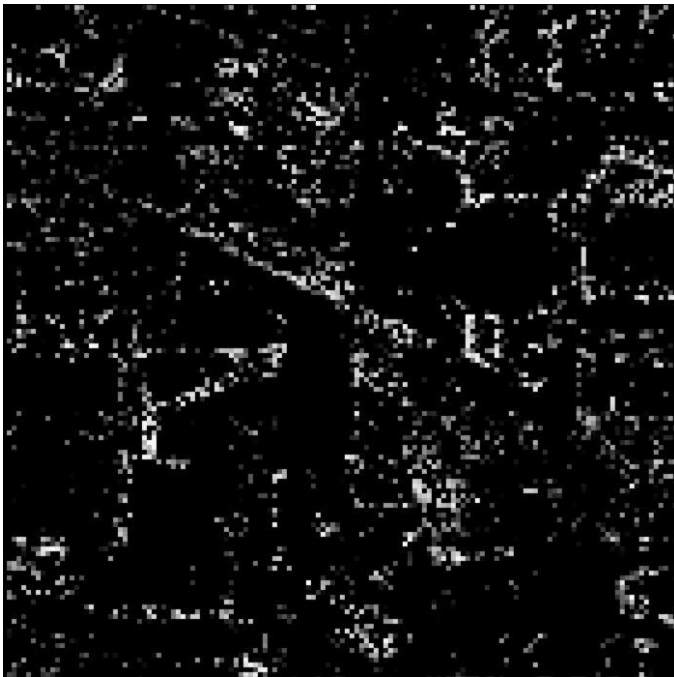
Reflectance



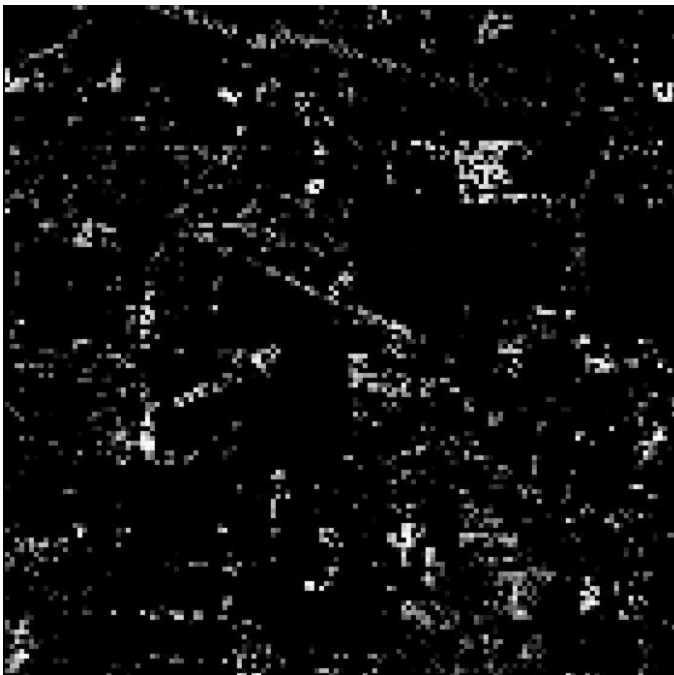
Optimal PCA



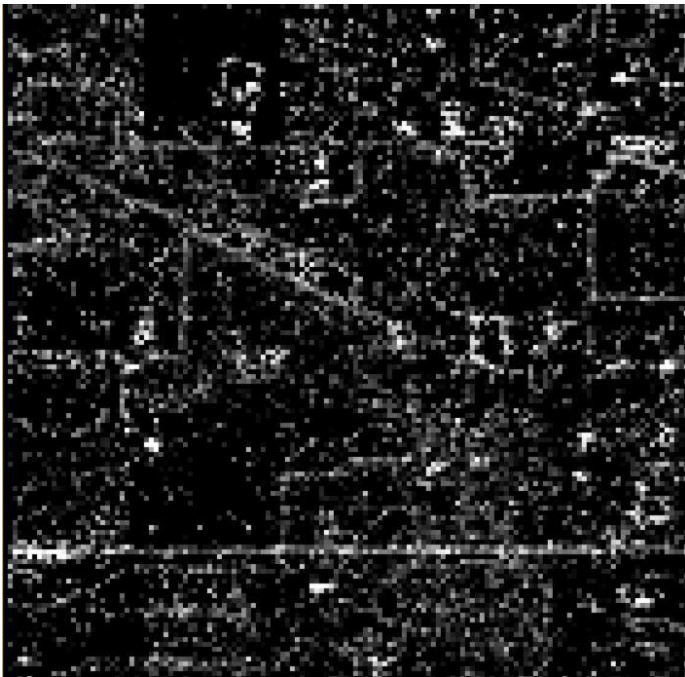
Optimal MNF



Full PCA

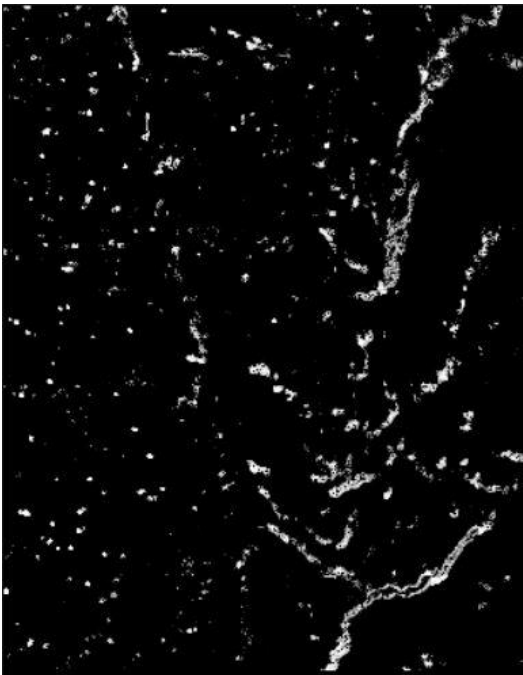


Full MNF

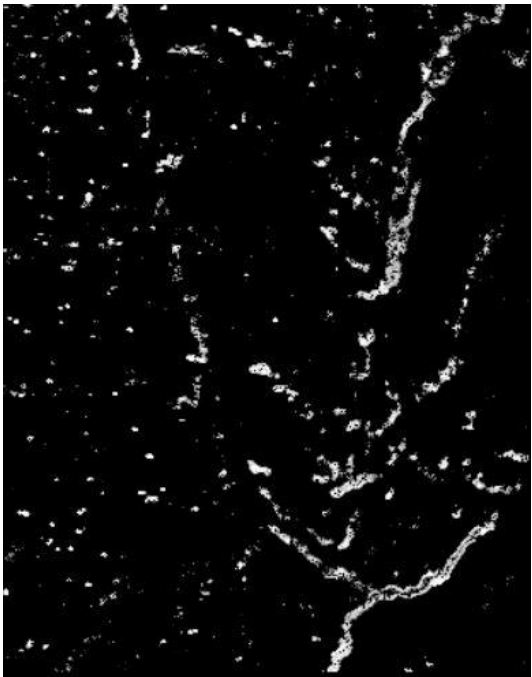


7. HySPADE Edge Detection Algorithm: Deepwater Horizon

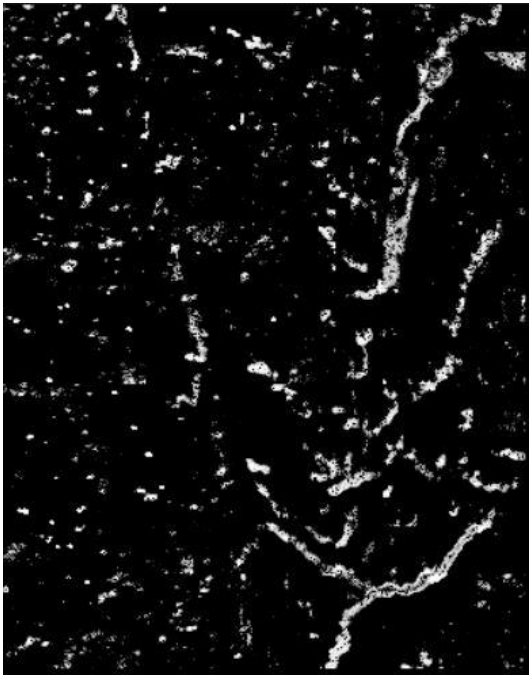
Radiance



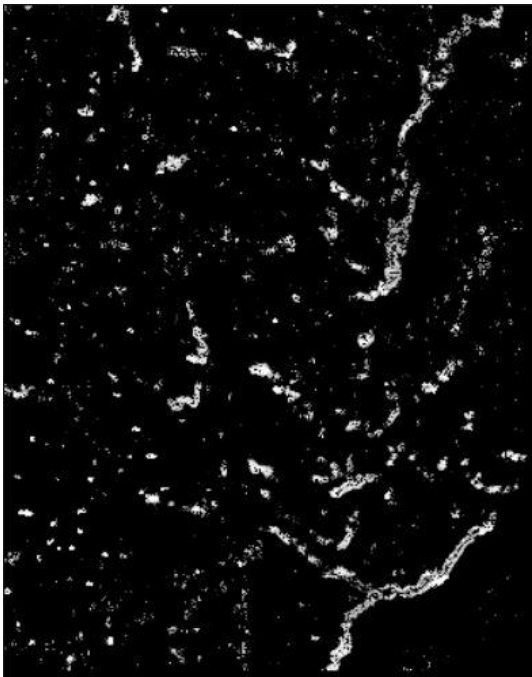
Reflectance



Optimal PCA



Optimal MNF



Full PCA

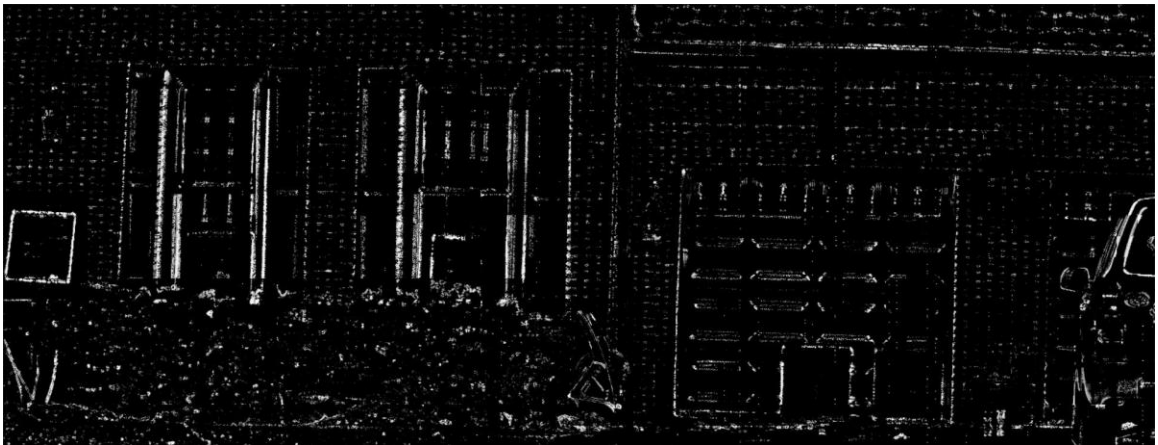


Full MNF

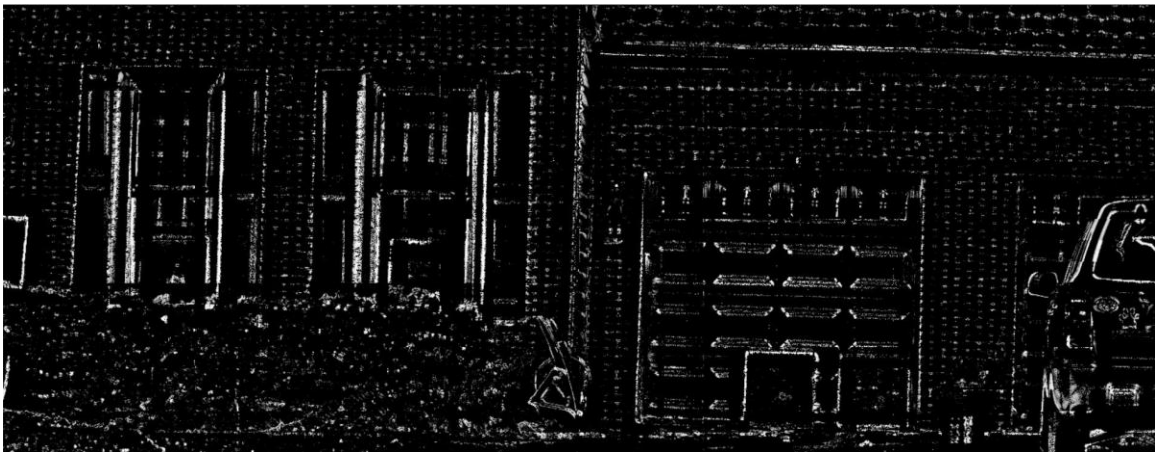


8. HySPADE Edge Detection Algorithm: Larkhaven

Reflectance



Optimal PCA



Optimal MNF



Full PCA

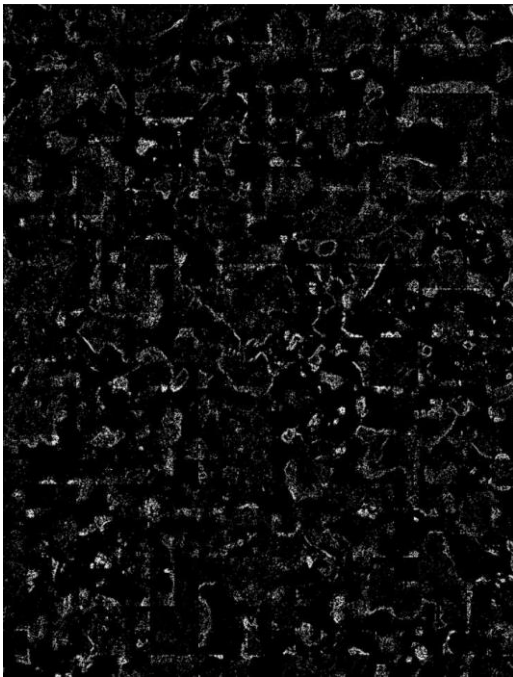


Full MNF

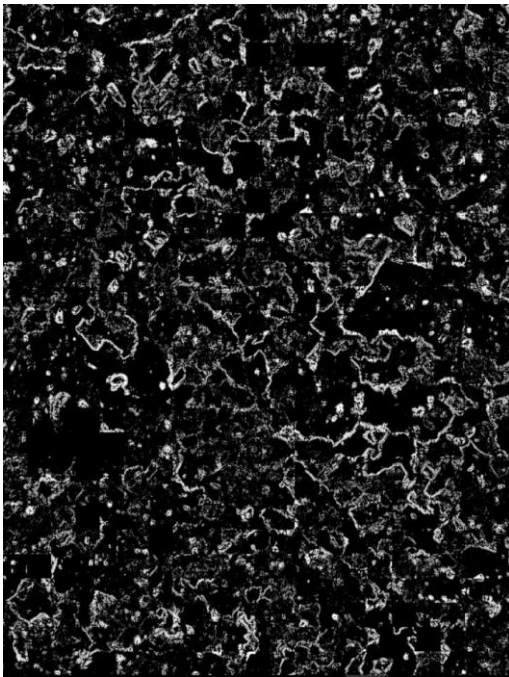


9. HySPADE Edge Detection Algorithm: Granite VNIR

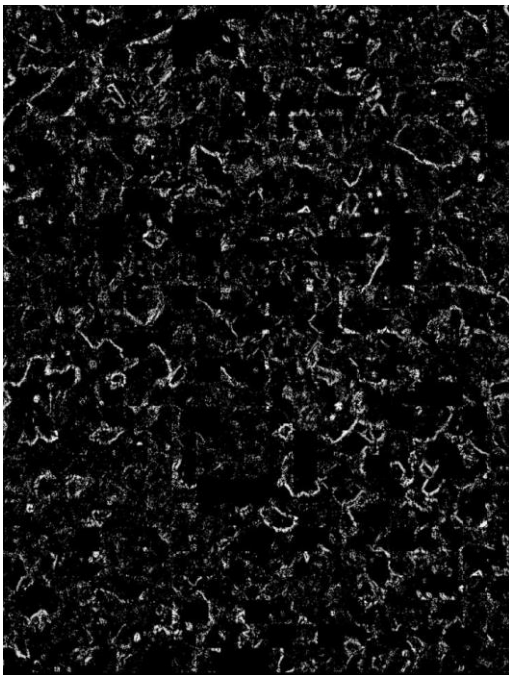
Reflectance



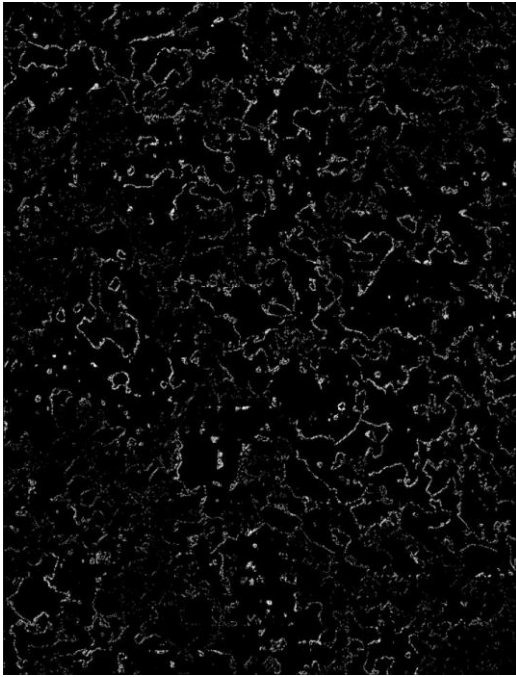
Optimal PCA



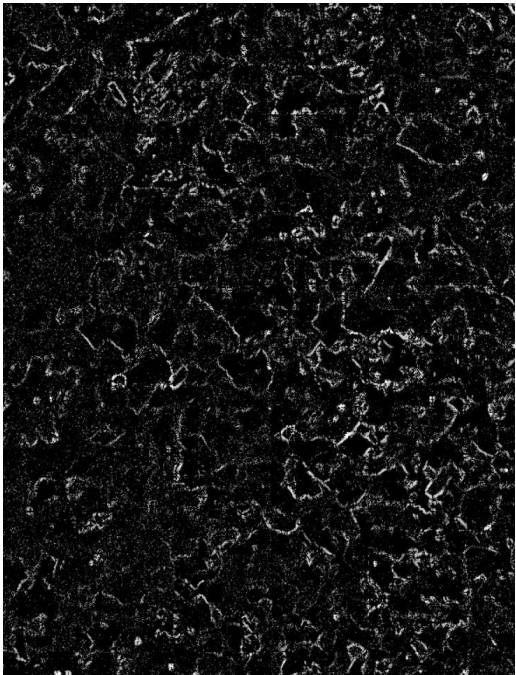
Optimal MNF



Full PCA

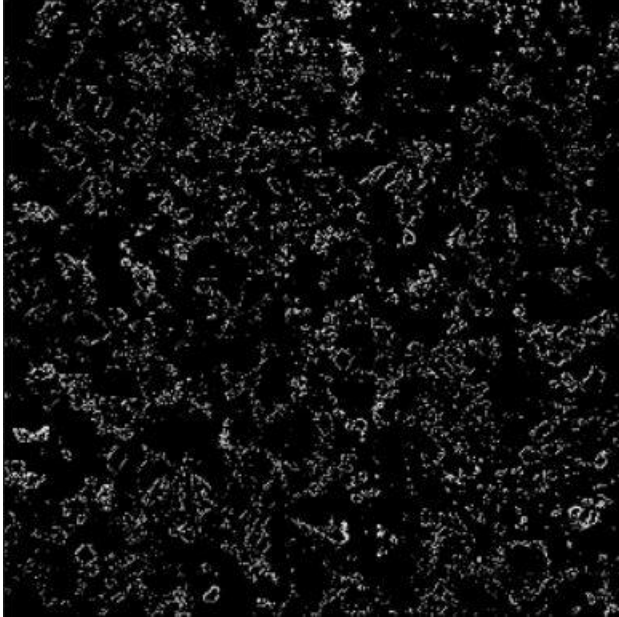


Full MNF

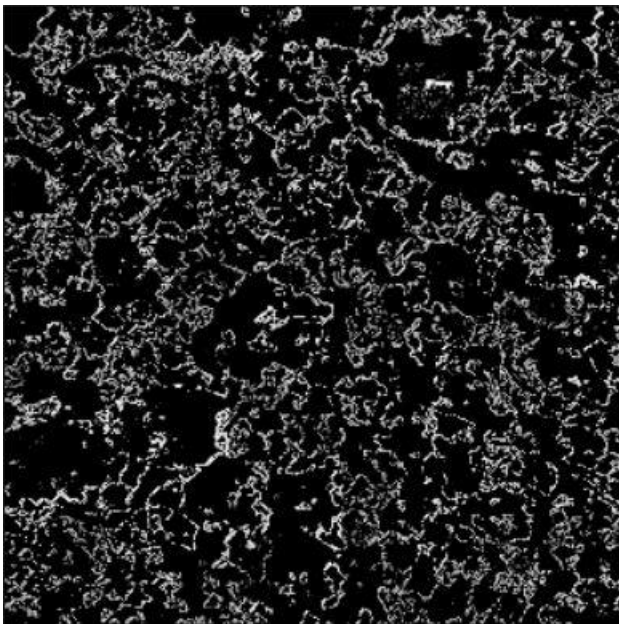


10. HySPADE Edge Detection Algorithm: Granite NIR/SWIR

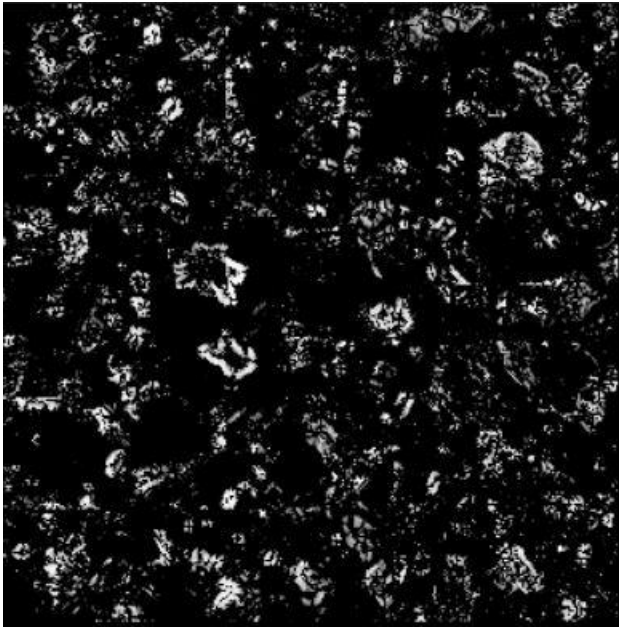
Reflectance



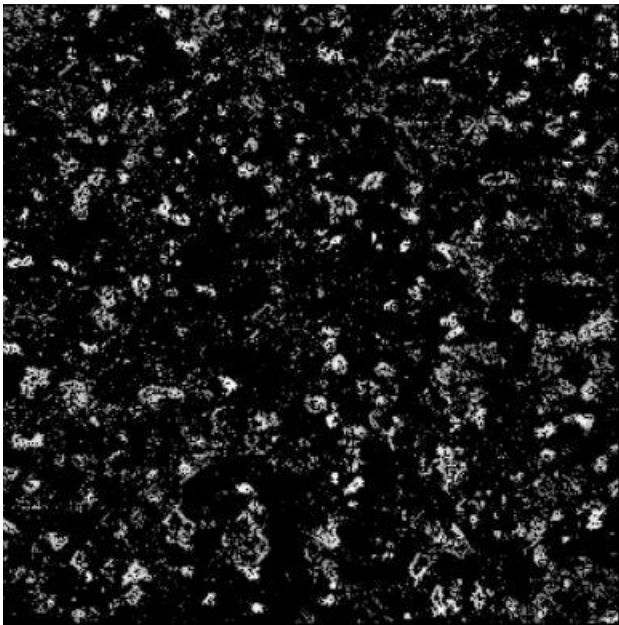
Optimal PCA



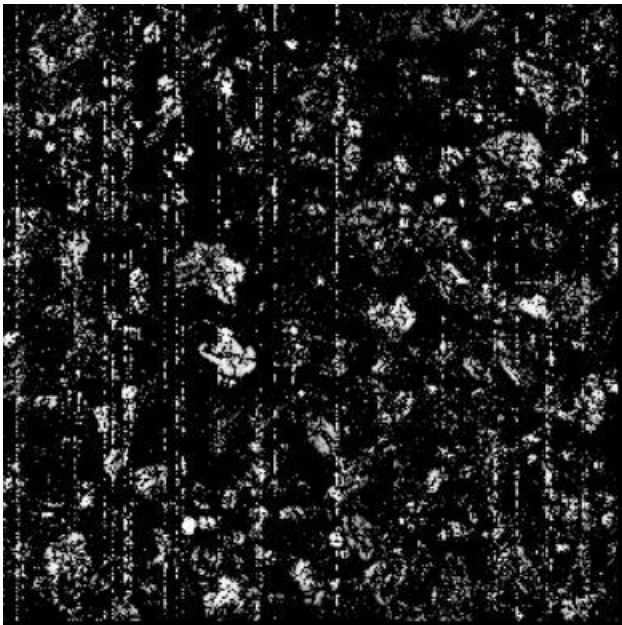
Optimal MNF



Full PCA

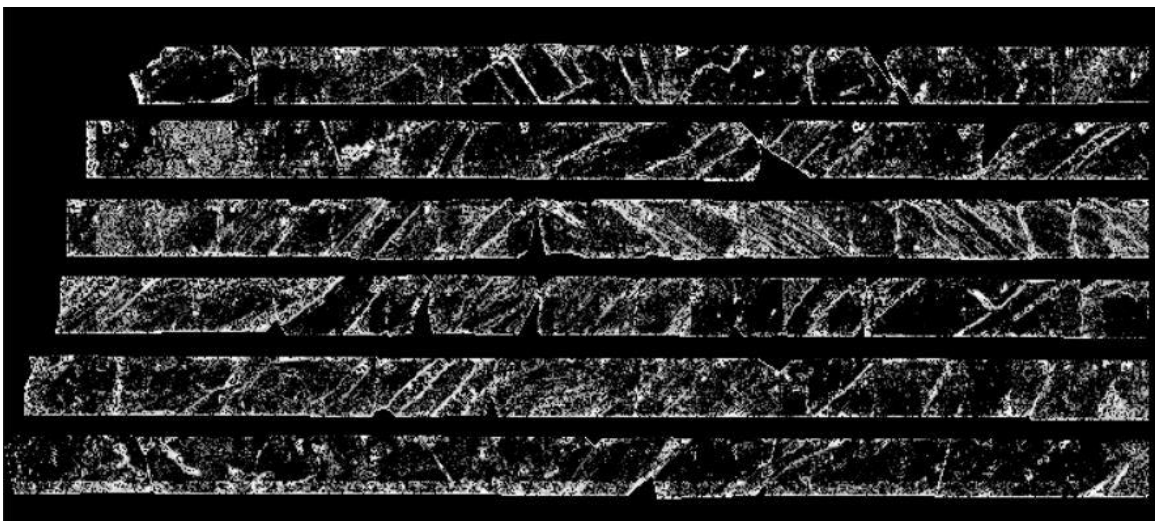


Full MNF

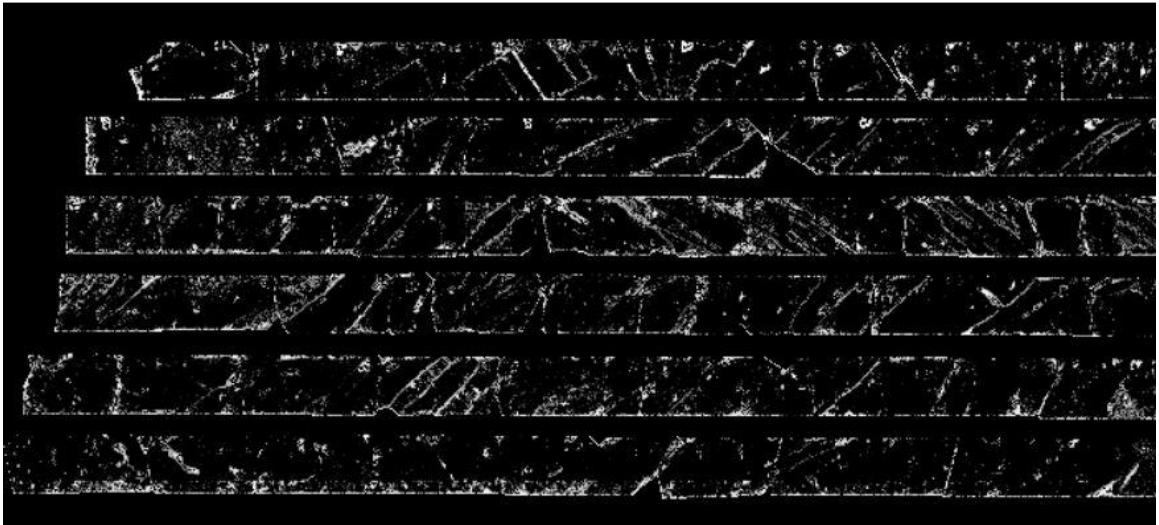


11. HySPADE Edge Detection Algorithm: South Africa Core Samples

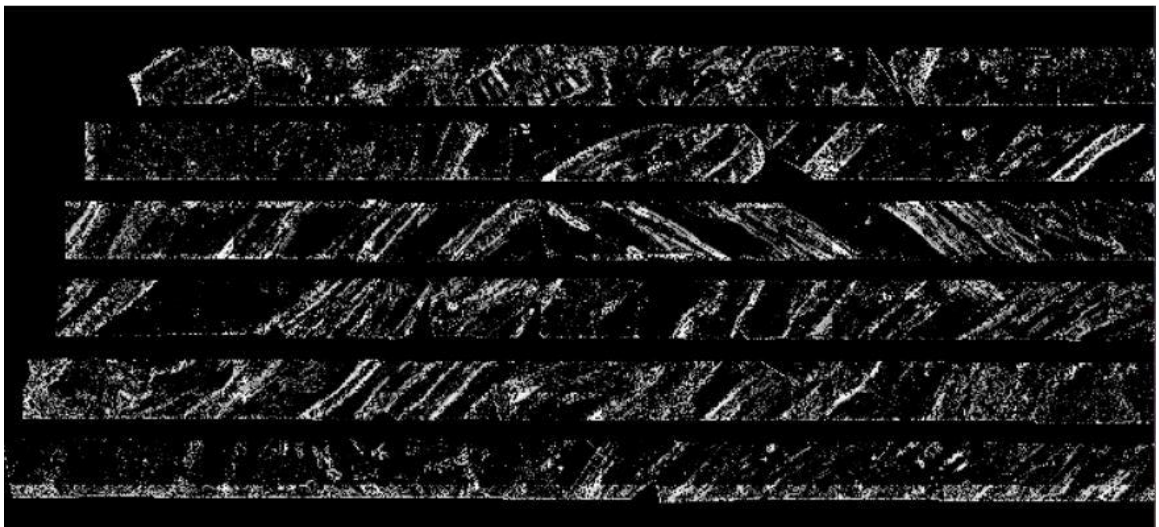
Reflectance



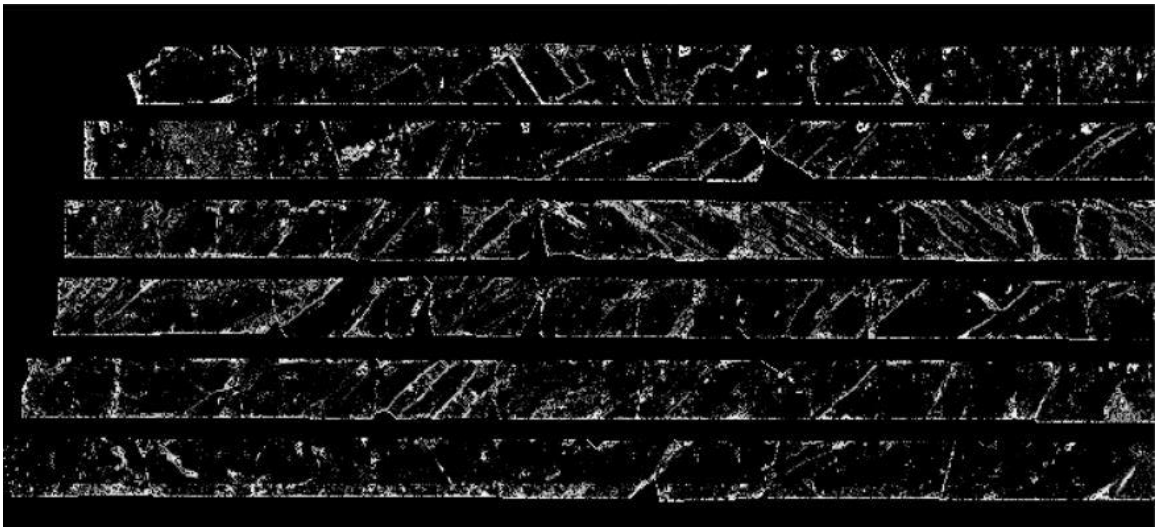
Optimal PCA



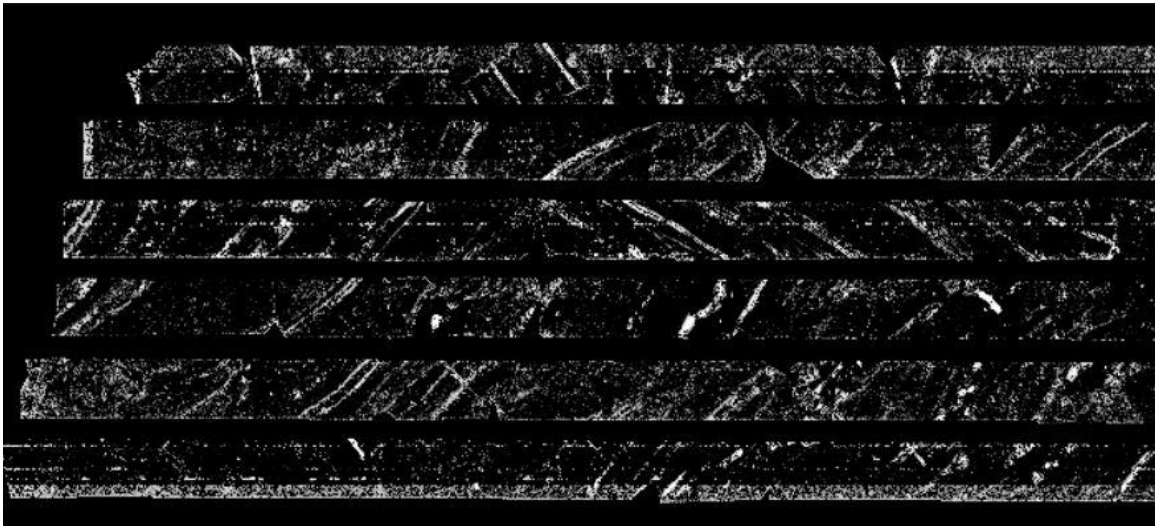
Optimal MNF



Full PCA



Full MNF

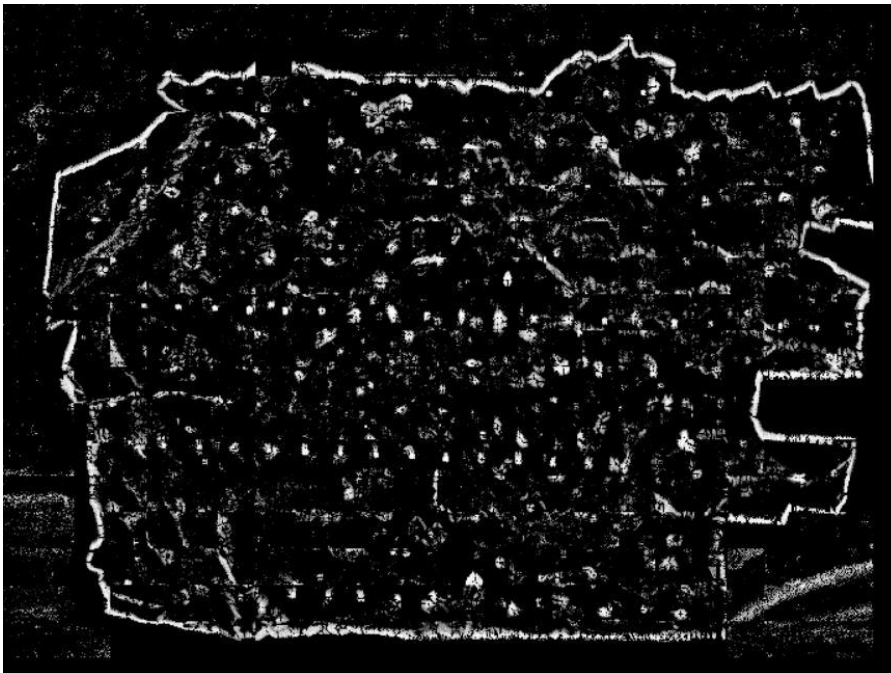


12. HySPADE Edge Detection Algorithm: Aluminum Panel

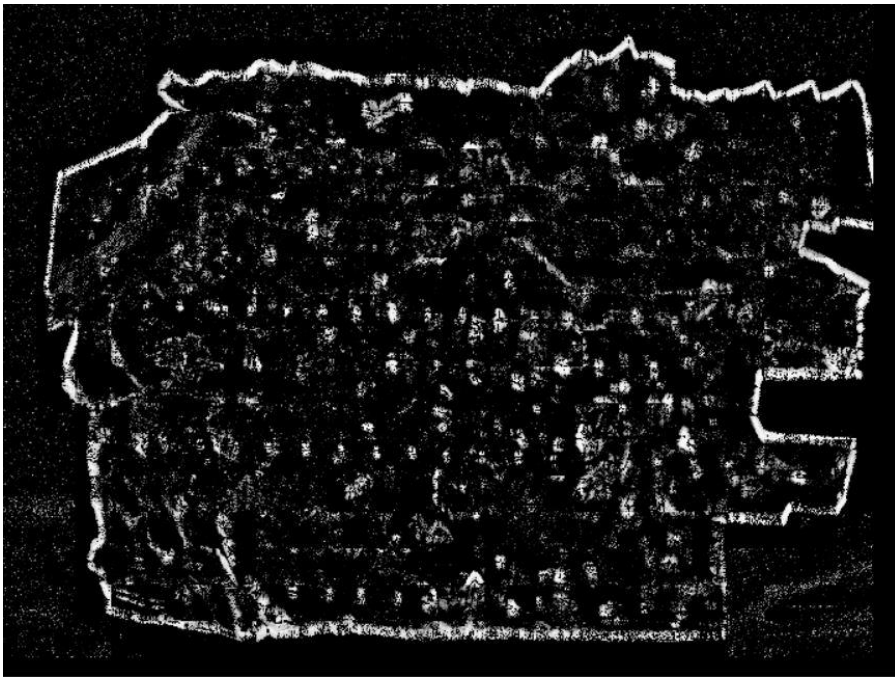
Reflectance



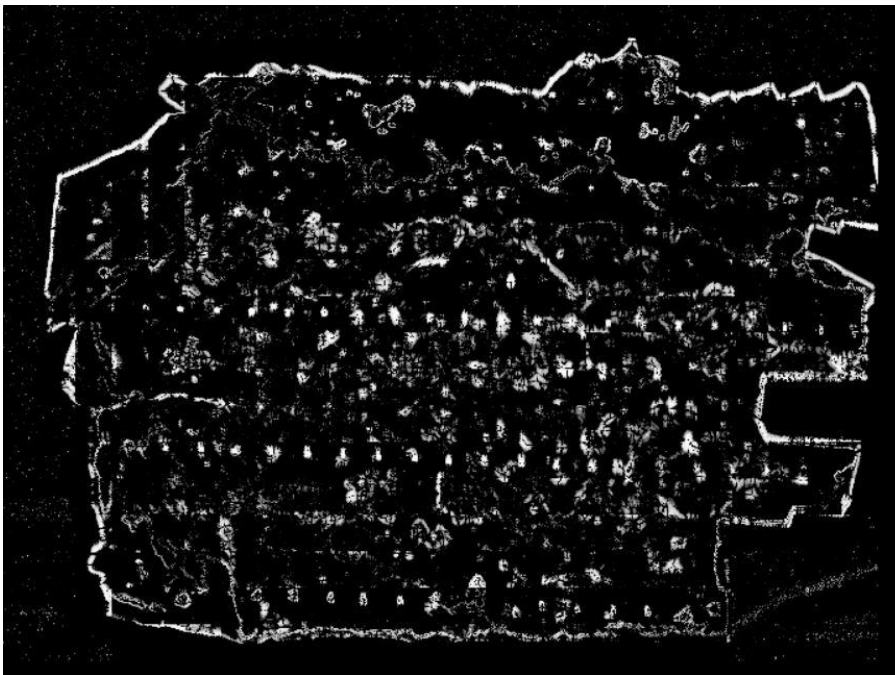
Optimal PCA



Optimal MNF



Full PCA

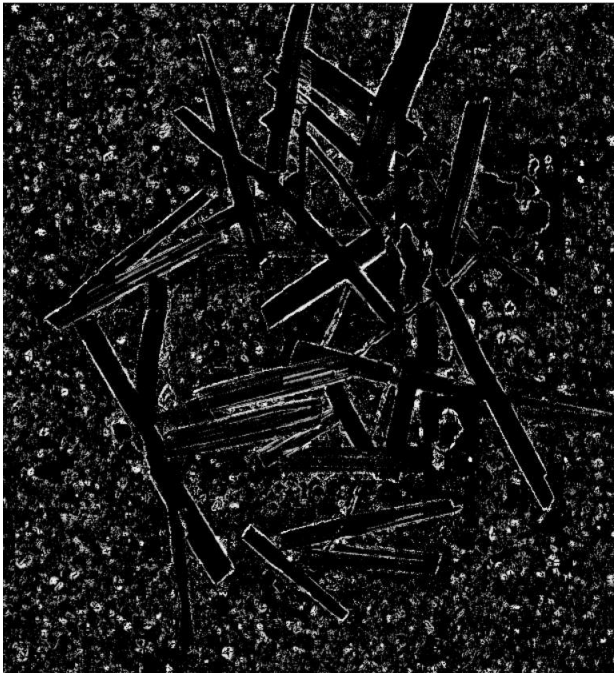


Full MNF

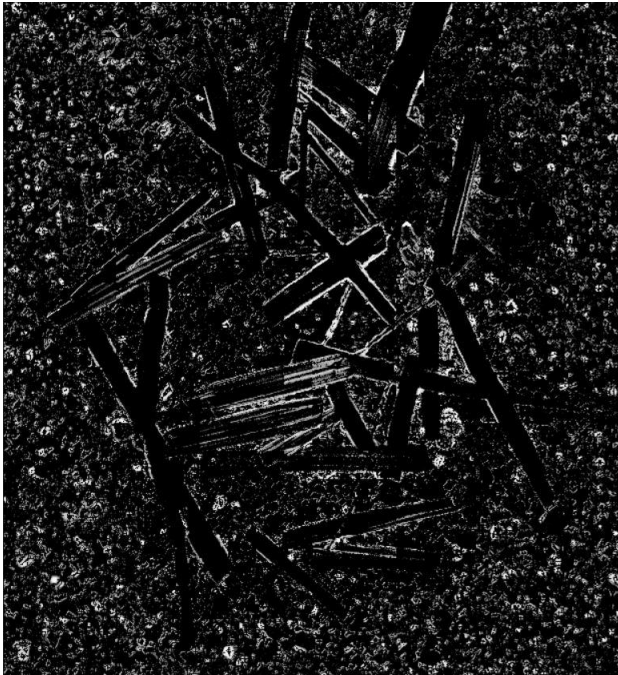


13. HySPADE Edge Detection Algorithm: Rare Target on Sand

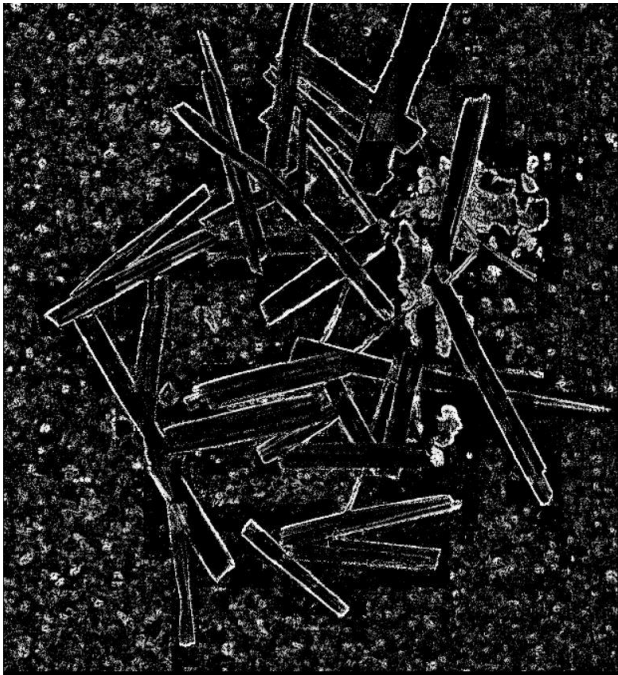
Reflectance



Optimal PCA



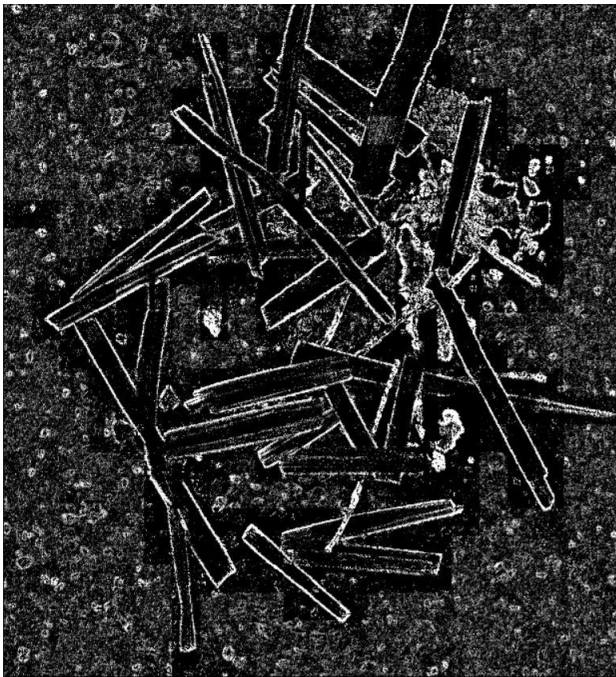
Optimal MNF



Full PCA

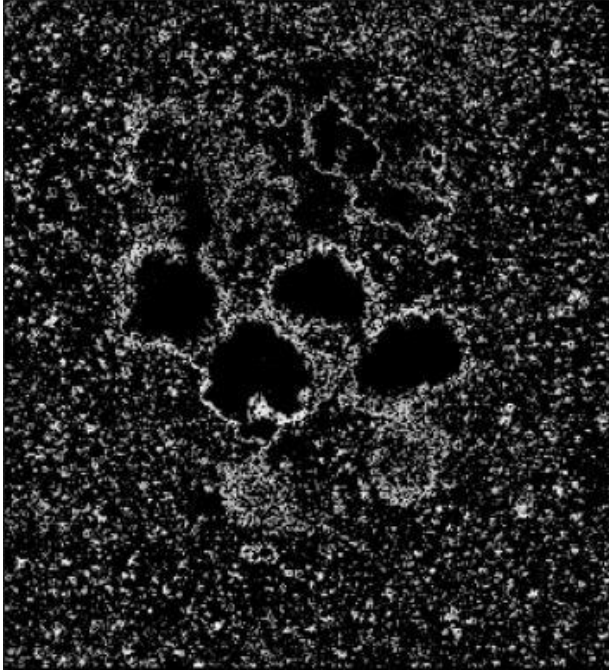


Full MNF



14. HySPADE Edge Detection Algorithm: Chemical Array

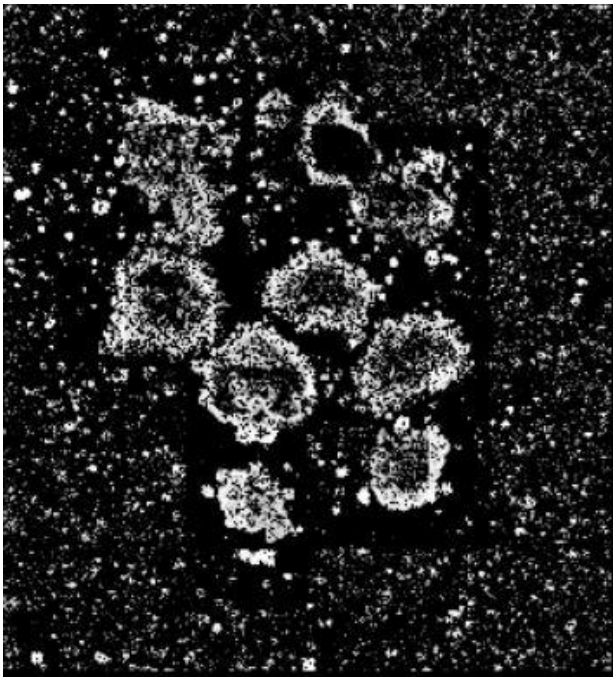
Reflectance



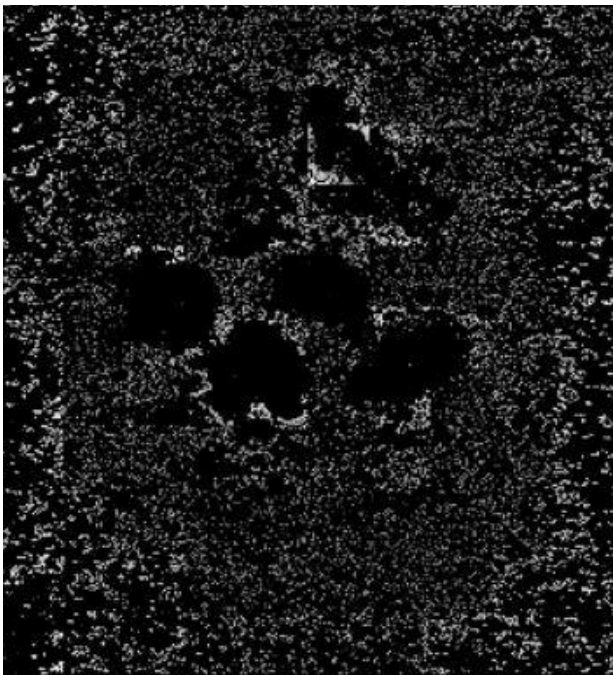
Optimal PCA



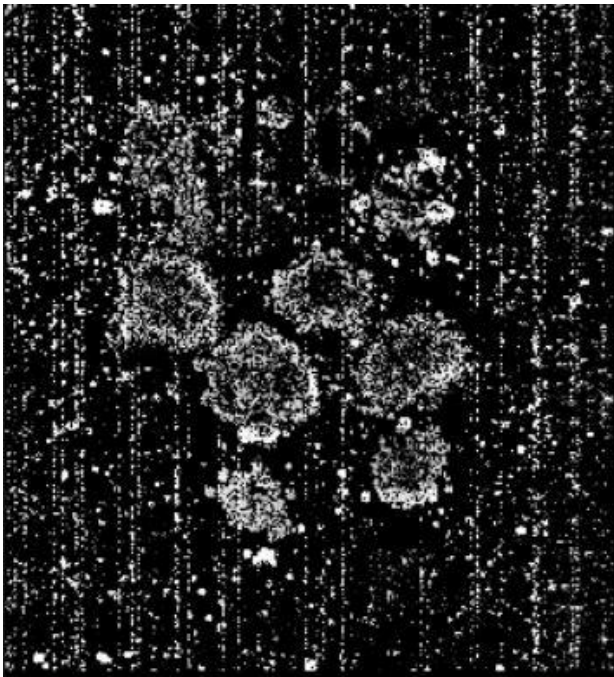
Optimal MNF



Full PCA

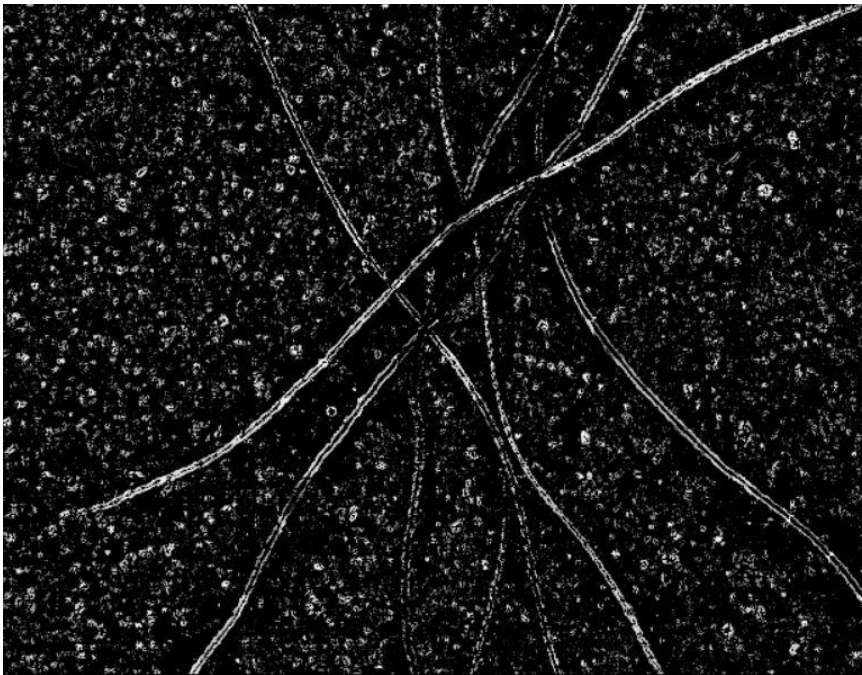


Full MNF

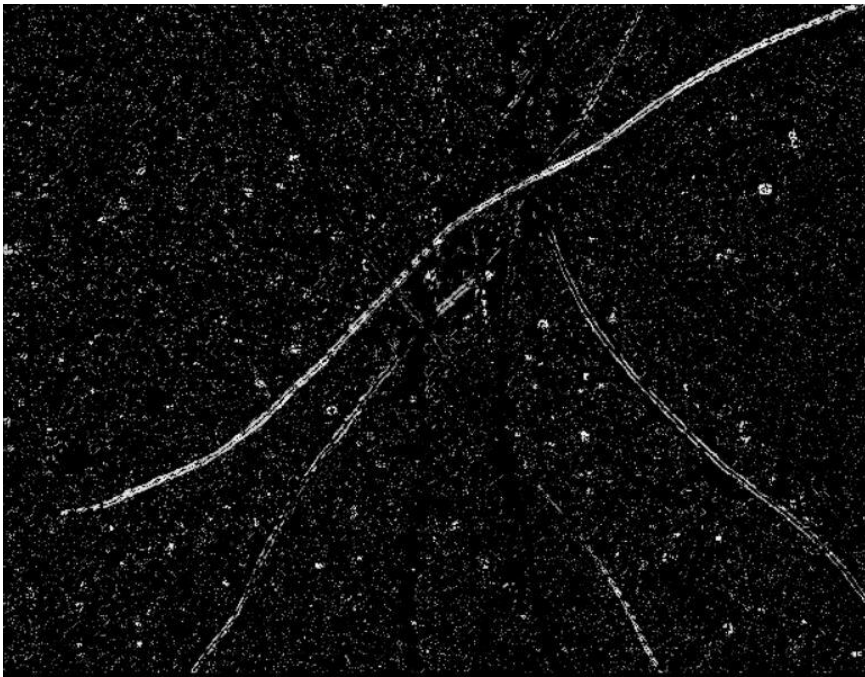


15. Level Set-Based Edge Detection Algorithm: Cloth Threads

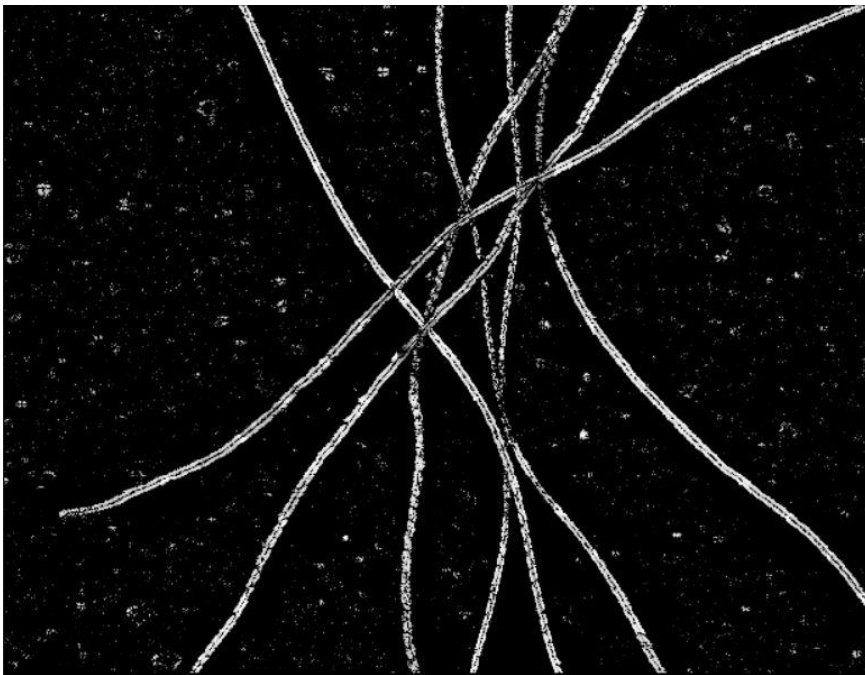
Reflectance



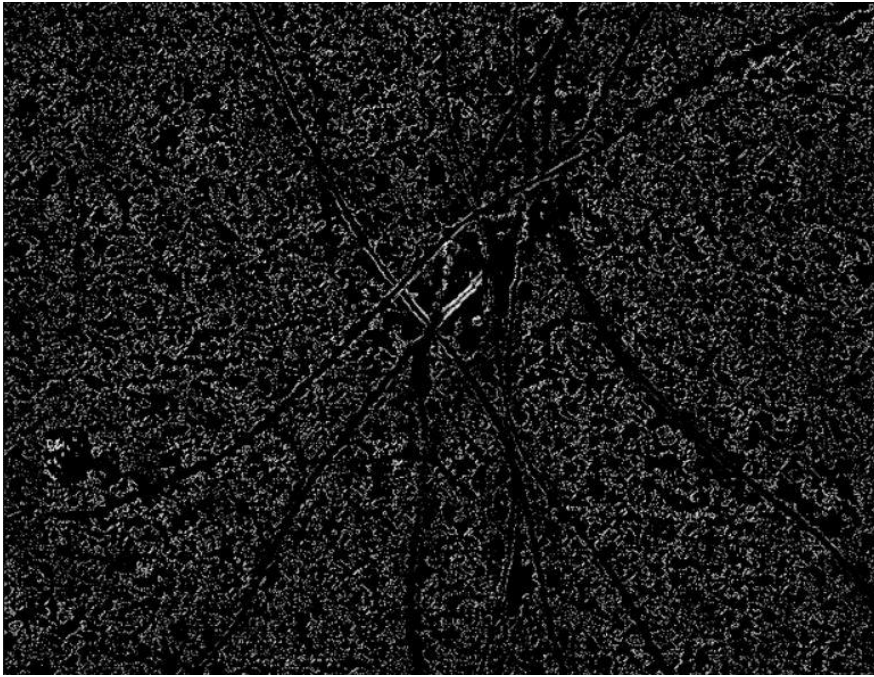
Optimal PCA



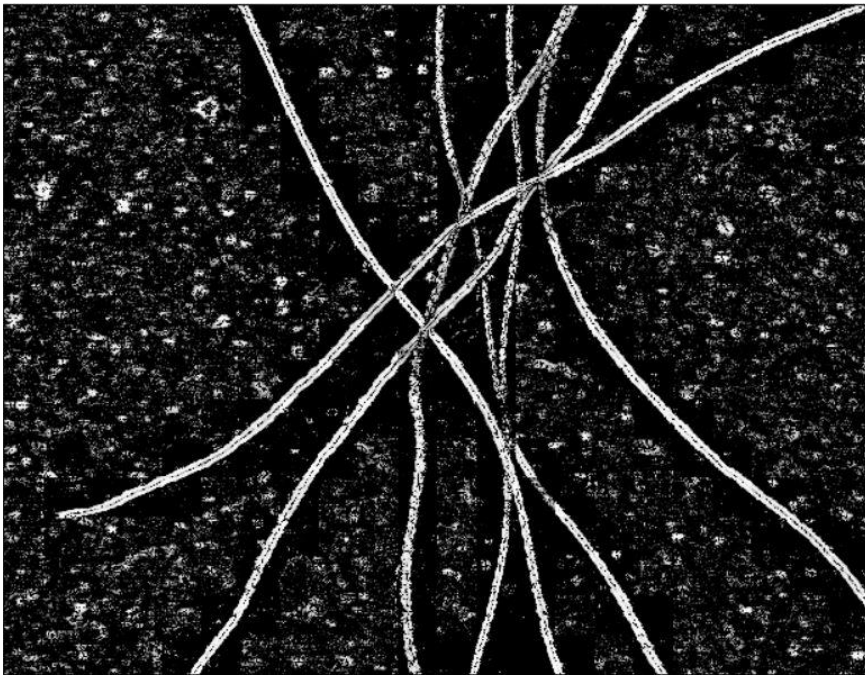
Optimal MNF



Full PCA



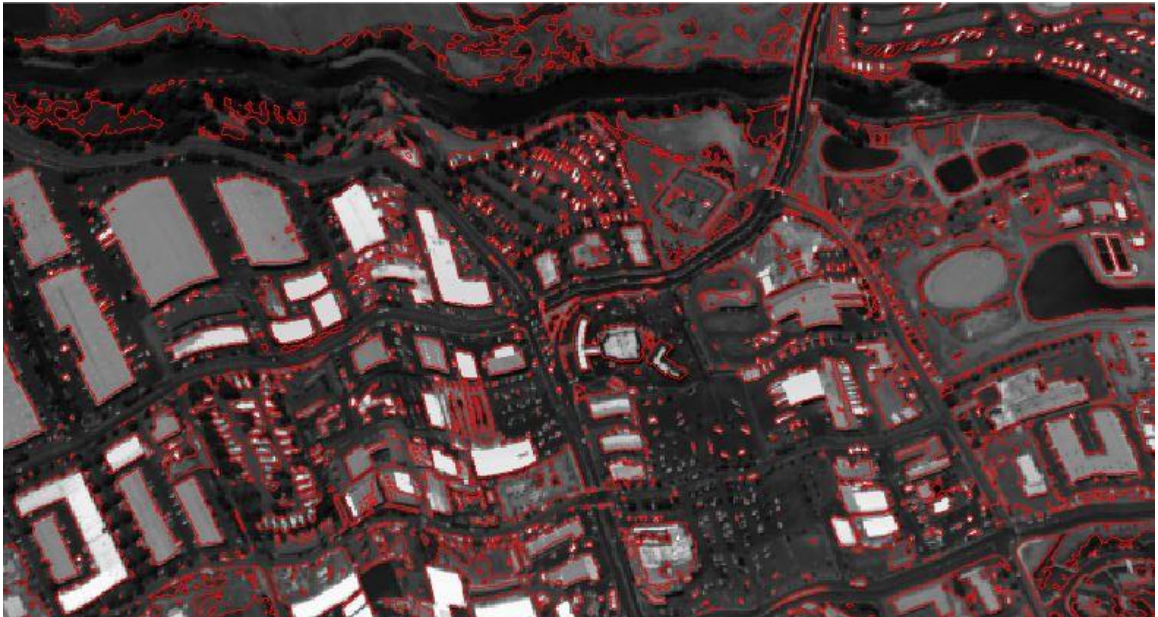
Full MNF



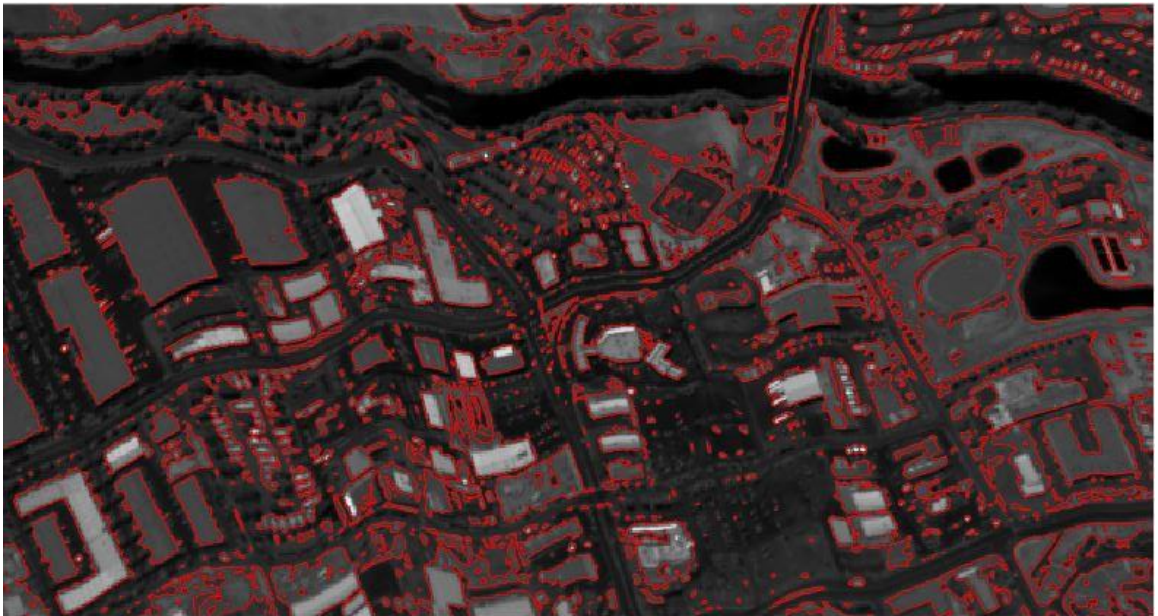
Level Set-Based Edge Detection Results

1. Level Set-Based Edge Detection Algorithm: Reno

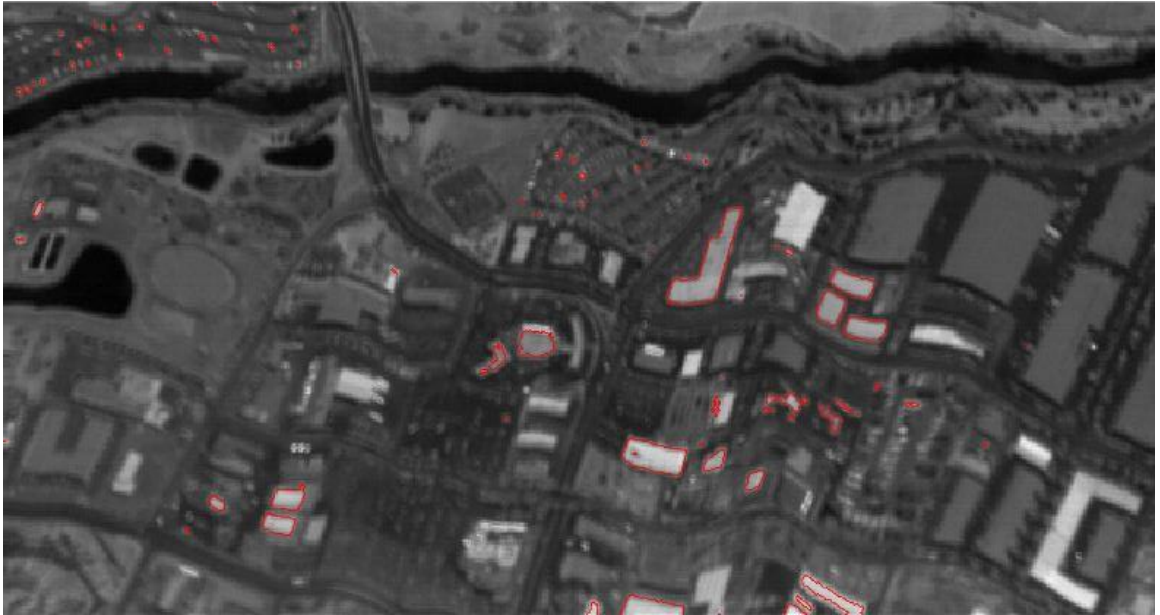
Reflectance



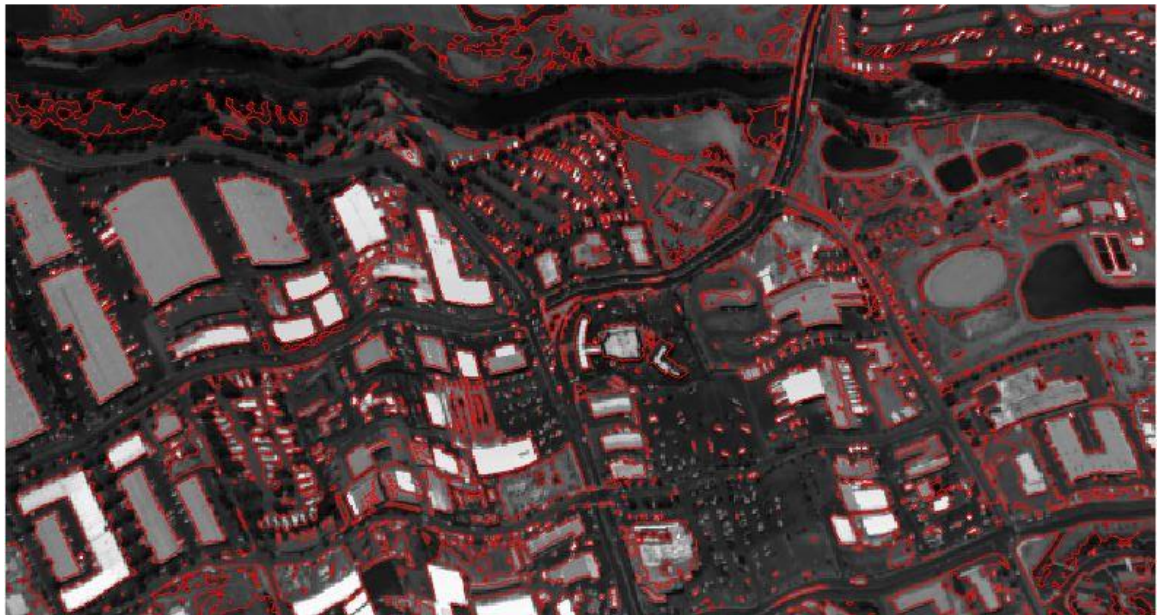
Optimal PCA



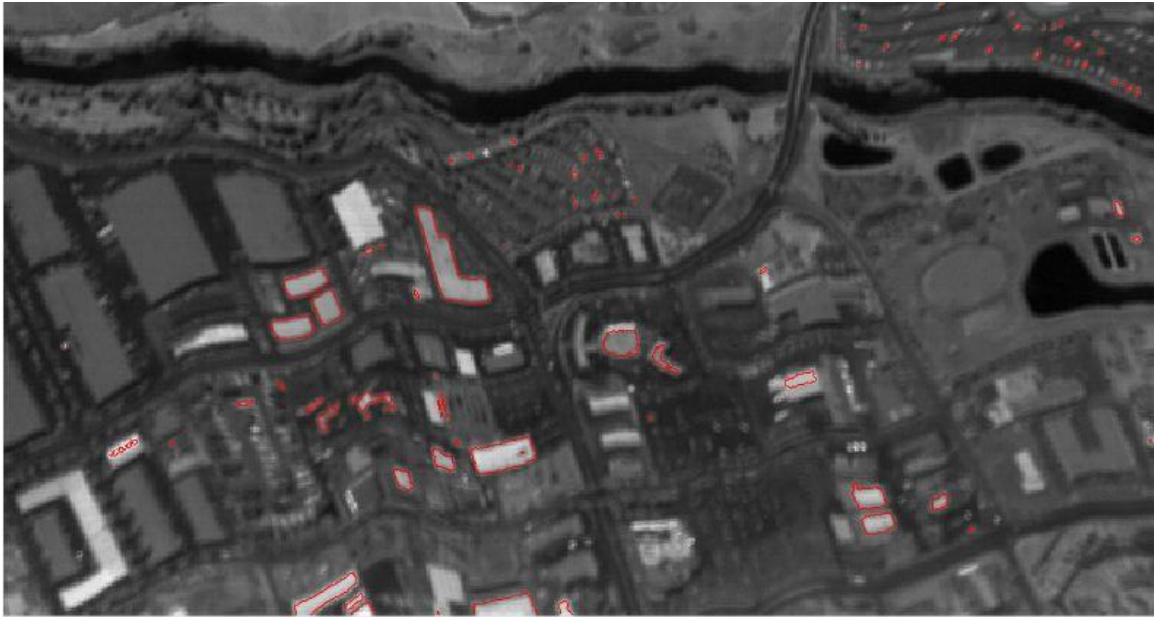
Optimal MNF



Full PCA

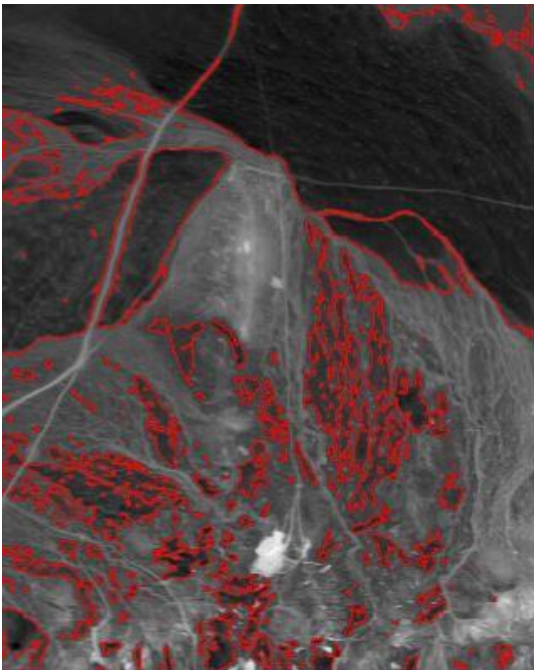


Full MNF

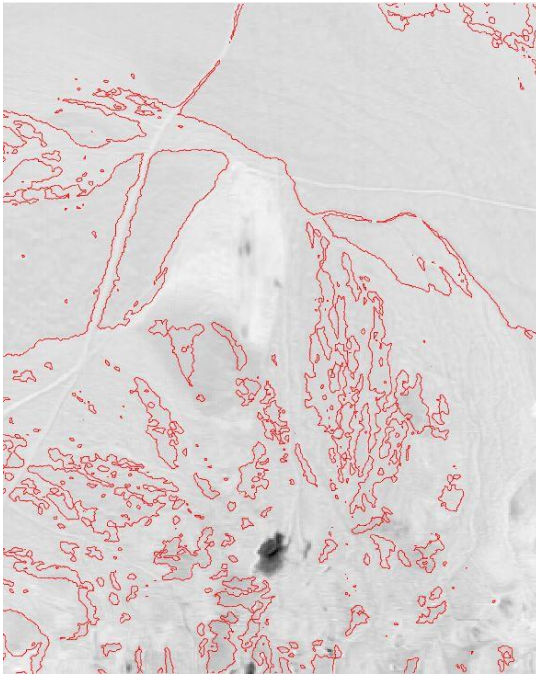


2. Level Set-Based Edge Detection Algorithm: Cuprite Flight Line #1

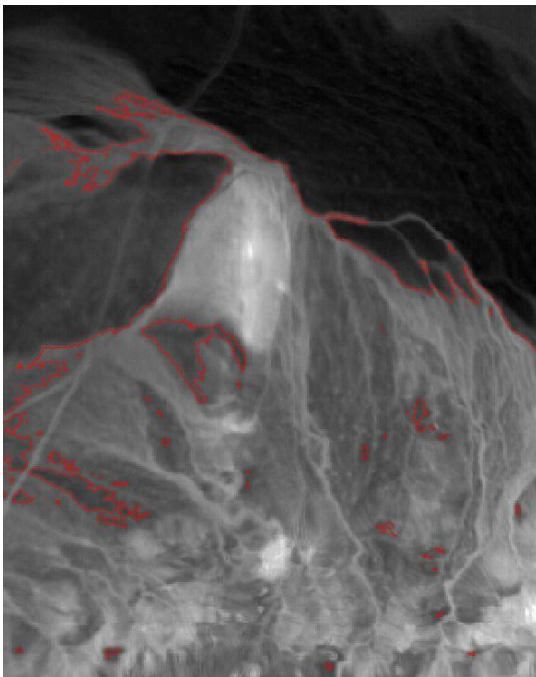
Reflectance



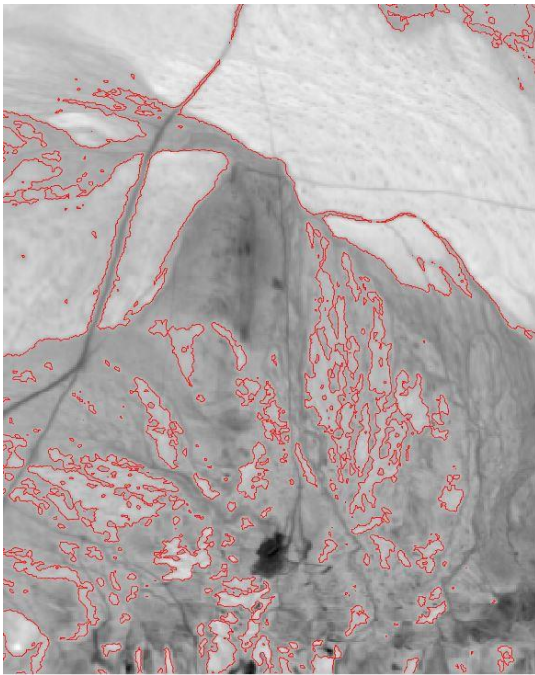
Optimal PCA



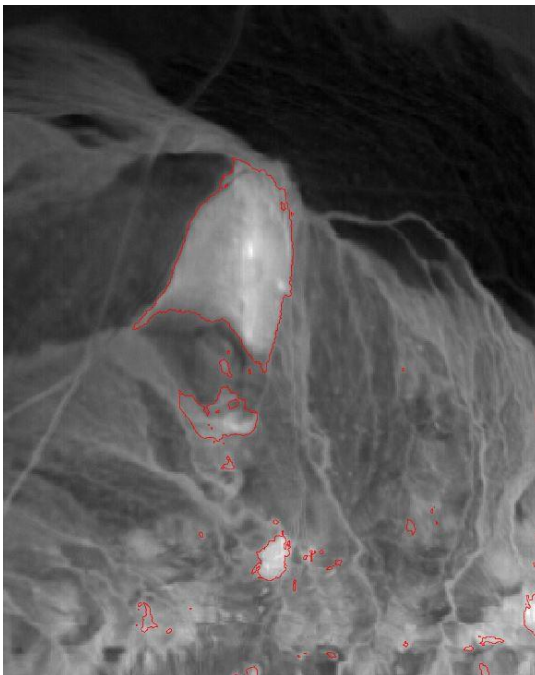
Optimal MNF



Full PCA

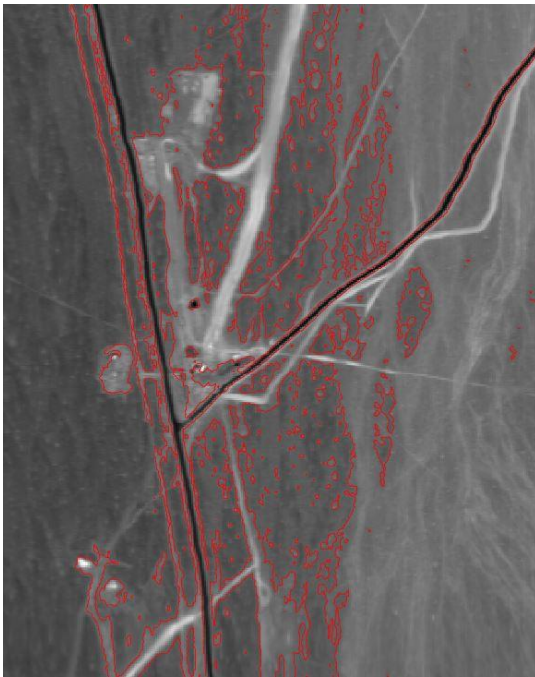


Full MNF

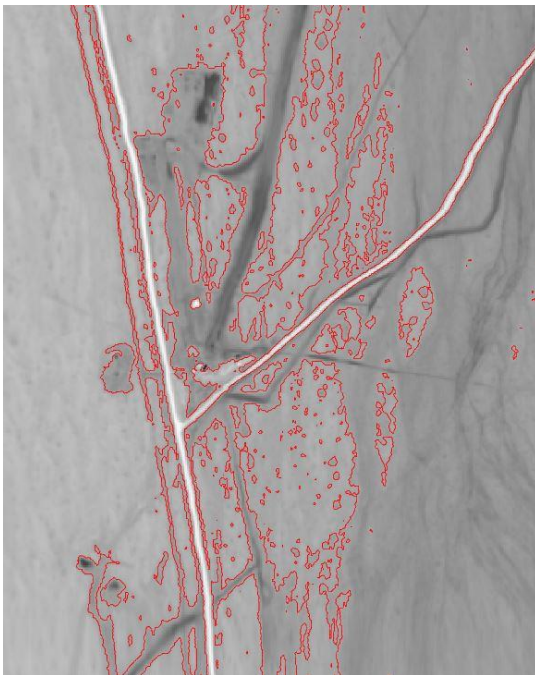


3. Level Set-Based Edge Detection Algorithm: Cuprite Flight Line #2

Reflectance



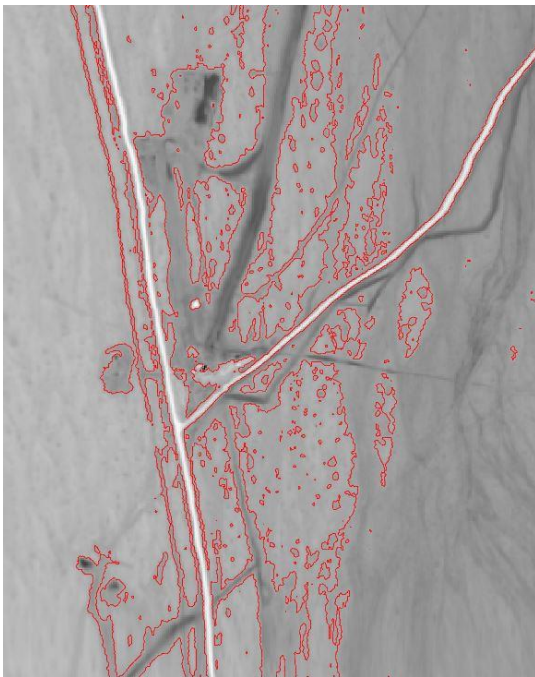
Optimal PCA



Optimal MNF



Full PCA

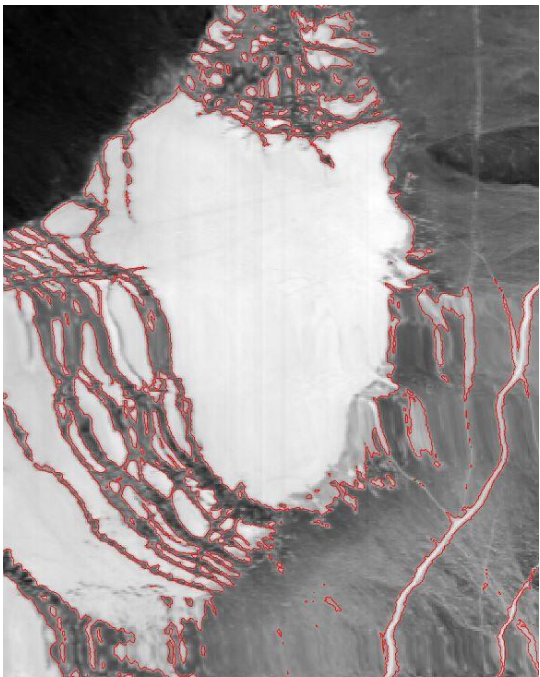


Full MNF

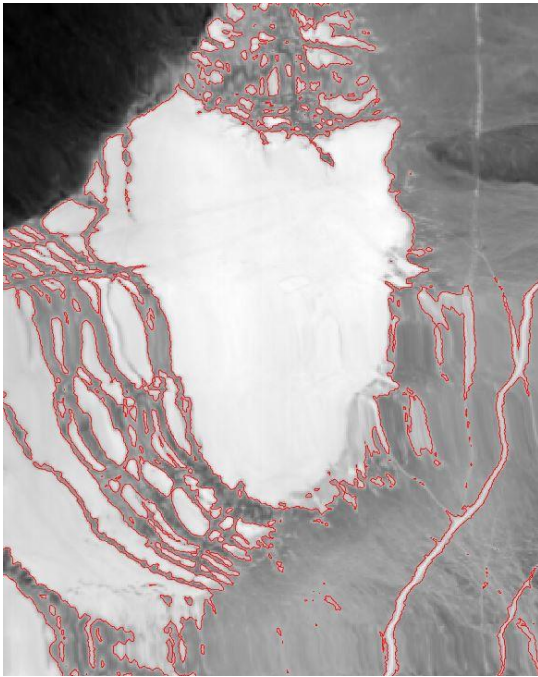


4. Level Set-Based Edge Detection Algorithm: Cuprite Flight Line #3

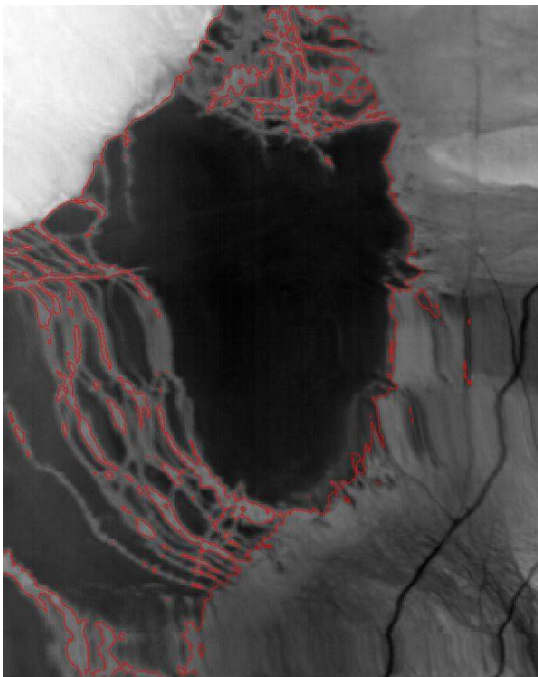
Reflectance



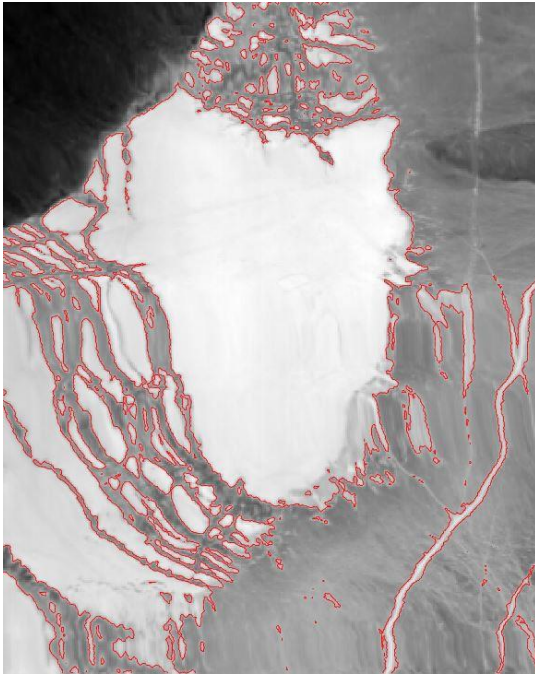
Optimal PCA



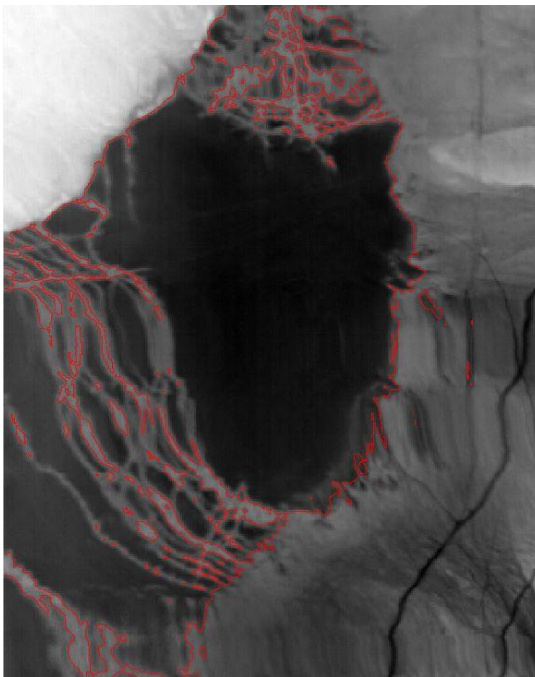
Optimal MNF



Full PCA

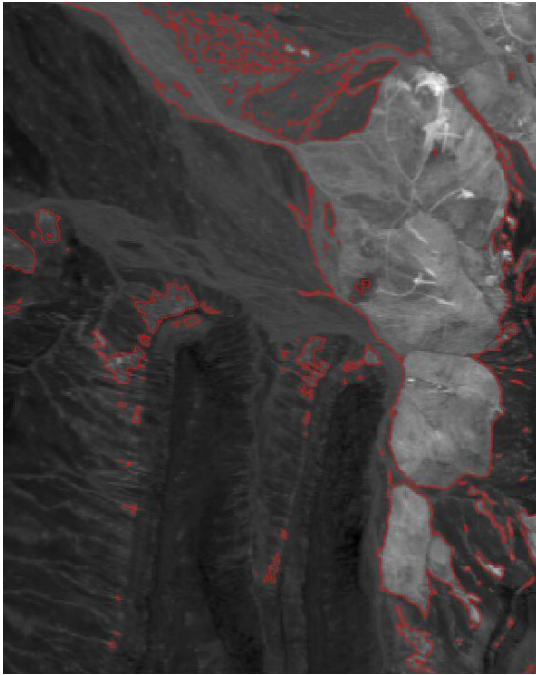


Full MNF

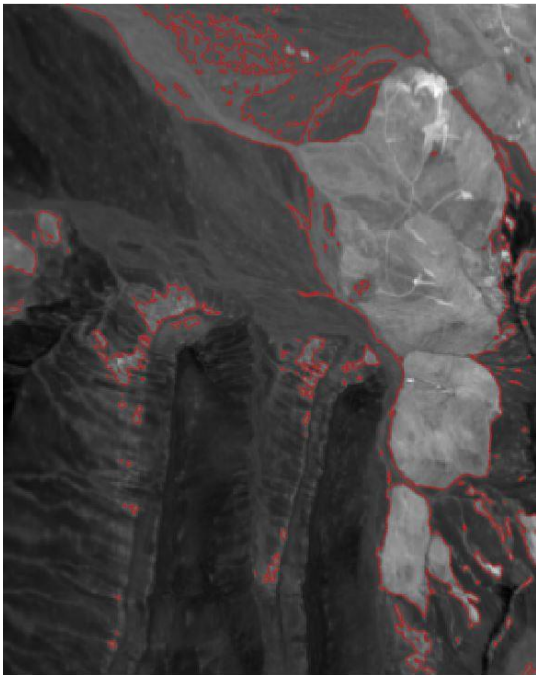


5. Level Set-Based Edge Detection Algorithm: Cuprite Flight Line #4

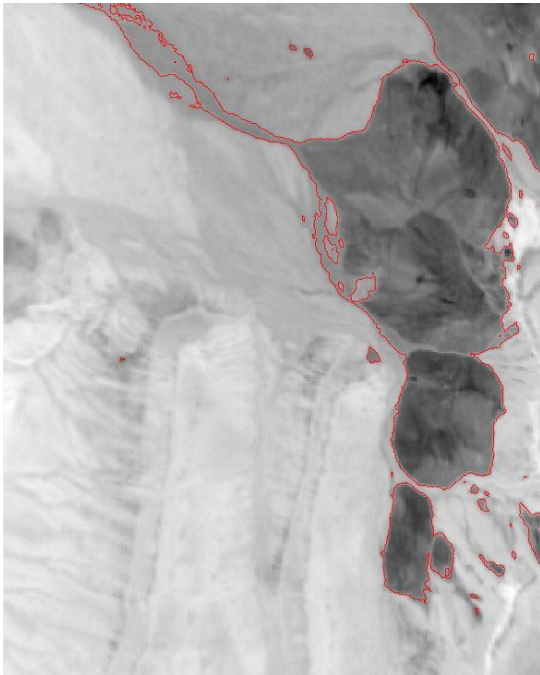
Reflectance



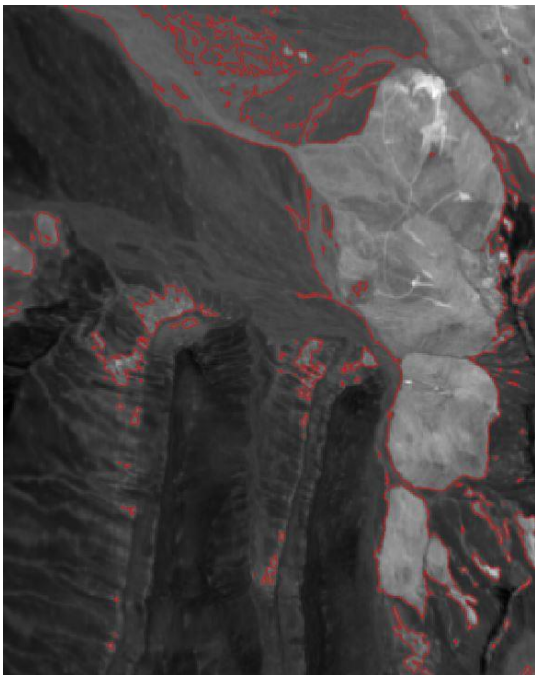
Optimal PCA



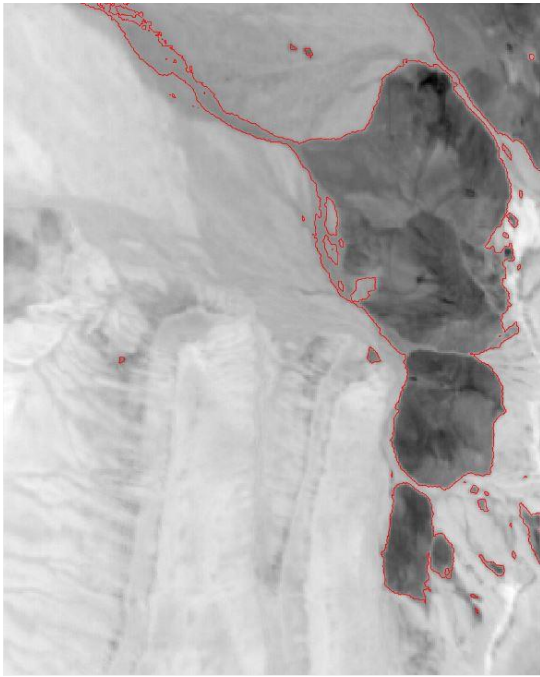
Optimal MNF



Full PCA



Full MNF

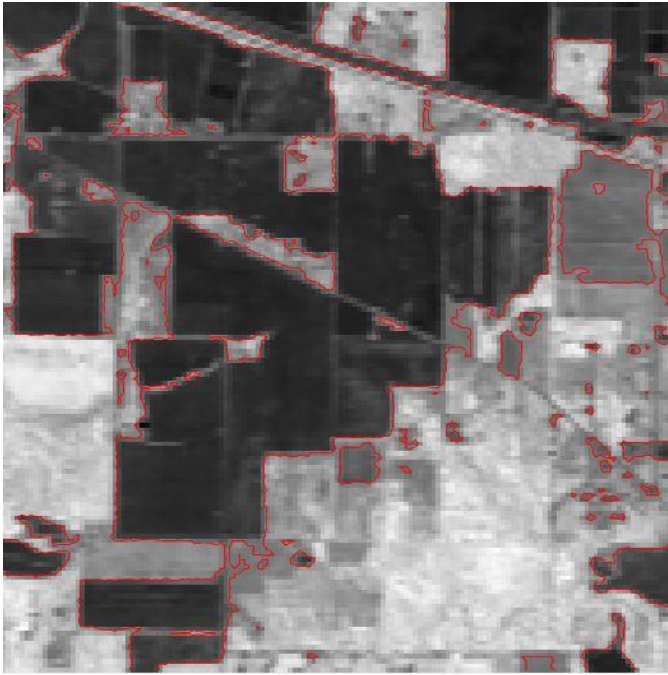


6. Level Set-Based Edge Detection Algorithm: Indian Pines

Reflectance



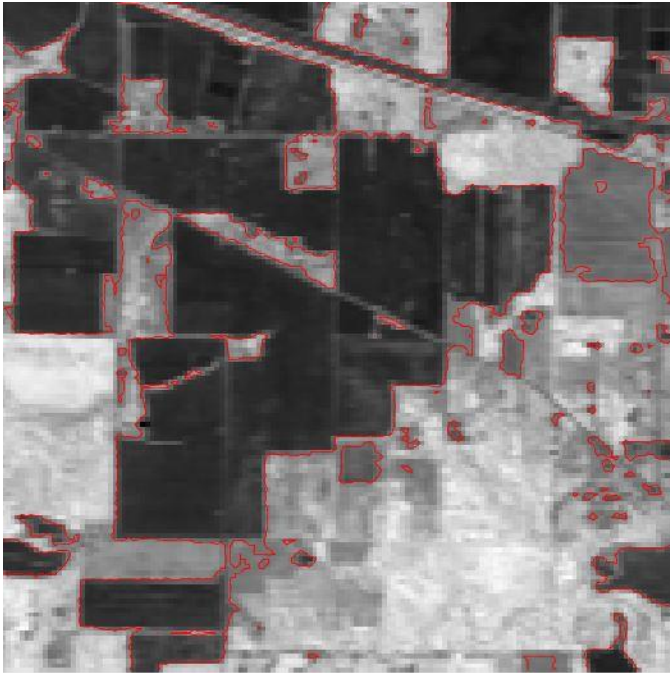
Optimal PCA



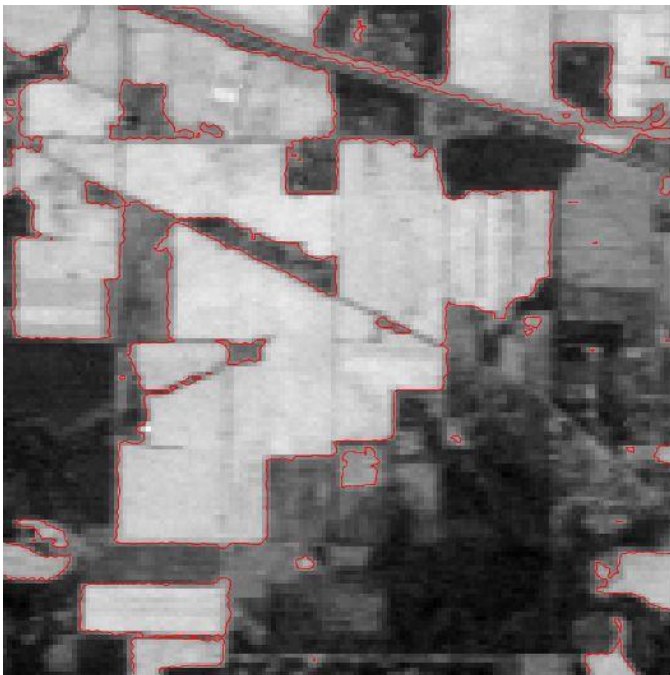
Optimal MNF



Full PCA

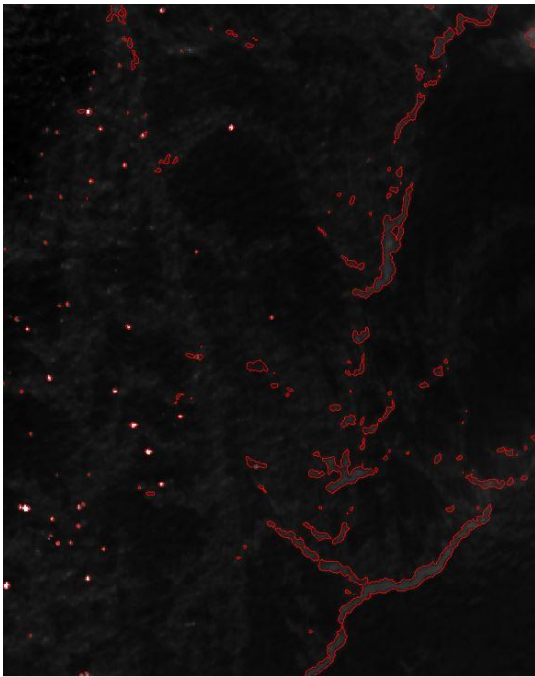


Full MNF

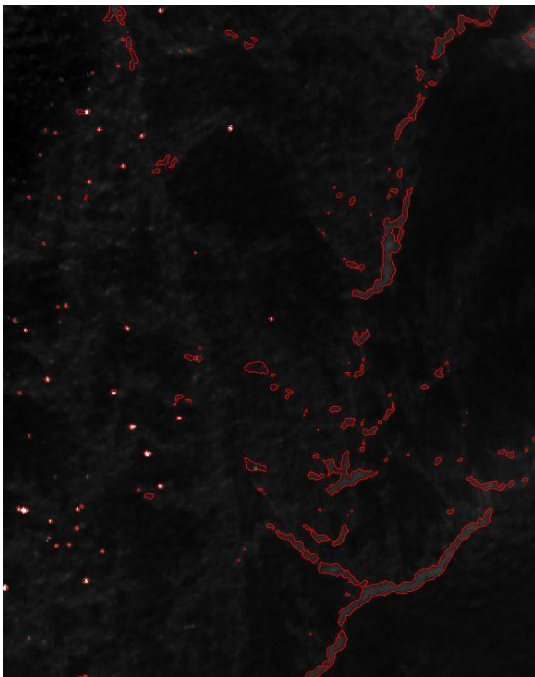


7. Level Set-Based Edge Detection Algorithm: Deepwater Horizon

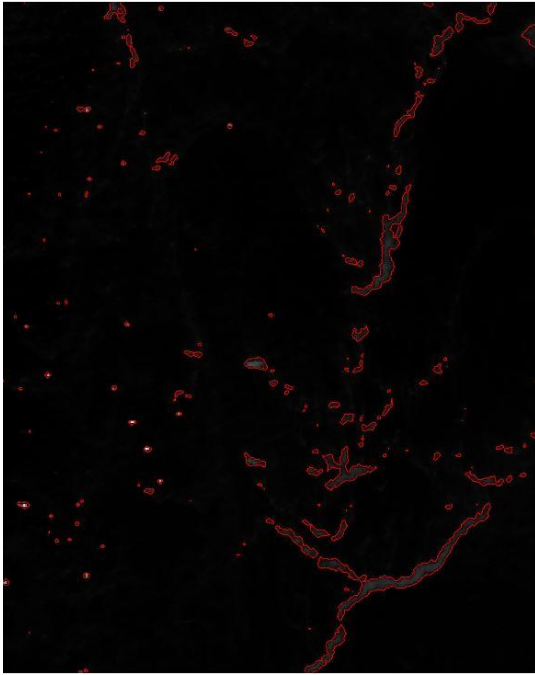
Radiance



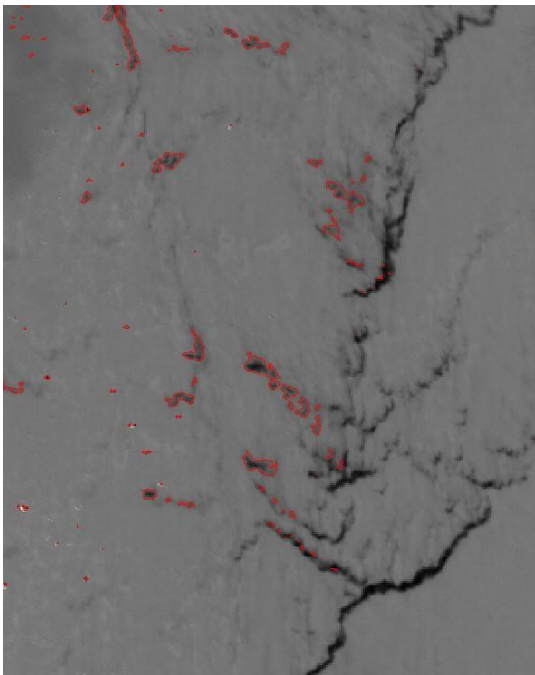
Reflectance



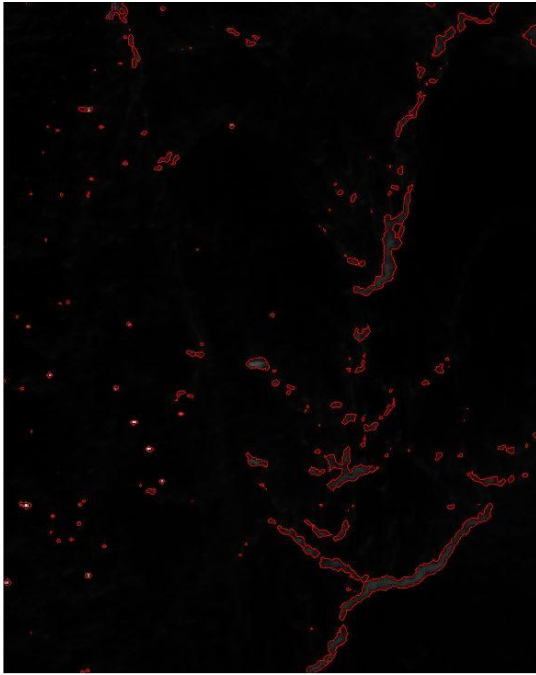
Optimal PCA



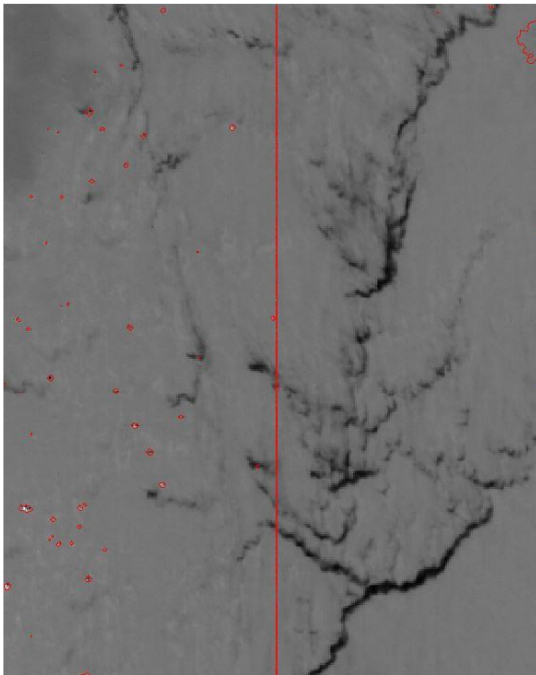
Optimal MNF



Full PCA

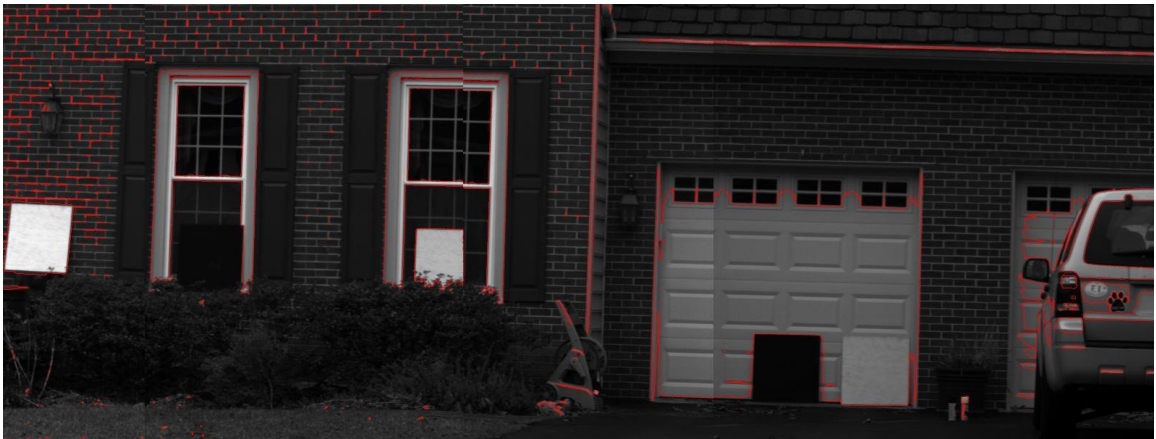


Full MNF



8. Level Set-Based Edge Detection Algorithm: Larkhaven

Reflectance



Optimal PCA



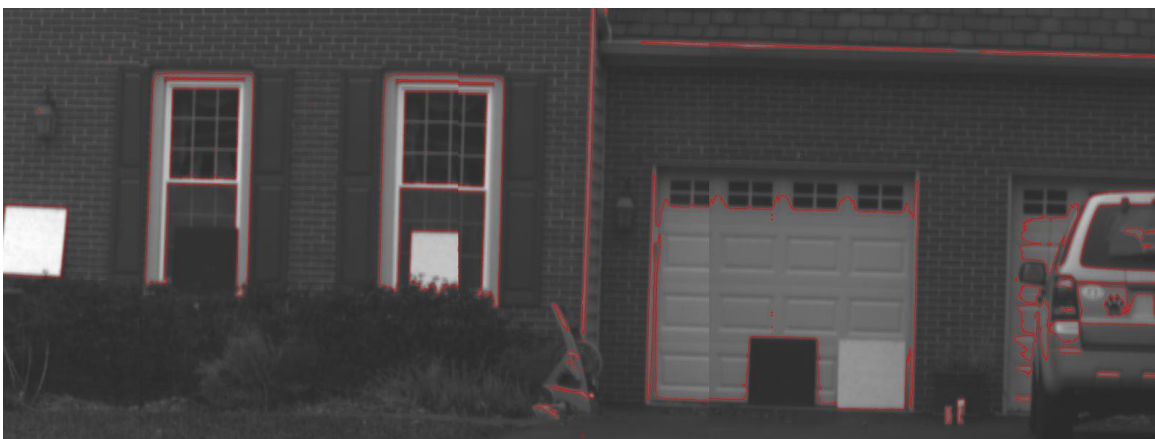
Optimal MNF



Full PCA

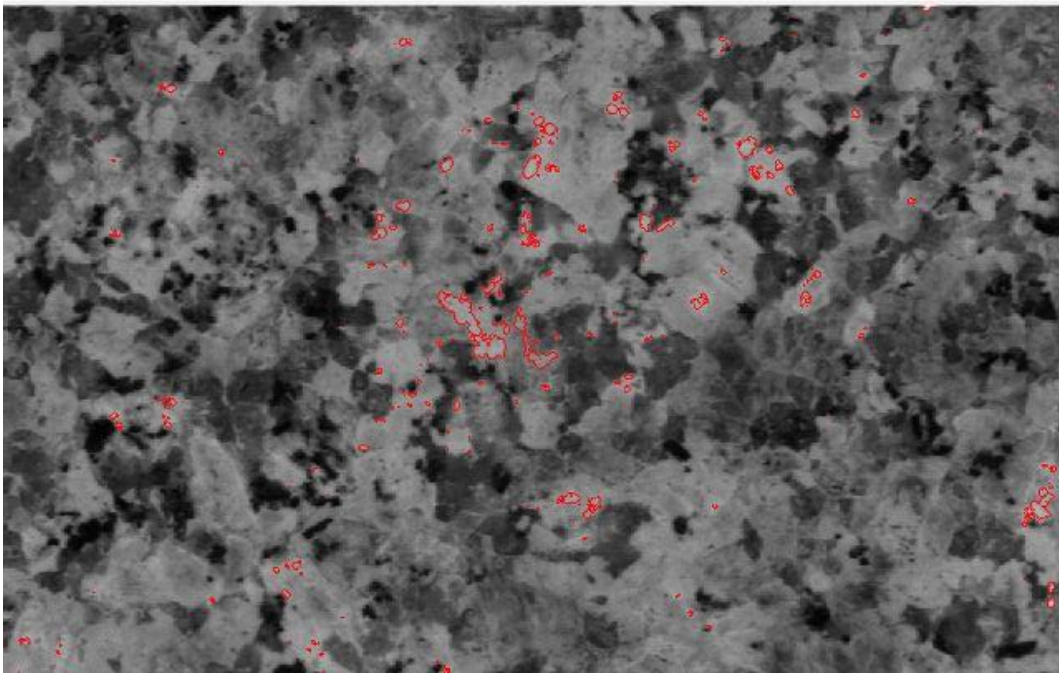


Full MNF

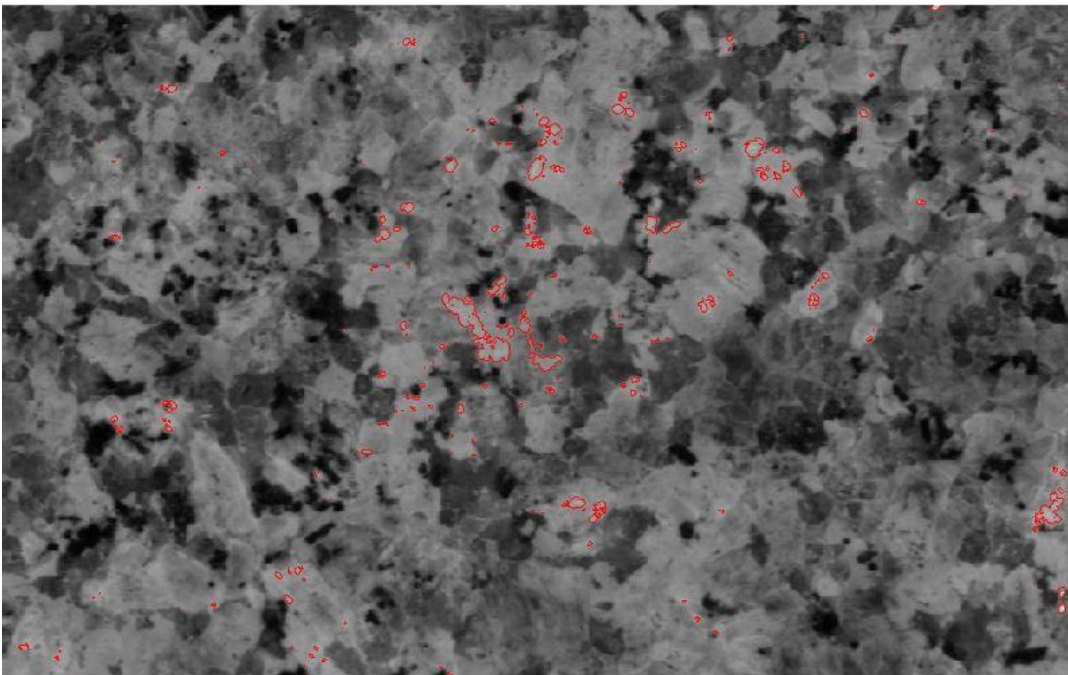


9. Level Set-Based Edge Detection Algorithm: Granite VNIR

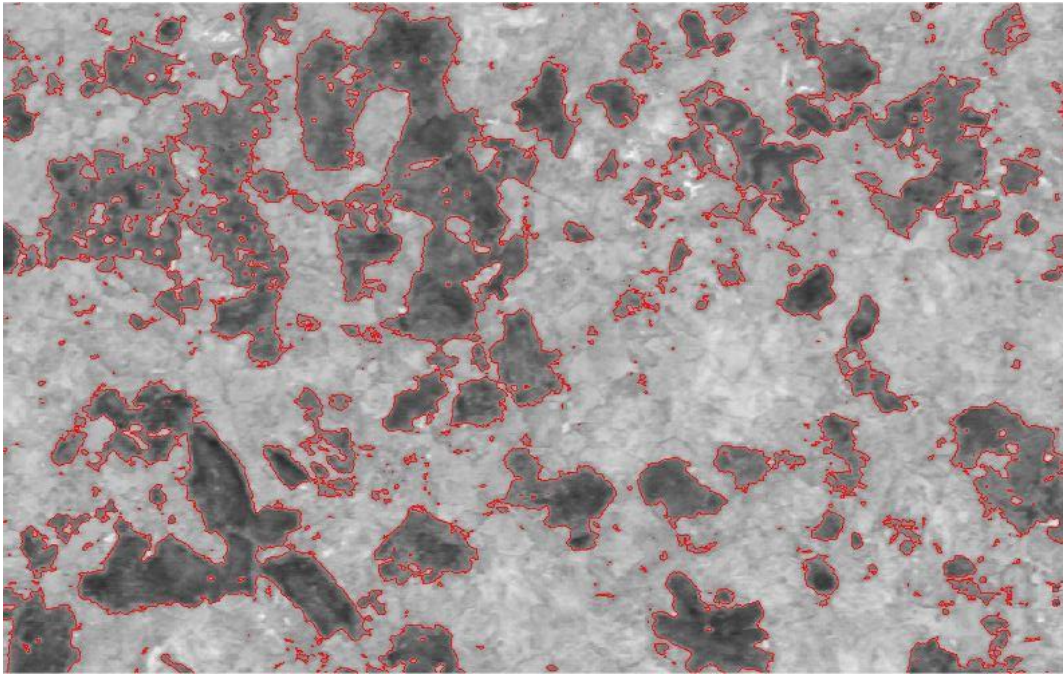
Reflectance



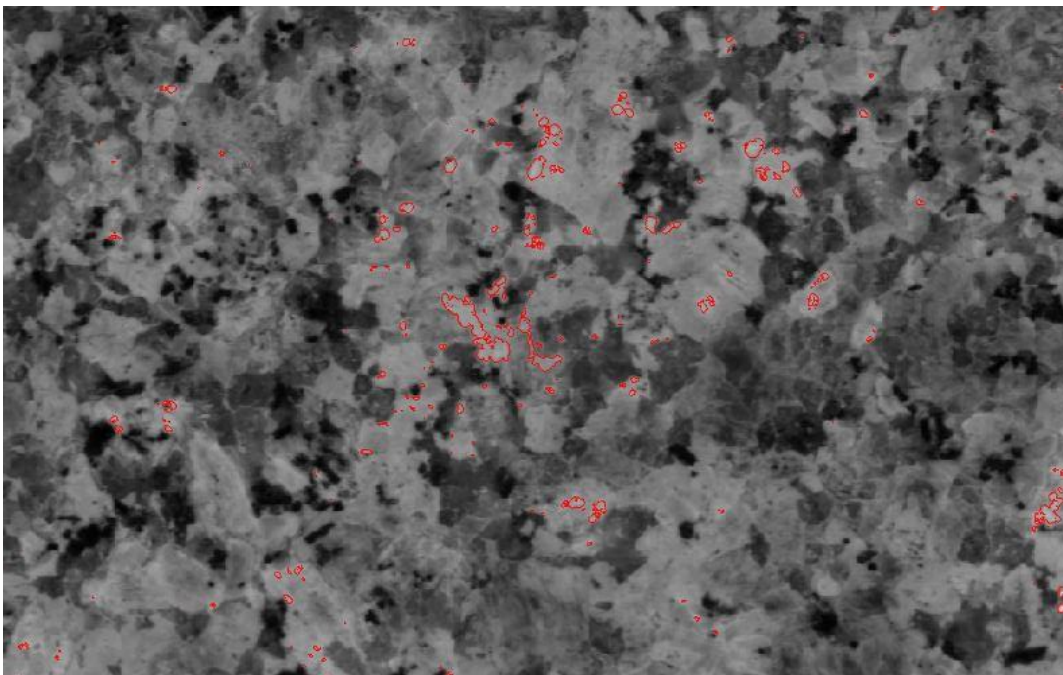
Optimal PCA



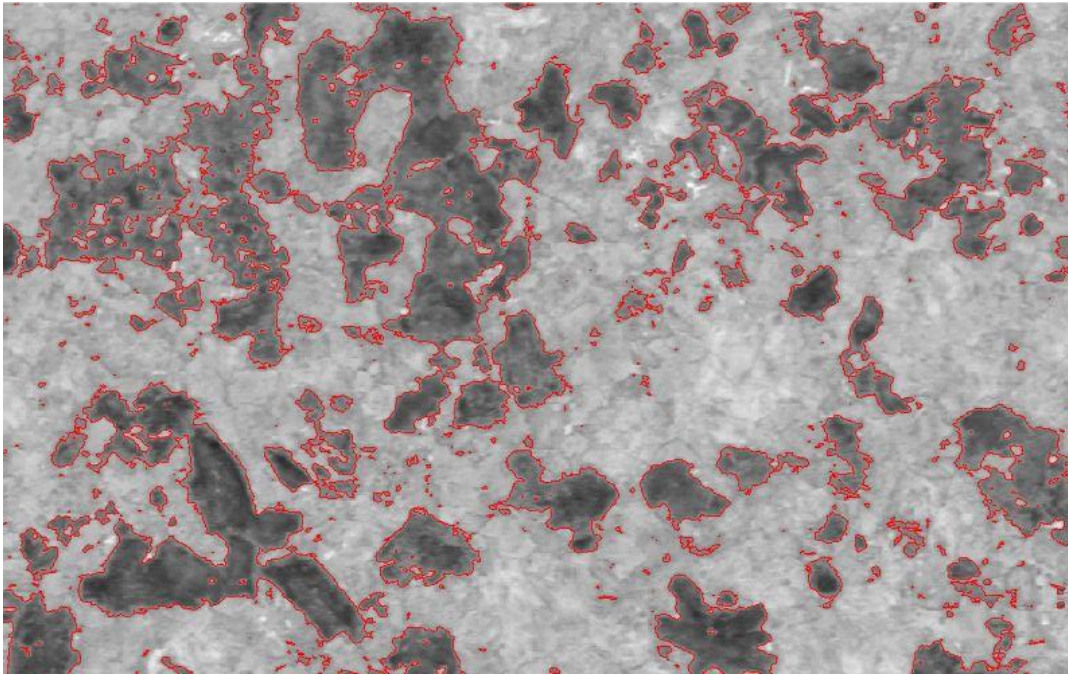
Optimal MNF



Full PCA

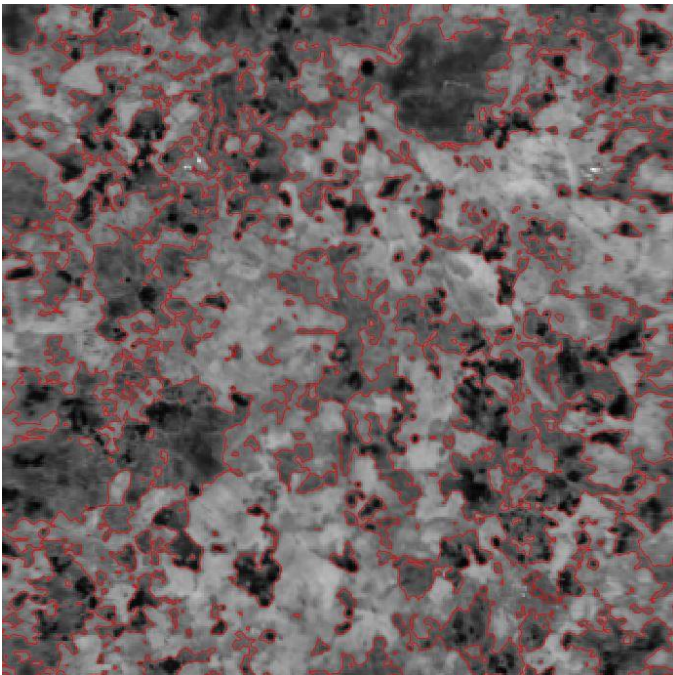


Full MNF

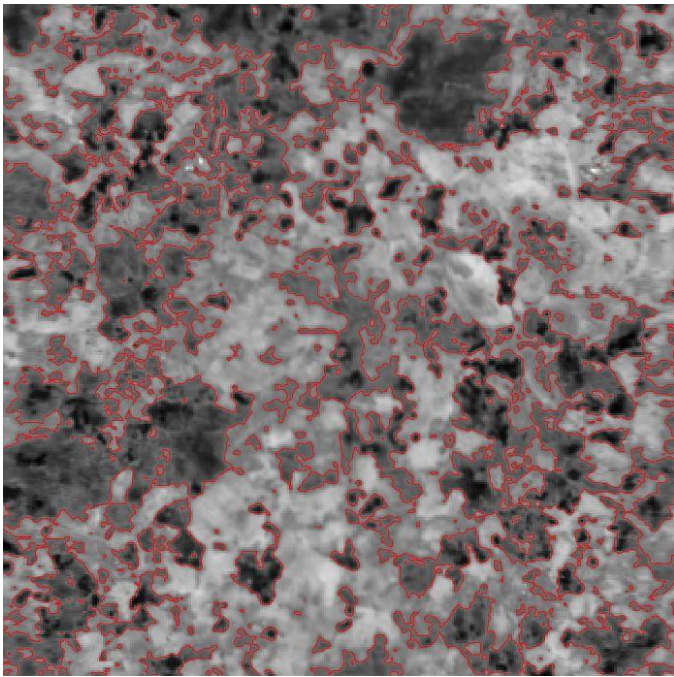


10. Level Set-Based Edge Detection Algorithm: Granite NIR/SWIR

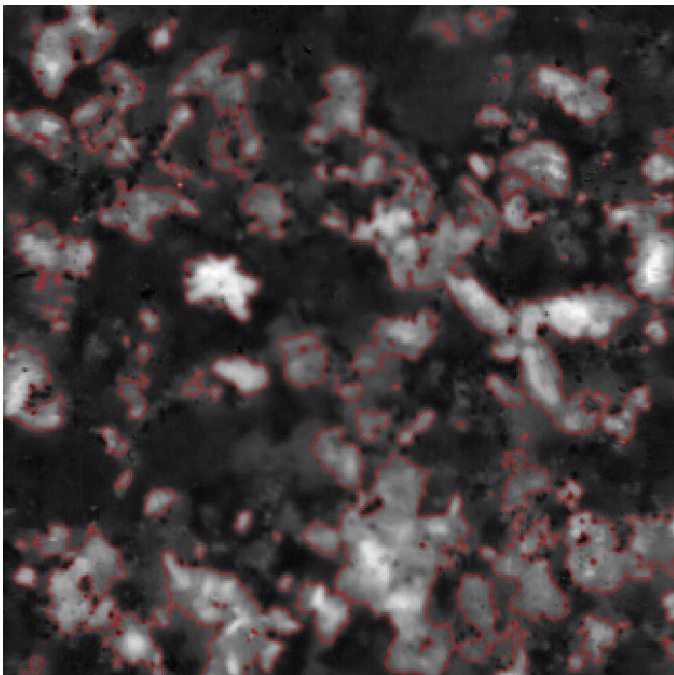
Reflectance



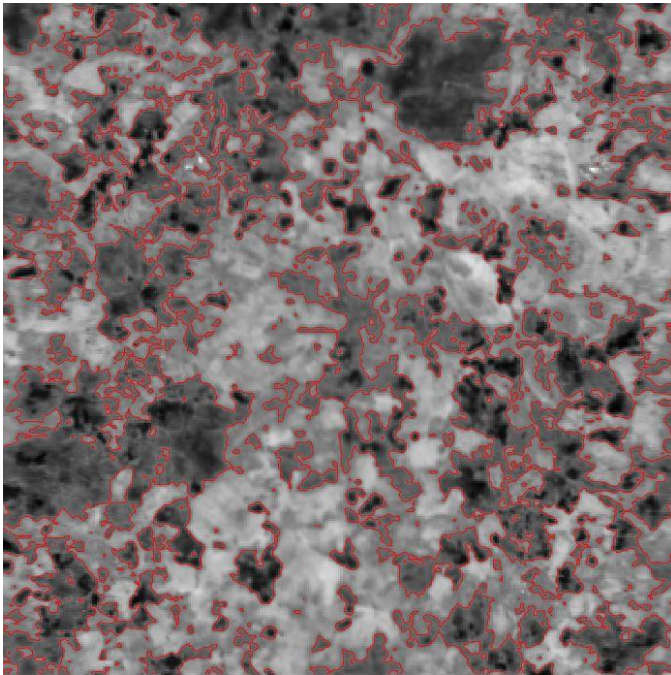
Optimal PCA



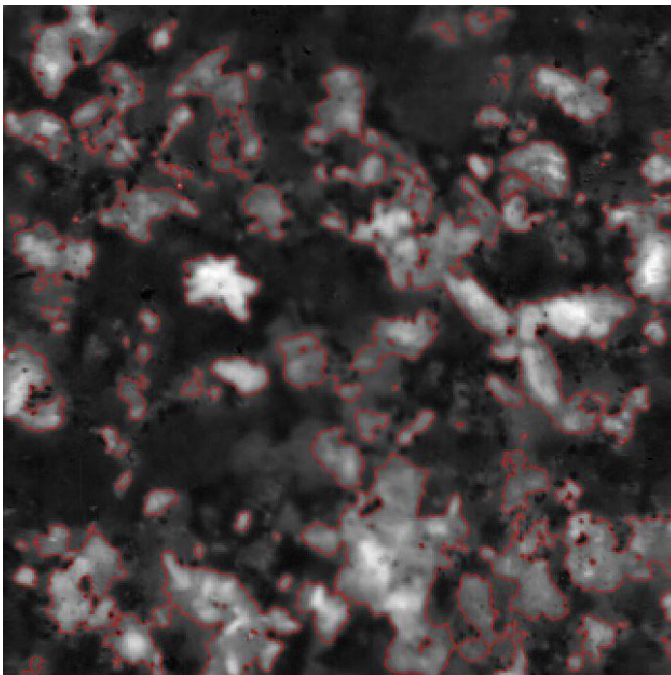
Optimal MNF



Full PCA



Full MNF

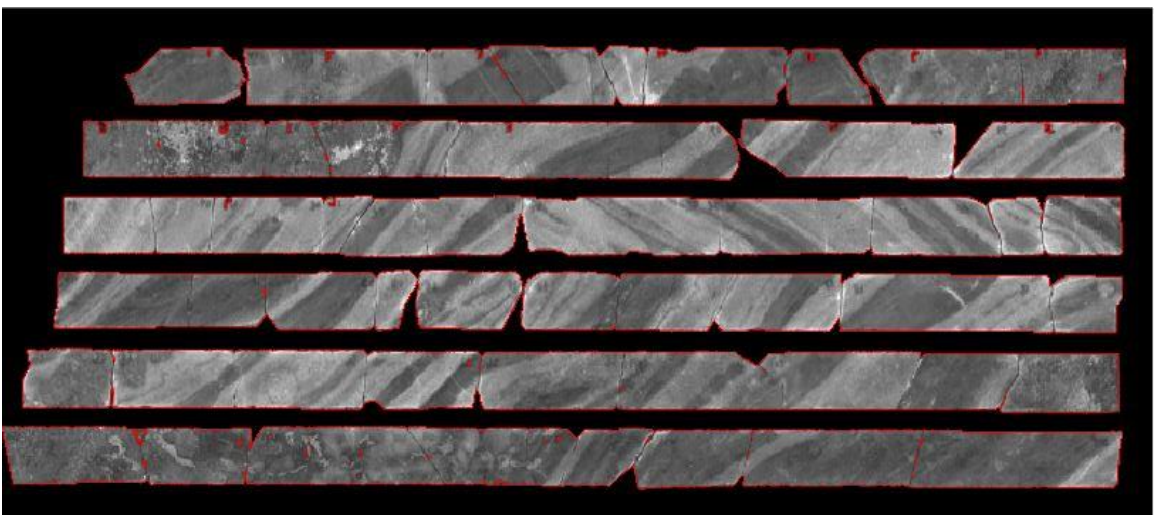


11. Level Set-Based Edge Detection Algorithm: South Africa Core Samples

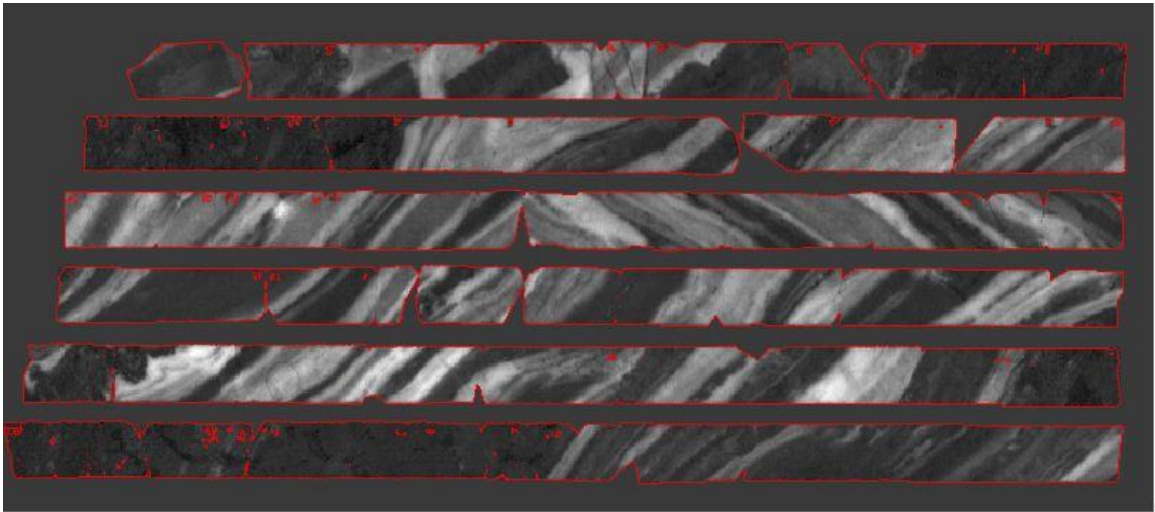
Reflectance



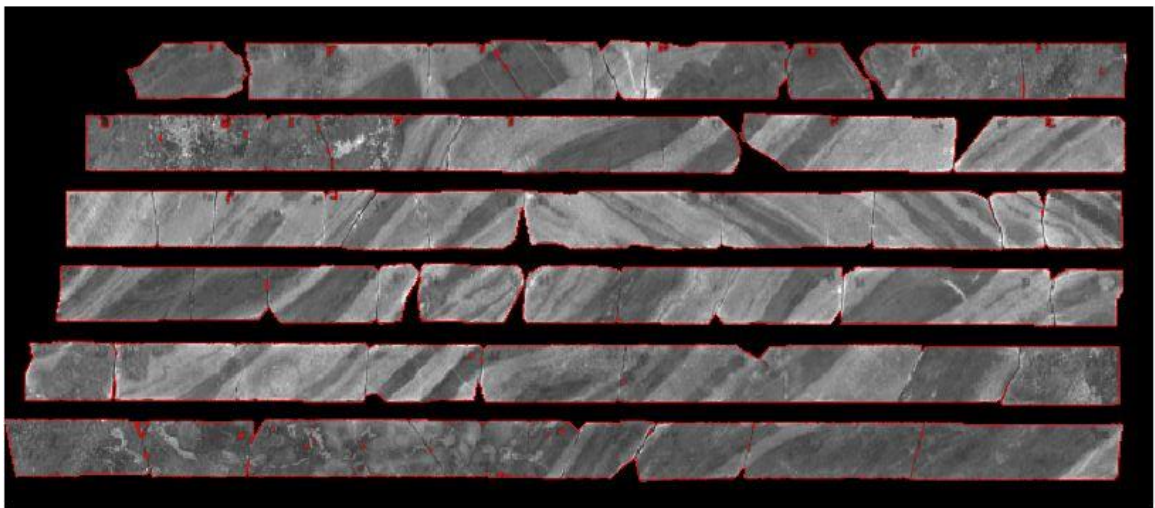
Optimal PCA



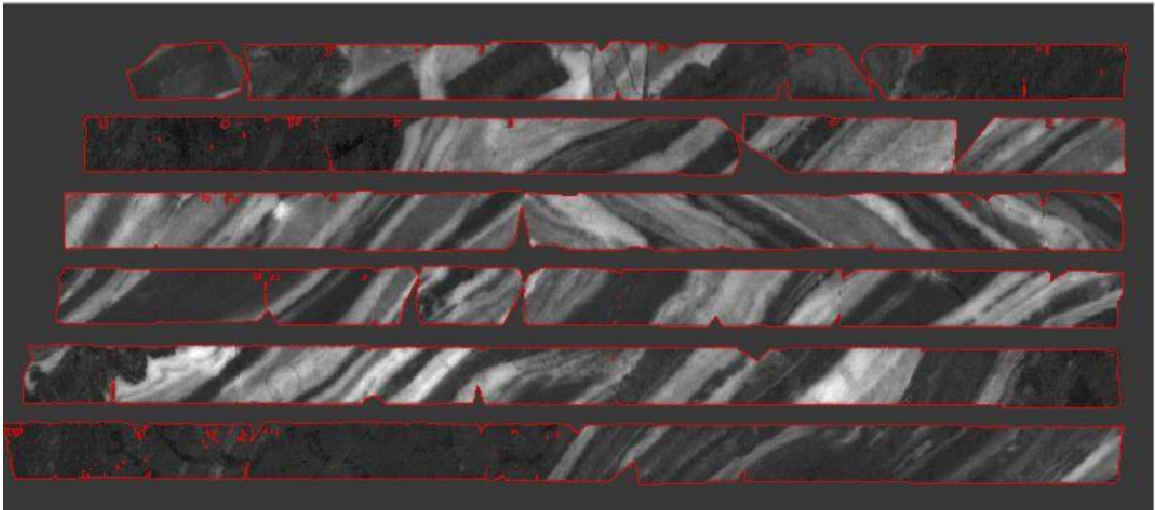
Optimal MNF



Full PCA

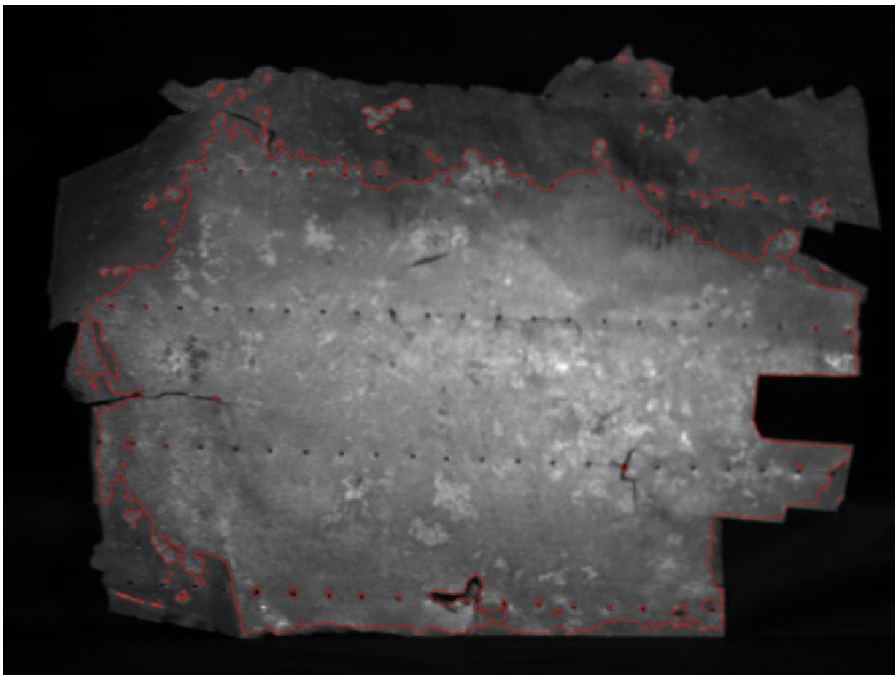


Full MNF

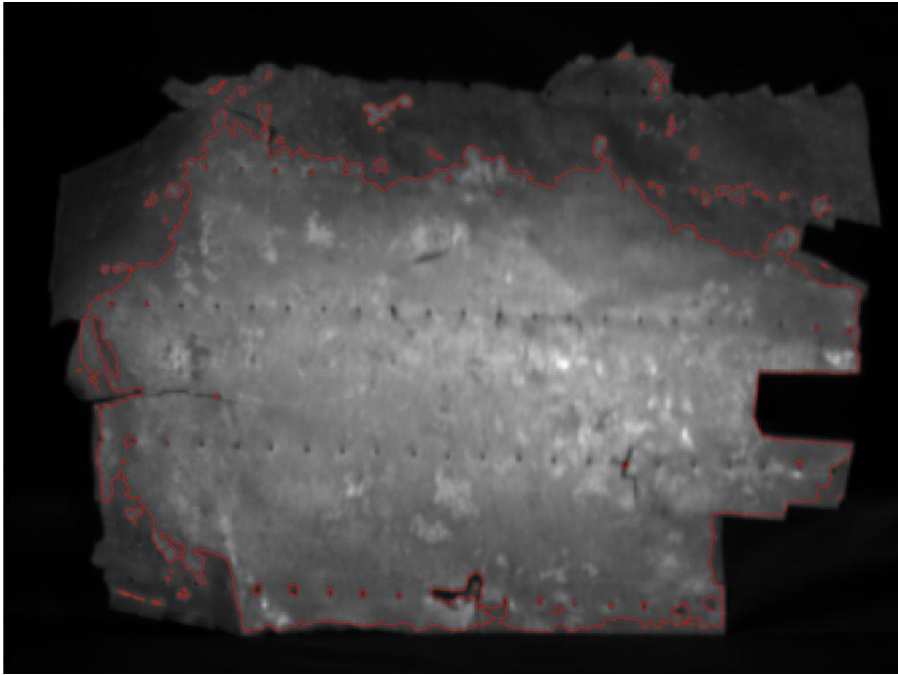


12. Level Set-Based Edge Detection Algorithm: Aluminum Panel

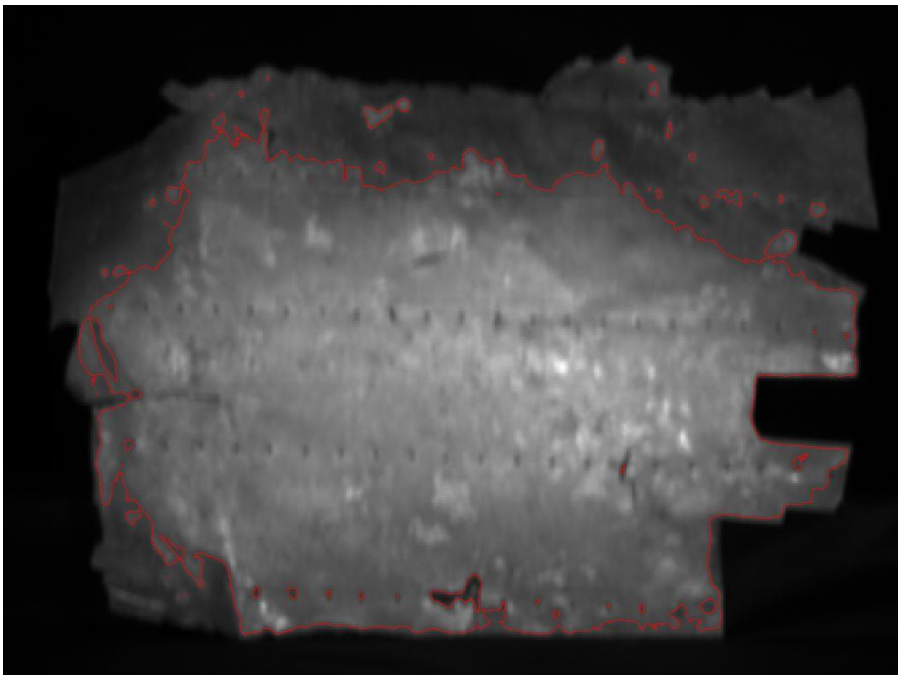
Reflectance



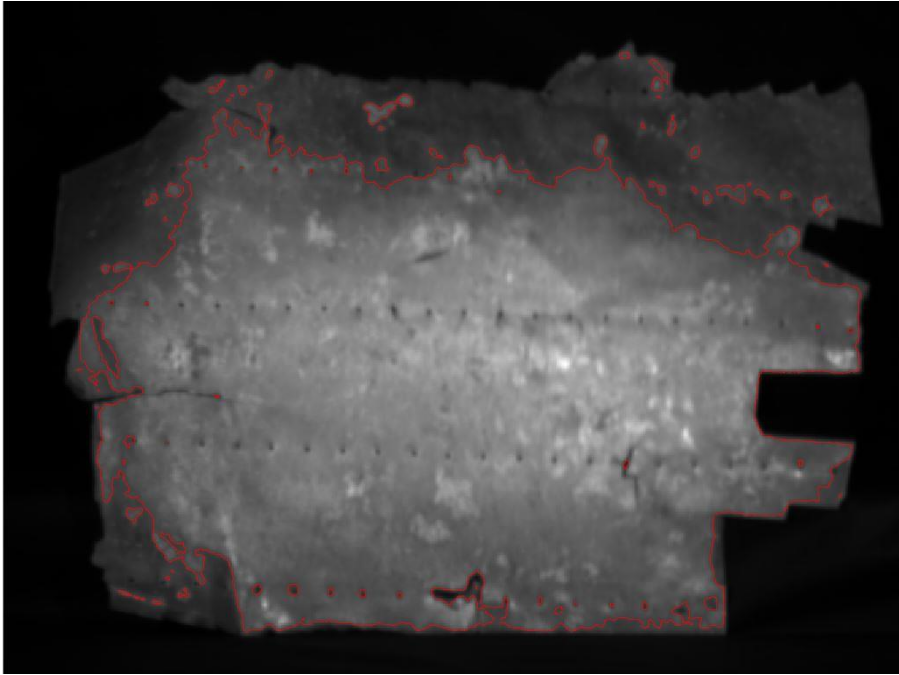
Optimal PCA



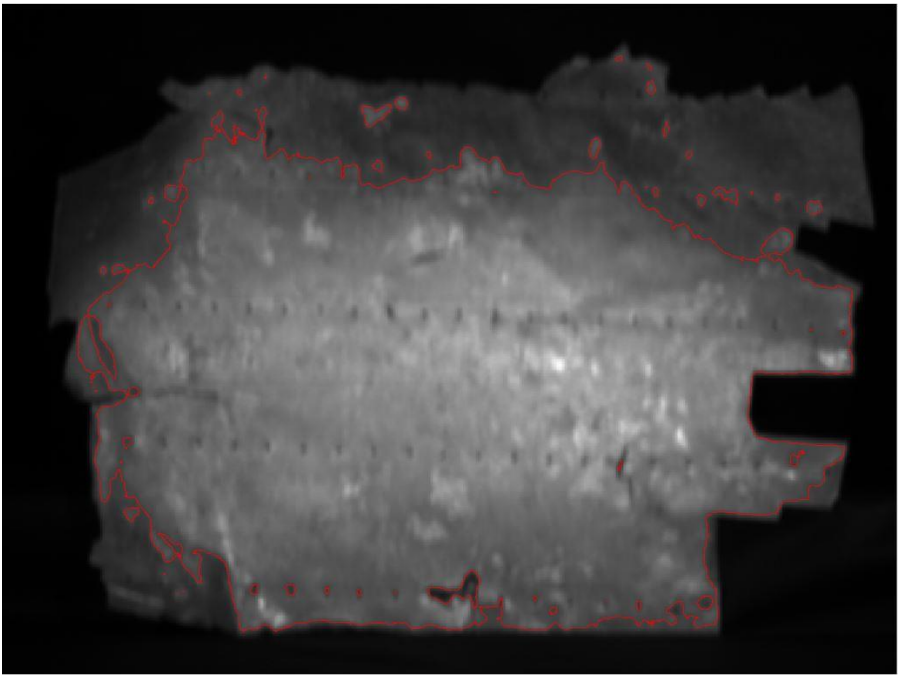
Optimal MNF



Full PCA

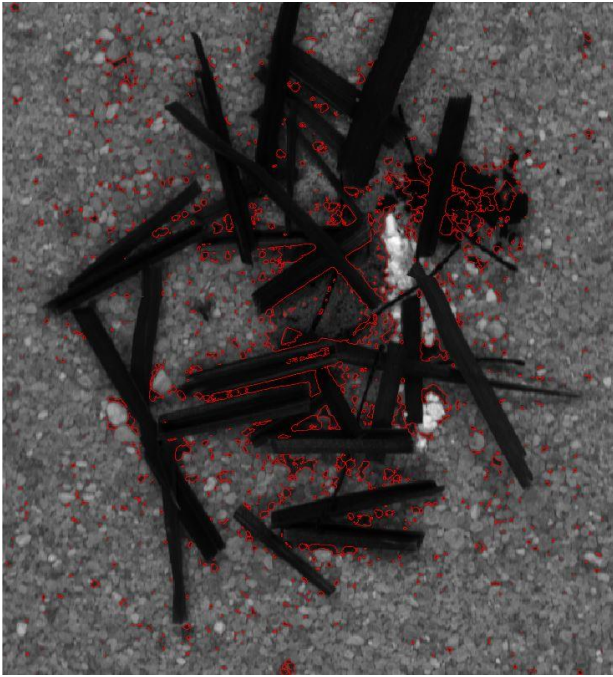


Full MNF

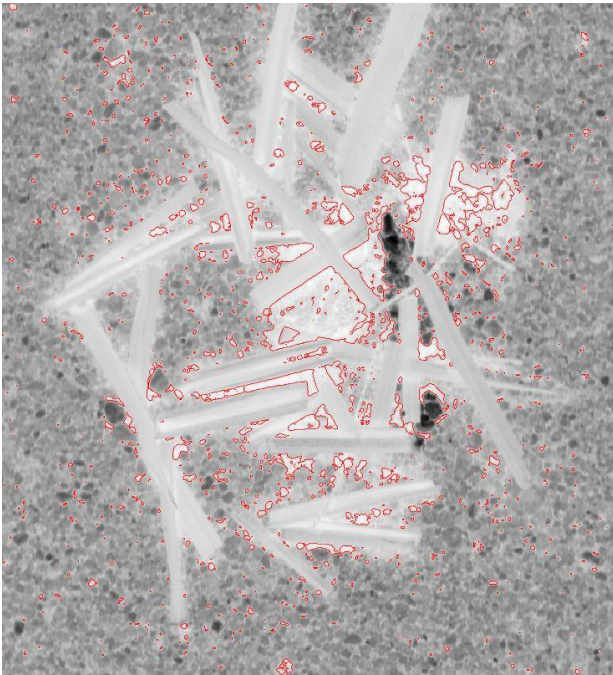


13. Level Set-Based Edge Detection Algorithm: Rare Target on Sand

Reflectance



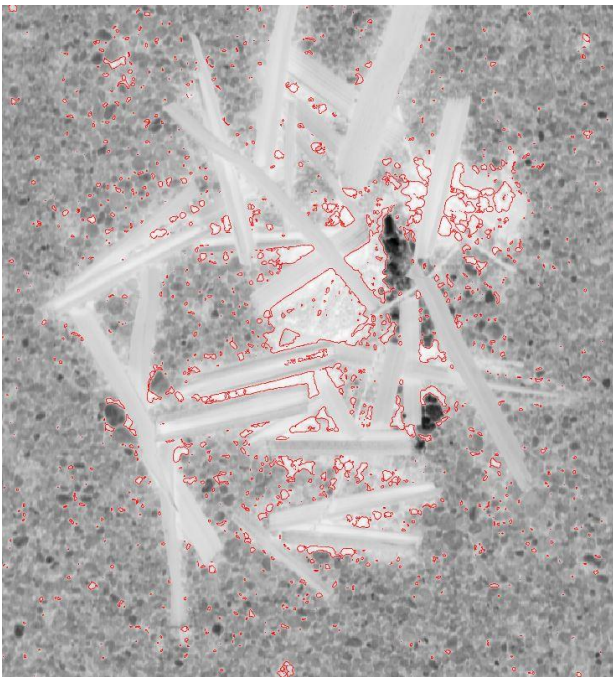
Optimal PCA



Optimal MNF



Full PCA

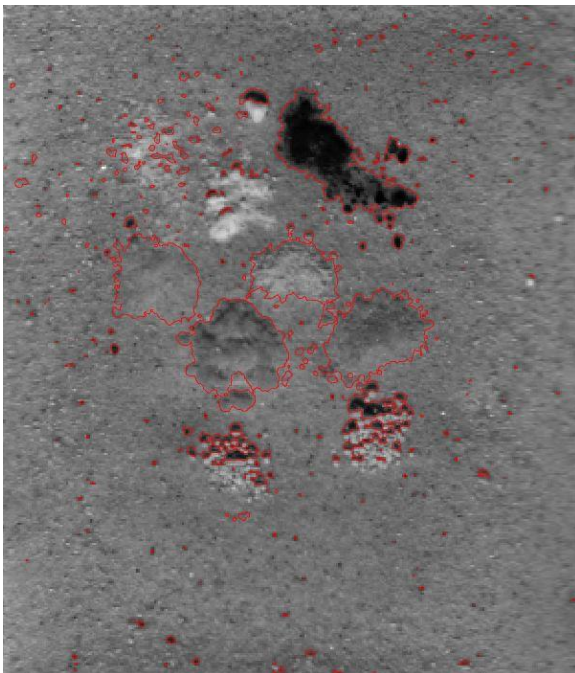


Full MNF

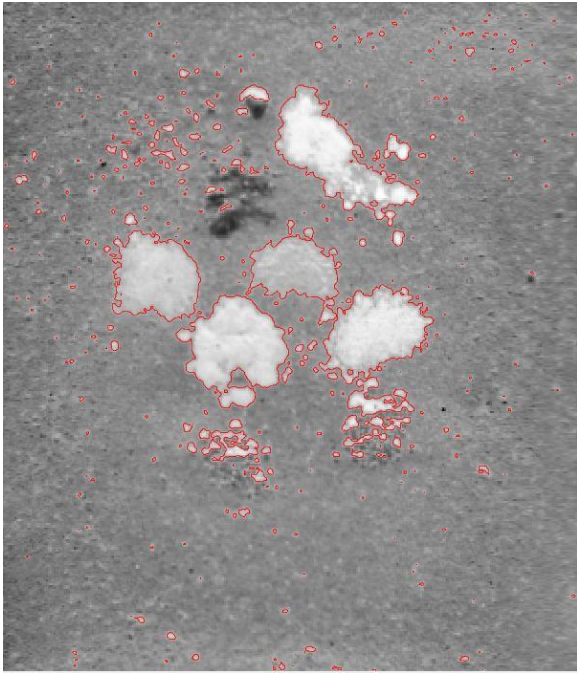


14. Level Set-Based Edge Detection Algorithm: Chemical Array

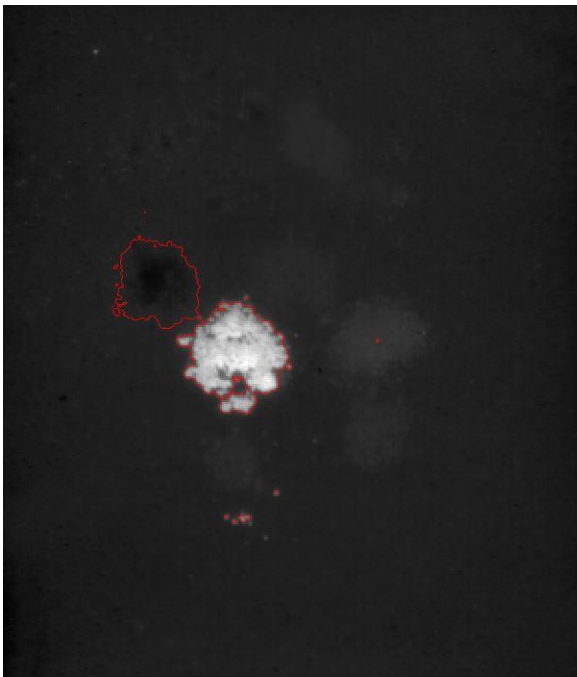
Reflectance



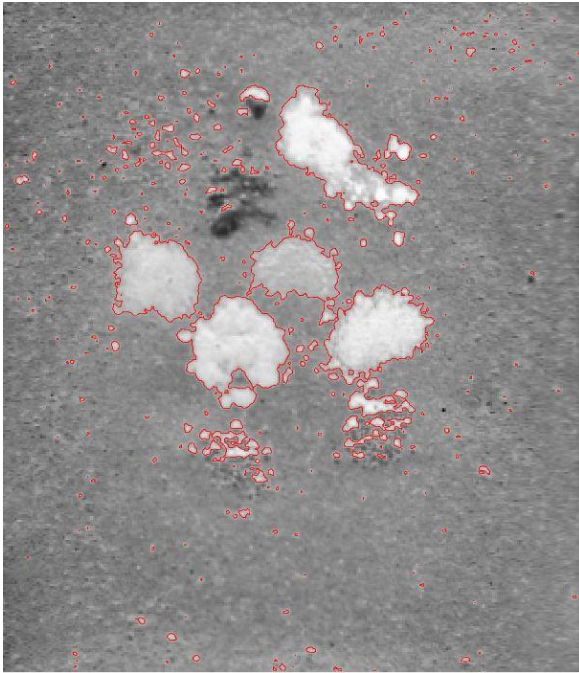
Optimal PCA



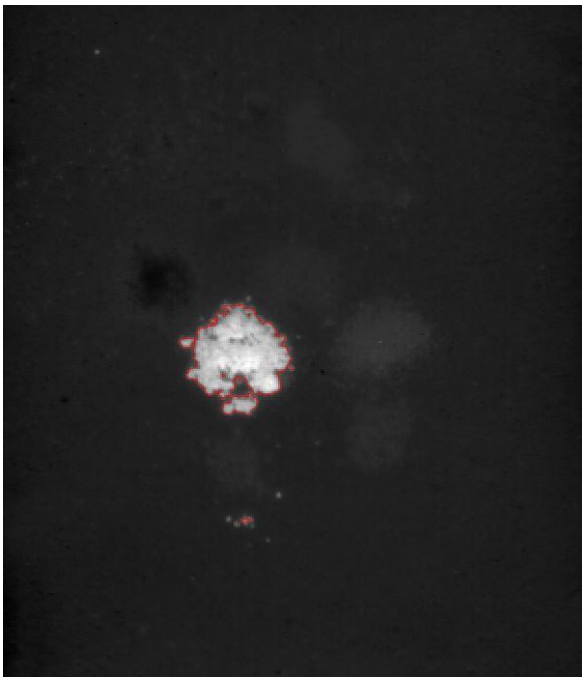
Optimal MNF



Full PCA

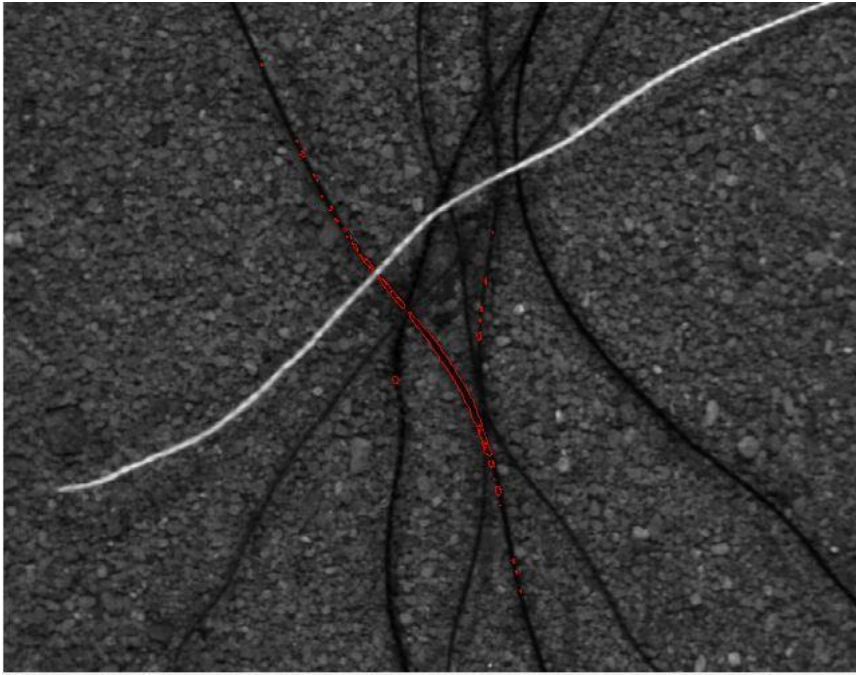


Full MNF

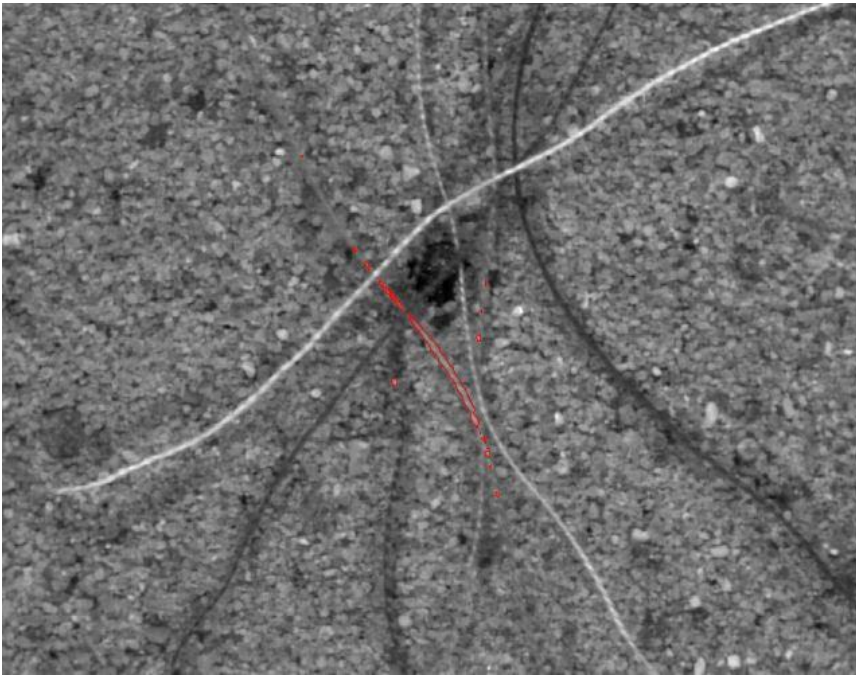


15. Level Set-Based Edge Detection Algorithm: Cloth Threads

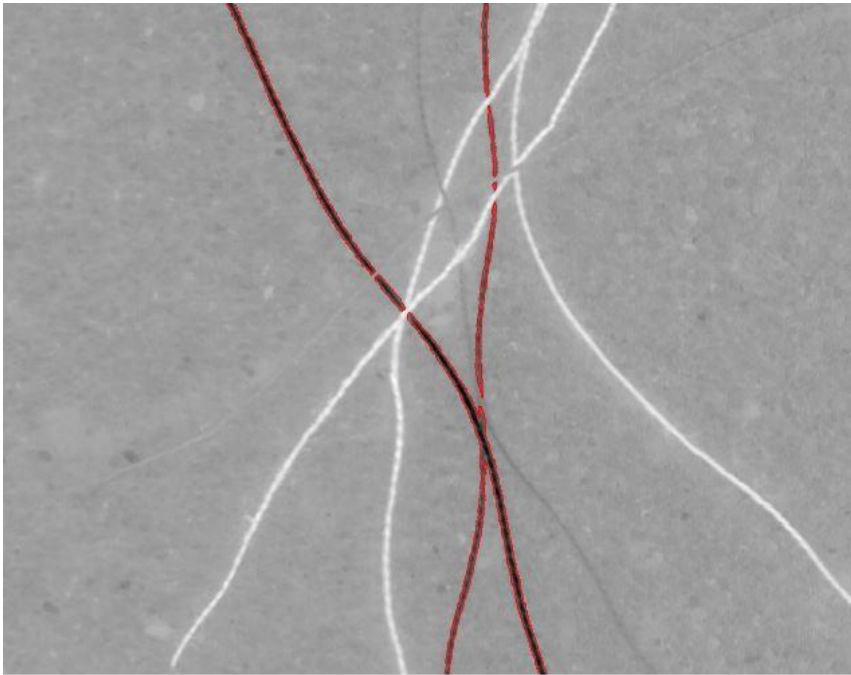
Reflectance



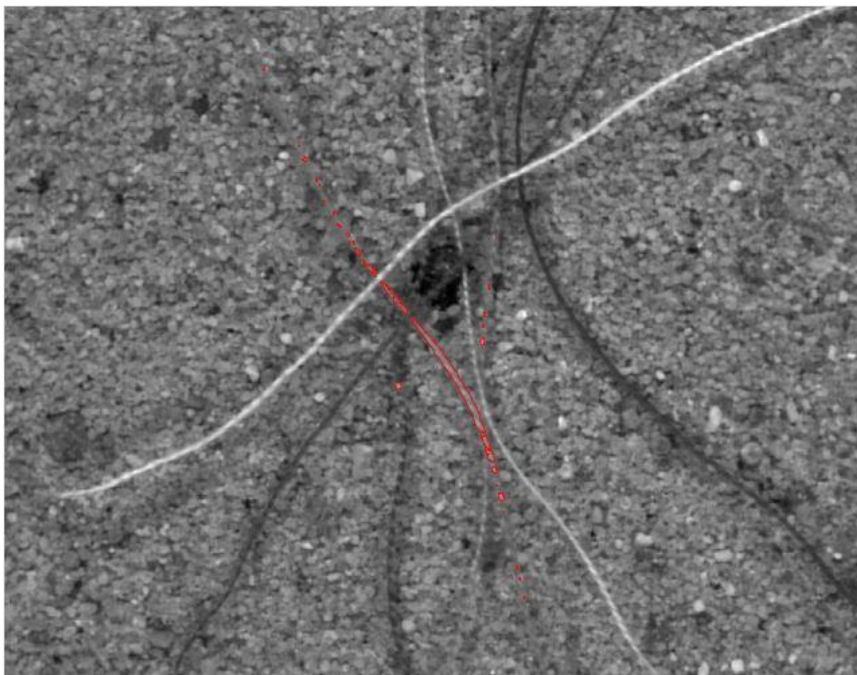
Optimal PCA



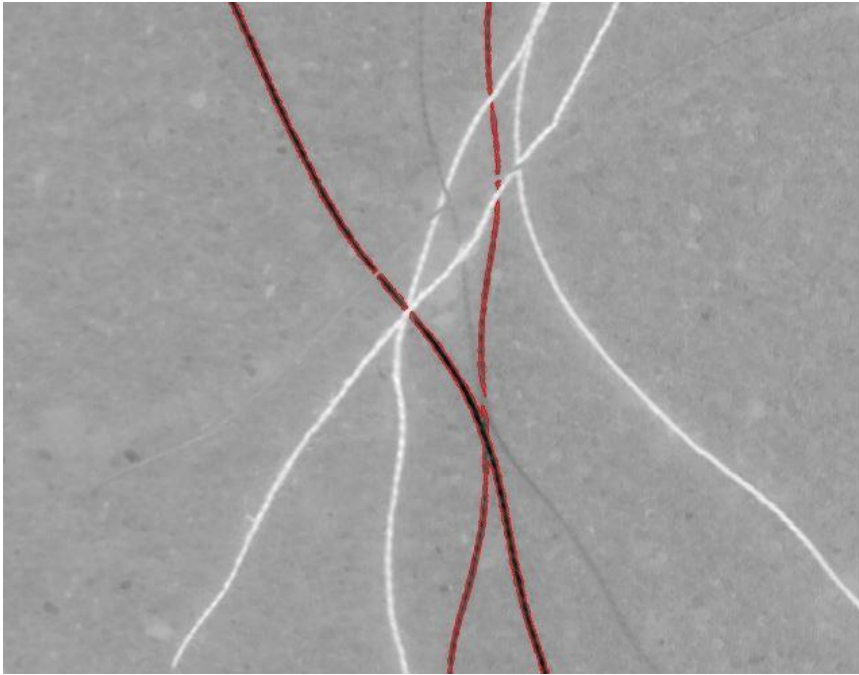
Optimal MNF



Full PCA



Full MNF



APPENDIX B: LIKERT SCORING

The Likert scale is inherently an ordinal ranking construct, meaning that the distances between the ratings do not have empirical meaning – an oft observed limitation of the Likert scale methodology. In order to mitigate this limitation, this dissertation establishes empirical traceability between each Likert rating and an underlying empirical measurement where possible, such as for the false positive criterion.

The key advantage of applying a Likert scale construct to this study's evaluation step is that Likert allows empirically derived evaluations (e.g., false alarms as measured against ground truth data) to be measured within the same evaluation construct as ratings derived by less empirical means (e.g., rating localization in the absence of ground truth). This study takes the position that remote sensing is both an art and a science, but that the art component should be informed by rigorous scientific measurement as much as possible. To that end, this dissertation relies on empirical measurement to its maximum effective range, and uses expert judgement to complete the journey to its conclusion.

Figure 323 presents the Likert scale for measuring false negatives in the edge plane. False negatives are more challenging to measure than false positives since they present as something missing that should be present, rather than something easily recognized as out of place such as a single pixel false alarm. As such, this work uses image sampling and image flickering techniques to measure false negatives on a per

feature basis rather than on a per pixel basis. Specifically, image sampling techniques are used to generate an estimate of how many features reside within the original HSI cube, and image flickering techniques are used to measure how many false negatives are present within the edge plane.

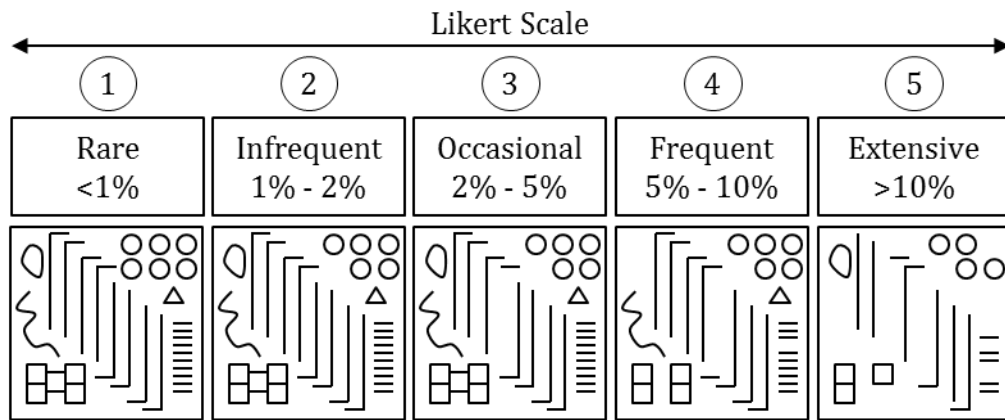


Figure 323: Likert Scale for Canny's False Negative Criterion

For example, consider Figure 323's image footprint, which models image features within a 100 x 100 pixel image. The model rating a rare rating contains all fifty features and represents the most accurate edge plane rendering achievable. As the edge planes degrade in quality, they begin to generate false negatives as seen as the Likert scale proceeds to a 5 rating, which is clearly a very weak edge plane.

Image sampling is a useful technique for creating the baseline for measuring false negatives because it obviates the need for manually truthing thousands of features across large datasets. Sampling takes advantage of the relatively even dispersal of features

across a scene or major subsections of a scene. For example, by manually truthing the volume of unique features within two to four 100 x 100 pixel samples of a hypercube, this methodology can confidently estimate the number of features across the overall scene. With a high-confidence estimate of the number of total unique features in the scene, a traditional image flickering procedure measures the number of false negatives across the full scene, after which the false negative rate is calculated using the estimated baseline and translated into a Likert score.

Figure 324 presents the Likert scale for measuring localization in the edge plane, where black features represent true features and red features edge plane localization errors. Similar to the evaluation techniques for false positives and false negatives, the localization evaluation technique measures how frequently an algorithm delineates an edge in the correct position (i.e., directly on top of the edge in the original image). A simple edge plane overlay onto the original image is used to measure localization.

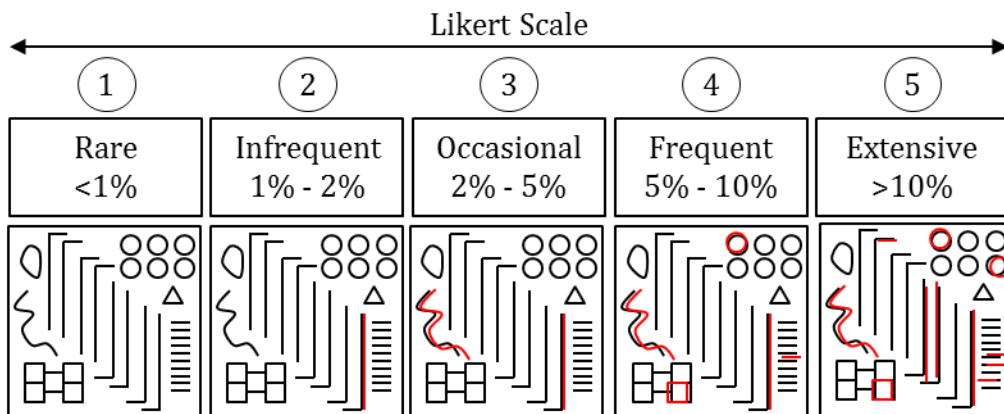


Figure 324: Likert Scale for Canny's Localization Criterion

For example, consider the models in Figure 324, where a simple edge plane overlay on the original image enables a quick and accurate count of localization errors. This technique also lends insight into the magnitude and direction of localization errors as well as which physical materials might increase the likelihood of localization errors. Again, note the natural break between Frequent/Extensive ratings and the Rare/Infrequent/Occasional ratings with respect to the barrier that a high volume of localization errors can present to reliable edge mapping.

Figure 325 presents the Likert scale for measuring robustness to noise in the edge plane, the first of Canny's secondary criteria addressed in this study. To measure robustness to noise, an initial understanding of the noise environment is required, a task accomplished within the preprocessing component for each HSI dataset. Specifically, the preprocessing component identifies and measures each dataset's noise behavior, which serves as the reference for measuring an experiment's performance against Canny's robustness to noise criterion.

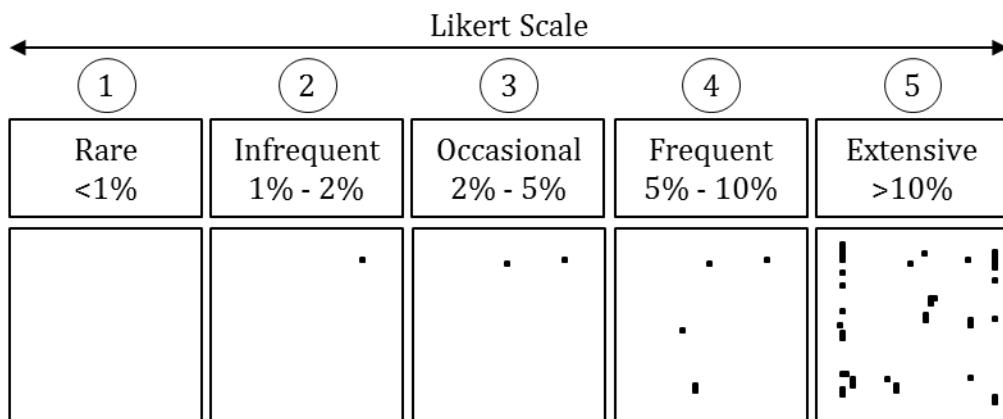


Figure 325: Likert Scale for Canny's robustness to noise Criterion

For example, consider the models in Figure 325, which are built on a reference model of 50 noise pixels within a 100 x 100 pixel cube. An experiment that is strongly robust to noise will earn a rare or infrequent rating by overcoming all but a handful of noise pixels. Tests that struggle to overcome noise will evident a comparatively high volume of noise pixels retained within the edge plane – a suboptimal result.

Figure 326 presents the Likert scale for measuring single-point response in the edge plane, where the optimal single-point response performance corresponds to thin, single-pixel edges consistent with Canny’s criterion for strong edge detection performance. Specifically, Canny specified that an optimal edge operator will confidently declare a single-pixel boundary between adjacent materials, a performance which corresponds to a Likert score of one. As seen in Figure 326, edges of one-pixel, two-pixel and three-pixel generally correspond to good performance, while edge widths beyond three pixels are unacceptably imprecise.

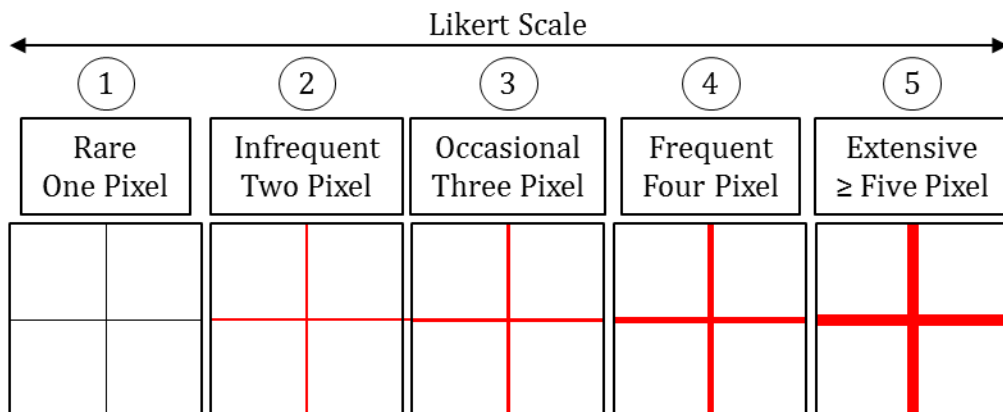


Figure 326: Likert Scale for Canny's Single-Point Response Criterion

Finally, Figure 327 presents the Likert scale for measuring the Unbroken Edge criterion, in which black features are edge features and red features are edge breaks. Similar to the localization evaluation technique, the unbroken edge evaluation technique is feature-based (as opposed to pixel based) in the sense that it counts the number of features that have one or more breaks along their edges. Specifically, this evaluation criterion equally scores a feature with one edge break equally to the same feature with three edge breaks. This structure strikes a balance between high performance standards and reasonable penalties by establishing a high premium on unbroken edges while not overly penalizing an algorithm if it generates several breaks in only a few features.

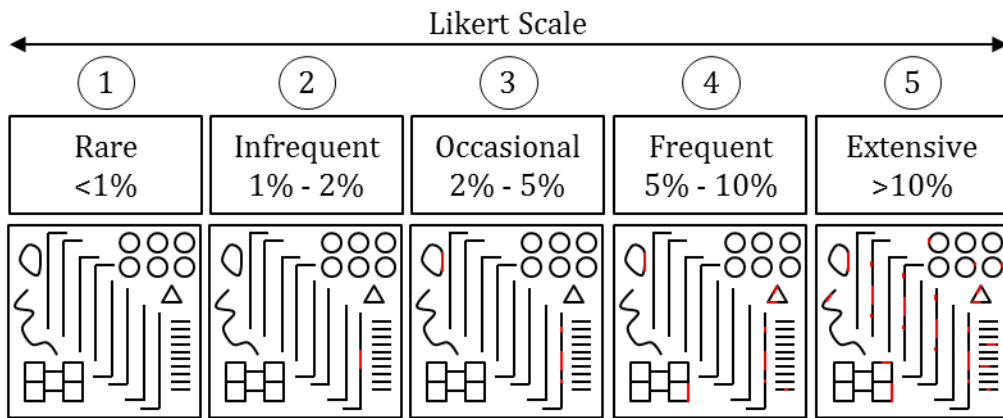


Figure 327: Likert Scale for Canny's Unbroken Edges Criterion

BIBLIOGRAPHY

- [1] J. Canny, "A Computational Approach to Edge Detection," *IEEE Transactions on Pattern Analysis and Machine Intelligence*, vol. 8, no. 6, pp. 679-698, 1986.
- [2] R. Sivanpillai and R. Congalton, "Future Landsat Data Needs at the Local and State Levels: An AmericaView Perspective," *Photogrammetric Engineering & Remote Sensing*, vol. 82, no. 8, p. 617-623, 2016.
- [3] Jet Propulsion Lab - California Institute of Technology, "AVIRIS Workshop Bibliographies," [Online]. Available: http://aviris.jpl.nasa.gov/documents/workshop_biblios.html. [Accessed 10 September 2010].
- [4] J. Schott, *Remote Sensing*, Second Edition, New York: Oxford University Press, 2007.
- [5] M. R. Elowitz, "What is Imaging Spectroscopy (Hyperspectral Imaging)?," [Online]. Available: <http://www.markelowitz.com/Hyperspectral.html>. [Accessed 4 9 2016].
- [6] T. Trautmann, "7. From Radiation Fields to Atmospheric Concentrations – Retrieval of Geophysical Parameters," 26 3 2007. [Online]. Available: http://atmos.caf.dlr.de/projects/scops/sciamachy_book/sciamachy_book_figures/chapter_7_figures.html. [Accessed 2016 4 9].
- [7] K. Szekiolda, J. Bowles, D. Gillis and W. Miller, "Interpretation of Absorption Bands in Airborne Hyperspectral Radiance Data," *Sensors*, vol. 9, no. 4, pp. 2907-2925, 2009.
- [8] A. Mariano and J. Grossmann, "Hyperspectral material identification on radiance data using single-atmosphere or multiple-atmosphere modeling," *Journal of Applied Remote Sensing*, vol. 4, pp. 1-17, 2010.
- [9] L. Bernstein, S. Adler-Golden, R. Sundberg, R. Levine, T. Perkins, A. Berk, A. Ratkowski and M. Hoke, "A new method for atmospheric correction and aerosol optical property retrieval for vis-swir multi- and hyperspectral imaging sensors: quick atmospheric correction," *Scientific and Technical Aerospace Reports*, vol. 44, no. 6, pp. 1-5, 2006.
- [10] L. Bernstein, X. Jin, B. Gregor and S. Adler-Golden, "Quick atmospheric correction code: algorithm description and recent upgrades," *Optical Engineering*, vol. 51, no. 11, pp. 1-12, 2012.

- [11 United States Geological Survey, "USGS Digital Spectral Library 06," 25 11 2013.
] [Online]. Available: <http://speclab.cr.usgs.gov/spectral.lib06/>. [Accessed 2 12 2010].
- [12 National Air and Space Administration, "MODIS: Moderate Resolution Imaging
] Spectroradiometer," [Online]. Available: <http://modis.gsfc.nasa.gov/>. [Accessed 7 2 2011].
- [13 National Air and Space Administration, "The Landsat Program," [Online].
] Available: <http://landsat.gsfc.nasa.gov/>. [Accessed 7 2 2011].
- [14 R. McCoy, J. Blake and K. Andrews, "Detecting hydrocarbon microseepage using
] hydrocarbon absorption bands of reflectance spectra of surface soils," *Oil and Gas Journal*, vol. 99, no. 22, pp. 40-45, 2001.
- [15 R. Gonzalez and R. Woods, Digital Image Processing, Third Edition, Upper Saddle
] River, New Jersey USA: Pearson Prentice Hall, 2008.
- [16 J. Townshend, T. Goff and C. Tucker, "Multitemporal dimensionality of images of
] normalized difference vegetation index at continental scales," *IEEE Transactions on Geoscience and Remote Sensing*, vol. 23, no. 6, pp. 888-895, 1985.
- [17 Y. Xie, X. Zhao, L. Li and H. Wang, "Calculating NDVI for Landsat 7-ETM data
] after atmospheric correction using 6S model: A case study in Zhangye City, China," in *18th International Conference on Geoinformatics*, Beijing, 2010.
- [18 B. Wilfong, D. Gorchov and M. Henry, "Detecting an Invasive Shrub in Deciduous
] Forest Understories Using Remote Sensing," *Weed Science*, vol. 57, no. 5, pp. 512 - 520, 2009.
- [19 Y.-C. Tian, K.-J. Gu, X. Chu, X. Yao, W.-X. Cao and Y. Zhu, "Comparison of
] different hyperspectral vegetation indices for canopy leaf nitrogen concentration estimation in rice," *Plant and Soil*, vol. 376, no. 1, pp. 193-209, 2014.
- [20 Q. Wang, C. Li, J. Wang, Y. Huang, X. Song and W. Huang, "Monitoring Winter
] Wheat Maturity By Hyperspectral Vegetation Indices," *Intelligent Automation & Soft Computing*, vol. 18, no. 5, pp. 537-546, 2012.
- [21 C. Unsalan and K. Boyer, "Classifying land development in high-resolution
] Satellite imagery using hybrid structural-multispectral features," *IEEE Transactions on Geoscience and Remote Sensing*, vol. 42, no. 12, pp. 2840-2850, 2004.
- [22 M. Chiliński, "Comparison of the results of modified NDVI indicator established on
] the basis of measurements by hyperspectral spectrometer and digital camera," *Ecological Questions*, vol. 17, pp. 35-42, 2013.
- [23 L. Galvão, "Sun and view angle effects on NDVI determination of land cover types
] in the Brazilian Amazon region with hyperspectral data," *International Journal of Remote Sensing*, vol. 25, no. 10, pp. 1861-1879, 2004.
- [24 R. Pu, S. Bell and D. P. R. English, "Developing Hyperspectral Vegetation Indices
] for Identifying Seagrass Species and Cover Classes," *Journal of Coastal Research*, vol. 31, no. 3, pp. 595-615, 2015.

- [25 G. S. Okin, D. A. Roberts, B. Murray and W. J. Okin, "Practical limits on
] hyperspectral vegetation discrimination in arid and semiarid environments," *Remote Sensing of Environment*, vol. 77, no. 2, pp. 212-225, 2001.
- [26 P. S. Thenkabail, R. B. Smith and E. De Pauw, "yperspectral Vegetation Indices
] and Their Relationships with Agricultural Crop Characteristics," *Remote Sensing of Environment*, vol. 71, no. 2, pp. 158-182, 2000.
- [27 C. Zhang, "Combining Hyperspectral and Lidar Data for Vegetation Mapping in the
] Florida Everglades," *Photogrammetric Engineering and Remote Sensing*, vol. 80, no. 8, pp. 733-743, 2014.
- [28 B. S. Lee, K. Mcgwire and C. Fritsen, "Identification and quantification of aquatic
] vegetation with hyperspectral remote sensing in western Nevada rivers, USA," *International Journal of Remote Sensing*, vol. 32, no. 24, pp. 9093-9117, 2011.
- [29 I. Herrmann, U. Shapira, S. Kinast, A. Karnieli and D. Bonfil, "Ground-level
] hyperspectral imagery for detecting weeds in wheat fields," *Precision Agriculture*, vol. 14, no. 6, pp. 637-659, 2013.
- [30 A. Olsson, "Feasibility of Invasive Grass Detection in a Desertscrub Community
] Using Hyperspectral Field Measurements and Landsat TM Imagery," *Remote sensing*, vol. 3, no. 12, pp. 2283 - 2304, 2011.
- [31 Z.-T. Ouyang, Y. Gao, X. Xie, H.-Q. Guo, T.-T. Zhang and B. Zhao, "Spectral
] Discrimination of the Invasive Plant *Spartina alterniflora* at Multiple Phenological Stages in a Saltmarsh Wetland," *PLoS One*, vol. 8, no. 6, pp. 1-13, 2013.
- [32 S. Ge, M. Xu, G. Anderson and R. Carruthers, "Estimating Yellow Starthistle
] (*Centaurea solstitialis*) Leaf Area Index and Aboveground Biomass with the Use of Hyperspectral Data," *Weed Science*, vol. 55, no. 6, pp. 671 - 678, 2007.
- [33 R. Pu, P. Gong, Y. Tian, X. Miao, R. Carruthers and G. Anderson, "Using
] classification and NDVI differencing methods for monitoring sparse vegetation coverage: a case study of saltcedar in Nevada, USA," *International Journal of Remote Sensing*, vol. 29, no. 14, pp. 3987 - 4011, 2008.
- [34 B. Somers and G. P. Asner, "Multi-temporal hyperspectral mixture analysis and
] feature selection for invasive species mapping in rainforests," *Remote Sensing of Environment*, vol. 136, pp. 14 - 27, 2013.
- [35 J. Zhang, L. Yuan, R. Pu, R. W. Loraamm, G. Yang and J. Wang, "Comparison
] between wavelet spectral features and conventional spectral features in detecting yellow rust for winter wheat," *Computers and Electronics in Agriculture*, vol. 100, pp. 79-87, 2014.
- [36 H. Z. Shafri and N. Hamdan, "Hyperspectral Imagery for Mapping Disease
] Infection in Oil Palm Plantation Using Vegetation Indices and Red Edge Techniques," *American Journal of Applied Sciences*, vol. 6, no. 6, pp. 1031-1035, 2009.

- [37 S. Ray, N. Jain, R. Arora, S. Chavan and S. Panigrahy, "Utility of Hyperspectral
] Data for Potato Late Blight Disease Detection," *Journal of the Indian Society of Remote Sensing*, vol. 39, no. 2, pp. 161-169, 2011.
- [38 X. Cao, Y. Luo, Y. Zhou, J. Fan, X. Xu, J. West, X. Duan and D. Cheng,
] "Detection of Powdery Mildew in Two Winter Wheat Plant Densities and Prediction of Grain Yield Using Canopy Hyperspectral Reflectance," *PLoS One*, vol. 10, no. 3, pp. 1-14, 2015.
- [39 A. Apan, A. Held, S. Phinn and J. Markley, "Detecting sugarcane 'orange rust'
] disease using EO-1 Hyperion hyperspectral imagery," *International Journal of Remote Sensing*, vol. 25, no. 2, pp. 489-498, 2004.
- [40 S. Oshigami, Y. Yamaguchi, M. Mitsuishi, A. Momose and T. Yajima, "An
] advanced method for mineral mapping applicable to hyperspectral images: the composite MSAM," *Remote Sensing Letters*, vol. 6, no. 7, pp. 499-508, 2015.
- [41 F. Kruse, J. Boardman and J. Huntington, "Comparison of airborne hyperspectral
] data and eo-1 hyperion for mineral mapping," *IEEE Transactions on Geoscience and Remote Sensing*, vol. 41, no. 6, pp. 1388-1400, 2003.
- [42 J. Wang, W. Wang, K. Zhou, J. Yan and H. Liu, "Hyper-Spectral Remote Sensing
] Apply on Alteration Mineral Mapping," *Applied Mechanics and Materials*, vol. 303, no. 306, pp. 729 - 733, 2013.
- [43 R. G. Resmini, M. E. Kappus, W. S. Aldrich, J. C. Harsanyi and M. Anderson,
] "Mineral mapping with HYperspectral Digital Imagery Collection Experiment (HYDICE) sensor data at Cuprite, Nevada, U.S.A.," *International Journal of Remote Sensing*, vol. 18, no. 7, pp. 1553-1570, 1997.
- [44 W. Ge, Q. Cheng, L. Jing, Y. Chen, X. Guo, H. Ding and Q. Liu, "Mineral mapping
] in the western Kunlun Mountains using Tiangong-1 hyperspectral imagery," *IOP Conference Series: Earth and Environmental Science*, vol. 34, no. 1, pp. 1-7, 2016.
- [45 P. Bierwirth, D. Huston and R. S. Blewett, "Hyperspectral mapping of mineral
] assemblages associated with gold mineralization in the central Pilbara, Western Australia," *Economic Geology and the Bulletin of the Society of Economic Geologists*, vol. 97, no. 4, pp. 819-826, 2002.
- [46 M. Xiong, F. Zhang, Q. Ran, W. Hu and W. Li, "Representation-based
] classifications with Markov random field model for hyperspectral urban data," *Journal Of Applied Remote Sensing*, vol. 8, no. 1, pp. 1-12, 2014.
- [47 J. Zou, W. Li, X. Huang and Q. Du, "Classification of hyperspectral urban data
] using adaptive simultaneous orthogonal matching pursuit," *Journal Of Applied Remote Sensing*, vol. 8, no. 1, pp. 1-14, 2014.
- [48 F. Dell'Acqua, P. Gamba, A. Ferrari, J. Palmason, J. Benediktsson and K. Arnason,
] "Exploiting Spectral and Spatial Information in Hyperspectral Urban Data With High Resolution," *IEEE Geoscience and Remote Sensing Letters*, vol. 1, no. 4, pp. 322-326, 2004.

- [49 D. Akbari, A. Safari and S. Homayouni, "Object-Based Hyperspectral
] Classification of Urban Areas by Using Marker-Based Hierarchical Segmentation,"
Photogrammetric Engineering and Remote Sensing, vol. 80, no. 10, pp. 963-970,
2014.
- [50 X. Tong, H. Xie and Q. Weng, "Urban Land Cover Classification With Airborne
] Hyperspectral Data: What Features to Use?," *IEEE Journal of Selected Topics in
Applied Earth Observations and Remote Sensing*, vol. 7, no. 10, pp. 3998-4009,
2014.
- [51 J. A. Xudong Kang, J. A. Shutao Li and J. A. Benediktsson, "Spectral–Spatial
] Hyperspectral Image Classification With Edge-Preserving Filtering," *IEEE
Transactions on Geoscience and Remote Sensing*, vol. 52, no. 5, pp. 2666-2677,
2014.
- [52 J. Xia, L. Bombrun, T. Adali, Y. Berthoumieu and C. Germain, "Spectral–Spatial
] Classification of Hyperspectral Images Using ICA and Edge-Preserving Filter via
an Ensemble Strategy," *IEEE Transactions on Geoscience and Remote Sensing*,
vol. 54, no. 8, pp. 4971-4982, 2016.
- [53 M. Herold, D. Roberts, V. Noronha and O. Smadi, "Imaging spectrometry and
] asphalt road surveys," *Transportation Research Part C*, vol. 16, no. 2, pp. 153-166,
2008.
- [54 M. Á. Fernández de La Ossa, C. García-Ruiz and J. M. Amigo, "Near infrared
] spectral imaging for the analysis of dynamite residues on human handprints,"
Talanta, vol. 130, pp. 315-321, 2014.
- [55 M. Á. Fernández de La Ossa, J. M. Amigo and C. García-Ruiz, "Detection of
] residues from explosive manipulation by near infrared hyperspectral imaging: A
promising forensic tool," *Forensic Science International*, vol. 242, pp. 228-235,
2014.
- [56 C. Kendziora, R. Furstenberg, M. Papantonakis, V. Nguyen, J. Byers and R. McGill,
] "Infrared photothermal imaging spectroscopy for detection of trace explosives on
surfaces," *Applied Optics*, vol. 54, no. 31, pp. F129-F138, 2015.
- [57 M. Phillips and B. Bernacki, "Hyperspectral microscopy of explosives particles
] using an external cavity quantum cascade laser," *Optical Engineering*, vol. 52, no.
6, pp. 1-8, 2013.
- [58 T. Dubroca, G. Brown and R. Hummel, "Detection of explosives by differential
] hyperspectral imaging," *Optical Engineering*, vol. 53, no. 2, pp. 1-7, 2014.
- [59 F. Fuchs, S. Hugger, M. Kinzer, R. Aidam, W. Bronner, R. Losch, Q. Yang, K.
] Degreif and F. Schnurer, "Imaging standoff detection of explosives using widely
tunable midinfrared quantum cascade lasers," *Optical Engineering*, vol. 49, no. 11,
pp. 1-8, 2010.
- [60 T. Blake, J. Kelly, N. Gallagher, P. Gassman and T. Johnson, "Passive standoff
] detection of RDX residues on metal surfaces via infrared hyperspectral imaging,"
Analytical And Bioanalytical Chemistry, vol. 395, no. 2, pp. 337-348, 2009.

- [61 R. Bhargava, R. Schwartz Perlman, D. Fernandez, I. Levin and E. Bartick, "Non-
] invasive detection of superimposed latent fingerprints and inter-ridge trace evidence
by infrared spectroscopic imaging," *Analytical and Bioanalytical Chemistry*, vol.
394, no. 8, pp. 2069-2075, 2009.
- [62 N. Boesche, C. Rogass, C. Lubitz, M. Brell, S. Herrmann, C. Mielke, S. Tonn, O.
] Appelt, U. Altenberger and H. Kaufmann, "Hyperspectral REE (Rare Earth
Element) Mapping of Outcrops—Applications for Neodymium Detection," *Remote
Sensing*, vol. 7, no. 5, pp. 5160-5186, 2015.
- [63 J. Dai, D. Wang, R. Wang and Z. Chen, "Quantitative estimation of concentrations
] of dissolved rare earth elements using reflectance spectroscopy," *Journal Of
Applied Remote Sensing*, vol. 7, no. 1, pp. 1-14, 2013.
- [64 S. Jay, M. Guillaume and J. Blanc-Talon, "Underwater Target Detection With
] Hyperspectral Data: Solutions for Both Known and Unknown Water Quality,"
*IEEE Journal of Selected Topics in Applied Earth Observations and Remote
Sensing*, vol. 5, no. 4, pp. 1213-1221, 2012.
- [65 B. B. aylor, M. H. Taylor, T. Dinter and A. Bracher, "Estimation of relative
] phycoerythrin concentrations from hyperspectral underwater radiance
measurements--A statistical approach," *Journal of Geophysical Research: Oceans*,
vol. 118, no. 6, pp. 2948-2960, 2013.
- [66 Q. Lu, M. Tang, J. Cai, J. Zhao and S. Vittayapadung, "Vis/NIR Hyperspectral
] Imaging for Detection of Hidden Bruises on Kiwifruits," *Czech Journal Of Food
Sciences*, vol. 29, no. 6, pp. 595-602, 2011.
- [67 L. Pan, Q. Zhang, W. Zhang, Y. Sun, P. Hu and K. Tu, "Detection of cold injury in
] peaches by hyperspectral reflectance imaging and artificial neural network," *Food
Chemistry*, vol. 192, pp. 134-141, 2016.
- [68 Z. Han, J. Wan, J. Zhang and H. Zhang, "Abundance quantification by independent
] component analysis of hyperspectral imagery for oil spill coverage calculation,"
Chinese Journal of Oceanology and Limnology, vol. 34, no. 145, pp. 1-9, 2016.
- [69 D. Liu, J. Zhang and X. Wang, "Reference spectral signature selection using
] density-based cluster for automatic oil spill detection in hyperspectral images,"
Optics Express, vol. 24, no. 7, pp. 7411-7425, 2016.
- [70 B. Liu, Y. Li, P. Chen and X. Zhu, "Extraction of Oil Spill Information Using
] Decision Tree Based Minimum Noise Fraction Transform," *Journal of the Indian
Society of Remote Sensing*, vol. 44, no. 3, pp. 421-426, 2016.
- [71 Y. Lu, Q. Tian, X. Wang, G. Zheng and X. Li, "Determining oil slick thickness
] using hyperspectral remote sensing in the Bohai Sea of China," *International
Journal of Digital Earth*, vol. 6, no. 1, pp. 76-93, 2013.
- [72 S. Sun, C. Hu, L. Feng, G. A. Swayze, J. Holmes, G. Graettinger, I. Macdonald, O.
] Garcia and I. Leifer, "Oil slick morphology derived from AVIRIS measurements of
the Deepwater Horizon oil spill: Implications for spatial resolution requirements of
remote sensors," *Marine Pollution Bulletin*, vol. 103, no. 1-2, pp. 276-285, 2016.

- [73 I. Leifer, W. J. Lehr, D. Simecek-Beatty, E. Bradley, R. Clark, P. Dennison, Y. Hu,
] S. Matheson, C. E. Jones, B. Holt, M. Reif, D. A. Roberts, J. Svejksky and G. Swayze, "State of the art satellite and airborne marine oil spill remote sensing: Application to the BP Deepwater Horizon oil spill," *Remote Sensing of Environment*, vol. 124, pp. 185-209, 2012.
- [74 R. F. Kokaly, B. R. Couvillion, J. M. Holloway, D. A. Roberts, S. L. Ustin, S. H.
] Peterson, S. Khanna and S. C. Piazza, "Spectroscopic remote sensing of the distribution and persistence of oil from the Deepwater Horizon spill in Barataria Bay marshes," *Remote Sensing of Environment*, vol. 129, pp. 210-230, 2013.
- [75 G. Sicot, M. Lennon, V. Miegbielle and D. Dubucq, "Estimation of the thickness
] and emulsion rate of oil spilled at sea using hyperspectral remote sensing imagery in the SWIR domain," *The International Archives of the Photogrammetry, Remote Sensing and Spatial Information Sciences*, Vols. XL-3, no. W3, pp. 445-450, 2015.
- [76 S. H. Peterson, D. A. Roberts, M. Beland, R. F. Kokaly and S. L. Ustin, "Oil
] detection in the coastal marshes of Louisiana using MESMA applied to band subsets of AVIRIS data," *Remote Sensing of Environment*, vol. 159, pp. 222-231, 2015.
- [77 M. Zare-Baghbidi and S. Homayouni, "Fast hyperspectral anomaly detection for
] environmental applications," *Journal Of Applied Remote Sensing*, vol. 7, no. 1, pp. 1-12, 2013.
- [78 R. Clark, G. Swayze, I. Leifer, K. Livo, R. Kokaly, T. Hoefen, R. Green, N.
] Pearson, C. Sarture, I. McCubbin, D. Roberts, E. Bradley, D. Steele, T. Ryan, R. Dominguez and T. AVIRIS, "A Method for Quantitative Mapping of Thick Oil Spills," *United States Geological Survey Open File Report 2010-1167*, pp. 1-51, 2010.
- [79 F. Salem, M. Kafatos, T. El-Ghazawi, R. Gomez and R. Yang, "Hyperspectral
] image assessment of oil-contaminated wetland," *International Journal of Remote Sensing*, vol. 26, no. 4, pp. 811-821, 2005.
- [80 H. Srivastava and T. Singh, "Assessment and development of algorithms to
] detection of oil spills using MODIS data," *Journal of the Indian Society of Remote Sensing*, vol. 38, no. 1, pp. 161-167, 2010.
- [81 J. Rivera, F. Valverde, M. Saldana and V. Manian, "Security inspection in ports by
] anomaly detection using hyperspectral imaging technology," *Proceedings of SPIE - The International Society for Optical Engineering*, vol. 8743, pp. 1-11, 2013.
- [82 F. Franch-Lage, J. M. Amigo, E. Skibsted, S. Maspocho and J. Coello, "Fast
] assessment of the surface distribution of API and excipients in tablets using NIR-hyperspectral imaging," *International Journal of Pharmaceutics*, vol. 411, no. 1, pp. 27-35, 2011.
- [83 J. Amigo, "Practical issues of hyperspectral imaging analysis of solid dosage
] forms," *Analytical and Bioanalytical Chemistry*, vol. 398, no. 1, pp. 93-109, 2010.

- [84 D. Goltz, M. Attas, G. Young, E. Cloutis and M. Bedynski, "Assessing stains on
] historical documents using hyperspectral imaging," *Journal of Cultural Heritage*,
vol. 11, no. 1, pp. 19-26, 2010.
- [85 Q. Li, W. Wang, C. Ma and Z. Zhu, "Detection of physical defects in solar cells by
] hyperspectral imaging technology," *Optics and Laser Technology*, vol. 42, no. 6,
pp. 1010-1013, 2010.
- [86 J. M. Medina and J. A. Diaz, "Scattering characterization of nanopigments in
] metallic coatings using hyperspectral optical imaging," *Applied Optics*, vol. 50, no.
31, pp. G47-G55, 2011.
- [87 G. Mirschel, O. Daikos, T. Scherzer and C. Steckert, "Near-infrared chemical
] imaging used for in-line analysis of inside adhesive layers in textile laminates,"
Analytica Chimica Acta, vol. 932, pp. 69-79, 2016.
- [88 National Air and Space Administration, "AVIRIS Airborne Visible/Infrared
] Imaging Spectrometer," 28 6 2016. [Online]. Available: <http://aviris.jpl.nasa.gov/>.
[Accessed 24 08 2016].
- [89 F. Kruse, A. Lefkoff and J. Dietz, "xpert system-based mineral mapping in northern
] death valley, California/Nevada, using the Airborne Visible/Infrared Imaging
Spectrometer (AVIRIS)," *Remote Sensing of Environment*, vol. 44, no. 2, pp. 309-
336, 1993.
- [90 A. Smailbegovic, K. J. Gray, V. Murphy and R. Holbrook, "Spectroscopic and
] hyperspectral evaluation of possible hydrocarbon occurrences in estuarine
sediments, North Charleston, South Carolina, USA," in *IEEE WHISPERS First
Workshop on Hyperspectral Image and Signal Processing: Evolution in Remote
Sensing*, Grenoble, 2009.
- [91 S. Veraverbeke, E. N. Stavros and S. J. Hook, "Assessing fire severity using
] imaging spectroscopy data from the Airborne Visible/Infrared Imaging
Spectrometer (AVIRIS) and comparison with multispectral capabilities," *Remote
Sensing of Environment*, vol. 154, pp. 153-163, 2014.
- [92 Harris Geospatial Solutions, "Push Broom and Whisk Broom Sensors," Harris
] Geospatial Solutions, 24 9 2013. [Online]. Available:
[http://www.harrisgeospatial.com/Company/PressRoom/Blogs/TabId/836/ArtMID/2
928/ArticleID/13618/Push-Broom-and-Whisk-Broom-Sensors.aspx](http://www.harrisgeospatial.com/Company/PressRoom/Blogs/TabId/836/ArtMID/2928/ArticleID/13618/Push-Broom-and-Whisk-Broom-Sensors.aspx). [Accessed 24 8
2016].
- [93 Natural Resources Canada, "Multispectral Scanning," Natural Resources Canada,
] 25 11 2015. [Online]. Available: [http://www.nrcan.gc.ca/earth-
sciences/geomatics/satellite-imagery-air-photos/satellite-imagery-
products/educational-resources/9337](http://www.nrcan.gc.ca/earth-sciences/geomatics/satellite-imagery-air-photos/satellite-imagery-products/educational-resources/9337). [Accessed 24 8 2016].
- [94 SPECIM Spectral Imaging, "AisaFENIX Hyperspectral Sensor," 1 6 2015.
] [Online]. Available: <http://www.specim.fi/products/aisafenix-hyperspectral-sensor/>.
[Accessed 29 8 2016].

- [95] SPECIM Spectral Imaging, "AisaFENIX 1K," 1 6 2015. [Online]. Available:
] <http://www.specim.fi/products/aisafenix1k/>. [Accessed 29 8 2016].
- [96] ProSpecTIR, "Free Data Samples," 2012. [Online]. Available:
] <http://www.spectir.com/free-data-samples/>. [Accessed 29 8 2016].
- [97] W. Roper and S. Dutta, "Oil Spill and Pipeline Condition Assessment Using
] Remote Sensing and Data Visualization Management Systems," 2006. [Online].
 Available:
<http://citeseerx.ist.psu.edu/viewdoc/download?doi=10.1.1.131.6669&rep=rep1&type=pdf>. [Accessed 29 8 2016].
- [98] K. Cawse-Nicholson, S. B. Damelin, A. Robin and M. Sears, "Determining the
] Intrinsic Dimension of a Hyperspectral Image Using Random Matrix Theory,"
IEEE Transactions on Image Processing, vol. 22, no. 4, pp. 1301-1310, 2013.
- [99] G. Vaughan and W. Calvin, "Mapping weathering and alteration minerals in the
] comstock and geiger grade areas using visible to thermal infrared airborne remote
 sensing data," *Scientific and Technical Aerospace Reports*, vol. 44, no. 23, pp. 1-20,
 2006.
- [10] F. Kruse, R. Bedell, J. Taranik, W. Peppin, O. Weatherbee and W. Calvin,
 0] "Mapping alteration minerals at prospect, outcrop and drill core scales using
 imaging spectrometry," *International Journal of Remote Sensing*, vol. 33, no. 6, pp.
 1780-1798, 2012.
- [10] J. Pontius, M. Martin, L. Plourde and R. Hallett, "Ash decline assessment in
 1] emerald ash borer-infested regions: A test of tree-level, hyperspectral technologies,"
Remote Sensing of Environment, vol. 112, no. 5, pp. 2665-2676, 2008.
- [10] S. T. Brantley, J. C. Zinnert and D. R. Young, "Application of hyperspectral
 2] vegetation indices to detect variations in high leaf area index temperate shrub
 thicket canopies," *Remote Sensing of Environment*, vol. 115, no. 2, pp. 514-523,
 2011.
- [10] M. J. Santos, J. A. Greenberg and S. L. Ustin, "Using hyperspectral remote sensing
 3] to detect and quantify southeastern pine senescence effects in red-cockaded
 woodpecker (*Picoides borealis*) habitat," *Remote Sensing of Environment*, vol. 114,
 no. 6, pp. 1242-1250, 2010.
- [10] X. Miao, R. Patil, J. Heaton and R. Tracy, "Detection and classification of invasive
 4] saltcedar through high spatial resolution airborne hyperspectral imagery,"
International Journal of Remote Sensing, vol. 32, no. 8, pp. 2131-2150, 2011.
- [10] M. Folkman, J. Pearlman, L. Liao and P. Jarecke, "EO-1/Hyperion hyperspectral
 5] imager design, development, characterization, and calibration," 2007. [Online].
 Available: http://www.ugpti.org/smartse/research/citations/downloads/Folkman-Hyperion_Design-2007.pdf. [Accessed 26 8 2016].
- [10] United States Geological Survey, "Sensors - Hyperion," 13 12 2011. [Online].
 6] Available: <https://eol.usgs.gov/sensors/hyperion>. [Accessed 29 8 2016].

- [10] United States Geological Survey, "EarthExplorer," 28 2016. [Online]. Available: <http://earthexplorer.usgs.gov/>. [Accessed 29 8 2016].
- [10] P. Baranowski, W. Mazurek and J. Pastuszka-Woźniak, "Supervised classification of bruised apples with respect to the time after bruising on the basis of hyperspectral imaging data," *Postharvest Biology and Technology*, vol. 86, pp. 249-258, 2013.
- [10] J. Pozo-Antonio, M. Fiorucci, A. Ramil, T. Rivas and A. López, "Evaluation of the effectiveness of laser crust removal on granites by means of hyperspectral imaging techniques," *Journal of Nondestructive Evaluation*, vol. 35, no. 3, pp. 1-8, 2016.
- [11] D. Allen, R. Resmini, C. Deloye and J. Stevens, "A microscene approach to the evaluation of hyperspectral system level performance," *Proceedings of SPIE - The International Society for Optical Engineering*, vol. 8743, pp. 1-13, 2013.
- [11] S. Adler-Golden, A. Berk, L. Bernstein, S. Richtsmeier, P. Acharya, M. Matthew, G. Anderson, C. Allred, L. Jeong and Chetwynd, "FLAASH, a MODTRAN4 atmospheric correction package for hyperspectral data retrievals and simulations," *Scientific and Technical Aerospace Reports*, vol. 38, pp. 9-14, 2000.
- [11] T. Perkins, S. Adler-Golden, M. Matthew, A. Berk, L. Bernstein, J. Lee and M. Fox, "Speed and accuracy improvements in FLAASH atmospheric correction of hyperspectral imagery," *Optical Engineering*, vol. 51, no. 11, pp. 1-7, 2012.
- [11] I. Reed and X. Yu, "Adaptive multiple-band CFAR detection of an optical pattern with unknown spectral distribution," *IEEE Transactions on Acoustics, Speech, and Signal Processing*, vol. 38, no. 10, pp. 1760-1770, 1990.
- [11] R. Govindan, A. Korre, S. Durucan and C. E. Imrie, "A geostatistical and probabilistic spectral image processing methodology for monitoring potential CO₂ leakages on the surface," *International Journal of Greenhouse Gas Control*, vol. 5, no. 3, pp. 589-597, 2011.
- [11] D. Wei, H. Yanbo, Z. Chunjiang, C. Liping and W. Xiu, "Bayesian discriminant analysis of plant leaf hyperspectral reflectance for identification of weeds from cabbages," *African Journal of Agricultural Research*, vol. 11, no. 7, pp. 551 - 562, 2016.
- [11] U. Balasubramanian, J. Saravanavel and S. Gunasekaran, "Ore mineral discrimination using hyperspectral remote sensing—a field-based spectral analysis," *Arabian Journal of Geosciences*, vol. 6, no. 12, pp. 4709-4716, 2013.
- [11] D. Manolakis, D. Marden and G. Shaw, "Hyperspectral image processing for automatic target detection applications," *Lincoln Laboratory Journal*, vol. 14, no. 1, pp. 79-116, 2003.
- [11] P. E. Dennison, K. Q. Halligan and D. A. Roberts, "A comparison of error metrics and constraints for multiple endmember spectral mixture analysis and spectral angle mapper," *Remote Sensing of Environment*, vol. 93, no. 3, pp. 359-367, 2004.

- [11 S. Kraut, L. Scharf and R. Butler, "The adaptive coherence estimator: a uniformly
9] most-powerful-invariant adaptive detection statistic," *IEEE Transactions on Signal
Processing*, vol. 53, no. 2, pp. 427-438, 2005.
- [12 L. Scharf and L. Mcwhorter, "Adaptive matched subspace detectors and adaptive
0] coherence estimators," in *Conference Record of The Thirtieth Asilomar Conference
on Signals, Systems and Computers*, Pacific Grove, California USA, 1996.
- [12 R. N. S. G. Clark, K. Livo, R. Kokaly, S. Sutley, J. Dalton, R. McDougal and C.
1] Gent, "Imaging Spectroscopy: Earth and Planetary Remote Sensing with the USGS
Tetracorder and Expert Systems," *Journal of Geophysical Research*, vol. 12, pp. 1-
44, 2003.
- [12 United States Geological Survey, "Pliocene Research, Interpretation and Synoptic
2] Mapping," USGS, 16 12 2016. [Online]. Available:
<http://geology.er.usgs.gov/egpsc/prism/>. [Accessed 27 03 2017].
- [12 T. Lillesand, R. Kiefer and J. Chipman, *Remote Sensing and Image Interpretation*,
3] Sixth Edition, Hoboken, New Jersey USA: John Wiley & Sons, Inc., 2008.
- [12 J. Gamon, J. Peñuelas and C. Field, "A narrow-waveband spectral index that tracks
4] diurnal changes in photosynthetic efficiency," *Remote Sensing of Environment*, vol.
41, no. 1, pp. 35-44, 1992.
- [12 A. V. Uhrin and P. A. Townsend, "Improved seagrass mapping using linear spectral
5] unmixing of aerial photographs," *Estuarine, Coastal and Shelf Science*, vol. 171,
pp. 11-22, 2016.
- [12 B. Jahne, *Digital Image Processing, Concepts, Algorithms, and Scientific
6] Applications*, Third Edition, New York, USA: Springer-Verlag, 1995.
- [12 L. Roberts, *Machine Perception of Three-Dimensional Solids, Doctoral
7] dissertation, Ph. D. Thesis*, Cambridge, Massachusetts USA: Massachusetts
Institute of Technology, 1963.
- [12 S. Kabir, P. Rivard, D.-C. He and P. Thivierge, "Damage assessment for concrete
8] structure using image processing techniques on acoustic borehole imagery,"
Construction and Building Materials, vol. 23, no. 10, pp. 3166-3174, 2009.
- [12 P. Wayalun, N. Laopracha, P. Songrum and P. Wanchanthuek, "Evaluation for
9] Edge Detection of Chromosome G-band Images for Segmentation," *Applied
Medical Informatics*, vol. 32, no. 1, pp. 25-32, 2013.
- [13 P. Sujatha and K. Sudha, "Performance Analysis of Different Edge Detection
0] Techniques for Image Segmentation," *Indian Journal of Science and Technology*,
vol. 8, no. 14, pp. 1-6, 2015.
- [13 K. Kumar, J.-. Li and S. Khan, "Comparative Study on Various Edge Detection
1] Techniques for 2-D Image," *International Journal of Computer Applications*, vol.
119, no. 22, pp. 1-6, 2015.
- [13 A. Fahrurrozi, S. Madenda, Ernastuti and D. Kerami, "Wood Texture Features
2] Extraction by Using GLCM Combined With Various Edge Detection Methods,"
Journal of Physics: Conference Series, vol. 725, no. 1, pp. 1-11, 2016.

- [13 L. Junyan, T. Qingju, W. Yang, L. Yumei and Z. Zhiping, "Defects' geometric
3] feature recognition based on infrared image edge detection," *Infrared Physics and
Technology*, vol. 67, pp. 387-390, 2014.
- [13 H. Li, X. Liao, C. Li, H. Huang and C. Li, "Edge detection of noisy images based
4] on cellular neural networks," *Communications in Nonlinear Science and Numerical
Simulation*, vol. 16, no. 9, pp. 3746-3759, 2011.
- [13 M. T. H and A. S. Rubia, "A Survey and Evaluation of Edge Detection Operators:
5] Application to Text Recognition," *International Journal of Computer Technology
and Applications*, vol. 3, no. 4, pp. 1481-1484, 2012.
- [13 X. Liu and S. Fang, "A convenient and robust edge detection method based on ant
6] colony optimization," *Optics Communications*, vol. 353, pp. 147-157, 2015.
- [13 I. Sobel and G. Feldman, "An Isotropic 3x3 Image Gradient Operator," 20 8 2015.
7] [Online]. Available:
[https://www.researchgate.net/publication/281104656_An_Isotropic_3x3_Image_Gr
radient_Operator](https://www.researchgate.net/publication/281104656_An_Isotropic_3x3_Image_Gradient_Operator). [Accessed 18 8 2016].
- [13 W. J. Kang, "Research on Extraction of Ship Target in Complex Sea-sky
8] Background," *Journal of Physics: Conference Series*, vol. 48, no. 1, pp. 354-358,
2006.
- [13 V. Sucharita, S. Jyothi and D. Mamatha, "Comparative Study on Various Edge
9] Detection Techniques used for the Identification of Penaeid Prawn Species,"
International Journal of Computer Applications, vol. 78, no. 6, pp. 1-6, 2013.
- [14 W.-K. Tsao, A. J. Lee, Y.-H. Liu, T.-W. Chang and H.-H. Lin, "A data mining
0] approach to face detection," *Pattern Recognition*, vol. 43, no. 3, pp. 1039-1049,
2010.
- [14 M. Khomyakov, "Comparative evaluation of linear edge detection methods,"
1] *Pattern Recognition and Image Analysis*, vol. 22, no. 2, pp. 291-302, 2012.
- [14 D. Kim, "Sobel Operator and Canny Edge Detector," 2013. [Online]. Available:
2] <http://www.egr.msu.edu/classes/ece480/capstone/fall13/group04/docs/danapp.pdf>.
[Accessed 18 9 2016].
- [14 B. Gong, "CSC5280 Project 1: Canny Edge Detection," [Online]. Available:
3] <http://www-scf.usc.edu/~boqinggo/Canny.htm>. [Accessed 19 9 2016].
- [14 Y. heng, Y. Zhou, H. Zhou and X. Gong, "Ultrasound Image Edge Detection Based
4] on a Novel Multiplicative Gradient and Canny Operator," *Ultrasonic Imaging*, vol.
37, no. 3, pp. 238-250, 2015.
- [14 J. Zhang, J. Hu and H. Zhu, "Contour extraction of glomeruli by using genetic
5] algorithm for edge patching," *IEEJ Transactions on Electrical and Electronic
Engineering*, vol. 6, no. 3, pp. 229-235, 2011.
- [14 M. Pan, J. Tang, Q. Rong and F. Zhang, "Medical image registration using
6] modified iterative closest points," *International Journal for Numerical Methods in
Biomedical Engineering*, vol. 27, no. 8, pp. 1150-1166, 2011.

- [14 Y. Zhang, X. Li, J. Zhang and D. X. J. Song, "A Study on Coastline Extraction and
7] Its Trend Based on Remote Sensing Image Data Mining," *Abstract and Applied
Analysis*, vol. 21, no. 1, pp. 1-6, 2013.
- [14 J. Wang, H. Zhao, Y. Bi, X. Chen, R. Zeng and S. Shao, "Quad-Rotor Helicopter
8] Autonomous Navigation Based on Vanishing Point Algorithm," *Journal of Applied
Mathematics*, vol. 2014, pp. 1-12, 2014.
- [14 F. Longsheng, W. Bin, C. Yongjie, S. Shuai, Y. Gejima and T. Kobayashi,
9] "Kiwifruit recognition at nighttime using artificial lighting based on machine
vision," *International Journal of Agricultural and Biological Engineering*, vol. 8,
no. 4, pp. 52-59, 2015.
- [15 Y. Chen, G. Zhang, Y. Yuan and Y. Zhao, "Weighted elliptic curve-fitting method
0] with sub-pixel level in the light-probe vision measuring system," *Transactions of
the Institute of Measurement and Control*, vol. 35, no. 5, pp. 698-702, 2013.
- [15 Y. Zhang, T. Li and Q. Li, "Defect detection for tire laser shearography image using
1] curvelet transform based edge detector," *Optics and Laser Technology*, vol. 47, pp.
64-71, 2013.
- [15 V. Rathod and R. Anand, "A novel method for detection and quantification of
2] incomplete penetration type flaws in weldments," *Journal Of X-Ray Science And
Technology*, vol. 19, no. 2, pp. 261-274, 2011.
- [15 W. Bakker and K. Schmidt, "Hyperspectral edge filtering for measuring
3] homogeneity of surface cover types," *ISPRS Journal of Photogrammetry and
Remote Sensing*, vol. 56, no. 4, pp. 246-256, 2002.
- [15 G. Noyel, J. Angulo and D. Jeulin, "A new spatio-spectral morphological
4] segmentation for multi-spectral remote-sensing images," *International Journal of
Remote Sensing*, vol. 31, no. 22, pp. 5895-5920, 2010.
- [15 M. Bouziani, K. Goita and K. Dong-Chen He, "Rule-Based Classification of a Very
5] High Resolution Image in an Urban Environment Using Multispectral
Segmentation Guided by Cartographic Data," *IEEE Transactions on Geoscience
and Remote Sensing*, vol. 48, no. 8, pp. 3198-3211, 2010.
- [15 I. Kopriva, M. Hadžija, M. Popović Hadžija, M. Korolija and A. Cichocki,
6] "Rational Variety Mapping for Contrast-Enhanced Nonlinear Unsupervised
Segmentation of Multispectral Images of Unstained Specimen," *The American
Journal of Pathology*, vol. 179, no. 2, pp. 547-554, 2011.
- [15 K. M. Saipullah, N. A. Ismail and D.-H. Kim, "The Pruning of Combined
7] Neighborhood Differences Texture Descriptor for Multispectral Image
Segmentation," *International Journal of Computer Technology and Electronics
Engineering*, vol. 1, no. 3, pp. 154-159, 2011.
- [15 C. Toro, C. Martin, A. Pedrero and E. Ruiz, "Superpixel-Based Roughness Measure
8] for Multispectral Satellite Image Segmentation," *Remote Sensing*, vol. 7, no. 11, pp.
14620-14645, 2015.

- [15] R. Khelifi, M. Adel and S. Bourennane, "Segmentation of multispectral images based on band selection by including texture and mutual information," *Biomedical Signal Processing and Control*, vol. 20, pp. 16-23, 2015.
- [16] F. Cánovas-García and F. Alonso-Sarría, "A local approach to optimize the scale parameter in multiresolution segmentation for multispectral imagery," *Geocarto International*, vol. 30, no. 8, pp. 937-961, 2015.
- [16] A. Wang, S. Wang and A. Lucieer, "Segmentation of multispectral high-resolution satellite imagery based on integrated feature distributions," *International Journal of Remote Sensing*, vol. 31, no. 6, pp. 1471-1483, 2010.
- [16] P. Li and X. Xiao, "An unsupervised marker image generation method for watershed segmentation of multispectral imagery," *Geosciences Journal*, vol. 8, no. 3, pp. 325-331, 2004.
- [16] P. Li and X. Xiao, "Multispectral image segmentation by a multichannel watershed-based approach," *International Journal of Remote Sensing*, vol. 28, no. 19, pp. 4429-4452, 2007.
- [16] L. Wang, P. Gong, Q. Ying, Z. Yang, X. Cheng and Q. Ran, "Settlement extraction in the North China Plain using Landsat and Beijing-1 multispectral data with an improved watershed segmentation algorithm," *International Journal of Remote Sensing*, vol. 31, no. 6, pp. 1411-1426, 2010.
- [16] B. Wuest and Y. Zhang, "Region based segmentation of QuickBird multispectral imagery through band ratios and fuzzy comparison," *ISPRS Journal of Photogrammetry and Remote Sensing*, vol. 64, no. 1, pp. 55-64, 2009.
- [16] P. Meyer, "Segmentation and symbolic description for a classification of agricultural areas with multispectral scanner data," *IEEE Transactions on Geoscience and Remote Sensing*, vol. 30, no. 4, pp. 673-679, 1992.
- [16] I. Pestunov, S. Rylov and V. Berikov, "Hierarchical Clustering Algorithms for Segmentation of Multispectral Images," *Optoelectronics, Instrumentation and Data Processing*, vol. 51, no. 4, pp. 329-338, 2015.
- [16] S. Kaur and S. Chawla, "Evaluation of Performance of Fuzzy C Means and Mean Shift based Segmentation for Multi-Spectral Images," *International Journal of Computer Applications*, vol. 120, no. 16, pp. 25-28, 2015.
- [16] J. Baumgartner, J. Gimenez, M. Scavuzzo and J. Pucheta, "A New Approach to Segmentation of Multispectral Remote Sensing Images Based on MRF," *IEEE Geoscience and Remote Sensing Letters*, vol. 12, no. 8, pp. 1720-1724, 2015.
- [17] A. Ahmadvand and P. Kabiri, "Multispectral MRI image segmentation using Markov random field model," *Signal, Image and Video Processing*, vol. 10, no. 2, pp. 251-258, 2016.
- [17] A. Bitam and S. Ameur, "A local-spectral fuzzy segmentation for MSG multispectral images," *International Journal of Remote Sensing*, vol. 34, no. 23, pp. 8360-8372, 2013.

- [17 S. Yildiz and M. Doker, "Monitoring urban growth by using segmentation-
2] classification of multispectral Landsat images in Izmit, Turkey," *Environmental Monitoring and Assessment*, vol. 188, no. 7, pp. 1-12, 2016.
- [17 I. Kerfoot and Y. Bresler, "Theoretical Analysis of Multispectral Image
3] Segmentation Criteria," *IEEE Transactions on Image Processing*, vol. 8, no. 6, pp. 798-820, 1999.
- [17 J. Lira, "Segmentation and morphology of open water bodies from multispectral
4] images," *International Journal of Remote Sensing*, vol. 27, no. 18, pp. 4015-4038, 2006.
- [17 M. Chen and J. Strobl, "Multispectral textured image segmentation using a multi-
5] resolution fuzzy Markov random field model on variable scales in the wavelet domain," *International Journal of Remote Sensing*, vol. 34, no. 13, pp. 4550-4569, 2013.
- [17 S. Pal and P. Mitra, "Multispectral Image Segmentation Using the Rough-Set-
6] Initialized EM Algorithm," *IEEE Transactions on Geoscience and Remote Sensing*, vol. 40, no. 11, pp. 2495-2501, 2002.
- [17 P. Paclík, R. Duin, G. van Kempen and R. Kohlus, "Segmentation of multi-spectral
7] images using the combined classifier approach," *Image and Vision Computing*, vol. 21, no. 6, pp. 473-482, 2003.
- [17 Y. Byun, Y. Han and T. Chae, "A Multispectral Image Segmentation Approach for
8] Object-based Image Classification of High Resolution Satellite Imagery," *KSCE Journal of Civil Engineering*, vol. 17, no. 2, pp. 486-497, 2013.
- [17 E. Freire Santana, L. Vidal Batista, R. Marques Da Silva and C. A. Guimarães
9] Santos, "Multispectral image unsupervised segmentation using watershed transformation and crossentropy minimization in different land use," *GIScience & Remote Sensing*, vol. 51, no. 6, pp. 613-629, 2014.
- [18 G.-C. Lin, W.-J. Wang, C.-C. Kang and C.-M. Wang, "Multispectral MR Images
0] Segmentation Based on Fuzzy Knowledge and Modified Seeded Region Growing," *Magnetic Resonance Imaging*, vol. 30, no. 2, pp. 230 - 246, 2012.
- [18 C. Mott, T. Anderson, S. Zimmermann, T. Schneider and U. and Ammer,
1] "'Selective" region growing – an approach based on object-oriented classification routines," in *Geoscience and Remote Sensing Symposium, 2002. IGARSS '02. 2002 IEEE International*, Toronto, 2002.
- [18 Y. Zhang, X. Feng and X. Le, "Segmentation on Multispectral Remote Sensing
2] Image Using Watershed Transformation," in *Congress on Image and Signal Processing.*, Sanya, 2008.
- [18 R. Adams and L. Bischof, "Seeded region growing," *IEEE Transactions on Pattern
3] Analysis and Machine Intelligence*, vol. 16, no. 6, pp. 641 - 647, 1994.
- [18 H. Soltanian-Zadeh, J. Windham and A. Yagle, "A Multidimensional Nonlinear
4] Edge-Preserving Filter for Magnetic Resonance Image Restoration," *IEEE Transactions on Image Processing*, vol. 4, no. 2, pp. 147-161, 1995.

- [18 R.-S. Kwan, A. Evans and G. Pike, "MRI Simulation-Based Evaluation of Image-
5] Processing and Classification Methods," *IEEE Transactions on Medical Imaging*,
vol. 18, no. 11, pp. 1085-1097, 1999.
- [18 I. Aarya, D. Jiang and T. A. I. Gale, "Edge localisation in MRI for images with
6] signal-dependent noise," *Electronics Letters*, vol. 51, no. 15, pp. 1151-1153, 2015.
- [18 V. Dharmale and P. A. Tijare, "Segmentation and Canny Edge Method in MRI
7] Brain Cyst Detection," *International Journal of Advanced Computer Research*, vol.
3, no. 4, pp. 289-293, 2013.
- [18 C. R. Tench, P. S. Morgan and C. S. Constantinescu, "Measurement of Cervical
8] Spinal Cord Cross-Sectional Area by MRI Using Edge Detection and Partial
Volume Correction," *Journal of Magnetic Resonance Imaging*, vol. 21, no. 3, pp.
197-203, 2005.
- [18 J.-M. Bonny, O. Boespflug-Tanguy, M. Zanca and J.-P. Renou, "Multi-exponential
9] analysis of magnitude MR images using a quantitative multispectral edge-
preserving filter," *Journal of Magnetic Resonance*, vol. 161, no. 1, pp. 25-34, 2003.
- [19 J. Chen, J. Li, J. Delu Pan, J. Qiankun Zhu and J. Zhihua Mao, "Edge-Guided
0] Multiscale Segmentation of Satellite Multispectral Imagery," *IEEE Transactions on
Geoscience and Remote Sensing*, vol. 50, no. 11, pp. 4513-4520, 2012.
- [19 T. Zhang, X. Yang, S. Hu and F. S. Su, "Extraction of Coastline in Aquaculture
1] Coast from Multispectral Remote Sensing Images: Object-Based Region Growing
Integrating Edge Detection," *Remote Sensing*, vol. 5, no. 9, pp. 4470-4487, 2013.
- [19 P. Toivanen, J. Ansamäki, J. Parkkinen and J. Mielikäinen, "Edge detection in
2] multispectral images using the self-organizing map," *Pattern Recognition Letters*,
vol. 24, no. 16, pp. 2987-2994, 2003.
- [19 M. Naraghi, M. Koohi and A. Shakery, "Edge detection in multispectral images
3] based on structural elements," *The International Journal of Multimedia & Its
Applications*, vol. 3, no. 1, pp. 90-99, 2011.
- [19 S. D. Zenzo, "A Note on the Gradient of a Multi-Image," *Computer Vision,
4] Graphics, and Image Processing*, vol. 33, pp. 116-125, 1986.
- [19 A. Cumani, "Edge Detection in Multispectral Images," *CVGIP: Graphical Models
5] and Image Processing*, vol. 53, no. 1, pp. 40-51, 1991.
- [19 H.-C. Lee and D. Cok, "Detecting boundaries in a vector field," *IEEE Transactions
6] on Signal Processing*, vol. 39, no. 5, pp. 1181-1194, 1991.
- [19 C. V. Dinh, R. Leitner, P. Pačlik, M. Loog and R. Duin, "SEDMI: Saliency based
7] edge detection in multispectral images," *Image and Vision Computing*, vol. 29, no.
8, pp. 546-556, 2011.
- [19 J. Lira and A. Rodríguez, "Edge enhancement in multispectral satellite images by
8] means of vector operators," *Geofísica Internacional*, vol. 53, no. 3, pp. 289-308,
2014.
- [19 C. Xu, L. H. W. Cao and J. Feng, "Multispectral image edge detection via Clifford
9] gradient," *Science China Information Sciences*, vol. 55, no. 2, pp. 260-269, 2012.

- [20 G. Sun and Z. Wang, "A Gravitational Edge Detection for Multispectral Images,"
0] *TELKOMNIKA Indonesian Journal of Electrical Engineering*, vol. 11, no. 7, pp. 3641-3647, 2013.
- [20 W. H. Farrand, J. F. Bell, J. R. Johnson, M. S. Rice and J. A. Hurowitz, "VNIR
1] multispectral observations of rocks at Cape York, Endeavour crater, Mars by the Opportunity rover's Pancam," *Icarus*, vol. 225, no. 1, pp. 709-725, 2013.
- [20 H. Ranjbar, F. Masoumi and E. M. Carranza, "Evaluation of geophysics and
2] spaceborne multispectral data for alteration mapping in the Sar Cheshmeh mining area, Iran," *International Journal of Remote Sensing*, vol. 32, no. 12, pp. 3309-3327, 2011.
- [20 W. Gao and A. Bertozzi, "Level Set Based Multispectral Segmentation with
3] Corners," *SIAM Journal on Imaging Sciences*, vol. 4, no. 2, pp. 597-617, 2011.
- [20 H. Tang, T. van Walsum, R. S. van Onkelen, R. Hameeteman, S. Klein, M. Schaap,
4] F. L. Tori, Q. J. van Den Bouwhuijsen, J. C. Witteman, A. van Der Lugt, L. J. van Vliet and W. J. Niessen, "Semiautomatic carotid lumen segmentation for quantification of lumen geometry in multispectral MRI," *Medical Image Analysis*, vol. 16, no. 6, pp. 1202-1215, 2012.
- [20 Y. Chen and Z. Cao, "Change detection of multispectral remote-sensing images
5] using stationary wavelet transforms and integrated active contours," *International Journal of Remote Sensing*, vol. 34, no. 24, pp. 8817-8837, 2013.
- [20 F. Bunyak, K. Palaniappan, S. K. Nath and G. Seetharaman, "Flux Tensor
6] Constrained Geodesic Active Contours with Sensor Fusion for Persistent Object Tracking," *Journal of Multimedia*, vol. 2, no. 4, pp. 20-33, 2007.
- [20 A. Maalouf, P. Carré, B. Augereau and C. Fernandez-Maloigne, "Cooperation of
7] the partial differential equation methods and the wavelet transform for the segmentation of multivalued images," *Signal Processing: Image Communication*, vol. 23, no. 1, pp. 14-30, 2008.
- [20 R. Ksantini, B. Boufama and S. Memar, "A new efficient active contour model
8] without local initializations for salient object detection," *Eurasip Journal On Image And Video Processing*, vol. 1, no. 40, pp. 1-13, 2013.
- [20 S. C. Zhu and A. Yuille, "Region competition: unifying snakes, region growing,
9] and Bayes/MDL for multiband image segmentation," *IEEE Transactions on Pattern Analysis and Machine Intelligence*, vol. 18, no. 9, pp. 884-900, 1996.
- [21 T. Chan and L. Vese, "Active contours without edges," *IEEE Transactions on
0] Image Processing*, vol. 10, no. 2, pp. 266-277, 2001.
- [21 B. Lu, M. Cui, Q. Liu and Y. Wang, "Automated grain boundary detection using
1] the level set method," *Computers and Geosciences*, vol. 35, no. 2, pp. 267-275, 2009.
- [21 S. Osher and J. A. Sethian, "Fronts propagating with curvature-dependent speed:
2] algorithms based on Hamilton-Jacobi formulations.," *Journal of computational physics*, vol. 79, no. 1, pp. 12-49, 1987.

- [21 M. Butenuth and C. Heipke, "Network snakes: graph-based object delineation with
3] active contour models," *Machine Vision and Applications*, vol. 23, no. 1, pp. 91-
109, 2012.
- [21 S. C. Zhu and A. Yuille, "Region competition: unifying snakes, region growing,
4] and Bayes/MDL for multiband image segmentation," *IEEE Transactions on Pattern
Analysis and Machine Intelligence*, vol. 18, no. 9, pp. 884-900, 1996.
- [21 X. Huang, L. Zhang and P. Li, "Classification of Very High Spatial Resolution
5] Imagery Based on the Fusion of Edge and Multispectral Information,"
Photogrammetric Engineering And Remote Sensing, vol. 74, no. 12, pp. 1585-1596,
2008.
- [21 R. Moreno and M. Graña, "About Gradient Operators on Hyperspectral Images," in
6] *Proceedings of the 1st International Conference on Pattern Recognition
Applications and Methods*, Vilamoura, Portugal, 2012.
- [21 S. Vantaram and E. Saber, "A method for improved localization of edges in
7] multi/hyperspectral imagery," *SPIE Optical Engineering+ Applications*, pp. 1-6,
2011.
- [21 M. Marin-Mcgee and M. Velez-Reyes, "A structure tensor for hyperspectral
8] images," in *Workshop on Hyperspectral Image and Signal Processing: Evolution in
Remote Sensing*, Grenoble, France, 2011.
- [21 R. Resmini, "Hyperspectral/Spatial Detection of Edges (HySPADE): An algorithm
9] for spatial and spectral analysis of hyperspectral information," in *Proceedings of the
SPIE, Algorithms and Technologies for Multispectral, Hyperspectral, and
Ultraspectral Imagery*, Orlando, Florida USA, 2004.
- [22 B. S. Paskaleva, S. E. Godoy, S. C. Woo-Yong Jang, S. Bender, M. M. Krishna and
0] M. M. Hayat, "Model-Based Edge Detector for Spectral Imagery Using Sparse
Spatiospectral Masks," *IEEE Transactions on Image Processing*, vol. 23, no. 5, pp.
2315-2327, 2014.
- [22 H. van Der Werff, F. van Ruitenbeek, M. van Der Meijde, F. van Der Meer, S. de
1] Jong and S. Kalubandara, "Rotation-Variant Template Matching for Supervised
Hyperspectral Boundary Detection," *IEEE Geoscience and Remote Sensing
Letters*, vol. 4, no. 1, pp. 70-74, 2007.
- [22 Q. Li, Y. Wang, J. Zhang, G. Xu and Y. Xue, "Quantitative Analysis of Protective
2] Effect of Erythropoietin on Diabetic Retinal Cells Using Molecular Hyperspectral
Imaging Technology," *IEEE Transactions on Biomedical Engineering*, vol. 57, no.
7, pp. 1699-1706, 2010.
- [22 F. van der Meer, F. van Ruitenbeek, H. van der Werff and C. Hecker, "apping PT
3] conditions in hydrothermal systems using hyperspectral remote sensing and object
based techniques," in *2nd Workshop on Hyperspectral Image and Signal
Processing: Evolution in Remote Sensing*, Reykjavik, Iceland, 2010.
- [22 F. J. van Ruitenbeek, T. J. Cudahy, F. D. van Der Meer and M. Hale,
4] "Characterization of the hydrothermal systems associated with Archean VMS-

- mineralization at Panorama, Western Australia, using hyperspectral, geochemical and geothermometric data," *van Ruitenbeek, Frank J.A. ; Cudahy, Thomas J. ; van Der Meer, Freek D. ; Hale, Martin*, vol. 45, pp. 33-46, 2012.
- [22 S. Salati, F. J. van Ruitenbeek, F. D. van der Meer, M. H. Tangestani and H. van
5] der Werff, "Lithological mapping and fuzzy set theory: Automated extraction of lithological boundary from ASTER imagery by template matching and spatial accuracy assessment," *International Journal of Applied Earth Observation and Geoinformation*, vol. 13, no. 5, pp. 753-765, 2011.
- [22 F. J. van Ruitenbeek, H. M. van Der Werff, K. A. Hein and F. D. van Der Meer,
6] "Detection of pre-defined boundaries between hydrothermal alteration zones using rotation-variant template matching," *Computers and Geosciences*, vol. 34, no. 12, pp. 1815-1826, 2008.
- [22 F. van Der Meer, H. van Der Werff and F. van Ruitenbeek, "Potential of ESA's
7] Sentinel-2 for geological applications," *Remote Sensing of Environment*, vol. 148, pp. 124-133, 2014.
- [22 A. S. Kumar, V. M. Keerthi, v. d. W. H. A. S. and F. van der Meer, "Hyperspectral
8] image classification by a variable interval spectral average and spectral curve matching combined algorithm," *International Journal of Applied Earth Observation and Geoinformation*, vol. 12, no. 4, pp. 261-269, 2010.
- [22 H. van der Werff and F. van der Meer, "Sentinel-2 for Mapping Iron Absorption
9] Feature Parameters," *Remote Sensing*, vol. 7, no. 10, pp. 12635-12653, 2015.
- [23 K. Kotwal and S. Chaudhuri, "Visualization of Hyperspectral Images Using
0] Bilateral Filtering," *IEEE Transactions on Geoscience and Remote Sensing*, vol. 48, no. 5, pp. 2308-2316, 2010.
- [23 J. A. Xudong Kang, J. A. Shutao Li and J. A. Benediktsson, "Spectral–Spatial
1] Hyperspectral Image Classification With Edge-Preserving Filtering," *IEEE Transactions on Geoscience and Remote Sensing*, vol. 52, no. 5, pp. 2666-2677, 2014.
- [23 J. Xia, L. Bombrun, T. Adali, Y. Berthoumieu and C. Germain, "Spectral–Spatial
2] Classification of Hyperspectral Images Using ICA and Edge-Preserving Filter via an Ensemble Strategy," *IEEE Transactions on Geoscience and Remote Sensing*, vol. 54, no. 8, pp. 4971-4982, 2016.
- [23 P. Perona and J. Malik, "Scale-space and edge detection using anisotropic
3] diffusion," *IEEE Transactions on Pattern Analysis and Machine Intelligence*, vol. 12, no. 7, pp. 629-639, 1990.
- [23 Y. Wang, R. Niu and X. Yu, " Anisotropic Diffusion for Hyperspectral Imagery
4] Enhancement," *IEEE Sensors Journal*, vol. 10, no. 3, pp. 469-477, 2010.
- [23 Y. Wang, R. Niu, L. Zhang and H. Shen, " Region-based adaptive anisotropic
5] diffusion for image enhancement and denoising," *Optical Engineering*, vol. 49, no. 11, pp. 1-19, 2010.

- [23 Y. Wang, K. Wu, Y. Yang and T. Chen, "Gradient and Laplacian-Based
6] Hyperspectral Anisotropic Diffusion," *IEEE Journal of Selected Topics in Applied Earth Observations and Remote Sensing*, vol. 8, no. 6, pp. 3235-3249, 2015.
- [23 L. Wang, Z. Li and J. Sun, "Anomaly Detection in Hyperspectral Imagery based on
7] Spectral Gradient and LLE," *Applied Mechanics and Materials*, vol. 121, no. 126, pp. 720-724 , 2011.
- [23 D. Connah, M. Drew and G. Finlayson, "Spectral edge image fusion: Theory and
8] applications," in *European Conference on Computer Vision*, Zurich, Switzerland, 2014.
- [23 D. Connah, M. S. Drew and G. D. Finlayson, "Spectral edge: gradient-preserving
9] spectral mapping for image fusion," *Journal of the Optical Society of America A: Optics, Image Science, and Vision*, vol. 32, no. 12, pp. 2384 - 2396, 2015.
- [24 X. Geng, K. Sun, L. Ji and Y. Zhao, "A Fast Volume-Gradient-Based Band
0] Selection Method for Hyperspectral Image," *IEEE Transactions on Geoscience and Remote Sensing*, vol. 52, no. 11, pp. 7111-7119, 2014.
- [24 C. Chen, J. Jiang, B. Zhang, W. Yang and J. Guo, "Hyperspectral Image
1] Classification Using Gradient Local Auto-Correlations," in *2015 3rd IAPR Asian Conference on Pattern Recognition*, Kuala Lumpur, Malaysia, 2015.
- [24 A. Erturk, M. K. Gullu and S. Erturk, "Hyperspectral Image Classification Using
2] Empirical Mode Decomposition With Spectral Gradient Enhancement," *IEEE Transactions on Geoscience and Remote Sensing*, vol. 51, no. 5, pp. 2787-2798, 2013.
- [24 X. Hadoux, S. Jay, G. Rabatel and N. Gorretta, "A Spectral–Spatial Approach for
3] Hyperspectral Image Classification Using Spatial Regularization on Supervised Score Image," *IEEE Journal of Selected Topics in Applied Earth Observations and Remote Sensing*, vol. 8, no. 6, pp. 2361-2369, 2015.
- [24 G. Noyel, J. Angulo and D. Jeulin, "Morphological Segmentation of Hyperspectral
4] Images," *Image Analysis and Stereology*, vol. 26, no. 3, pp. 101-109, 2011.
- [24 S. R. Vantaram, E. Saber and D. Messinger, "An intensity-gradient-texture guided
5] methodology for spatial segmentation of remotely sensed multi/hyperspectral imagery," in *18th IEEE International Conference on Image Processing*, Brussels, Belgium, 2011.
- [24 J. Xiaoli Ma, J. Wang Cheng, J. Zhuo Sun, J. Chenglu Wen and J. Li,
6] "Hyperspectral image classification using Primal Laplacian SVM in preconditioned conjugate gradient solution," in *IEEE International Geoscience and Remote Sensing Symposium - IGARSS*, Beijing, China, 2013.
- [24 S. Vantaram, S. Piramanayagam, E. Saber and D. Messinger, "Spatial segmentation
7] of multi/hyperspectral imagery by fusion of spectral-gradient-textural attributes," *Journal Of Applied Remote Sensing*, vol. 9, no. 1, pp. 1-38, 2015.
- [24 M. Marin-Mcgee and M. Velez-Reyes, "Enhancement of hyperspectral imagery
8] using spectrally weighted tensor anisotropic nonlinear diffusion for classification,"

- SPIE Defense, Security, and Sensing. International Society for Optics and Photonics*, pp. 1-8, 2013.
- [24 R. Resmini, "Simultaneous spectral/spatial detection of edges for hyperspectral
9] imagery: the HySPADE algorithm revisited," *SPIE Defense, Security, and Sensing*,
pp. 1-13, 2012.
- [25 C. Cox, "Hyperspectral/Spatial Detection of Edges (HySPADE) Analysis of
0] Mineral Assemblages and Linear Features at Cuprite, Nevada, U.S.A.," in
ASPRS/MAPPS 2009 Fall Conference, San Antonio, Texas USA, 2009.
- [25 S. Godoy, "A PhD Dissertation: Communication-theoretic Approach for Skin
1] Cancer Detection using Dynamic Thermal Imaging," The University of New
Mexico, Albuquerque, New Mexico USA, 2015.
- [25 Q. Li, "Hyperspectral Imaging Technology Used in Tongue Diagnosis," in *Recent
2] Advances in Theories and Practice of Chinese Medicine*, Rijeka, Croatia, InTech,
2012, pp. 112-136.
- [25 R. R. B. P. & B. A. Juang, "Level set segmentation of hyperspectral images using
3] joint spectral edge and signature information," in *IEEE 11th International
Conference on Information Fusion*, Cologne, Germany, 2008.
- [25 J. Ball and L. Bruce, "Level Set Hyperspectral Image Classification Using Best
4] Band Analysis," *IEEE Transactions on Geoscience and Remote Sensing*, vol. 45,
no. 10, pp. 3022-3027, 2007.
- [25 K. Karantzalos and D. Argialas, "A Region-based Level Set Segmentation for
5] Automatic Detection of Man-made Objects from Aerial and Satellite Images,"
Photogrammetric Engineering and Remote Sensing, vol. 75, no. 6, pp. 667-677,
2009.
- [25 E. Pasolli, F. Melgani, N. Alajlan and N. Conci, "Optical Image Classification: A
6] Ground-Truth Design Framework," *IEEE Transactions on Geoscience and Remote
Sensing*, vol. 51, no. 6, pp. 3580-3597, 2013.
- [25 A. Alarcon-Ramirez, M. R. Rwebangira, M. F. Chouikha and V. Manian, "A New
7] Methodology Based on Level Sets for Target Detection in Hyperspectral Images,"
IEEE Transactions on Geoscience and Remote Sensing, vol. 54, no. 9, pp. 5385-
5396, 2016.
- [25 R. Resmini and D. Allen, "The microscene: a novel method for hyperspectral image
8] generation for algorithm development and testing," The MITRE Corporation,
McLean, VA USA, 2014.
- [25 M. F. Baumgardner, L. L. Biehl and D. A. Landgrebe, "220 Band AVIRIS
9] Hyperspectral Image Data Set: June 12, 1992 Indian Pine Test Site 3," 2015.
[Online]. Available: <https://purr.purdue.edu/publications/1947/1>. [Accessed 13 11
2016].
- [26 J.-S. Qiu, D.-Z. Wang, B. McInnes, S.-Y. Jiang, R.-C. Wang and S. Kanisawa,
0] "Two subgroups of A-type granites in the coastal area of Zhejiang and Fujian

- Provinces, SE China: age and geochemical constraints on their petrogenesis," *Geological Society of America Special Papers*, vol. 95, pp. 227-236, 2004.
- [26 S. Pruitt, "Researchers Identify Fragment of Amelia Earhart's Plane," *The History Channel*, 29 10 2014. [Online]. Available: <http://www.history.com/news/researchers-identify-fragment-of-amelia-earharts-plane>. [Accessed 13 11 2016].
- [26 he International Group for Historic Aircraft Recovery, "The Earhart Project," 2016. 2] [Online]. Available: <https://tighar.org/Projects/Earhart/AEdescr.html>. [Accessed 13 11 2016].
- [26 The International Group for Historic Aircraft Recovery, "New Discovery: 3] Comparing Earhart to the Bones on Nikumaroro," 2016 22 10. [Online]. Available: https://tighar.org/Projects/Earhart/Archives/Research/Bulletins/78_EarhartArms/78_EarhartArms.html. [Accessed 2016 13 11].
- [26 T. I. G. f. H. A. Recovery, "The Window, the Patch, & the Artifact," 28 10 2014. 4] [Online]. Available: https://tighar.org/Projects/Earhart/Archives/Research/Bulletins/73_StepbyStep/73_Step_by_Step.html. [Accessed 13 11 2016].
- [26 Surface Optics Corporation, "Hyperspectral Imaging Possible Amelia Earhart 5] Wreckage," 14 08 2014. [Online]. Available: <https://surfaceoptics.com/hyperspectral-imaging-amelia-earhart-wreckage/>. [Accessed 13 11 2016].
- [26 C. Gias, "Gradient image of multi-spectral image," 21 8 2011. [Online]. Available: 6] <https://www.mathworks.com/matlabcentral/fileexchange/32623-gradient-image-of-multi-spectral-image?focused=5197187&tab=function>. [Accessed 14 10 2015].
- [26 C. Li, "Level Set for Image Segmentation," 3 6 2013. [Online]. Available: 7] <https://www.mathworks.com/matlabcentral/fileexchange/12711-level-set-for-image-segmentation>. [Accessed 21 10 2015].
- [26 N. Otsu, "A Threshold Selection Method from Gray-Level Histograms," *IEEE 8] Transactions on Systems, Man and Cybernetics*, Vols. SMC-9, no. 1, pp. 62-66, 1979.
- [26 Mathworks, "Image segmentation using Otsu thresholding," 10 3 2010. [Online]. 9] Available: <https://www.mathworks.com/matlabcentral/fileexchange/26532-image-segmentation-using-otsu-thresholding>. [Accessed 3 4 2017].
- [27 Mathworks, "MathWorks - Makers of MATLAB and Simulink," 15 3 2017. 0] [Online]. Available: <https://www.mathworks.com/>. [Accessed 3 4 2017].
- [27 Microsoft Corporation, "Visual C++ | Visual Studio," 20 2 2017. [Online]. 1] Available: <https://www.visualstudio.com> > Visual Studio IDE. [Accessed 3 4 2017].
- [27 Harris Geospatial Solutions, "ENVI," 31 3 2017. [Online]. Available: 2] www.harrisgeospatial.com/. [Accessed 3 4 2017].
- [27 J. Sweet, J. Granahan and M. Sharp, "An objective standard for hyperspectral image 3] quality," in *Proceedings of AVIRIS Workshop*, Honolulu, Hawaii USA, 2000.

- [27] Yale University, "Confidence Intervals," [Online]. Available:
4] <http://www.stat.yale.edu/Courses/1997-98/101/confint.htm>. [Accessed 10 4 2017].
- [27] D. Rumsey, "Choosing a Confidence Level for a Population Sample," [Online].
5] Available: <http://www.dummies.com/education/math/statistics/choosing-a-confidence-level-for-a-population-sample/>. [Accessed 10 4 2017].
- [27] Math Boot Camps, "Interpreting Confidence Intervals," 2016. [Online]. Available:
6] <http://www.mathbootcamps.com/interpreting-confidence-intervals/>. [Accessed 10 4 2017].
- [27] Penn State University Eberly College of Science, "An Interval's Length," [Online].
7] Available: <https://onlinecourses.science.psu.edu/stat414/node/198>. [Accessed 10 4 2017].
- [27] United States Geological Survey, "Materials Maps," 9 June 2000. [Online].
8] Available: <https://speclab.cr.usgs.gov/maps.html>. [Accessed 23 12 2016].
- [27] C. Schmid, R. Mohr and C. Bauckhage, "Evaluation of Interest Point Detectors,"
9] *International Journal of Computer Vision*, vol. 37, no. 2, pp. 151-172, 2000.
- [28] S. Baker and S. Nayar, "Global measures of coherence for edge detector
0] evaluation," in *IEEE Computer Society Conference on Computer Vision and Pattern Recognition*, Ft. Collins, Colorado, 1999.
- [28] A. Singh, "Review article digital change detection techniques using remotely-
1] sensed data," *International journal of remote sensing*, vol. 10, no. 6, pp. 989-1003, 1989.
- [28] Roper Scientific Germany, "Spectroscopic Etaloning in Back Illuminated CCDs,"
2] [Online]. Available: <http://www.roperscientific.de/etaloning.html>. [Accessed 6 4 2017].
- [28] S. Veraverbeke, E. N. Stavros and S. J. Hook, "Assessing fire severity using
3] imaging spectroscopy data from the Airborne Visible/Infrared Imaging Spectrometer (AVIRIS) and comparison with multispectral capabilities," *Remote Sensing of Environment*, vol. 154, pp. 153-163, 2014.
- [28] R. Fisher, S. Perkins, A. Walker and E. Wolfart, "Canny Edge Detector," 2003.
4] [Online]. Available: <http://homepages.inf.ed.ac.uk/rbf/HIPR2/canny.htm>. [Accessed 18 9 2016].
- [28] Y. Wu, X. Zhao, Y. Jin and X. Zhang, "Extracting Golden Area from Image Based
5] on Canny Operator," *Applied Mechanics and Materials*, vol. 731, pp. 201-204, 2015.
- [28] J. Chen, C. Richard, H. Lantéri, C. Theys and P. Honeine, "A gradient based
6] method for fully constrained least-squares unmixing of hyperspectral images," in *2011 IEEE Statistical Signal Processing Workshop*, Nice, France, 2011.
- [28] A. Zandifar, M. Babaie-Zadeh and C. Jutten, "A projected gradient-based algorithm
7] to unmixing," in *20th European Signal Processing Conference*, Bucarest, Romania, 2012.

- [1] J. Canny, "A Computational Approach to Edge Detection," *IEEE Transactions on Pattern Analysis and Machine Intelligence*, vol. 8, no. 6, pp. 679-698, 1986.
- [2] R. Sivanpillai and R. Congalton, "Future Landsat Data Needs at the Local and State Levels: An AmericaView Perspective," *Photogrammetric Engineering & Remote Sensing*, vol. 82, no. 8, p. 617–623, 2016.
- [3] Jet Propulsion Lab - California Institute of Technology, "AVIRIS Workshop Bibliographies," [Online]. Available: http://aviris.jpl.nasa.gov/documents/workshop_biblios.html. [Accessed 10 September 2010].
- [4] J. Schott, *Remote Sensing*, Second Edition, New York: Oxford University Press, 2007.
- [5] M. R. Elowitz, "What is Imaging Spectroscopy (Hyperspectral Imaging)?," [Online]. Available: <http://www.markelowitz.com/Hyperspectral.html>. [Accessed 4 9 2016].
- [6] T. Trautmann, "7. From Radiation Fields to Atmospheric Concentrations – Retrieval of Geophysical Parameters," 26 3 2007. [Online]. Available: http://atmos.caf.dlr.de/projects/scops/sciamachy_book/sciamachy_book_figures/chapter_7_figures.html. [Accessed 2016 4 9].
- [7] K. Szekiolda, J. Bowles, D. Gillis and W. Miller, "Interpretation of Absorption Bands in Airborne Hyperspectral Radiance Data," *Sensors*, vol. 9, no. 4, pp. 2907-2925, 2009.
- [8] A. Mariano and J. Grossmann, "Hyperspectral material identification on radiance data using single-atmosphere or multiple-atmosphere modeling," *Journal of Applied Remote Sensing*, vol. 4, pp. 1-17, 2010.
- [9] L. Bernstein, S. Adler-Golden, R. Sundberg, R. Levine, T. Perkins, A. Berk, A. Ratkowski and M. Hoke, "A new method for atmospheric correction and aerosol optical property retrieval for vis-swir multi- and hyperspectral imaging sensors: quick atmospheric correction," *Scientific and Technical Aerospace Reports*, vol. 44, no. 6, pp. 1-5, 2006.
- [10] L. Bernstein, X. Jin, B. Gregor and S. Adler-Golden, "Quick atmospheric correction code: algorithm description and recent upgrades," *Optical Engineering*, vol. 51, no. 11, pp. 1-12, 2012.
- [11] United States Geological Survey, "USGS Digital Spectral Library 06," 25 11 2013. [Online]. Available: <http://speclab.cr.usgs.gov/spectral.lib06/>. [Accessed 2 12 2010].
- [12] National Air and Space Administration, "MODIS: Moderate Resolution Imaging Spectroradiometer," [Online]. Available: <http://modis.gsfc.nasa.gov/>. [Accessed 7 2 2011].

- [13 National Air and Space Administration, "The Landsat Program," [Online].
] Available: <http://landsat.gsfc.nasa.gov/>. [Accessed 7 2 2011].
- [14 R. McCoy, J. Blake and K. Andrews, "Detecting hydrocarbon microseepage using
] hydrocarbon absorption bands of reflectance spectra of surface soils," *Oil and Gas Journal*, vol. 99, no. 22, pp. 40-45, 2001.
- [15 R. Gonzalez and R. Woods, Digital Image Processing, Third Edition, Upper Saddle
] River, New Jersey USA: Pearson Prentice Hall, 2008.
- [16 J. Townshend, T. Goff and C. Tucker, "Multitemporal dimensionality of images of
] normalized difference vegetation index at continental scales," *IEEE Transactions on Geoscience and Remote Sensing*, vol. 23, no. 6, pp. 888-895, 1985.
- [17 Y. Xie, X. Zhao, L. Li and H. Wang, "Calculating NDVI for Landsat 7-ETM data
] after atmospheric correction using 6S model: A case study in Zhangye City, China," in *18th International Conference on Geoinformatics*, Beijing, 2010.
- [18 B. Wilfong, D. Gorchoy and M. Henry, "Detecting an Invasive Shrub in Deciduous
] Forest Understories Using Remote Sensing," *Weed Science*, vol. 57, no. 5, pp. 512 - 520, 2009.
- [19 Y.-C. Tian, K.-J. Gu, X. Chu, X. Yao, W.-X. Cao and Y. Zhu, "Comparison of
] different hyperspectral vegetation indices for canopy leaf nitrogen concentration estimation in rice," *Plant and Soil*, vol. 376, no. 1, pp. 193-209, 2014.
- [20 Q. Wang, C. Li, J. Wang, Y. Huang, X. Song and W. Huang, "Monitoring Winter
] Wheat Maturity By Hyperspectral Vegetation Indices," *Intelligent Automation & Soft Computing*, vol. 18, no. 5, pp. 537-546, 2012.
- [21 C. Unsalan and K. Boyer, "Classifying land development in high-resolution
] Satellite imagery using hybrid structural-multispectral features," *IEEE Transactions on Geoscience and Remote Sensing*, vol. 42, no. 12, pp. 2840-2850, 2004.
- [22 M. Chiliński, "Comparison of the results of modified NDVI indicator established on
] the basis of measurements by hyperspectral spectrometer and digital camera," *Ecological Questions*, vol. 17, pp. 35-42, 2013.
- [23 L. Galvão, "Sun and view angle effects on NDVI determination of land cover types
] in the Brazilian Amazon region with hyperspectral data," *International Journal of Remote Sensing*, vol. 25, no. 10, pp. 1861-1879, 2004.
- [24 R. Pu, S. Bell and D. P. R. English, "Developing Hyperspectral Vegetation Indices
] for Identifying Seagrass Species and Cover Classes," *Journal of Coastal Research*, vol. 31, no. 3, pp. 595-615, 2015.
- [25 G. S. Okin, D. A. Roberts, B. Murray and W. J. Okin, "Practical limits on
] hyperspectral vegetation discrimination in arid and semiarid environments," *Remote Sensing of Environment*, vol. 77, no. 2, pp. 212-225, 2001.
- [26 P. S. Thenkabail, R. B. Smith and E. De Pauw, "yperspectral Vegetation Indices
] and Their Relationships with Agricultural Crop Characteristics," *Remote Sensing of Environment*, vol. 71, no. 2, pp. 158-182, 2000.

- [27 C. Zhang, "Combining Hyperspectral and Lidar Data for Vegetation Mapping in the Florida Everglades," *Photogrammetric Engineering and Remote Sensing*, vol. 80, no. 8, pp. 733-743, 2014.
- [28 B. S. Lee, K. Mcgwire and C. Fritsen, "Identification and quantification of aquatic vegetation with hyperspectral remote sensing in western Nevada rivers, USA," *International Journal of Remote Sensing*, vol. 32, no. 24, pp. 9093-9117, 2011.
- [29 I. Herrmann, U. Shapira, S. Kinast, A. Karnieli and D. Bonfil, "Ground-level hyperspectral imagery for detecting weeds in wheat fields," *Precision Agriculture*, vol. 14, no. 6, pp. 637-659, 2013.
- [30 A. Olsson, "Feasibility of Invasive Grass Detection in a Desertscrub Community Using Hyperspectral Field Measurements and Landsat TM Imagery," *Remote sensing*, vol. 3, no. 12, pp. 2283 - 2304, 2011.
- [31 Z.-T. Ouyang, Y. Gao, X. Xie, H.-Q. Guo, T.-T. Zhang and B. Zhao, "Spectral Discrimination of the Invasive Plant *Spartina alterniflora* at Multiple Phenological Stages in a Saltmarsh Wetland," *PLoS One*, vol. 8, no. 6, pp. 1-13, 2013.
- [32 S. Ge, M. Xu, G. Anderson and R. Carruthers, "Estimating Yellow Starthistle (*Centaurea solstitialis*) Leaf Area Index and Aboveground Biomass with the Use of Hyperspectral Data," *Weed Science*, vol. 55, no. 6, pp. 671 - 678, 2007.
- [33 R. Pu, P. Gong, Y. Tian, X. Miao, R. Carruthers and G. Anderson, "Using classification and NDVI differencing methods for monitoring sparse vegetation coverage: a case study of saltcedar in Nevada, USA," *International Journal of Remote Sensing*, vol. 29, no. 14, pp. 3987 - 4011, 2008.
- [34 B. Somers and G. P. Asner, "Multi-temporal hyperspectral mixture analysis and feature selection for invasive species mapping in rainforests," *Remote Sensing of Environment*, vol. 136, pp. 14 - 27, 2013.
- [35 J. Zhang, L. Yuan, R. Pu, R. W. Loraamm, G. Yang and J. Wang, "Comparison between wavelet spectral features and conventional spectral features in detecting yellow rust for winter wheat," *Computers and Electronics in Agriculture*, vol. 100, pp. 79-87, 2014.
- [36 H. Z. Shafri and N. Hamdan, "Hyperspectral Imagery for Mapping Disease Infection in Oil Palm Plantation Using Vegetation Indices and Red Edge Techniques," *American Journal of Applied Sciences*, vol. 6, no. 6, pp. 1031-1035, 2009.
- [37 S. Ray, N. Jain, R. Arora, S. Chavan and S. Panigrahy, "Utility of Hyperspectral Data for Potato Late Blight Disease Detection," *Journal of the Indian Society of Remote Sensing*, vol. 39, no. 2, pp. 161-169, 2011.
- [38 X. Cao, Y. Luo, Y. Zhou, J. Fan, X. Xu, J. West, X. Duan and D. Cheng, "Detection of Powdery Mildew in Two Winter Wheat Plant Densities and Prediction of Grain Yield Using Canopy Hyperspectral Reflectance," *PLoS One*, vol. 10, no. 3, pp. 1-14, 2015.

- [39] A. Apan, A. Held, S. Phinn and J. Markley, "Detecting sugarcane 'orange rust' disease using EO-1 Hyperion hyperspectral imagery," *International Journal of Remote Sensing*, vol. 25, no. 2, pp. 489-498, 2004.
- [40] S. Oshigami, Y. Yamaguchi, M. Mitsuishi, A. Momose and T. Yajima, "An advanced method for mineral mapping applicable to hyperspectral images: the composite MSAM," *Remote Sensing Letters*, vol. 6, no. 7, pp. 499-508, 2015.
- [41] F. Kruse, J. Boardman and J. Huntington, "Comparison of airborne hyperspectral data and eo-1 hyperion for mineral mapping," *IEEE Transactions on Geoscience and Remote Sensing*, vol. 41, no. 6, pp. 1388-1400, 2003.
- [42] J. Wang, W. Wang, K. Zhou, J. Yan and H. Liu, "Hyper-Spectral Remote Sensing Apply on Alteration Mineral Mapping," *Applied Mechanics and Materials*, vol. 303, no. 306, pp. 729 - 733, 2013.
- [43] R. G. Resmini, M. E. Kappus, W. S. Aldrich, J. C. Harsanyi and M. Anderson, "Mineral mapping with HYperspectral Digital Imagery Collection Experiment (HYDICE) sensor data at Cuprite, Nevada, U.S.A.," *International Journal of Remote Sensing*, vol. 18, no. 7, pp. 1553-1570, 1997.
- [44] W. Ge, Q. Cheng, L. Jing, Y. Chen, X. Guo, H. Ding and Q. Liu, "Mineral mapping in the western Kunlun Mountains using Tiangong-1 hyperspectral imagery," *IOP Conference Series: Earth and Environmental Science*, vol. 34, no. 1, pp. 1-7, 2016.
- [45] P. Bierwirth, D. Huston and R. S. Blewett, "Hyperspectral mapping of mineral assemblages associated with gold mineralization in the central Pilbara, Western Australia," *Economic Geology and the Bulletin of the Society of Economic Geologists*, vol. 97, no. 4, pp. 819-826, 2002.
- [46] M. Xiong, F. Zhang, Q. Ran, W. Hu and W. Li, "Representation-based classifications with Markov random field model for hyperspectral urban data," *Journal Of Applied Remote Sensing*, vol. 8, no. 1, pp. 1-12, 2014.
- [47] J. Zou, W. Li, X. Huang and Q. Du, "Classification of hyperspectral urban data using adaptive simultaneous orthogonal matching pursuit," *Journal Of Applied Remote Sensing*, vol. 8, no. 1, pp. 1-14, 2014.
- [48] F. Dell'Acqua, P. Gamba, A. Ferrari, J. Palmason, J. Benediktsson and K. Arnason, "Exploiting Spectral and Spatial Information in Hyperspectral Urban Data With High Resolution," *IEEE Geoscience and Remote Sensing Letters*, vol. 1, no. 4, pp. 322-326, 2004.
- [49] D. Akbari, A. Safari and S. Homayouni, "Object-Based Hyperspectral Classification of Urban Areas by Using Marker-Based Hierarchical Segmentation," *Photogrammetric Engineering and Remote Sensing*, vol. 80, no. 10, pp. 963-970, 2014.
- [50] X. Tong, H. Xie and Q. Weng, "Urban Land Cover Classification With Airborne Hyperspectral Data: What Features to Use?," *IEEE Journal of Selected Topics in Applied Earth Observations and Remote Sensing*, vol. 7, no. 10, pp. 3998-4009, 2014.

- [51] J. A. Xudong Kang, J. A. Shutao Li and J. A. Benediktsson, "Spectral–Spatial
] Hyperspectral Image Classification With Edge-Preserving Filtering," *IEEE Transactions on Geoscience and Remote Sensing*, vol. 52, no. 5, pp. 2666-2677, 2014.
- [52] J. Xia, L. Bombrun, T. Adali, Y. Berthoumieu and C. Germain, "Spectral–Spatial
] Classification of Hyperspectral Images Using ICA and Edge-Preserving Filter via an Ensemble Strategy," *IEEE Transactions on Geoscience and Remote Sensing*, vol. 54, no. 8, pp. 4971-4982, 2016.
- [53] M. Herold, D. Roberts, V. Noronha and O. Smadi, "Imaging spectrometry and
] asphalt road surveys," *Transportation Research Part C*, vol. 16, no. 2, pp. 153-166, 2008.
- [54] M. Á. Fernández de La Ossa, C. García-Ruiz and J. M. Amigo, "Near infrared
] spectral imaging for the analysis of dynamite residues on human handprints," *Talanta*, vol. 130, pp. 315-321, 2014.
- [55] M. Á. Fernández de La Ossa, J. M. Amigo and C. García-Ruiz, "Detection of
] residues from explosive manipulation by near infrared hyperspectral imaging: A promising forensic tool," *Forensic Science International*, vol. 242, pp. 228-235, 2014.
- [56] C. Kendziora, R. Furstenberg, M. Papantonakis, V. Nguyen, J. Byers and R. McGill,
] "Infrared photothermal imaging spectroscopy for detection of trace explosives on surfaces," *Applied Optics*, vol. 54, no. 31, pp. F129-F138, 2015.
- [57] M. Phillips and B. Bernacki, "Hyperspectral microscopy of explosives particles
] using an external cavity quantum cascade laser," *Optical Engineering*, vol. 52, no. 6, pp. 1-8, 2013.
- [58] T. Dubroca, G. Brown and R. Hummel, "Detection of explosives by differential
] hyperspectral imaging," *Optical Engineering*, vol. 53, no. 2, pp. 1-7, 2014.
- [59] F. Fuchs, S. Hugger, M. Kinzer, R. Aidam, W. Bronner, R. Losch, Q. Yang, K.
] Degreif and F. Schnurer, "Imaging standoff detection of explosives using widely tunable midinfrared quantum cascade lasers," *Optical Engineering*, vol. 49, no. 11, pp. 1-8, 2010.
- [60] T. Blake, J. Kelly, N. Gallagher, P. Gassman and T. Johnson, "Passive standoff
] detection of RDX residues on metal surfaces via infrared hyperspectral imaging," *Analytical And Bioanalytical Chemistry*, vol. 395, no. 2, pp. 337-348, 2009.
- [61] R. Bhargava, R. Schwartz Perlman, D. Fernandez, I. Levin and E. Bartick, "Non-
] invasive detection of superimposed latent fingerprints and inter-ridge trace evidence by infrared spectroscopic imaging," *Analytical and Bioanalytical Chemistry*, vol. 394, no. 8, pp. 2069-2075, 2009.
- [62] N. Boesche, C. Rogass, C. Lubitz, M. Brell, S. Herrmann, C. Mielke, S. Tonn, O.
] Appelt, U. Altenberger and H. Kaufmann, "Hyperspectral REE (Rare Earth Element) Mapping of Outcrops—Applications for Neodymium Detection," *Remote Sensing*, vol. 7, no. 5, pp. 5160-5186, 2015.

- [63 J. Dai, D. Wang, R. Wang and Z. Chen, "Quantitative estimation of concentrations of dissolved rare earth elements using reflectance spectroscopy," *Journal Of Applied Remote Sensing*, vol. 7, no. 1, pp. 1-14, 2013.
- [64 S. Jay, M. Guillaume and J. Blanc-Talon, "Underwater Target Detection With Hyperspectral Data: Solutions for Both Known and Unknown Water Quality," *IEEE Journal of Selected Topics in Applied Earth Observations and Remote Sensing*, vol. 5, no. 4, pp. 1213-1221, 2012.
- [65 B. B. aylor, M. H. Taylor, T. Dinter and A. Bracher, "Estimation of relative phycoerythrin concentrations from hyperspectral underwater radiance measurements--A statistical approach," *Journal of Geophysical Research: Oceans*, vol. 118, no. 6, pp. 2948-2960, 2013.
- [66 Q. Lu, M. Tang, J. Cai, J. Zhao and S. Vittayapadung, "Vis/NIR Hyperspectral Imaging for Detection of Hidden Bruises on Kiwifruits," *Czech Journal Of Food Sciences*, vol. 29, no. 6, pp. 595-602, 2011.
- [67 L. Pan, Q. Zhang, W. Zhang, Y. Sun, P. Hu and K. Tu, "Detection of cold injury in peaches by hyperspectral reflectance imaging and artificial neural network," *Food Chemistry*, vol. 192, pp. 134-141, 2016.
- [68 Z. Han, J. Wan, J. Zhang and H. Zhang, "Abundance quantification by independent component analysis of hyperspectral imagery for oil spill coverage calculation," *Chinese Journal of Oceanology and Limnology*, vol. 34, no. 145, pp. 1-9, 2016.
- [69 D. Liu, J. Zhang and X. Wang, "Reference spectral signature selection using density-based cluster for automatic oil spill detection in hyperspectral images," *Optics Express*, vol. 24, no. 7, pp. 7411-7425, 2016.
- [70 B. Liu, Y. Li, P. Chen and X. Zhu, "Extraction of Oil Spill Information Using Decision Tree Based Minimum Noise Fraction Transform," *Journal of the Indian Society of Remote Sensing*, vol. 44, no. 3, pp. 421-426, 2016.
- [71 Y. Lu, Q. Tian, X. Wang, G. Zheng and X. Li, "Determining oil slick thickness using hyperspectral remote sensing in the Bohai Sea of China," *International Journal of Digital Earth*, vol. 6, no. 1, pp. 76-93, 2013.
- [72 S. Sun, C. Hu, L. Feng, G. A. Swayze, J. Holmes, G. Graettinger, I. Macdonald, O. Garcia and I. Leifer, "Oil slick morphology derived from AVIRIS measurements of the Deepwater Horizon oil spill: Implications for spatial resolution requirements of remote sensors," *Marine Pollution Bulletin*, vol. 103, no. 1-2, pp. 276-285, 2016.
- [73 I. Leifer, W. J. Lehr, D. Simecek-Beatty, E. Bradley, R. Clark, P. Dennison, Y. Hu, S. Matheson, C. E. Jones, B. Holt, M. Reif, D. A. Roberts, J. Svejksky and G. Swayze, "State of the art satellite and airborne marine oil spill remote sensing: Application to the BP Deepwater Horizon oil spill," *Remote Sensing of Environment*, vol. 124, pp. 185-209, 2012.
- [74 R. F. Kokaly, B. R. Couvillion, J. M. Holloway, D. A. Roberts, S. L. Ustin, S. H. Peterson, S. Khanna and S. C. Piazza, "Spectroscopic remote sensing of the

- distribution and persistence of oil from the Deepwater Horizon spill in Barataria Bay marshes," *Remote Sensing of Environment*, vol. 129, pp. 210-230, 2013.
- [75 G. Sicot, M. Lennon, V. Miegebielle and D. Dubucq, "Estimation of the thickness and emulsion rate of oil spilled at sea using hyperspectral remote sensing imagery in the SWIR domain," *The International Archives of the Photogrammetry, Remote Sensing and Spatial Information Sciences*, Vols. XL-3, no. W3, pp. 445-450, 2015.
- [76 S. H. Peterson, D. A. Roberts, M. Beland, R. F. Kokaly and S. L. Ustin, "Oil detection in the coastal marshes of Louisiana using MESMA applied to band subsets of AVIRIS data," *Remote Sensing of Environment*, vol. 159, pp. 222-231, 2015.
- [77 M. Zare-Baghbidi and S. Homayouni, "Fast hyperspectral anomaly detection for environmental applications," *Journal Of Applied Remote Sensing*, vol. 7, no. 1, pp. 1-12, 2013.
- [78 R. Clark, G. Swayze, I. Leifer, K. Livo, R. Kokaly, T. Hoefen, R. Green, N. Pearson, C. Sarture, I. McCubbin, D. Roberts, E. Bradley, D. Steele, T. Ryan, R. Dominguez and T. AVIRIS, "A Method for Quantitative Mapping of Thick Oil Spills," *United States Geological Survey Open File Report 2010-1167*, pp. 1-51, 2010.
- [79 F. Salem, M. Kafatos, T. El-Ghazawi, R. Gomez and R. Yang, "Hyperspectral image assessment of oil-contaminated wetland," *International Journal of Remote Sensing*, vol. 26, no. 4, pp. 811-821, 2005.
- [80 H. Srivastava and T. Singh, "Assessment and development of algorithms to detection of oil spills using MODIS data," *Journal of the Indian Society of Remote Sensing*, vol. 38, no. 1, pp. 161-167, 2010.
- [81 J. Rivera, F. Valverde, M. Saldana and V. Manian, "Security inspection in ports by anomaly detection using hyperspectral imaging technology," *Proceedings of SPIE - The International Society for Optical Engineering*, vol. 8743, pp. 1-11, 2013.
- [82 F. Franch-Lage, J. M. Amigo, E. Skibsted, S. MasPOCH and J. Coello, "Fast assessment of the surface distribution of API and excipients in tablets using NIR-hyperspectral imaging," *International Journal of Pharmaceutics*, vol. 411, no. 1, pp. 27-35, 2011.
- [83 J. Amigo, "Practical issues of hyperspectral imaging analysis of solid dosage forms," *Analytical and Bioanalytical Chemistry*, vol. 398, no. 1, pp. 93-109, 2010.
- [84 D. Goltz, M. Attas, G. Young, E. Cloutis and M. Bedynski, "Assessing stains on historical documents using hyperspectral imaging," *Journal of Cultural Heritage*, vol. 11, no. 1, pp. 19-26, 2010.
- [85 Q. Li, W. Wang, C. Ma and Z. Zhu, "Detection of physical defects in solar cells by hyperspectral imaging technology," *Optics and Laser Technology*, vol. 42, no. 6, pp. 1010-1013, 2010.

- [86] J. M. Medina and J. A. Diaz, "Scattering characterization of nanopigments in metallic coatings using hyperspectral optical imaging," *Applied Optics*, vol. 50, no. 31, pp. G47-G55, 2011.
- [87] G. Mirschel, O. Daikos, T. Scherzer and C. Steckert, "Near-infrared chemical imaging used for in-line analysis of inside adhesive layers in textile laminates," *Analytica Chimica Acta*, vol. 932, pp. 69-79, 2016.
- [88] National Air and Space Administration, "AVIRIS Airborne Visible/Infrared Imaging Spectrometer," 28 6 2016. [Online]. Available: <http://aviris.jpl.nasa.gov/>. [Accessed 24 08 2016].
- [89] F. Kruse, A. Lefkoff and J. Dietz, "xpert system-based mineral mapping in northern death valley, California/Nevada, using the Airborne Visible/Infrared Imaging Spectrometer (AVIRIS)," *Remote Sensing of Environment*, vol. 44, no. 2, pp. 309-336, 1993.
- [90] A. Smailbegovic, K. J. Gray, V. Murphy and R. Holbrook, "Spectroscopic and hyperspectral evaluation of possible hydrocarbon occurrences in estuarine sediments, North Charleston, South Carolina, USA," in *IEEE WHISPERS First Workshop on Hyperspectral Image and Signal Processing: Evolution in Remote Sensing*, Grenoble, 2009.
- [91] S. Veraverbeke, E. N. Stavros and S. J. Hook, "Assessing fire severity using imaging spectroscopy data from the Airborne Visible/Infrared Imaging Spectrometer (AVIRIS) and comparison with multispectral capabilities," *Remote Sensing of Environment*, vol. 154, pp. 153-163, 2014.
- [92] Harris Geospatial Solutions, "Push Broom and Whisk Broom Sensors," Harris Geospatial Solutions, 24 9 2013. [Online]. Available: <http://www.harrisgeospatial.com/Company/PressRoom/Blogs/TabId/836/ArtMID/928/ArticleID/13618/Push-Broom-and-Whisk-Broom-Sensors.aspx>. [Accessed 24 8 2016].
- [93] Natural Resources Canada, "Multispectral Scanning," Natural Resources Canada, 25 11 2015. [Online]. Available: <http://www.nrcan.gc.ca/earth-sciences/geomatics/satellite-imagery-air-photos/satellite-imagery-products/educational-resources/9337>. [Accessed 24 8 2016].
- [94] SPECIM Spectral Imaging, "AisaFENIX Hyperspectral Sensor," 1 6 2015. [Online]. Available: <http://www.specim.fi/products/aisafenix-hyperspectral-sensor/>. [Accessed 29 8 2016].
- [95] SPECIM Spectral Imaging, "AisaFENIX 1K," 1 6 2015. [Online]. Available: <http://www.specim.fi/products/aisafenix1k/>. [Accessed 29 8 2016].
- [96] ProSpecTIR, "Free Data Samples," 2012. [Online]. Available: <http://www.spectir.com/free-data-samples/>. [Accessed 29 8 2016].
- [97] W. Roper and S. Dutta, "Oil Spill and Pipeline Condition Assessment Using Remote Sensing and Data Visualization Management Systems," 2006. [Online]. Available:

<http://citeseerx.ist.psu.edu/viewdoc/download?doi=10.1.1.131.6669&rep=rep1&type=pdf>. [Accessed 29 8 2016].

- [98 K. Cawse-Nicholson, S. B. Damelin, A. Robin and M. Sears, "Determining the
] Intrinsic Dimension of a Hyperspectral Image Using Random Matrix Theory,"
IEEE Transactions on Image Processing, vol. 22, no. 4, pp. 1301-1310, 2013.
- [99 G. Vaughan and W. Calvin, "Mapping weathering and alteration minerals in the
] comstock and geiger grade areas using visible to thermal infrared airborne remote
sensing data," *Scientific and Technical Aerospace Reports*, vol. 44, no. 23, pp. 1-20,
2006.
- [10 F. Kruse, R. Bedell, J. Taranik, W. Peppin, O. Weatherbee and W. Calvin,
0] "Mapping alteration minerals at prospect, outcrop and drill core scales using
imaging spectrometry," *International Journal of Remote Sensing*, vol. 33, no. 6, pp.
1780-1798, 2012.
- [10 J. Pontius, M. Martin, L. Plourde and R. Hallett, "Ash decline assessment in
1] emerald ash borer-infested regions: A test of tree-level, hyperspectral technologies,"
Remote Sensing of Environment, vol. 112, no. 5, pp. 2665-2676, 2008.
- [10 S. T. Brantley, J. C. Zinnert and D. R. Young, "Application of hyperspectral
2] vegetation indices to detect variations in high leaf area index temperate shrub
thicket canopies," *Remote Sensing of Environment*, vol. 115, no. 2, pp. 514-523,
2011.
- [10 M. J. Santos, J. A. Greenberg and S. L. Ustin, "Using hyperspectral remote sensing
3] to detect and quantify southeastern pine senescence effects in red-cockaded
woodpecker (*Picoides borealis*) habitat," *Remote Sensing of Environment*, vol. 114,
no. 6, pp. 1242-1250, 2010.
- [10 X. Miao, R. Patil, J. Heaton and R. Tracy, "Detection and classification of invasive
4] saltcedar through high spatial resolution airborne hyperspectral imagery,"
International Journal of Remote Sensing, vol. 32, no. 8, pp. 2131-2150, 2011.
- [10 M. Folkman, J. Pearlman, L. Liao and P. Jarecke, "EO-1/Hyperion hyperspectral
5] imager design, development, characterization, and calibration," 2007. [Online].
Available: [http://www.ugpti.org/smartse/research/citations/downloads/Folkman-
Hyperion_Design-2007.pdf](http://www.ugpti.org/smartse/research/citations/downloads/Folkman-Hyperion_Design-2007.pdf). [Accessed 26 8 2016].
- [10 United States Geological Survey, "Sensors - Hyperion," 13 12 2011. [Online].
6] Available: <https://eo1.usgs.gov/sensors/hyperion>. [Accessed 29 8 2016].
- [10 United States Geological Survey, "EarthExplorer," 2 8 2016. [Online]. Available:
7] <http://earthexplorer.usgs.gov/>. [Accessed 29 8 2016].
- [10 P. Baranowski, W. Mazurek and J. Pastuszka-Woźniak, "Supervised classification
8] of bruised apples with respect to the time after bruising on the basis of
hyperspectral imaging data," *Postharvest Biology and Technology*, vol. 86, pp. 249-
258, 2013.

- [10] J. Pozo-Antonio, M. Fiorucci, A. Ramil, T. Rivas and A. López, "Evaluation of the effectiveness of laser crust removal on granites by means of hyperspectral imaging techniques," *Journal of Nondestructive Evaluation*, vol. 35, no. 3, pp. 1-8, 2016.
- [11] D. Allen, R. Resmini, C. Deloye and J. Stevens, "A microscene approach to the evaluation of hyperspectral system level performance," *Proceedings of SPIE - The International Society for Optical Engineering*, vol. 8743, pp. 1-13, 2013.
- [11] S. Adler-Golden, A. Berk, L. Bernstein, S. Richtsmeier, P. Acharya, M. Matthew, G. Anderson, C. Allred, L. Jeong and Chetwynd, "FLAASH, a MODTRAN4 atmospheric correction package for hyperspectral data retrievals and simulations," *Scientific and Technical Aerospace Reports*, vol. 38, pp. 9-14, 2000.
- [11] T. Perkins, S. Adler-Golden, M. Matthew, A. Berk, L. Bernstein, J. Lee and M. Fox, "Speed and accuracy improvements in FLAASH atmospheric correction of hyperspectral imagery," *Optical Engineering*, vol. 51, no. 11, pp. 1-7, 2012.
- [11] I. Reed and X. Yu, "Adaptive multiple-band CFAR detection of an optical pattern with unknown spectral distribution," *IEEE Transactions on Acoustics, Speech, and Signal Processing*, vol. 38, no. 10, pp. 1760-1770, 1990.
- [11] R. Govindan, A. Korre, S. Durucan and C. E. Imrie, "A geostatistical and probabilistic spectral image processing methodology for monitoring potential CO₂ leakages on the surface," *International Journal of Greenhouse Gas Control*, vol. 5, no. 3, pp. 589-597, 2011.
- [11] D. Wei, H. Yanbo, Z. Chunjiang, C. Liping and W. Xiu, "Bayesian discriminant analysis of plant leaf hyperspectral reflectance for identification of weeds from cabbages," *African Journal of Agricultural Research*, vol. 11, no. 7, pp. 551 - 562, 2016.
- [11] U. Balasubramanian, J. Saravanavel and S. Gunasekaran, "Ore mineral discrimination using hyperspectral remote sensing—a field-based spectral analysis," *Arabian Journal of Geosciences*, vol. 6, no. 12, pp. 4709-4716, 2013.
- [11] D. Manolakis, D. Marden and G. Shaw, "Hyperspectral image processing for automatic target detection applications," *Lincoln Laboratory Journal*, vol. 14, no. 1, pp. 79-116, 2003.
- [11] P. E. Dennison, K. Q. Halligan and D. A. Roberts, "A comparison of error metrics and constraints for multiple endmember spectral mixture analysis and spectral angle mapper," *Remote Sensing of Environment*, vol. 93, no. 3, pp. 359-367, 2004.
- [11] S. Kraut, L. Scharf and R. Butler, "The adaptive coherence estimator: a uniformly most-powerful-invariant adaptive detection statistic," *IEEE Transactions on Signal Processing*, vol. 53, no. 2, pp. 427-438, 2005.
- [12] L. Scharf and L. Mcwhorter, "Adaptive matched subspace detectors and adaptive coherence estimators," in *Conference Record of The Thirtieth Asilomar Conference on Signals, Systems and Computers*, Pacific Grove, California USA, 1996.
- [12] R. N. S. G. Clark, K. Livo, R. Kokaly, S. Sutley, J. Dalton, R. McDougal and C. Gent, "Imaging Spectroscopy: Earth and Planetary Remote Sensing with the USGS

- Tetracorder and Expert Systems," *Journal of Geophysical Research*, vol. 12, pp. 1-44, 2003.
- [12 United States Geological Survey, "Pliocene Research, Interpretation and Synoptic
2] Mapping," USGS, 16 12 2016. [Online]. Available:
<http://geology.er.usgs.gov/egpsc/prism/>. [Accessed 27 03 2017].
- [12 T. Lillesand, R. Kiefer and J. Chipman, Remote Sensing and Image Interpretation,
3] Sixth Edition, Hoboken, New Jersey USA: John Wiley & Sons, Inc., 2008.
- [12 J. Gamon, J. Peñuelas and C. Field, "A narrow-waveband spectral index that tracks
4] diurnal changes in photosynthetic efficiency," *Remote Sensing of Environment*, vol. 41, no. 1, pp. 35-44, 1992.
- [12 A. V. Uhrin and P. A. Townsend, "Improved seagrass mapping using linear spectral
5] unmixing of aerial photographs," *Estuarine, Coastal and Shelf Science*, vol. 171, pp. 11-22, 2016.
- [12 B. Jahne, Digital Image Processing, Concepts, Algorithms, and Scientific
6] Applications, Third Edition, New York, USA: Springer-Verlag, 1995.
- [12 L. Roberts, *Machine Perception of Three-Dimensional Solids, Doctoral
7] dissertation, Ph. D. Thesis*, Cambridge, Massachusetts USA: Massachusetts Institute of Technology, 1963.
- [12 S. Kabir, P. Rivard, D.-C. He and P. Thivierge, "Damage assessment for concrete
8] structure using image processing techniques on acoustic borehole imagery," *Construction and Building Materials*, vol. 23, no. 10, pp. 3166-3174, 2009.
- [12 P. Wayalun, N. Laopracha, P. Songrum and P. Wanchanthuek, "Evaluation for
9] Edge Detection of Chromosome G-band Images for Segmentation," *Applied Medical Informatics*, vol. 32, no. 1, pp. 25-32, 2013.
- [13 P. Sujatha and K. Sudha, "Performance Analysis of Different Edge Detection
0] Techniques for Image Segmentation," *Indian Journal of Science and Technology*, vol. 8, no. 14, pp. 1-6, 2015.
- [13 K. Kumar, J.-. Li and S. Khan, "Comparative Study on Various Edge Detection
1] Techniques for 2-D Image," *International Journal of Computer Applications*, vol. 119, no. 22, pp. 1-6, 2015.
- [13 A. Fahrurozi, S. Madenda, Ernastuti and D. Kerami, "Wood Texture Features
2] Extraction by Using GLCM Combined With Various Edge Detection Methods," *Journal of Physics: Conference Series*, vol. 725, no. 1, pp. 1-11, 2016.
- [13 L. Junyan, T. Qingju, W. Yang, L. Yumei and Z. Zhiping, "Defects' geometric
3] feature recognition based on infrared image edge detection," *Infrared Physics and Technology*, vol. 67, pp. 387-390, 2014.
- [13 H. Li, X. Liao, C. Li, H. Huang and C. Li, "Edge detection of noisy images based
4] on cellular neural networks," *Communications in Nonlinear Science and Numerical Simulation*, vol. 16, no. 9, pp. 3746-3759, 2011.

- [13 M. T. H and A. S. Rubia, "A Survey and Evaluation of Edge Detection Operators: 5] Application to Text Recognition," *International Journal of Computer Technology and Applications*, vol. 3, no. 4, pp. 1481-1484, 2012.
- [13 X. Liu and S. Fang, "A convenient and robust edge detection method based on ant 6] colony optimization," *Optics Communications*, vol. 353, pp. 147-157, 2015.
- [13 I. Sobel and G. Feldman, "An Isotropic 3x3 Image Gradient Operator," 20 8 2015. 7] [Online]. Available:
https://www.researchgate.net/publication/281104656_An_Isotropic_3x3_Image_Gradient_Operator. [Accessed 18 8 2016].
- [13 W. J. Kang, "Research on Extraction of Ship Target in Complex Sea-sky 8] Background," *Journal of Physics: Conference Series*, vol. 48, no. 1, pp. 354-358, 2006.
- [13 V. Sucharita, S. Jyothi and D. Mamatha, "Comparative Study on Various Edge 9] Detection Techniques used for the Identification of Penaeid Prawn Species," *International Journal of Computer Applications*, vol. 78, no. 6, pp. 1-6, 2013.
- [14 W.-K. Tsao, A. J. Lee, Y.-H. Liu, T.-W. Chang and H.-H. Lin, "A data mining 0] approach to face detection," *Pattern Recognition*, vol. 43, no. 3, pp. 1039-1049, 2010.
- [14 M. Khomyakov, "Comparative evaluation of linear edge detection methods," 1] *Pattern Recognition and Image Analysis*, vol. 22, no. 2, pp. 291-302, 2012.
- [14 D. Kim, "Sobel Operator and Canny Edge Detector," 2013. [Online]. Available: 2] <http://www.egr.msu.edu/classes/ece480/capstone/fall13/group04/docs/danapp.pdf>. [Accessed 18 9 2016].
- [14 B. Gong, "CSC5280 Project 1: Canny Edge Detection," [Online]. Available: 3] <http://www-scf.usc.edu/~boqinggo/Canny.htm>. [Accessed 19 9 2016].
- [14 Y. heng, Y. Zhou, H. Zhou and X. Gong, "Ultrasound Image Edge Detection Based 4] on a Novel Multiplicative Gradient and Canny Operator," *Ultrasonic Imaging*, vol. 37, no. 3, pp. 238-250, 2015.
- [14 J. Zhang, J. Hu and H. Zhu, "Contour extraction of glomeruli by using genetic 5] algorithm for edge patching," *IEEJ Transactions on Electrical and Electronic Engineering*, vol. 6, no. 3, pp. 229-235, 2011.
- [14 M. Pan, J. Tang, Q. Rong and F. Zhang, "Medical image registration using 6] modified iterative closest points," *International Journal for Numerical Methods in Biomedical Engineering*, vol. 27, no. 8, pp. 1150-1166, 2011.
- [14 Y. Zhang, X. Li, J. Zhang and D. X. J. Song, "A Study on Coastline Extraction and 7] Its Trend Based on Remote Sensing Image Data Mining," *Abstract and Applied Analysis*, vol. 21, no. 1, pp. 1-6, 2013.
- [14 J. Wang, H. Zhao, Y. Bi, X. Chen, R. Zeng and S. Shao, "Quad-Rotor Helicopter 8] Autonomous Navigation Based on Vanishing Point Algorithm," *Journal of Applied Mathematics*, vol. 2014, pp. 1-12, 2014.

- [14 F. Longsheng, W. Bin, C. Yongjie, S. Shuai, Y. Gejima and T. Kobayashi,
9] "Kiwifruit recognition at nighttime using artificial lighting based on machine
vision," *International Journal of Agricultural and Biological Engineering*, vol. 8,
no. 4, pp. 52-59, 2015.
- [15 Y. Chen, G. Zhang, Y. Yuan and Y. Zhao, "Weighted elliptic curve-fitting method
0] with sub-pixel level in the light-probe vision measuring system," *Transactions of
the Institute of Measurement and Control*, vol. 35, no. 5, pp. 698-702, 2013.
- [15 Y. Zhang, T. Li and Q. Li, "Defect detection for tire laser shearography image using
1] curvelet transform based edge detector," *Optics and Laser Technology*, vol. 47, pp.
64-71, 2013.
- [15 V. Rathod and R. Anand, "A novel method for detection and quantification of
2] incomplete penetration type flaws in weldments," *Journal Of X-Ray Science And
Technology*, vol. 19, no. 2, pp. 261-274, 2011.
- [15 W. Bakker and K. Schmidt, "Hyperspectral edge filtering for measuring
3] homogeneity of surface cover types," *ISPRS Journal of Photogrammetry and
Remote Sensing*, vol. 56, no. 4, pp. 246-256, 2002.
- [15 G. Noyel, J. Angulo and D. Jeulin, "A new spatio-spectral morphological
4] segmentation for multi-spectral remote-sensing images," *International Journal of
Remote Sensing*, vol. 31, no. 22, pp. 5895-5920, 2010.
- [15 M. Bouziani, K. Goita and K. Dong-Chen He, "Rule-Based Classification of a Very
5] High Resolution Image in an Urban Environment Using Multispectral
Segmentation Guided by Cartographic Data," *IEEE Transactions on Geoscience
and Remote Sensing*, vol. 48, no. 8, pp. 3198-3211, 2010.
- [15 I. Kopriva, M. Hadžija, M. Popović Hadžija, M. Korolija and A. Cichocki,
6] "Rational Variety Mapping for Contrast-Enhanced Nonlinear Unsupervised
Segmentation of Multispectral Images of Unstained Specimen," *The American
Journal of Pathology*, vol. 179, no. 2, pp. 547-554, 2011.
- [15 K. M. Saipullah, N. A. Ismail and D.-H. Kim, "The Pruning of Combined
7] Neighborhood Differences Texture Descriptor for Multispectral Image
Segmentation," *International Journal of Computer Technology and Electronics
Engineering*, vol. 1, no. 3, pp. 154-159, 2011.
- [15 C. Toro, C. Martin, A. Pedrero and E. Ruiz, "Superpixel-Based Roughness Measure
8] for Multispectral Satellite Image Segmentation," *Remote Sensing*, vol. 7, no. 11, pp.
14620-14645, 2015.
- [15 R. Khelifi, M. Adel and S. Bourenane, "Segmentation of multispectral images
9] based on band selection by including texture and mutual information," *Biomedical
Signal Processing and Control*, vol. 20, pp. 16-23, 2015.
- [16 F. Cánovas-García and F. Alonso-Sarría, "A local approach to optimize the scale
0] parameter in multiresolution segmentation for multispectral imagery," *Geocarto
International*, vol. 30, no. 8, pp. 937-961, 2015.

- [16 A. Wang, S. Wang and A. Lucieer, "Segmentation of multispectral high-resolution
1] satellite imagery based on integrated feature distributions," *International Journal of Remote Sensing*, vol. 31, no. 6, pp. 1471-1483, 2010.
- [16 P. Li and X. Xiao, "An unsupervised marker image generation method for
2] watershed segmentation of multispectral imagerY," *Geosciences Journal*, vol. 8, no. 3, pp. 325-331, 2004.
- [16 P. Li and X. Xiao, "Multispectral image segmentation by a multichannel watershed-
3] based approach," *International Journal of Remote Sensing*, vol. 28, no. 19, pp. 4429-4452, 2007.
- [16 L. Wang, P. Gong, Q. Ying, Z. Yang, X. Cheng and Q. Ran, "Settlement extraction
4] in the North China Plain using Landsat and Beijing-1 multispectral data with an improved watershed segmentation algorithm," *International Journal of Remote Sensing*, vol. 31, no. 6, pp. 1411-1426, 2010.
- [16 B. Wuest and Y. Zhang, "Region based segmentation of QuickBird multispectral
5] imagery through band ratios and fuzzy comparison," *ISPRS Journal of Photogrammetry and Remote Sensing*, vol. 64, no. 1, pp. 55-64, 2009.
- [16 P. Meyer, "Segmentation and symbolic description for a classification of
6] agricultural areas with multispectral scanner data," *IEEE Transactions on Geoscience and Remote Sensing*, vol. 30, no. 4, pp. 673-679, 1992.
- [16 I. Pestunov, S. Rylov and V. Berikov, "Hierarchical Clustering Algorithms for
7] Segmentation of Multispectral Images," *Optoelectronics, Instrumentation and Data Processing*, vol. 51, no. 4, pp. 329-338, 2015.
- [16 S. Kaur and S. Chawla, "Evaluation of Performance of Fuzzy C Means and Mean
8] Shift based Segmentation for Multi-Spectral Images," *International Journal of Computer Applications*, vol. 120, no. 16, pp. 25-28, 2015.
- [16 J. Baumgartner, J. Gimenez, M. Scavuzzo and J. Pucheta, "A New Approach to
9] Segmentation of Multispectral Remote Sensing Images Based on MRF," *IEEE Geoscience and Remote Sensing Letters*, vol. 12, no. 8, pp. 1720-1724, 2015.
- [17 A. Ahmadvand and P. Kabiri, "Multispectral MRI image segmentation using
0] Markov random field model," *Signal, Image and Video Processing*, vol. 10, no. 2, pp. 251-258, 2016.
- [17 A. Bitam and S. Ameer, "A local-spectral fuzzy segmentation for MSG
1] multispectral images," *International Journal of Remote Sensing*, vol. 34, no. 23, pp. 8360-8372, 2013.
- [17 S. Yildiz and M. Doker, "Monitoring urban growth by using segmentation-
2] classification of multispectral Landsat images in Izmit, Turkey," *Environmental Monitoring and Assessment*, vol. 188, no. 7, pp. 1-12, 2016.
- [17 I. Kerfoot and Y. Bresler, "Theoretical Analysis of Multispectral Image
3] Segmentation Criteria," *IEEE Transactions on Image Processing*, vol. 8, no. 6, pp. 798-820, 1999.

- [17 J. Lira, "Segmentation and morphology of open water bodies from multispectral
4] images," *International Journal of Remote Sensing*, vol. 27, no. 18, pp. 4015-4038,
2006.
- [17 M. Chen and J. Strobl, "Multispectral textured image segmentation using a multi-
5] resolution fuzzy Markov random field model on variable scales in the wavelet
domain," *International Journal of Remote Sensing*, vol. 34, no. 13, pp. 4550-4569,
2013.
- [17 S. Pal and P. Mitra, "Multispectral Image Segmentation Using the Rough-Set-
6] Initialized EM Algorithm," *IEEE Transactions on Geoscience and Remote Sensing*,
vol. 40, no. 11, pp. 2495-2501, 2002.
- [17 P. Paclík, R. Duin, G. van Kempen and R. Kohlus, "Segmentation of multi-spectral
7] images using the combined classifier approach," *Image and Vision Computing*, vol.
21, no. 6, pp. 473-482, 2003.
- [17 Y. Byun, Y. Han and T. Chae, "A Multispectral Image Segmentation Approach for
8] Object-based Image Classification of High Resolution Satellite Imagery," *KSCE
Journal of Civil Engineering*, vol. 17, no. 2, pp. 486-497, 2013.
- [17 E. Freire Santana, L. Vidal Batista, R. Marques Da Silva and C. A. Guimarães
9] Santos, "Multispectral image unsupervised segmentation using watershed
transformation and crossentropy minimization in different land use," *GIScience &
Remote Sensing*, vol. 51, no. 6, pp. 613-629, 2014.
- [18 G.-C. Lin, W.-J. Wang, C.-C. Kang and C.-M. Wang, "Multispectral MR Images
0] Segmentation Based on Fuzzy Knowledge and Modified Seeded Region Growing,"
Magnetic Resonance Imaging, vol. 30, no. 2, pp. 230 - 246, 2012.
- [18 C. Mott, T. Anderson, S. Zimmermann, T. Schneider and U. and Ammer,
1] "'Selective" region growing – an approach based on object-oriented classification
routines," in *Geoscience and Remote Sensing Symposium, 2002. IGARSS '02. 2002
IEEE International*, Toronto, 2002.
- [18 Y. Zhang, X. Feng and X. Le, "Segmentation on Multispectral Remote Sensing
2] Image Using Watershed Transformation," in *Congress on Image and Signal
Processing.*, Sanya, 2008.
- [18 R. Adams and L. Bischof, "Seeded region growing," *IEEE Transactions on Pattern
3] Analysis and Machine Intelligence*, vol. 16, no. 6, pp. 641 - 647, 1994.
- [18 H. Soltanian-Zadeh, J. Windham and A. Yagle, "A Multidimensional Nonlinear
4] Edge-Preserving Filter for Magnetic Resonance Image Restoration," *IEEE
Transactions on Image Processing*, vol. 4, no. 2, pp. 147-161, 1995.
- [18 R.-S. Kwan, A. Evans and G. Pike, "MRI Simulation-Based Evaluation of Image-
5] Processing and Classification Methods," *IEEE Transactions on Medical Imaging*,
vol. 18, no. 11, pp. 1085-1097, 1999.
- [18 I. Aarya, D. Jiang and T. A. I. Gale, "Edge localisation in MRI for images with
6] signal-dependent noise," *Electronics Letters*, vol. 51, no. 15, pp. 1151-1153, 2015.

- [18 V. Dharmale and P. A. Tijare, "Segmentation and Canny Edge Method in MRI
7] Brain Cyst Detection," *International Journal of Advanced Computer Research*, vol. 3, no. 4, pp. 289-293, 2013.
- [18 C. R. Tench, P. S. Morgan and C. S. Constantinescu, "Measurement of Cervical
8] Spinal Cord Cross-Sectional Area by MRI Using Edge Detection and Partial Volume Correction," *Journal of Magnetic Resonance Imaging*, vol. 21, no. 3, pp. 197-203, 2005.
- [18 J.-M. Bonny, O. Boespflug-Tanguy, M. Zanca and J.-P. Renou, "Multi-exponential
9] analysis of magnitude MR images using a quantitative multispectral edge-preserving filter," *Journal of Magnetic Resonance*, vol. 161, no. 1, pp. 25-34, 2003.
- [19 J. Chen, J. Li, J. Delu Pan, J. Qiankun Zhu and J. Zhihua Mao, "Edge-Guided
0] Multiscale Segmentation of Satellite Multispectral Imagery," *IEEE Transactions on Geoscience and Remote Sensing*, vol. 50, no. 11, pp. 4513-4520, 2012.
- [19 T. Zhang, X. Yang, S. Hu and F. S. Su, "Extraction of Coastline in Aquaculture
1] Coast from Multispectral Remote Sensing Images: Object-Based Region Growing Integrating Edge Detection," *Remote Sensing*, vol. 5, no. 9, pp. 4470-4487, 2013.
- [19 P. Toivanen, J. Ansamäki, J. Parkkinen and J. Mielikäinen, "Edge detection in
2] multispectral images using the self-organizing map," *Pattern Recognition Letters*, vol. 24, no. 16, pp. 2987-2994, 2003.
- [19 M. Naraghi, M. Koochi and A. Shakery, "Edge detection in multispectral images
3] based on structural elements," *The International Journal of Multimedia & Its Applications*, vol. 3, no. 1, pp. 90-99, 2011.
- [19 S. D. Zenzo, "A Note on the Gradient of a Multi-Image," *Computer Vision,
4] Graphics, and Image Processing*, vol. 33, pp. 116-125, 1986.
- [19 A. Cumani, "Edge Detection in Multispectral Images," *CVGIP: Graphical Models
5] and Image Processing*, vol. 53, no. 1, pp. 40-51, 1991.
- [19 H.-C. Lee and D. Cok, "Detecting boundaries in a vector field," *IEEE Transactions
6] on Signal Processing*, vol. 39, no. 5, pp. 1181-1194, 1991.
- [19 C. V. Dinh, R. Leitner, P. Paclik, M. Loog and R. Duin, "SEDMI: Saliency based
7] edge detection in multispectral images," *Image and Vision Computing*, vol. 29, no. 8, pp. 546-556, 2011.
- [19 J. Lira and A. Rodríguez, "Edge enhancement in multispectral satellite images by
8] means of vector operators," *Geofísica Internacional*, vol. 53, no. 3, pp. 289-308, 2014.
- [19 C. Xu, L. H. W. Cao and J. Feng, "Multispectral image edge detection via Clifford
9] gradient," *Science China Information Sciences*, vol. 55, no. 2, pp. 260-269, 2012.
- [20 G. Sun and Z. Wang, "A Gravitational Edge Detection for Multispectral Images,"
0] *TELKOMNIKA Indonesian Journal of Electrical Engineering*, vol. 11, no. 7, pp. 3641-3647, 2013.

- [20 W. H. Farrand, J. F. Bell, J. R. Johnson, M. S. Rice and J. A. Hurowitz, "VNIR
1] multispectral observations of rocks at Cape York, Endeavour crater, Mars by the
Opportunity rover's Pancam," *Icarus*, vol. 225, no. 1, pp. 709-725, 2013.
- [20 H. Ranjbar, F. Masoumi and E. M. Carranza, "Evaluation of geophysics and
2] spaceborne multispectral data for alteration mapping in the Sar Cheshmeh mining
area, Iran," *International Journal of Remote Sensing*, vol. 32, no. 12, pp. 3309-
3327, 2011.
- [20 W. Gao and A. Bertozzi, "Level Set Based Multispectral Segmentation with
3] Corners," *SIAM Journal on Imaging Sciences*, vol. 4, no. 2, pp. 597-617, 2011.
- [20 H. Tang, T. van Walsum, R. S. van Onkelen, R. Hameeteman, S. Klein, M. Schaap,
4] F. L. Tori, Q. J. van Den Bouwhuijsen, J. C. Witteman, A. van Der Lugt, L. J. van
Vliet and W. J. Niessen, "Semiautomatic carotid lumen segmentation for
quantification of lumen geometry in multispectral MRI," *Medical Image Analysis*,
vol. 16, no. 6, pp. 1202-1215, 2012.
- [20 Y. Chen and Z. Cao, "Change detection of multispectral remote-sensing images
5] using stationary wavelet transforms and integrated active contours," *International
Journal of Remote Sensing*, vol. 34, no. 24, pp. 8817-8837, 2013.
- [20 F. Bunyak, K. Palaniappan, S. K. Nath and G. Seetharaman, "Flux Tensor
6] Constrained Geodesic Active Contours with Sensor Fusion for Persistent Object
Tracking," *Journal of Multimedia*, vol. 2, no. 4, pp. 20-33, 2007.
- [20 A. Maalouf, P. Carré, B. Augereau and C. Fernandez-Maloigne, "Cooperation of
7] the partial differential equation methods and the wavelet transform for the
segmentation of multivalued images," *Signal Processing: Image Communication*,
vol. 23, no. 1, pp. 14-30, 2008.
- [20 R. Ksantini, B. Boufama and S. Memar, "A new efficient active contour model
8] without local initializations for salient object detection," *Eurasip Journal On Image
And Video Processing*, vol. 1, no. 40, pp. 1-13, 2013.
- [20 S. C. Zhu and A. Yuille, "Region competition: unifying snakes, region growing,
9] and Bayes/MDL for multiband image segmentation," *IEEE Transactions on Pattern
Analysis and Machine Intelligence*, vol. 18, no. 9, pp. 884-900, 1996.
- [21 T. Chan and L. Vese, "Active contours without edges," *IEEE Transactions on
0] Image Processing*, vol. 10, no. 2, pp. 266-277, 2001.
- [21 B. Lu, M. Cui, Q. Liu and Y. Wang, "Automated grain boundary detection using
1] the level set method," *Computers and Geosciences*, vol. 35, no. 2, pp. 267-275,
2009.
- [21 S. Osher and J. A. Sethian, "Fronts propagating with curvature-dependent speed:
2] algorithms based on Hamilton-Jacobi formulations.," *Journal of computational
physics*, vol. 79, no. 1, pp. 12-49, 1987.
- [21 M. Butenuth and C. Heipke, "Network snakes: graph-based object delineation with
3] active contour models," *Machine Vision and Applications*, vol. 23, no. 1, pp. 91-
109, 2012.

- [21 S. C. Zhu and A. Yuille, "Region competition: unifying snakes, region growing,
4] and Bayes/MDL for multiband image segmentation," *IEEE Transactions on Pattern Analysis and Machine Intelligence*, vol. 18, no. 9, pp. 884-900, 1996.
- [21 X. Huang, L. Zhang and P. Li, "Classification of Very High Spatial Resolution
5] Imagery Based on the Fusion of Edge and Multispectral Information," *Photogrammetric Engineering And Remote Sensing*, vol. 74, no. 12, pp. 1585-1596, 2008.
- [21 R. Moreno and M. Graña, "About Gradient Operators on Hyperspectral Images," in
6] *Proceedings of the 1st International Conference on Pattern Recognition Applications and Methods*, Vilamoura, Portugal, 2012.
- [21 S. Vantaram and E. Saber, "A method for improved localization of edges in
7] multi/hyperspectral imagery," *SPIE Optical Engineering+ Applications*, pp. 1-6, 2011.
- [21 M. Marin-Mcgee and M. Velez-Reyes, "A structure tensor for hyperspectral
8] images," in *Workshop on Hyperspectral Image and Signal Processing: Evolution in Remote Sensing*, Grenoble, France, 2011.
- [21 R. Resmini, "Hyperspectral/Spatial Detection of Edges (HySPADE): An algorithm
9] for spatial and spectral analysis of hyperspectral information," in *Proceedings of the SPIE, Algorithms and Technologies for Multispectral, Hyperspectral, and Ultraspectral Imagery*, Orlando, Florida USA, 2004.
- [22 B. S. Paskaleva, S. E. Godoy, S. C. Woo-Yong Jang, S. Bender, M. M. Krishna and
0] M. M. Hayat, "Model-Based Edge Detector for Spectral Imagery Using Sparse Spatospectral Masks," *IEEE Transactions on Image Processing*, vol. 23, no. 5, pp. 2315-2327, 2014.
- [22 H. van Der Werff, F. van Ruitenbeek, M. van Der Meijde, F. van Der Meer, S. de
1] Jong and S. Kalubandara, "Rotation-Variant Template Matching for Supervised Hyperspectral Boundary Detection," *IEEE Geoscience and Remote Sensing Letters*, vol. 4, no. 1, pp. 70-74, 2007.
- [22 Q. Li, Y. Wang, J. Zhang, G. Xu and Y. Xue, "Quantitative Analysis of Protective
2] Effect of Erythropoietin on Diabetic Retinal Cells Using Molecular Hyperspectral Imaging Technology," *IEEE Transactions on Biomedical Engineering*, vol. 57, no. 7, pp. 1699-1706, 2010.
- [22 F. van der Meer, F. van Ruitenbeek, H. van der Werff and C. Hecker, "apping PT
3] conditions in hydrothermal systems using hyperspectral remote sensing and object based techniques," in *2nd Workshop on Hyperspectral Image and Signal Processing: Evolution in Remote Sensing*, Reykjavik, Iceland, 2010.
- [22 F. J. van Ruitenbeek, T. J. Cudahy, F. D. van Der Meer and M. Hale,
4] "Characterization of the hydrothermal systems associated with Archean VMS-mineralization at Panorama, Western Australia, using hyperspectral, geochemical and geothermometric data," *van Ruitenbeek, Frank J.A. ; Cudahy, Thomas J. ; van Der Meer, Freek D. ; Hale, Martin*, vol. 45, pp. 33-46, 2012.

- [22 S. Salati, F. J. van Ruitenbeek, F. D. van der Meer, M. H. Tangestani and H. van
5] der Werff, "Lithological mapping and fuzzy set theory: Automated extraction of lithological boundary from ASTER imagery by template matching and spatial accuracy assessment," *International Journal of Applied Earth Observation and Geoinformation*, vol. 13, no. 5, pp. 753-765, 2011.
- [22 F. J. van Ruitenbeek, H. M. van Der Werff, K. A. Hein and F. D. van Der Meer,
6] "Detection of pre-defined boundaries between hydrothermal alteration zones using rotation-variant template matching," *Computers and Geosciences*, vol. 34, no. 12, pp. 1815-1826, 2008.
- [22 F. van Der Meer, H. van Der Werff and F. van Ruitenbeek, "Potential of ESA's
7] Sentinel-2 for geological applications," *Remote Sensing of Environment*, vol. 148, pp. 124-133, 2014.
- [22 A. S. Kumar, V. M. Keerthi, v. d. W. H. A. S. and F. van der Meer, "Hyperspectral
8] image classification by a variable interval spectral average and spectral curve matching combined algorithm," *International Journal of Applied Earth Observation and Geoinformation*, vol. 12, no. 4, pp. 261-269, 2010.
- [22 H. van der Werff and F. van der Meer, "Sentinel-2 for Mapping Iron Absorption
9] Feature Parameters," *Remote Sensing*, vol. 7, no. 10, pp. 12635-12653, 2015.
- [23 K. Kotwal and S. Chaudhuri, "Visualization of Hyperspectral Images Using
0] Bilateral Filtering," *IEEE Transactions on Geoscience and Remote Sensing*, vol. 48, no. 5, pp. 2308-2316, 2010.
- [23 J. A. Xudong Kang, J. A. Shutao Li and J. A. Benediktsson, "Spectral–Spatial
1] Hyperspectral Image Classification With Edge-Preserving Filtering," *IEEE Transactions on Geoscience and Remote Sensing*, vol. 52, no. 5, pp. 2666-2677, 2014.
- [23 J. Xia, L. Bombrun, T. Adali, Y. Berthoumieu and C. Germain, "Spectral–Spatial
2] Classification of Hyperspectral Images Using ICA and Edge-Preserving Filter via an Ensemble Strategy," *IEEE Transactions on Geoscience and Remote Sensing*, vol. 54, no. 8, pp. 4971-4982, 2016.
- [23 P. Perona and J. Malik, "Scale-space and edge detection using anisotropic
3] diffusion," *IEEE Transactions on Pattern Analysis and Machine Intelligence*, vol. 12, no. 7, pp. 629-639, 1990.
- [23 Y. Wang, R. Niu and X. Yu, " Anisotropic Diffusion for Hyperspectral Imagery
4] Enhancement," *IEEE Sensors Journal*, vol. 10, no. 3, pp. 469-477, 2010.
- [23 Y. Wang, R. Niu, L. Zhang and H. Shen, " Region-based adaptive anisotropic
5] diffusion for image enhancement and denoising," *Optical Engineering*, vol. 49, no. 11, pp. 1-19, 2010.
- [23 Y. Wang, K. Wu, Y. Yang and T. Chen, "Gradient and Laplacian-Based
6] Hyperspectral Anisotropic Diffusion," *IEEE Journal of Selected Topics in Applied Earth Observations and Remote Sensing*, vol. 8, no. 6, pp. 3235-3249, 2015.

- [23 L. Wang, Z. Li and J. Sun, "Anomaly Detection in Hyperspectral Imagery based on
7] Spectral Gradient and LLE," *Applied Mechanics and Materials*, vol. 121, no. 126,
pp. 720-724 , 2011.
- [23 D. Connah, M. Drew and G. Finlayson, "Spectral edge image fusion: Theory and
8] applications," in *European Conference on Computer Vision*, Zurich, Switzerland,
2014.
- [23 D. Connah, M. S. Drew and G. D. Finlayson, "Spectral edge: gradient-preserving
9] spectral mapping for image fusion," *Journal of the Optical Society of America A: Optics, Image Science, and Vision*, vol. 32, no. 12, pp. 2384 - 2396, 2015.
- [24 X. Geng, K. Sun, L. Ji and Y. Zhao, "A Fast Volume-Gradient-Based Band
0] Selection Method for Hyperspectral Image," *IEEE Transactions on Geoscience and Remote Sensing*, vol. 52, no. 11, pp. 7111-7119, 2014.
- [24 C. Chen, J. Jiang, B. Zhang, W. Yang and J. Guo, "Hyperspectral Image
1] Classification Using Gradient Local Auto-Correlations," in *2015 3rd IAPR Asian Conference on Pattern Recognition*, Kuala Lumpur, Malaysia, 2015.
- [24 A. Erturk, M. K. Gullu and S. Erturk, "Hyperspectral Image Classification Using
2] Empirical Mode Decomposition With Spectral Gradient Enhancement," *IEEE Transactions on Geoscience and Remote Sensing*, vol. 51, no. 5, pp. 2787-2798, 2013.
- [24 X. Hadoux, S. Jay, G. Rabatel and N. Gorretta, "A Spectral–Spatial Approach for
3] Hyperspectral Image Classification Using Spatial Regularization on Supervised Score Image," *IEEE Journal of Selected Topics in Applied Earth Observations and Remote Sensing*, vol. 8, no. 6, pp. 2361-2369, 2015.
- [24 G. Noyel, J. Angulo and D. Jeulin, "Morphological Segmentation of Hyperspectral
4] Images," *Image Analysis and Stereology*, vol. 26, no. 3, pp. 101-109, 2011.
- [24 S. R. Vantaram, E. Saber and D. Messinger, "An intensity-gradient-texture guided
5] methodology for spatial segmentation of remotely sensed multi/hyperspectral imagery," in *18th IEEE International Conference on Image Processing*, Brussels, Belgium, 2011.
- [24 J. Xiaoli Ma, J. Wang Cheng, J. Zhuo Sun, J. Chenglu Wen and J. Li,
6] "Hyperspectral image classification using Primal Laplacian SVM in preconditioned conjugate gradient solution," in *IEEE International Geoscience and Remote Sensing Symposium - IGARSS*, Beijing, China, 2013.
- [24 S. Vantaram, S. Piramanayagam, E. Saber and D. Messinger, "Spatial segmentation
7] of multi/hyperspectral imagery by fusion of spectral-gradient-textural attributes," *Journal Of Applied Remote Sensing*, vol. 9, no. 1, pp. 1-38, 2015.
- [24 M. Marin-Mcgee and M. Velez-Reyes, "Enhancement of hyperspectral imagery
8] using spectrally weighted tensor anisotropic nonlinear diffusion for classification," *SPIE Defense, Security, and Sensing. International Society for Optics and Photonics*, pp. 1-8, 2013.

- [24 R. Resmini, "Simultaneous spectral/spatial detection of edges for hyperspectral
9] imagery: the HySPADE algorithm revisited," *SPIE Defense, Security, and Sensing*, pp. 1-13, 2012.
- [25 C. Cox, "Hyperspectral/Spatial Detection of Edges (HySPADE) Analysis of
0] Mineral Assemblages and Linear Features at Cuprite, Nevada, U.S.A.," in *ASPRS/MAPPS 2009 Fall Conference*, San Antonio, Texas USA, 2009.
- [25 S. Godoy, "A PhD Dissertation: Communication-theoretic Approach for Skin
1] Cancer Detection using Dynamic Thermal Imaging," The University of New Mexico, Albuquerque, New Mexico USA, 2015.
- [25 Q. Li, "Hyperspectral Imaging Technology Used in Tongue Diagnosis," in *Recent
2] Advances in Theories and Practice of Chinese Medicine*, Rijeka, Croatia, InTech, 2012, pp. 112-136.
- [25 R. R. B. P. & B. A. Juang, "Level set segmentation of hyperspectral images using
3] joint spectral edge and signature information," in *IEEE 11th International Conference on Information Fusion*, Cologne, Germany, 2008.
- [25 J. Ball and L. Bruce, "Level Set Hyperspectral Image Classification Using Best
4] Band Analysis," *IEEE Transactions on Geoscience and Remote Sensing*, vol. 45, no. 10, pp. 3022-3027, 2007.
- [25 K. Karantzas and D. Argialas, "A Region-based Level Set Segmentation for
5] Automatic Detection of Man-made Objects from Aerial and Satellite Images," *Photogrammetric Engineering and Remote Sensing*, vol. 75, no. 6, pp. 667-677, 2009.
- [25 E. Pasolli, F. Melgani, N. Alajlan and N. Conci, "Optical Image Classification: A
6] Ground-Truth Design Framework," *IEEE Transactions on Geoscience and Remote Sensing*, vol. 51, no. 6, pp. 3580-3597, 2013.
- [25 A. Alarcon-Ramirez, M. R. Rwebangira, M. F. Chouikha and V. Manian, "A New
7] Methodology Based on Level Sets for Target Detection in Hyperspectral Images," *IEEE Transactions on Geoscience and Remote Sensing*, vol. 54, no. 9, pp. 5385-5396, 2016.
- [25 R. Resmini and D. Allen, "The microscene: a novel method for hyperspectral image
8] generation for algorithm development and testing," The MITRE Corporation, McLean, VA USA, 2014.
- [25 M. F. Baumgardner, L. L. Biehl and D. A. Landgrebe, "220 Band AVIRIS
9] Hyperspectral Image Data Set: June 12, 1992 Indian Pine Test Site 3," 2015. [Online]. Available: <https://purrr.purdue.edu/publications/1947/1>. [Accessed 13 11 2016].
- [26 J.-S. Qiu, D.-Z. Wang, B. McInnes, S.-Y. Jiang, R.-C. Wang and S. Kanisawa,
0] "Two subgroups of A-type granites in the coastal area of Zhejiang and Fujian Provinces, SE China: age and geochemical constraints on their petrogenesis," *Geological Society of America Special Papers*, vol. 95, pp. 227-236, 2004.

- [26] S. Pruitt, "Researchers Identify Fragment of Amelia Earhart's Plane," *The History Channel*, 29 10 2014. [Online]. Available: <http://www.history.com/news/researchers-identify-fragment-of-amelia-earharts-plane>. [Accessed 13 11 2016].
- [26] The International Group for Historic Aircraft Recovery, "The Earhart Project," 2016. [Online]. Available: <https://tighar.org/Projects/Earhart/AEdescr.html>. [Accessed 13 11 2016].
- [26] The International Group for Historic Aircraft Recovery, "New Discovery: Comparing Earhart to the Bones on Nikumaroro," 2016 22 10. [Online]. Available: https://tighar.org/Projects/Earhart/Archives/Research/Bulletins/78_EarhartArms/78_EarhartArms.html. [Accessed 2016 13 11].
- [26] T. I. G. f. H. A. Recovery, "The Window, the Patch, & the Artifact," 28 10 2014. [Online]. Available: https://tighar.org/Projects/Earhart/Archives/Research/Bulletins/73_StepbyStep/73_Step_by_Step.html. [Accessed 13 11 2016].
- [26] Surface Optics Corporation, "Hyperspectral Imaging Possible Amelia Earhart Wreckage," 14 08 2014. [Online]. Available: <https://surfaceoptics.com/hyperspectral-imaging-amelia-earhart-wreckage/>. [Accessed 13 11 2016].
- [26] C. Gias, "Gradient image of multi-spectral image," 21 8 2011. [Online]. Available: <https://www.mathworks.com/matlabcentral/fileexchange/32623-gradient-image-of-multi-spectral-image?focused=5197187&tab=function>. [Accessed 14 10 2015].
- [26] C. Li, "Level Set for Image Segmentation," 3 6 2013. [Online]. Available: <https://www.mathworks.com/matlabcentral/fileexchange/12711-level-set-for-image-segmentation>. [Accessed 21 10 2015].
- [26] N. Otsu, "A Threshold Selection Method from Gray-Level Histograms," *IEEE Transactions on Systems, Man and Cybernetics*, Vols. SMC-9, no. 1, pp. 62-66, 1979.
- [26] Mathworks, "Image segmentation using Otsu thresholding," 10 3 2010. [Online]. Available: <https://www.mathworks.com/matlabcentral/fileexchange/26532-image-segmentation-using-otsu-thresholding>. [Accessed 3 4 2017].
- [27] Mathworks, "MathWorks - Makers of MATLAB and Simulink," 15 3 2017. [Online]. Available: <https://www.mathworks.com/>. [Accessed 3 4 2017].
- [27] Microsoft Corporation, "Visual C++ | Visual Studio," 20 2 2017. [Online]. Available: <https://www.visualstudio.com> > Visual Studio IDE. [Accessed 3 4 2017].
- [27] Harris Geospatial Solutions, "ENVI," 31 3 2017. [Online]. Available: www.harrisgeospatial.com/. [Accessed 3 4 2017].
- [27] J. Sweet, J. Granahan and M. Sharp, "An objective standard for hyperspectral image quality," in *Proceedings of AVIRIS Workshop*, Honolulu, Hawaii USA, 2000.
- [27] Yale University, "Confidence Intervals," [Online]. Available: <http://www.stat.yale.edu/Courses/1997-98/101/confint.htm>. [Accessed 10 4 2017].

- [27] D. Rumsey, "Choosing a Confidence Level for a Population Sample," [Online].
5] Available: <http://www.dummies.com/education/math/statistics/choosing-a-confidence-level-for-a-population-sample/>. [Accessed 10 4 2017].
- [27] Math Boot Camps, "Interpreting Confidence Intervals," 2016. [Online]. Available:
6] <http://www.mathbootcamps.com/interpreting-confidence-intervals/>. [Accessed 10 4 2017].
- [27] Penn State University Eberly College of Science, "An Interval's Length," [Online].
7] Available: <https://onlinecourses.science.psu.edu/stat414/node/198>. [Accessed 10 4 2017].
- [27] United States Geological Survey, "Materials Maps," 9 June 2000. [Online].
8] Available: <https://speclab.cr.usgs.gov/maps.html>. [Accessed 23 12 2016].
- [27] C. Schmid, R. Mohr and C. Bauckhage, "Evaluation of Interest Point Detectors,"
9] *International Journal of Computer Vision*, vol. 37, no. 2, pp. 151-172, 2000.
- [28] S. Baker and S. Nayar, "Global measures of coherence for edge detector
0] evaluation," in *IEEE Computer Society Conference on Computer Vision and Pattern Recognition*, Ft. Collins, Colorado, 1999.
- [28] A. Singh, "Review article digital change detection techniques using remotely-
1] sensed data," *International journal of remote sensing*, vol. 10, no. 6, pp. 989-1003, 1989.
- [28] Roper Scientific Germany, "Spectroscopic Etaloning in Back Illuminated CCDs,"
2] [Online]. Available: <http://www.roperscientific.de/etaloning.html>. [Accessed 6 4 2017].
- [28] S. Veraverbeke, E. N. Stavros and S. J. Hook, "Assessing fire severity using
3] imaging spectroscopy data from the Airborne Visible/Infrared Imaging Spectrometer (AVIRIS) and comparison with multispectral capabilities," *Remote Sensing of Environment*, vol. 154, pp. 153-163, 2014.
- [28] R. Fisher, S. Perkins, A. Walker and E. Wolfart, "Canny Edge Detector," 2003.
4] [Online]. Available: <http://homepages.inf.ed.ac.uk/rbf/HIPR2/canny.htm>. [Accessed 18 9 2016].
- [28] Y. Wu, X. Zhao, Y. Jin and X. Zhang, "Extracting Golden Area from Image Based
5] on Canny Operator," *Applied Mechanics and Materials*, vol. 731, pp. 201-204, 2015.
- [28] J. Chen, C. Richard, H. Lantéri, C. Theys and P. Honeine, "A gradient based
6] method for fully constrained least-squares unmixing of hyperspectral images," in *2011 IEEE Statistical Signal Processing Workshop*, Nice, France, 2011.
- [28] A. Zandifar, M. Babaie-Zadeh and C. Jutten, "A projected gradient-based algorithm
7] to unmixing," in *20th European Signal Processing Conference*, Bucarest, Romania, 2012.

BIOGRAPHY

Cary M. Cox graduated from Odessa High School, Odessa, Texas, in 1997. He received his Bachelor of Arts in Geography from The University of Texas at Austin in 2001. He also received a Master of Science in Applied Geography from the University of North Texas in 2003, and a Master of Science in Strategic Intelligence from American Military University in 2004. He has been employed in the defense and aerospace industry for 13 years.